europhysics conference abstracts

23rd European Physical Society Conference on

Controlled Fusion and Plasma Physics

Kiev, 24-28 June,1996

Editors: D.Gresillon, A.Sitenko and A.Zagorodny

Contributed Papers, Part I

Published by: The European Physical Society

Series Editor: Prof. R.Pick, Paris

Managing Editor: G.Thomas, Geneva

Volume 20C

Part I

23rd European Physical Society Conference on

Controlled Fusion and Plasma Physics

Bogolyubov Institute for Theoretical Physics, Kiev, Ukraine

24-28 June 1996

Editors: D Gresillon, A.Sitenko and A.Zagorodny

europhysics
conference
abstracts

23rd European Physical Society Conference on

Controlled Fusion and Plasma Physics

Kiev, 24-28 June 1996

Editors: D Gresillon, A.Sitenko and A.Zagorodny

Contributed Papers, Part I

Published by: The European Physical Society
Series Editor: Prof. R Pick, Paris
Managing Editor: G.Thomas, Geneva

Volume 20C
Part I

EUROPHYSICS CONFERENCE ABSTRACTS is published by the European Physical Society © 1996

PREFACE

The 23rd EPS Conference on Controlled Fusion and Plasma Physics was organized on behalf of the European Physical Society by the National Academy of Sciences of Ukraine, State Committee on Science, Technologies, and Industrial Policy of Ukraine, and the Bogolyubov Institute for Theoretical Physics (BITP) in Kiev, Ukraine.

The 1996 Conference included the topics: A - Tokamaks, B - Stellarators, C - Alternative Magnetic Confinement, D - Plasma Edge Physics, E - Plasma Heating and Current Drive, F - Diagnostics, G - Basic Collisionless Plasma Physics, H - High Intensity Laser Produced Plasmas and Inertial Confinement, I - Astrophysical and Geophysical Plasmas, J - Low-Temperature Plasmas.

The Conference Proceedings are published in three parts, including:

Part I - Topic A; Part II - Topics B,C,D,E;
Part III - Topics F.G,H,I,J, and postdeadline papers.

The four-page papers are arranged within topical groups in the ascending order of file numbers. An exception is made for 24 contributions which were selected for oral presentation at the Conference. Such papers are presented at the beginning of each topical group.

According to EPS Plasma Physics Division regulations, the Conference Proceedings contain the four-page papers of all those contributions for which at least one author was a registered participant at the Conference. There are 371 papers which satisfy this condition. The three parts of the proceedings will be mailed to all registered participants of the Conference.

The papers of five Review Lectures and 21 Topical Lectures will be published in a special issue of the journal "Plasma Physics and Controlled Fusion", which will also be mailed to all registered participants.

D.Gresillon, A.Sitenko, A.Zagorodny

July 1996

Program Committee

D.Gresillon	(Ecole Polytechnique, CNRS, Palaiseau France - *Chairman*)
G.Fussmann	(MPI fur Plasmaphysik, Bereich Berlin, Germany)
X.Garbet	(CEA, Cadarache, France)
C.Hidalgo	(CIEMAT Fusion, Madrid, Spain)
L.Kovrizhnykh	(General Physics Institute, Moscow, Russia)
S.Prager	(University of Wisconsin, Madison USA)
A.Sitenko	(BITP, Kiev, Ukraine)
F.Sluijter	(Eindhoven University, The Netherlands - *Chairman of the EPS PlasmaPhysics Division*)
M.Tendler	(Royal Institute. of Technology, Stockholm, Sweden)
P.Thomas	(JET Joint Undertaking, Abingdon, UK)
H.Weisen	(CRPP-EPFL, Lausanne, Switzerland)
J.Winter	(KFA, Juelich, Germany)

Local Organizing Committee

A.Sitenko	*Chairman*
A.Zagorodny	*Vice-Chairman*
O.Pavlichenko	*Vice-Chairman*
I.Goutych	*Scientific Secretary*
G.Bugrij	
Yu.Chutov	
S.Fomina	
O.Kocherga	
Ya.Kolesnichenko	
V.Krol'	
A.Polozov	
P.Schram	
P.Sosenko	
K.Stepanov	
I.Yakimenko	

CONTENTS

PART I

PART II

PART III

A

TOKAMAKS

Electron Temperature Fluctuations in Drift-Resistive Ballooning Turbulence

A. Zeiler, J. F. Drake and D. Biskamp
Max-Planck-Institut für Plasmaphysik, EURATOM Association,
85748 Garching, Germany

1. Introduction

Turbulence and anomalous transport in the cool plasma edge of toroidal confinement devices are usually investigated using models based on two-fluid equations in the drift approximation. Previous three-dimensional simulations [1,2] were based on an electrostatic drift-wave model containing density and potential fluctuations as well as magnetic shear and curvature, but assuming a constant electron temperature T_e and cold ions ($T_i = 0$). The main result was, that the system is characterized by two different regimes: one driven by the resistive ballooning mode; and the other by a nonlinear instability [3].

In this paper we extend the equations by adding electron temperature fluctuations. Since T_e-fluctuations strongly destabilize the two-dimensional sheared slab [4], they may alter the properties of the three-dimensional turbulence significantly. A similar set of equations was previously treated by Scott, but without attempting to estimate the scaling of the system [5].

2. Equations

The equations are derived from the two-fluid Braginskii-equations by assuming $T_i = 0$, using the usual drift-approximations for the motion perpendicular to $\vec{B}$, and neglecting the electron inertia as well as electromagnetic corrections. As in refs. [1,2] we define the characteristic time scale $t_0 = (RL_p/2)^{1/2}/c_s$ and the perpendicular scale length $L_0 = 2\pi q_a(\nu_{ei}R\rho_s/2\Omega_e)^{1/2}(2R/L_p)^{1/4}$ based on the resistive ballooning modes, and choose the connection length $2\pi q_a R$ as parallel scale length. Normalizing the fluctuating quantities to $\tilde{\phi} \sim BL_0^2/ct_0$, $\tilde{n} \sim n_0 L_0/L_p$, $\tilde{T_e} \sim T_{e,0}L_0/L_p$, and $v_\parallel \sim c_s L_0/L_p$, we obtain the dimensionless equations for the normalized fluctuating quantities ϕ, n, T_e, $v_\parallel$ in field aligned flux-tube coordinates (see ref. [2] for details)

$$\frac{d}{dt}\nabla_\perp^2\phi + \hat{C}p + \frac{\partial^2 h}{\partial z^2} = D_\phi \nabla_\perp^4 \phi, \tag{1}$$

$$\frac{dn}{dt} + \frac{1}{1+\eta_e}\frac{\partial \phi}{\partial y} - \epsilon_p \hat{C}(\phi - \alpha p) + \epsilon_p \alpha \frac{\partial^2 h}{\partial z^2} + \gamma \frac{\partial v_\parallel}{\partial z} = D_n \nabla_\perp^2 n, \tag{2}$$

$$\frac{dT_e}{dt} + \frac{\eta_e}{1+\eta_e}\frac{\partial \phi}{\partial y} - \frac{2}{3}\left\{\epsilon_p \hat{C}(\phi - \alpha p) - 1.71\epsilon_p \alpha \frac{\partial^2 h}{\partial z^2} - \gamma \frac{\partial v_\parallel}{\partial z} + \kappa_\parallel \frac{\partial^2 T_e}{\partial z^2}\right\} = D_T \nabla_\perp^2 T_e, \tag{3}$$

	$\eta_e = 0.5$	$\eta_e = 1.0$	$\eta_e = 2.0$	without T_e
$D/D_{0,L_n}$, outside	0.077 ± 0.016	0.076 ± 0.016	0.078 ± 0.018	0.070 ± 0.015
$D/D_{0,L_n}$, inside	0.023 ± 0.007	0.020 ± 0.008	0.021 ± 0.009	0.035 ± 0.010
$\chi_e/D_{0,L_n}$, outside	0.11 ± 0.03	0.13 ± 0.02	0.16 ± 0.03	—
$\chi_e/D_{0,L_n}$, inside	0.06 ± 0.01	0.06 ± 0.02	0.07 ± 0.01	—

Table 1: Ballooning dominated regime: Transport at outside/inside midplane at $\alpha = 0.5$ and different values of η_e.

$$\frac{dv_\parallel}{dt} + \gamma \frac{\partial p}{\partial z} = 0, \tag{4}$$

with $h = \phi - \alpha(n + 1.71T_e)$, $p = n + T_e$, $d/dt = \partial/\partial t - \nabla_\perp \phi \times \vec{z} \cdot \nabla_\perp$, the curvature operator $\hat{C} = [\cos(2\pi z) + 2\pi \hat{s}(z - z_0)\sin(2\pi z) - (a/R)]\partial/\partial y + \sin(2\pi z)\partial/\partial x$, $\nabla_\perp^2 = [\partial/\partial x + 2\pi\hat{s}(z - z_0)\partial/\partial y]^2 + \partial^2/\partial y^2$, the parameters

$$\alpha = \frac{\rho_s c_s t_0}{L_p L_0}, \ \gamma = \frac{c_s t_0}{L_z}, \ \epsilon_p = \frac{2L_p}{R}, \ \eta_e = \frac{L_n}{L_{T_e}}, \ \kappa_\parallel = \frac{\kappa}{n_0}\frac{t_0}{L_z^2}, \ \hat{s} = \frac{a}{q_a}\frac{\partial q_a}{\partial r}, \tag{5}$$

and the viscosities D_ϕ, D_n and D_T. The anomalous particle diffusion coefficient and the heat conductivity are related to the dimensionless fluxes by

$$D = -(1 + \eta_e) D_0 \langle n \frac{\partial \phi}{\partial y} \rangle, \ \chi_e = -(1 + \eta_e^{-1}) \frac{3}{2} D_0 \langle T_e \frac{\partial \phi}{\partial y} \rangle, \ D_0 = \frac{L_0^2}{t_0}. \tag{6}$$

3. Simulations Results

In the ballooning dominated regime (characterized by $\alpha < 1$) we performed several runs at $\alpha = 0.5$, $\epsilon_p = 0.02$, $\hat{s} = 1$, $a/R = 0.25$, $\gamma = 0.02$, $\kappa_\parallel = 0.05$, and various values for η_e. The resolution is 48×48 complex modes in the perpendicular plane and 96 collocation points along the magnetic field. The box dimensions are $L_x = 5.72$, $L_y = 6$, $L_z = 3$ and the viscous damping parameters are $D_\phi = D_n = D_T = 2 \times 10^{-3}$. The resistive ballooning instability forms radial streams at the unfavourable curvature location $z = 0, \pm 1$ similar to the ones observed for $T_e = const$ [2], which break up nonlinearly and drive a transport strongly peaked at the outside of the torus. The turbulent structures of ϕ, n and T_e are very similar on large scales, whereas on small scales ϕ is smoother than n and T_e. In table 1 we summarize the transport results for different values of η_e. To investigate the influence of L_{T_e} more easily we extract the η_e-dependence of D_0 leading to $D_0 = D_{0,L_n}(1 + \eta_e)$ with D_{0,L_n} being independent of η_e and L_{T_e}. The particle flux is practically independent of η_e and on the outside of the torus remains at almost the same level as in the system without T_e-dynamics [2]. Note, however, that the inside/outside-asymmetry is enhanced with T_e included. The heat flux shows only a weak dependence on η_e: increasing η_e by a factor of four increases χ_e by only 50 %.

ϵ_p	η_e	$\hat{\rho}_s^2$	$D/\hat{D}_0$ outside	$D/\hat{D}_0$ inside	$\chi_e/\hat{D}_0$ outside	$\chi_e/\hat{D}_0$ inside
0.01	1.0	0.027	0.047 ± 0.006	0.030 ± 0.003	0.031 ± 0.002	0.023 ± 0.002
0.02	0.5	0.045	0.030 ± 0.003	0.016 ± 0.003	$.0065 \pm .0008$	$.0040 \pm .0008$
0.02	1.0	0.055	0.015 ± 0.003	0.008 ± 0.002	0.011 ± 0.002	0.008 ± 0.002
0.02	2.0	0.071	0.011 ± 0.002	$.0015 \pm .0003$	0.012 ± 0.002	$.0020 \pm .0003$
0.03	1.0	0.082	0.006 ± 0.002	0.002 ± 0.001	0.003 ± 0.001	$.0019 \pm .0009$

Table 2: Nonlinearly driven regime: Transport at outside/inside midplane at $\alpha = 1.5$ and different values of η_e and ϵ_p.

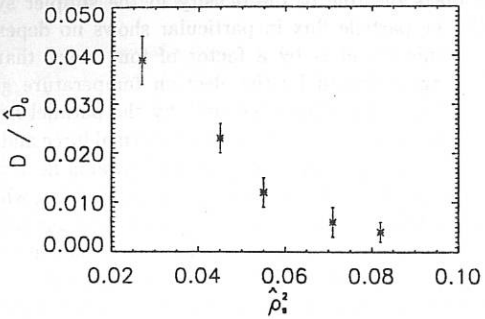

Figure 1: Transport $D/\hat{D}_0$ versus $\hat{\rho}_s^2$ (values of table 2)

For large α the ballooning growth-rate is weak [6], and the turbulence is mainly driven by the nonlinear instability discussed in refs. [2,3]. We discuss runs for $\alpha = 1.5$, $L_x = 7.63$, $L_y = 8$, various ϵ_p and η_e and all other parameters as in the runs for $\alpha = 0.5$. The radial streams observed in the ballooning regime are replaced by almost completely isotropic structures similar to the $T_e = const$ system [2]. The theory of the nonlinear instability predicts for the anomalous particle diffusion coefficient [2,3] a scaling according to

$$D = \hat{D}_0 \cdot f(\hat{\rho}_s^2, \eta_e),\ \hat{D}_0 = D_0 \frac{\alpha^{4/3}(1+\eta_e)^{2/3}}{\hat{s}^{2/3}},\ \hat{\rho}_s^2 = \epsilon_p \alpha^{4/3}(1+\eta_e)^{2/3}\hat{s}^{4/3}. \quad (7)$$

We therefore express the anomalous transport coefficients in terms of $\hat{D}_0$. The results of several runs are summarized in table 2. For small $\hat{\rho}_s^2$ the inside/outside transport asymmetry is 1.5 compared to 4.0 in the ballooning regime. For large $\hat{\rho}_s^2$ the nonlinear drive is suppressed and the residual ballooning instability again produces a large outside/inside asymmetry but at a low transport level. The transport level in table 2 is a factor of four lower than that obtained for constant T_e [2]. To check the

influence of the variation of η_e on the transport we plot the average transport as a function of $\hat{\rho}_s^2$ (Fig. 1). The diagram shows the strong reduction of the transport for increased $\hat{\rho}_s^2$ expected from the system with $T_e = const$ [2]. Since the values for $\eta_e = 2.0$ and $\eta_e = 0.5$ fit well into this relation and $\hat{D}_0$ does not depend on η_e, D seems to be independent of L_{T_e}; χ_e in contrast reacts sensitively to η_e, increasing with steepened temperature gradient.

In summary the particle flux is independent of η_e in both the resistive ballooning and nonlinear instability regimes, and the electron heat conductivity depends strongly on η_e only in the nonlinearly driven regime.

4. Physical Mechanism

Comparing equations (1-4) to the system with $T_e = const$ [1,2], we notice that the electron pressure takes the role of the density in the simpler system, but as pointed out previously the particle flux in particular shows no dependence on the electron temperature gradient and is by a factor of four lower than without T_e-dynamics instead of being increased by the electron temperature gradient. The analogy between the two systems is modified only by the parallel heat conduction and the thermal force. Various runs with and without thermal force and with different values of $\kappa_\parallel$ confirm this analogy, if thermal force and parallel heat conduction are discarded, and show in summary, that the qualitative change occurs, when the parallel heat conductivity $\kappa_\parallel$ is switched from zero to 0.05, which is of a realistic magnitude compared to experimental values. The thermal force and an increase of $\kappa_\parallel$ lead only to a quantitative modification by further reducing the transport level. The nonlinear drive mechanism reacts particularly sensitive to parallel diffusion regardless whether the diffusion is caused by the parallel Ohm's law (increment of $\hat{\rho}_s$) or by the parallel heat conduction. This also explains the observed difference between the transport level in the two regimes, which is strongly emphasized, if the T_e-dynamics and the parallel heat conduction are included.

In summary we observe, that the contribution of T_e-fluctuations to the two (in principle pressure driven) instabilities is strongly suppressed by parallel heat conduction. Hence the transport coefficients are weakly affected by a change of η_e.

References

[1] P. N. Guzdar, *et. al.* , Phys. Fluids B **5**, 3712 (1993)

[2] A. Zeiler, J. F. Drake, D. Biskamp, P. N. Guzdar,"Three-dimensional fluid simulations of tokamak edge turbulence", Phys. Plasmas, in press (1996)

[3] J. F. Drake, A. Zeiler, D. Biskamp, Phys. Rev. Lett. **75**, 4222 (1995)

[4] B. D. Scott, Phys. Rev. Lett. **65**, 3289 (1990)

[5] B. D. Scott, in *Proceedings of the 22nd EPS Conference on Controlled Fusion and Plasma Physics* (Bournemouth, 1995), Vol. 1, p. 229

[6] S. V. Novakovskii, *et. al.* , Phys. Plasmas **2**, 781 (1995)

Temperature Profile Perturbations measured by High Resolution ECE diagnostics

P.C. de Vries, G. Waidmann, A. Krämer-Flecken, A.J.H. Donné* and F.C. Schüller*

Trilateral Euregio Cluster

Institut für Plasmaphysik, Forschungszentrum Jülich, GmbH.
Association EURATOM-KFA, D-52425 Jülich, Germany

*FOM-Instituut voor Plasmafysica 'Rijnhuizen', Associatie EURATOM-FOM
P.O.Box 1207, 3430 BE Nieuwegein, The Netherlands

An experimental investigation into temperature profile perturbations due to MHD modes has been performed by means of high resolution electron cyclotron emission (ECE) diagnostics on TEXTOR. The position and width of large $m = 2$ magnetic islands have been determined. A secondary temperature maximum inside the island has been observed.

1. Introduction

The ideal MHD equilibrium of a tokamak plasma can be violated in the vicinity of rational q surfaces. Here, because of finite resistivity, the flux surfaces may tear and reconnect forming so-called tearing modes or magnetic islands. These MHD modes are frequently observed as precursors to major disruptions. Therefore intense studies are devoted to magnetic islands.

The magnetic perturbation can cause a change in the temperature distribution because the reconnected flux surfaces act as short circuits for the heat flow. The balance between parallel and perpendicular transport over the flux surfaces of the magnetic island is determined by the local collisionality [1]. Sustained temperature gradients over a magnetic island have been observed in other devices [2]. It is predicted, however, that an $m = 2$ island with a minimum width of 2.5cm in TEXTOR will flatten the temperature profile over the O-point in absence of internal sources [1]. In the presence of a toroidal plasma rotation the asymmetric temperature perturbations appear as MHD oscillations on diagnostic time traces. The radial variation of the MHD oscillation amplitude reflects the difference between the temperature profile over an X- and O-point.

Flat temperature regions have been observed near the $q = 2$ surface in the TEXTOR tokamak previously [3]. At TEXTOR ($R_o = 1.75$m, $a = 0.46$m, $I_p = 350$kA and $q_a \approx 3.8$) two new six-channel ECE diagnostics monitor the temperature perturbations in the vicinity of the $q = 1$ and $q = 2$ surface, respectively, with a good radial spacing of $1 - 2$cm. In this way the temperature profile flattening due to magnetic islands can be studied in more detail. For the cases treated in this paper the optical thickness in the vicinity of the $q = 2$ surfaces was above 3.

2. Temperature Profile Perturbations

Using the fact that the temperature profile will be flattened over the magnetic island, its width and position can be determined. As an example a specific ohmic discharge will be shown. It exhibits large MHD activity, i.e. coupled $m/n = 1/1$ and $2/1$ modes, which is observable from the time the current reaches its flat-top phase ($t = 300$ms). However the central temperature and density are still increasing. The rotating modes locks at $t = 570$ms and the discharge disrupts afterwards. Flattening of the temperature profile has been observed in the vicinity of the $q = 2$ surface. The flattening causes the MHD oscillations on opposite sides of the rational q surface to be in counter phase. The MHD

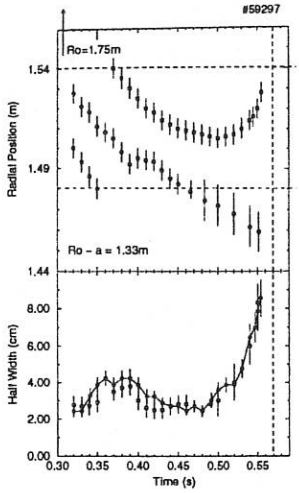

Figure 1: *(a) Temporal behaviour of the $q = 2$ surface (circles) and the islands separatrix (squares) versus the major radial position for an ohmic TEXTOR discharge. Both are deduced from the minimum and maximum MHD oscillation amplitude. After about $t = 450ms$ the position of the minimum and maximum deviated rapidly from each other which shows the island is growing. (b) The half island width deduced from figure 1(a). The vertical dashed line indicates the time of disruption. The measurements have been performed by tuning the toroidal magnetic field to , $B_t = 1.96T$, $R_o = 1.75m$, and shifting six ECE channels in the vicinity of the HFS $q = 2$ surface.*

oscillation amplitude will have a minimum at the rational surface. Outside the separatrix the tearing mode resembles an ideal helical kink perturbation. Its amplitude decreases with the distance from the magnetic island. Hence the largest MHD oscillation amplitude is expected at the islands separatrix. The radial location of the phase reversal and maximum amplitude, monitored within the range of the ECE diagnostic provides information on the location of the $q = 2$ surface and the island width as shown in figure 1. The radial resolution is $\sim$ 1cm.

Although the discharge is already in the current flat-top phase the $q = 2$ surface is still moving radially outwards. This can be explained by the increasing central temperature and density causing a peaking of the current profile. In other identical discharges, exhibiting MHD activity, the $m/n = 1/1$ mode appears about 150ms later as the $m/n = 2/1$ mode and couples immediately to the earlier mode. Before the appearance of the $m/n = 1/1$ the central q value is apparently larger than unity. Later on due to current peaking it decreases below unity. The time scale for the increase of radius of the q surfaces, $\tau_{r_{q=2}} = 125$ms, gives an indication for order of magnitude of the current diffusion time in TEXTOR. Shortly before the disruption the current flowing inside the $q = 2$ surface is about 72% of the total plasma current.

The width of the $m = 2$ magnetic island, in figure 1, is first nearly constant ($\sim \frac{1}{2}w = 3 - 4$cm) but after $t = 450$ms it starts to increase rapidly. Just before the disruption it reached its maximum value $\frac{1}{2}w = 7$cm. Only the half width of the island is given because, as we shall see later on, the shape of the island may be asymmetric. Because the small magnetic island was located deep in the plasma detection with magnetic probes was difficult the first 200ms.

3. The Temperature Distribution over a Magnetic Island

The temperature distribution over a magnetic island, with no internal sources, will be flattened; of course not only in radial but also in helical direction. Some ECE channels observing regions effected by the magnetic island show therefore a 'clipping' effect as

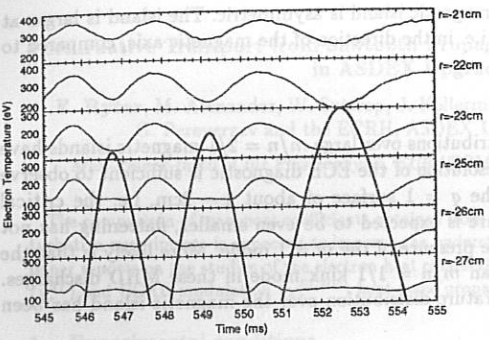

Figure 2: *Time traces of the six ECE channels monitoring the vicinity of the HFS $q = 2$ region. Only a part of the magnetic island lies within the range of the ECE channels. A clipping of the MHD oscillations is clearly visible on the outer three channels. Later on the clipping appears on the channel at $r = -23cm$ which shows the separatrix moves through the range of the ECE channels as indicated schematically.*

demonstrated in figure 2. The signals contain a flat part in toroidal rotation direction. In this figure a part of the growing magnetic island is visualized. A Fourier analysis identifies the clipping as an increase of higher harmonic in the frequency spectrum as explained in ref. [1].

A doubled frequency with respect to the main MHD frequency has been observed on ECE time traces monitoring near to the rational q surface. In this case the second harmonic component of oscillation may even be larger than the first harmonic. In figure 3 the doubling of the MHD frequency is shown. This doubled frequency is caused by the fact that the temperature distribution over the magnetic island shows a relative maximum at the O-point with respect to the separatrix. This is also shown in a contour plot of the temperature distribution in figure 4. Closed equi-temperature contours around the O-point are observed. The maximum temperature was found to be about $\sim 25 - 50$eV above that of the separatrix in ohmically heated discharges. However the topology of the magnetic island requires a lower current density inside the island than in the surrounding plasma. An explanation of this unexpected phenomenon of heat confinement may be sought in degraded transport properties inside the magnetic island.

Figure 3: *ECE channel monitoring outside the magnetic island (top) and another ECE channel which is for a part of time monitoring the inside of the magnetic island. The top trace shows a harmonic oscillation. The bottom trace shows a doubled frequency because the temperature increases from the separatrix to the centre of the magnetic island. Certain times the separatrix (S), X- and O-point pass the toroidal position of the ECE diagnostic have been indicated for one oscillation period.*

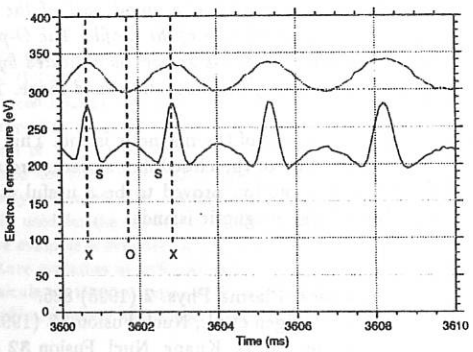

As shown in figure 4 the observed magnetic island is asymmetric. The island is larger at the inside of the rational q surface, i.e. in the direction of the magnetic axis, compared to the outer part.

4. Conclusions

In this paper only temperature distributions over large $m/n = 2/1$ magnetic islands have been shown. Although the radial resolution of the ECE diagnostic is sufficient to observe flat temperature regions around the $q = 1$ surface of about $1 - 2$cm, i.e. the critical width for flattening the temperature is expected to be even smaller, flattening has not been observed not withstanding the presence of the $m = 1$ mode. More likely is that the $m/n = 2/1$ mode has coupled to an $m/n = 1/1$ kink mode in these MHD discharges. A relative maximum in the temperature distribution over the magnetic island has been

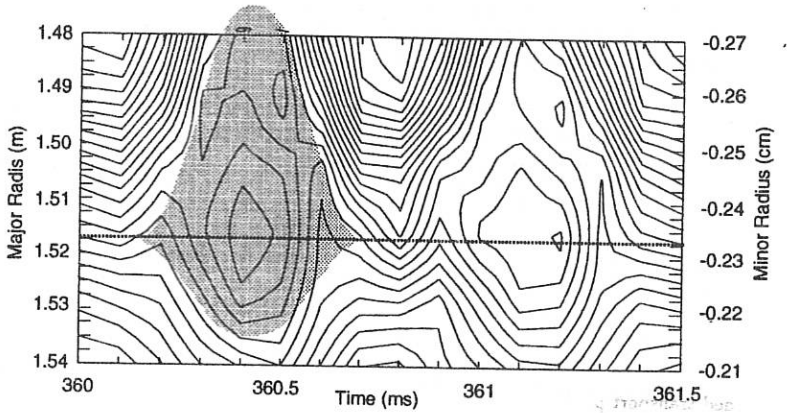

Figure 4: *A contour plot of a small part of the temperature profile. A small rotating island causes a perturbation of the profile. The O-point is hotter than the separatrix of the magnetic island. The $q = 2$ surface is indicated by the dashed line and the shaded region gives an impression of the magnetic island shape. The contour lines are separated by $5eV$.*

found near the centre of the magnetic island. This may be interpreted as an improvement of confinement due to the closed flux surfaces around the O-point. ECE radiometry with a good radial resolution proved to be a useful diagnostic to reveal information on the properties of large magnetic islands.

References

[1] R. Fitzpatrick, Plasma Phys. **2** (1995) 825.
[2] B.Ph. van Milligen et al., Nucl. Fusion **33** (1993) 8.
[3] G. Waidmann and G. Kuang, Nucl. Fusion **32** (1992) 645.

Perturbative Transport from Sawtooth Propagation and ECRH Modulation in ASDEX Upgrade

F. Ryter, M. Alexander, W. Suttrop, J. Köllermeyer, F. Leuterer, A.G. Peeters, G. Pereverzev and the ECRH, ASDEX Upgrade and NI Teams

Max-Planck-Institut für Plasmaphysik, EURATOM Association, D-85748 Garching

The comparison of transport coefficients obtained from power balance analyses and from perturbative experiments is expected to improve the understanding of transport physics [1]. This paper reports on the studies of the electron heat conductivity (χ_e) using sawtooth propagation (χ_e^{ST}) and ECRH modulation (χ_e^{ECRH}) heat pulse propagation in ASDEX Upgrade.

1. Experimental conditions

The key diagnostic in this work is the ECE radiometer which provides T_e measurements with the necessary high time resolution (31 kHz) and sensitivity (0.1 eV). This diagnostic has 45 channels generally covering 80% of the plasma minor radius (a $\approx$ 0.5 m) with a radial resolution below 1cm for each channel. The other experimental data necessary for the analyses are provided by the standard diagnostics usually available on a modern tokamak.
The recently installed first phase of the ECRH system for ASDEX Upgrade consists of one gyrotron at 140 GHz (central deposition at the second harmonic for $B_T = 2.5$ T) which delivers up to 400 kW for 0.5 s and can be modulated up to 30 kHz [2]. The modulation experiments were generally performed with 100% on/off power modulation with a duty-cycle of 50% at frequencies between 10 Hz and 1 kHz. The system allows on-axis and off-axis deposition depending on the magnetic field (B_T) and angle of injection, adjustable with a mirror.
The sawtooth and ECRH modulation studies were performed in Ohmic and NBI heated L-mode plasmas, in the standard single-null divertor configuration of ASDEX Upgrade. Plasma current, magnetic field and density as well as working gas (H^+ or D^+) were varied. All the discharges were sawtoothing which provides a wide set of data for the sawtooth analysis and a direct comparison between χ_e^{ECRH} and χ_e^{ST} in the shots where ECRH modulation was applied. We generally performed the ECRH modulation with off-axis deposition at r/a $\approx$ 0.5 because this configuration offers the best conditions for χ_e analyses in the confinement region.

2. Analysis methods

Two methods were applied to analyse the data: i) a time-dependent code (TDC); ii) a Fourier transform interpreted with a slab model (FT). In the TDC analysis the diffusion equation is solved in cylindrical geometry using a forced boundary method in which the T_e time trace of one ECE channel is taken as the corresponding inner boundary condition [3]. The damping terms (electron-ion exchange, modulation of P_{OH}, radiation) are explicitly calculated. The density perturbation is generally small and not taken into account because of the lack of precise measurement. This code was recently extended with a maximum entropy fit procedure to determine χ_e [4]. TDC was essentially used for the sawtooth analysis because of the large amplitude they provide. A representative example is depicted in Fig. 1 which shows a comparison between the experimental temperature evolution at different radii and the corresponding simulation. A good agreement of the calculated time evolution of T_e with the data for r/a $\leq$ 0.7 is generally obtained with flat χ_e profiles, however with larger value than χ_e^{PB} from power balance, as discussed in sect. 3.

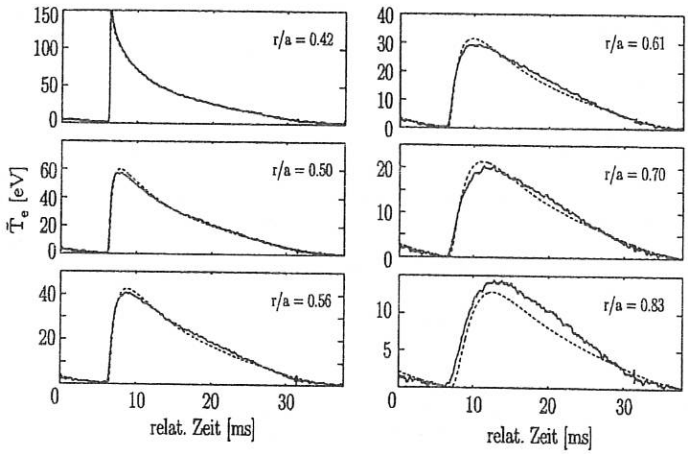

Figure 1: *Fit of a sawtooth with TDC, with $\chi_e^{sim} = 4.8$ m^2/s. The time evolution versus relative time is shown. The solid lines are the experimental time trace, the dashed lines the fit. To correctly reproduce the channels with r/a $\geq$ 0.7 an outward convection of the form $U = 80(r/a)^4$ m/s was necessary.*

An outward convection at the plasma edge is necessary to reproduce the only weakly decreasing amplitude and the flattening phase of the perturbation for r/a $\geq$ 0.7. This behaviour is not modified by taking as outer boundary condition $\tilde{T}_e(a) = 0$ or $\tilde{T}_e(a)$ provided by the corresponding T_e measurement.

The FT analysis is less time consuming than TDC and therefore better suited for an overview of large datasets. We have verified that the TDC and FT methods give the same χ_e results within the error bars which are around ± 1 m^2/s for both methods. The FT analysis is illustrated in Fig. 2 for an ECRH modulation dataset. It is well-known that in the slab model interpretation the amplitude and phase data for a given frequency yield χ_e^{amp} and χ_e^{phase} respectively [1]. The difference between these two values depends on the damping term, which is eliminated by taking the geometric mean, $\chi_e^{FT} = \sqrt{\chi_e^{amp}\chi_e^{phase}}$, which gives the actual χ_e^{FT} used here. It is clearly seen in Fig. 2, that the amplitude decay on the LFS and HFS of the deposition, outwards and inwards respectively, is not symmetrical. This is essentially due to the geometry effect, and it can be shown, following reference [5], that the mean value of the χ_e^{amp} values on both sides should be taken. This correction was done in this work. Note that the phase is not affected by geometry and is therefore symmetrical. It is expected that χ_e^{amp} and χ_e^{phase} reach the same value χ_e^{FT} at high frequency where the relative influence of the damping becomes weak. This behaviour is clearly observed in our experiments. For the modulation scheme used here with 50% duty-cycle, the Fourier frequency spectrum of the T_e measurement essentially shows the odd harmonics and no or very small even harmonics, as expected in the absence of non-linear reaction of the plasma to the power modulation. We also observed that, both for sawteeth and ECRH modulation, χ_e does not depend on the frequency, which excludes a T_e dependence of χ_e [6].

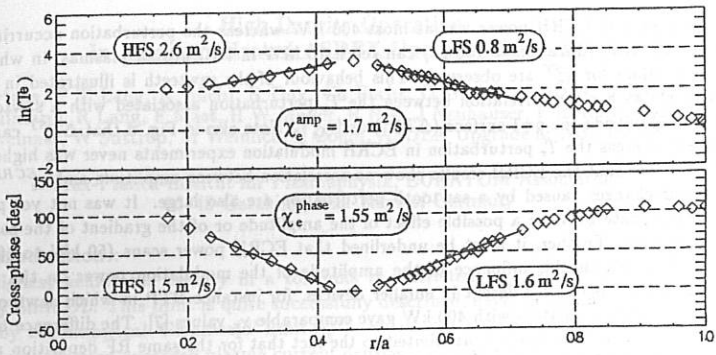

Figure 2: *Example of FT results showing amplitude and cross-phase at the fundamental frequency (29.41 Hz). The linear fits for HSF and LFS are indicated as well as the mean values obtained for χ_e^{amp}, χ_e^{phase}, giving $\chi_e^{FT} = 1.6\ m^2/s$.*

3. Experimental results

In this section we compare χ_e^{ST} and χ_e^{ECRH} with χ_e^{PB}, where χ_e^{PB} is given either by the power balance analysis when it is available or by $\chi_e^{Global} = a^2\kappa/4\tau_E$ (κ elongation, τ_E global energy confinement time). In the cases where χ_e^{PB} was available, it has been verified that χ_e^{Global} is close to χ_e^{PB} within 25%. The analyses of our sawtooth dataset yields $\chi_e^{PB} \leq \chi_e^{ST} \leq 6\chi_e^{PB}$ as appears in Fig. 3. Moreover there is obviously no correlation between χ_e^{ST} and χ_e^{PB}. In contrast, for the ECRH modulation experiments Fig. 3 clearly shows that χ_e^{ECRH} is at most 2 times larger than χ_e^{PB}, in agreement with the assumption $\chi_e \propto \nabla T_e^{\alpha}$ with $\alpha \leq 1$, [6].

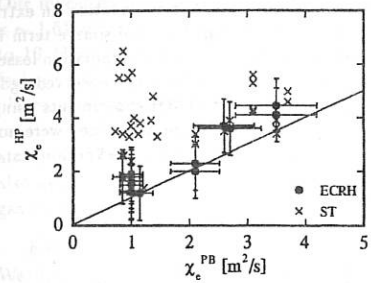

Figure 3: *χ_e^{FT} or χ_e^{ECRH} versus χ_e^{PB} for Ohmic and L-mode discharges under different conditions. The χ_e^{PB} values above 2 m^2/s are obtained from NBI-heated discharges in pure hydrogen.*

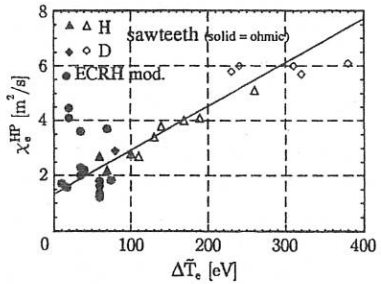

Figure 4: *χ_e^{ST} plotted versus the amplitude of the temperature perturbation caused by the sawteeth as measured just outside the inversion radius.*

In the shots where ECRH modulation was applied one observes that χ_e^{ST} is larger than χ_e^{ECRH} in most of the cases. An essential difference between the heat pulses from sawteeth and ECRH modulation resides in the size of the induced perturbation which is larger for sawteeth.

The modulated ECRH power was at most 400 KW whereas the perturbation occurring at a sawtooth crash (duration $\approx$ 100 μs) can reach 10 MW in NBI heated plasmas, in which the largest values for χ_e^{ST} are observed. This behaviour of the sawteeth is illustrated in Fig. 4 which shows a clear correlation between the T_e perturbation associated with a sawtooth as measured outside the q=1 surface (ΔT_e^{ST}) and χ_e^{ST}. Note also in Fig. 4 that ΔT_e^{ST} can reach 400 eV whereas the T_e perturbation in ECRH modulation experiments never was higher than 60 eV. Note that the ECRH results show no correlation between amplitude and χ_e^{ECRH}. The gradient changes caused by a sawtooth perturbation are also large. It was not yet possible to discriminate between a possible effect of the amplitude or of the gradient of the sawtooth perturbation. Further, it must be underlined that ECRH power scans (50 kW to 400 kW) showed no measurable influence of the amplitude of the modulation power on the results. However, this may be different in smaller devices, for instance RTP in which sawtooth and ECRH power modulation with 400 kW gave comparable χ_e values [7]. The difference between RTP and ASDEX Upgrade is attributed to the fact that for the same RF deposition at mid-radius, the ECRH power density in RTP is larger than in ASDEX Upgrade by more than one order of magnitude due to the larger volume. A second reason might be that in ASDEX Upgrade the large discrepancies between χ_e^{ST} and χ_e^{PB} occur with auxiliary heating (up to 5 MW) where the sawteeth are the strongest. Small Ohmic sawteeth in ASDEX Upgrade yield $\chi_e^{ST} \leq 3\chi_e^{PB}$. In ASDEX Upgrade an experimental simulation of sawtooth effects with ECRH would require an installed power of several MW, which will be available in the future.

4. Discussion

Simulations of the ECRH modulation experiments described above were performed with the ASTRA code [8]. The best agreement with the data is obtained with flat χ_e profiles having values higher than that required for power balance. Similarly to the TDC results for sawteeth, for ECRH modulation also, the amplitude and phase behaviour for channels outside r/a = 0.7 are well reproduced with outward convection. However, the observed behaviour might also be caused by a non-local transport, which introduces into the diffusion equation an extra modulated source term linked to the steady-state source [6]. In our case, the source term is dominated by the heating power inside r/a = 0.7 whereas it is dominated by the radiation losses outside this radius. In particular, the latter term qualitatively reproduces the observed egde behaviour of the perturbation at the edge. The simulations of our ECRH experiments using a non-local transport model also show that even harmonics should be created. They were not experimentally observed, perhaps due to a lack of sensitivity. Therefore, in our experiments, a non-local character of transport cannot yet be fully excluded.

References

[1] LOPES-CARDOZO, N. J., Plasma Phys. Controlled Fusion **37** (1995) 799.

[2] LEUTERER, F. et al., This Conference (1996).

[3] RIEDEL, K. S. et al., Nucl. Fusion **38** (1988) 1509.

[4] GIANNONE, L. et al., Plasma Phys. Controlled Fusion **38** (1996) 477.

[5] JACCHIA, S. et al., Phys. Fluids **B 3** (1991) 3033.

[6] STROTH, U. et al., Plasma Phys. Controlled Fusion **38** (1996) 611.

[7] JACCHIA, S. et al., Nucl. Fusion **34** (1994) 1629.

[8] PEREVERZEV, G. V. et al., IPP report 5/42 (1991) .

High Density Operation In Auxiliary Heated ASDEX Upgrade Discharges

V Mertens, P T Lang, K Büchl, R Dux, Ch Fuchs, O Gruber, G Haas, A Kallenbach, M Kaufmann, R Lang, F Mast, H W Müller, R Neu, J Neuhauser, F Ryter, H Salzmann, J Schweinzer, W Suttrop, M Weinlich, H Zohm, ASDEX Upgrade & NBI Teams

Max-Planck-Institut für Plasmaphysik, EURATOM Association,
85748 Garching, Fed. Rep. of Germany

Introduction :

The highest achievable density in a tokamak is restricted by the normally disruptive density limit DL. This limit is quite successfully described, even on machines of different sizes, by the empirical 'Greenwald' limit $\bar{n}_e^{GW} = \kappa < j >$ (κ is the plasma elongation and $< j >$ the area averaged plasma current density) [1]. Since the ITER (EDA) concept aspires an operation density significantly beyond this limit ($\approx 1.5\ \bar{n}_e^{GW}$ [2]), one needs reliable scenarios to overcome it without deterioration of the energy confinement time τ_E. At large heating powers, however, the particle fuelling efficiency of gas injection degrades such that high densities are difficult to achieve. Furthermore, the corresponding high neutral particle densities cause normally the backtransition of the favourable H-mode to an L-mode, yielding divertor detachment and probably a 'classic' DL. Presently, the only methode to achieve long lasting phases with $\bar{n}_e > \bar{n}_e^{GW}$ seems to be the repetitive injection of pellets.

This paper deals mainly with the characteristics of the L-mode phase preceeding every density limit disruption including impurity gas injection forced L-modes. The latter is found to prevent effectively detrimental divertor heat load.

Discharge Parameters :

Our investigations concentrate on lower single null discharges (R = 1.65 m, a = 0.5 m, $\kappa \sim 1.6$) with plasma currents between 0.6 MA and 1.2 MA and NBI heating powers up to 10 MW. The corresponding safety factors q_{95} vary between 2.5 and 5. The plasma facing vessel components are boronized. The ion ∇B drift is directed towards the target plates. A centrifuge enables to inject strings of pellets with velocities up to 1.2 km/s and repetition rates up to 80 Hz (representing a maximum fuelling rate of $\Phi \sim 3 \cdot 10^{22}$ D atoms/s). The working gas is mostly deuterium but in a smaller amount of discharges also hydrogen. Highly radiative discharges are performed by injecting Ne, Ar or Nitrogen gas into the main chaimber.

Experimental Observations :

We first describe the typical sequence from reaching very high line averaged densities finally ending in a DL disruption. At the applied high heating power levels P_{heat} the discharges stay normally in the ELM'y H-mode. During this mode the Greenwald limit could so far not be surpassed only by applying excessive gas puffing ($\Phi \lesssim 3 \cdot 10^{22}$ D atoms/s) as can be seen on Fig. 1 a) summarizing the highest achieved $\bar{n}_e$ in various regimes.

If the separatrix electron temperature in the H-mode decreases below $\approx$ 130 eV according to the strong particle influx and radiation cooling the discharge falls back into the

L-mode [3]. Owing to the reduced particle confinement of the L-mode the line averaged density decreases transiently until the density feedback control system rises the external gas flux and $\bar{n}_e$ grows again. Thereupon the divertor detaches, visible e.g. by the strong drop of the ion saturation current measured by langmuir probes mounted in the target plates. After the divertor electron temperature falls to a few eV a small Marfe forms close to the active X-point observable in a slight enhancement of the bolometer signals measuring the X-point region. If $\bar{n}_e$ raises further, the divertor throats become so cold that the radiating zone shifts up to the X-point and the Marfe starts to expand smoothly into the region of closed flux surfaces. This leads to a concentration of the boundary density into the X-point region observed by Li-beam and Thomson scattering diagnostics measuring close to the midplane and near the X-point, respectively. Correspondingly, the electron temperature close to the X-point reduces strongly from values of up to 100 eV to a few eV. An analysis of the electron pressure at the outside midplane boundary and in front of the divertor plates shows a clear pressure drop as signature of detachment. The smooth Marfe expansion is an unambiguous precursor of the local instability of the Marfe and hence of the DL. There is a large density operational window found with detached plasmas between q_{95} values of ≈ 3 and 4.

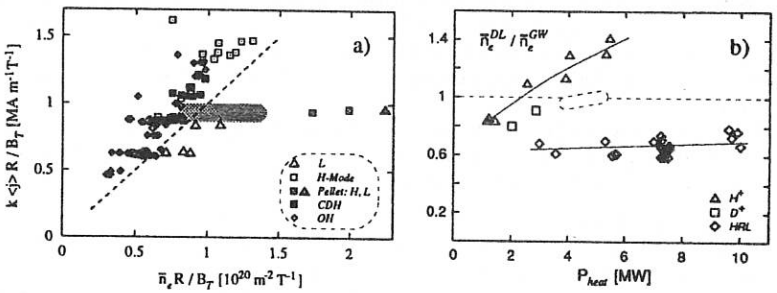

Figure 1: *a) shows the Greenwald plot indicating the typical ASDEX Upgrade density operating space. The dark area represents the region of feedback controlled pellet fuelled plasmas in H- as well as in L-mode. The white dashed surrounded area in Fig. b) corresponds to the $\bar{n}_e$ achieved up to now. Technical reasons prevent the further increase of $\bar{n}_e$. HRL denotes highly radiating L-modes.*

To obtain quickly and stationary high densities, we combined moderate gas puffing and repetitive pellet injection (with pellet injection alone $\bar{n}_e$ could not be successfully increased). Each pellet causes a quick (< 1 ms) raise in density, followed up by a slow decay of the density increment. In parallel, each pellet triggers an ELM expelling a part of the injected fuel [4]. The magnitude of the pellet induced increment is governed by the pellet fuelling efficiency ϵ_f. As during the injection sequence plasma cooling occurs (see Fig. 2 a), the pellets penetrate deeper into the plasma starting with roughly half minor radius ending up to approximately central deposition. Concomittantly, the fuelling efficiencies rise markedly. It has been shown that ϵ_f is a clear function of the penetration depth ranging between 30 % and 40 % in L-mode plasmas and dropping down to ≈ 0 %

in ELM'y H-mode phases for shallow penetration.

As a special tool to maintain long lasting high density phases we performed a control circuit using a bremsstrahlung signal as a measure of the line averaged density and inhibit the injection of pellets when the preprogrammed $\bar{n}_e$ is reached. Using this setup stationary phases ($>> \tau_E$) of up to 1.5 $\bar{n}_e^{GW}$ have been achieved as demonstrated in Fig. 2 a). In this example a smooth H $\rightarrow$ L transition occurs at about 1.9 s.

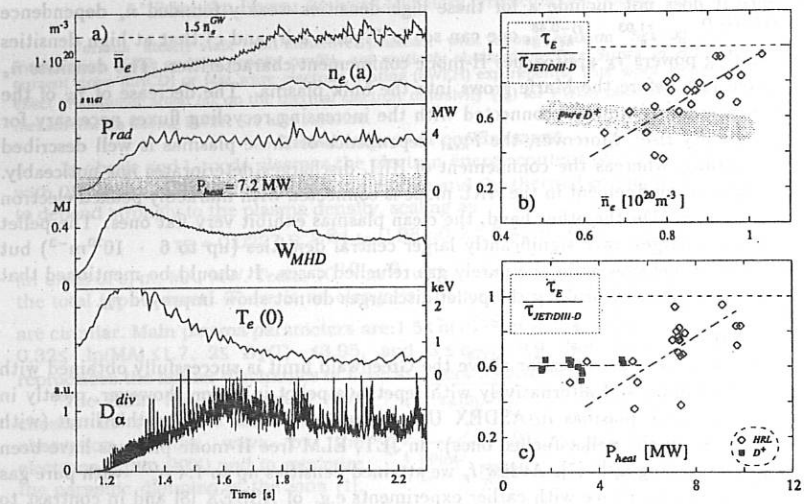

Figure 2: *a) shows a feedback controlled pellet fuelled discharge with preprogrammed $1.5\bar{n}_e^{GW}$. The shaded area in b) corresponds to the full squares of c) and represent clean deuterium L-mode plasmas.*

The fact that clean hydrogen/deuterium discharges normally do not detach in the H-mode at high densities, since at least the ELM's always burn through the divertor plasma, forced us to reduce the divertor power load by means of impurity gas injection. During ELM's peak power densities of up to 25 MWm^{-2} have been measured on the plates. This so achieved highly radiating and completely detached H-mode is known as CDH-mode [5]. The impurity injection can lead to radiative fractions $P_{rad}/P_{heat} > 90$ % before the plasma falls back into the L-mode. The highly radiating L-mode HRL shows qualitatively the same detachment and Marfe sequence as the clean hydrogen/deuterium discharges. No disruption has been observed without preceeding violent Marfe expansion.

The Greenwald scaling supposes the density limitation to be independent of heating power. The experiments, however, exhibit in the case of purely hydrogen/deuterium puffing a clear increase of the DL with heating power. At low plasma currents, $\bar{n}_e^{GW}$ is surpassed by up to 40 %. In contrast, the impurity dominated DL seems to be independent on P_{heat} (see Fig. 1 b). In the HRL-mode the disruption occurs normally at densities 0.6 -

0.8 $\bar{n}_e^{GW}$. The line averaged $\bar{Z}_{eff}$ there is about 4, whereas it is $\approx$ 1.8 in the clean plasmas. Generally, the DL of clean hydrogen discharges is systematically about 10 % higher than those in deuterium.

If one compares the energy confinement times of the two extremes (clean deuterium $\leftrightarrow$ HRL) one gets the interesting situation that the highly radiating plasmas have significantly larger τ_E than the clean ones. Taking the JET/DIII-D H-mode scaling as reference [6] since it does not include a for these high densities weakly founded $\bar{n}_e$ dependence $\tau_E^{JET/DIII-D} \propto I_p^{1.03} \cdot P_{heat}^{-0.46}$, one can see in Figures 2 b) and c) that at high densities and heating powers τ_E approaches H-mode confinement characteritics. The densities $\bar{n}_e$ are taken just before the Marfe grows into the bulk plasma. The decrease of τ_E of the clean deuterium plasmas is connected with the increasing recycling fluxes necessary for strong density rise. Moreover, the P_{heat} dependence of these plasmas is well described by the scaling, whereas the confinement of HRL discharges deteriorates not noticeably. The improved confinement in the HRL mode is connected with markedly peaked electron density profiles. On the other hand, the clean plasmas exhibit very flat ones. The pellet refuelled discharges have significantly larger central densities (up to 6 $\cdot$ $10^{20} m^{-3}$) but the boundary behaves as in the purely gas refuelled cases. It should be mentioned that despite strong density peaking the pellet discharges do not show improved τ_E.

Summary :

The aim to achieve densities far above the Greenwald limit is successfully obtained with strong gas puffing and alternatively with repetitive pellet injection, however, mostly in L-mode. H-mode plasmas in ASDEX Upgrade so far do not surpass this limit (with the exception of the pellet fuelled ones). In JET, ELM free H-mode plasmas have been observed exceeding $\bar{n}_e^{GW}$ [7]. At low I_p we attained densities up to 1.4 $\bar{n}_e^{GW}$ with pure gas refuelling. In accordance with earlier experiments e.g. of ASDEX [8] and in contrast to the Greenwald scaling, $\bar{n}_e^{DL}$ has been shown to increase clearly with P_{heat}. In the extreme case of strong impurity puffing the DL is markedly reduced, the heating power dependence on the DL evanesces, but τ_E can reach H-mode quality. With pellet injection we achieved controlled long lasting phases up to 1.5 $\bar{n}_e^{GW}$ and transiently maximum densities of about 2 $\bar{n}_e^{GW}$ in type-I ELM'y H-modes and $\approx$ 2.5 $\bar{n}_e^{GW}$ in L-modes. The related confinement in the H-mode is, however, degraded.

With respect to ITER one can conclude that operation at the projected density seems to be possible, but there are serious difficulties to maintain H-mode confinement. The injection of impurities unburdens the divertor and improves the L-mode confinement but reduces noticeably the achievable densities.

References :

[1] M Greenwald et al, Nuclear Fusion **28**, 1988, 2199
[2] G Janeschitz et al, Plasma Physics and Controlled Fusion **37** 11A, A19
[3] W Suttrop et al, this conference
[4] P T Lang et al, Nuclear Fusion, in press
[5] O Gruber et al, Phys Rev Lett **74**, 1995, 4217
[6] D Schissel et al, Nuclear Fusion **31**, 1991, 73
[7] D Campbell et al, Controlled Fusion and Plasma Physics (Proc. 21th Europ. Conf. Montpellier 1994) **18B** I 2
[8] A Stäbler et al, Nuclear Fusion **32**, 1992, 1557

Transport and density fluctuations in non-inductive current drive experiments in Tore Supra.

G.T. Hoang, I. Voitsekhovitch *, P. Devynck, T. Aniel,
V. Basiuk, A. Bécoulet, R.V. Budny **, C. Gil, E. Joffrin

Association EURATOM-CEA sur la Fusion Contrôlée
C.E. Cadarache, 13108 St Paul lez Durance, FRANCE
* Permanent address: SRC Kurchatov Institute, Moscow, Russia
**Princeton Plasma Physics Laboratory, Princeton, NJ 08543, USA

Various steady-state non-inductive plasmas, with strong electron heating and significant modification of the current density profile, are routinely obtained on Tore Supra in either lower hybrid current drive (LHCD) or fast wave electron heating (FWEH) experiments. This work focuses only on the effect of magnetic shear (s), on the thermal electron diffusivity (χ_e) for FWEH plasmas. Density fluctuation measurements during FWEH are also reported.

Global improved confinement

In ohmic and L-mode plasmas the electron energy content (W_e) is in good agreement with 0D Rebut-Lallia-Watkins (RLW) prediction and the thermal confinement time is found to depend strongly to the plasma density, scaling as

$$\tau_E = 0.0227\ R^{1.84}\ I_p^{0.98}\ B^{0.2}\ \bar{n}^{0.43}\ P^{-0.75} \qquad (1)$$

(in units of s, m, MA, MW, Tesla, 10^{19} m^{-3}, with $\bar{n}$ the central line averaged density, and P the total input power). There is no elongation dependence since the Tore Supra plasmas are circular. Main plasma parameters are: $1.5 \le \bar{n}(10^{19}\ m^{-3}) \le 4.9$, $0.4 \le P(MW) \le 9.8$, $0.32 \le I_p(MA) \le 1.7$, $2 \le B_T(T) \le 3.95$, and $3 \le q_{cyl} \le 9.9$. Note that this scaling also reproduces the limiter discharges of several others tokamaks.

The main FWEH scenario was chosen in order to maximize the absorption of the wave by the electrons (up to 90%) and to minimize the parasitic damping of the ions [1]. The working gas is helium. In these experiments, strong electron heating was observed, while the ions were weakly heated by ion-electron equipartition: $T_e(0)$ increased from 1 keV to about 7 keV and $T_i(0)$ reached a value below 2.5 keV with 9.5 MW of FW power. Large fractions of bootstrap current (up to 70%) [2], due to the peaked pressure profile, are routinely obtained. During FWEH, the total thermal energy (W_{tot}) is found to exceed the L-mode prediction by a factor of 1.7. Also, W_e exceeds the 0D Rebut-Lallia-Watkins scaling by a factor up to 2.2. A typical shot (Ip=0.68 MA, B=2.8T) is shown on Fig. 1 with three different heating schemes (FWEH, ICRH minority,

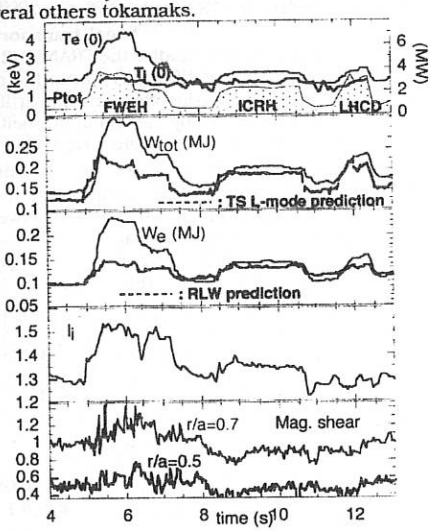

Fig.1: Time evolution of discharge with both L-mode and improved confinement regimes

LHCD) applied one after the other one. During ICRH and LHCD, the total thermal stored energy (W_{tot}) follows well the Tore Supra L-mode prediction. In contrast, FWEH phase displays an improvement over TS L-mode scaling by a factor H=1.4, which is provided by improved confinement in electron channel (We exceeds the 0D-RLW scaling by a factor of 1.7). At the same time a significant modification of the current profile (increase of plasma inductance, l_i, and magnetic shear in the gradient zone) during the FWEH phase has been observed. The good correlation between the increase of s (at r/a = 0.5) and the enhancement factors of the confinement is shown in figure 2.

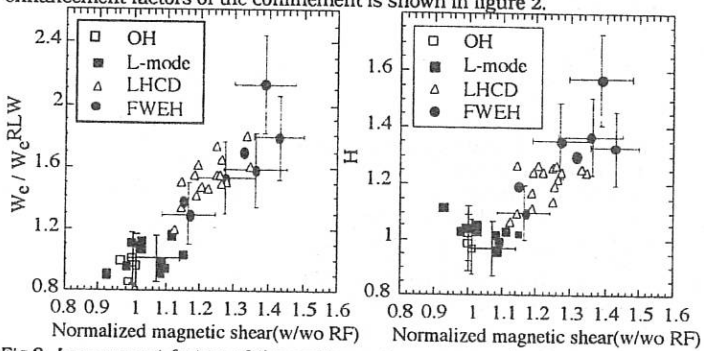

Fig.2: Improvement factors of the confinement versus normalized magnetic shear taken at r/a =0.5. H is defined as τ_E / TS L-mode prediction (Eq. 1)

Local transport analysis

For local transport studies the TRANSP [2], ASTRA [3] and LOCO [4] codes are used to determine the electron diffusivity within the region 0.2< r/a < 0.7. In our analyses, we only take into account the ion-electron equipartition (which is much less than the additional power mainly coupled to the electrons) but neither radiation nor convection terms, which are dominant only in the edge region, typically for r/a>0.8. The improvement of the energy confinement is clearly observed by the decrease of χ_e in the gradient region (0.3 < r/a < 0.7) during FWEH, compared to the L-mode LHCD and ICRH phases (Fig.3) for the same power level. The comparison between the 3.7 MW of FWEH and 2.2MW of ICRH displays the same thermal diffusivity in spite of the higher power in the first case. This reduction of χ_e is correlated to the increase of magnetic shear in the gradient zone. A statistical analysis also confirms this correlation. In Fig. 4, the normalized values of s and χ_e versus the total power are plotted for both L-mode and FWEH improved confinement regimes. These parameters are normalized to the corresponding ohmic levels

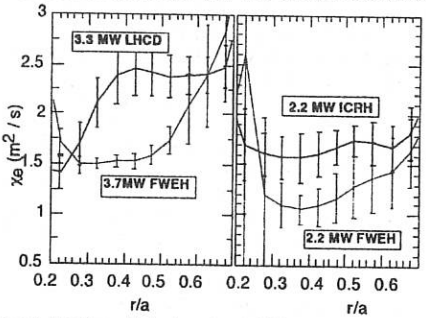

Fig. 3: Profiles of electron heat diffusivity, for the discharge shown in Fig.1:3.7 MW FWEH (t=6s), 3.3MW LHCD (t=12s), 2.2 MW ICRH (t=9.5s), 2.2 MW FWEH (t=7s)

The slopes of s and χ_e curves indicates the benefical effect of magnetic shear on electron heat diffusivity. The degradation of χ_e with increasing power for high shear discharges is lower than the levels of corresponding L-mode.

Simulations using some 1D transport models include the dependence on ∇T_e, q and s. We restrict here to two empirical models proposed respectively by Taroni [5] and Rebut-Lallia-Watkins [6]. The Taroni model, without the effect of s in the explicit form, provides the good agreement with the experimental temperature profile for L-mode without current modification (Fig. 5). However, the simulation for FWEH phase displays the good fit in the inner part of the confinement region along with the discrepancy in the outer part (r/a >0.4) where the magnetic shear increases.

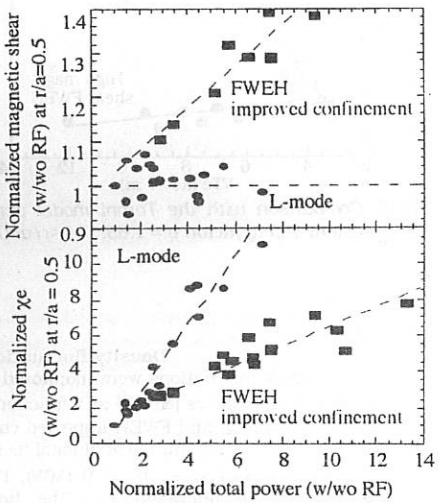

Fig. 4: Variation of s and χ_e with total power for L-mode and FWEH improved confinement regimes. (circles: L-mode, squares: Improved confinement)

Furthermore, a statistical analyis (dataset of 40 shots using various heating schemes) shows a disagreement with this model in dependence on ∇T_e. In Fig. 6, the ratio χ_e / χ_e^{Taroni} is plotted versus ∇T_e for both the L-mode and FWEH high shear improved confinement discharges in which the main plasma parameters were kept constant, namely q = 1.65 (0.4 < r/a < 0.6), except ∇T_e by increasing the total power up to about 10MW. Discrepancy with increasing ∇T_e is observed for L-mode. For FWEH shots the increase of ∇T_e modifies, at the same time, the magnetic shear profile through the increase of bootstrap current fraction. Therefore, the effect of s compensates the disagreement in ∇T_e dependence (change in the slope). This also indicates that the improved confinement in our FWEH experiments is clearly linked to the increase of s, but not simply to the change in safety factor.

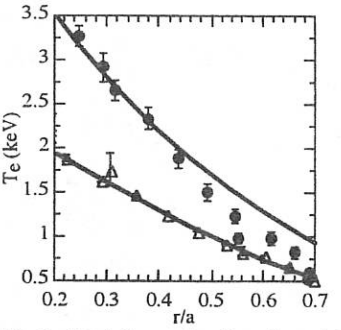

Fig. 5: Simulation using Taroni model (solid lines) for L-mode (triangles) and FWEH (circles).

Concerning to the RLW model, a good agreement is only obtained when ∇T_e is much higher than critical temperature gradient given by RLW [7]. The comparison with both Taroni and RLW models is illustrated in Fig. 7. For Taroni model, the discrepancy at high ∇T_e could be explained by the existence of a critical temperature gradient experimentally observed [7].

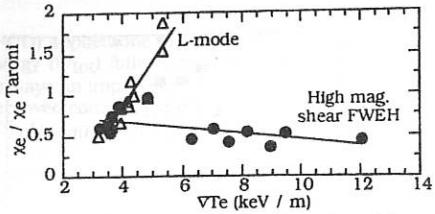

Fig. 6: Comparison with the Taroni model versus ∇Te (constant safety factor: q = 1.65, 0.4 <r/a<0.6)

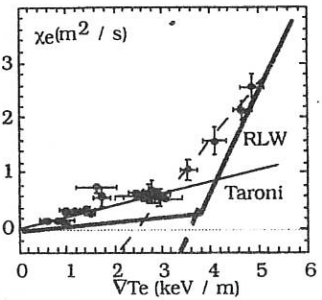

Fig. 7: Comparison with Taroni and RLW models versus ∇Te

Density fluctuation behaviour

The density fluctuations were monitored with an heterodyne CO2 laser scattering diagnostic [8]. Fig. 8 shows $(\delta n/n)^2$ as a function of ∇T_e (taken at r/a=0.7) for the ICRH L-mode(minority heating) and FWEH improved confinement regimes. Note that the density was kept constant throughout the additional heating phase. Variation of ∇T_e was obtained by increasing the total power (up to 9.4MW). The rms signal monitored is for k=5 cm^{-1}, and corresponds to fluctuations at the bottom of the plasma, located between $0.5 < r/a < 1$, with a maximum around r/a=0.7. For high magnetic shear discharges the increase of $(\delta n/n)^2$ with ∇T_e is notably weaker compared to L-mode regime. There is therefore an indication that the density fluctuations could be efficiently reduced by increasing s.

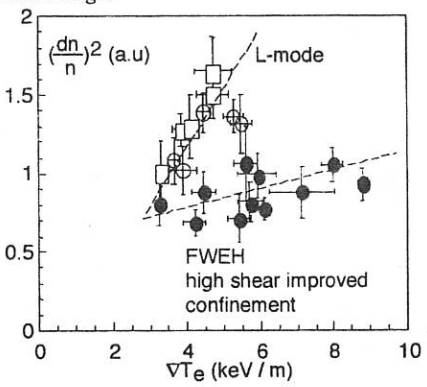

Fig. 8: Density fluctuation versus ∇Te
circles: CO2 laser scattering for FWEH (full: Improv. confinement, open: L-mode)
squares: reflectometry for ICRH L-mode [9]

Conclusions

Improvement in global confinement thanks to current modification (increased magnetic shear in the confinement zone) is clearly demonstrated. Simultaneously the reductions of χ_e and density fluctuation were observed. The 1D Taroni and RLW models can fit the experimental result with some restrictions. For Taroni model a discrepancy takes place when s or ∇T_e increases. The RLW model is in good agreement only for high ∇T_e cases.

Ref:

[1]: Equipe Tore Supra, 21th EPS, Montpellier.
[2]: Budny, R.V., et al., Nuclear Fusion 32 (1992)
[3]: Pereverzev G. V., et al., Nucl. Fus., vol (1992)
[4]: Harris, G.R., et al., Nuclear Fusion 32 (1992)
[5]: Taroni, A., et al., 20th EPS, Lisboa.
[6]: Rebut, P.H., et al., Phys. Fluids B3 (1991)
[7]: Guiziou L., et al., 22th EPS, Bournemouth.
[8]: Devynck P., Plas. Phys. Cont. Fus., 35,(1993)
[9]: Clairet F., et al., 22th EPS, Bournemouth.

Particle simulation of alpha-particle-driven modes in tokamaks

S. Briguglio

Associazione Euratom-ENEA sulla Fusione, C.R.E. Frascati,
C.P. 65 - 00044 - Frascati, Rome, Italy.

Toroidal Alfvén Eigenmodes (TAE's) and their kinetic counterpart (KTAE's) can play a relevant role in determining the confinement properties of energetic particles in Tokamak plasmas close to ignition conditions. TAE's and KTAE's can indeed be driven unstable by the resonant interaction with energetic ions characterized by velocities of the same order of magnitude of the Alfvén speed and, in turn, enhance their losses.

For resonant drive larger than the continuum damping, a new unstable mode can appear: the Energetic-Particle (continuum) Mode (EPM).[1] The EPM does not correspond to any MHD normal mode (it would not exist in the absence of the energetic particles), and its frequency is determined by the resonance condition with the parallel motion of energetic particles ($\omega \approx k_{\|} v_{\|H}$). It is a close relative of the fishbone mode, in the sense that it can, in principle, continuously adjust its frequency and "follow" the energetic particles while displacing them. One of the major points in the investigation of the properties of these modes concerns their nonlinear saturation and the fluctuation level at which the saturation takes place. Different saturation mechanisms have been proposed in literature, related either to mode-mode coupling[2,3] or to trapping of resonant particles in the potential well of the wave.[4] Each of these mechanisms could dominate in appropriate regimes, but they are all based on the assumption of perturbative energetic-particle contribution. A powerful tool for the investigation of the relative importance of these as well as of other mechanisms is represented by the Hybrid MHD-Gyrokinetic Code[5] which allows to fully retain all the relevant kinetic effects related to the energetic-particle population. The code evolves the $O(\epsilon^3)$-reduced MHD equations for the fluctuating (scalar and parallel vector) potentials, with the term related to the energetic-particle pressure. To compute this term, at each time step, the gyro-averaged Vlasov equation for the energetic-particle distribution function is solved by particle-in-cell techniques. In order to better resolve the low-amplitude linear-growth stage of the mode evolution, the low-noise δF algorithm is adopted, which consists in representing only the deviation of the distribution function from a known background distribution function in terms of (weighted) particles.[5] Switching to a standard full-F simulation is allowed in the nonlinear stage, if the deviation becomes of the same order of the equilibrium distribution function.

In order to limit the requirements for spatial resolution and hence for computational resources, we refer here to low toroidal mode numbers ($n \approx O(1)$). Although this case is not directly relevant for reactor scenarios (high-n modes are predicted to be the most unstable[6]), it shows important features that are expected to be present also in more realistic situations.

In Fig. 1 the results of linear simulations are reported. The linear growth rate and the real frequency of the most unstable mode are shown, normalized to the Alfvén time τ_A, at different values of the ratio between the energetic-particle on-axis density n_H and the bulk-ion one n_i. Only modes with toroidal mode number $n = 4$ and poloidal mode numbers ranging from $m = 4$

and $m = 8$ are retained (the safety factor q ranges from 1.1 to 1.9). The initial energetic-particle population is Maxwellian, with thermal speed equal to the Alfvén velocity. At low values of energetic-particle density, a "perturbative" regime (i.e., a regime in which the effect of particle dynamics on the mode structure is negligible), characterized by weakly unstable TAE with growth rate increasing linearly with n_H, is observed. The real frequency, in this regime, is well inside the gap. At intermediate values of n_H/n_i, the real frequency decreases, merging into the lower continuum. Correspondingly, the KTAE, given by the toroidal coupling of two counterpropagating Kinetic Alfvén Waves, turns out to be the most unstable mode. Its growth rate exhibits a weak dependence on n_H/n_i, because increasing n_H tends to enhance both drive and radiative damping.[7] Above a certain threshold in n_H/n_i, the Energetic Particle continuum Mode appears, with growth rate sharply increasing with n_H. The real frequency is deeply inside the lower continuum. In this regime, wave-particle resonances cannot be treated within a perturbative approach.

Concerning the nonlinear saturation, our attention is focused on the mechanisms related to energetic-particle dynamics. This is first examined by following the particles in a fluctuating field with given radial profile and time-dependent amplitude driven by the resonant wave-particle interaction. The dependence of the saturation level on the linear-phase growth rate is shown in Fig. 2 (squares), for simulations with $n = 1$ modes. It can be seen that, at low values of γ_L, the agreement with the theoretical predictions ($\delta B_r|_{sat} \propto \gamma_L^2$) of Ref.[4] is qualitatively good. At higher values of γ_L, the radial width of the wave-particle resonance is limited by the finite extent of the fluctuating field, and the mode saturates at lower amplitude.

The nonperturbative effects of energetic particles on the mode structure are then included. The results of such self-consistent simulations correspond to the triangles in the same figure. As far as low values of the energetic-particle density are considered (low values of γ_L), the two kinds of simulations yield very similar results. Above the threshold for the EPM destabilization, however, saturation amplitudes depart from the previous perturbative results. The indication that a different mechanism is active in this regime is supported by the examination of the typical particle orbit in the meridian plane, obtained in a simulation with $n_H/n_i = 0.03$ and shown in Fig. 3. The wave-particle interaction induces a secular radial drift of the particle, instead of a small oscillation around the unperturbed orbit. Saturation is then reached because the source of the instability is macroscopically displaced, rather than because of trapping of resonant particles in the potential well of the wave.

As a consequence, in spite of the lower level of the saturation amplitude, the effect of this mechanism on the energetic-particle confinement can be dramatic. Figure 4 shows the radial profile of the energetic-particle line density, for the same case as Fig. 3, at two different times: during the linear growth of the mode and after saturation, respectively. In Fig. 5, the fraction of energetic-particle population displaced out of a given radial position ($r = 0.7a$, in this case) is shown, at different values of n_H/n_i, for the cases $n = 1$ and $n = 4$ (open triangles and squares, respectively). The corresponding linear growth rates are also shown (full triangles and squares). It is apparent that the destabilization of EPM's corresponds to a sharp increase of the fraction of displaced particles and then, potentially, of the fraction of lost particles.

Although the threshold for this dangerous saturation mechanism corresponds to unrealistically high values of energetic-particle density, it can be seen that such a threshold decreases with increasing n. Realistic values of n_H/n_i could then cause the same phenomenology in the more unstable high-n cases.[6] Nonperturbative studies of the saturation of high-n Alfvén modes are then required for investigating the α-particle confinement properties of plasmas close to ignition conditions.

References

[1] L. Chen, Phys. Plasmas **1**, 1519 (1994).

[2] G. Vlad, C. Kar, F. Zonca, and F. Romanelli, Phys. Plasmas **2**, 418 (1995).

[3] T.S. Hahm, L. Chen, Phys. Rev. Lett. **74**, 266 (1995)

[4] H. L. Berk and B. N. Breizman, Phys. Fluids B **2**, 2246 (1990).

[5] S. Briguglio, G. Vlad, F. Zonca, and C. Kar, Phys. Plasmas, **2**, 3711 (1995).

[6] S. Briguglio, C. Kar, F. Romanelli, G. Vlad and F. Zonca, Plasma Phys. and Controlled Fusion, **37**, A279 (1995).

[7] R. R. Mett and S. M. Mahajan, Phys. Fluids B **4**, 2885 (1992).

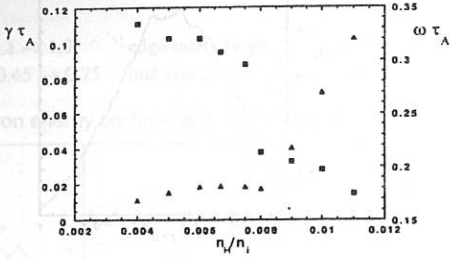

Figure 1: Normalized linear growth rate (triangles) and real frequency (squares) at different values of n_H/n_i. Only modes with toroidal mode number $n = 4$ have been retained.

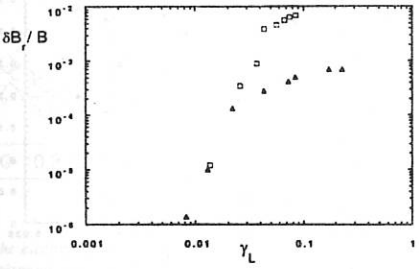

Figure 2: Saturation level of the fluctuating magnetic field versus the linear-phase growth rate, for "perturbative" (squares) and self-consistent (triangles) nonlinear simulations with $n = 1$.

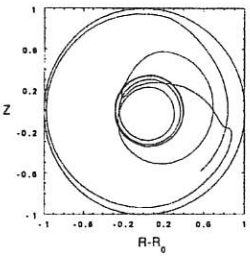

Figure 3: Typical particle orbit in the meridian plane, obtained in a simulation with $n_H/n_i = 0.03$, $n = 1$. A secular radial drift is observed.

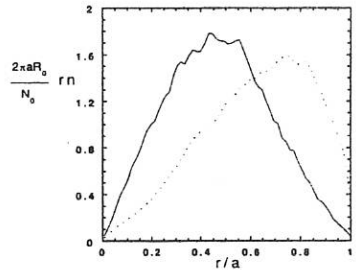

Figure 4: Radial profile of the energetic-particle line density, for the same case as Fig.3, during the linear growth of the mode (solid line) and after saturation is reached (dashed line).

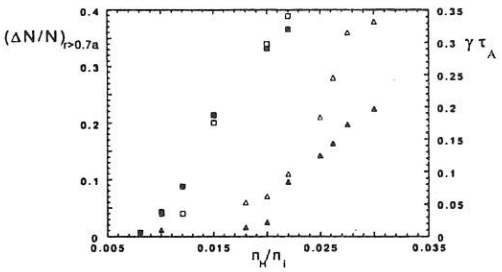

Figure 5: Fraction of energetic-particle population displaced out of $r = 0.7a$, at different values of n_H/n_i, for the cases $n = 1$ and $n = 4$ (open triangles and squares, respectively). The corresponding linear growth rates are also shown (full triangles and squares).

How the Shape Influences the TCV Plasma Properties

J.-M. Moret, M. Anton, R. Behn, F. Bühlmann, M.J. Dutch, B.P. Duval, A. Fasoli, S. Franke, F. Hofmann, B. Joye, J.B. Lister, Y. Martin, C. Nieswand, Z.A. Pietrzyk, R.A. Pitts, A. Pochelon, F.N. Skiff, W. van Toledo, G. Tonetti, M.Q. Tran, H. Weisen

Centre de Recherches en Physique des Plasmas
Association EURATOM - Confédération Suisse
École Polytechnique Fédérale de Lausanne, CH-1015 Lausanne, Switzerland

TCV has the unique capability of creating a wide variety of plasma shapes [1], controlled by 16 independent coils. This opens a new domain in Tokamak operation which has been explored to investigate the influence of the shape on plasma properties. In limited ohmic L-mode stationary discharges ($R = 0.88$ m, $a = 0.25$ m, $B_T = 1.4$ T), the following parameters have been systematically scanned:

elongation	$\kappa = 1.1 \rightarrow 1.9$	edge safety factor	$q_a = 2 \rightarrow 6$
triangularity	$\delta = -0.45 \rightarrow 0.75$	line average density	$n_e = 2.5 \rightarrow 8.5 \times 10^{19}$ m^{-3}

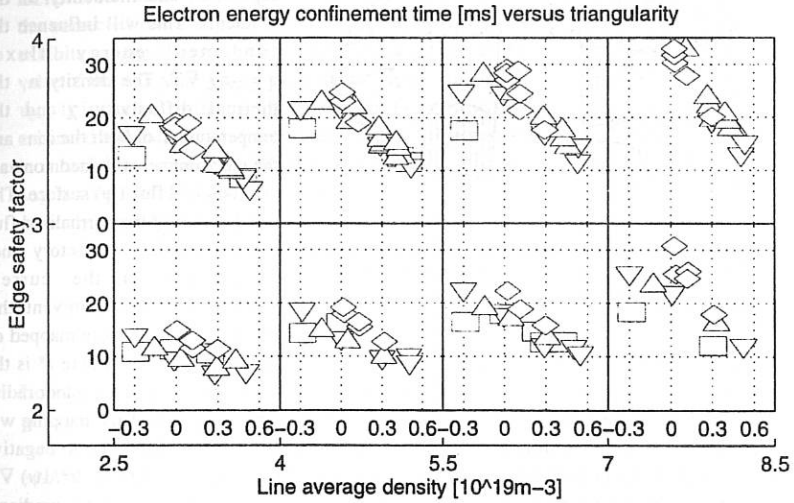

Fig. 1. Dependence of the electron energy confinement time on the shape for 4 classes of density and 2 classes of safety factor. The horizontal axis in each plot is the triangularity. Symbols represent the elongation: □ $\kappa = 1 \rightarrow 1.25$, ▽ $\kappa = 1.25 \rightarrow 1.5$, △ $\kappa = 1.5 \rightarrow 1.75$, ◇ $\kappa = 1.75 \rightarrow 2$.

The confinement properties of these plasmas are quantified by the electron energy confinement time, $\tau_{Be} = W_e/P_{oh}$, where P_{oh} is the ohmic input power. The total electron energy, W_e, is obtained by volume integration of Thomson scattering measurements at 10 spatial positions.

The ratio P_{rad}/P_{oh} was observed to be remarkably constant in all conditions [2] so a correction for the total radiated power P_{rad} does not modify the observed variations in τ_{Ee}. For a given plasma shape, τ_{Ee} exhibits the usual increase with q_a and the usual linear dependence on the density (fig. 1); the density saturation occurs at values slightly higher than the highest one used in this work. In all conditions a strong dependence of τ_{Ee} on the plasma shape was found: a slight improvement with elongation and a marked degradation with positive triangularity, both at fixed value of q_a (fig. 1). The degradation factor over the scanned triangularity range is typically 2 and reaches 3 at the highest density. The improved confinement at negative triangularity leads to a reduction in the ohmic power which is necessary to drive the plasma current. This is also reflected in reduced sawtooth ramp rates, which are proportional to the central ohmic power deposition in all conditions. The electron energy confinement keeps increasing when going to negative triangularity so that the influence of triangular shape is not symmetric. Some data points however indicate a reduced confinement correlated with MHD activity seen both on magnetic probes and soft X-ray tomography.

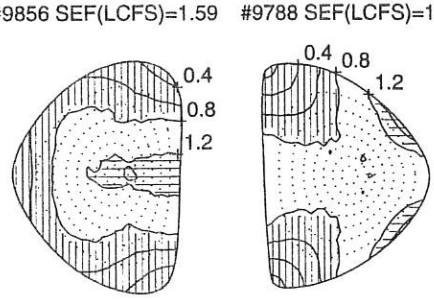

Fig. 2. Distribution of the gradient geometrical factor for a negative (left) and positive (right) triangularity. Vertical and horizontal hatching shows the reduced and increased gradient regions respectively.

Geometrical effects. A direct consequence of the shaping is a modification of the flux surface separation and incidently of the gradients. This will influence the conducted energy fluxes $q = -n\chi \nabla T$. The density n, the thermal diffusivity χ and the temperature T of both the ions and the electrons are assumed constant on a poloidal flux (ψ) surface. The usual choice of the normalised flux coordinate is not satisfactory since it depends on the current distribution. To circumvent this effect the profiles were mapped on to the equatorial plane. The energy flux becomes $-n\chi\ (dT/dr^*)\ (dr^*/d\psi)\ \nabla\psi$ where r^* is the outer horizontal distance from the magnetic axis normalised such that it equals the minor radius (half the horizontal plasma width) on the last closed flux surface (LCFS). This mapping was necessary to handle flux surface compression in the outer equatorial plane due to negative triangularity and Shafranov shift. The spatial distribution of the geometrical factor $(dr^*/d\psi)\ \nabla\psi$ is plotted in figure 2 for two shapes: a value smaller than unity implies smaller gradients compared to a cylindrical plasma of same horizontal width. This plot allows to identify the regions where energy fluxes are increased or decreased. In particular, the compression of flux surfaces toward the outer tip of a positive triangularity shape creates an extended region with increased gradients. At negative triangularity, this region shrinks due to increasing separation of the flux surfaces away from the equatorial plane, so that a large part of the plasma can benefit from shaping geometrical effects. Only the surface integral of the energy flux enters the 1-D

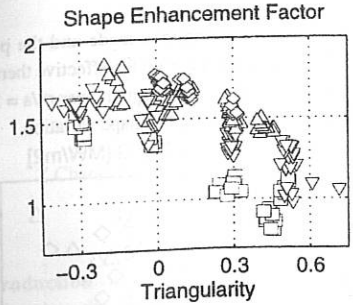

Fig. 3. Shape enhancement factor on the LCFS. See fig. 1 for symbols.

radial power balance and it is therefore convenient to define a shape enhancement factor (SEF) $s = d\psi/dr^* <\nabla\psi>^{-1}$, where the average is taken on a flux surface. The value of the SEF on the LCFS is shown in figure 3 for all the shapes studied, clearly demonstrating that a considerable reduction in the average gradients in the plasma outer region can be obtained not only with elongated shapes but also with shapes with negative triangularity at modest elongation. High positive triangularity can even lead to an SEF bellow unity.

Global confinement. If thermal conduction processes dominate the electron energy losses, the SEF directly multiplies the global energy confinement time. The SEF varies in space, being closer to one in the plasma center where the flux surfaces are less shaped and increasing towards the LCFS. If its value in the temperature gradient region is used, the corrected electron energy confinement time τ_{Ee}/s still exhibits a dependence on the shape (fig. 4). Applying the value of the SEF at the edge cancels almost all the variation of τ_{Ee}. It is then clear that confinement can be considerably enhanced by geometrical effects alone. But these are averaged in an unfoldable manner in the global confinement time and any intrinsic influence of the shape on transport properties will only be revealed by a local power balance analysis.

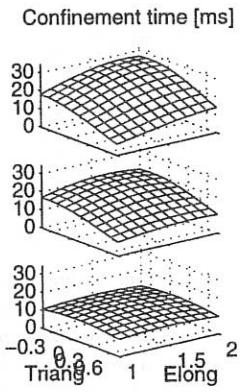

Fig. 4. At fixed value of $q_a = 4$ and $n_e = 5.5 \times 10^{19}$ m^{-3}, dependence on the shape of (from top to bottom) : raw electron energy confinement time; corrected with SEF in the gradient region; corrected with SEF on the LCFS.

Local transport. A simplified radial power balance was used in which: (i) the local ohmic power deposition is estimated from the current distribution obtained from an equilibrium reconstruction and a uniform electrical field; (ii) the radiated power is localised near the plasma edge [2] and has not been introduced; (iii) in the absence of an adequate measurement of the ion temperature T_i and its profile, ion and electron channel losses were not separated. Combining the power balance of both species leads to the definition of an effective thermal diffusivity χ_{eff} such that $q_{oh} = -n_e\chi_{eff}\,(dT_e/dr^*)\ s^{-1}$ and $\chi_{eff} = \chi_e + \chi_i\,(\nabla T_i/\nabla T_e)$, where q_{oh} is the input power flux. Well pronounced geometrical effects near the plasma edge are evident in the electron temperature profile (fig. 5): the mapped gradient at the edge is steeper for large SEF, indicating the beneficial effect of good flux surface separation and allowing a broader profile to build up. This generalises to all shapes as seen in figure 6 where the usual plot of the power flux

versus the temperature gradient is drawn. Given the rough assumptions made and the poor accuracy of a local power balance, no significative influence of the shape on the effective thermal diffusivity can be detected. The same observation is true for the gradient region, near $r^*/a = 3/4$. Thus no dramatic changes in the transport coefficient are brought about by shape variation.

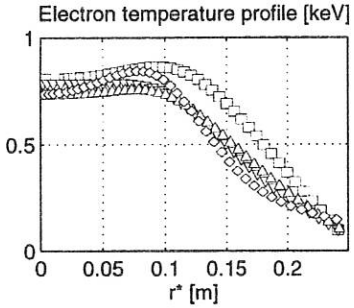

Fig. 5. Electron temperature profile mapped on the outer equatorial plane at $\kappa = 1.4$, $q_a = 2.5$ *and* $n_e = 5.5 \times 10^{19}$ m^{-3}:
□ δ = -0.3 SEF = 1.61
▽ δ = 0 SEF = 1.45
◇ δ = 0.3 SEF = 1.29
δ = 0.5 SEF = 1.00

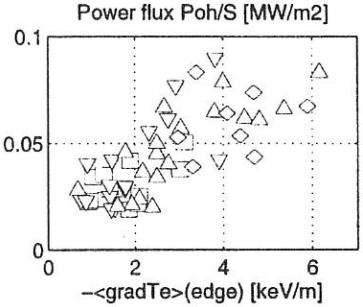

Fig. 6. Power flux near the edge versus electron temperature gradient for all shapes and currents at $n_e = 4.0 \rightarrow 5.5 \times 10^{19}$ m^{-3}. *For symbols see fig. 1.*

Conclusion. In summary, the large variation in global confinement time within the domain of explored shapes can possibly be explained by direct geometrical effects. No important influence of the shape on local transport coefficients has been found. Of course this statement may have to be revised in other operational regimes, for example with significant auxiliary heating or when approaching stability limits, as suggested by DIII-D [3]. This work however indicates that a global confinement optimisation can be achieved by tuning the plasma shape. Negative triangularity, which may exhibit poor MHD or vertical stability performance [4], is not the only option. More subtle shape variations can be envisaged and the result of this optimisation would be a compromise between the benefit of the geometry and other constraints.

This work was partly supported by the Fonds National Suisse de la Recherche Scientifique.

[1] F. Hofmann, M.J. Dutch, J.-M. Moret, *22nd EPS Conf. on Cont. Fusion and Plasma Phys., Bournemouth, 1995*, p. 101, vol. 19B part II.

[2] H. Weisen et al., *Measurement and Modelling of Light Impurity Behaviour in TCV*, this conference.

[3] A.W. Hyatt, E.A. Lazarus, T.H. Osborne, *21st EPS Conf. on Cont. Fusion and Plasma Phys., Montpellier, 1994*, p. 14, vol. 18B part I.

[4] M.J. Dutch, F. Hofmann, O. Sauter, D.J. Ward, M. Anton, J.-M. Moret, *22nd EPS Conf. on Cont. Fusion and Plasma Phys., Bournemouth, 1995*, p. 77, vol. 19C part IV.

Stability of TFTR Reverse Shear Discharges

T.C.Hender, C.G.Gimblett, R.J.Hastie

UKAEA Fusion, Culham, Abingdon OX14 3DB, UK
(UKAEA/EURATOM Fusion Association)

Z.Chang, E.Fredrickson, J.Manickam and M.Okabayashi and the TFTR group

Princeton Plasma Physics Laboratory, Princeton, NJ, USA

Introduction

To improve the economics of tokamak fusion power plants a high bootstrap fraction is desirable. Since there is no bootstrap current driven at the magnetic axis, such high bootstrap fraction equilibria will have currents peaked off-axis and non-monotonic or reverse shear q-profiles. An additional attraction of reverse shear in the core is that this gives access to the second stability regime for ballooning modes [1]. Reverse shear operation in TFTR has been achieved by applying moderate NBI heating during the current rise and high power heating (up to 34MW) early in the flat-top [2]. In some discharges there is a transition to an enhanced reverse shear (ERS) confinement regime, in the central inverted shear region, leading to very peaked pressure profiles (with P(0)/<P> up to about 8). Motional Stark Effect measurements indicate during the ERS phase that $2<q_{min}<3$. The highest β discharges can end in a disruption, though this can be controlled by tailoring the NBI heating. In this paper the MHD stability of these TFTR discharges is discussed.

Observed Reverse Shear MHD

A range of coherent low-n MHD is observed in reverse shear discharges. During the high power heating phase of most reverse shear discharges low level intermittent n=1 activity is observed. Also in nearly half of all ERS discharges n=2 activity is observed. Figure 1 shows a typical discharge in which n=1 and n=2 activity is observed.

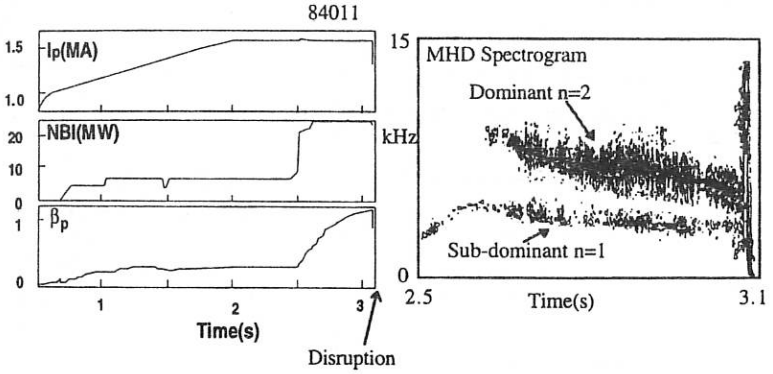

Fig 1 MHD power spectrum as a function of time showing long lived n=1 and 2 activity during the ERS phase. Note there is a disruption at 3.1s.

In some discharges long lived n=3 activity is also observed. This long-lived n=1-3 activity has been determined to rotate at approximately the measured plasma velocity. The n=2 activity is found to be radially localised near q=5/2, and just outside q_{min}, with an island parity indicated by ECE measurements (Fig 2). From the ECE measurements the long lived n=1 is found to be located at slightly larger minor radii than the n=2 activity.

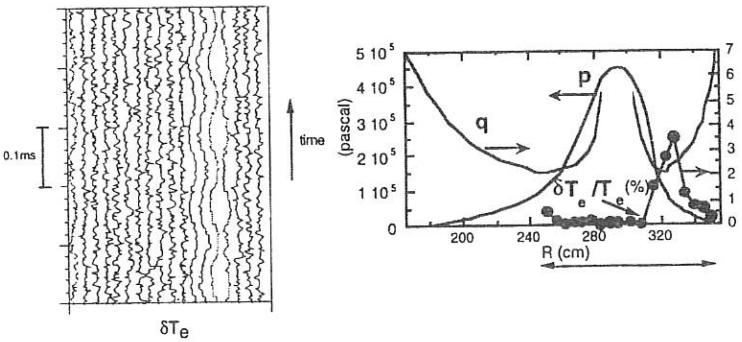

Fig 2 Multi-channel ECE temperature perturbations (LHS) across portion of major radius indicated by the arrow in RHS plot, which shows pressure (P) and q-profiles and ECE temperature perturbation.

As can be seen from Fig 1 a disruption occurs which limits performance. Analysis of the Mirnov data shows a short lived n=1 precursor to the disruption which rotates in the ion diamagnetic direction (distinguishing this from the long lived low level n=1 activity). In a discharge in which the long lived n=2 activity is absent, the n=1 precursor to the disruption can clearly be seen in the ECE data (Fig 3). This ECE data indicates an even-m mode and given the MSE measurement that q_{min}~2 this suggests an m=2,n=1 mode. There is no clear evidence for tearing-type phase inversions occurring during these n=1 disruption precursors.

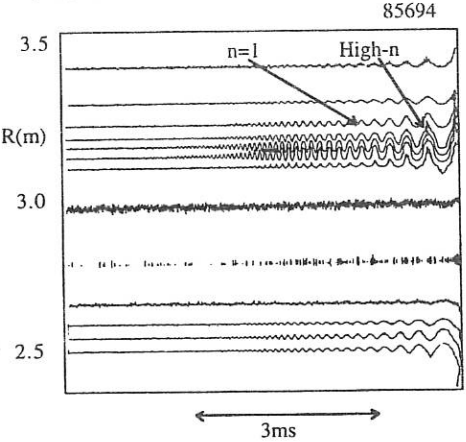

Fig 3 ECE temperature contours showing an n=1 mode growing before a high performance disruption at β_n=1.6%mTMA^{-1}. Note the high frequency ballooning activity superimposed on the n=1 kink.

In addition to this MHD activity during the high power heating phase, there is also evidence for n=1 double tearing activity in reverse shear discharges both before and after the high power heating phase. This double tearing activity is indicated by radial flat-spots observed in the (ECE) temperature profile data. The ECE measurements show the flat-spots occurring alternately at different radial locations, indicating two distinct islands chains with a relative poloidal phase of ~90°. Preceding the high power heating phase this double tearing activity can cause disruptions, possibly linked to a coupling to an external kink mode as the edge-q passes through an integer value during the current ramp. In the post high power heating phase this double tearing activity can lead to full or partial sawteeth [3]. The full sawteeth have the normal characteristics of a rapid central temperature collapse and a clear temperature inversion radius, but with $q_{min}>1$.

Theory Considerations

Here we discuss likely theory explanations for the MHD activity observed during the ERS phase.

The reverse shear in the core region guarantees stability to the high-n ballooning modes, though just outside the shear reversal region the ballooning modes can be close to instability. This may be correlated to the observed high-n ballooning activity observed in a few discharges, superimposed on the n=1 disruption precursor (see Fig 3).

The rotation directions of the low-n MHD tends to indicate the long-lived n=1-3 activity is resistive in origin while the n=1 disruption precursor is an ideal mode. This is verified by ideal stability calculations, using the PEST code [4], which show the n=1 kink is unstable at β-values close to those at which the n=1 precursored disruption occurs. Further the eigenfunction structure of this n=1 kink mode is found to be in close agreement with that determined experimentally from ECE measurements.

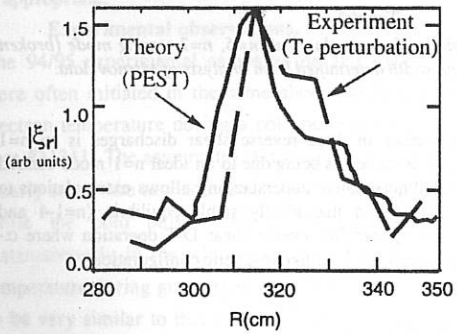

Fig 4 Comparison showing good agreement between the experimentally derived radial displacement of the n=1 disruption precursor and the equivalent quantity derived from the ideal PEST stability calculation.

An analytic theory has been developed which quantitatively describes the properties of these reverse shear ideal instabilities; by analogy with double tearing modes they are termed double kink modes. For these modes $\beta_{crit} \propto \varepsilon^{8/5}$ so they tend to be more limiting than external kinks ($\beta_{crit} \propto \varepsilon$).

The resistive stability of these discharges has been calculated with the FAR code [5]. In particular the discharge shown in Fig 1 has been studied; the results show n=1 and 2 resistive modes are unstable in this discharge and as discussed above, near the disruption β-value, an ideal n=1 becomes unstable (Fig 5).

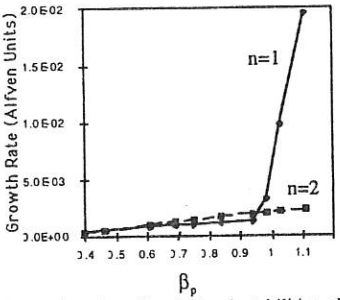

Fig 5 Resistive stability ($S=10^7$) of n=1 and 2 modes for discharge shown in Fig 1. For β_p>0.95 the n=1 mode is ideally unstable. This sequence of instabilities with rising β is in good agreement with experiment (c.f. Fig 1) but there are difficulties over the mode characteristics (see below). NB $S\sim10^9$ in TFTR, this reduces the resistive mode growth rates ($\sim S^{1/3}$) but does not qualitatively alter the picture.

The n=1 and n=2 resistive instabilities observed in the simulation are resistive interchange modes which are unstable in the reverse shear region for sufficiently high pressure gradients, even though q>>1. These modes are strongly radially localised just within the shear reversal region; this appears to be at variance with experimental observations for the n=2 (cf Fig 2). An explanation for this may be that in the core region these discharges are in the collisionless regime. In this regime both the tearing [6] and twisting parity modes [7], driven by the bootstrap current, are stable in the negative shear region. Just outside q_{min} however, these modes are unstable and comparisons with the computed evolution of the 5/2 island width ($dW/dt \propto \eta(\Delta'+C\beta p/W)$, where C is an equilibrium dependent constant) shows reasonable agreement:-

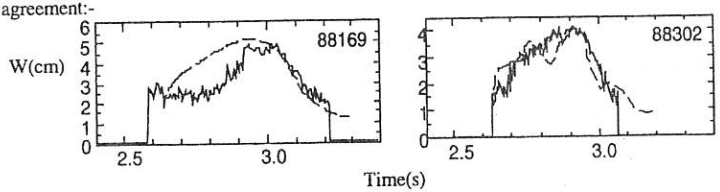

Fig 6 Computed island width (W) evolution for neo-classical m=5, n=2 tearing mode (broken line) compared with experimental island width determined from analysis of Mirnov data.

Discussion

The primary MHD limitation to performance in these reverse shear discharges is an n=1 precursored disruption. This limit is well described as being due to an ideal n=1 mode centred near the shear reversal surface. This good quantitative understanding allows extrapolations to higher current (Ip=2.5MA), where it is found that ideally stable equilibria (n=1-4 and ballooning) exist. This indicates suitable regimes for reverse shear D-T operation where α-particle physics can be examined for advanced tokamak like magnetic configurations.

References

[1] A Sykes et al, EPS Oxford **2** (1979) EP21
[2] F M Levinton et al, Phys Rev Lett, **75** (1995) 4417
[3] Z Chang et al, Submitted to Phys Rev Lett
[4] R C Grimm et al, Meth Comp Phys **16** (1976) 253.
[5] L A Charlton et al, Journal of Computational Physics **86** (1990) 270
[6] C C Hegna et al, Phys Fluids **B4** (1992) 1855
[7] J W Connor and L Chen, Phys Fluids **28** (1985) 2201

Acknowledgement This work was jointly supported by the US Department of Energy (Contract DE-AC02-76-CH03073), the UK Department of Trade and Industry and EURATOM.

Numerical analysis of the heat pulses in JET

V.V.Parail, A. Cherubini, M. Erba, P. Galli*, R. Giannella, L. Porte, A. Rookes, F. Romanelli#, E. Springmann, A. Taroni
JET Joint Undertaking, Abingdon, Oxon OX14 3EA, UK
*Dipartimento di Fisica,Universita Degli Studi di Milano, I-20133, Milano, Italy.
Associazione EURATOM-ENEA sulla Fusione, C.R.E. Frascati, C.P. 65, 00044, Frascati, Roma, Italy

Introduction.

Predictive modelling of different kind of heat pulses is a powerful tool to test the validity of transport models. The last experimental campaign in JET gave high quality information of the electron temperature evolution during five types of heat pulses: the L-H transition, sawtooth crashes, giant ELMs, cold pulses triggered by laser impurity ablation and slow roll-over. All relatively strong pulses triggered from the plasma edge show a fast global modification of at least the electron heat conductivity which, in principle, permits different interpretations. A first one involves the idea of a critical temperature gradient (or strong profile consistency) [1-3], an other one uses the idea of a global turbulent structures produced by a toroidal or a non-linear coupling of the unstable modes [4-6]. Numerical analysis of above mentioned heat pulses will be presented to assess which of these models is appropriate.

Experimental observations.

The 94/95 experimental campaign on JET gave examples of heat and cold pulses which were often initiated in the same shot. Figure 1 shows, for example, the evolution of the electron temperature during a cold pulse and subsequent sawtooth crashes for the H-mode shot #31341. The asymmetry in the speed of pulses which propagate inward and outward is clearly seen - the sawtooth crash heat pulse propagates outward in the usual diffusive way, while the cold pulse changes the behaviour of the electron temperature almost instantaneously in the whole outer half of the plasma column. The evolution of electron temperature during giant (type I) ELMs on JET, after a very short MHD phase, was shown to be very similar to that of the cold pulses [7]. Figure 2 shows temporal evolution of the main plasma parameters during the so called slow roll-over, the event which often terminates high performance phase of the hot ion H-mode on JET. All these transient phenomena were analysed in a semi-predictive way with the transport code JETTO, using either a "global" or a critical temperature gradient model of anomalous transport.

Transport models.

In our analysis we used a modified version of the RLW [2] critical temperature gradient model with:

$$\chi_{e,i}^{anom} = \alpha_{e,i}\chi_{RL}(\nabla T_e - \beta\nabla T_{crit})\theta(\nabla T_e - \beta\nabla T_{crit}) \qquad (1)$$

as an example of a critical marginality model. Here T_{crit} defined by $T'_c = (\frac{6}{q}\frac{\eta jB3}{nT1/2})1/2$, $\chi_{RL} = 2(1-\sqrt{\frac{r}{R}}\sqrt{1+Z_{ef}}\sqrt{\frac{T_e}{T_i}}\left[\frac{\nabla T_e}{T_e} + 2\frac{\nabla n_e}{n_e}\right]\frac{q^2}{\nabla qB_T\sqrt{R}}$ and numerical coefficients $\alpha_{e,i}$ and β were varied in order to test a different degree of profile consistency. The original RLW model has soft profile consistency with $\alpha_{e,i} = \beta = 1$. Analysis shows however that we should increase $\alpha_{e,i}$ up to ten times in order to be able to get fast propagation of the cold pulses (which corresponds to a strong profile consistency transport model). Simultaneously we should increase coefficient β to reproduce experimental temperature profile.

Our "global" model is based on the assumption that due to either toroidal or non-linear coupling plasma turbulence organises long correlated structures (with the radial correlation length being proportional to the plasma minor radius). In this case the magnitude of the transport coefficients depends not only on the local plasma parameters but also on the source of the turbulence near plasma edge (we will assume that plasma turbulence emerges near the separatrix due to either temperature or pressure gradients and propagates inside with the group velocity of the unstable waves). In order to reproduce such a behaviour, in further analysis we will assume that both electron and ion thermal diffusivities consist of a local gyrobohm term (which could be produced by the ITG instability, for example) and a global bohm-type term (produced by either ballooning or interchange instability near the separatrix) which depends on the relative electron temperature or pressure gradient near the separatrix [7]:

$$\chi_{e,i} = \alpha_{e,i}^{GB}\rho_i\left|\frac{\nabla T_e}{B_T}\right| + \alpha_{e,i}^{B}\left|\frac{\nabla nT_e}{nB_T}\right|a^2q^2\left|\frac{\nabla T_e(r\approx a)}{T_e(r\approx a)}\right| + \chi_{e,i}^{incl} \qquad (2)$$

where $\alpha_{e,i}^{GB}$, $\alpha_{e,i}^{B}$ are numerical coefficients. In a sense the global model is similar to the critical marginality one because the global confinement in both models depends on the plasma quantities near the separatrix. The main difference between the models is that transport properties of the global model are not symmetrical but depend on whether the transient phenomena are initiated near the edge or near the centre of the plasma column. Indeed, if we assume for simplicity that only the electron temperature is perturbed in the course of the heat pulse and that this perturbation is small $\delta T_e/T_e << 1$ we obtain the following equation for the evolution of δT_e:

$$\frac{\partial\delta T_e}{\partial t} \approx div\left\{\chi_e^{(0)}\frac{\partial\delta T_e}{\partial r} + \frac{\partial\chi_e^{(0)}}{\partial\nabla T_e}\nabla T_e\frac{\partial\delta T_e}{\partial r} + \frac{\partial\chi_e}{\partial T_e(r\approx a)}\nabla T_e\delta T_e(r\approx a)\right\} \qquad (3)$$

The first two terms in the right hand side of equation (3) describe the usual diffusive propagation of the heat pulse independently of the localisation of the pulse origin. The last term emerges from the global model and only if the heat pulse is initiated near the plasma edge. It works as a perturbation of the heat source and is distributed over the whole plasma

volume. As was discussed earlier, the characteristic time of propagation of such a heat source inward is controlled by the group velocity of the turbulence and it is much faster than the typical transport time $\tau \approx a^2/\chi$.

Result of numerical analysis.

We have performed a predictive numerical modelling of selected JET discharges with different kind of the pulses. The selection covers both the heat pulses, initiated near the plasma centre (caused by the sawtooth crash) and pulses initiated near the plasma edge (cold pulse, ELMs, L-H transition and slow roll-over).

Figure 3 compares the result of the numerical simulation of the cold pulse and sawtooth heat pulse with the corresponding experimental evolution from shot #31341. Direct comparison of the change in slope of the simulated electron temperature at different radii at the onset of the pulses shows, that the global model (2) can reproduce the observed asymmetry. The critical marginality model with soft profile consistency underestimates the speed of propagation of the cold pulse while the model with strong profile consistency overestimates the speed of the sawtooth heat pulse.However simulation of slow roll-overs seem to indicate that a combination of the global transport and ITG mode might be at work. The result of the numerical analysis of the central ion temperature evolution during the roll-over with different transport models is shown in Figure 4.

Conclusions.

In summary, even though the critical marginality models considered here can reproduce some of the features of the global and local transport, they seem to fail to reconstruct the asymmetry in the time scales observed during transient phenomena. A "global" model gives a better agreement with experimental results in these situations. However modelling of the slow roll-over indicates that a combination of the global turbulence, which dominates in the outer part of the plasma volume, and of the local ITG mode, which could be important at mid-radius, might be responsible of the variety of phenomena observed.

References.

[1] F. Romanelli, W.M. Tang and R.B. White, Nucl. Fusion 26, (1986), 1515;

[2] P.H. Rebut, P. Lallia, M. Watkins in Plasma Physics and Controlled Nuclear Fusion Research 1988 (Proc. 12th Int. Conf. Nice 1988), Vol. 2, IAEA, Vienna (1991) 191;

[3] W. Dorland et al., 15th Int. Conf. on Plasma Phys. and Contr. Nucl. Fus. Res., Seville, Spain 1994, CN-60/D-P-I-6;

[4] J.W. Connor, R.J. Hastie, J.B. Taylor, Proc. Roy. Soc. London Ser. A 365, 1(1979)

[5] F. Romanelli, F. Zonca, Phys. Fluids, B 5, (1993), 4081;

[6] J.G. Cordey et al., Plasma Phys. and Contr. Fusion, 36, suppl..(7A),(1994), A267;

[7] V. Parail et al., JET-P(95)49, to be published in Plasma Phys. and Contr. Fusion, 1996

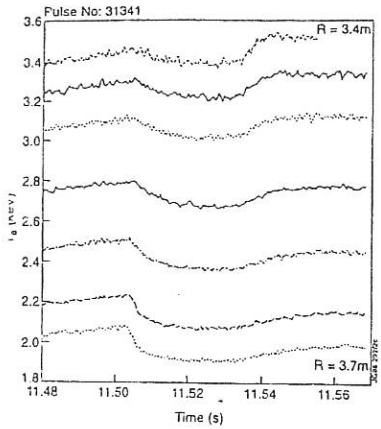

Figure 1. Experimental electron temperature evolution on different radii for the cold pulse followed by sawteeth heat pulses.

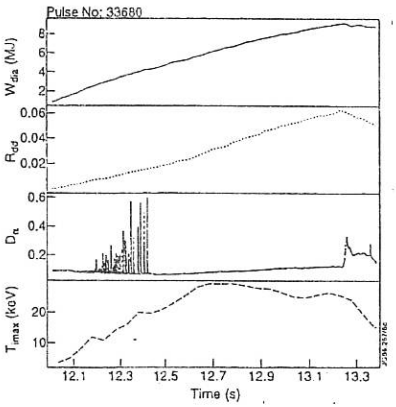

Figure 2. Evolution of the main plasma parameters in the hot ion H-mode which is terminated by the slow roll-over.

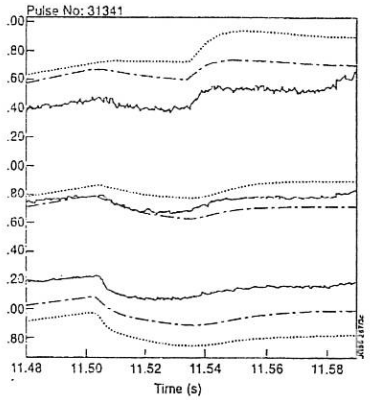

Figure 3. Comparison of the experimental electron temperature evolution (solid lines) with the simulated one: global model- chain, soft profile consistensy - dotted.

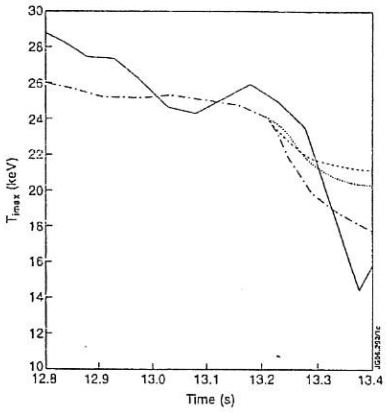

Figure 4. Temporal evolution of the central ion temperature during roll-over: solid- experiment, dashed - global model, dotted- ITG model, chain - combination of global and ITG models.

Figure captions.

H-mode Confinement Scaling and ELMs on COMPASS-D

M Valovič, C Silva[1], M Booth, J Dowling, S J Fielding, D A Gates, C Hunt,
S J Manhood, A W Morris, T Pinfold, M Price
and the COMPASS-D and ECRH Teams
UKAEA, Fusion, Culham, Abingdon, Oxon OX14 3DB, U.K.
(UKAEA/Euratom Fusion Association)

1. Introduction

Combination of good global energy confinement and steady power exhaust in a Tokamak is a difficult problem. Steady power exhaust require the presence of a substantial level of fluctuations at the edge such as continuous ELMs or L-mode turbulence. This edge 'noise', however, increases the transport to a considerable depth within the plasma. Moreover, the associated reduction of edge pressure leads to an unfavourable boundary condition for global transport. Quantitatively these two conflicting requirements on energy confinement have been formulated for ITER as [1, 2]:

$$H_H = \frac{\tau_E}{0.85 \times \tau_{E,ITERH93P}} \geq 1 \qquad (1)$$

$$\delta W/W < 0.8\% \quad during \ \delta t \leq 1ms\,(ELM), \qquad (2)$$

Criterion (1) sets a minimum energy confinement normalised to ITERH93P ELM-free H-mode scaling, with the factor 0.85 accounting for the reduction due to ELMs. Criterion (2) represents the maximum energy δW which can be tolerated by the divertor during a single event of energy loss.

The objective of this work is to compile a 0-D confinement database for COMPASS-D and compare it with the requirements (1) and (2). The data contains deuterium plasmas with ITER-similar geometry (Single Null Divertor, R=0.56m, a=0.17m, κ=1.6), Ohmic and ECR heating, fuelling by gas puffing and with boronised walls. Energy confinement data are obtained from diamagnetic measurement with typical accuracy of ±15%. The data are described in terms of plasma physics variables: normalised beta β_N, normalised collisionality $\nu^*=(R/a)^{3/2}qR/\lambda_{mfp}$ [3] and the role of atomic physics is represented here by the Hugill number defined as $N=n/n_{Gr}$ where $n_{Gr,20}=I_p(MA)/(\pi a^2)$ is the Greenwald limit. In these variables $\tau_{E,ITERH93P} \propto \tau_{Bohm}\, \rho^{*-0.7}\beta_N^{-1.2}\nu^{*-0.3}$, where $\rho^*\sim\rho/a$ is the normalised Larmor radius. This type of transport can be interpreted as Gyro-Bohm, due to pressure driven micro-instabilities [4]. The ITER operation point (β_N=2.4, ν^*=0.02, N=1.5) is outside the H-mode

[1]Permanent address: Instituto Superior Tecnico, Assosc. Euratom-IST, Lisboa, Portugal

Confinement database DB2 [5] and therefore it is desirable to investigate the experimental dependence of $H_H=F(\beta_N, \nu^*, N)$, particularly in the direction of this point.

2. H-mode Confinement

H-mode on COMPASS-D has been achieved so far only with the ion-gradB drift towards the X-point. Data occupy the intervals: (β_N=0.6-1.6, ν^*=0.015-7, N=0.1-0.6) and thus the ITER point has not been reached.

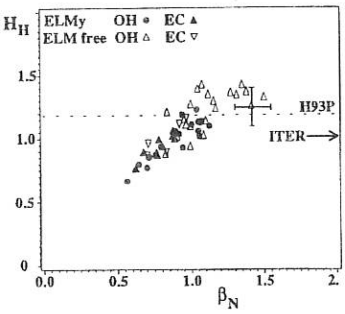

Figure 1. Normalised energy confinement in COMPASS-D H-mode as a function of β_N.

$H_H=F(\beta_N, \nu^*, N)$ shows no systematic dependence on ν^* and N and also no signs of decrease towards the ITER operational point. However, the relevant region ν^*~0.02 is sparsely populated and also ELMy data exists only for ν^*>0.3. The only systematic dependence of H_H appears on β_N, showing an increase up to β_N~1 (Fig. 1). The relevant ELMy plasmas which satisfy $H_H \geq 1$ exist only in a small interval around β_N=1. So far we have have been unable to extend this region towards higher β_N. Increasing β_N in OH plasma leads to ELM-free H-mode. With ECRH, ELMy plasmas have been achieved at ω_{ce} but, so far, an increase of power only results in a transition to the ELM-free regime.

3. ELMs

ELMs observed at β_N=1 are large and regular. It is of interest, therefore, to compare them with the ITER requirement on the maximum allowed energy loss per ELM (2). The energy loss is measured using the fast diamagnetic flux signal $\Delta\Phi$, corrected for poloidal vessel current and using box car averaging over a stationary ELMy period. The power loss is calculated as $P_L=<P_{OH}>-3\pi/\mu_0(d\Delta\Phi/dt)RB_T$. The contribution to P_L from the paramagnetic flux due to changes in plasma current and radial position during an ELM has been estimated using the m=0, 1 moments from internal Mirnov coils. These corrections are small (<15%). We also compare the power loss P_L with the power P_{div} flowing to the divertor as measured by an array of Langmuir probes. The approximation $P_{div}=\int 8\times j_{sat}\times(kT_e/e)dS$ is used where the integration over the surface S assumes toroidal symmetry. Figure 2 shows both power traces together with the D_α emission. Good agreement between P_L and P_{div} is found, suggesting that no substantial edge radiation losses are involved during the ELM. The power loss increases by a factor of ~5 over its average and this increase lasts about δt~200μs during which $\delta W/W \approx 4\%$ of the plasma energy is lost. Such an energy loss clearly exceeds the condition (2). One can

imagine three ways that these large ELMs may be extrapolated to lead to acceptable ELMs in ITER. The first is that the ELM duration scales with machine size. This, however, seems unlikely. The electron temperature during an ELM, measured by Langmuir probes at the X-point and also by a reciprocating probe at the top stagnation point, is T_e=40-55eV. Such temperatures provide a characteristic SOL time-scale of 0.5 L/c_s~150μs which is in agreement with the duration of energy loss δt. Here, L~20m is the connection length, $c_s=((T_e+T_i)/M_D)^{1/2}$ with $T_e=T_i$. The time $\delta t \sim L/c_s$, however, scales only weakly with machine size. The second possibility is a significant broadening of the wetted area during an ELM. On COMPASS, similarly to other divertor tokamaks, the wetted area at the divertor broadens only by a factor of 2 during the ELM. Finally the possibility exists that δW/W will decrease as one moves closer to the ITER operational point (β_N, ν*, N).

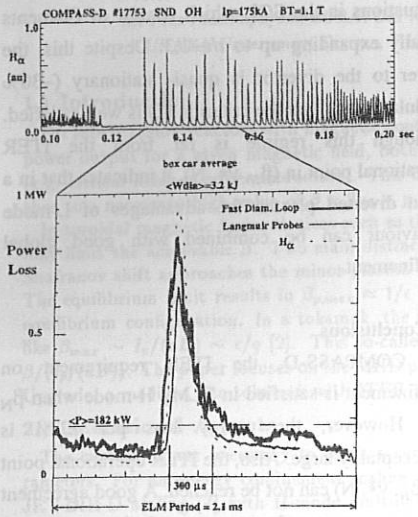

Figure 2. Modulation of power loss during an ELM.

4. L-mode Confinement

Good energy confinement is also achieved in L-mode in two different regimes: high density Ohmically heated plasma with ion-gradB drift away from X-point and low density high power ECRH at $2\omega_{ce}$. Figure 3 shows the normalised energy confinement $H_H=F(\beta_N, \nu^*, N)$ along the β_N and N-axes. For ECRH, $H_H>1$ above $\beta_N \approx 1$. These plasmas show a deviation from the ITERH93P scaling over the whole range of data. There is no saturation of H_H for $\beta_N \geq 1$ and also there is a strong decrease of H_H with increasing ν*. The low collisionality, ν*=0.004–0.01 due to the high electron temperature and low density ($T_{dia} \leq 10$keV, $n_e<1.5\times 10^{19}m^{-3}$) could be responsible for this anomaly. For high β_N, the contribution of non-thermal electrons may also be substantial. The high density Ohmically heated plasmas were achieved during dedicated experiments where q_{95}=3.0 was kept constant and the toroidal field varied from 0.9 to 1.3 T. Fresh boronisation was applied. The maximum values of β_N were limited by the maximum achievable density, which in most cases was due to the limited duration of the discharge and the finite gas puffing rate. The high β_N is, however, achieved at the expense of very high collisionality ν*=1–10. The normalised energy confinement saturates above

β_N~1, at a level H_H=0.9. These values still marginally satisfy the ITER confinement criterion (1). No degradation of H_H=F(N) in the direction of the ITER point is observed over the limited range of data (Fig. 3). In this regime, fast (40kHz) videos of the plasma reveal large fluctuations in the SOL which consist of filaments radially expanding up to r/a~1.3. Despite this, the power to the divertor is quasi- stationary (~30% modulation) so that the criterion (2) is well satisfied. Although this regime is far from the ITER operational point in (β_N, ν*, N), it indicates that in a clean diverted plasma the advantages of L-mode behaviour can be combined with good global confinement.

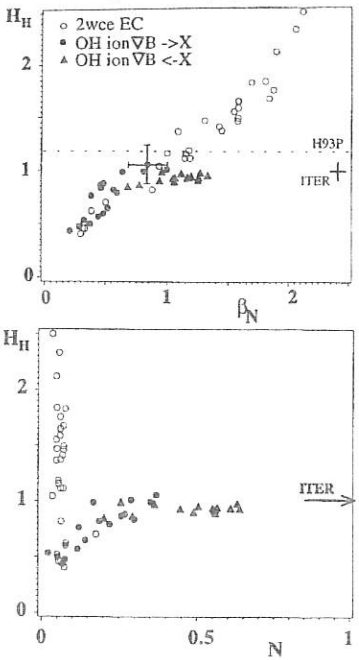

Figure 3. Normalised energy confinement in L-mode as a function of β_N and Hugill number N.

6. Conclusions

On COMPASS-D, the ITER requirement on confinement is satisfied in ELMy H-mode when β_N =1. However, the energy loss per ELM is unacceptably large. Also, the ITER operational point in (β_N, ν*, N) can not be reached. A good agreement between energy loss measured by very fast diamagnetic loop and Langmuir probes during an individual ELM indicates that all energy loss during the ELM is conducted to the target. L-modes can be generated in COMPASS-D, with good confinement, H_H=0.9, satisfying the ITER requirement.

Discussions with J W Connor are gratefully acknowledged. This work was jointly funded by the UK Department of Trade of Industry and Euratom.

[1] G Janeshitz *et al*, *Plasma Phys. Control. Fusion* **37** (1995) A19
[2] ITER Team, *Design Description Document, Plasma Physics*, June 1995
[3] $\nu^*=(R/a)^{3/2}q_{95}Rne^2Z_{eff}ln\Lambda/(12\pi^{3/2}\varepsilon_0^2T^2)$, $T=1/3(W/Vol)/(en)$,
see also F Perkins et al. *Phys. Fluids* **B5** (1993) 477
[4] J W Connor and H R Wilson, *Plasma Phys. Control. Fusion* **36** (1994) 719
[5] ITER H-mode Database Working Group, *Nucl.Fusion* **34** (1994) 13

β-Limiting Phenomena in ASDEX Upgrade

H. Zohm, M.Alexander, *R. Buttery, S. de Peña Hempel, O. Gruber, *T.C. Hender, T. Kass, M. Maraschek, W. Sandmann, S. Sesnic, M. Sokoll, A. Stäbler, *H.R. Wilson, H.P. Zehrfeld, ASDEX Upgrade Team, NBI-Group

MPI für Plasmaphysik, EURATOM Association, D-85748 Garching, Germany

** UKAEA Government Divison, Fusion, Culham, Abingdon OX143DB, UK*

1.) Introduction

For future fusion reactors with magnetic confinement it is necessary to maximize the fusion power output for a given magnetic field, both for economic as well as for technical reasons (e.g. critical fields of superconductors). This directly translates to a high stored energy and thus to a necessary high value of $\beta = 2\mu_0 < p > / B^2$ [1].

In toroidal magnetic fusion devices such as the tokamak or the stellarator, different factors may limit the achievable β. Two main distinct reasons are the equilibrium limit (when the Shafranov shift approaches the minor plasma radius) and the β-limit due to MHD activity. The equilibrium limit results in $\beta_{p,max} \approx 1/\epsilon$ and can thus be avoided by chosing a proper equilibrium configuration. In a tokamak, the second limit has been shown to roughly scale like $\beta_{max} \sim I_p/(aB) \sim \epsilon/q$ [2]. This so-called Troyon-limit led to the definition of $\beta_N = \beta/(I_p/(aB))$. The paper focuses on the MHD phenomena giving rise to the β-limit in ASDEX Upgrade, a medium size tokamak with ITER relevant geometry [3].

2.) Operational Aspects

The heating power necessary to reach a certain β depends on plasma geometry and parameters. For an energy confinement scaling $\tau_E \sim 0.05 \times H I_p R^{3/2}/P^{1/2}$ (derived from the JET-DIII-D scaling [4] with H-mode multiplier H), we obtain for ASDEX Upgrade ($R = 1.65$ m, $a = 0.5$ m, $\kappa = 1.6$) $P(\beta_N) = 2.15(\beta_N/H)^2 B_t^2$. With an available heating power of 10 MW, using $\beta_{N,max} \approx 3$ and $H \approx 2$, β-limit studies can only be conducted at $B_t \leq 1.5$ T unless improved confinement occurs. Thus, our database is acquired at $B_t \leq 1.9$ T.

For the discussion of neoclassical tearing modes, the collisionality $\nu^* = \nu q R/(2\epsilon v_{\|})$ is an important parameter. It scales like $\nu^* \sim (n/T^2)(qa/\epsilon^2)$ whereas $\beta \sim nT/B^2$. Thus, at constant β, we find $\nu^* \sim (an^3/B^4)(q/\epsilon^2)$ and we have to use a scaling $n \sim B^{4/3}/a^{1/3}$ to match ITER in the dimensionless numbers β, ν^*, ϵ and q. For ITER parameters $B_t = 5.7$ T, $n = 1.25 \times 10^{20}$ m^{-3} and $a = 2.8$ m, we find that an ASDEX Upgrade shot at 1.5 T should be run at $n = 0.38 \times 10^{20}$ m^{-3}. The lowest possible density in ELMy H-mode is proportional to I_p, which itself is fixed by the requirement $q = 3$. For the example above (corresponding to $I_p = 0.8$ MA) the minimum density is about 0.5×10^{20} m^{-3}. Therefore, we cannot run at exactly the ITER dimensionless parameters: at the right q, the collisionality is higher by a factor of $(0.5/0.38)^3 = 2.4$. Increasing the density will increase this factor $\sim n^3$.

The β-limit may either occur as a saturation (W does not follow a rise in P), as a β-drop (W decreases with increasing P) or as a β-limit disruption. It has been shown before that in ASDEX Upgrade, below $q = 3$, the β-limit is disruptive whereas above $q = 3$, a saturation or drop occurs [5]. In [5], only the energy from magnetic reconstruction was considered; we have now found good agreement between these values and the total kinetic energy. From the Troyon-scaling, we would expect $\beta_{N,max} \neq f(q)$. In ASDEX Upgrade, we usually find $\beta_{N,max} \approx 3$ for $q \geq 3$, but for $q \leq 3$, $\beta_{N,max}$ drops with q to values around 2 for $q \rightarrow 2$ [5]. The highest values of β_N were achieved with the highest triangularity ($\delta \approx 0.4$). In this configuration, we transiently achieve $\beta_N \approx 3.3$ without I_p ramp.

Another extension of the Troyon-scaling has been proposed in DIII-D by including ℓ_i into

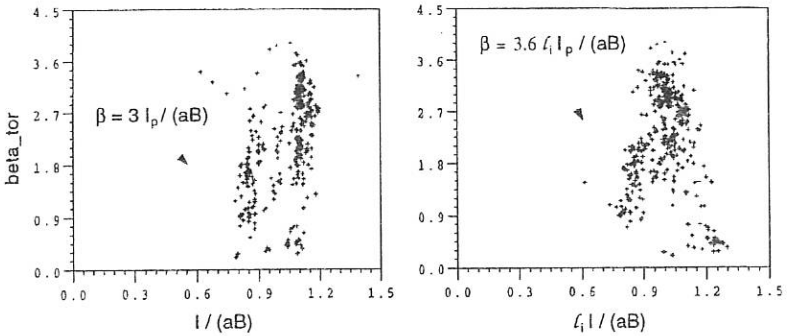

Figure 1: *Plot of β against the normalization $I_p/(aB)$ (left) or $\ell_i I_p/(aB)$ (right). Including ℓ_i can account for the high β cases obtained in I_p ramp-down experiments.*

the scaling [6]. In ASDEX Upgrade, we have varied ℓ_i by I_p ramp-down and thus achieved the highest values of $\beta_p \approx 3$ and $\beta_N \approx 4.5$. As shown in Fig. 1, including ℓ_i into the scaling also provides a reasonable fit to the ASDEX Upgrade data. Note that, due to a slightly different definition, our ℓ_i is about 10 % smaller than that of DIII-D.

3.) MHD Mode Behaviour at the β-limit

An analysis of the ideal kink stability of typical ASDEX Upgrade high β equilibria using the ERATO code [7] reveals stability for $\beta_N \leq 3.5$ even without a conducting wall with the limit given by the (2,1) mode. Including the ASDEX Upgrade vacuum vessel stabilizes this mode up to $\beta_N \approx 4.1$. The (3,2) mode appears at $\beta_N \approx 3.7$ without wall, but can also be wall-stabilized here. However, for $\beta_N = 4.1$, it cannot be stabilized and now dominates the mode pattern. The pressure gradient is usually below the critical gradient for ideal ballooning except at the plasma edge, where it is linked to the occurrence of type I ELMs in these discharges. Thus, ideal MHD cannot explain the usual limit of $\beta_N \leq 3.3$.

In the experiment, we can distinguish two types of mode activity giving rise to a β-limit:

$q = 1$ activity: β-saturation is mostly connected to activity on the $q = 1$ surface. This is often a continuous (1,1) mode which probably is connected to a (1,1) island (as it may last for several 100 ms, a time scale on which an internal kink should form an island). This mode leads to a saturation of β_N. In discharges with high beam power at nearly perpendicular injection, we also see fishbone bursts with a dominant (1,1) structure, but also higher helicity components [8]. Occurrence of repetitive fishbones may lead to a drop of β_N by less than 10 %. Usually, sawteeth persist, but their repetition rate slows down. The sawtooth losses do not play a significant role in the β-limit.

$q > 1$ activity: In addition to the (1,1) activity, we often see tearing modes on surfaces with $q > 1$. An example for a time sequence is given in Fig. 2. Here, initially a (1,1) mode exists. At $t = 1.84$ s, a (4,3) mode develops and, 40 ms later, a (3,2) develops. From the plot of the amplitudes of the different modes, it can be seen that the $q > 1$ islands drive the initial (1,1) mode and produce higher harmonics with equal toroidal mode number via toroidal mode coupling. During this sequence, β_N can drop significantly (by up to 30 %).

These tearing modes at high β are usually attributed to the neoclassical tearing mode where the island is driven nonlinearly by the loss of bootstrap current due to a flattening of the pressure inside the island [9]. In a more recent theory [10], it is found that, due to diamagnetic stabilization, a threshold island width W_{thr} exists below which no neoclassical

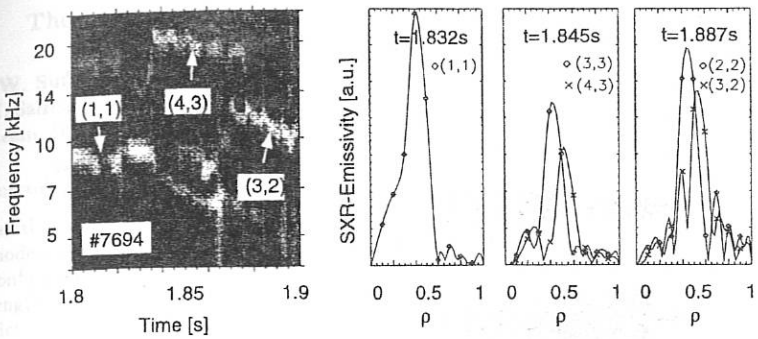

Figure 2: *Typical sequence of resistive modes at the β-limit. The left plot shows SXR-signal frequencies as a function of time, the right plots show the amplitudes of various modes from a deconvolution of SXR line integrals.*

island will occur and thus one needs a 'seed island' of $W > W_{thr}$ to start neoclassical tearing. For $\nu_i/(\epsilon\omega_{*pe}) < 1$, this width is greatly reduced. To check this theory in ASDEX Upgrade, we performed a β-limit experiment where, at fixed I_p and B_t, the density was increased by a factor of 2. Following the scaling above, this corresponds to a change in ν^* by a factor of 8. Although there was no pronounced effect on $\beta_{N,max}$, the MHD behaviour changed: at the lowest collisionality, the rise in β was limited by (1,1) activity whereas at the highest collisionality, the sequence shown in Fig. 2 involving neoclassical tearing modes occured. For the whole collisionality scan, we are in the regime $\nu_i/(\epsilon\omega_{*pe}) < 1$, but due to $W_{thr} \sim \rho_{pi}$, the threshold island size decreases at constant β but lower temperature. It turns out that a comparison of local parameters at the (3,2) surface yields good agreement with this theory, assuming a seed island width of $\approx$ 2 cm [11]. The onset of such tearing modes usually coincides with ELMs or sawteeth, therefore it is likely that a seed island of the right helicity is produced by these events.

To independently prove that the observed islands are of neoclassical origin, we calculated the difference in bootstrap current ΔI_{bs} for a typical pressure profile at the β-limit when the pressure is flattened at the (3,2) surface in a region of 5 cm (corresponding to the saturated island width estimated from Mirnov analysis). Then, we calculate the width of the magnetic island produced by a helical current of magnitude ΔI_{bs} (for an 800 kA discharge at the β-limit, $\Delta I_{bs} \approx 3.5$ kA). The island width calculated in this manner is close to the 5 cm we started with, indicating that this would be a saturated neoclassical island. Also, these islands often grow linearly in $\tilde{B}$ for $\approx$ 10 ms, which is another feature of the neoclassical tearing mode [9]. Finally, for reasonable current profiles, one would always expect $\Delta' < 0$ for the (4,3) mode, so we have to rely on the neoclassical drive.

An interesting difference between the $q = 1$ and the $q > 1$ activity is their influence on the toroidal plasma rotation. Fig. 3 shows an example where a $q = 1$ limit occurs ($t = 1.3$ s). An increase in beam power leads to another rise in β followed by a drop due to the occurence of a (3,2) tearing mode. Only the (3,2) mode leads to a significant drop of toroidal rotation of the core (inside the (3/2) surface). This may be explained by an increase in the viscosity due to the MHD activity, and also by the interaction of the rotating (3,2) mode with the resistive wall and the static error field. Both effects would be much more pronounced for the (3,2) mode than for the (1,1) mode. Note that, as stated above, the (3,2) has a bigger effect on

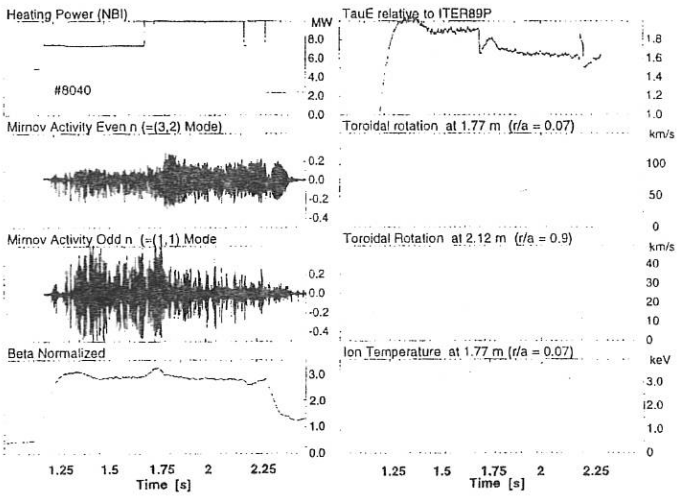

Figure 3: *β-limit by (1,1) activity (1.3 s) and then by a (3,2) tearing mode (1.78 s). The (3,2) mode has a significant influence on toroidal rotation of the core.*

confinement then the (1,1), as indicated by the decreased H-mode multiplier (for the same T_i and density, one needs more beam power).

Thus, we conclude that the β-limit with $q > 1$ mode activity in ASDEX Upgrade is mainly given by the stability of the neoclassical tearing mode. This is especially important as these modes sometimes 'accidentally' occur at β_N-values well below the values stated above, maybe due to a change in Δ' or due to an especially large seed island (there are examples down to $\beta_N = 2.4$). The β-drop introduced can be restored by increasing the heating power, but at the expense of a reduced confinement due to the mode as shown in Fig. 3.

Finally, it should be noted that β-limit disruptions in ASDEX Upgrade happen only several 100 ms after the occurrence of the actual β-limit and seem to be due to a loss of confinement caused by the (3,2) mode with subsequent H-L transition, and the occurrence of a MARFE causing a (2,1) mode. Thus, a typical β-limit disruption, as has been identified in TFTR [12], does not appear in ASDEX Upgrade, even at the lowest q-value of 2.3.

[1] ITER-JCT and Home Teams, Plasma Phys. Controlled Fusion **37** (1995) A19.
[2] TROYON, F. et al., Plasma Phys. Controlled Fusion **26** (1984).
[3] KÖPPENDÖRFER, W. et al., 14th IAEA Conference, IAEA-CN-56 / A-2-3 (1992).
[4] SCHISSEL, D. et al., Nucl. Fusion **31** (1991) 73.
[5] ZOHM, H. et al., Plasma Phys. Controlled Fusion **37** (1995) A313.
[6] LAO, L. L. et al., 14th IAEA Conference, Würzburg, IAEA-CN-56 / A-7-19 (1992).
[7] LÜTJENS, H. et al., Comput. Phys. Commun. **69** (1992) 287.
[8] KASS, T. et al., 22nd EPS Conference, Bournemouth **IV** (1995) 41.
[9] CHANG, Z. et al., Phys. Rev. Lett. **74** (1995) 4663.
[10] WILSON, H. et al., Phys. of Plasmas **3** (1996) 248.
[11] WILSON, H. et al., this conference, to appear in Plasma Phys. Controlled Fusion (1996).
[12] FREDERICKSON, E. et al., Phys. of Plasmas **2** (1995) 4216.

The Role of Edge parameters for L-H Transitions and ELM Behaviour on ASDEX Upgrade

W. Suttrop, H. J. de Blank, G. Haas, H. Murmann, O. Gehre, H. Reimerdes, F. Ryter, H. Salzmann, J. Schweinzer, J. Stober, H. Zohm, ASDEX Upgrade team, NBI team, ICRH team, Max-Planck-Institut für Plasmaphysik, EURATOM Association, D-85748 Garching

Introduction

Local plasma parameters play an important role for transition to high-confinement mode (H-mode) since loss mechanisms which drive the radial electrical field associated with improved confinement [1] critically depend on collisionality and ion temperature and density gradient lengths at the plasma edge. However, partly due to diagnostical difficulties, the clearest picture of L- to H-mode transitions exists so far with respect to global quantities [2, 3]. Few measurements of local parameters have been reported as yet, including an early observation of constant T_e at L-H and H-L transitions on ASDEX [4]. More recent results of JET [5] and of a parameter scan on DIII-D [6] agree on the role of edge temperature as a critical parameter but are ambiguous about the dependence on B_t. Edge Localized Modes (ELMs), always observed during stationary H-mode, impose a stability limit on the edge pressure gradient, but ELM parameters (e.g. ELM type) themselves depend on edge conditions.

Here, we report local T_e, T_i and n_e measurements made at the plasma edge of ASDEX Upgrade at L-H and H-L transitions and ELMs in an attempt to describe the local edge parameter space of L-mode, L-H transitions, and H-mode with various ELM types. A detailed quantitative comparison of edge T_i, n_e, T_e profiles and neutral flux measurements with transition theory for a limited number of dicharges is addressed in a separate paper [7].

For the present investigation, a set of 98 discharges is randomly selected from recent ASDEX Upgrade deuterium discharges with similar geometry (lower single null, ion-∇B direction towards the X-point, $R = 1.65$ m, $a = 0.5$ m, elongation $\kappa \approx 1.7$, triangularity $\delta \approx 0.07$). Varying discharge parameters are $B_t = 1.5 \ldots 3$ T, $I_p = 0.6 \ldots 1.2$ MA, $P_{NBI} = 2.5 \ldots 7.5$ MW, and $P_{ICRF} = 0 \ldots 2$ MW. The set contains shots with and without Neon impurity gas puff. Diagnostics include DCN FIR laser interferometry and Li beam for density measurements, 16-channel Thomson scattering and 45-channel ECE radiometry for electron temperature measurements, and two ionization gauges installed near the divertor and in the main chamber to measure the neutral gas flux.

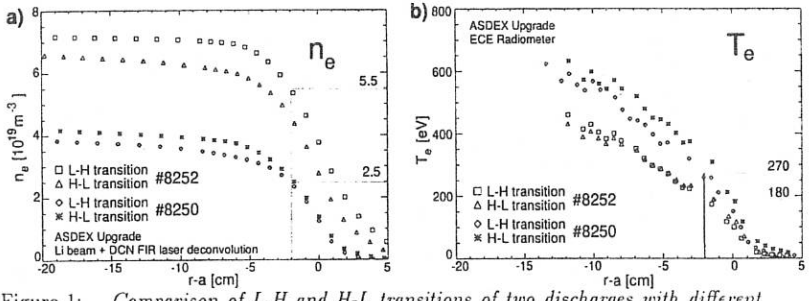

Figure 1: *Comparison of L-H and H-L transitions of two discharges with different line averaged density a) electron density b) electron temperature profiles*

L-H and H-L transitions

We first consider an example to illustrate the relevance of local parameters at the L-H and H-L thresholds. Fig. 1 shows a pair of discharges (ASDEX Upgrade #8250, #8252) with electron density varied and otherwise identical parameters (B_t = 2.5 T, I_p = 1.0 MA). Slow L-H transitions are achieved by switching a 2.5 MW neutral beam at 34 Hz rate. Line averaged densities (in $10^{19}\mathrm{m}^{-3}$) / NBI duty cycles at the L-H and H-L transitions are 3.9/50% (#8250, L-H), 7/100% (#8252, L-H), 4/30% (#8250, H-L), and 6.4/30% (#8252, H-L). Edge densities of the two discharges differ by a factor of 2.5 (Fig.1 a). The edge electron temperature (Fig.1 b), taken at 2 cm inside the nominal separatrix, differs by 50% for the two shots, where a higher temperature is found at lower density. The difference in T_e between L-H and H-L transitions is small, of the order of few percent, with the tendency of lower ratio T_e/n_e at L-H compared to H-L.

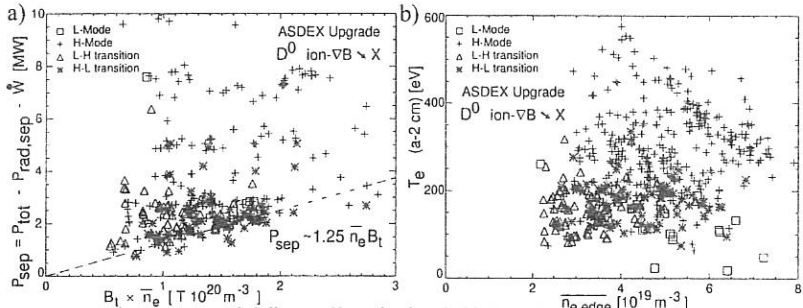

Figure 2: *Comparison of different H-mode threshold dependencies a) P_{sep} vs. $\overline{n_e}B_t$. b) T_e (edge) vs. $\overline{n_e}$ (edge)*

We now compare the global scaling of $P_{sep} = P_{tot} - dW/dt - P_{rad,sep}$ with the dependence of edge T_e on edge density for the set of 98 recent discharges characterized above. Fig. 2 a) shows P_{sep} as a function of $\overline{n_e}B_t$ for L-H, H-L transitions, stationary H-mode, and few L-mode phases with auxiliary heating. The dashed line represents the scaling of P_{sep} (MW) = $1.25\overline{n_e}$ (10^{20} m^{-3}) B_t (T) derived from earlier ASDEX Upgrade discharges [8]. Although there is a fair agreement with the global $\overline{n_e}B_t$-scaling, several data points depart, which probably reflects the difficulties to determine accurately the fraction of power radiated from inside the separatrix and dW/dt during fast changes of heating power. Fig. (Fig. 2 b) shows a plot of edge electron temperature T_e at $r = a - 2$ cm (obtained by interpolation of two adjacent Thomson channels) vs. edge line-averaged density $\overline{n_{e,edge}}$ for the same data set. A radial position 2 cm (corresponding to $\rho_p = 0.97$) inside the nominal separatrix is selected, because it is believed to be relevant for transition physics but sufficiently distant from the separatrix to avoid T_e being entirely determined by the heat flux to the divertor. There is a large scatter in the T_e data, but no significant dependence on $\overline{n_{e,edge}}$ and also no significant difference in T_e for L-H and H-L transitions is observed. Values of $T_e(r = a - 2$ cm) at the transition center around $\approx$ 160 eV, with T_e above during H-mode and below during L-mode. H- and L-modes can exist over the entire experimental edge density range of $2 \ldots 7 \times 10^{19}\mathrm{m}^{-3}$.

At high neutral densities (main chamber neutral flux $\Gamma_0 \geq 5 \times 10^{21}\mathrm{m}^{-2}\mathrm{s}^{-1}$). L-modes are

obtained even for high heating power (P_{tot} = 8 MW). This illustrates that H-mode can be inaccessible above certain neutral densities. However, since these discharges also have high n_e, high bulk radiation and low edge T_e, it is not exactly clear which mechanism causes this effect.

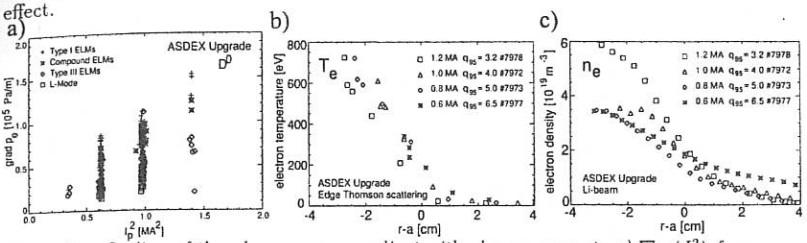

Figure 3: *Scaling of the edge pressure gradient with plasma current: a) $\nabla p_e(I_p^2)$ for a set of discharges, b) edge T_e and c) n_e profiles measured for q_a varied by I_p variation.*

Edge Localized Modes

Following the DIII-D classification [9], ELMs of type I and III are observed on ASDEX Upgrade [10]. In addition, compound ELMs exist which are identified as ELM events with subsequent brief transition to L mode [11]. As for pressure gradient driven instabilities, one would expect that edge n, T profiles reflect the stability limit of type I ELMs at [12, 10] and type III ELMs below the ideal ballooning limit [13]. In the first stability region at high shear or in the cylindrical approximation, the normalized pressure gradient $\alpha = 2\nabla p \mu_0 R q^2 / B_t^2$ at the ideal ballooning limit is approximately proportional to the normalized shear $S = (dq/dr) \times (r/q)$ [14]. Assuming that S is approximately independent of q_a, one would expect the maximum $\nabla p = \nabla p_{crit}$ to be proportional to I_p^2 and independent of B_t. This is indeed observed for the set of discharges as shown in Fig. 3 a). For given I_p, highest pressure gradients are observed during type I ELMy H-mode. Pressure gradients in phases with type III ELMs are significantly lower but still above ∇p_e in L-mode. An I_p-scan (Fig. 3 b, c) with otherwise identical parameters (P_{NBI} = 5 MW, B_t = 2.5 T) reveals that the change in ∇p is almost entirely due to different edge densities, while edge T_e profiles change much less with I_p, consistent with expectation that $\tau_p \propto I_p$. For all discharges except at I_p = 0.6 MA gas puff was switched off during H-mode.

Apart from stability limits imposed by ELMs on the edge pressure gradient, the occurrence of the various ELM types can be parametrized by local edge quantities. Fig. 4 a) shows the edge electron pressure gradient normalized to I_p^2 vs. T_e at $r = a - 2$ cm for the set of discharges in deuterium. Type I ELMs mainly populate the region above $\nabla p_e / I_p^2 = 1.5 \times 10^5$ Pa/m/MA^2 and $T_e(a - 2cm) \approx 300$ eV while type III ELMs predominate below. From a plot of T_e vs. n_e at $r = a - 2$ cm (Fig. 4 b) one sees that type III ELMs occur at lower T_e than type I ELMs but both types are observed independent of density. At high resistivity, type III ELMs are destabilized at lower pressure gradient than type I ELMs, while at low resistivity, the fixed stability limit of type I ELMs is reached first, consistent with the picture of a resisitive instability [11]. Compound ELMs appear mainly at high edge density (or high neutral gas flux, which is correlated), regardless of B_t, which varies by a factor of 2 in the set. They are found either at intermediate or at low pressure gradient, and can therefore be attributed to type I ELMs or type III ELMs, respectively, followed by a brief L-mode period.

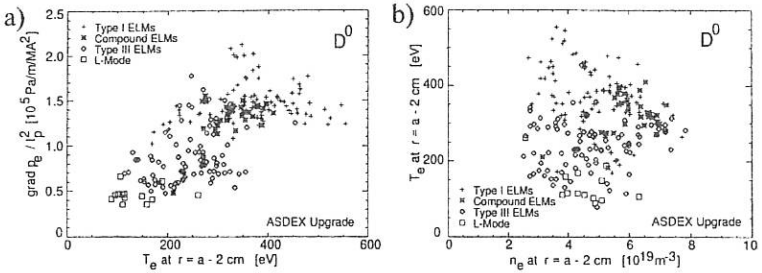

Figure 4: *Occurrence of various ELM types a) $\nabla p_e / I_p^2$ vs. T_e and b) T_e vs. n_e*

Conclusion

On ASDEX Upgrade, T_e at the edge at L-H and H-L transitions is found to be independent of a number of plasma parameters, in particular P_{tot}, B_t, I_p, although there is considerable scatter ($\pm 30\%$) in the data set. Also, no density dependence is obvious from the data set. However, comparison of individual discharges shows that T_e and T_i decrease by $\approx 50\%$ when the edge density is raised by a factor of 2.5. This finding indicates a possible weak dependence of T_e and T_i on density, but also implies that L-H transitions are obtained at very different edge collisionalities. More detailed measurements are necessary to check whether the departure from constant T_e found on other experiments [4, 6] is significant. There is only a weak difference of T_e at the L-H and H-L transitions, indicating that the hysteresis in P_{tot} is owed mainly to the change in confinement. At highest neutral densities, the H-mode is quenched even at high heating powers. This may indicate that an upper limit to neutral densities in H-mode exists, but the mechanism still has to be identified.

A much clearer picture exists with respect to ELMs. As expected for ideal ballooning, $\nabla p_{e,max} \propto I_p^2$ for type I ELMs. ∇p_e is significantly below $\nabla p_{e,max}$ for type III ELMs. The occurrence of ELM types depends on edge T_e, but not density. Consistent with resistive modes, type III ELMs are found at lower T_e than type I ELMs.

References

[1] Itoh, K. and Itoh, S.-I. 1996 Plasma Phys. Contr. Fus. **38**, 1
[2] Ryter, F., H-Mode Database Working Group 1995 IPP-4/269
[3] Carlstrom, T. N., 1995 IAEA H-Mode workshop, Princeton, GA-A22191
[4] ASDEX Team, 1989 Nucl. Fusion **29**, 1959
[5] Righi, E. *et. al.* 1995 Proceedings of the 22nd EPS Conf. on Contr. Fusion and Plasmaphys., Bournemouth, Vol. 19C, p. II-073
[6] Groebner, R. J., 1995 IAEA H-Mode workshop, Princeton, GA-A22184
[7] de Blank, H. *et. al.* 1996 *this conference*
[8] Kallenbach, A. *et. al.* 1995 Proceedings of the 22nd EPS Conf. on Contr. Fusion and Plasmaphys., Bournemouth, Vol. 19C, p. II-005
[9] Doyle, E. J. *et. al.* 1991 Phys. Fluids **B3**, 2300
[10] Suttrop, W. *et. al.* 1995 Proceedings of the 22nd EPS Conf. on Contr. Fusion and Plasmaphys., Bournemouth, Vol. 19C, p. III-237
[11] Zohm, H. 1996 Plasma Phys. Control. Fusion **38**, 105
[12] Gohil, P. *et. al.* 1995 Phys. Rev. Lett. **61**, 1603
[13] Zohm, H. *et. al.* 1995 Nucl. Fusion **35**, 543
[14] Wesson, J. 1987 Tokamaks (Oxford), p. 156

Three Dimensional Computation of Collisional Drift Wave Turbulence and Transport in Tokamak Geometry

B Scott

Max-Planck-IPP, Garching, Germany

Computations of fluid drift turbulence in a nonlocal model tokamak geometry are presented. Profiles and fluctuations interact with each other self-consistently. A self-consistent limiter scrape-off layer (SOL) is incorporated. Electron drift wave dynamics dominate the fluctuation energetics. Parallel correlation lengths in the SOL are in agreement with experimental observations, even though the dynamics is still three-dimensional. The results reproduce well the qualitative and quantitative properties of observed fluctuations, but predict overly strong transport in the SOL.

It is of general interest to directly simulate the process of anomalous transport of thermal energy and particles in a magnetically confined plasma, with a fluid model system of equations. Ideally, the domain of computation would extend from center to edge, and the run time would be of order a global confinement time. As this is not yet feasible, the traditional approach is to carry a computation for a small domain whose extent perpendicular to the magnetic field lines is much less than the profile scale length, $L_\perp$. The fluctuation dynamics would be local, with profiles given as system parameters. An alternative approach is to carry an intermediate domain, whose extent is one or two $L_\perp$, so that the system's thermodynamics can be studied while still faithfully representing the scale, $\Delta \ll L_\perp$, at which the turbulence actually occurs [1]. This is already feasible for small tokamaks, from which we have the best data.

The computations are done in the geometry of an axisymmetric tokamak, with shifted-circular flux surfaces and a toroidal limiter in an outer portion. The reference flux surface is the last closed flux surface (LCFS), with minor and major radii a and R_0, and volume $V_a = 2\pi^2 a^2 R_0$. The coordinate system begins with the Hamada (V, θ, ζ), with θ and ζ periodic on $[0, 1]$, and then transformed via $\xi = \zeta - q\theta$, with $q(V)$ the field line pitch parameter. Only one contravariant component of the magnetic field, $B^\theta = \chi'$, with $\chi(V)$ the poloidal flux, is nonzero. The field line connection length is $L_\parallel = B_0/\chi' \approx 2\pi q R_0$, with B_0 the average field strength. The periodicity constraint, $f(V, \theta + 1, \xi - q) = f(V, \theta, \xi)$, serves as the boundary condition in θ in the closed field line region; in the SOL the standard Debye sheath model is used. The dependent variable V-derivatives are assumed to vanish on inner and outer boundaries, at which sources are prescribed. Domain sizes are quoted in terms of V_a and a toroidal periodicity, k_0, in terms of which ξ is periodic on $[0, k_0^{-1}]$, equivalent to keeping only multiples of k_0 in a Fourier expansion in ξ (as well as mode zero). This amounts to a flux-tube truncation which retains the periodicity constraint.

The equations are those of Braginskii [2], with perpendicular dissipation neglected and with a model for electron and ion Landau damping in the form of limits placed on the parallel dissipation. The ions are cold. The electrostatic drift approximation is used, such that a parameter $\delta_0 = \rho_0/a \ll 1$, with a the area-averaged minor radius of the LCFS and ρ_0 the ion gyroradius at reference parameters [n_0, T_0, and B_0 at $r/a = (V/V_a)^{1/2} = 1$]. This gives the electron and ion perpendicular velocities and heat fluxes in terms of their

drifts: $\mathrm{v}_\perp{}^\mu = \mathrm{v}_E^\mu + \mathrm{v}_*^\mu$ with $ne\mathrm{v}_*^\mu = \hat{F}^{\mu\nu}\nabla_\nu p_e$ and $\mathrm{q}_{e\wedge}^\mu = (5/2e)nT_e\hat{F}^{\mu\nu}\nabla_\nu T_e$ for the electrons, and $\mathrm{u}_\perp{}^\mu = \mathrm{v}_E^\mu$ for the ions, where $\mathrm{v}_E^\mu = -\hat{F}^{\mu\nu}\nabla_\nu\phi$ is the ExB velocity of both, and $\hat{F}^{\mu\nu} = (c/B^2)\epsilon^{\mu\nu}{}_\eta B^\eta$ is the drift operator. The ion polarisation drift, due to the inertia, is retained: $\mathrm{v}_p^\mu = -\hat{F}^\mu{}_\nu\left[(\partial/\partial t) + \left(\mathrm{v}_E^\eta + u_\parallel b^\eta\right)\nabla_\eta\right]\mathrm{u}_\perp{}^\nu$, where $u_\parallel = b^\mu u_\mu$ and $b^\mu = B^\mu/B$. The equations appear as

$$
\begin{aligned}
-\nabla_\mu ne\mathrm{v}_p^\mu &= \nabla_\mu\left(b^\mu J_\parallel - ne\mathrm{v}_*^\mu\right)\\
\frac{\partial n}{\partial t} &= -\nabla_\mu n\left(b^\mu v_\parallel + \mathrm{v}_\perp{}^\mu\right)\\
1.5\frac{\partial T_e}{\partial t} &= -1.5\left(b^\mu v_\parallel + \mathrm{v}_\perp{}^\mu\right)\nabla_\mu T_e - T_e\nabla_\mu\left(b^\mu v_\parallel + \mathrm{v}_\perp{}^\mu\right) - n^{-1}\nabla_\mu\left(b^\mu q_{e\parallel} + \mathrm{q}_{e\wedge}^\mu\right)\\
\frac{\partial u_\parallel}{\partial t} &= -\left(b^\mu u_\parallel + \mathrm{v}_E^\mu\right)\nabla_\mu u_\parallel - (nM_i)^{-1}\left(\nabla_\parallel p_e + \nabla_\mu b^\mu nM_i D_{i\parallel} b^\nu\nabla_\nu u_\parallel\right)\\
J_\parallel &= ne(u_\parallel - v_\parallel) = neD_{e\parallel}\left(1.71T_e^{-1}\nabla_\parallel T_e + n^{-1}\nabla_\parallel n - eT_e^{-1}\nabla_\parallel\phi\right)\\
q_{e\parallel} &= -1.6nD_{e\parallel}\nabla_\parallel T_e + 0.71nT_e(v_\parallel - u_\parallel)
\end{aligned}
$$

where the first is an equation for ϕ, $\nabla_\parallel = b^\mu\nabla_\mu$, and the dissipation parameters are given by $D_{e\parallel}^{-1} = 0.51\nu_e V_e^{-2} + (L_\parallel V_e)^{-1}$ and $D_{i\parallel} = L_\parallel c_s$ with $V_e^2 = T_e/m_e$ and $c_s^2 = T_e/M_i$.

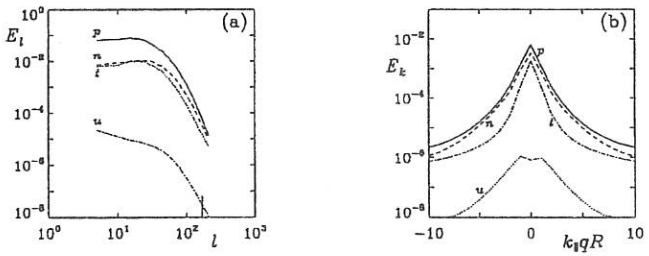

Figure 1. Fluctuation spectra, perpendicular (a) and parallel (b) wavenumbers, of the mean squared amplitudes of $\widetilde{\phi}$ (p), $\widetilde{n}$ (n), $\widetilde{T}$ (t), and $\widetilde{u}_\parallel$ (u). The long vertical hash denotes $k_\xi\rho_s \sim 1$. The source and sink curves [1] show ∇T as the strongest free energy source, low-k_ξ as a sink region, and low-$k_\parallel$ as the only source region.

Most of the results obtained from this system so far have been limited by the use of drift-ordering, which drops terms formally small by $\Delta \ll L_\perp$ (*e. g.*, $u_\parallel\nabla_\parallel$ in the fluctuations or magnetic divergences like $\nabla_\mu ne\mathrm{v}_*^\mu$ in the profiles) while still still allowing the profiles and fluctuations to self-consistently interact [1]. An example of such a result is shown in Fig. 1, the parallel and perpendicular spectra of fluctuations in a domain $V/V_a \in [0.9, 1.1]$ and $k_0 = 5$ for TEXT edge parameters ($a = 27\,\mathrm{cm}$, $R_0 = 4.0$, $B_0 = 2\,\mathrm{T}$, $T_0 = 30\,\mathrm{eV}$ and $n_0 = 3\times10^{12}\,\mathrm{cm}^{-3}$). The radial extent was two $L_\perp$. The collisionality parameter was $C_0 = (0.51\nu_e L_n)(m_e/M_i)(qR/L_n)^2 = 5.8$ and δ_0 was 0.002. The profiles were maintained by feedback control, where n/n_0 and T_e/T_0 were damped towards 2.5 and 0.4 at the inner and outer boundaries, respectively (numerical details appear in [1]). Fig. 2 shows the parallel transfer between neighboring regions of parallel wavenumber space and the

scaling with C_0 of such "local" runs. The runs with the tokamak metric were compared to counterparts with a sheared slab metric, both with and without the magnetic divergences ("ballooning"). This shows that the importance of ballooning depends strongly on the geometry; it is relatively unimportant compared to the tokamak's poloidal variation of the drift scale $\rho_s = c(T_e M_i)^{1/2}/eB$ in exciting asymmetries in the more collisional regime, but as C_0 drops the range of $k_\parallel$-interaction narrows and the ballooning is relatively more important. The parallel transfer rates were found to be more than twice as strong in tokamak as in slab-metric geometry. The slab-metric runs reproduce the gist of other current work [3].

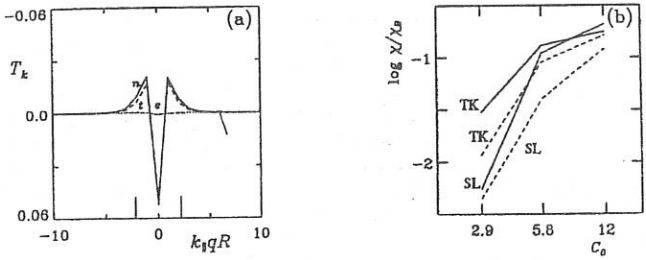

Figure 2. (a) Normalised parallel transfer rates, in ExB (e), density (n), and temperature (t) free energy components. Transfer is out of the $k_\parallel = 0$ region, with the ExB contribution negligible. (b) Dependence of energy transport, $\chi/\chi_B = (q_H/n\nabla T)(eB/cT)$, on the drift wave collisional parameter, C_0, for tokamak (TK) and slab (SL) geometry, with (solid) and without (dashed) the magnetic divergences (see text).

Another run was carried out, with $V/V_a \in [0.9, 1.1]$ and $k_0 = 10$, for ASDEX-Upgrade Ohmic edge parameters ($a = 60\,\mathrm{cm}$, $R_0 = 2.75$, $B_0 = 2\,\mathrm{T}$, $T_0 = 60\,\mathrm{eV}$, and $n_0 = 10^{13}\,\mathrm{cm}^{-3}$), with a SOL for $V/V_a > 1.0$. The drift wave parameters were $C_0 = 7.5$ and $\delta_0 = 0.0012$, not very different from the TEXT case. The SOL was determined by an inboard toroidal limiter at $\theta = \pm 0.5$. An inner-edge heat flux of $Q_0 = 0.6\,\mathrm{MW}(4\pi^2 aR)^{-1}$ was set, and the SOL was left as the sink according to the Debye-sheath boundary conditions. The profiles are shown in Fig. 3; these were not equilibrated over the $\sim 0.8\,\mathrm{msec}$ run time, but there has been reaction to the turbulence and to Q_0. In the SOL itself the confinement time is much shorter, as the gradients were flattened within 0.2 msec. The fluctuations were somewhat different in the closed and open field line regions; the turbulence and transport were stronger in the SOL. The parallel correlation length, $\lambda_\parallel$, for $\tilde{T}$ was twice as long in the SOL. For $\tilde{n}$ and $\tilde{\phi}$ the difference was closer to 50%. The main point of this, however, is that the three-dimensional parallel dynamics, *i. e.*, the exchange of free energy between $k_\parallel = 0$ and $k_\parallel = \pm qR$ components, continues to play a strong role even in the SOL and even with the long $\lambda_\parallel$. Although the turbulence notices the existence of open field lines, there is no specialised role for the flute-like target-plate instability [4,5], since the collisional drift wave nonlinear instability is more robust.

It is important at this stage to point out two discrepancies between these simulations and the situation observed in tokamak edges. The profiles were found to be too flat in the

SOL, indicating that the turbulence is too strong there in the numerical model. The amplitude itself was in good agreement but the coupling among $\widetilde{\phi}$, $\widetilde{n}$, and $\widetilde{T}$ appears to be too immediate in the collisional drift wave model. It may be that the addition of electromagnetic effects, usually considered to be small for these parameters ($\hat{\beta} = 4\pi n T L_\parallel^2 / B^2 L_\perp^2 \ll 1$), may subtly interrupt the dissipative coupling one has in the electrostatic model; in pure two-dimensional simulations this appears to be the case [6]. The other discrepancy is the lack of a particle pinch. When there are no sources and no particle flux, ∇n is close to zero. Although the need for a particle pinch in tokamak edges depends on inferences from a (perhaps irrelevant) diffusion model [7], it is well known that in the interior there is a $\nabla n \neq 0$ well within the source regions. The mechanism for that will have to be something other than collisional drift wave physics. Finally, it is to be noted that this type of turbulence is not effective at all above about 120 eV in the ASDEX-Upgrade case, and the model indeed loses validity at about this point. This makes the collisional drift wave model by itself invalid for the study of the L-to-H transition.

It is important as well to note the successes: the fluctuation amplitudes agree well with observations ($e\widetilde{\phi}/T \sim 0.2 \gtrsim \widetilde{n}/n \gtrsim \widetilde{T}/T$), the computed thermal energy flux on closed field lines is about 0.3 to 0.5 of observed values. Concerning the parallel mode structure, observed fluctuations in both tokamak and stellarators preserve a correlation of 0.8 over 10 m [5], and this has been used to advance two-dimensional flute-like turbulence models with the inference that $k_\parallel$ should be nearly zero [4,5]. However, the correlation function measured here drops to 0.8 in about $0.2 L_\parallel$, or about 8 m, in good agreement. This does however correspond to enough of a parallel gradient that collisional drift wave physics is robustly excited, and the special case of collisional drift waves on open field lines such that $k_\parallel \to 0$ with the Debye sheath providing dissipative coupling among $\widetilde{\phi}$, $\widetilde{n}$, and $\widetilde{T}$, elsewhere called the target-plate instability model [5], never enters.

References

[1] B. Scott, in *Proceedings of the 22th European Conference on Controlled Fusion and Plasma Physics, Bournemouth, 1995* (European Physical Society, Bournemouth, 1995), p I-229; *Plasma Phys. Contr. Fusion* , in press.

[2] S. I. Braginskii, *Rev. Plasma Phys.* 1, 205 (1965).

[3] A. Zeiler, D. Biskamp, J.F. Drake and P.N. Guzdar, *Phys. Plasmas* , in press; see also J. F. Drake *et al*, in *Plasma Physics and Controlled Nuclear Fusion Research 1994* (IAEA, Vienna 1995), paper D-P-I-8.

[4] A. V. Nedospasov, *Sov. J. Plasma Phys.* 15, 659 (1989).

[5] A. Rudyj, R. D. Bengston, A. Carlson, L. Giannone, M. KrÄmer, H. Niedermeyer, Ch. P. Ritz, N. Tsois, and the ASDEX Team, in *Proceedings of the 16th European Conference on Controlled Fusion and Plasma Physics, Venice, 1989* (European Physical Society, Venice, 1989), p I-27; M. Endler, H. Niedermeyer, L. Giannone, E. Holzhauer, A. Rudyj, G. Theimer, N. Tsois, and the ASDEX Team, *Nucl. Fusion* 35, 1307 (1995).

[6] S. J. Camargo, B. Scott, and D. Biskamp, *Phys. Plasmas* , in press.

[7] A. J. Wooton, B. A. Carreras, H. Matsumoto, K. McGuire, W. A. Peebles, Ch. P. Ritz, P. W. Terry, and S. J. Zweben, *Phys. Fluids B* 2, 2879 (1990).

OCCURRENCE OF SAWTEETH IN ITER AND THEIR EFFECTS ON ALPHA PARTICLES AND STABILITY

R.V. Budny, G.-Y. Fu, N.N. Gorelenkov, J. Manickam, M.P. Petrov,
M.H. Redi, S. Sabbagh, R.B. White, **L. Zakharov**, Y. Zhao, and S.J. Zweben
Princeton University, P.O. Box 451, Princeton NJ, 08543, USA

I - Introduction Sawteeth alter the plasma, current, and fast ion profiles in present tokamak experiments. The central electron temperature, density, and neutron emission profiles are observed to flatten within the radius where the safety factor, $q_\psi = 1$; so sawteeth reduce the central reactivity and fusion power. The plasma current also mixes to some degree since the safety factor in the center, $q_\psi(0)$, is observed to increase after sawtooth crashes [1]. Sawteeth may have beneficial effects as well. In TFTR, discharges with sawteeth do not have major high-β disruptions, suggesting that sawteeth and/or fishbones may inhibit these disruptions.

It is not known whether sawteeth will occur in ITER. If they do, they could have both beneficial and detrimental effects. Since ITER must achieve sustained ignition, it is important to know to what extent and how the alpha particles will mix during sawteeth crashes, since this mixing will affect the alpha heating, and thus the reheat rate. The alpha particle mixing might shift alphas to regions where the losses are large, possibly damaging wall components. Also, the MHD and TAE stability will depend sensitively on the total pressure, p_{tot}, and q_ψ profiles, which are altered by sawtooth mixing.

This paper studies the occurrence and effects of sawteeth in ITER. Many of the plasma parameters in present tokamak experiments are very different from those anticipated in ITER, so large extrapolations are needed to predict ITER conditions and performance. This paper uses codes and semi-empirical models to study ITER plasmas. Since sawtooth mixing of alphas has been observed in TFTR, we use these measurements to calibrate the sawtooth mixing models. We apply them to sets of profiles for two representative ITER plasmas from the Interim Design database [2] producing 1.5 GW of fusion power, one with a flat electron density, and one with a more peaked density. Profiles are shown in Figures a-c.

The TRANSP plasma analysis code [3] is used to derive profiles for q_ψ and p_{tot} and the effects of current and alpha particle mixing after sawtooth crashes. The stability of sawteeth in these plasmas is assessed using a semi-empirical model of ω^* stabilization. The MHD and TAE stability before and after the sawteeth crashes is calculated using the PEST and NOVA-K codes. The ripple losses of alpha particles is computed by TRANSP and FPPT. These codes and models for predicting the sawteeth stability and sawteeth effects in TFTR are in approximate agreement with measurements.

II - Steady state conditions in ITER The TRANSP plasma analysis code has been used to analyze these ITER plasmas [4]. The vertically asymmetric flux surfaces are computed from the equilibrium modeling. The code also models the alpha source, orbits, slowing down, and heating profiles. The central alpha pressure is approximately 10% of the thermal pressure. Total pressure profiles are shown in Fig. c.

One of the present unknowns of the ITER design is how the non-inductive plasma currents will be driven. The bootstrap currents for the flat and peaked profile cases are 3.0 and 5.5 MA respectively, out of a total current of 21 MA. Several methods have been proposed to drive the extra current, including using energetic neutral beam injection and fast wave current drive. The profile of the driven current will greatly effect the total current and q_ψ profiles. We assume that the driven current profile will have the same shape as if the

ohmic current were used. This current profile depends on the Z_{eff} profile (taken from the ITER database) and the assumed neo classical resistivity. The computed q_ψ profiles (shown in Fig. c) have $q_\psi = 1$ near $x \equiv \sqrt{\text{normalized toroidal flux}} \approx 0.40 - 0.50$.

Another unknown is the amount of current mixing during sawteeth crashes in ITER. This is discussed in Section IV. The conclusions of this paper are that the sawtooth effects on sustained ignition appear to be benign for standard ITER plasmas if the $q_\psi = 1$ surface is not greater than $x \approx 0.5$.

III - Sawtooth stability A semi-empirical model of ω^* stabilization [5] is consistent with the sawtooth stability observed in TFTR plasmas with auxiliary heating. The stability criterion is expressed as a critical shear at the $q_\psi = 1$ surface. The prediction of this criterion for ITER is that the peaked profile plasma is stable, and the flat profile plasma is unstable to sawteeth.

Trapped fast ions might stabilize sawteeth [6]. In beam-heated supershots in TFTR there does not appear to be enough deeply trapped energetic beam ions to stabilize sawteeth [7]. One important parameter for the trapping is the average energy of the trapped ions. The beam ions in TFTR have $\langle E_{bm} \rangle \approx 40$ keV. The alpha particles in the ITER cases are computed to have $\langle E_\alpha \rangle \approx 1.5$ MeV in the center.

Other models have been used to analyze the stability of ITER plasmas to sawteeth. A model invoking a threshold criterion and alpha stabilization has been used to predict ITER sawtooth periods of 120 sec [8].

IV - Current and alpha particle mixing in ITER TRANSP models sawteeth assuming Kadomstev mixing of flux surfaces [3]. Partial current mixing is modeled by computing a weighted average of the fully mixed and unmixed plasma currents after the crash. The q_ψ profiles in TFTR L-mode and supershot plasmas are generally simulated accurately with this model by assuming that about 20% of the current is mixed [1]. A comparison of pre-crash q_ψ profiles assuming 20% and 100% mixing is shown in Fig. c. The sawtooth period is assumed here to be 50 sec. Longer periods allow $q_\psi(0)$ to decrease further between crashes.

TRANSP models the fast ion sawtooth mixing by shifting the guiding centers with the flux surfaces, randomizing the poloidal distribution, and conserving v_{par} and μ [3]. The TRANSP model has been generalized using a Fokker-Planck Post TRANSP processor (FPPT) [9], which solves the bounce averaged drift kinetic equation using the plasma parameters from TRANSP. The FPPT mixing model is based on the ExB drift of fast ions at the crash. This mechanism has negligible effects on passing particles, and on the total fast ion density profile, but alters the distribution of the trapped particles.

Comparisons of simulations and alpha profile measurements in TFTR are shown in Figs. d-e. The pellet charge exchange (PCX) data [10], shown in Fig. d, are normalized to calculations in a similar sawtooth free discharge. Only deeply trapped alphas contribute to the measurement, and the FPPT modification of the TRANSP mixing is in approximate agreement with the measurements.

The TRANSP alpha mixing model alone achieves good agreement with the alpha energy measured by alpha charge exchange recombination spectroscopy (alpha CHERS). Comparisons with measurements [11] before and after a sawtooth crash are shown in Fig. e. This measurement averages a wide range of alphas with positive pitch angles, and thus includes mainly passing alpha particles.

TRANSP predictions for the alpha mixing in ITER are shown in Fig. f. The central alpha density and heating power are reduced to about 1/2 for 1-2 sec. The shifted profile depends strongly on the location of $q_\psi = 1$. We have not modeled the mixing of the thermal plasma.

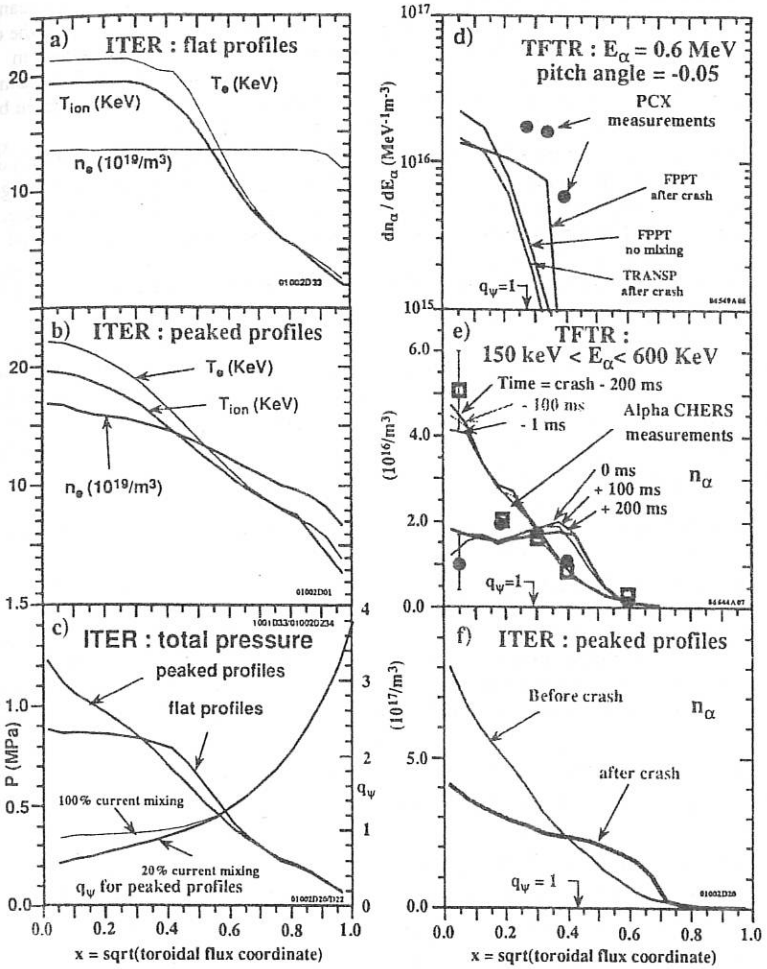

Profiles of the temperatures and electron density for an ITER discharge with a) flat, and b) peaked profiles; c) total pressure for both cases, and q_ψ for the peaked case before a sawtooth crash, computed with two choices of current mixing; d) comparison of TRANSP and FPPT simulations and measurements of the alpha particle energy in a TFTR supershot deduced from alpha charge exchange with a Li pellet cloud; e) comparison of TRANSP simulations and measurements of the alpha energy in a TFTR supershot deduced from spectroscopy of emission from He^0 resulting from charge exchange with beam ions before and after a sawtooth crash; f) predicted alpha density in the peaked ITER discharge before, and 1 sec after a sawtooth crash.

V - Consequences of alphas mixing in ITER The driven current profile and sawteeth can have considerable effects on the MHD stability by changing the p_{tot} and q_ψ profiles. If the q_ψ = 1 surface is pushed to large radii then the poloidal mode m = 1 can couple to the high m modes in the edge, causing instability. PEST code [12] results indicate the two ITER plasmas are ideal MHD stable to low-n modes. Their β_{norm} values of around 2.5 can be increased by about 15% before reaching the critical β_{norm} for high-n ideal MHD stability.

The TAE stability of these ITER plasmas has been analyzed using the kinetic-MHD code NOVA-K [13]. It is found that TAE global modes, at least up to n=10 are stable due to large ion Landau damping for both the flat and peaked profile cases. For the peaked profile case, core-localized TAE modes can exist and are unstable at relatively higher temperatures and lower plasma densities. The stability of these localized modes is reduced as the shear of q_ψ is reduced. As discussed above, the shear is affected by the amount of current mixing. The TAE stability after crashes needs to be investigated further.

Sawteeth in TFTR have been observed to increase the ripple losses of energetic alpha particles. The ripple losses are calculated by TRANSP [14] and FPPT. Calculations of these losses by both codes show good agreement in TFTR plasmas. For instance, for the supershot shown in Fig. d, the number of alpha particles that are ripple lost as a result of the sawtooth crash is calculated by TRANSP to be 1.5×10^{15} and by FPPT to be 1.4×10^{15}. FPPT does not have Coulomb pitch angle scattering, which is the reason of additional losses in TRANSP.

TRANSP calculates the ripple losses for the ITER plasmas considered here to be less than 1% of the alpha power during steady state. The alpha mixing shown in Fig. f increases the loss rate by less than 1% [14].

VI - Conclusions The q_ψ profile has important consequences for alpha mixing, MHD stability, and TAE activity in ITER. With the assumed current and sawtooth mixing assumptions in this paper, the q_ψ = 1 radius is at x ≈ (0.4-0.5). We conclude that sawteeth in the ITER plasmas studied are not likely to adversely affect the MHD stability, or the TAE activity, or to significantly increase the ripple losses. Specification of the method of current drive in ITER will be important for substantiating these consequences.

This work is supported by the U. S. D.o.E. under Contract No. DE-AC02-76-CHO3073.

[1] M. Yamada, F.M. Levinton, N. Pomphrey, *et al.*, Phys. Plasmas **1** (1994) 3269-3276.

[2] The ITER database is available on internet: http//picard.iterus.org.

[3] R.V. Budny, M.G. Bell, A.C. Janos, *et al.*, Nucl. Fusion **35** (1995) 1497-1508.

[4] R.V. Budny, D. McCune, *et al.*, "TRANSP Analysis...", submitted to Phys. of Plasmas.

[5] L. Zakharov, R. Budny, *et al.*, "Triggering Disruptions in TFTR at High-β", this conf.

[6] Y. Wu, C.Z. Cheng, and R.B. White, Phys. Plasmas **1** (1994) 3369.

[7] Y. Zhao and R. White, private communication.

[8] F. Porcelli, D. Boucher, and M. Rosenbluth, proceedings of the 20th EPS conf. III-169.

[9] N.N. Gorelenkov, R. Budny, *et al.*, PPPL Report #3184, submitted to Nucl.Fusion.

[10] M.P. Petrov, N.N. Gorlenkov, R.V. Budny, *et.al.*, "Aspects of Trapped ..", this conf.

[11] B. Stratton, R. Fonck, G. McKee, R. Budny, *et al.*, to be published in Nuclear Fusion.

[12] R.C. Grimm, R.L. Dewar, and J. Manickam, J. Comput. Phys. **49** (1983) 94.

[13] G.-Y. Fu, C.Z. Chen, R. Budny, *et al.*, Phys. Rev. Letters, **75** (1995), 2336.

[14] M.H. Redi, R.J. Goldston, R.B. White, *et al.*, "TF Ripple Loss of Alpha....", this conf.

Transport Barrier Formation in TFTR Reversed Magnetic Shear Plasmas

R. E. Bell, S. H. Batha†, M. Beer, C.E. Bush‡, Z. Chang, P. C. Efthimion, T. S. Hahm, G. Hammett, F. Levinton†, B. LeBlanc, E. Mazzucato, D. Mikkelsen, H. Park, S. Paul, G. Rewoldt, G. L. Schmidt, S.D. Scott, E. J. Synakowski, G. Taylor, M.C. Zarnstorff, and the TFTR Group

Princeton Plasma Physics Laboratory, Princeton, New Jersey, 08543 USA
†Fusion Physics and Technology, Torrance, California 90503 USA
‡Oak Ridge National Laboratory, Oak Ridge, Tennessee 37831 USA

I. Introduction

Tokamak plasmas with reversed magnetic shear are being studied due to their potential for improved core confinement and stability. Recent experiments have demonstrated improved core particle and ion thermal confinement inside an internal barrier that coincides with a region of negative magnetic shear.[1,2] Magnetic shear is defined by $s=(r/q)(dq/dr)$ where q is the safety factor and r is the minor radius. In TFTR reversed magnetic shear plasmas, two types of transitions to improved confinement have now been observed. The signature of the type I transition (as described in Ref. [1]) is an abrupt increase in the rate of rise of central electron density, $n_e(0)$, and a broadening of the ion temperature, T_i, and electron temperature, T_e, profiles. The more recently observed type II transitions are characterized by an abrupt increase in T_i and T_e with a more gradual peaking of n_e, and have been obtained with a significantly lower neutral beam (NB) power. Both transition types lead to a peaking of the pressure profile.

One possible mechanism for the formation of the internal transport barrier is a decorrelation of turbulence by $E\times B$ flow shear.[3,4] This mechanism can be tested by comparing the $E\times B$ shear rate, $\omega_{E\times B}=(RB_\theta/B)\cdot d/dr(E_r/RB_\theta)$, to the maximum calculated linear growth rates of the plasma turbulence, γ^{ℓ}_{max}. The $E\times B$ shear rate is evaluated using measured background profiles of the carbon temperature, density, toroidal flow, and poloidal magnetic field and calculated poloidal flow. The rate of the fastest growing mode is determined with a comprehensive numerical model [5] which calculates eigenmodes and eigenfrequencies of electrostatic and electromagnetic modes using measured profiles and calculations from the time-dependent, kinetic code, TRANSP.[6]

The peaked pressure profiles across the type I transition yield $E\times B$ shear rates that are comparable to γ^{ℓ}_{max}, suggesting that the shear in the quantity E_r/B_θ may play a role in reducing turbulent-driven transport in this case. However, calculated values of γ^{ℓ}_{max}, at the time of the type II transition are much larger than the values determined for $\omega_{E\times B}$, suggesting that another mechanism may be responsible for this transition. This point is further tested by varying the co/counter mix of the NB power to examine the relative influence of the toroidal velocity shear and ∇p on the $E\times B$ shear. The timing of the type I transition can be varied with respect to the evolving q profile, in contrast, the type II transition seems to be linked to the current profile evolution since it occurs when q_{min} is near 2. The differences in the power

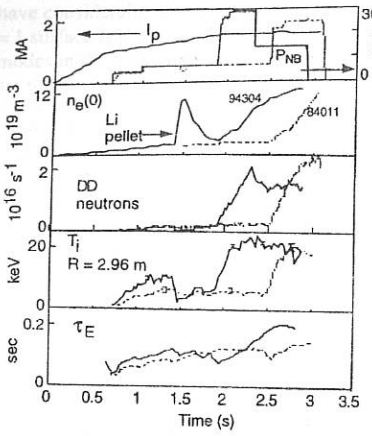

Fig. 1 Parameters of ERS type I with early and late heating phase.

threshold for the two types of transitions, the ratio of the shear rate to the maximum growth rate of turbulence, and the timing of the transitions suggest different triggering mechanisms. These two transitions once triggered may be sustained by similar mechanisms, since they share similar improvements in particle, ion thermal, and momentum confinement.

II. Enhanced Reverse Shear - Type I

The reversed magnetic shear condition is established in TFTR during the plasma startup using ramps in the plasma current and early low power neutral beam injection (See Fig. 1) to produce a hollow current profile. Higher power neutral beam injection is then added in a heating phase, and may be reduced in a "postlude" phase. Some reversed shear (RS) plasmas transit into an "enhanced reverse shear" (ERS) mode with improved confinement properties. Sometimes a lithium pellet is injected before the high power phase to precipitate a transition.

The type I transition into the ERS mode on TFTR has a power threshold ~20 MW, and is distinguished by a rapid rise in the central electron density, which can reach values in excess of 10^{20} m^{-3}. The T_i profile broadens as does the T_e profile, though to a lesser extent. The transport coefficients of electron diffusion, D_e, and ion conductivity, χ_i, are reduced inside the transport barrier. There is no corresponding improvement in χ_e. The momentum diffusivity, χ_ϕ, evaluated in the postlude period when the beam torque can be adjusted, is also reduced in the core.

In recent experiments, the timing of the heating phase has been moved earlier to overlap the current ramp phase (see Fig. 1 shot #94304). By achieving the transition to ERS earlier, a longer postlude is possible, and by properly adjusting the postlude heating power, a more "steady state" ERS mode can be maintained during the postlude. Note in Fig. 1 that shot 94304 has an increasing global energy confinement time, τ_E, and the neutron rate is steady during the postlude period.

The *E×B* shear rate is calculated for shot 84011 and plotted with the maximum growth rate in Fig. 2. At the time of the ERS transition, these two rates are comparable, supporting the idea that *E×B* shear can improve transport through a reduction in turbulence. γ^{ℓ}_{max} is shown to decrease with time even before the transition. This is consistent with the stabilizing influence of an increasing Shafranov shift, which is already large for these reverse shear plasmas, due to their low central current density. After the transition, the gap between $\omega_{E\times B}$ and γ^{ℓ}_{max} widens as they both respond to the higher confinement of the ERS mode. The shear rate grows as the

pressure gradient increases the E_r/B_θ shear, and the higher pressure increases the Shafranov shift providing more stabilization of the turbulence.

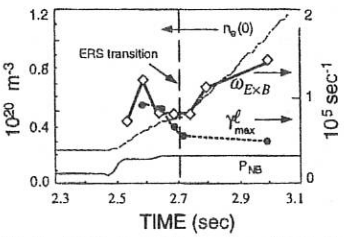

Fig. 2. E x B shear rate is comparable to the calculated maximum linear growth rate at the time of the ERS transition and is a possible mechanism for triggering the transition by suppressing turbulence.

III. Enhanced Reverse Shear - Type II

The plasma startup for the discharges which undergo a type II transition is the same as described above for type I transitions. The neutral beam power in the heating phase, however, is much lower. Type II transitons with 5 MW of input power have been seen. A typical discharge is show in Fig. 3 for a case where the neutral beam power is 14 MW in the heating phase. Just before 3.5 sec, there is a sudden increase in the core T_i , which is accompanied with an abrupt increase in core T_e (not shown). The profiles of T_i and n_e are plotted in Figs. 3b and 3c at three times (before and 40 ms, 180 ms after transition, denoted A, B, and C). A sudden increase in core T_i is seen within 50 ms of the transition (profile B in Fig. 3b). The steady increase in the electron density can be seen in Fig. 3c. The corresponding profiles of χ_i and D_e show the improvement in ion thermal and particle confinement (Figs. 3d and 3e). Like the type I transition, there is also an improvement in the core χ_ϕ, and no change in χ_e.

The sudden increase in both T_i and T_e at the time of the type II transition allows the location and timing of the transition to be determined, especially with the faster measurements of T_e from electron cyclotron emission. As the internal transport barrier is formed, the outward transport of energy across the barrier is reduced; the stored energy just inside the barrier increases while the region just outside the barrier is deprived of energy. Plotted in Fig. 4 is the normalized heating rate, $(1/T_e) / dT_e/dt$, at the time of the type II transition along with the q profile measured by the motional stark effect (MSE) diagnostic. The inversion radius of the heating rate indicates the location of the transport barrier just outside of q_{min}. This value of q_{min} is typical of the value at the type II transition regardless of the applied neutral heating power or beam torque.

Due to the lower power threshold for the type II transitions, it is possible on TFTR to vary substantially the toroidal plasma rotation, thereby changing the relative influence of rotation and pressure gradient on the radial electric field. Type II transitions can be obtained with co-rotating, balanced or counter-rotating plasmas (see Fig. 5). In the rotating cases E_r is dominated by the plasma rotation and the relative influence of ∇p is small. This is consistent with the calculation of $\gamma^{\ell}_{max} >> \omega_{E\times B}$ at the time of the type II transition. The $E\times B$ shear does not seem to play a role in the type II transition. The slightly co-rotating plasmas have the strongest transitions. Highly co- or counter-rotating plasmas have weaker transitions.

In summary, both the type I and type II transitions to enhanced confinement show similar improvements in χ_i, D_e, and χ_ϕ near the core, with little or no change in χ_e. The type I

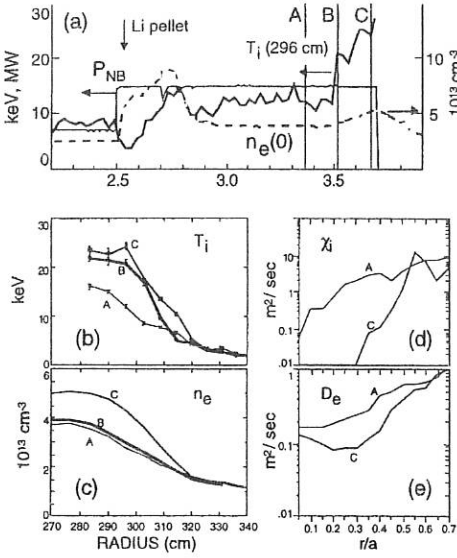

Fig. 3 Type II ERS transition results in sudden increase in Ti and gradual increase in n_e with improved core ion and particle confinement.

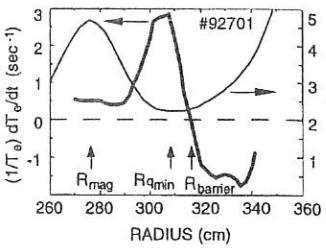

Fig. 4 Inversion of the normalized heating rate at the time of a type II transition shows the location of the transport barrier. The q profile is measured by MSE diagnostic.

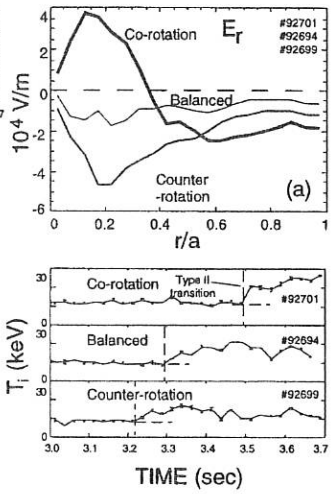

Fig. 5 E_r which is dominated by plasma rotation does not influence the type II transition.

transition has a power threshold $\gtrsim$ 20 MW, while the type II has a power threshold $\lesssim$ 5MW. Different triggering mechanisms are likely for the two transitions. Sheared $E{\times}B$ flow may be important for the type I transition, but not for the type II transition. The timing of the type II transition may be linked to the current density profile; type II transitions occur with $q_{min} \gtrsim 2$. The performance of plasmas with the type I transition seem better than plasmas with the type II transition, e.g. the reduction in D_e is larger for type I transitions.

This work was supported by the U.S. DOE Contract No. DE-AC02-76-CHO-3073.

1 F. M. Levinton, *et al.*, Phys. Rev. Lett. **75**, 4417 (1995).
2 E. J. Strait, *et al.*, Phys. Rev. Lett. **75**, 4421 (1995).
3 R.E.Waltz *et.al.* Phys. Plasmas **1**, 2229 (1994).
4 T. S. Hahm and K. Burrell, Phys. Plasmas **2**, 1648 (1995).
5 G. Rewoldt, W. M. Tang, and R. J. Hastie, Phys. Fluids **30**, 807 (1987).
6 R.V. Budny, M.G. Bell, A.C. Janos, *et al.*, Nucl. Fusion **35**, 1497 (1995).

Aspects of Trapped Confined Alpha Physics on TFTR

M. P. Petrov
A. F.I offe Physical-Technical Institute, St. Petersburg, 194021 Russia

N. N. Gorelenkov
TRINITI, Troitsk 142092 Russia

R. V. Budny, D. K. Mansfield, S. S. Medley
Princeton Plasma Physics Laboratory, P. O. Box 451, Princeton, New Jersey 08543 USA

H. H. Duong, R. K. Fisher, J. M. McChesney, P. B. Parks
General Atomics, San Diego, California 92186 USA

1. Introduction

The energy distributions and radial density profiles of the fast confined trapped alpha particles in DT experiments on TFTR are being measured in the energy range 0.5 - 3.5 MeV using a Pellet Charge eXchange (PCX) diagnostic. This technique uses the active neutral particle analysis with the ablation cloud of an injected lithium or boron pellet as the neutralizer [1]. Initial measurements of the fast confined alpha energy distributions and alpha density radial profiles in the presence of stochastic ripple diffusion and sawtooth oscillations were reported previously [2,3]. This paper focuses on more detailed analysis of some aspects of fast confined alpha physics on the basis of modeling of PCX experimental results with and without the presence of stochastic ripple diffusion and sawtooth mixing.

2. PCX Technique and Data Analysis

The PCX diagnostic on TFTR uses lithium and boron pellets injected along a midplane major radius. The neutral particle analyzer views the pellet from behind with a sightline at a toroidal angle of 2.75^{o} to the pellet trajectory. Consequently, only trapped alphas with velocities close to $v_{||}/v = -0.048$ are detected in these experiments. The radial position of the pellet as a function of time is measured with a linear photodiode array situated on the top of the vacuum vessel. From the time dependence of the PCX signal, radially resolved fast ion energy spectra and density radial profiles can be derived with a radial resolution ~5 cm. Further details of the PCX measurements were presented in [4].

The experimental data are compared with modeling results obtained with a specially developed Fokker-Planck Post TRANSP (FPPT) processor code [5]. TRANSP [6] follows the orbits of alphas as they slow down and takes into account the spatial and temporal distributions of the background plasma parameters for each particular shot. The FPPT code is

based on a numerical solution of the drift-averaged Fokker-Planck equation for the particular PCX pitch angle ($v_{||}/v = -0.048$):

$$\delta f/\delta t = \langle St(f_\alpha)\rangle + \langle S_\alpha\rangle - f_\alpha/\tau_\delta - f_\alpha/t_{conf} \qquad (1)$$

where f_α is the distribution function of alphas including the thermal broadening effect, $St(f_\alpha)$ is the collisional integral describing the slowing down of alphas, S_α is the alpha source taken from TRANSP code, t_δ is the confinement time of alphas determined by the effect of toroidal field ripple, and τ_{conf} is the confinement time of alphas determined by alpha radial transport of any other type excluding ripple effects.

3. Alpha Slowing Down in the Core of Quiescent Discharges

In the TFTR D-T experiments, pellets for the PCX diagnostic typically are injected 0.2 to 0.5 s after termination of neutral beam heating. This timing delay allows T_e and n_e to decrease, resulting in deeper penetration of the pellet as well as enhancement of the signal-to-noise ratio because the neutron background decays significantly faster than the confined alpha population. Here we present studies of the distribution functions of alphas in the plasma core of a quiescent discharge where there is neither significant ripple nor MHD influence on alpha particles. Fig. 1 shows the energy spectrum of alphas in the plasma center which was obtained using a Boron pellet injected 0.2 s after the termination of 1.0 s, 15 MW beam pulse (#86291). The alpha slowing down time in this case is equal to $\tau_{sl} = 0.32$ s. The solid line shows the FPPT calculation assuming that $\tau_{conf} >> \tau_{sl}$ ($\tau_{conf} = 300\tau_{sl}$). The dotted lines present the cases where $\tau_{conf}/\tau_{sl} = 3.0$, 1.5, 0.8 and 0.4. It is seen from Fig. 1 that the case $\tau_{conf} >> \tau_{sl}$ provides the best modeling fit to the data. This supports the statement that the alpha energy spectra is determined only by the classical slowing down without significant transport during the slowing down.

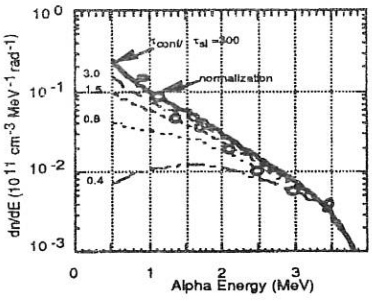

Fig. 1 Alpha energy spectra in the plasma core.

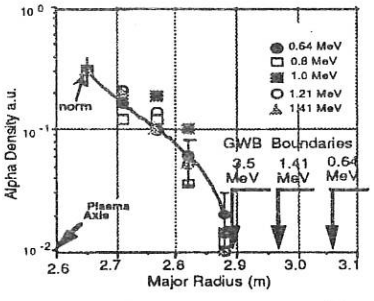

Fig.2 Alpha radial density profiles.

4. Studies of the Effect of Toroidal Ripple on Trapped Alphas

Fig. 2 presents PCX radial density profiles of alphas with energies of 0.64, 0.8, 1.0, 1.21 and 1.41 MeV measured 0.3 s after termination of 20 MW beam injection, normalized at R = 2.65 m (#84550). Also shown is the Goldston-White-Boozer (GWB) stochastic ripple diffusion radial boundaries [7] for alpha energies of 0.64, 1.41 and 3.5 MeV. These boundaries are defined by the following expression: $\delta_{TF}\rho q' (\pi N q/\varepsilon)^{3/2} > 1$, where δ_{TF} is toroidal field ripple, ρ is the alpha gyroradius, N is the number of toroidal field coils, q is the safety factor, $q'=dq/dr$, and ε is the inverse aspect ratio. Inside the GWB boundaries the alpha behavior is classical while outside there exists a domain where alpha particles are strongly affected by stochastic ripple diffusion. It is seen that alpha density radial profiles are consistent with the GWB boundary for $E_\alpha = 3.5$ MeV. This demonstrates the absence of significant alpha transport outward during slowing down from the birth energy to at least 0.64 MeV and the strong ripple influence on alphas outside the GWB boundary. Ripple diffusion causes alphas born outside the GWB boundary to be promptly lost while alphas born inside this boundary are confined and slowing down there in the absence of any outward transport. Note that at the time of measurement (0.3s after the termination of neutral beam heating) the generation of alphas is practically absent. This result is consistent with the data presented in Fig. 1. Fig. 3 presents the experimental alpha density profiles and the FPPT code predictions for $E_\alpha = 0.64$ MeV and 1.21 MeV with and without ripple. Modeling results are normalized to the PCX data separately for both energies. It is seen that experimental data are in good agreement with the ripple modeling. It is seen also that the modeling without ripple predicts much broader radial density profiles than experimentally measured.

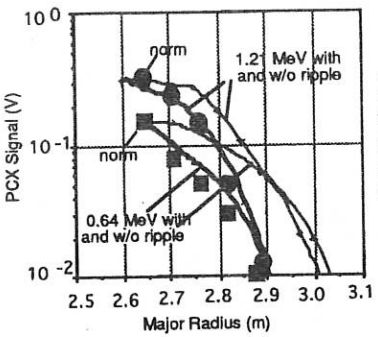

Fig.3 Alpha density profiles with and without ripple

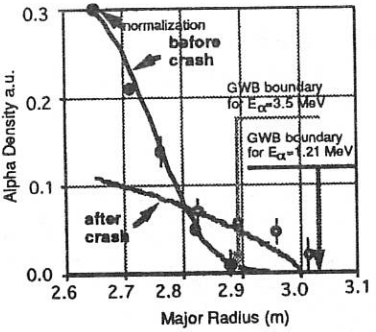

Fig.4 Sawtooth mixing of alphas

5. Sawtooth Mixing of Alpha Particles

Sawtooth crashes in TFTR usually occur 0.3 - 0.4 s after termination of neutral beam injection. For PCX measurement of the sawtooth mixing of the alphas, a Li pellet was injected immediately before the first sawtooth crash in one discharge and immediately after the sawtooth crash for a similar discharge. Fig. 4 presents the alpha radial density profiles (E_α = 1.21 MeV) before and after the crash. A significant outward transport of alphas beyond the q=1 surface is clearly seen. The magnitude of this sawtooth mixing is observed to decrease with increasing alpha energy. Sawtooth models [8] based on magnetic reconnection and the conservation of magnetic flux and particle energy and density can not provide the strong outward transport of trapped alphas observed experimentally. Recently, a model of the sawtooth mixing of trapped alphas was implemented in the FPPT code in which a helical electric field produced by the sawtooth crash leads to a change in the alpha energy [5]. In Fig. 4, results from this model before and after the sawtooth crash are shown by the solid lines. Also shown are the GWB boundaries for E_α =1.21 MeV and 3.5 MeV. The modeling results are in agreement with the PCX experimental data and the alpha density profiles are consistent with the GWB boundaries. It is seen that the sawtooth oscillations transport trapped alphas radially to near the stochastic ripple loss region, which can lead to enhanced ripple losses.

6. Summary

In the plasma core of quiescent TFTR D-T plasmas, the trapped alpha particles are well confined and slow down classically without any significant losses. In outer regions, trapped alphas are strongly affected by magnetic field ripple and by sawtooth mixing which can be modeled on the basis of a perturbed helical electric field.

Acknowledgments

Work supported by US DoE Contract DE-AC02-76-CH0-3073 and US DoE Grant DE-FG03-92ER54150

References

[1] R. K. Fisher, *et al.*, Rev. Sci. Instrum. **63**, 4499 (1992)
[2] R. K. Fisher, *et al.*, Phys. Rev. Lett. **72**, 649 (1995)
[3] M. P. Petrov, *et al.*, Nuclear Fusion **35**, 1437 (1995)
[4] S. S. Medley, *et al.*, Proc. of the 22nd EPS Conference on Controlled Fusion and Plasma Physics, (Bournemouth, United Kingdom, 3-7 July 1995), Vol. **19C**, I-409.
[5] N. N. Gorelenkov, *et al.*, PPPL-3184 (April, 1996) 17 pp. To be submitted to Nuclear Fusion
[6] R. V. Budny, *et al.*, Nuclear Fusion **35**, 1497 (1995)
[7] R. J. Goldston, R. B. White, A. H. Boozer, Phys. Rev. Lett., **47**, 647 (1981)
[8] Ya. I. Kolesnichenko *et al.*, Phys. Rev. Lett. **68**, 388 (1992)

Triggering Disruptions in TFTR at High-β[1]

L. Zakharov, R. Budny, Z. Chang, E. Fredrickson
Princeton Plasma Physics Laboratory, PU, Princeton NJ 08543

B. Rogers
Institute for Plasma Research, University of Maryland, College Park

In this report, the triggering of disruptions in high performance supershots in the Test Fusion Tokamak Reactor is theoretically explained and compared with experimental data. These high-β disruptions represent a major obstacle for increasing fusion power in TFTR. Although they are related to the enhanced plasma pressure, their triggering cannot be described by only one global parameter like Troyon β_N.

At high-β, both minor and major disruptions in TFTR start with the internal collapse (thermal quench) involving $m = 1$ and ballooning modes. It may occur abruptly without (or at best with a very short) precursor[1]. This fact is difficult to explain assuming crossing some stability limit. One explanation[2] is based on numerical studies of the nonlinear dynamics of ballooning modes. In situations, where the low-n mode is present, ballooning modes can provide fast transport of the plasma thermal energy from the center through a toroidally (and poloidally) localized channel with well developed instabilities. Although this approach is very successful in reproducing many features which are experimentally observed, it does not address the problem of triggering.

Here, we reveal the positive feedback coupling between the the $m = 1$ mode and ballooning modes which exists in TFTR and can explain the fast triggering. Earlier[3], we found that despite the fact that $q_0 < 1$ in TFTR supershots, the stability of the $m = 1$ mode is provided by FLR stabilization related to the pressure gradient at the $q = 1$ surface. As $1\ \beta_{1/1}$ at $q = 1$ reaches the level determined by the criterion

$$1.4\beta_{1/1}^{2/3}\left(\frac{m_i}{2Z_{eff}m_p}\right)^{1/6}\left|\frac{n'R}{n}\right|_{1/1}^{2/3}\left|\frac{p'R}{p}\right|_{1/1}^{1/3} > q'r_{1/1} \qquad (1)$$

sawtooth oscillations become stabilized (here, p, n are the plasma pressure and density, $r_{1/1}$ ane R are the $q = 1$ minor and major radii). The fact that an increase in pressure stabilizes the $m = 1$ instability in TFTR provides a triggering mechanism for the internal disruptions when the plasma β approaches the ballooning limit:

- Ballooning modes, when excited near the $q = 1$ surface, destroy ω_* stabilization of the $m = 1$ mode.
- In turn, the $m = 1$ perturbation ξ disturbs the pressure profile

$$\xi = \xi(r)\cos(\theta - \phi), \quad p = p(r + \xi\cos(\theta - \phi)) \qquad (2)$$

- The pressure gradient is thereby significantly enhanced near the $q = 1$ surface as

$$p' = p'_r[1 + \xi'\cos(\theta - \phi)], \quad \xi' \simeq 1 \qquad (3)$$

Local (in both radial and azimuthal directions, where $\xi'\cos(\theta - \phi) > 0$) enhancement in the pressure gradient amplifies the ballooning modes, thus, closing the positive feedback loop.

[1]This work was supported by the U.S. DOE, Contract No. DE-AC02-76-CHO-3073

This generic coupling between the $m = 1$ and ballooning modes gives a self-consistent explanation of triggering the internal collapses. It is also consistent with observations of the azimuthal and radial localization of the ballooning modes excited during the disruption. This is novel and is not present in previous studies[4] of ballooning modes in configurations perturbed by the $m = 1$ mode as well as in numerical simulations[2].

The straightforward prediction of our model is that internal disruptions in supershots occur as soon as the ballooning stability limit is violated in the vicinity of the $q = 1$ surface (at 25-30% of the minor radius). Also, the model reveals that the central $\beta_N(1/3) = \beta_N(r = 1/3a)$, corresponding approximately to the $q = 1$ region (a is the plasma minor radius), rather than the global Troyon β_N, is a critical parameter for triggering the disruptions in TFTR.

The positive feedback coupling predicts *mutual* amplification of both $m = 1$ and ballooning modes and allows for disruptions starting either with or without any significant precursors ($m = 1$ or ballooning modes).

Fig. 1a presents the contour plot of fast oscillations of the Electron Cyclotron Emission (ECE) signal for one of the best TFTR DT shot # 76778, which disrupted prior to the end of the heating phase. It shows presence of a saturated $n = 1$ (which is, presumably, the $m = 1$ mode) existed in this discharge for a long time. Although this discharge had other developed high-n perturbations ($n > 5$), time evolution of the ECE signal as function of major radius R (Fig. 1b) clearly indicates that triggering occurs just when both $m = 1$ and ballooning modes start to grow together and near the $q = 1$ surface. This behavior is consistent with the positive feedback mechanism, mentioned above.

The comparison of the central core normalized β_N

$$\beta_N(r) \equiv 100 \frac{2\mu_0 < p - p(r) >}{B^2} \frac{Br}{I(r)}, \tag{4}$$

(which is a generalization of the Troyon definition on an arbitrary minor radius r), calculated using the ballooning code and TRANSP simulations of the plasma profiles, shows $\beta_N(r = 1/3a)$ (upper black dots) approaching the theoretical ballooning limit (Fig. 1c) just prior to disruption.

Fig. 2a shows experimental data for another kind of discharge (with a more peaked pressure profile), when the predisruptive stage was much quieter with almost no indication of the low-n mode. Very small ballooning modes did not exhibit any azimuthal modulations on the ECE signal, and have a very clean spectrum. Nevertheless this discharge was terminated by a major disruption at lower global Troyon $\beta_N(a)$ (calculated for the whole plasma) than that in Fig. 1. While this particular disruption event is difficult to reconcile with other models of triggering, it fits well our feedback mechanism, which considers only central core ballooning stability as the essential feature. It allows lack of precursors before the disruptions. Accordingly, ballooning calculations found the same violation of the central core stability.

Based on this model, we performed extensive scanning of about 80 high performance TFTR discharges with comparison of calculations of ballooning stability using TRANSP plasma profiles and experimental observations of MHD activity. Despite lack of measurements to corraborate the TRANSP computed safety factor $q(r)$ profile, we found no deep penetration of β_N (at any radii) into the theoretically unstable space. In addition, it was found that the criterion based on comparison of $\beta_N(1/3)$ with its theoretical limit can be used as a good indicator of the threshold for internal collapses in supershots.

Table shows results of comparison of predictions of ballooning theory with experimental observations. The model does not distinguish between subsequent minor and major disruptions. Although it underestimates the stability of certain shots, it shows good correlation with the data.

Theory / Experiment	Stable	Internal Collapse
Stable	38 shots	8
Minor Disruption	0	8
Major Disruption	1	5

Comparison of the pressure gradient profiles found good alignment with the limiting profiles inside 1/4–1/3 of the minor radius preceding the triggering the internal collapses.

As a further development of the model, we included the two-fluid FLR effects, which allows to to consider not only stability limits but also the frequency and wave numbers of the ballooning modes.

In the collisionless TFTR regime, FLR effects lead to stabilization of the high-n ballooning modes starting with some critical n-number. Because of limitations on the possible toroidal n-number, the excitation of ballooning modes requires a finite radial size of the zone, where local pressure gradient exceeds its ballooning limit. Extensive comparison of the same set of experimental data found many local violations of the ballooning criterion in a region of about 5 cm wide ($\simeq 1/20a$). These local violation of ballooning stability gives possible interpretation of observed quiet ballooning modes, (referred frequently as "KBM" and shown on Fig. 2a) as local two-fluid MHD ballooning modes, which are too limited in space and, thus, do not lead to macroscopic events.

Table shows comparison of the two-fluid MHD ballooning model in prediction of local ballooning modes and internal collapses with experiments in TFTR. The model overestimates the stability with respect to disruptions. The reason needs to be established and, presumably, may be related to the presence of a saturated $m = 1$ mode in some of the shots.

Theory, n=5 / **Experiment**	Stable	Local Balloon.	Internal Collapse
Stable	19	7	0
Local Balloonning	1	14	0
Minor Disruption	0	5	1
Major Disruption	1	3	1

For local ballooning modes, the two-fluid model is consistent with frequency (which is close to the the half of diamagnetic frequency of the whole ion species) as well as with the range of observable toroidal wave numbers. Fig. 3 shows typical comparison of the experimental pressure gradient profile with the theoretical limits, when quiet modes have been seen in experiment and stability was violated in the limited zone.

In conclusion, a self-consistent model of triggering internal collapses at high-β in TFTR has been developed, which reveals the role of the central normalized $\beta_N(r = 1/3a)$ as a critical parameter for internal disruptions. The same model also describes localization, frequency and toroidal wave number of the quiet ballooning modes.

1. E.D.Fredrickson, K.McGuire, et al. PPPL Report PPPL-3023, 1994.
2. W.Park, E.D.Fredrickson, A.Janos, et al. Phys.Rev.Lett. **75** (1995) 1763.
3. F. Levinton, L. Zakharov, S. H. Batha, et al, Phys. Rev. Lett. **72** (1994) 2895.
4. M. N. Bussac, R. Pellat, Phys. Rev. Lett. **59** (1987) 2650.

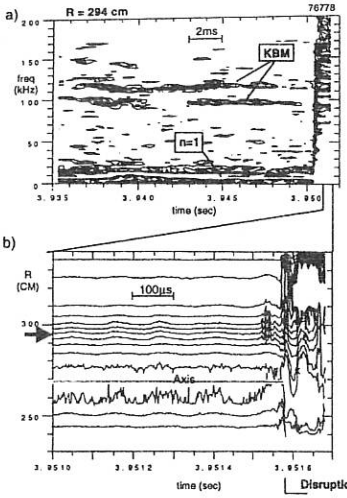

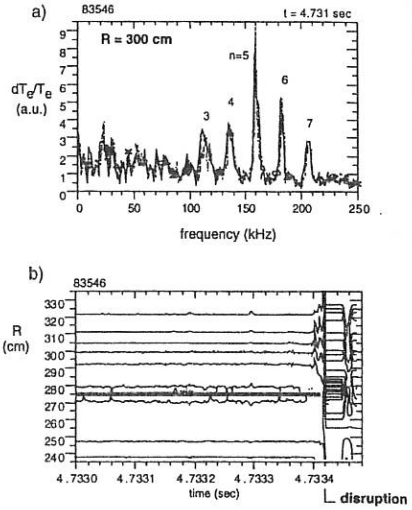

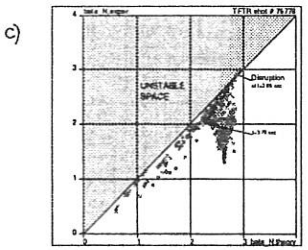

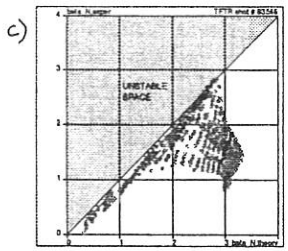

Fig. 1. ECE contour plots on a) frequency—time and b) R—time planes for high β shot 76778; c) $\beta_N(1/3a)$ (upper black dots) approaching the theoretical stability limit before the disruption. Low-right black dots represent the Troyon $\beta_N(a)$.

Fig. 2. a) Spectrum of quiet high-n perturbations and b) R—time ECE contour plot for the lower β shot 83546; c) Similar approach of the central $\beta_N(1/3a)$ to its threshold. Global $\beta_N(a)$ is lower due to a more peaked pressure profile in this shot.

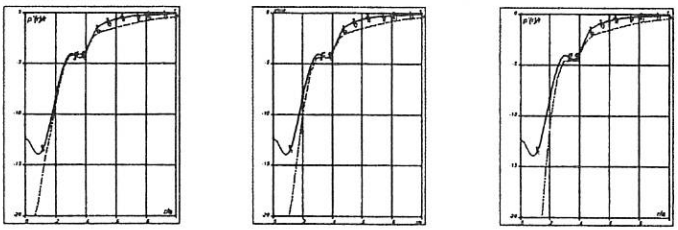

Fig. 3. Pressure gradient profile in shot 77309 showing instability of two-fluid ballooning modes with a) $n = 5$, b) $n = 8$, and stabilization starting with c) $n = 10$

TF Ripple Loss of Alpha Particles from the ITER Interim Design: Simulation and Theory

M. H. Redi[a], R. J. Goldston[a], R. B. White[a], R. V. Budny[a],
D. C. McCune[a], C. O. Miller[b], S. J. Zweben[a]
[a] Princeton Plasma Physics Laboratory, Princeton University, Princeton, NJ 08543
[b] Richard Stockton College of New Jersey, Pomona, N. J. 08240, U. S. A.

1. Introduction

Ripple loss of alphas can result in reduced alpha heating and potentially severe localized wall damage in fusion reactors. In this paper we show guiding center code (GC) calculations of ripple-induced alpha loss in ITER, under a number of different operating conditions for the ITER Interim Design [1]: L-mode, H-mode, post-sawtooth, and reversed-shear configurations. In all cases except for the last, alpha loss is very small [2,3]. In the case of reversed-shear operation, alpha banana convection loss can be important. We also present a new theoretical calculation of the stochastic threshold [2], which gives excellent agreement with the much more computationally intensive GC calculations.

2. Guiding Center Code Method

Recently, the ORBIT Hamiltonian coordinate guiding center code [4] has been used to quantitatively evaluate TF ripple losses for TFTR alpha particles [5] and to adjust the normalization of a simple model for stochastic ripple losses within the TRANSP code [6]. Collisions were found to be far more important than had been expected, with pitch angle scattering during the alpha particle slowing down time moving particles into the stochastic regions and thus causing losses about twice those without collisional effects. Good agreement was found in comparing appropriately normalized TRANSP simulations to measured confined alpha profiles [6].

3. Application to ITER

ORBIT GC simulations for the 21 MA, 20 TF coil ITER Interim design are based on comprehensive, self-consistent TRANSP simulations of two scenarios: moderately peaked density profiles (L-mode) and flat profiles (H-mode). ITER equilibria were obtained with the PEST code using pressure and q profiles from TRANSP, based on cases in the ITER database. TRANSP simulations of ITER also provided alpha source profiles, before and after sawtooth broadening, and collision rates.

The TF ripple data field was fit to $\delta(R, Z) = \delta_0 \exp\{[(R - R_{MIN}(Z))^2 + b_r Z^2]^{0.5} / w_r\}$. Here b_r is the ellipticity, w_r is the scale length of the ripples, δ_0 is the minimum value of the ripple field, and $R_{MIN} = 6.75 - 0.034 Z^2$ is the radius at which this minimum occurs. The magnetic axis is typically at Z = 1.5 m.The ripple field strength increases exponentially with R, and with vertical distance from the midplane, Z. We find $\delta_0 = 3.75 \times 10^{-6}$, with w_r and b_r 0.535 m and 0.268, respectively.

Monte Carlo simulations were carried out for 256 alpha particles of birth energy 3.5 MeV, including collisional pitch angle scattering over one alpha slowing down time and with R = 8.14 m, a = 2.8 m, Ip = 21 MA, B = 5.7 T and edge q of 3.3. The alpha particle source profiles were calculated by TRANSP from simulation of DT fusion, with prescribed D and T profiles and a simple Kadomtsev sawtooth model. Two different alpha source profiles occur in the TRANSP L-mode simulations. A peaked, pre-sawtooth profile was fit by $(1 - |r/a|)^3$ and a sawtooth-broadened profile was fit by uniform density out to r/a = 0.7, and zero for r/a > 0.7. Constant collision rates used were $\nu_{perp}^{\alpha} = 0.126$ sec^{-1} and $\nu_{\varepsilon}^{\alpha} = 5.0$ sec^{-1}.

GC simulations of ITER with the presawtooth, L-mode alpha profile showed no losses of the 256 particles followed, Monte Carlo errors in the particle loss calculations are approximated by $n^{0.5}/n_T$ where n is the number of particles lost and n_T is the total number of

Monte Carlo particles followed. When simulations yield no particles lost, the error should be less than calculated for one lost particle (±0.4%), thus an upper bound to alpha ripple losses is ~ 0.4% in the new design.

The physics of the sawtooth instability is an active area of present research with the details of the sawtooth magnetic field reconnection and its effect on the fast particle distribution function not yet well known. (See for example Ref. 7 where energetic ions were detected very near the plasma edge immediately after sawtooth events in PDX.) The sawtooth broadened L-mode alpha profile led to particle (power) losses of 0.8 (0.7%) ±0.6%. Because of the very short duration of sawtooth broadened alpha profiles in experiments and in present models of the sawtooth instability, the pulse-averaged power losses should be virtually unaffected by the existence of sawteeth and so described by the upper bound 0.4%. However pulsed energy loss may be significant, particularly if large sawteeth give rise to associated MHD activity. Alpha losses from the sawtooth broadened L-mode ITER, with reversed direction of toroidal field, were 1.6 (0.8)±0.8% particle (power) losses.

Simulations were also carried out for the H-mode scenario. The source profile was modelled as trapezoidal, flat to r/a = 0.4, decreasing to zero at r/a = 0.7. The slowing down and pitch angle scattering times are similar to those for L-mode, as are the alpha profiles outside r/a = 0.3. No losses were simulated so that alpha particle energy losses are < 0.4%.

Initial simulations of a Reversed Shear ITER plasma [1] led to no first orbit losses, but 16% alpha ripple power loss and 19% alpha particle losses due to strong banana convection (see Sec. 4 below). An alternative ITER/RS equilibrium [8], with reduced elongation to make the plasma more nearly centered within the TF coil set, is found to lose only 2.9±0.4% of alpha particles. Figs. 1 and 2 show the ripple trapping regions for the ITER 21 MA case and the Interim Design Reversed Shear plasma.

We estimate the heat load for maximum alpha ripple losses for the 21 MA case of 0.4% gives ~ 0.01 MW/m^2, and for the RS cases 0.07 - 0.40 MW/m^2. The wall heat load may be increased by MHD and TAE enhanced losses, in addition to toroidal peaking factors.

4. Theory

In principle, since the mechanisms of ripple-induced alpha loss are well understood, it should be possible to provide a very fast algorithm for determining alpha loss, without the large computational effort associated with unaccelerated GC orbit calculations. Previous efforts [6] in this direction have been based on using a very simplified version of the stochastic loss criterion, given as Eq. 3 in Ref. 9. To provide a match between GC calculations and the stochastic loss criterion, substantial ad hoc normalization factors were required. This is understandable, since the loss criterion used in that work ignored the poloidal dependence of the stochasticity threshold, as well as the effects of toroidal precession.

As indicated in Ref. 9, the transition to chaos occurs when the radial step size in the banana map reaches a critical value, scaled either by the spacing between precession resonances (where the banana precession distance, $R\phi_p$, changes by $2\pi R/N$) or between banana-length resonances (where the banana length, $R\phi_b$, changes by $2\pi R/N$). For the usual case where the the banana-length resonances are much more closely spaced than the precession resonances, detailed calculations of the transition to chaos give the threshold radial displacement:

$$\text{Eq (1)} \qquad \Delta_s = c \,/\, [N\,(|\phi_b'| + d\,|\phi_p'|)]$$

with c = 1.0 and d = 0.5, as opposed to c = 1.0, d = 1.0 estimated in Eq. 15 of Ref. 9. (Primes indicate radial derivatives.) Investigation of the underlying map shows that the transition to chaos in this case occurs as the islands centered at precession resonances replicate across the banana-length resonances and begin to fill all of space. In the region where ϕ_b'/ϕ_p' is not large, the phasing between the two kinds of resonant surfaces becomes important, as represented by $w_k \equiv N\phi_b/2 + N\phi_p/2$, evaluated at resonant surface k. In particular, for $w_k = \pi/2$ and $\phi_b'/\phi_p' = \pm 1$, the stochastic threshold goes to infinity! In the region $|\phi_b'/\phi_p'| < 4$, the stochasticity

threshold must be evaluated as a function of w_k as well as ϕ_b'/ϕ_p' (Fig. 3), and used instead of Eq. (1), above. Eq. (1) has also been generalized for top-bottom asymmetry, giving

Eq (2) $$\Delta_s = 1 / [N ((2-r^p) |\phi_b'| + 0.5\, r^q |\phi_p'|)]$$

with r equal to the ratio of the smaller to the larger ripple strength at the banana tips, p = 0.2, and q = 0.55. Δ_s is the threshold value of the larger ripple. The result of comparing this calculation with GC calculations of stochastic loss for a wide range of equilibria in ITER and TFTR is very favorable, with no evidence of error outside of the expected Monte Carlo statistical noise, as shown in Fig. 4.

In order to provide detailed comparison with full GC calculations (and to predict overall losses), other loss mechanisms must be taken into account. When banana tips are located in regions of ripple wells, two very important processes must be included. If the ripple wells are on the gradB drift side of the plasma, then in most magnetic geometries collisionless ripple trapping is likely to be very rapid [10]. On the other hand, if ripple wells are located on the opposite side of the device, and no ripple wells are located on the gradB drift side - due to up-down asymmetry - then a rapid net outward convective drift of alpha particles is induced. A calculation of this drift rate is shown in Fig. 12 of Ref. [10] and discussed in some detail in Ref. [11]. Finally, any of these loss mechanisms must persist along a near vertical trajectory of constant |B|, for an alpha to be fully lost from the system.

In order to include the collisional effects of pitch-angle scattering and slowing down, all three loss criteria are evaluated 10 to 100 times as the alphas slow down. This permits the GC slowing-down calculation to take place in toroidally symmetric fields, and with greatly accelerated collisions. A factor ~ 200 improvement in computer run time is achieved, while preserving accuracy to within the Monte-Carlo noise of the GC runs, for cases examined to date.

5. Conclusions

Encouraging results are presented for predicted alpha losses in most ITER cases. However, since the losses are so small, more careful evaluation of the alpha birth profiles and sawtooth ejection patterns may be in order to give quantitively accurate results. Potentially serious wall damage issues appear to be avoidable for the 20 TF coil ITER, if the first wall is carefully designed to allow for predicted levels of alpha ripple loss and wall heating and if MHD and TAE enhanced loss is controllable. Attractive reversed shear regimes also appear acessible.

A first principles algorithm with no adjustable normalization factors has been developed which provides an accurate and computationally economical method of evaluating alpha losses. It is well suited for detailed parameter scans in support of ITER flexibility studies.

Acknowledgment

We are grateful to W. Nevins and S. Putvinski, for their interest and help in this work and also to R. J. Hawryluk, K. McGuire and N. Sauthoff for their interest and encouragement. This research was supported by the U. S. Department of Energy Contract No. DE-AC02-76-CHO-3073. C. O. Miller was suppported by a DOE National Undergraduate Research Fellowship.

References

[1] ITER EDA, Documentation Series No. 7, IAEA, Vienna (1995); private communication, S. Putvinski (1996).
[2] White, R. B. *et al.*, " Ripple-Induced Energetic Particle Loss in Tokamaks", Phys. Plas. in press.
[3] Redi, M. H.*et al.*, "Simulations of Alpha Ripple Loss from ITER", Phys. Plas. in press.
[4] White, R. B. and Chance, M. S., Phys. Fluids **27** (1984) 2455.
[5] Redi, M. H. *et al*, Nucl. Fusion, **35** (1995) 1191.
[6] Redi, M. H. *et al*, Nucl. Fusion, **35** (1995) 1509.

[7] Goldston, R. J., *et al*, Nucl. Fusion **27** (1987) 921.
[8] Nevins, W. M., LLNL, private communication (1996).
[9] Goldston, R. J., *et al*, Phys. Rev. Lett. **47** (1981) 647.
[10] Goldston, R. J., *et al*, J. Plasma Phys. **26** (1981) 283.
[11] Yushmanov, P. N., *et al*, Nucl. Fusion **33** (1993) 1293.

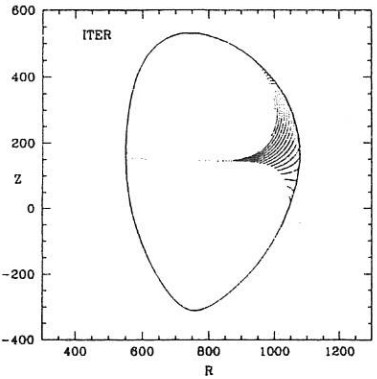

Fig. 1. Ripple well domain in 21 MA ITER

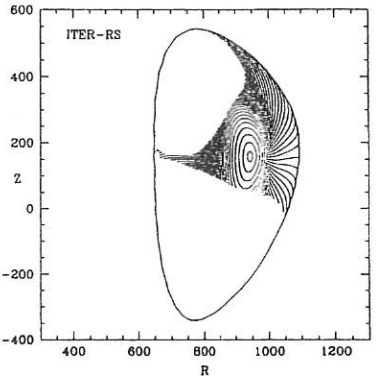

Fig. 2 Ripple well domain in ITER, reversed shear

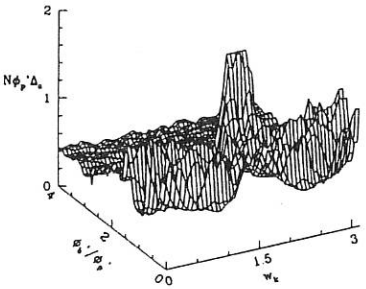

Fig. 3 Stochastic threshold for small ϕ_b'/ϕ_p'

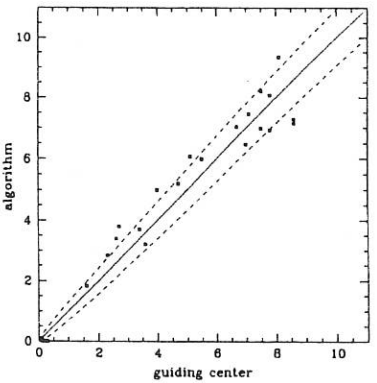

Fig. 4 Loss (%) from algorithm and gc simulation

Extension of TFTR Enhanced Reversed Shear Regime to Larger Core Volume and Higher Current

G.L.Schmidt, S.H.Batha(*), M.G.Bell, F.Levinton(*), J.Manickam, M.Zarnstorff,
and TFTR Group

Princeton Plasma Physics Laboratory, Princeton University, Princeton NJ, USA

(*) Fusion Physics and Technology, Torrance CA, USA

1.0 Introduction: Discharges with weak or negative magnetic shear have recently been produced in TFTR and a number of other tokamaks which exhibit enhanced core confinement. [1,2,3] On TFTR this is termed the ERS regime and has been produced in both D and DT plasmas.

The ERS plasma is marked by strongly reduced thermal and particle transport within the region of shear reversal. The change from high to low diffusivity can occur over a region in minor radius which is small in radial extent, often refered to as an internal transport barrier.

Control and expansion of this barrier allows further improvements in discharge performance by increasing volume of the enhanced core. This paper presents the results of initial experiments in TFTR using increased current ramp rate and higher total plasma current to expand the ERS region. This is a critical issue for the extrapolation of ERS performance. The transition to ERS and MHD stability in the ERS regime are discussed in detail in a separate papers in these proceedings [4,5].

2.0 Scenario: The TFTR ERS scenario consists of an initial ohmic current ramp followed by three periods of beam heating: Prelude, High Power and Postlude phases. The ERS initial ohmic current ramp is different from standard TFTR discharges. Normally, the axis position varies in time to adjust the plasma cross-section, increase axial current density and limit the development of MHD oscillations during the current ramp. In the ERS scenario, the axial current density is limited during the current ramp by positioning the plasma axis near the center of the vacuum vessel from the onset of the discharge which increases the distance the current must diffuse[6]. Early in the current ramp, low power prelude beam injection is begun using predominantly co-injection. Beam driven current develops which maintains the current distribution established during the ohmic phase of the discharge. High power injection is begun during or just prior to the period of constant plasma current. The transition to the ERS regime[4] typically occurs during this phase. Following the transition, a significant bootstrap current develops.

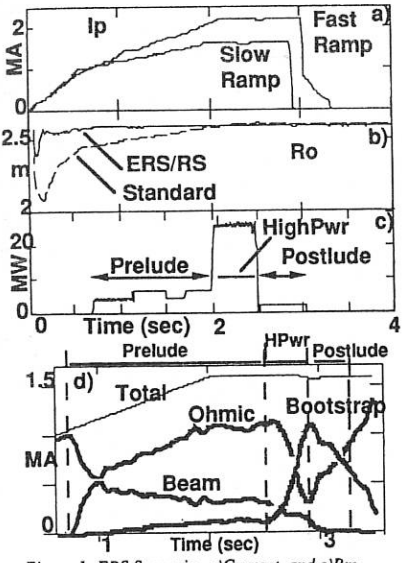

Figure 1: ERS Scenario -a)Current and c)Bm Pwr(93517/94394),b)Radial Position(88170/82528), d) Calculated current components (88170a10)

The ERS regime, once established, can be maintained during a period of reduced heating power (postlude). If modest beam power is applied during this phase the pressure decreases while the core density is sustained. At higher postlude power the pressure and neutron rates can be maintained while both the density and plasma rotation continue to increase.

3.0 q Profile at Larger Rmin The rate of current increase can be used to alter the evolution of the q profile and in particular the location (Rmin) of the minimum value

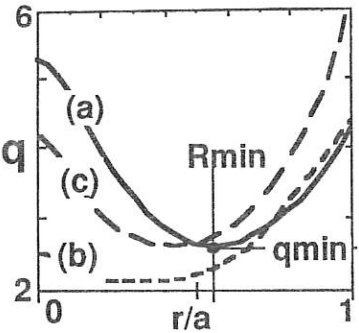

Figure 2: Radial profile of q at ~50ms before start of high power phase; a) fast ramp - 2.2MA, b) slow ramp - 2.2MA, c) slow ramp 1.6 MA

(qmin) of q(r). Increasing the current ramp rate was successful in expanding the region of weak shear and in increasing Rmin, as shown in Figure 2. ERS plasmas were first obtained at a current of 1.6 MA using a "slow" current ramp with a final ramp rate of 0.4 MA/s. The radius of minimum q in this case [curve (c)] is located at r/a=0.4 with a narrow region of near-zero shear. Continuing with the same current ramp rate to 2.2MA total current results in a lower qmin and a smaller region of shear reversal. Increasing the ramp rate to 0.8 MA/s causes the discharge to reach 2.2 MA at 2.0 s and allows earlier beam injection. In this case, curve (a), the rapid addition of current outside the qmin radius acts to broaden the region of negative shear and to maintain the location of qmin near the r/a=0.6 radial position. The volume enclosed within r/a=0.5 is ~30% of the total volume and roughly 50% greater than in the 1.6MA case. The faster ramp rate causes the value of qmin to be slightly lower than for the slow ramp rate, but remains above 2 during high power heating in both slow and fast ramp cases.

4.0 Plasma Response to Larger Rmin q Profiles Differences in power threshold, barrier location and global performance are observed in ERS plasmas at large Rmin.

4.1 ERS Transition (Type I): The presence of larger Rmin affects the conditions required for ERS transition. High power in combination with Li pellet injection are required for transition in the present TFTR large Rmin scenario. With Rmin ~0.4, ERS transitions have been obtained at power levels >16MW at 1.6MA and at 23.5MW for 2.2MA using Li pellet injection. In particular, using Li pellet during the prelude phase appears to improve the reproduciblity of the transition and lowers the power threshold for Type I transitions [Bell]. With Rmin~0.5 in the fast ramp scenario however, transitions were not obtained using this approach with Li pellets 0.8 or 0.15 seconds prior to high power injection and power levels up to 28MW. Transitions in the fast ramp case have been obtained only when power levels of 28MW are used in conjunction with injection of a Li pellet precisely at the start of the high power phase.

These requirements suggest that issues such as beam deposition, the presence of strong gradients in electon and impurity density in the target plasma and the volume of the Rmin region as well as wall conditions could play a role in the transition threshold level. Use of lithium immediately prior to high power produces a high density target plasma at the start of high power injection. This high density target broadens the initial beam deposition profile. Transitions produced under these conditions then occupy a larger volume of the discharge than in cases with smaller Rmin.

The need to use a Li target plasma results in ERS discharges with significant impurity levels. While the impurity level decreases immediately following the pellet perturbation, once a transition has taken place the loss of impurities from the plasma core is reduced and a high core impurity level is maintained.

4.2 Barrier Location:

The enhanced core region is expanded in the presence of large Rmin. In the fast ramp case, the pellet depostion profile of the Li pellet produces a peaked high density plasma with large density gradient near the Rmin radius at the start of the high power phase. This target profile is illustrated in figure 3a by the profile shown at 2.1s. The high density target establishes a broad deposition profile from the start of high power injection. The altered deposition and the formation of a transport barrier combine to produce strong gradients in Te and Ti and to sustain

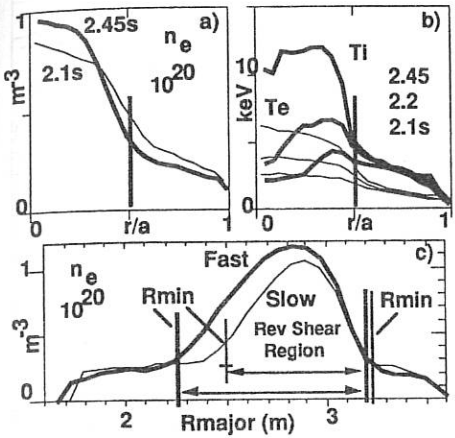

Figure 3: Radial Profiles - Fast and Slow Ip Ramp - Vertical Bar indicates position of Rmin; a) and b) 93517 High Power 2.0 to 2.5s (Fast Ramp) c) Fast/Slow Ramp cases - (93260/88170)

the initial peaked density profile. The strong gradient regions are located just inside the Rmin position at r/a~0.5 calculated using the TRANSP code.

Density profiles for fast and slow ramp cases are compared in figure 3c. While the central density is subject to some uncertainty, the expanded core region in the fast ramp case can be seen from the profiles. The region of improved core transport can be identified by the level of density fluctuations [7]. Low fluctuation levels are observed within the enhanced core. In fast ramp discharges the region of low fluctuation levels is observed to expand in minor radius compared to the slow ramp case extending to the region of strong temperature gradients at larger Rmin.

4.3 Global Parameters: The presence of an enhanced core region can be clearly seen from differences in global discharge parameters when plasmas with and without transitions are compared. Figures 4a,4b and 4c compare RS and ERS plasmas in the fast ramp case. Following the transition the global confinement increases steadily during the high power phase as the core pressure increases. The stored energy continues to increase until the end of high power injection. During the postlude phase, energy confinement increases further and is maintained until the enhanced regime is lost. In the ERS regime confinement is increasing in time. At the end of the high power phase global confinement is almost three times that obtained in the RS regime.

High power injection is ended to avoid, if possible, a plasma disruption. In such a scenario, discharge parameters have not reached steady state levels at high power. Comparison with other regimes which approach steady state must be made with this in mind. With the termination of high power injection, the ERS regime is retained but stored energy begins to decrease at low postlude power. In discharges with large Rmin the ERS regime can be retained for an extended period ~0.5s during this decrease. If the postlude power is increased, plasma pressure and the ERS plasma can be maintained. Performance in this constant pressure postlude is more suitable for comparison with other quasi-steady state regimes. Figure 4d shows the evolution of the DD neutron rate in such a discharge at 1.6MA (slow ramp).

For discharges with peaked pressure profiles the quantity $\beta^* = \beta \sqrt{\langle p^2 \rangle} / \langle p \rangle$ is an appropriate figure of merit which emphasizes the pressure within the core of the discharge. Figure 5 indicates the range of β^* obtained in TFTR ERS discharges and compares these values to super-shot plasmas at several power levels. In the present data set, β^* obtained in ERS discharges is limited at high power by plamsa stability and at low power by the power threshold.

Nonetheless, β* in the range from 1.1 to 1.3% has been obtained in ERS plasmas, comparable to values obtained in steady state supershots at similar powers. β* in present large Rmin experiments is comparable to that obtained in other ERS discharges and is roughly 1.4x the level achieved under similar conditions in RS plasmas which have reached steady state. An indication of potential ERS performance is shown by the steady state ERS point at 14MW which is roughly 2x the RS level at this power level.

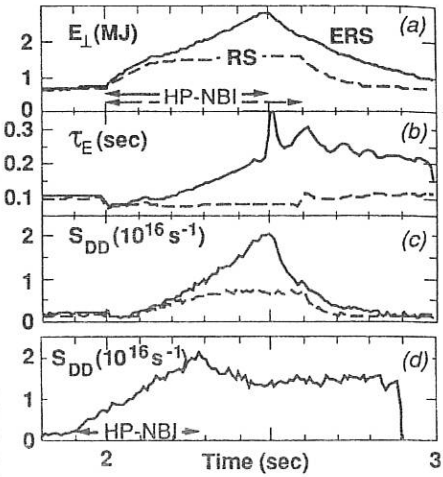

Figure 4- Comparison of ERS (solid) and RS (dashed) discharges through high-power (HP) and postlude phases: (a),(b),(c): 2.2MA with low power (3-7MW) postludes; (d): 1.6MA with higher power (14MW) postlude.

5.0 Stability At Larger Rmin: MHD stability analysis of the high I_p [q(a) ≈ 4.6] discharges shows that they are close to the ideal stability limit just prior to disruption. This observation is similar to that in the lower current discharges. However, there is a distinct difference in the nature of the instability. At the low current [q(a) ≈ 6.3] β limit, the mode is observed to be predominantly internal and extends over the low shear region. In contrast, at higher current and larger Rmin the mode has a distinct external kink component. The reduced shear outside the qmin surface, q(a) - qmin, and the shift of the pressure gradient outwards contribute to a reduced β limit. Theoretical simulations of ERS discharges keeping q(a) > 5, show stability at $\beta_N \approx 2$. This regime can be accessed by slowly ramping down the current as the beam power is increased.

6.0 Summary: Expansion of the ERS core has been obtained by operation with faster current ramp producing plasmas with larger Rmin. The volume of the high confinement region is increased but the use of a high density target plasma produced by injection of a Li pellet limts core power deposition and performance. Transitions in the absence of Li injection and with increased central power deposition will be pursued.

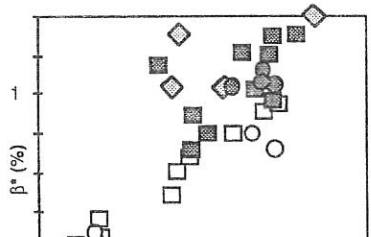

Figure 5: β for ERS and SuperShot Discharges. Circles (Shaded/Open) - ERS/RS at 2.2MA; Squares (Shaded/Open) - ERS/RS at 1.6MA; Diamonds - SuperShots*

Work supported by U.S DoE Contract DE-AC02-76-CH0-3073

1- Levinton et al PRL-75, 4417 (1996)
2- Strait et al PRL- 75,4421 (1996)
3- Koide et al PRL 72,3662 (1994)
4-Bell et al - paper A011 these preceedings
5-Hender et al - these preceedings
6-Batha et al 22nd EPS Conf, Bournemouth II,p 113.
7-Mazzucato et al submitted to PRL

The Fishbone-Instability in ASDEX Upgrade

T Kass, HS Bosch, F Hoenen*, K Lackner, M Maraschek, H Zohm,
ASDEX Upgrade Team, NI Team, ICRH Team and ECRH Team

Max-Planck-Institut für Plasmaphysik, EURATOM Association,
Boltzmannstr. 2, D-85748 Garching, Germany
*IPP Forschungszentrum Jülich GmbH, EURATOM Association,
D-52425 Jülich, Germany

1. Introduction

Stability and confinement are important features of tokomak fusion plasmas. It has been shown, that the fishbone instability [1,2] directly deteriorates the confinement of fast ions in a fusion plasma. As for example the α-particles from the D(T,n)α-reaction are responsible for the heating of a future fusion reactor, this instability can affect ignition of a fusion plasma. Understanding the fishbone instability is therefore an important topic in nuclear fusion research. As all experiments presented here have been examined in pure deuterium discharges the α-particles were simulated throughout by fast deuterium particles injected with an energy of 60 keV.

2. General Features of the Fishbone-Instability

The fishbone instability can be easily identified because of its (namegiving) typical burstlike structure on the signal of the magnetic probes. Fishbones not only vary in amplitude but also in frequency. The temporal variation of the frequency within one single fishbone burst can be calculated with the help of a wavelet analysis (differential Fourier analysis). The result of such an analysis is shown in Fig. 1.

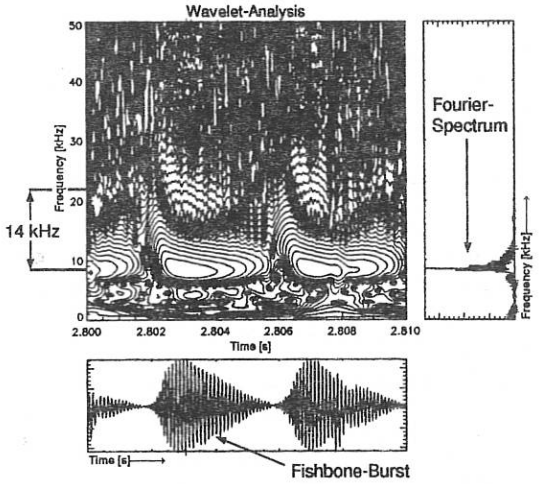

Fig. 1: *A wavelet analysis (differential Fourier analysis) during a fishbone burst shows clearly a frequency decrease within each single burst. Furthermore it exhibits, that the mode amplitude reaches its maximum right at the time, when the mode frequency has whistled down [3].*

In the bottom box the raw signal of a magnetic probe during two fishbone bursts is shown. The plot above displays the result of the wavelet analysis. The vertical axis represents the frequency in kHz, whereas the horizontal axis represents the time in sec. The lines connect areas with equal spectral power. This analysis shows, that a fishbone burst starts with an oscillation frequency of approximately 22 kHz, which decreases continuously within one third of the duration of the burst to the much lower frequency of the plasma rotation ($\approx$ 8.5 kHz in the lab-frame). Thus the difference of 14 kHz represents the actual start frequency of the fishbone burst in the plasma rest frame. Furthermore it can be observed, that the mode amplitude reaches its maximum right at the moment, when the mode frequency has whistled down. Integrating this 2-dimensional distribution over time, one gets the known Fourier spectrum shown in the right box.
A mode analysis exhibits, that the fishbone mode has a toroidal number of n=1 and a poloidal number of m=1 mainly. However higher poloidal mode numbers are also observed during each single burst. The rotation direction of this mode is the ion-diamagnetic drift direction. The amplitude distribution of magnetic probes located at different poloidal positions shows, that the fishbone activity is enhanced at the low-field side of the mid-plane plasma. As the fast trapped ions stay in majority in this area too, a coupling between these ions and the fishbone mode is indicated. During each fishbone burst an ejection of fast ions is detected via a correlated (up to) 20%-reduction of the neutron flux. Measurements of the charge exchange flux confirm this fact directly in showing, that fast particles are ejected from the plasma [4].
A correlation between the fishbone instability and the ELM (Edge Localized Mode) instability located on the plasma edge (far away from the fishbones at the q=1-flux surface) was observed in a high-β-discharge. This might be due to the ejection of the resonant fast trapped particles through the fishbone instability. These ions may enhance the plasma gradient on the plasma edge and thus cause an ELM. But to clear up this issue fully further investigations have to be done.

3. Mechanism

The initial frequency of the fishbone oscillation in the plasma rest frame is identified as the toroidal precession frequency of the injected fast trapped ions. From this, and the observation that the trapped content of the injected fast particles plays the dominant role in destabilizing the fishbone instability, a more detailed understanding of the basic fishbone mechanism can be derived.
The underlying destabilization mechanism is based on the fact, that the deeply trapped ions always stay in the bad curvature region of the magnetic field. Hence they can cause plasma interchange on the resonant q=1-surface, resulting in a resistive (m=1,n=1)-interchange mode. In this case the gradient of the spatial fast trapped ion distribution at the q=1-surface drives the fishbone instability. Because of the precessional movement of the fast trapped ions, the fishbone mode oscillates with the same frequency. Since the fishbone instability continuously ejects the resonant and driving ions it is successively driven unstable by lower energetic ions in the fast-ion-distribution. The fact, that the precession frequency is proportional to the energy of the fast trapped ions explains the observed whistling down of the frequency. If the gradient has been removed, the mode will not be driven any longer and slows down, as shown in Fig 1. It vanishes within the resitive time scale.
The inherent mechanism of successive fishbone cycles can be described in good accordance with the experimental data, if the mode amplitude and the destabilizing fast trapped ions are considered as predator and prey [5]. With this relationship it is possible to model the fishbone instability quite well.

4. Operational Regime

An evaluation of the experimental data leads directly to a stability diagram for the fishbone instability. Fig. 2 plots the toroidal precession frequency of the fast trapped ions against the fast particle pressure $\beta_{fast} = \beta_{tor}/(1+\tau_E/\tau_{sd})$, where τ_E represents the energy confinement time and τ_{sd} the slowing-down time of the fast ions) of several discharges showing fishbone activity (full symbols) and some without (open symbols). It exhibits clearly, that a distinct threshold in the fast particle pressure exists ($\beta_{fast} > 0.009$), above which the fishbone instability can be destabilized in ASDEX Upgrade.

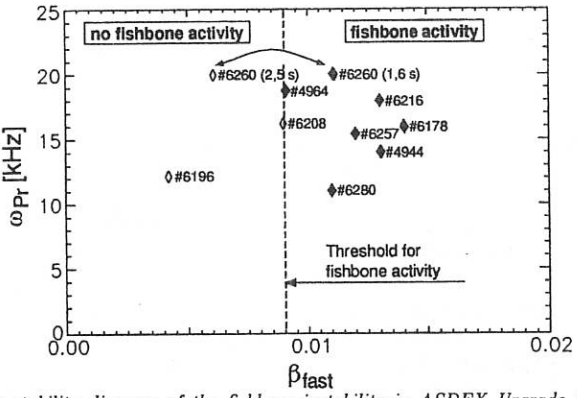

Fig. 2: *The stability diagram of the fishbone instability in ASDEX Upgrade [3]. It shows directly, that the fishbone activity occurs only above a distinct threshold in the fast particle pressure $\beta_{fast} = \beta_{tor}/(1+\tau_E/\tau_{sd})$ (where τ_E is the energy confinement time of the plasma and τ_{sd} the slowing-down time of the fast injected deuterium particles).*

As β_{fast} is a very inconvenient parameter it is useful to express the information of this diagram in terms of adjustable plasma parameter in order to derive a general operational regime of the fishbone instability. This can be achieved by replacing all parameter in the equation for β_{fast} through their explicite terms. For the confinement time τ_E one has to insert the ITER H92P scaling law [6]. Thus it is possible to calculate the operational regime via an evaluation of the following expression [3]:

$$\beta_{fast} = \frac{2\mu_0 n_e T_e/B_t^2 \cdot 3,1 \cdot 10^8 A_b T_e^{2/3}/n_e \ln\Lambda}{0,051 \cdot A_i^{0,51} \cdot I_P^{0,83} \cdot P_{tot}^{-0,51} \cdot R^{1,87} \cdot (\frac{a}{R})^{0,11} \cdot \kappa^{0,5} \cdot B_{tor}^{0,1} \cdot n_e^{0,05}} > 0.009 \qquad (1)$$

It can be seen, that the destabilization of the fishbone mode is more or less independent of the plasma density n_e at constant heating power P_{tot}. Figure 3 displays the calculated general operational regime (for $n_e = 5 \cdot 10^{19}$ m^{-3} and $P_{tot} = 6$ MW) including the location of some discharges with and without fishbone activity. By means of this diagram it is possible to predict the appearance of the fishbone instability depending on the plasma current I_P, the toroidal magnetic field B_{tor} and the central plasma temperature T_e.

Following from that, within the flattop phase of a plasma discharge with constant current, toroidal magnetic field and additional heating power the single free parameter for destabilizing the fishbone mode is the plasma temperature. Thus in a discharge located very close to the destabilization region for fishbones, only small changes in the plasma temperature are necessary to suppress or to destabilize fishbone activity.

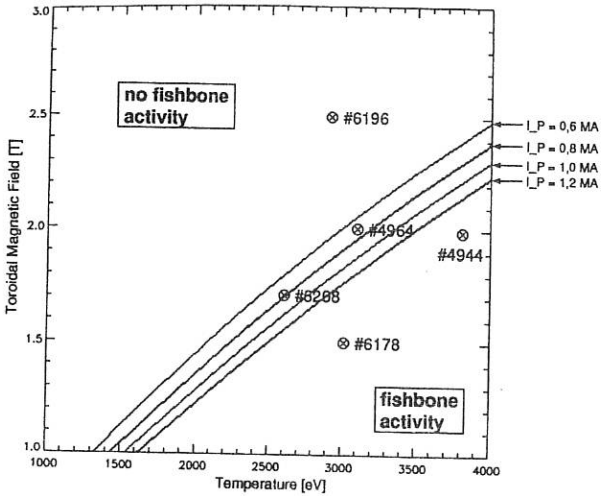

Fig. 3: *The calculated operational regime of the fishbone instability in ASDEX Upgrade [3]. The parameter space is divided into two regions by the line for the plasma current ranging between 0.6 - 1.2 MA. In the upper left area (above the corresponding plasma current line) no fishbone activity is possible, wheras in the lower right area (below the corresponding plasma current line) fishbone activity can be observed.*

5. Summary

The fishbone instability has been investigated in the tokamak experiment ASDEX Upgrade. It can easily be identified due to its burstlike structure on the magnetic probes and the characteristic frequency reduction within each single burst. The basic destabilization mechanism is essentially based on the fact, that the fast trapped ions always stay in the bad curvature region of a toroidal plasma. Thus they can destabilize interchange. Because of their toroidal precession these ions transport this magnetic perturbation in the same direction. As the toroidal precession frequency depends on the energy of the fast trapped ions, the ejection of these particles results in a frequency reduction during each burst. Fishbones occur in ASDEX Upgrade only above the threshold $\beta_{fast} > 0.009$. From this it is possible to calculate generally the operational regime in terms of adjustable plasma parameters like plasma current, toroidal magnetic field and temperature. It turns out, that the destabilization depends only marginally on the plasma density. Thus within the flattop phase of a discharge the single free parameter for destabilizing fishbone activity is the plasma temperature [3].

References

[1] McGuire K et al, *Phys. Rev. Lett.* **50** 891 (1983)
[2] Coppi B and Porcelli F, *Phys. Rev. Lett.* **57** 2722 (1986)
[3] Kass T, PhD thesis, TU Munich, *IPP-Report* **1/298** (1996)
[4] Kass T et al, 22nd EPS Conference, Bournemouth **IV** 41 (1995)
[5] Heidbrink W-W et al, *Phys. Fluids B* **5(7)** 2176 (1993)
[6] Kardaun O et al, *Plasma Phys. and Controlled Fusion Research* (Proc. 14th Int. Conf., Würzburg, 1992), IAEA, Vienna, 3, 251 (1992)

Optimization of radiative H-mode operation

A. Kallenbach, R. Dux, S. de Peña Hempel, G. Becker, H.-S. Bosch, J. C. Fuchs, H. Salzmann, K.-H. Steuer, and the ASDEX Upgrade-, NI-, and ICRH-Teams
MPI für Plasmaphysik, EURATOM Association, Garching & Berlin, Germany

1 Introduction

The optimization of a radiative scenario for the required reduction of the power flow onto the target plates of a fusion reactor needs to consider confinement degradation, fuel dilution and target plate protection. Given that good H-mode confinement is indispensible, but intense type-I ELMs are not tolerable, the power flow through the separatrix must be adjusted into the type-III ELMy region close to the H→L threshold power. To decide on the optimum radiating species, important parameters are the achieved radiated power per central Z_{eff} increase[1], $P_z = \Delta P_{rad}/\Delta Z_{eff}$, and, with regard to the H-L power threshold, the fraction of the main chamber radiation emitted inside the separatrix, $f_z^{in} = P_{rad}^{in}/P_{rad}^{main}$. Both quantities depend on plasma parameters n_e, T_e and transport coefficients[2]. Parameter dependencies of P_z and f_z^{in} are investigated for ASDEX Upgrade and envisaged ITER conditions using an extended version of the impurity transport code STRAHL which was validated against radiative ASDEX Upgrade discharges with Ne injection[3]. We focus on the main chamber radiation, because total divertor radiation below the X-point was found to be always low in ASDEX Upgrade highly radiative regimes.

2 Experimental parameter variations in ASDEX Upgrade

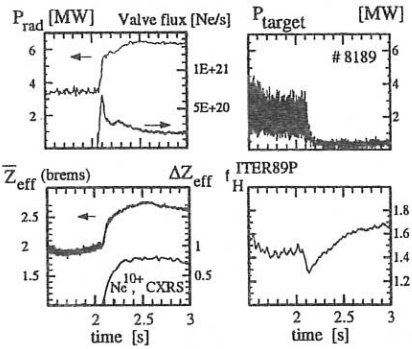

Figure 1: Radiated power in the main chamber, feedback-controlled Ne flux, total divertor power load from thermography, central line-averaged Z_{eff} from bremsstrahlung and the contribution of Ne^{10+} at $\rho_{pol} \approx 0.65$ from CXRS and energy confinement normalized to the ITER89P scaling for a CDH-mode discharge.
P_z= 4 MW, f_{in}= 0.65, P_{heat}= 7.5 MW, $n_0^{div} = 1.5 \cdot 10^{20}\ D_2/m^3$.

Fig. 1 shows time traces for a typical completely detached H-mode (CDH-mode)[4] discharge in ASDEX Upgrade. Right after switching on the Ne radiation feedback at t= 2.05 s, the CDH-mode is obtained, as indicated by a peak target power load below 1 MW and energy confinement improvement. An important ingredient for efficient (i.e. high P_z) radiative cooling is the presence of sawtooth activity. For typical CDH-mode parameters in ASDEX Upgrade (q_{95}= 4), the preservation of sawtooth activity is just marginal. Fig. 2 compares Ne^{10+} profiles measured by CXR spectroscopy for CDH-mode discharges with and without sawtooth activity. If sawteeth are lost, central impurity peaking is always

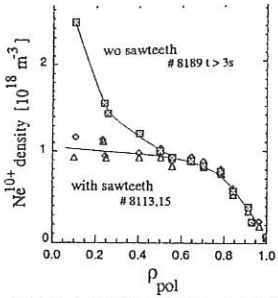

Figure 2: Radial profiles of fully stripped Neon from CXR spectroscopy for standard CDH discharges with and without sawtooth activity. Standard rate coefficients taken from the ADAS database[5] for the $Ne^X(11 \rightarrow 10)$ line emission at 525 nm are corrected by a factor 1/3 to R= $1.7 \cdot 10^{-14}$ m^3/s for the beam energy of E= 30 keV/amu, for E= 60 keV/amu, the original R= $2.9 \cdot 10^{-14}$ m^3/s appears to be correct.

#	t/s	$\bar{n}_e^{main}/m^3$	el.	P_z/MW	f_{in}	$f_H^{ITER89P}$	comments
8113	3.1	$9.8 \cdot 10^{19}$	Ne	4	0.66	1.55	CDH, ST
8189	3.3	$11.3 \cdot 10^{19}$	Ne	3.9	0.67	1.67	CDH, without ST
7546	2.8	$8.5 \cdot 10^{19}$	Ne	3.15	0.67	1.55	radiative H-mode, ST
7548	2.6	$7.1 \cdot 10^{19}$	Ne	3.0	0.69	1.3	radiative L-mode, ST
8178	2.7	$10.3 \cdot 10^{19}$	N_2	$\approx$4	0.46	1.44	divertor-puff CDH, ST
8246	2.4	$9.6 \cdot 10^{19}$	Ar	$\approx$9	0.78	1.35	CDH, transient, ST

Table 1: Radiative discharges near the H/L power threshold with $P_{rad}^{seed} \approx 0.5 \cdot P_{rad}^{main}$.

observed, while with sufficiently high sawtooth frequency, the profiles remain flat. Table 1 compares the most relevant parameters of a number of radiative discharges. Besides a slight increase in energy content, sawtooth suppression has no beneficial effect on the radiative characteristics and should be avoided under all circumstances. N_2 puffing in the divertor does not lead to high divertor radiation, but yet results in peaking of P_{rad} outside the separatrix ($f_{in} < 0.5$). Ar exhibits quite favourable values of P_z, but the confinement is reduced by the more central bulk radiation.

3 STRAHL modelling of radiative discharges and parameter variation

Starting from a well-diagnosed discharge, the influence of individual parameters is investigated using the impurity transport code STRAHL. Electron density and temperature profiles were taken from a measurement with moderate additional neon radiation (Fig. 3a). The radial profile of the diffusion coefficient $D(\rho_{pol})$ in Fig. 3b was determined by dynamic pulse analysis[1], using time-resolved mesurements of Ne profiles from CXRS and soft-X emission data. The discharge kept sawteeth, and no drift had to be introduced for the transport modelling. Good agreement is obtained between STRAHL calculations and measurements for the radiated power in the bulk plasma, Ne^{10+} densities and soft-X emission. The scrape-off layer (SOL) is treated in a simplified way using exponential decay lengths for temperature and density (L_n, L_T) and a parallel loss time $\tau_{parallel}$. Radiated power densities and cooling rates for the experimental case and one with increased D_{edge} are given in Fig. 3 c+d. P_z turns out to be quite independent of D_{edge}, while the distribution of radiation is shifted inward. Keeping the central neon density constant, the contribution to P_{rad} from inside the separatrix increases with D_{edge} due to

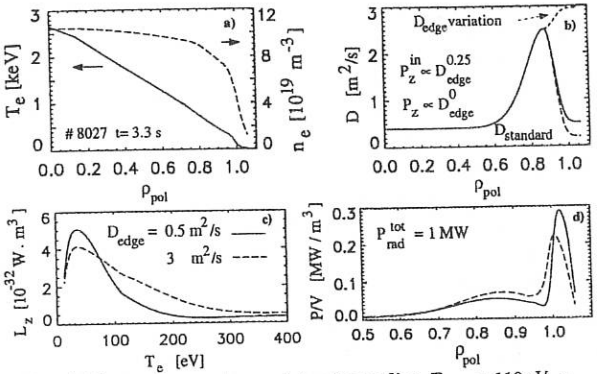

Figure 3: a) Electron temperature and density profiles. $T_{e,sep}$= 110 eV, $n_{e,sep}$= $4.7 \cdot 10^{19}$ m^{-3}, P_{heat}=7.5 MW, P_{rad}=5 MW. b) Diffusion coefficients $D(\rho_{pol})$. c) cooling rate L_z and d) radiated power density, normalized to P_{rad}^{main}=1 MW, for the measured case (solid line) and for high D_{edge}.

the broadening of the H-, He- and Li like radiating Ne shells[2]. The radiation outside the separatrix decreases due to the lower SOL particle confinement time. Fig. 4 shows the influence of the electron density and temperature at the edge on the radiation characteristics. While the contribution to P_z from inside the separatrix is hardly effected, a rise in edge density increases the radiation outside the separatrix considerably. A nearly quadratic increase of $P_z \propto \bar{n}_e^{1.8}$ is obtained, if the electron density profile is scaled with fixed shape. A similar variation of T_e exhibits a much smaller effect. The experimental uncertainty of $n_{e,sep}$ and $T_{e,sep}$ and the crudeness of the SOL model impose some uncertainty on the STRAHL calculations for the radiation outside the separatrix, but P_{rad}^{in} is considered reliable within 25 %.

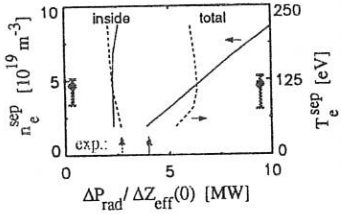

Figure 4: Influence of the *edge* electron density and temperature on radiative characteristics. STRAHL calculations were done with variations of n_e and T_e around the measured values (see Fig. 3a), with L_n and T_n kept fixed. The diagram can also be used to estimate the influence of uncertainties in n_e^{sep} and T_e^{sep}, caused by deficiencies of the flux surface mapping. Generally, the contribution to P_z from inside the separatrix is quite insensitive against variations of n_e^{sep} and T_e^{sep}.

4 Variation of the radiating species for ITER conditions

Fig. 5 shows the radiative efficiencies P_z of different radiative species for ITER conditions. T_e and n_e profiles are taken from a self-consistent reactor study[6], slighty modified with respect to the actual ITER parameters. D(r) was taken from the ASDEX Upgrade results, divided by a factor of 2 resulting in τ_p= 6 s for the ITER case. The atomic data are either taken from the ADAS database or put together by estimating and scaling of the most prominent lines of the individual ionization stages. Except for some individual variations,

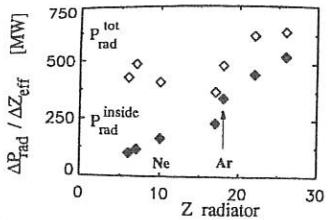

Figure 5: Total radiated power and radiated power inside the separatrix for ITER parameters and various seed elements. $n_e(0) = n_e(sep) = 1.3 \cdot 10^{20}\ m^{-3}$, $T_e(0) = 16.4$ keV, $T_e(sep) = 77$ eV. Hydrogenic bremsstrahlung of $P_{rad} = 47$ MW is not included.

the total P_z appears to be quite independent of the species chosen. Regarding bulk plasma radiation, P_z^{in} increases approximately linear with Z. The individual variations can be important for the development of radiative reactor scenarios, however, the uncertainties of the underlying atomic data are of the same order.

5 Discussion

Increasing the electron density is found to be the most robust way to achieve high radiative losses with a given seed impurity concentration. In ASDEX Upgrade, operation with a high neutral density in the divertor has the beneficial effect of high electron densities near the separatrix and good impurity compression in the divertor, which is favourable for reliable feedback control and necessary for efficient helium ash removal ($\tau^*_{He}/\tau_E < 10$ for the CDH-mode). Therefore, operation in the CDH mode would be an optimum for ITER. If its H-L transition power is low, and given that the power flow across the separatrix has to be reduced at least close above P^{sep}_{H-L} to avoid type-I ELMs, cold divertor conditions will occur naturally[7] for the high electron densities anticipated in ITER at $P_{target} = 5$ MW/m^2. The relatively small values of the energy confinement time associated with high neutral densities in the main chamber can hopefully be improved by a more closed divertor, like the divertor II experiment under construction for ASDEX Upgrade.

Since the edge plasma parameters in ASDEX Upgrade are not too far away from those anticipated for a reactor, it is appropriate to extrapolate measurements and modelling of neon radiative boundary experiments to ITER. Scaling $P_z = 4$ MW with the ratios of the plasma surface[8] (1250/43) and $\overline{n}_e^2$, we obtain $P_z = 205$ MW per unit Z_{eff} increase. STRAHL modelling for ITER parameters results in $P_z = 410$ MW, with a contribution $P_z^{in} = 170$ MW from inside the separatrix, quite consistent with the direct scaling of the ASDEX Upgrade results with its higher f_{in}=0.66 and lower $n_{e,sep}/\overline{n}_e$ values.

The use of alternative impurity species with higher or lower Z will depend on the actual value of the H-L power threshold in ITER. High values of P^{sep}_{H-L} will favour low Z-impurities, supporting divertor power handling by strong SOL radiation. A low P_{H-L} favours higher-Z impurities, with a better core P_z and less dilution. However, the increasing tendency to central impurity accumulation will impose the upper limit on Z. Preservation of sawtooth activity is indispensable, urgently calling for q profile control.

References

[1] A. Kallenbach et al., Nucl. Fusion **35** (1995) 1231. [2] M. Z. Tokar, Nucl. Fusion **34** (1994) 853.
[3] R. Dux et al., this conference. [4] O. Gruber et al., PRL **74** (1995) 4217.
[5] http://patiala.phys.strath.ac.uk/adas/adas.html [6] G. Becker, Nucl. Fus. **35** (1995) 869.
[7] M. Kaufmann et al., to be published. [8] G. Matthews et al , PSI 96 conference.

Online Confinement Regime Identification for the Discharge Control System at ASDEX Upgrade

P. Franzen, V. Mertens, G. Neu, T. Zehetbauer, G. Raupp,
M. Kaufmann, the ASDEX Upgrade Team, and the NI Team

Max-Planck-Institut für Plasmaphysik, EURATOM Association, Germany;
POB 1533, D-85740 Garching, Germany

Introduction

In present experimental fusion devices, the online control of plasma discharges is necessary to achieve certain plasma configurations. For example, the CDH regime at ASDEX Upgrade [1] is established by feedback control of the radiated power from the plasma and the neutral density in the divertor. In order to avoid applying a not adequate set of control parameters to unexpected plasma configurations, the control system has to 'know' the actual plasma regime during the discharge in real time. This knowledge enables the control system to react dynamically to regime changes enhancing the plasma performance and e.g. reducing the disruption rate.

For this purpose, we developed a regime identification algorithm for the discharge control system of ASDEX Upgrade [2]. The basic requirement was a high identification rate provided by a small number of involved plasma parameters which are also online available to the plasma performance controller [3]. This controller has a cycle time of 2.5 ms which is much lower than the energy confinement time.

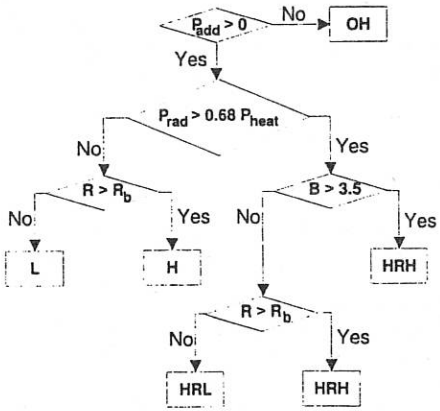

Fig. 1: *Flow chart of the regime identification algorithm at a given moment during a discharge. Additionally, the high confinement regimes H and HRH require the heating power exceeding the H mode threshold power, and the transition from H to HRL is forbidden (see text).*

Regime Identification Algorithm

Figure 1 shows the logical flow chart of a first realization of the regime identification algorithm for the discharge control system at ASDEX Upgrade for a given moment during a discharge. Apart from the OH regime for that the additional heating power P_{add} equals zero, the regimes are divided in low and high confinement regimes with low radiative (L and H regime) and high radiation (HRL and HRH regime) levels, distinguished by the radiated power P_{rad} provided by 10 bolometer channels being below or above 68% of the total heating power P_{heat}.

In the following we describe the regime identification algorithm for the different radiative regimes. The different threshold values and weight parameters (see below) were optimized to match empirically identified plasma

regimes for more than 1200 stationary plasma configurations. With the given values more than 95% of these regimes are recognized correctly offline. The hitting rate is slightly lower online due to small deviations of the online signals from their respective offline values.

For low radiative conditions, low and high confinement regimes are distinguished by using two plasma parameters: the internal inductivity l_i of the plasma and the energy confinement time $\tau_E = W/P_{heat}$, W being the stored energy, provided by magnetic data. H regime is established if the ratio of τ_E to the 1989 JET, DIIID H mode scaling law, $\tau_{E_{JET,DIIID}}$, exceeds a value of 0.7. ($\tau_{E_{JET,DIIID}} = 0.16\, M^{0.5}\, I_p^{1.03}\, P_{heat}^{-0.48}$[4], M being the (mean) mass of the plasma ions in amu, I_p the plasma current in MA and P_{heat} given in MW, respectively.) However, with a few exceptions, this is a necessary, but no sufficient condition for the H regime.

A necessary and sufficient condition for H regime is provided by the internal inductivity which characterizes globally the current profile: lower values represent a flatter profile — i.e. H regime —, whereas higher values are characteristical for the L regime. However, l_i reacts rather slowly — within about 100 ms — to regime changes. Figure 2 shows the dependence of the internal inductivity on the value of q at 95% of the poloidal flux radius, q_{95}, for stationary phases (> 200 ms). As can be seen, the boundary between L and H regime, $l_{i,L\to H}$, is with a few exception unambiguous and depends on q_{95}, as well as on the plasma gas but it seems to be independent on the kind of injected gas by the neutral beams.

From the signals discussed above we can derive a single function R which 'measures' the plasma regime in the low radiative scenario:

$$R = \left(\frac{w_{\tau_E}\,\tau_E}{\tau_{E_{JET,DIIID}}}\right)\left(\frac{w_{l_i}}{l_i}\right), \quad w_{\tau_E} = \left(\frac{\tau_E}{0.7\tau_{E_{JET,DIIID}}}\right)^{\alpha}, \quad w_{l_i} = \left(\frac{l_{i,L\to H}(q_{95})}{l_i}\right)^{\beta}, \qquad (1)$$

introducing the weights w_{l_i} and w_{τ_E} of the respective parameter in order to reduce the influence of the ambiguous τ_E parameter on R. They are chosen in such a way that they equal unity when the respective parameter equal the L to H boundary value ($\tau_E = 0.7\tau_{E_{JET,DIIID}}$ and $l_i = l_{i,L\to H}$, respectively), hence being a measure for the distance to the boundary. The powers α and β are optimized empirically by the number of identified stationary regimes (see above), resulting in $\alpha = 0$ ($\Rightarrow w_{\tau_E} = 1$) and $\beta = 10$.

The L $\to$ H boundary (and vice versa) for low radiative scenarios, R_b, can be expressed as a combination of the respective boundary values of l_i and $\tau_E/\tau_{E_{JET,DIIID}}$

$$R_b = 0.7/l_{i,L\to H}(q_{95}) \qquad (2)$$

Hence, an unambiguous condition for H regime is that R is larger than R_b. A second condition for H regime is that the total heating power exceeds the H regime threshold power P_{th} including the L$\to$H$\to$L hysteresis.

In spite of the fact that l_i reacts rather slowly to changes of the plasma properties — typical time constants are of the order of 100 ms — also the transitions between L and H regime are described sufficiently well within a few 10 ms due to the influence of τ_E on the time constants of R.

As can be seen in the flow chart the high radiative regimes HRL and HRH are obtained if more than 68% of the input power is radiated by injected impurities like Ne or Ar. The CDH regime is a special case of the HRH regime, but up to now the regime identification algorithm does not distinguish the CDH regime with a detached plasma from an attached H regime with a high radiated power level.

For the detached regime, l_i also is increased with respect to the attached H regime; hence it cannot be used for identifying the detached HRH regime. However, this regime can be identified by the changes in the plasma radiation profile characteristic for the detachment. This radiation profile can be characterized by a combination of several line integrated radiation power densities

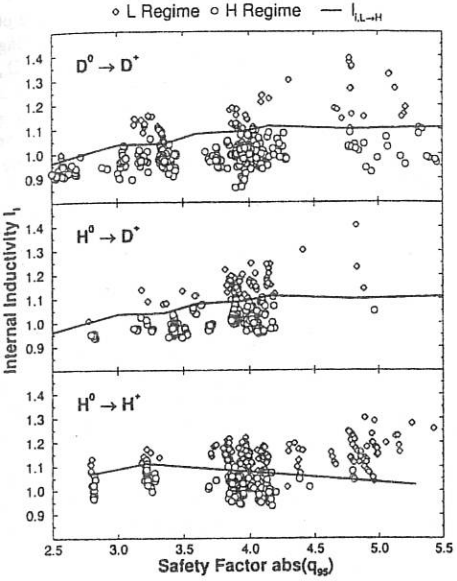

$l_{i,L\to H}(q_{95})$

Plasma Gas: Deuterium		Hydrogen	
q_{95}	l_i	q_{95}	l_i
2.2	0.92	2.8	1.07
3.0	1.035	3.21	1.113
3.35	1.04	5.27	1.023
3.6	1.08		
3.95	1.09		
4.15	1.112		
4.8	1.1		
6.5	1.12		

Fig. 2: *Internal inductivity l_i for L and H regime as function of the safety factor q_{95} for different combinations of plasma ions and injected neutrals. The boundary lines are fitted by a composition of straight lines fixed at the points given in the tables.*

along certain line-of-sights through the plasma measured by bolometer. The resulting parameter B is given by [1]

$$B = \frac{\int \epsilon_{21}\, dl}{\int \epsilon_1\, dl} \frac{\int \epsilon_7\, dl}{\int \epsilon_{11}\, dl}, \tag{3}$$

where ϵ_i denotes the emission from a point $l\,dl$ of the line-of-sight with index i. $\int \epsilon_1\, dl$ gives the radiated power just above the outer divertor plates, $\int \epsilon_7\, dl$ close to the X-point, $\int \epsilon_{11}\, dl$ from a region just above the X-point, and $\int \epsilon_{21}\, dl$ from the equatorial plane, respectively. The first ratio (#21/#1) in Eq. 3 is a measure for the radiated power in the divertor with respect to the main plasma region, being high in the case of detachement. This signal, however, can be falsified by MARFEs which is corrected by the second ratio (#7/#11).

B being larger than a threshold value of 3.5 is an unambiguous condition for the (detached) HRH regime [1], but only for ELM free plasma conditions. In the case that B is lower than 3.5, the plasma might be still attached in spite of the high radiation level, and $R = F(l_i, \tau_E)$ (Eq. 1) is again a 'good' function distinguishing low and high confinement regimes.

A further restriction of the regime identification algorithm is that the H $\to$ HRL transition is forbidden. The radiation profile in the plasma needs a certain time (some 10 ms) for the rearrangement if the radiation level is increased during an H regime, so that the combination of a still low value of B and an increase of l_i due to a possible detachment might lead to the wrong conclusion the plasma being in the HRL regime.

Up to now, the regime identification algorithm can only be used in the flattop phase of the plasma current. This is due the influence of current changes on l_i which might lead to wrong regime predictions.

Example of a dynamically controlled discharge

Figure 3 shows a main application of the regime identification algorithm: the avoidance of disruptions caused by unexpected plasma states. The goal of this discharge was a long lasting CDH regime which is established at about 2 s by neon gas puffing, as can be seen from the D_α and C_{III}^{div} signals. However, due to the high set value of $P_{rad}/P_{heat} = 0.78$, the neon input flux is still increased by the control system after the onset of the CDH regime. Because of the resulting too high impurity concentration, the plasma falls back to the HRL regime, e.g. indicated by the increase of l_i.

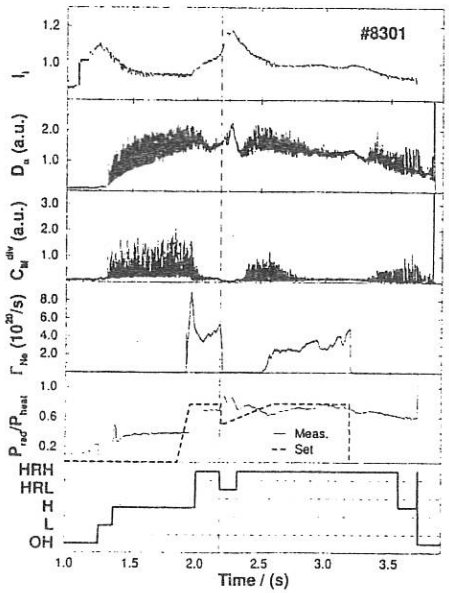

Fig. 3: *Example of a dynamically controlled discharge at ASDEX Upgrade. I_p = 1 MA, B_T = -1.9 T. Neutral beam injection starts at 1.3 second with 7.2 MW. At 2.19 seconds the Ne valve was dynamically switched off by the control system.*

Without online regime control, as it was done earlier, the set of controlling parameters would have not been adequate and the discharge might be e.g. driven into a radiation collapse due to too much Ne puffing. But in the case of this discharge, the control system recognizes the falling back to the HRL regime and closes the Ne valve by setting the set value of P_{rad}/P_{heat} down to 0.5 at the moment the plasma leaves the high confinement regime. Due to the further slow increase of the P_{rad}/P_{heat} set value, the high confinement regime is even recovered.

Summary

A regime identification algorithm was developed and tested successfully for the discharge control system of ASDEX Upgrade. The algorithm distinguishes high and low confinement regimes in low and high radiative scenarios by using only a small number of online available plasma parameters — about 20 signals including 10 bolometer channels —, allowing the control system to react dynamically to plasma regime changes within a cycle time of 2.5 ms.

A main application was demonstrated for the first time in a fusion device: an unwanted and unexpected regime transition was dynamically corrected and the planned regime was recovered reducing the disruption probability and enhancing the plasma performance. In a next step, more regimes will be recognized, e.g. detached regimes using the C_{III} signal from the divertor.

References

[1] Dux, R. and Kallenbach, A., Technical Report IPP 10/1, Max-Planck-Institut für Plasmaphysik, 1996, submitted to Nuclear Fusion.

[2] Raupp, G., et al., in *Proceedings of the 17th SOFT*, p. 1072, Roma, 1992.

[3] Neu., G. et al., in *Proceedings of the 18th SOFT*, p. 675, Karlsruhe, 1994.

[4] Schissel, D.P. et al., Nuclear Fusion **31** (1991) 73.

Bootstrap current derived from different model collision operators

W. Feneberg,
Max-Planck-Institut für Plasmaphysik
EURATOM-IPP Association, Garching, Germany

Introduction

The bootstrap current is an important quantity for the construction of the advanced Tokamak reactor. For this reason it is often studied experimentally and theoretically. The comparison between experiment and theory is always done using the famous formula of Hirshman and Sigmar (1) which is based on an asymptotic solution of the kinetic equation in the limit of very small collision frequency. This calculation was extended by Kikuchi (2) to the range of higher collisionality. In this theory are all collisions described by the Lorentz operator containing only pitch angle scattering.

In order to proof the accuracy of the coefficients entering the bootstrap current the kinetic equation was solved for arbitrary collisionality without the assumption of large aspect ratio and without neglecting energy scattering. Is is statet in the literature (1) that energy scattering has no effect on the parallel viscosity. On the other hand the results from a precise numerical calculation presented here show a small change of the viscous force due to energy scattering such, that the contribution of bootstrap current related to the temperature gradient is in the range of low collisionality reduced by about 30 % compared with the results from the pitch angle scattering model. For the coefficient of the pressure gradient in the bootstrap current one finds always the same value. This quantity is obviously insensitive against a change in the collision model.

Drift kinetic equation and collision operator

The linearized drift kinetic equation for a pure plasma consisting of electrons and ions with charge Z = 1 takes the form given elsewhere in the literature (3). It calculates the solution for the distribution function $g_l = g_l(\eta, w)$ defined as the deviation from a Maxwellian ($f = f_M^{(0)} + g_l$) according to an expansion into the gyroradius parameter $\delta = \rho_\Theta / L$. The velocity variables used here are the random velocity $\vec{w}$ and $\eta = w_\parallel / w_l$, which is the pitch angle. The dependence of g_l from the random velocity involves the condition

$$\int w_{\parallel} g_l \delta^3 w = 0, \tag{1}$$

where $w_{\parallel}$ is the random velocity parallel to the magnetic field (the condition perpendicular to the magnetic field $\int \vec{w}_\perp g_l \delta^3 w = 0$ is fulfilled automatically, because g_l is independet from the gyrophase). In this work, circular magnetic surfaces are assumed with the magnetic field having the standard form

$$(B_\rho, B_\Theta, B_t) = (0, B_{\Theta,_o} R_o / R, B_{t,o} \frac{R_o}{R}),$$

where $R = R_o(1 - \epsilon cos\Theta)$ is the major radius and $\epsilon = \rho / R_o$ the inverse aspect ratio. The collision operator for like particle collisions used here is a model operator close to that

as described in the paper of Bolton-Ware (4). This operator has all the properties of the full collision operator: conservation of particles, momentum and energy. It contains also the decrease of the Coulomb cross section with velocity of the colliding particle as w^{-3}. It reads for the electrons

$$I_{e,e} = \frac{3\sqrt{2\pi}}{4}\nu_{e,i}\left(\frac{A_o(x)}{x^3}\frac{\partial}{\partial\eta}\left((1-\eta^2)\frac{\partial g_l}{\partial\eta}\right) - \tilde{\lambda}B_o(x)g_l\right.$$
$$+ \frac{4}{3\sqrt{2\pi}}xP_l f_M^{(o)}\int_o^\infty \left(A_o + 0.5\tilde{\lambda}x^3B_o\right)a_l e^{-x^2/2}\delta x - f_M^{(o)}\frac{P_o}{\sqrt{2\pi}}(x^2-5)\int_o^\infty \tilde{\lambda}B_o a_o x^2 e^{-x^2/2}\delta_2$$
$$\left. + f_M^{(o)}\frac{P_o}{3\sqrt{2\pi}}(x^2-3)\int_o^\infty \tilde{\lambda}B_o a_o x^4 e^{-x^2/2}\delta x\right) \tag{2}$$

where $x = w/(T_e/m_e)^{1/2}$. The functions A_o, B_o are given in paper (4). The same expression holds for the ions, replacing $\nu_{e,i}$ with $\sqrt{2}\nu_{i,i}$ the Braginskii ion-ion collision time (in the case of ions one has $x = w/(T_i/m_i)^{1/2}$). The first term in equ. (2) is the well known pitch angle cross section which enters also the electron-ion collision term $I_{e,i}$. The second term looks like a modified Krook term which contains energy scattering, but contributes also to momentum exchange. The correction terms proportional to the Legendre ploynomials P_o and P_l are needed to guarantee the conservation properties. The parameter $\tilde{\lambda}$ is used to modify the energy scattering effect.

Method of Solution:
With this model collision operator, the distribution function g_l could easily be expanded in terms of orthogonal functions: That is, Legendre polynomials in η

$$g_l = f_M^{(o)}\sum_{n=o}^{N} a_n(\Theta_l x)P_n(\eta) \tag{3}$$

and a Fourier series in the poloidal angle Θ. Each Legendre polynomial coefficinet a_n consists of $2M+1$ Fourier modes where M is the Fourier mode number. In the equations for the Legendre ploynomials P_o and P_l there enter the unknown integral relations from equ. (2). These where calculated from a system of $6M+1$ linear equations which exists between these $6M+1$ variables: In order to find this system the solution for the Legendre polynomials $a_2 \ldots, a_N$ was inserted into the equ. for P_l and the remaining equations for a_o and a_l, where resolved such, that the quantities a_o and a_l could be expressed by the driving terms and the unknown integral variables. Multiplying each Fourier quantity of a_o and a_l with the functions within the integrals of equ. (2) and integration over the volocity space established the system of equations. The side condition (1) which reads

$$\int_o^\infty e^{-x^2/2}x^3 a_l(\Theta_l x)\delta x = 0 \tag{4}$$

is a condition for only one constant C_o which is posed to be zero: From the zero moment equation for particle conservation it is found that the solution of the kinetic equation fulfills the relationsship $< \int_o^\infty e^{-x^2/2} x^3 a_l \delta x >= C_o$, where $< \ldots >$ is the flux average.

With $C_o = 0$ the momentum is conserved and the solution takes the form (given here for the electrons):

$$\frac{eU_L q}{2\pi T} C_1 + 2\alpha \tilde{d}_{ll}^{(o)} C_2 + \frac{2\alpha q \pi P'}{B_{t,o} e n_e (T_e/m_e)^{1/2}} C_3 + \frac{\rho_g q T'}{12T} C_4 - \frac{q}{\epsilon} \tilde{V}_{\Theta,o} C_5 = 0 \qquad (5)$$

(that is: $e-$ the charge (here is $e > 0$), n_e- density, $P'-$ pressure gradient, U_L the Loop Voltage, $\alpha = \frac{3\sqrt{2\pi}}{4} R_o q \nu_{e,i}/(T_e/m_e)^{1/2}, q-$ safety factor, $\tilde{d}_{ll}^{(o)} = (V_{e,ll}^{(o)} - V_{i,ll}^{(o)})/(T_e/m_e)^{1/2}$, $\tilde{V}_{\Theta,o} = V_{\Theta,o}^{(e)}/(T_e/m_e)^{1/2}, \rho_g-$ electron gyroradius)

In this formula the visours force and the $e-i$ friction force are not seperated. The ion momentum law looks much simpler neglecting terms of order $(m_e/m_i)^{1/2}$, that is

$$\frac{\rho_g^{(i)} q T_i'}{12 T_i} C_4 + \frac{q}{\epsilon} \tilde{V}_{\Theta,o}^{(i)} C_5 = o \qquad (6)$$

The most difficult parameter ranges in the calculation are where collision frequency is very small. Here about 50 Legendre polynomials and 11 to 13 Fourier components (corresponding to M = 5 or 6) are needed to obtain convergence.

Results

The bootstrap current is calculated with the formula

$$j_{bs} = -\frac{q}{\sqrt{\epsilon} B_t} \left(\frac{L_{31}}{\sqrt{\epsilon}} P' + \frac{L_{32}^{(e)}}{\sqrt{\epsilon}} n_e T_e' - \delta_3 \frac{L_{31}}{\sqrt{\epsilon}} n_e T_i' \right) \qquad (7)$$

(here $P = P_e + P_i$ is the total pressure).

Values for the coefficients are given in the tabels 1 to 3. The energy scattering parameter $\tilde{\lambda}$ varies from 10^{-2} to 5.4. The results for $\tilde{\lambda} = 10^{-2}$ (the programm does not allow for $\tilde{\lambda} = 0$) agree perfect with that given by Kikuchi (2). The parameter $\tilde{\lambda} = 5.4$ was choosen by Bolton-Ware (4) because this value fits perfect to the Spitzer-Härm parallel conductivity.

ν^*	$\tilde{\lambda} = 10^{-2}$	$\tilde{\lambda} = 1.0$	$\tilde{\lambda} = 5.4$
0.025	1.41	1.42	1.46
0.05	1.34	1.35	1.38
0.1	1.24	1.25	1.27
0.2	1.11	1.11	1.11
0.3	1.02	1.01	0.99

Table 1: The bootstrap current coefficient $L_{31}/\sqrt{\epsilon}$ for $\epsilon = 0.22$.

ν^*	$\tilde{\lambda} = 10^{-2}$	$\tilde{\lambda} = 1.0$	$\tilde{\lambda} = 5.4$
0.025	−0.29	−0.434	−0.715
0.05	−0.161	−0.30	−0.541
0.1	−0.020	−0.14	−0.34
0.2	0.13	0.026	−0.12
0.3	0.21	0.12	−0.001

Table 2: The bootstrap current coefficient $L_{32}^{(e)}/\sqrt{\epsilon}$ for $\epsilon = 0.22$.

ν^*	$\bar{\lambda} = 10^{-2}$	$\bar{\lambda} = 1.0$	$\bar{\lambda} = 5.4$
0.025	0.62	0.68	0.73
0.05	0.56	0.615	0.65
0.1	0.48	0.53	0.55
0.2	0.39	0.43	0.41
0.3	0.33	0.36	0.32

Table 3: The coefficient δ_3 of the ion poloidal rotation $V_\Theta^{(i)} = \delta_3 T_i'/eB$ for $\epsilon = 0.22$

Conclusion

The effect of energy scattering reduces the amount of bootstrap current related to the temperature gradient: For equal electron and ion temperature one can write $j_{bs} = -q/\sqrt{\epsilon} B_T (L_n \cdot T \cdot n_e' + L_T n_e T')$.

For the example $\nu^* = 0.025$ and $\epsilon = 0.22$ one finds from the results in the tables:

$L_n = 2.82$ $\quad L_T = 1.66$ (for $\bar{\lambda} = 10^{-2}$)

and $L_n = 2.92$ $\quad L_T = 1.14$ (for $\bar{\lambda} = 5.4$)

Central peaking of density is needed in order to achieve a reasonable large bootstrap-current.

References

|1| Hirshmann, S.P., Sigmar, D.J., Nucl. Fusion 21 (1981)

|2| Kikuchi, M. et al, Nucl. Fusion, 30, 2 (1990)

|3| Hirshmann, S.P. et al, Phys. Fluids 29 (9), September 1986

|4| Bolton, C. and Ware, A.A., Phys. Fluids 26 (2), February 1983

Measurement and Modelling of Impurity Transport in Radiating Boundary Discharges in ASDEX Upgrade

R. Dux, A. Kallenbach, K. Behringer, R. Neu, S. de Peña-Hempel, M. Sokoll, and the ASDEX Upgrade-,NI- and ICRH-teams

MPI für Plasmaphysik, EURATOM Association, Garching & Berlin, Germany

Introduction

Radiative cooling of the plasma boundary by controlled injection of medium Z impurities has been demonstrated to yield substantial reductions of the power flow onto the target plates as required for future reactors. Important key numbers for such scenarios are fuel dilution and central radiation loss caused by increased central density of the added impurity depending on the radial transport parameters of the impurity in the bulk plasma. Radiating boundary CDH-mode discharges in the ASDEX Upgrade tokamak with high-power neutral beam injection and neon as radiating species [1] were analyzed and the impurity transport in the plasma bulk was investigated.

CDH-mode types of discharges with different bulk transport

A comparison of two CDH-mode discharges with neon is shown in fig. 1. Both discharges have plasma current I_p=1MA, toroidal field B_T=2.5T and safety factor q_{95}=4. Constant NBI-heating with P_{NI}=7.5MW is used and #8115 has additional 400kW central ICRH-heating. Neon is puffed into the main chamber and the neon puff rate Γ_{Ne} is feedback controlled to reach a constant power fraction P_{rad}/P_{heat} ≈0.9. With the increase of P_{rad} the ELM-type changes from type-I to type-III and the plasma detaches from the target plates as indicated by the CIII signal measured directly above the outer target plate (CDH-mode).

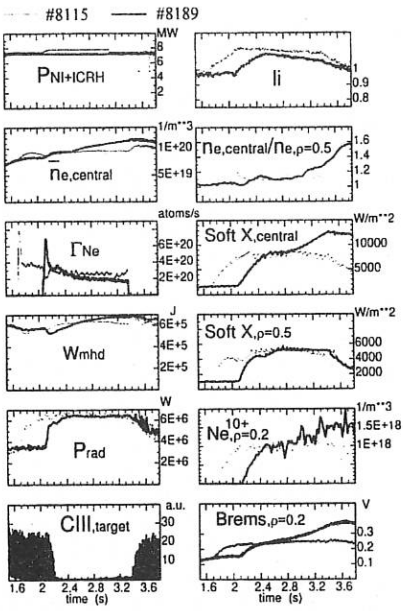

Figure 1: Comparison of two CDH-discharges with different central transport behaviour.

After the onset of the CDH-mode both discharges show similar behaviour for the first 0.4s. For the rest of the CDH-phase, however, the bulk transport for both discharges is very different. The electron density profile, represented by line-averaged values of a central line-of-sight and the density ratio $n_{e,central}/n_{e,rho=0.5}$, remains constant for #8115 while it peaks for #8189. The soft x-ray time traces of a central chord and a chord with $\rho_{pol,tan}$=0.5, stay nearly constant for #8115 and show a strong peaking for #8189. As will be shown later, this strong peaking of the soft x-ray profile for #8189 can only be explained by a central accumulation of neon. Some indication to this is also given by the density of the fully

ionized neon at ρ_{pol}=0.2 measured by charge exchange recombination spectroscopy and by visible bremsstrahlung measurement on a chord with $\rho_{pol,tan}$=0.2. The internal inductivity l_i is a measure of the current profile peaking. For #8189 lower l_i values, i.e. flatter current profiles, are observed due to higher resistivity in the plasma center: $\eta \propto Z_{eff} T_e^{-3/2}$. The stored energy W_{mhd} reaches higher values in the case of peaked electron and impurity density profiles(#8189).

The development of the peaking in #8189 is accompanied by a suppression of sawteeth and the growth of an m=1-mode while #8115 shows strong sawteeth during the whole discharge. In a number of radiating boundary discharges (CDH-mode and H-mode) with parameters nearly identical to the ones presented here sawteeth are always found to suppress central peaking of electron density and neon while the lack of sawteeth always leads to peaked profiles. When reaching high levels of radiated power fraction the plasma is very close to the limit of sawtooth instability. We observed discharges with and without sawteeth in type-I ELM'y H-modes as well as in CDH-modes. For L-mode the database is not very large, but here sawteeth were always present. Triggering of sawteeth by central ICRH-heating could not clearly be seen for the heating powers reached so far ($\approx 500kW$).

Modelling of Impurity Transport in the Case of no Sawteeth

The neon transport and radiation has been modelled with the radial impurity transport code STRAHL [2] using atomic data from the ADAS [3] database. The code uses measured profiles of electron density and temperature in the main plasma, the scrape-off layer is treated in a simplified manner applying decay lengths which are fitted to measured data. The radial transport equations are solved by an ansatz of anomalous and/or neoclassical diffusivities and radial drift velocities. The neon source function is evaluated from the measured valve fluxes using an empirical description of recycling and pumping with a simple chamber model [4].

In fig. 2 various profiles are given for three time points of the discharge #8189 and are compared with measured values. The first time point represents the case with flat impurity profile and sustained sawtooth action, the second with peaked impurity profile at the end of the CDH-mode shortly before the neon puff stops and the third 0.5 s after neon puffing. The total neon density and the according ΔZ_{eff} is shown in fig. 2a and 2b. Fig. 2d gives the measured electron densities for these times. Note that the peaking of neon coincides with a peaking of the electron density.

Fig. 2c and 2e show a comparison of measured and calculated radiation fluxes for two soft x-ray pinhole cameras, which cover the total poloidal plasma cross section, plotted over the minimal poloidal flux label of the according line-of-sight (negative flux labels for chords below the plasma center). One camera is equipped with an $8\mu m$ thick beryllium filter, cutting out all radiation below ≈1keV. It is sensitive to line radiation of hydrogen-like and partly helium-like neon ions, but from all other ionization stages of neon and from other lighter impurities only bremsstrahlung and recombination radiation contribute. The other camera has a $100\mu m$ thick beryllium filter, which makes the camera insensitive for all line radiation of the light impurities due to an energy limit of ≈2.5keV. Thus the $100\mu m$-camera observes always peaked profiles, while the $8\mu m$-camera measures hollow or peaked profiles because there is always a second maximum of the emissivity around ρ_{pol}=0.85 due to line radiation of H- and He-like neon. The signals of both cameras are dominated by the neon radiation and the neon on/off ratios are about 5:1 to 10:1. The background radiation due to intrinsic impurities was treated by just considering carbon

and adjusting the carbon level to such a level, that the pre-puff radiation profiles could be fitted. Then the transport parameters for Ne and C were adjusted to get the best agreement of the modelled and measured soft x-ray radiation fluxes.

In fig. 2g the modelled densities of fully ionized neon are shown together with the measured values from charge exchange recombination spectroscopy (CXRS). The fit to the soft x-ray data gives also good agreement with the CXRS-data. Unfortunately the innermost point at ρ_{pol}=0.11 has a high uncertainty due to low signal.

As one can see from the time traces in fig. 1, the impurity peaking coincides with a peaking of the electron density. Thus we tested, whether the impurity profiles can be explained by neoclassical pinch terms being proportional to the slope of the proton profile ($v_{drift,neo} \propto dn_p/dr$), which in turn is self-consistently modelled from the given electron density and the impurity density (drifts due to friction between impurities were neglected). However, since the profile shape is determined by the ratio of drift velocity and diffusivity a serious test can only be performed when the anomalous diffusion coefficient D_{an} is known. In former investigations [5] we found hollow profiles for the diffusion coefficient with central values of 2-3 times the neoclassical value (thick grey line in fig. 2f), however, these values are sawtooth-averaged. Now we assumed that in the sawtooth-free period of the discharge the diffusion reduces to neoclassical values in the center (solid line in fig. 2f). With this low central diffusion and by increasing the neoclassical drift velocities by a factor of 1.5 (fig. 2h) the peaking of impurity and soft x-ray emission could be described. The gradients of T_e and n_e are rather uncertain in the steep gradient zone $\rho_{pol} > 0.9$ and only anomalous transport was used in this region.

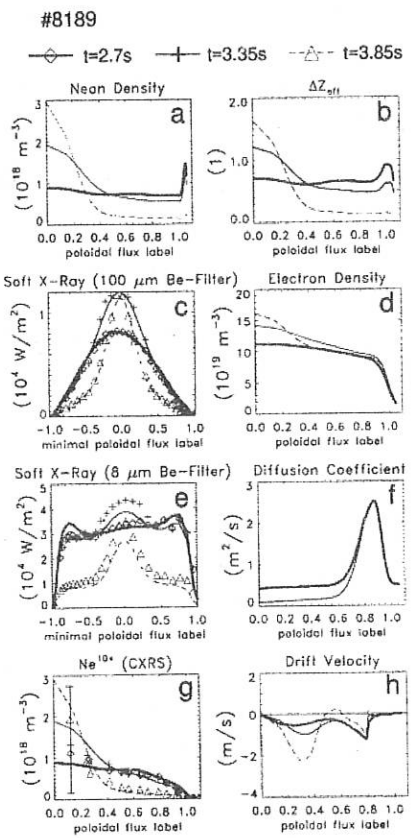

Figure 2: Neon density and soft-x radiation profiles for three time points of discharge #8189 modelled with impurity transport code STRAHL in comparison with measured profiles.

Due to the uncertainties in the profiles of density, temperature, safety factor and anomalous diffusion this analysis of impurity peaking in terms of neoclassical theory is certainly not a real quantitative check but the qualitative features of the strong impurity peaking are described well.

Central Impurity Transport with Sawteeth

For a first investigation of sawteeth induced impurity transport in discharge #8115 an unfolding of the additional soft x-ray radiation fluxes after the neon puff (measured with $100\mu m$ Be-filter) was performed assuming constant emissivity on flux surfaces. Fig. 3b shows the large modulation of the central soft x-ray emission in comparison to the variation of the central electron temperature in fig. 3c and the electron density in fig. 3a. From the soft x-ray emissivities the total neon densities in the center and at ρ_{pol}=0.5 (fig. 3d) were calculated taking into account the central variation of T_e while at $\rho_{pol} = 0.5$ constant T_e was used. It is clearly seen that in the CDH-phase every sawtooth leads to a completely flattened or even slightly hollow profile, which develops into a peaked profile until the onset of the next sawtooth. Just after the neon puff starts the neon profile is of course hollow and the sawteeth cause central filling of the neon profile. These observations are consistent with the picture that sawteeth produce a mixing of the impurity inventories inside and outside the q=1-radius [6]. From the time constant for profile recovery after a sawtooth crash and the sawtooth frequency the peaking for zero frequency can be calculated being only ≈10% higher than the observed mean peaking. Thus, even between sawtooth crashes the central transport of #8115 has a lower inward drift parameter compared with #8189 because n_e is only slighlty peaked.

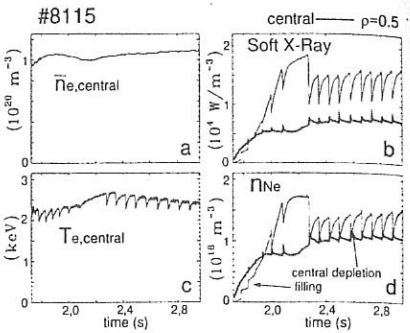

Figure 3: Sawtooth modulations of neon densities evaluated from the variation of soft x-ray emissivity, electron density and temperature.

Conclusions

For CDH-mode discharges in ASDEX Upgrade neon density profiles have been determined from soft x-ray measurements using the impurity transport/radiation code STRAHL. For constant radiated power the central neon density varies strongly for discharges with and without sawteeth. All discharges in ASDEX-Upgrade with high radiation level are close to the stability limit of sawteeth. For discharges without sawteeth there is a strong neon peaking which can be explained qualitatively by neoclassical drifts due to peaked proton profiles. For discharges with sawteeth the neon peaking is reduced. The neon inventories inside and outside the q=1-radius are effectively mixed during a sawtooth crash. Only CDH-modes with sawteeth and flat electron profiles give useful values of $\Delta P_{rad}/\Delta Z_{eff}$ [7] and further experiments to preserve sawteeth by central heating will be performed.

References

[1] J. Neuhauser et al., PPCF. **37** Suppl. 11A, A37 (1995).
[2] K. Behringer, JET-R(87)08, JET Joint Undertaking , Culham (1987).
[3] H. P. Summers, JET-IR 06, Jet Joint Undertaking, Culham (1994).
[4] R. Dux et al., to appear in PPCF. [5] A. Kallenbach et al., Nucl. Fus., **35** 1231 (1995).
[6] A. Ödblum et al., Phys. Plasmas, **3** 956 (1996). [7] A. Kallenbach et al., this conference.

Radial Current Balance in ASDEX Upgrade discharges in the L and H-mode phases

H.J. de Blank, J. Stober, W. Suttrop, ASDEX Upgrade and Neutral Injection teams
Max-Planck Institut für Plasmaphysik, EURATOM-Association, 85740 Garching, FRG

1. Introduction

The radial electric field E_r near the last closed flux surface in tokamak plasmas can differ markedly between the L- and H-mode states and, indeed, may play a central role in the bifurcation mechanism between these two modes. It has been proposed[1,2] that:
a. a sheared radial electric field is responsible for the suppression of fluctuations and the improvement of confinement in the H-mode.
b. near the plasma edge non-ambipolar radial particle fluxes can be identified which depend non-linearly on E_r. The steady state condition of vanishing radial current yields one or more solutions for E_r.
The combination of these two ingredients may give rise to a bifurcated state because modified transport leads to changes in the density and temperature profiles, the non-ambipolar particle fluxes, and hence to different solutions E_r. This paper leaves open the question whether mechanism (a) is active in creating the L-H bifurcation, or merely describes how transport levels respond to bifurcated values of E_r determined solely by (b), although recent experiments [3] show that the E_r increase takes much longer than the actual L-H transition. In the present paper, the second assertion (b) is tested for specific ASDEX-Upgrade L-mode and H-mode plasmas, by evaluating several sources of non-ambipolar radial particle flux as a function of E_r which, because its value is poorly known, is treated here as a free parameter. The following fluxes are considered:
1. The ion orbit loss flux, mainly caused by pitch-angle scattering of ions into loss orbits onto the divertor plates. The vertical drift is essential in explaining the preferential loss of ions over electrons.
2. The neoclassical radial current in the collisional and plateau regimes, which can be non-ambipolar in the presence of an electric field.
3. Charge exchange friction between the ions and atoms.
In most cases only one solution is found, usually at a low value of E_r. Very close to the separatrix this is the case because a large charge exchange flux limits E_r, while far inward the ion orbit loss flux simply is too low to generate a substantial field. By contrast, in an intermediate region 4–8 mm inside the separatrix in H-mode plasmas (but not in L-mode), two solutions are found. This bifurcated solution may be responsible for the hysteresis in the heating power at transitions between L-mode and H-mode.

2. Prior discussion of the non-ambipolar fluxes

ion orbit loss The ion orbit loss flux Γ_{OL} can generate a radial electric field $E_r < 0$ because it is non-zero even if $E_r = 0$. The dominant contribution to this loss process comes from ions with a large vertical drift (barely circulating) and a few times the thermal velocity, which are pitch-angle scattered into loss orbits. This flux is relevant in a layer of width $\sim \rho_{pi}\sqrt{\epsilon}$ inside the last closed flux surface, where, importantly, it is a strictly increasing function of radius. Here $\rho_{pi} = mv_{ti}/\epsilon B_p$ is the poloidal ion gyroradius, and ϵ is the inverse aspect ratio.

The results of Ref. [4] are adopted, where the ion orbit loss process is described as a combination of pitch angle scattering and radial diffusion, with two modifications: *(i)* the effect of $E_r \neq 0$ on the loss boundaries in phase space for the ASDEX-Upgrade single-null X-point geometry has been studied, and has been modeled by a 1-parameter fit to the explicit expressions for $\Gamma_{OL}(E_r)$ at the separatrix in Refs. [1,2], and *(ii)* it is recognized that the non-ambipolar loss flux is reduced depending on the collisionality ν_* of the loss orbit. For simplicity, we take ν_* to be the collisionality of the originally confined ion. In fact, we believe the effect of collisions on the loss orbit to be important and a source of high uncertainty, requiring detailed drift orbit calculations. In particular, the average length of the loss orbits strongly depends on the ion drift direction, being much longer in case the drift is away from the X-point. Indeed, if the collisionality on the loss orbit is artificially doubled in our calculations to simulate unfavourable drift, the H-mode solutions (presented below) disappear. The discharges analysed in this paper all have the favourable ion drift direction.

neoclassical flux In response to a radial electric field there will be a neoclassical radial current $\epsilon\Gamma_{NC}$, for which the expressions of Ref. [5] will be used. This flux is a non-monotonic function of E_r. Hence the current balance $\epsilon\Gamma_{OL} + \epsilon\Gamma_{NC} = 0$ may, depending on ν_*, give rise to multiple solutions in E_r and the L-H bifurcation [1].

charge exchange flux As pointed out in Ref. [6], the rotation velocity associated with E_r can be subject to charge exchange friction between ions and neutral particles, leading to a non-ambipolar flux Γ_{CX}. This flux increases roughly linearly with E_r so that, at a sufficiently high neutral density n_N, it completely cancels the non-monotonic character of Γ_{NC}, thus barring the possibility of an H-mode solution at the considered flux surface. This is what will happen close to the edge, where n_N is highest. Thus, Γ_{CX} forces the H-mode bifurcation somewhat inward, away from the separatrix. This also resolves a technical point: the expressions for Γ_{OL} and Γ_{NC} do not properly take into account the X-point geometry, and the equation $\Gamma_{OL} + \Gamma_{NC} = 0$ breaks down at the separatrix.

Summarizing, the possibility of a H-mode will depend critically on the existence of a layer some distance inside the separatrix, sufficiently far so that n_N is low, but not so far that $\Gamma_{OL}(r)$ is too small. In the following, this possibility will be investigated for several ASDEX-Upgrade discharges.

3. Experimental data

The analysis requires knowledge of T_e, T_i, n_e and their gradients, and of n_N, with high spatial resolution in the vicinity of the separatrix. A Li beam and FIR laser interferometry provide the $n_e(r)$ measurements, while $T_e(r)$ is obtained from 16-channel Thomson scattering and 45-channel ECE radiometry. The used profiles are averaged over a quasi-steady state time interval lasting 0.04–0.55 s, which in most H-mode cases is an average over many type-I edge localized modes. These profiles, together with a parametrized T_i profile, have also been used as plasma background in Monte-Carlo neutral particle calculations with the EIRENE code [7]. The T_i parameters are fitted to measured energy-resolved neutral flux data [8]. These calculations yield $T_i(r)$, $n_N(r)$, and $T_N(r)$ ($\approx T_i$ in the domain of interest).

4. Analysis and discussion

The case presented in detail here is a discharge (ASDEX Upgrade #6138), with $B_t = 2.5\,\mathrm{T}$ and $I_p = 1.0\,\mathrm{MA}$, which is in ELMy H-mode during heating with $P_{\mathrm{NBI}} = 7.5\,\mathrm{MW}$. A time interval $t = 2.4$–$2.6\,\mathrm{s}$ has been chosen where the line-averaged density is constant, $\overline{n}_e = 8.9\,10^{19}\mathrm{m}^{-3}$. The radial fluxes Γ_{OL} and $-\Gamma_{\mathrm{NC}} - \Gamma_{\mathrm{CX}}$ have been calculated for 10 radial positions $\hat{\rho} = 0.94, \cdots, 1.03$ around the assumed separatrix position, neglecting ion orbit squeezing effects. The radial coordinate $\hat{\rho}$ is defined in terms of the normalized poloidal flux, $\hat{\rho} \equiv \sqrt{\psi/\psi_{\mathrm{sep}}}$. All particle fluxes Γ have been made dimensionless by normalization with respect to $nv_{ti}^2/\Omega_i r$ (*i.e.*, current densities normalized to p/rB). As a measure of E_r the poloidal Mach number $M_p = -E_r/v_{ti}B_p$ is used.

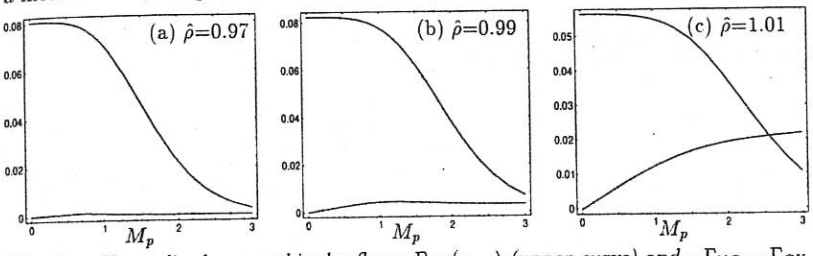

Fig. 1 *Normalized non-ambipolar fluxes $\Gamma_{\mathrm{OL}}(r_{\mathrm{sep}})$ (upper curve) and $-\Gamma_{\mathrm{NC}} - \Gamma_{\mathrm{CX}}$ (lower curve), as a function of M_p, for 3 values of the radius, $\hat{\rho} = 0.97, 0.99, 1.01$.*

Figure 1 shows the orbit loss flux Γ_{OL} and the balancing flux $-\Gamma_{\mathrm{NC}} - \Gamma_{\mathrm{CX}}$, for the profile data taken at the radii $\hat{\rho} = 0.97, 0.99, 1.01$. Here, Γ_{OL} is the total ion orbit loss flux through the separatrix for the density and collisionality measured at the position $\hat{\rho}$, not the smaller fraction of the flux $\Gamma_{\mathrm{OL}}(r) \sim \exp\big((r - r_{\mathrm{sep}})/\rho_{pi}\sqrt{\epsilon}\big)$ at the distance $r_{\mathrm{sep}} - r$ inside the separatrix that coresponds to $\hat{\rho}$. The latter value, $\Gamma_{\mathrm{OL}}(r)$, is so sensitive to uncertainties in the separatrix that we treat it as an unknown.

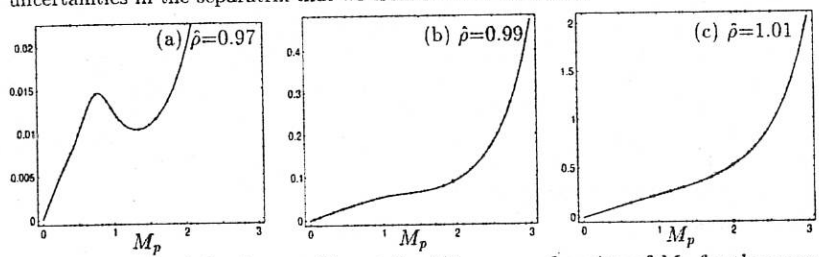

Fig. 2 *Ratio of the fluxes, $-(\Gamma_{\mathrm{NC}} + \Gamma_{\mathrm{CX}})/\Gamma_{\mathrm{OL}}$, as a function of M_p for the same discharge and radii as Fig. 1.*

With this in mind, the quantity $-(\Gamma_{\mathrm{NC}} + \Gamma_{\mathrm{CX}})/\Gamma_{\mathrm{OL}}$ is plotted in Fig. 2. It is equal to the ratio $\Gamma_{\mathrm{OL}}(r)/\Gamma_{\mathrm{OL}}(r_{\mathrm{sep}})$ that is required for current balance. This ratio being a free parameter, curves like those in Fig. 2 determine if bifurcated values of E_r can exist at a given $\hat{\rho}$: in Fig. 2, the curve for $\hat{\rho} = 0.97$ is non-monotonic, allowing for multiple solutions in E_r, while the other curves do not. Note that non-monotonicity of $\Gamma_{\mathrm{NC}} + \Gamma_{\mathrm{CX}}$ alone, as shown in Fig. 1 for $\hat{\rho} = 0.99$, is not sufficient for a bifurcation.

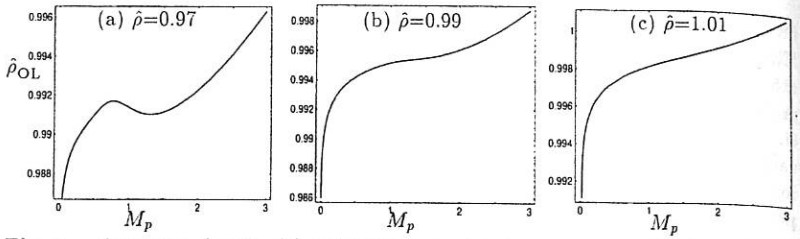

Fig. 3 *Assuming that $\Gamma_{OL}(r)$ inside the separatrix has an exponential decay length $\rho_{pi}\sqrt{\epsilon}$, the data of Fig. 2 is expressed as a normalized radius $\hat{\rho}_{OL}$. This radius indicates how far inside the separatrix $\Gamma_{OL}(r)$ is smaller than $\Gamma_{OL}(r_{sep})$ by the exact amount needed for current balance. These radii need not agree with the positions where the data were taken ($\hat{\rho}$ =0.97, 0.99, 1.01).*

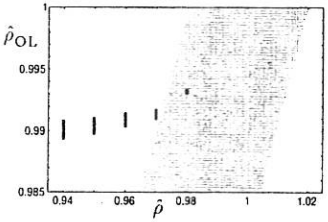

Fig. 4 *As in Fig. 3, the vertical scale is the radius $\hat{\rho}_{OL}$ where $\Gamma_{OL}(r)$ has the value required for current balance. On the horizontal scale is the normalized radius $\hat{\rho}$ at which the data is taken. The vertical lines show the range where a bifurcation in M_p exists. The shaded area gives the correspondence between $\hat{\rho}_{OL}$ and $\hat{\rho}$, with a ± 2 cm uncertainty in the separatrix position.*

Earlier during the same discharge, the L-mode exists at a heating power $P_{NBI} = 2.5$ MW. At that time, $-(\Gamma_{NC} + \Gamma_{CX})/\Gamma_{OL}$ is a monotonic function of M_p in the entire range $\hat{\rho} = 0.94$–1.03, *i.e.*, a bifurcation exists nowhere. However, later in the discharge the plasma remains in H-mode when P_{NBI} is stepped down from 7.5 MW to 2.5 MW thanks to the hysteresis effect. In this case $-(\Gamma_{NC} + \Gamma_{CX})/\Gamma_{OL}$ indicates that a bifurcation is possible in the range $\hat{\rho} = 0.94$–0.95. This is, however, far inward: there is a large mismatch $\hat{\rho}_{OL} < \hat{\rho}$, and the overlap that was found in Fig. 4 is absent.

Analysis of several other discharges confirms these findings: the data of discharges that are deep in the H-mode are consistent with a bifurcation of E_r just inside the separatrix. In cases with H-mode just above the power threshold, the higher charge exchange friction near the edge forces the zone suitable for a bifurcation inward, where Γ_{OL} is found to be insufficient for H-mode. This may indicate that the present model underestimates Γ_{OL}. The analysed L-mode cases are all far away from a possible bifurcation, independent of uncertainties in Γ_{OL}.

References

[1] K.C. Shaing, and E.C. Crume, Phys. Rev. Lett. **63** (1989) 2369.
[2] K.C. Shaing, E.C. Crume, and W.A. Houlberg, Phys. Fluids B **2** (1990) 1496.
[3] W. Herrmann, *et al.*, Phys. Rev. Lett. **75** (1995) 4401.
[4] K.C. Shaing, Phys. Fluids B **4** (1992) 3310.
[5] K.C. Shaing, C.T. Hsu, and P.J. Christenson, Plasma Phys. Control. Fusion **36** (1994) A75.
[6] K.C. Shaing, and C.T. Hsu, Phys. Plasmas **2** (1995) 1801.
[7] D. Reiter, KFA Jülich reports, Jül-1947 (1984) and Jül-2599 (1992).
[8] J. Stober et al., this conference, paper f010.

Transport Investigations using "Dimensionally Similar" Discharges in ASDEX Upgrade

M. Alexander, O. Gruber, H. -U. Fahrbach, O. Gehre, S. de Peña Hempel, K. Lackner, H.- D. Murmann, G. Pereverzev, H. Salzmann, J. Schweinzer, W. Suttrop, ASDEX Upgrade and NI groups

MPI für Plasmaphysik, EURATOM Assoziation, D-85748 Garching, Germany

Introduction

The diffusion of heat across magnetic flux surfaces is of fundamental importance to magnetic confinement fusion research. Heat diffusion in tokamaks and stellarators is much faster than allowed by neoclassical theory, and it is commonly assumed, that plasma turbulence is responsible for anomalous transport, but the specific nature of it is still unknown. Using the scale invariance approach to confinement scaling [1,2] the thermal diffusivity can be expressed as a power law in the normalized gyroradius $\rho_* = \rho_I/a \sim (A_i T)^{1/2}/(Ba)$ in a dimensionally correct form as

$$\chi = \chi_B \rho_*^{\alpha} F(\nu_*, \beta, q, \text{shape}, \ldots.) \qquad (1),$$

with the Bohm diffusivity $\chi_B \sim T/B$, collisionality $\nu_* \sim qn/T^2$ and normalized pressure $\beta \sim nT/B^2$ (safety factor q, plasma density n, electron or ion temperature T, magnetic field B). If the scaling with ρ_* is known, then the transport behavior of existing experiments can be scaled to larger ignition devices having similar q, ν_* and β, even without a complete understanding of the process of turbulent diffusion [3]. The exponent α of ρ_* can be interpreted as an indication for the characteristic turbulence wavelength λ, if $v_{phase} \approx v_{drift}$ is assumed: (a) $\alpha = 1$ implies $\lambda \sim \rho_s$ which is called gyro Bohm like scaling, (b) $\alpha = 0$ implies $\lambda \sim a$ which is called Bohm like scaling, (c) $\alpha = -1$ implies $\lambda >> a$ which could arise from stochastic fields throughout the plasma [4]. A scaling with an exponent $\alpha = -1/2$ leads to the so called Goldston confinement scaling.

The scaling of confinement with the single parameter ρ_* has been examined in ASDEX Upgrade with so called "dimensionally similar" discharges by varying just ρ_* while keeping all other dimensionless parameters fixed. To keep q, ν_* and β constant the relations $I_p \sim B$, $n_e \sim B^{4/3}$ and $T \sim B^{2/3}$ have been fulfilled in these ρ_* scans in single null configuration ($q_{95} = 4$, $\kappa = 1.7$, $\langle\delta\rangle = 0.2$) at densities between 4 and 10×10^{19} m^{-3}. We report here on scans in L- and H- mode approaching the L - H and H - L transition threshold, respectively, and deep in the H- mode at even higher heating powers.

Results and Discussion

1. L- Mode Scaling Experiments

The dimensionless ρ_* scan in H^+ was outlined in such a way that the discharge with the lowest value of n_e (4×10^{19} m^{-3}) and B_t (1.5T) was near to the L- to H- mode threshold. Combining the L to H threshold power P_{th}, which is proportional to $\langle n_e\rangle B_t$, and the scaling condition $n_e \sim B^{4/3}$ the threshold power scales $\sim B^{7/3}$. As we performed the scan assuming a Bohm like behavior the power input for dimensionally similar scaling had to increase with $P_{heat} \sim B^{5/3}$ and the discharges at higher toroidal fields have a larger distance to the threshold and are deep in L- Mode (Fig. 1). The parameters of the L-Mode series are given in Table 1. The heating method used was neutral beam injection. We kept the power deposition profiles as self similar as possible by changing the beam energy from 30 keV at $\langle n_e\rangle = 4\times10^{19}$ m^{-3} to the maximum value of 55 keV at $\langle n_e\rangle = 10\times10^{19}$ m^{-3}. The global analysis of the L-Mode series showed the expected behavior of $W \sim B^2$ resulting in a slight increase of $\tau_{E,th}$ with B (Fig. 2).

Local analysis of the series revealed the constancy of β and ν_* over a large part of the cross section as shown in Fig. 3. The absolute values of ν_* around half radius are about 0.3. The q profiles should be identical as well, as q_{95} was kept constant and the inversion radius for sawteeth was found to be around

$\rho_{tor} = 0.25$ for all investigated discharges. Local thermal diffusivities were calculated with the transport code ASTRA and compared in Fig. 4 with scaling predictions mentioned in the introduction. It was not possible to resolve thermal diffusivities of electron and ion channels separately due to the high densities which produce a large error in the exchange power flux between ions and electrons. Therefore we used $\chi_{eff} = (n_e\chi_e + n_i\chi_i)/(n_e + n_i)$. By inspection of the relation between local thermal diffusivities it is concluded that confinement scales Bohm like or even worse for this L- Mode series. No distinct improvement of confinement of discharges close to the L to H threshold (B_t = 1.5T) compared to the discharges deep in L- mode (B_t = 2.5T, 3T) is exhibited.

2. H- Mode Investigations

In both H- mode scans in H^+ and D^+ reaching the H to L threshold at the highest field of 3T (see Fig. 1 for D^+) no gyro Bohm like transport behavior was found even at the lower fields. Therefore scans were performed with higher heating powers staying deep in the H- mode regime (Fig. 1, table 2). But again it was not possible to achieve a $W_{th} \sim B_t^2$ behavior as demanded for dimensionally similar discharges neither for gyro Bohm (✙, ◇), Bohm (●) or Goldston (▲) like assumptions on transport (Fig. 2).
For a closer inspection of this unexpected phenomenon which is in clear contrast to results from JET and DIII-D we looked for additional loss channels or other hidden parameters influencing the scaling experiments. First we looked for a possible influence of the radiated power and the type I ELM behavior on the global confinement (represented by the H- factor $\tau/\tau_{ITER89\text{-}P}$) of the ASDEX Upgrade discharges. The radiated power normalized to heating power was nearly constant and around 0.3. No dependence of confinement deterioration with increasing B on radiation could be detected. The ELM frequency at the different magnetic fields was nearly constant or even decreased with enhanced heating. In addition, the energy losses per ELM exhibited a nearly constant value of about 20-25kJ per ELM. Thus no dramatic change in ELM induced losses could be detected.
By inspection of confinement deterioration as a function of neutral gas pressure we found that the decrease in H- factor in the dimensionless scaling series is strongly correlated with an increasing neutral gas pressure in the divertor. The divertor neutral gas density is in turn closely coupled to the main chamber neutral gas and the plasma density, and it can hardly be decoupled without higher pumping rates. Recent experiments in JET revealed that the decisive parameter for confinement deterioration is the neutral gas pressure and not the plasma density [5]. Clearly the neutral gas density is a crucial parameter for H- mode confinement. For the L- mode discharge series no such dependence could be verified although variation of neutral gas pressure was up to a factor of two higher.
Finally we accounted for the varying power deposition profiles in the H- mode series which could not be kept as constant as wanted even by changing the beam energy. For this purpose we determined the necessary heating powers at high fields to get dimensionally similar profiles under the assumption of different confinement laws using the calculated beam deposition profiles. The H- mode discharge at B_t = 2T, I_{pl} = 0.8MA and $\langle n_e \rangle = 5.6\times10^{19}\ m^{-3}$ was used as starting point for this investigation. The analyzed χ_{eff} profiles were now fitted by the expression:

$$\chi = \frac{T^{1+s}}{B^{1+2s}} \cdot F_s(\rho_{tor}) \qquad (2)$$

with s = ½ for gyro Bohm and s = 0 for Bohm like behavior. $F_S(\rho_{tor})$ is a profile factor accounting for the gross radial variation of χ due to the unknown dependence on ν_*, β, q,... of transport. After scaling of $n(\rho_{tor})$ of the analyzed low field discharge to the necessary values at B_t = 3T according to $n \sim B^{4/3}$, T was simulated with the ASTRA code for different heating powers and the deposition profile calculated for the scaled density. By adjusting the simulated temperature to the scaled one ($T \sim B^{2/3}$) the power necessary to establish a dimensional similar discharge was found. In case of gyro Bohm behavior a heating power of about 7 MW is necessary compared to 5.5 MW estimated for a fixed power deposition profile. In the case of Bohm scaling a total power of about 9 MW compared to 7.3 MW from scaling prediction had to be used. A cross check with the normalized heat deposition profile of the starting discharge kept fixed resulted in the scaled powers of 5.5 and 7.3 MW, respectively, for reproducing the scaled temperature profiles. In the experiments we used powers up to 8.6 MW and could not establish temperature profiles necessary for a dimensionless similar discharge. Thus we

predict the confinement behavior in deep H- mode discharges in ASDEX Upgrade to be limited to Bohm behavior at best.

Conclusions

In ASDEX Upgrade both L- and H- mode discharges at high plasma and neutral gas densities show a Bohm like confinement at best. For the L- mode such a behavior is in agreement with the ITER89-P scaling. For H- mode this is quite different from results of scaling experiments obtained in DIII-D and JET [6,7] and of global energy H- mode confinement scalings done for ITER. The plasma densities in our dimensionally similar ρ_* scans are higher than those in [6,7] and exhibit high neutral gas densities, both in the divertor and the main chamber. This points to a hidden parameter like the nonlinear relation between neutral gas and plasma density which may lead to changes in the transport behavior not covered in the scaling relations of eq. (1) not taking into account atomic processes. This offers another explanation of the recent JET results [6] showing a confinement degradation from gyro Bohm like to more Bohm or Goldston like behavior in the H- mode when approaching the H to L transition threshold as this was connected with an increased plasma density of 7.5×10^{19} m^{-3}.
Another obvious difference is in the collisionality being around $\nu_* \approx 0.1$ at $\rho_{tor} = 0.5$ in our H- mode scans compared to values about 10 times lower in the two other experiments. If this is the cause for the discrepancy a simple power law for ρ_* as described in (1) would be discarded. Additionally the necessary strong ν_* dependence would be in contrast to the ITER92-P H- mode scaling showing only a very weak ν_* dependence.

References

[1] B. B. Kadomtsev, Sov. J. Plasma Phys. 1, 295 (1995)
[2] J. W. Connor and J. B. Taylor, Nucl. Fusion 17, 1047 (1977)
[3] R. E. Waltz, J. C. DeBoo, and M. N. Rosenbluth, Phys. Rev. Lett. 65, 2390 (1990)
[4] J. P. Christiansen et al., Plasma Phys. Controlled Fusion 34, 1881 (1992)
[5] G. Saibene et al. PSI 1996, preprint
[6] B. Balet et al., 22nd European Physical Society Conference on Controlled Fusion an Plasma Physics, Bournemouth, 3rd - 7th July 1995
[7] C. C. Petty et al., Phys. Rev. Lett. 74, 1763 (1995)

Tables

shot no.	B (T)	I (MA)	<n_e> (10^19m^-3)	P (MW)	W/W(1.5T)
# 7785	1.5	0.6	4.0	1.6	1.0
# 7778	2.0	0.8	5.9	2.6	1.8
# 7784	2.5	1.0	8.0	4.4	2.8
# 7768	3.0	1.2	10.1	5.2	4.1

Table 1: Discharge parameters of L- Mode scan in H^+. The plasma energy W represents an average from magnetic and kinetic data.

shot no.	B (T)	I (MA)	<n_e> (10^19m^-3)	P (MW)	W/W(2T)
# 8120	2.0	0.8	5.6	3.7	1.0
# 8121	2.5	1.0	7.5	4.6	1.3
# 8123	3.0	1.2	9.6	5.6	1.6
# 8126	2.5	1.0	7.5	5.2	1.3
# 8125	3.0	1.2	9.6	7.6	1.8
# 8257	3.0	1.2	9.6	8.6	2.0

Table 2: Discharge parameters of H- mode scans in D^+. # 8121, 23 gyro Bohm, # 8126, 25 Bohm and #8257 Goldston.

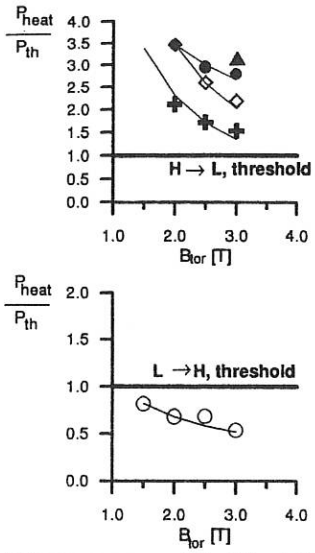

Fig. 1: Heating power norm. to L - H threshold power (L- mode scan in H^+: ○) or H - L threshold power (H- mode scan in D^+: ✚ ◇, ●, ▲)

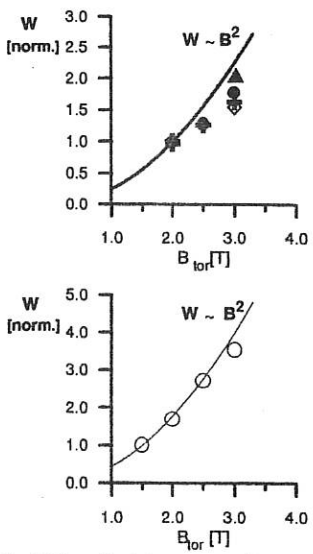

Fig. 2: Normalized plasma energy in ρ_* scans.

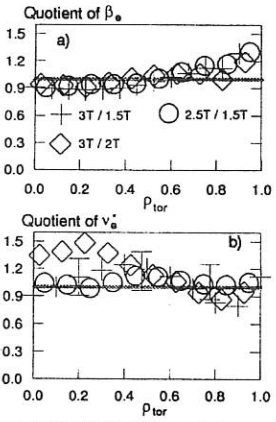

Fig. 3: Quotients of dimensionless variables β and ν_* for the L- mode ρ_* scan (H^+). Error in (a) equal to symbol height, in (b) indicated by bars.

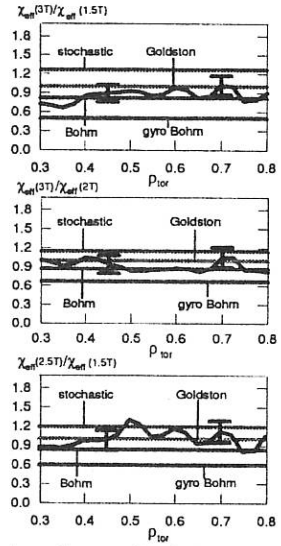

Fig. 4 Quotients of χ_{eff} profiles for L- Mode ρ_* scan (H^+).

Error Fields, Low Collisionality and High β on COMPASS-D

D. A. Gates, A. M. Edwards, T. C. Hender, A. W. Morris, H. R. Wilson
and the COMPASS-D and ECRH teams

UKAEA Fusion, Culham, Abingdon, Oxfordshire, OX14 3DB, UK

(UKAEA/EURATOM Fusion Association)

1. Introduction

Much attention has been focused recently upon the effects of neoclassical MHD on the pressure limits to tokamak operation [1]. This is primarily due to the observation on several divertor tokamaks (COMPASS-D [2], DIII-D [3], and ASDEX-U [4]) that the β-limit at low density (and hence low collisionality) is often determined by low *m/n* modes, and not the ideal-MHD kink modes underlying the conventional β-limit models. It has also been observed that plasmas become more sensitive to error-fields as β is increased, with error-field driven islands much larger than expected from classical non-linear tearing-mode models.

Initial calculations of the stability of bootstrap driven islands indicated instability for all values of β_p and all collisionalities (as long as the bootstrap current flows). More recent calculations suggest that collisionality-dependent stabilising mechanisms determine mode onset. Of the two proposed mechanisms for stabilisation [5,6] we provide evidence that the polarisation current model is consistent with the observed instability regimes as a function of collisionality. We also show that the island dynamics match neoclassical theory (see also [7]) and present a model for the observed q-scaling of the low density β-limit.

2. Background

The equation that determines the evolution of the island is given by [5,6]:

$$\frac{dw}{dt} = \left(\frac{1.22\eta_{nc}}{\mu_o}\right)\left[\Delta' + C_1\varepsilon^{1/2}\beta_p\frac{L_q}{L_p}\left(\frac{w}{w^2+w_c^2}\right) - C_2\frac{\rho_{\theta i}^2\beta_p g(\varepsilon)}{w^3}\left(\frac{L_q}{L_p}\right)^2\right] \quad (1)$$

where w = island width, η_{nc} = the neoclassical resistivity, Δ'= the jump in logarithmic derivative of the flux, ε = the inverse aspect ratio, β_p = the local poloidal β, and L_p and L_q are, respectively, the scale lengths of the pressure and the q (all quantities to be evaluated at the rational surface of interest, $r=r_s$ where $m = nq(r_s)$). The second term on the right is the bootstrap drive term with the effects of radial transport represented by w_c [5] (important for small islands). For COMPASS-D it is estimated to be not critical. The third term in Eqn. (1) is the contribution due to ion polarisation currents, with $\rho_{\theta i}$ the poloidal ion Larmor radius, and $g(\varepsilon)$ defined by: $g(\varepsilon) = \varepsilon^{3/2}$ for $\nu_i/\varepsilon\omega_{*e} << 1$ (collisionless) and $g(\varepsilon) = 1$ *for* $\nu_i/\varepsilon\omega_{*e} >> 1$ (collisional). From Eqn. (1) it is found that: (a) at any moderate or low collisionality, $\beta_p > \beta_p(\min)$ is required for islands to grow at all (for $\Delta' < 0$); (b) at any collisionality a critical island size (w_{crit}) must be exceeded before the pressure term can cause the island to grow further (i.e. for the pressure drive to dominate the stabilisation terms), but $w_{crit} \sim g^{1/2}\varepsilon^{-1/4}\rho_{\theta i}$ is much smaller at low collisionalities through the change in $g(\varepsilon)$; (c) once the critical island size is exceeded the final saturated island size increases with increasing β_p. The critical "seed" island can be provided by various mechanisms - e.g. mode coupling from sawteeth and error-field modes. The various behaviours are all observed to greater or lesser degree on COMPASS-D in low density plasmas.

3. Density scaling of MHD onset

For COMPASS-D high-β discharges which are heated with high power Electron Cyclotron Resonant Heating (ECRH), neutral particle analyser measurements indicate that T_i remains roughly constant as P_{ECRH} is increased, implying that $\rho_{\theta i}$ is also roughly constant. This, combined with the assumption that L_p/L_q does not change significantly during a discharge, implies that the only significant variation of w_{crit} is due to the change in the "collisionality-like" parameter $\sigma \equiv \nu_i / \varepsilon\omega_{*e} \sim n/(T_e T_i^{3/2})$. Onset of MHD is predicted if this parameter crosses ~0.3 during the discharge [1]. Since T_i is approximately constant, lowering n_e lowers σ, as does raising T_e. The separation between the high and low collisionality regimes for T_i=*const.* becomes a β threshold, $\beta_p \sim n^2$. Since the high collisionality regime requires a higher β before pressure-driven islands can occur, the theory can be tested by scanning β at various densities - the critical β for island growth should scale as n^2 until β is high enough for the high collisionality regime (where w_{crit}~4cm as opposed to ~2cm) to become unstable. The experimental results are shown in Fig. 1 (open symbols, no RMP), and while there are fitting parameters, the trend with n^2 is clear. The error-field points are described below.

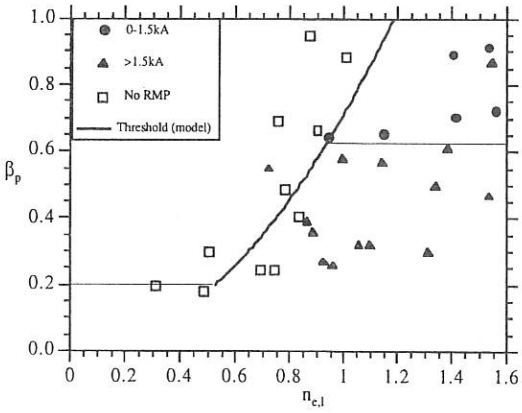

Fig. 1

Open symbols: Onset of m=2 modes as a function of β_p and line average density ($10^{19}m^{-3}$).

Solid symbols: where error-field islands appear for two different ranges of current in the resonant magnetic perurbation (RMP) windings on COMPASS-D.

The parabola indicates the low-high collisionality threshold and the horizontal lines the instability thresholds in β_p

4. Island dynamics

Another way to test the threshold features of the model is from the island dynamics. This is illustrated in Fig. 2. Here the rotating island was created by applying an error-field with the RMP coils at high β and then removing the error field. The island width is seen to fall as the power falls in time. The curve matching the measured island width is derived from Eqn. 1. As the island gets smaller, its width should fall below w_{crit}, where the ion polarisation stabilisation term dominates, and it is reasonable to suppose that the sudden decay at *t*=289.5ms is due to this.

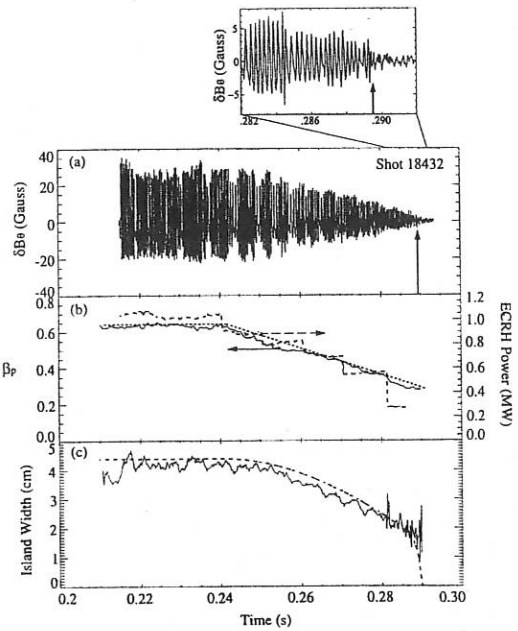

Fig. 2 Evolution of magnetic island as the pressure is reduced by dropping the ECRH power in time. The island width is deduced from wall-corrected B_r measurements (which removes frequency change effects), and the dotted line in (b) is a fit to the β_p decay. The inset shows the sudden drop associated with $w<w_{crit}$

5. q-scaling of β-limit

If the β-limit is not due to ideal-MHD instabilities, then there is no reason to suppose it follows an I/aB_T scaling. To determine the actual scaling, a q-scan was performed at constant B_T (to maintain central ECRH). The results are shown in Fig. 3 where it is seen that there is an optimum q_{95}~4.5. These shots have heating alone in order to minimise changes in the current profile, but at the expense of slightly lower maximum β (counter-ECCD gives higher β on COMPASS-D [2]). All shots have strong m=2 activity, and so represent a limit due to MHD (not background confinement), but the limit is not always disruptive (nor are disruptions always at the limit).

The simple model proposed here is that the β limit is determined by the condition that the saturated bootstrap driven island extends to a prescribed distance from the edge or axis/q=1. This can be simply stated as: $w_{max} = \alpha Min[r_s, a - r_s]$ where α is the fractional island width required for this interaction. A simple scaling of the β-limit with q_{95} is found by assuming a specific form for the q-profile. For simplicity we assume a quadratic form, $q = q_0 + (r/a)^2(q_a - q_0)$. Solving for r_s and substituting the definition of β_N and $A \equiv R/a$:

$$\beta_{N\max} = \frac{C(-\alpha r_s \Delta')}{A^{1/2}} \left[\frac{\langle p \rangle L_p}{p_{r_s} L_q} \right] \frac{q_a}{q^2} \left(\frac{q - q_0}{q_a - q_0} \right)^{3/4} Min\left[1, \sqrt{\frac{q_a - q_0}{q - q_0}} - 1 \right] \qquad (2)$$

where $\langle p \rangle$ is the volume averaged pressure and p_{r_s} is the pressure at the rational surface. C is a (known) constant. Fig. 3 shows the overlay of the curves predicted by Eqn. (2) as calculated

with data from COMPASS-D. The relevant mode is m/n=2/1. It is assumed that $q_0 = 1$ and the terms without explicit q dependence in Eqn. (2) are roughly independent of q_{95}; $\alpha r_s \Delta'$ is used as a fitting parameter to the data envelope, and reasonable values result. A more detailed model including pressure profile effects gives similar results [1].

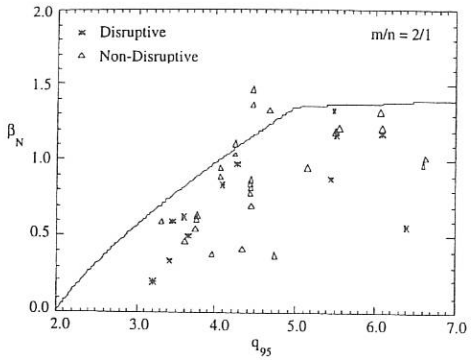

Fig. 3 Dependence of the experimental β-limit on q_{95}, together with a limit deduced from neoclassical MHD theory.

6. Error Field Effects

The conventional theory of error-field penetration does not consider the stabilising effects of the polarisation current. If the driven island calculated with conventional considerations is smaller than w_{crit} for the appropriate collisionality range, then the island may be partially stabilised. As β_p increases the stronger bootstrap drive may lead to both lower thresholds to error-fields and to larger final islands. Thus one would expect that to produce a substantial island a smaller error-field is needed at higher β_p, and this is supported by the data of Fig. 1, where the resonant magnetic perturbation (RMP) system on COMPASS-D is used to provide controlled error-fields to test the penetration threshold. Error-field experiments at low density or high β_p show that, once penetrated, the island grows and often unlocks, indicating that after the seed island has been generated the subsequent dynamics are independent of the applied error-field, again as expected from neoclassical MHD theory.

7. Summary

There is a growing body of evidence that neoclassical MHD and bootstrap-current-driven islands are important at low collisionality and most of the predicted features are observed on COMPASS-D. A simple scaling matches the observed β-limit (though it is dependent on the pressure and current profiles), and survives more detailed examination on several tokamaks [1]. Further support comes from the details of the island dynamics, where the island size increases with β_p and a stability threshold with the expected density dependence is seen. This model gives a low critical island width (≤3cm) suggesting neoclassical tearing modes may be a problem in ITER and the β-limit may be reduced. This model also indicates why large islands are produced by small error-fields, and hence confirms the importance of correction coils.

References

[1] H.R. Wilson, this conference, to be published in Plasma Physics and Controlled Fusion
[2] D. A. Gates, D. A., et al., 22nd EPS Conf. on Controlled Fusion and Plasma Physics **IV**, 117, (1995)
[3] R. La Haye, et al., submitted to Nuclear Fusion
[4] H. Zohm, et al., Plasma Physics and Controlled Fusion, **37**, A313 (1995)
[5] R. Fitzpatrick, Physics of Plasmas **2**, 825 (1995)
[6] H R Wilson, et al., Physics of Plasmas. **3**, 248 (1996)
[7] Z. Chang, et al., Physical Review Letters., **74** 4663 (1994)

This work is jointly funded by the UK Department of Trade and Industry and EURATOM.

Measurement and Modelling of Light Impurity Behaviour in TCV

H. Weisen, V. Piffl+, A. Weller*, J. Moravec+, A. Krejci+, J. Raus+, M. Anton, R.A. Pitts, B. Joye, Ch. Deschenaux, R. Behn, F. Bühlmann, M.J. Dutch, B.P. Duval, S. Franke, F. Hofmann, Y. Martin, J.-M. Moret, Ch. Nieswand, A. Pietrzyk

Centre de Recherches en Physique des Plasmas
Association EURATOM - Confédération Suisse
Ecole Polytechnique Fédérale de Lausanne, Switzerland

+*Institute of Plasma Physics, Czech Academy of Sciences, Prague, Czech Republic*
**Max Planck Institut für Plasmaphysik, Garching, Germany*

Abstract. Light impurity radiation from the TCV tokamak is permanently monitored using a four-channel ultrasoft X-ray (USX) monochromator based on multilayer mirrors, allowing low-resolution ($\lambda/\Delta\lambda$≈30) measurements in the range 200-850 eV [1]. The strongest lines accessible to the instrument are responsible for about two third of the total radiated power of helium- and hydrogen-like ionization stages of the impurities Boron, Carbon, Nitrogen and Oxygen. The instrument can provide a direct measurement of radiation losses from H- and He-like light impurities. USX measurements and absolute emissivities from soft X-ray tomography [2] are used together with the IONEQ code to determine impurity levels. Total plasma radiation is obtained from three 16-channel bolometric cameras with nearly horizontal viewing lines.

Modelling of ionization equilibria using IONEQ

The ionization and radiation code IONEQ is used for modelling of emission from light impurities in TCV. The code uses measured electron density and temperature profiles from Thomson scattering and calculates radiation profiles associated with the main lines of each charge state of the impurity under consideration. It is however necessary to assume ad-hoc transport coefficients in order to obtain sensible results. In order to reproduce the observed line-brightness ratios of He- to H-like lines it is necessary to assume a diffusion coefficient $D \geq 0.5$ m^2/s [1]. By default we have adopted $D=1$ m^2/s. It is also assumed that the impurity concentration profile $c_z=n_z/n_e$ is constant in radius. This is equivalent to assuming the existence of an inward particle pinch with a profile which is adjusted as to produce an impurity density profile which match the measured electron density profiles. The comparison of predicted (for n_z/n_e = 1%) and measured H-like line emission, which is only moderately sensitive to assumptions on transport coefficients, can be used for estimates of absolute impurity concentrations. IONEQ simulations with $0.5 \leq D \leq 2$ m^2/s show that the uncertainty on impurity concentrations based on USX line brightness measurements is a factor of 2. Additional uncertainties are associated with errors in the absolute instrumental throughput. Estimates of $Z_{eff} = 1 + \Sigma\, c_z(z-1)z$ with (z=5,6,7,8) from USX and IONEQ alone are consistent with those from X-ray emissivity [3] and near infrared Bremstrahlung within the expected uncertainty.

The relative proportions of light impurities, such as $p_C=n_C/(n_B + n_C + n_N + n_O)$, are

used for quantitative interpretation of soft X-ray emission and are less sensitive to modelling assumptions than impurity concentrations. X-ray emissivities, normalized to $n_e n_i$, have been tabulated for the species of interest as a function of T_e using IONEQ [3]. Since most of the soft X-ray radiation, which is filtered using Be windows to contain only photon energies in excess of 1 keV, originates from fully ionized impurities in the core plasma, these emissivities are insensitive to assumptions on particle transport, and are hence more appropriate for absolute estimates of impurity concentrations. Soft X-ray based measurements of light impurity concentrations are however dependent on the assumption that the impurities monitored are responsible for most of the soft X-ray radiation. This assumption is supported by preliminary measurements of FeXVII line emission at 826 eV. The identification of the Fe line remained inconclusive because of the proximity of an OVIII line at 820 eV. The measurements however give an upper limit, $n_{Fe}/n_e \leq 10^{-5}$, at which level metallic impurities from untiled parts of the stainless steel vessel are expected to contribute less than 10% of the total soft X-ray emission.

The total power emitted from H and H-like light impurities, which contribute to radiation losses, can also be obtained from the measured line brightnesses. To this effect the radiation profiles calculated by IONEQ are volume integrated using the flux surface geometry from the equilibrium reconstruction. The estimate is fairly insensitive to assumptions on particle transport coefficients which only affect the position and width of the radiation shells. Note that although lower ionization stages may be responsible for a large fraction of the radiated power, their radiation is emitted too close to the plasma edge to make a significant impact on confinement.

Monitoring of impurity levels

Long term monitoring of vessel conditions is achieved by means of a reproducible 'standard discharge' in a Single Null diverted configuration, which is produced at least once every operational day. The relative proportions of light impurities undergo dramatic changes as a result of vessel conditioning such as glow discharge cleaning and boronization [4].

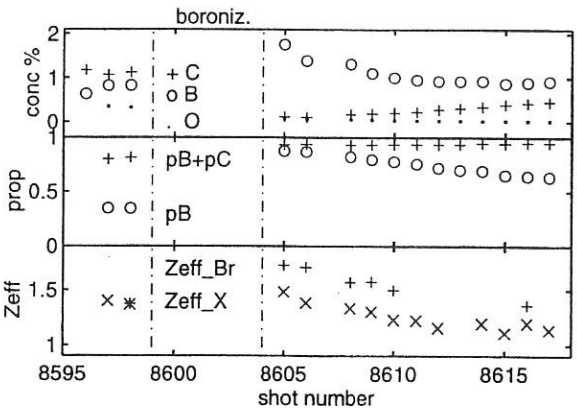

Fig.1 Evolution of light impurity concentration and plasma purity after a boronization

On the first discharge after a reboronization carbon levels are reduced by a factor of 10, Oxygen levels by a factor of 2-3, while Boron accounts for more than 90% of the light impurities (fig.1). Over the subsequent ~ 10-20 discharges Carbon and Boron concentrations return to their pre-boronization levels (~1%) while Oxygen levels continue to drop by a further factor of 2-3 to about 0.1%. After the first 10-20 discharges, impurity levels, including the reduced Oxygen level, remain fairly constant for hundreds of discharges.

Influence of discharge conditions and plasma shape

The core impurity concentrations were inferred from the tomographically reconstructed core X-ray emisivity together with light impurity proportions from USX measurements and IONEQ simulations for a wide range of inner-wall limited ohmic L-mode conditions ($120 \le I_p \le 600$kA, $3 \le \langle n_e \rangle \le 9 \times 10^{19} m^{-3}$, $1.1 \le \kappa_{95} \le 1.8$, $-0.3 \le \delta_{95} \le 0.5$, [5]). The corresponding values of Z_{eff} are shown versus $\langle n_e \rangle$ in fig.2 for $\delta_{95} \ge 0$, where the symbols refer to classes of ohmic power density at the last closed flux surface, P_{oh}/S. Low power and high density is favourable for plasma purity. These dependences were not observed for $\delta_{95} < 0$. In this set of experiments the proportion of Carbon increased with δ for $\kappa \ge 1.4$ (fig.3). The higher Carbon concentrations may be due to the higher ohmic power necessary to sustain discharges with high triangularity [5] and to differences in the boron coverage of the wall areas wetted by the SOL. During the course of these experiments (~150 shots) the part of Carbon in the impurity mixture of standard discharges increased from 0.4 to 0.6, suggesting a stronger than usual erosion of the Boron layer, possibly due to the higher power discharges in the series [4]. Despite the differences in the impurity mixture, the radiated power fraction P_{rad}/P_{oh}, as determined from bolometry, is remarkably independent of plasma shape, showing that differences in radiation losses cannot explain the reduction of energy confinement time with increasing triangularity [5].

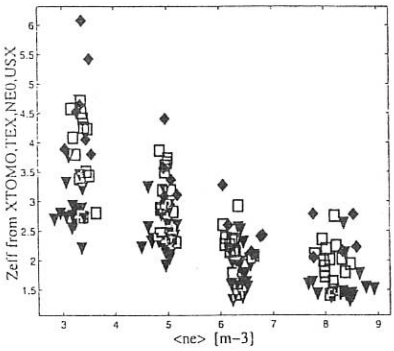

Fig.2. Dependence of core Zeff from X-ray tomography on line average density. Diamonds: 100 kW m^2>P_{oh}/S > 68 kW/m^2 Triangles: 42 kW/m^2>P_{oh}/S > 17kW/m^2

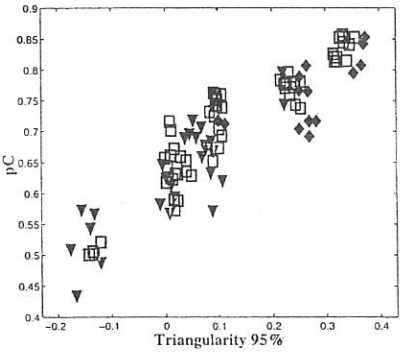

Fig.3. Dependence of Carbon proportion on plasma triangularity for κ>1.5. (For low δ no significant dependence) Squares : 68 kW m^2>P_{oh}/S > 42 kW/m^2

P_{rad}/P_{oh} depends mainly on the electron temperature near the LCFS (fig.4a), which itself increases with P_{oh}/Sn_e (fig.4b). In fig.4c the ratio P_{USX}/P_{rad} is shown to rise sharply as a function of Te(0.9a). The increase corresponds to changes in the dominantly radiating ionization stages, with He and H-like stages dominating at Te(0.9a) > 200 eV. Comparison of absolute values shows that the overall throughput of the USX diagnostic is underestimated by a factor of 2-3.

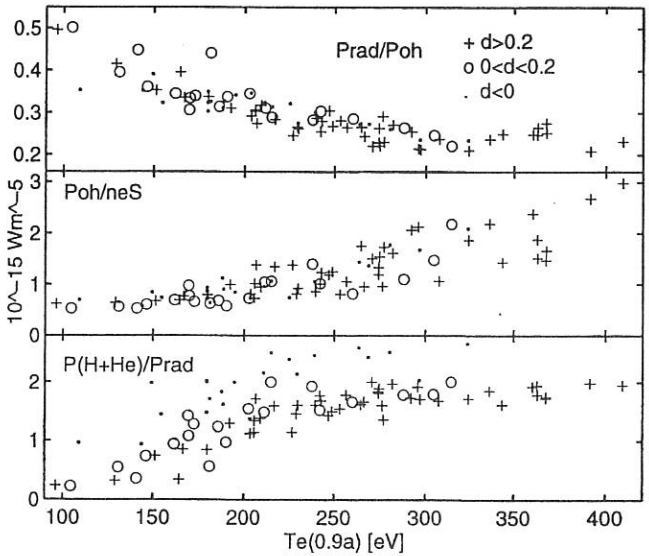

Fig. 4. Dependence of radiated power fraction (a) on edge temperature measured at r/a ≈ 0.9. Relation (b) between P_{oh}/Sn_e(0.9a) and Te(0.9a). Dependence (c) of ratio of H- and He-like radiation to P_{rad} on Te(0.9a). The set of data was restricted to intermediate values of elongation for clarity, 1.4<k<1.7. Symbols refer to classes of triangularity (+ δ>0.2, o 0<δ<0.2, · δ<0).

Conclusions. Altough the impurity mixture varies with plasma shape, overall impurity content and radiation losses depend mainly on edge conditions such as P_{oh}/S, Te(0.9a) and n_e. The dependence of energy confinement on triangularity reported in [5] cannot be accounted for by radiation losses. The USX 4-channel multi-layer mirror monochromator has proven to be a valuable diagnostic for monitoring the content and radiation losses of H- and He-like light impurities.

Ackn: This work was partly supported by the Fonds National Suisse de la Recherche Scientifique.

References:

[1] Weisen H, V. Piffl, A. Kreijci et al, 22nd EPS on CFPP, 1995, ECA 19C II-393
[2] M. Anton, H. Weisen, M.J. Dutch et al, this conference
[3] H. Weisen, D Pasini, A Weller & AW Edwards, Rev. Sci. Instrum 62 (1991), 1531.
[4] R. Pitts, Ch. Nieswand, H. Weisen et al, 12th PSI, St. Raphael, May 1996
[5] J.-M. Moret, M. Anton, R. Behn et al, this conference (oral presentation)

Electron Density Profiles during Ohmic H-modes in TCV

Z. A. Pietrzyk, R. Behn, S. Franke, M. Anton, M.J. Dutch, B.P. Duval, F. Hofmann, Y. Martin, J-M. Moret, Ch. Nieswand and H. Weisen

Centre de Recherches en Physique des Plasmas, EPFL
Association EURATOM - Confédération Suisse
CH-1015 Lausanne, Switzerland

Ohmic H-modes have been obtained in the TCV tokamak ($R \approx 0.89$ m, $a \leq 0.25$ m, $B_T \leq 1.5$ T) in large range of configurations for different κ and δ [1]. For certain discharge parameters and wall conditions, long ELM free H-modes have been obtained. These ELM free H-modes terminate by a disruption or often by a transition to the L-mode during current ramp-down. Following the L-H transition, a rapid density increase is observed. In TCV this density increase can have either a flat or peaked profile. In such long lasting ELM free H-mode the particle transport can be studied to examine the difference between flat and peaked density profiles. The electron density profiles are measured using a 10 point repetitive (every 50 ms) Thomson scattering system together with a 6 channel interferometer. The behavior of the density in ELM free H-mode discharges for $\kappa \approx 1.66$ and $\delta \approx 0.43$ is described in this paper.

The initial high density increase, following the L-H transition, levels off to a plateau or low level density increase after 30 ms at the plasma edge and 200 ms at the center. Due to the rapid density increase at the plasma edge just after the L-H transition the electron density profiles are initially always flat or slightly hollow. The subsequent evolution can however lead to the formation of either a flat or peaked profile in an otherwise similar discharge as seen in Fig. 1 and Fig. 2 for Single Null configurations. Since the particle source is localized in the plasma periphery and the density profile is initially flat, the peaking in the case shown in Fig. 2 must correspond to a strong inward convection of particles.

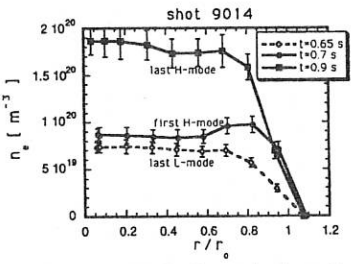

Fig. 1 Shot with flat electron density profile
I_p = 426 kA, κ = 1.67, δ = 0.42

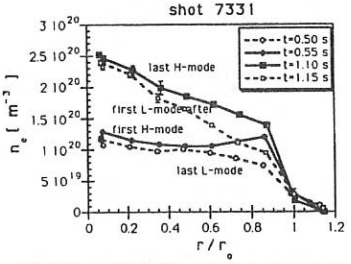

Fig. 2 Shot with highly peaked electron density profile
I_p = 420 kA, κ = 1.64, δ = 0.46

L-mode -- dashed line, H-mode solid line in these figures.

We also observed cases where the density peaking occurs after a period where the profiles are flat or where the profile peaks only in the central part of plasma. The temperature profiles are very similar for both categories of density profiles. Since the electron temperature is always peaked and usually increases only near the plasma edge just after the L-H transition, the pressure profiles are peaked even for flat density profiles.

In order to determine whether the observed density peaking is due to impurity accumulation at the plasma center, we investigated the spatial and temporal variation of Z_{eff} obtained from multicore Bremstrahlung and reconstructed X-ray emissivity(2). In both cases (peaked and flat profile) the Z_{eff} profile remains flat or slightly hollow for the duration of the H-mode. This indicates that the observed spontaneous peaking of the density profile is not concomitant with central impurity accumulation. The overall impurity concentrations do however increase during ELM free H-modes, with Z_{eff} rising to near 3 after 0.5 seconds of ELM-free H-mode, but the rate of increase is the same for peaked and flat n_e profiles.

A study of the inversion radius q=1 and the sawtooth amplitude have been made using a soft X-ray tomographic reconstruction technique(3). The inversion radius and sawtooth relative amplitude (in "energy") is calculated from Single Value Decomposition (SVD) of the local emissivity matrix. The inversion radius increases rapidly at the L-H transition, which is expected from the rapid temperature rise (in about 10 ms) at the plasma edge, causing changes the current profile. However, shortly after transition, the inversion radius drops and is the same for both peaked and flat profiles. We observed a larger increase of the inversion radius for the flat than for the peaked profiles. The sawtooth amplitude decreases rapidly after the L-H transition and the decrease is the same for flat and peaked profiles. This behavior of sawtooth amplitude and inversion radius suggests that the flattening of the n_e profile is not simply a consequence of the reduced sawtooth activity.

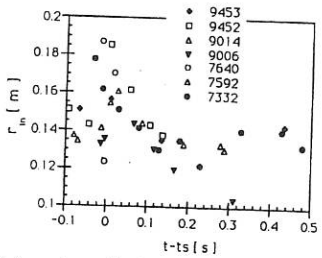

Fig. 3 Inversion radius (vertical) after transition solid points are the shots with peaked and open symbols refers to flat profiles for both of these figures

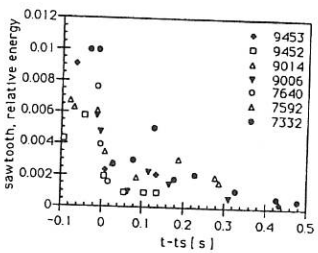

Fig. 4. Sawtooth "energy" from SVD of soft X-ray matrix

We examine particle transport in these H mode plasmas by calculating the diffusion coefficient and inward drift from the experimental data. At the L-H transition, as observed in other experiments a strong particle and energy barrier is created near the plasma edge. Therefore we assume that D is very small near the plasma edge in the H-mode. Due to limits on spatial resolution of the Thomson scattering system (about 4 cm) the n_e gradient cannot be resolved in this region. The expected gradient length of density near the plasma edge is about 1 cm. We analyze the central plasma region r/r_O=0.05 to 0.7, only, as r=0 has to be also excluded due to 1/r term in the equation.

The density profiles can be analyzed using the particle conservation equation in quasi-cylindrical approximation:

$$\frac{\partial n_e}{\partial t} + \frac{1}{r}\left(\frac{\partial}{\partial r}(r\Gamma_e)\right) = S_e. \qquad (1)$$

where: S_e is the electron source, which in our case is non-zero only at the plasma edge, so $S_e(r,t)=0$. is assumed for our calculations. Γ is the particle flux which can be expressed as $\Gamma_e = -D\frac{\partial n_e}{\partial r} + n_e V$, where V is the inward pinch velocity. Substituting Γ_e into (1) after integration one gets:

$$D\frac{\partial n_e}{\partial r} - n_e V = \frac{1}{r}\int_0^r r\frac{\partial n_e}{\partial t}\,dr \qquad (2)$$

so that if n_e is known as a function of both r and t, we have an equation with two unknowns D and V. In the following calculations we assume that D and V are time independent functions during the ELM free H-mode. With this assumption one can write the equation (2) for two different times and this way gets two equations with two unknown D(r) and V(r). However it is possible to do this only for the peaked profiles since for the flat profile the first term is zero.

For flat profiles $\frac{\partial n_e}{\partial r} = 0.$ and, $-n_e V = \frac{1}{r}\int_0^r r\frac{\partial n_e}{\partial t}\,dr$ from which V(r) can be calculated.

It should have been realized that this is only a maximum V for which the flat profile can persist. Smaller V could also lead to flat profile as the plasma would be filled with particles, if there is a very small diffusion near the plasma edge, typical for the H-mode and larger in the rest of the profile. This can happen as the accumulation of the particles near the plasma edge would produced the gradient in the opposite to "normal" direction, thus the plasma interior would be filled by diffusion. Taking this to the limit a flat profile can exist with V=0.

and D≠0. The diffusion coefficient D cannot thus be determined from the experimental data for the flat profiles.

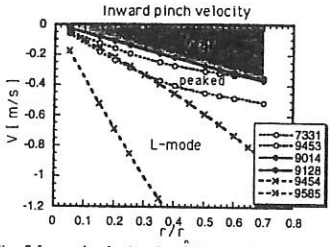

Fig. 5 Inward velocity for different plasma discharges,. solid line: max. V for flat profile, dotted lines: peaked H-mode profiles, and dashed: line L-mode.

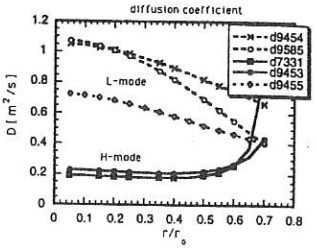

Fig. 6 Diffusion coefficient for selected L (dashed line) and H-mode (solid line) discharges (peaked profiles)

The radial dependence of the pinch velocity (Fig. 5) shows that the absolute value is always smaller in H-mode than in for L-mode and that flat profiles have a smaller inward velocity than the peaked profiles. Fig. 6 shows the difference between L-mode and H-mode diffusion coefficients. The L-mode diffusion coefficient, for shots with the same configuration as H mode but for which the H-mode was not achieved, is largest in the central part of plasma and larger than ELM free H-mode discharges. The diffusion coefficient for the H-mode increases with radial position. We know that at the edge it must become smaller, so a maximum must exist at some normalized radius between 0.6 and 1. Indeed, calculations performed for DIIID ELM free H-mode plasmas(4) gives the region of maximum D to be between r/r_0=0.3 and 0.7 and similar magnitude of D from 0.25 to 0.5 [m^2/s].

We have observed large differences of the density profiles for very similar global discharge parameters. Once the peaked profile is established it remain peaked till the end of ELM free H-mode period. A simple picture of particle transport shows that for the flat profile the inward drift is smaller than for the peaked profiles, which in turn is smaller than for L-mode discharges. Extending the range of plasma condition and shapes (q, κ, δ) in the future should give further insight into the physical processes leading to peaked density profiles.

Acknowledgments: This work was partially supported by the Fonds National Suisse de la Recherche Scientifique.

(1) Y. Martin at al at this Conference

(2) H.Weisen, D.Pasini, A.Weller and A.W. Edwards, Rev Sci. Inst. 62 (1991) 1531

(3) M. Anton at al at this Conference

(4) D.R. Baker and G.L. Jackson, APS 6Q23 Louisville, 1995

Shape Dependence of Ohmic H-mode Accessibility in TCV

Y. Martin, B.P. Duval, J.-M. Moret, H. Weisen

Centre de Recherches en Physique des Plasmas,
Association Confédération Suisse-EURATOM,
Ecole Polytechnique Fédérale de Lausanne, 1015 Lausanne, Switzerland.

1. Introduction

TCV, (Tokamak à Configuration Variable), is a compact, highly elongated tokamak, built to study the influence of the plasma properties on the plasma shape. The design parameters are R=0.88 m, a≤0.25 m, Bt ≤ 1.5 T, $\kappa \leq 3$. 16 independent shaping coils allow precise control of shape parameters such as plasma elongation, triangularity, squareness, X-point(s) location and divertor geometry. Plasmas with up to 810 kA, $0.9 \leq \kappa_{95} \leq 2.1$ and $-0.45 \leq \delta_{95} \leq 0.7$ have to date been achieved. Since TCV does not, as yet, have auxiliary heating, power is provided to the plasma by the Ohmic heating only.

Following a first observation of a clear L-mode to H-mode transitions in a Single Null plasma discharge, H-mode transitions have been obtained in a large variety of limited and diverted, Single Null (SN) and Double Null (DN) configurations. All the L-H transitions, from ~600 discharges, have been compiled into a database containing plasma and configuration parameters during a short period preceding the L-H transition.

2. H-mode accessibility - operational domain

For the major configurations, L-mode to H-mode transitions have been obtained for plasma parameters in the ranges summarised in the table below. I_p and Bt are defined positive when anti-clockwise viewed from the top of the machine.

Configuration		Limited	SN	DN	
Mag. Field	(Bt)	1.0 & 1.4	-1.4, 1 & 1.4	1.4	[T]
Plasma Cur.	(I_p)	300 -> 600	-350 -> -280	230 -> 520	[kA]
	&		200 -> 450		[kA]
Plasma Dens.	(ne)	7.0 -> 11.0	2.5 -> 10.0	3.5 -> 11.0	[$10^{19}m^{-3}$]
Elongation	(κ_{95})	1.3 -> 2.0	1.05 -> 1.75	1.2 -> 1.7	
Triangularity	(δ_{95})	0.2 -> 0.45	-0.1 -> 0.65	0.35 -> 0.65	

Figures 1 and 2 plot all the documented L-H transitions for the major plasma parameters and the shape parameters respectively.The suffix '95' refers to the parameter value on the plasma surface enclosing 95% of the poloidal flux.

Such a presentation only attempts to show where H-mode plasmas have been observed. It does not imply that H-mode would not be achievable outside these domains. Thus, parameter values at the boundaries can not be considered as threshold values. As an example of this, the apparent limit at q=2 (fig 1) is due to MHD stability. The differences in plasma elongation and triangularity between the plasma configurations is due to the presence of a belt limiter in the vacuum vessel, which does not permit up-down symmetric plasma shapes. Moreover, the wide dispersion in the data, caused by diversity of the preprogrammed plasma conditions, indicates that the triggering of the L-H transition is probably not a simple function of any of these parameters.

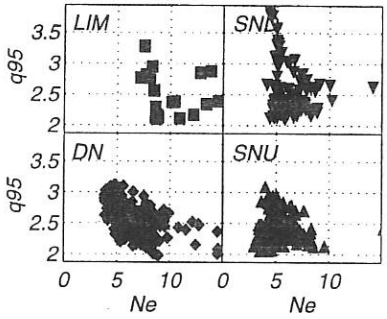

Fig1: H-mode accessibility in the ne q_{95} domain.

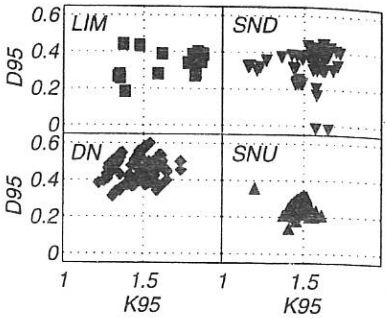

Fig 2: H-mode accessibility domain in the $\kappa\delta$ domain.

The global database approach does not thus allow the determination of the parameters responsible for triggering the L-H transition, so another approach is required. The versatile control system of TCV can be programmed such that the conditions of an L to H transition are reached by modifying each parameter separately. In order that the L-H transition occurs when required shape and plasma parameter values have been established, and not before, two startup scenarios have been developed. In the first , the distance between the inner wall and the plasma is increased from a limited configuration and is used in the next section.

In the second scenario, the plasma density is slowly increased after the desired configuration has been established. As already presented in [1,2], we found that the L-H transition occurred once the plasma density exceeded a certain value, called the "density threshold". This density threshold was shown to increase as the wall conditioning degraded and to increase with the plasma triangularity. The variations of the density threshold indicate that the density is not really a threshold in itself, but a parameter which acts on threshold parameters such as the edge temperature, density and/or their gradients. The fact that the first H-mode on TCV was obtained shortly after the first boronisation and that only after recent conditioning (by boronisation or He glow cleaning discharge), H-mode at densities lower than 3 10^{19} m^{-3} have been obtained, corroborate this impression. Moreover, when H-mode could not be obtained in conditions where it was expected, conditioning of the vacuum vessel often allows it to be recovered.

This influence of the wall conditioning on the H-mode implies that care must be taken to limit and quantify any changes in the vessel conditioning. This kind of experiment should be performed on a time scale of about an operating day, with as few intervening disruptions as possible, in order to avoid sharp degradations in the wall conditioning. The H-mode accessibility in the I_p-κ_{95} domain was examined on TCV following this prescription.

3. H-mode accessibility - I_p κ_{95} domain

To study the boundary of the H-mode operational domain, we performed a series of SND discharges with negative magnetic field such that the ion grad B drift is directed towards the X-point. A plasma with the desired elongation, triangularity and current was created in limited configuration, on the central column and the plasma density raised to a value above the expected H-mode threshold. The plasma was then moved off the wall resulting in a single null diverted configuration.

For each elongation in the range 1.05 →1.65, the plasma current was increased, from shot to shot, until an L-H transition occurred. Typically, when the plasma current was sufficient, the transition occurred when the inner gap was larger than ~1cm. The TCV shaping system allowed us to change κ_{95} with only minor changes in the other shaping parameters.

The lowest κ obtained (1.05) was limited by difficulties in creating these configurations with a set of discretely located shaping coils and the approach of the edge safety factor to q_{95}=2. The upper limit on κ (1.65) was in turn restricted by the vertical plasma stability. The installation of internal vertical control coils should allow this value to be increased.

Figures 3 show the results of the H-mode accessibility in the I_p - κ domain. Each discharge in the experimental series is represented by up to 3 symbols, linked by a line. Discharges in which an H-mode transition was not observed are indicated by hollow diamonds with time slices taken at 100ms intervals after the divertor was formed and the plasma density is being further increased. The H-mode accessibility boundary is revealed by the first discharges which show an H-mode transition. These discharges are represented in figure 3 by groups of symbols containing diamonds and a square. The time slices are indicated by: a) diamonds during the inner wall separation and b) a square just prior to the H-mode transition. The squares thus delimit the H-mode accessibility in that another discharge with higher I_p would also transit into H-mode. This boundary divides the I_p - κ graph into L-mode and H-mode regions, showing that more current is required for discharges with higher κ.

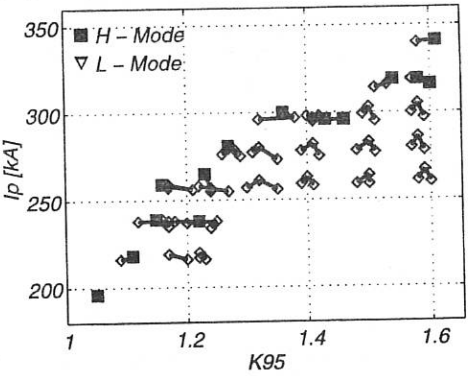

Fig 3: Squares represent the boundary between L and H-mode accessibility in the Ip -κ domain.

It is worth remarking that an Ohmic H-mode has been obtained with I_p lower than 200 kA and an almost circular discharge (κ ~ 1.05).

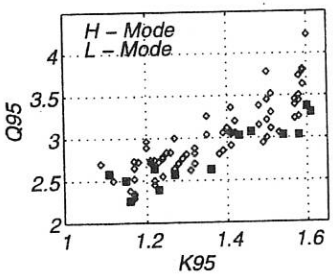

Fig 4: H-mode boundary limit in the q_{95} / K_{95} domain

The threshold values of the safety factor increase with the elongation, as shown in figure 4. This shows that the safety factor near the edge can not be a parameter which directly determines the threshold. Since the average plasma current density also varies at the boundary it can be similarly excluded.

Although this experiment did not allow us to determine the parameter responsible of the L-H transition triggering, a clear boundary was found in the Ip κ domain.

4. Discussion

The success of this experiment emphasises the importance of the configuration evolution in the determination of the boundaries of the H-mode accessibility domain. This must kept in mind when looking for threshold values of heating power. With additional heating, the input power may be approximately considered as a free parameter so the determination of a power threshold is possible. For ohmic heating, due to its dependence on plasma density, current and shape, a precise determination of the ohmic power threshold is difficult. However, from the database, the ohmic power which was applied to the plasma for all the compiled transitions can be plotted. The comparison of the ohmic power per unit surface against the product of the plasma density and the magnetic field, as shown in figure 5, with the ASDEX scaling represented by the solid line, indicates that the ohmic power is in the range of the usual power needed to get an H-mode. (The effects of radiation are neglected)

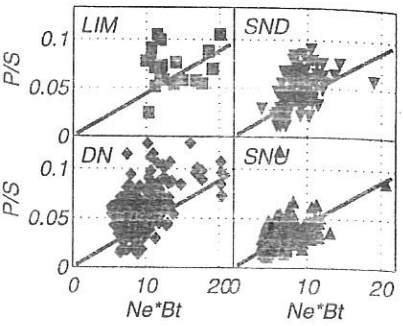

Fig 5: Ohmic power at the L-H transition compared with the ASDEX scaling.

5. Conclusion

Following boronisation, TCV has shown a remarkable facility to access H-mode with Ohmic heating alone. H-modes have been observed in virtually all categories of configurations (SND DND and limiter) and over a wide range of plasma parameters. The accessibility has been found to depend on the wall conditioning and, if this is sufficient, a minimum density and plasma heating current for a given configuration have been found necessary to obtain an H-mode transition. These threshold behaviours, indicate that other parameter(s) (such as edge density, temperature, or their gradients) may determine the occurrence of the L-H transition.

These experiments emphasise the requirement that a single parameter at a time be varied at least until the dominant factors have been determined.

As an example, the results of the H-mode boundary limit in the Ip-κ domain have been described. It is seen that less plasma current was required at lower values of κ with an H-mode obtained for a near circular plasma with Ip ~ 200kA. This demonstrates the ability of TCV to examine the H-mode threshold as a function of a single shaping parameter while keeping other parameters as constant as possible.

Acknowledgements: This Work was partly supported by the Fonds National Suisse de la Recherche.

References

[1] H. Weisen et al, *H-mode Workshop, Princetn,* 1995.
[2] Duval et al., 22th EPS Conference, Bornemouth, 1995.
[3] Ryter et al., 20th EPS Conference, Lisbon, 1993, ECA Vol 17C, I-23.

Breakdown in a Continuous Low Resistivity Vessel in TCV

J.-M. Moret, F. Hofmann, B.P. Duval, J.B. Lister

Centre de Recherches en Physique des Plasmas
Association EURATOM - Confédération Suisse
École Polytechnique Fédérale de Lausanne, CH-1015 Lausanne, Switzerland

The TCV vacuum vessel is continuously welded and has a low toroidal resistance (45 μΩ) for passive stabilisation the plasma vertical motion. Consequently large vessel currents, up to 200 kA, are induced by the loop voltage during breakdown. They create a vertical magnetic field of the order of 10 to 20 mT that must be carefully compensated to achieve discharge breakdown. This compensation as well as the creation of a poloidal field quadrupole rely on accurate magnetic measurements and a precise model of the electromagnetic properties of the vacuum vessel.

Magnetic diagnostics. TCV magnetic measurements consist of: (i) 38 poloidal flux loops wound on the outside of the vessel: (ii) 4 arrays of 38 magnetic probes measuring the tangential field inside the vacuum vessel; (iii) one flux loop on each of the 23 poloidal field coils; (iv) 20 current sensors for the poloidal and toroidal field coils. In addition to an accurate calibration, the consistency of all these measurements has been enhanced by small corrections in their calibration and in the sensor position, leading to an error better than 0.5 mWb and 0.5 mT for the flux and field values, and about 1 mm for their position [1].

Vessel model. The vacuum vessel is made of stainless steel, 15 mm thick in the cylindrical parts and 20 mm thick on the top and bottom. Port holes in the vessel make its electromagnetic modeling difficult. Instead of a complicated 3-D representation, a toroidaly symmetric model with an experimentally determined spatial distribution of the effective resistivity was chosen. The vessel is divided in current filaments I_v whose voltage equation writes

$$0 = R_{vv} I_v + M_{vv} dI_v/dt + M_{va} dI_a/dt \qquad (1)$$

R_{vv} is the diagonal matrix of the sought filament resistances, I_a are the currents in the active coils and the M's are the mutual inductance matrices. These depend only on the geometry and are assumed to be known exactly. Trapezoidal current waveforms much longer than the vessel time constant (13 ms) are separately injected in each active coil. During the ramps I_v and dI_a/dt are constant and from eq. (1) one derives the vessel currents

$$I_v = - Y_{vv} M_{va} dI_a/dt, \qquad (2)$$

where $Y_{vv} = R_{vv}^{-1}$. The flux and field measured by the magnetic sensors are

$$\begin{aligned} \psi_f &= M_{fa} I_a + M_{fv} I_v \\ B_m &= B_{ma} I_a + B_{mv} I_v \end{aligned} \qquad (3)$$

The vessel filament resistances can be deduced from these measurements by solving for Y_{vv} in a least square sense the equations

$$\psi_f - M_{fa} I_a = M_{fv} I_v = - M_{fv} Y_{vv} M_{va} dI_a/dt$$
$$B_m - B_{ma} I_a = B_{mv} I_v = - B_{mv} Y_{vv} M_{va} dI_a/dt \quad (4)$$

The differences in the rhs are calculated using the flux and field values during the current flat top. In fact the available data allow the determination of only a limited number of filament resistances. Thus the latter are combined either in vessel segments, appropriate base functions or vessel eigenmodes by mean of a rectangular matrix T_{vw} and by replacing Y_{vv} by T_{vw} Y_{ww} in eq. (4). Figure 1 compares the measured vessel resistivity with a rough estimation obtained from the vessel geometry and its specific resistivity. The influence of the ports holes is clear and leads to an average discrepancy of 20% which must be accounted for in programming the breakdown field.

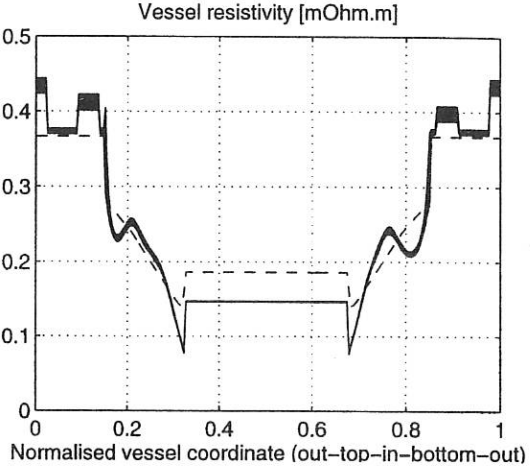

Fig. 1. Vessel resistivity distribution along the vessel perimeter. Dotted line: constructional estimate. Solid: measurement and its error.

Estimatin of the magnetic field configuration. The basic ingredients in determining the magnetic field topology inside the vacuum vessel prior to plasma breakdown are the currents in the active coils and in the vessel. These can be derived from the magnetic measurements by solving in a least square sense and with appropriate weights the set of equations

$$\psi_f = M_{fa} I_a + M_{fv} I_v$$
$$B_m = B_{ma} I_a + B_{mv} I_v \quad (5)$$
$$J_a = I_a$$

The last equation has been introduced to account for errors between the measured (J_a) and adjusted (I_a) coil currents. This method however has proven inadequate and gave a poloidal field null location that did not coincide with that of the breakdown seen on H_α detectors. Equation (1) was then also used to account for the time dependent vessel currents in a consistent way. This new set of equations (5+1) is then solved over a time period prior to breakdown, using a two point difference operator for the time derivatives. The difference in the vessel current distribution estimated by these two methods is large (fig. 2). The latter however results in a estimation of the field inside the vessel and has been extensively used to optimise

the breakdown conditions. The drawback is the large size of the system to be solved, typically 6000 x 2000. To circumvent this, a Kalman filter was set up [2] which works as a best state estimator for the state space system whose states are (I_a,I_v), whose inputs are dI_a/dt and whose outputs are the (ψ_f,B_m,J_a). This approach gives comparable results at much reduced computation time. Because it is fast and it relies only on past samples, it could be implemented in real time as part of the future TCV digital control system.

Creation of plasma breakdown. Breakdown conditions are established in TCV by the MGAMS plasma control algorithm [3]. As part of the shot preparation, MGAMS computes the coil currents as functions of time such that the poloidal field vanishes at the desired breakdown position, at time t=0. In addition, we prescribe a positive vertical field gradient, $dBz/dr > 0$, in order to ensure vertical stability of the initial plasma. These calculations involve a complete simulation of the experiment, including induced currents in the vacuum vessel and plasma current startup. The main difficulty with this approach is that the precision of the poloidal field configuration that can be achieved in the experiment depends on the accuracy of the tokamak model used in the simulation. In TCV, this problem is particularly severe since the vacuum vessel has very low toroidal resistance. Reliable breakdown at loop voltages of the order of 10V can only be achieved when the poloidal field errors are less than about 0.5mT. This accuracy can be obtained by adding small corrections to the prescribed values of Bz, Br, dBz/dr, dBr/dr, at the desired breakdown position, at time t=0. The corrections are deduced from off-line vacuum field analysis, as described in the previous paragraph.. Plasma breakdown has been set up at various position in the vessel: z = 0, ±0.23 and ±0.40 m, for both directions of plasma current and of toroidal field. In all situations the vessel currents is similar to that plotted in figure 2. An example of the magnetic field configuration prior to breakdown is shown on figure 3 (left) for z = -0.23 m. The field modulus is less than 1 mT in a region of more than 0.2 m in diameter. The example on the right of this figure is the field configuration for a simultaneous breakdown at z = ±0.40 m used for the creation of a doublet [4].

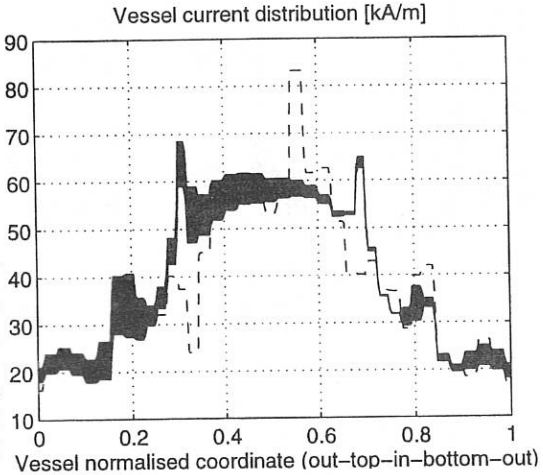

Fig. 2. Vessel current distribution along the vessel perimeter. Dotted line: estimation without vessel current dynamics. Solid: estimation with vessel current dynamics and typical error.

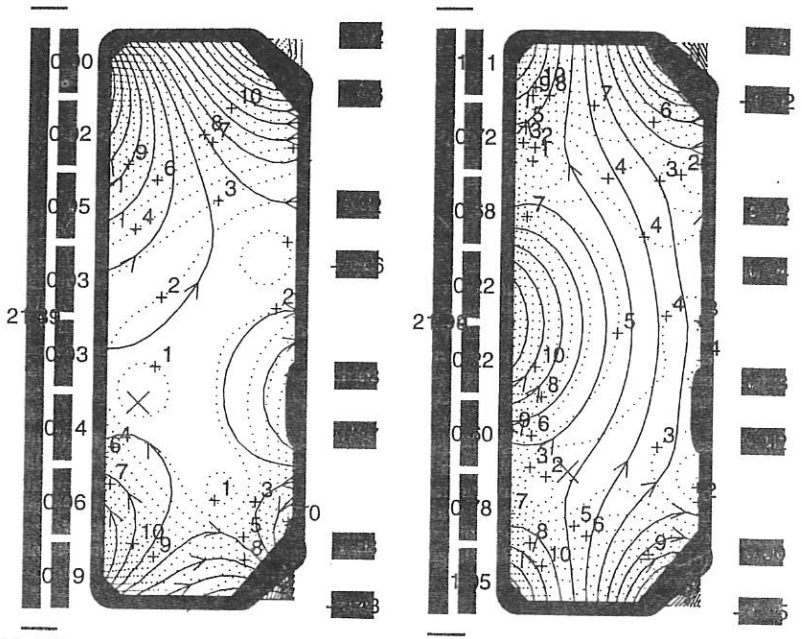

Fig. 3. Vacuum magnetic field configuration prior to plasma breakdown. Dotted lines are the magnetic field modulus contours labelled in [mT]. Numbers on the coils are their current estimation in [kA]. Left: breakdown at z = -0.23 m. Right: simultaneous breakdown at ±40 cm for doublet creation.

This work was partly supported by the Fonds National Suisse de la Recherche Scientifique.

[1] J.-M. Moret, F. Buhlmann, F. Hofmann, G. Tonetti, *22nd EPS Conf. on Cont. Fusion and Plasma Phys., Bournemouth, 1995,* p. 417, vol. 19B part I.

[2] F.L. Lewis and V.L. Syrmos, *Optimal Control,* 2nd edition, John Wiley & Sons, New-York, 1995.

[3] F. Hofmann, M.J. Dutch, J.-M. Moret, *22nd EPS Conf. on Cont. Fusion and Plasma Phys., Bournemouth, 1995,* p. 101, vol. 19B part II.

[4] F. Hofmann, M.J. Dutch, J.B. Lister, Y. Martin, J.-M. Moret, *On the Possibility of Creating Doublet-Shaped Plasmas in TCV,* this conference.

On the Possibility of Creating Doublet-Shaped Plasmas in TCV

F. Hofmann, M.J. Dutch, J.B. Lister, Y. Martin, J.-M. Moret
Centre de Recherches en Physique des Plasmas, EPFL
Association EURATOM - Confédération Suisse,
CH-1015 Lausanne, Switzerland

1. Introduction

Doublet-shaped plasmas were studied at General Atomics for many years [1,2]. Research in this field was stopped in 1984, when Doublet III was converted into DIII-D. Recently, the doublet has received renewed interest [3] because it has an intrinsic zone of negative shear, which is tied to the magnetic configuration and does not depend on a hollow current profile. Negative magnetic shear is thought to have beneficial effects on plasma confinement in tokamaks [4]. Another important property of doublets is the fact that vertical instability growth rates are much lower than in D-shaped plasmas with the same overall elongation [3].

In this paper, we consider three different scenarios for creating doublets and we summarize initial experimental work in this field on TCV.

2. Theoretical Scenarios for Creating Doublets

2.1. Lateral Constriction of a Highly Elongated, Racetrack-Shaped Plasma

Figure 1. shows a sequence of theoretical free-boundary tokamak equilibria illustrating this scenario. Stability analysis of these equilibria shows that the vertical growth rate first increases, as the elongation grows, then goes through a maximum, and finally decreases. The maximum growth rate is reached at the time when the internal separatrix begins to form. Its value depends on the assumed profile functions. For typical TCV profiles, the predicted maximum growth rate is beyond the ideal stability limit and for this reason, no experimental work has been devoted to this scenario so far.

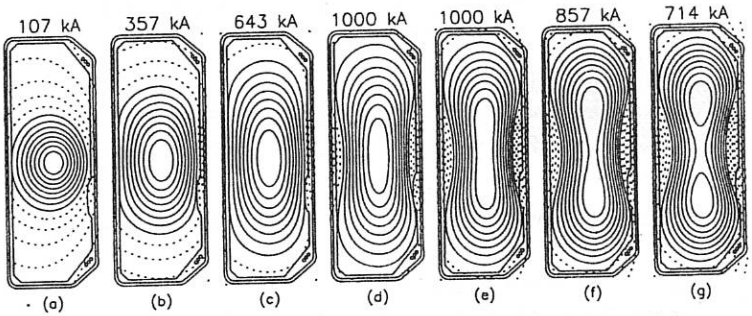

Fig.1. Theoretical scenario for creating doublets by lateral constriction

2.2. Hour-glass scenario

This scenario (Fig.2.) starts with a pear-shaped plasma representing the upper lobe of the doublet. The poloidal flux is controlled in such a way that it stays constant on the boundary of the final doublet shape. When the current is gradually increased under these conditions, the plasma spills over into the lower lobe, an internal separatrix appears and finally the currents in the two lobes become equal.

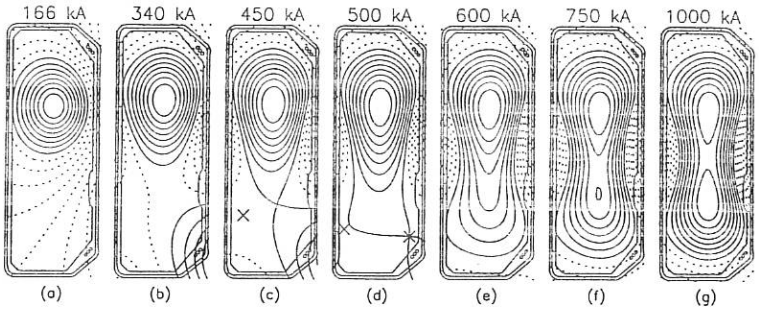

Fig.2. Theoretical scenario for creating doublets by "spill-over"

However, the existence of the intermediate equilibria in this scenario depends on the assumed current profile. For broad current profiles, all equilibria exist, as shown in Fig.2., whereas for peaked profiles, the highly asymmetric doublets (Fig.2e) can not exist in the sense that they cannot be generated with the TCV poloidal field coils. The boundary between existing and non-existing equilibria manifests itself by an extreme sensitivity of the plasma shape to small variations in the coil currents.

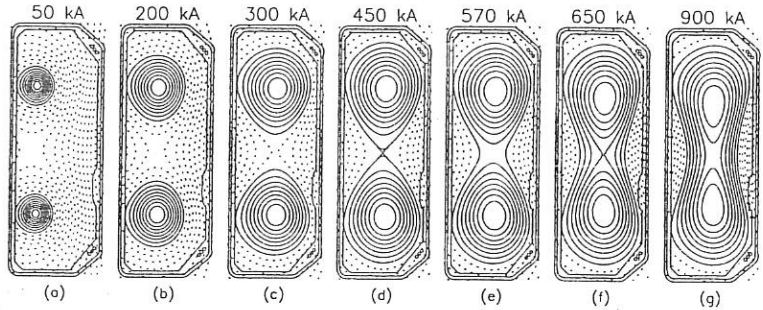

Fig.3. Theoretical scenario for creating doublets by merging two plasmas

2.3. Merging of two Droplet-Shaped Plasmas

This was the preferred scenario in the original doublet experiments at GA [2]. A sequence of theoretical equilibria based on TCV geometry is shown in Fig.3.

3. Doublet Experiments in TCV

3.1. Pear-Shaped Plasmas

The hour-glass scenario described above has been investigated experimentally in TCV: Pear-shaped plasmas have been created in the upper half of the vacuum vessel and a constant flux has been produced on a doublet-shaped contour (Fig.4.). However, when the current is increased, q drops below 2 before the plasma spills over to the lower lobe. This behaviour seems to be connected with the shape of the current profile. Plasma current profiles cannot yet be measured directly on TCV, but we can get some information on the width of the profile from equilibrium reconstructions. We find that in TCV ohmic plasmas, the profiles are rather peaked. If we try to compute the theoretical scenario (Fig.2.) using current profiles resembling the experimental ones, we discover that some of the intermediate equilibria cannot be generated and that the end of the experimental scenario (Fig.4.) roughly corresponds to the boundary between existing and non-existing equilibria.

The hour-glass scenario may be feasible in the future, when current profile modification with ECRH will become possible on TCV.

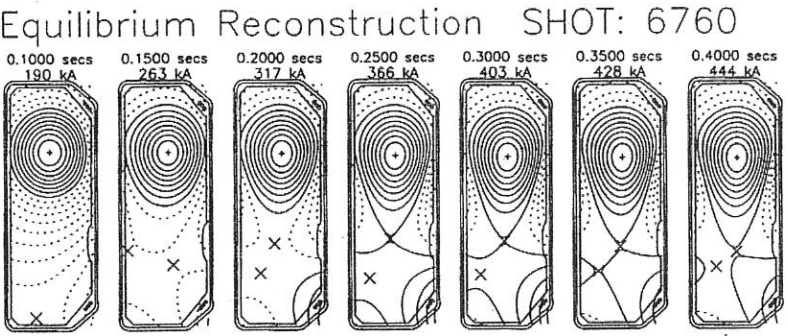

Fig.4. Experimental TCV equilibria showing the initial phase of the hour-glass scenario

3.2. Merging of two Plasmas

The TCV poloidal field coil set allows the creation of two quadrupole nulls inside the vacuum vessel, as described in [5]. In order to create two plasmas, the breakdown at the two nulls must be exactly simultaneous, because if one plasma starts up slightly too early it destroys the field null for the other plasma. If the two currents are roughly equal, they can both grow and finally merge to form a doublet. Initial experiments along these lines have produced doublet shaped plasmas with Ip=110kA and κ=2.6, lasting for about 10ms. As an example we show the reconstruction of an experimental equilibrium (Fig.5a). Plotting this result in κ-I_p space, together with the TCV data base, shows how far the doublet lies from all other plasmas produced in TCV up to now (Fig. 5b).

Acknowledgements: It is a pleasure to acknowledge the support of the entire TCV team. This work was partly supported by the Fonds National Suisse de la Recherche Scientifique.

References:

[1] T. Ohkawa et al., in Plasma Physics and Controlled Nuclear Fusion Research 1974 (Proc. 5th Int. Conf. Tokyo, 1974), Vol. 1, IAEA (1975) 281.

[2] J.C. Wesley et al., in Plasma Physics and Controlled Nuclear Fusion Research 1980 (Proc. 8th Int. Conf. Brussels, 1980), Vol 1, IAEA (1981) 35.

[3] L. Degtyarev et al. in Controlled Fusion and Plasma Physics (Proc. 21st Eur. Conf. Montpellier, 1994), Vol 18B, Part II, EPS (1994) 556.

[4] S.H. Batha et.al., in Controlled Fusion and Plasma Physics (Proc. 22nd Eur. Conf. Bournemouth, 1995), Vol 19C, Part II, EPS (1995) 113.

[5] J.M. Moret, et al., this Conference.

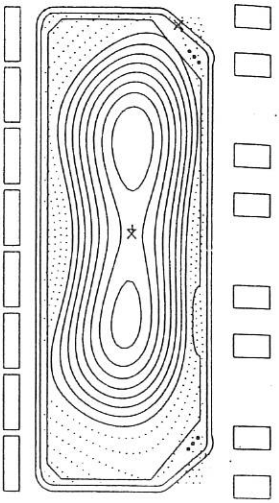

Fig. 5a. Reconstruction of experimental doublet equilibrium in TCV (I_p=110kA, κ=2.6)

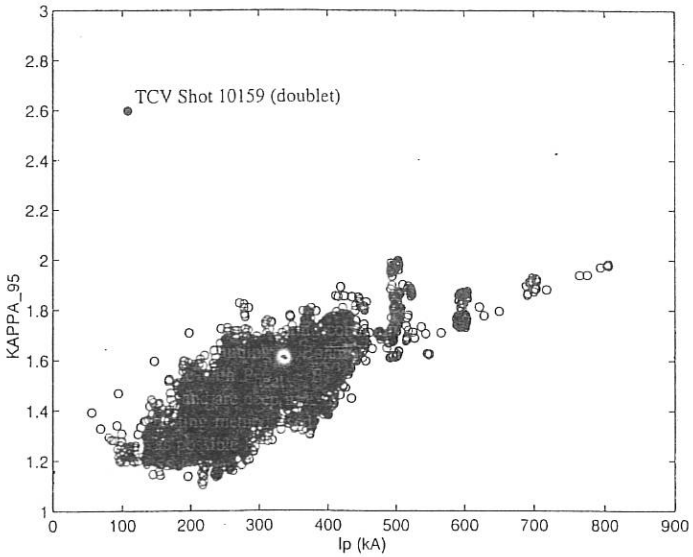

Fig. 5b. κ vs.I_p for TCV plasmas

Scalings of Resistive Mode of Finite Pressure

D. H. Liu, J. Li* and T. Hellsten

Fusion Plasma Physics, Alfven Laboratory, Royal Institute of Technology

* Present address: ABB Industrial System AB, Dept. HSK

Abstract: Stability analyses of internal resistive MHD modes resonating at the q=1,2 or higher surfaces in Tokamak are examined. Special attention is paid to the resistive scalings of modes with different poloidal mode numbers and their different transitions induced by reducing the resistivity, beta value, or shaping the current density profile.

1. Introduction: In recent experiments, it has been observed that peaking the plasma current by different techniques has resulted in high beta and good confinement[1,2,3,4,5]. However, many of the discharges disrupt after beta has reached saturation. The arising of 2/1 and 3/2 or 4/3 modes (often at lower amplitude) are usually associated with degradation of confinement time and beta values. Thus it is necessary to study the internal low n modes carefully to provide detail understanding of these instabilities and means of avoiding them. A vanishing of current density and its gradient at the edge are necessary for stabilising the external kink mode. Since complete stabilization of these instabilities is possible for a sufficiently peaked current density[6], we concentrate on the internal modes, especially, the behaviour of resistive scalings of internal modes with different poloidal mode numbers, their transitions, and effects of on-axis safety factor, resistivity, beta, Suydam criterion as well as shaping of the current and pressure profiles.

To study the effects of the current density and pressure profile, we represent these as

$$j_z = j_{z0}(1-r^{\alpha_{j1}})^{\alpha_{j2}} + c_j e^{-\frac{(r-r_s)^2}{d}} \sin\frac{(r-r_s)}{d}\pi$$

$$p = p_0(1-r^{\alpha_{p1}})^{\alpha_{p2}} + c_p e^{-\frac{(r-r_s)^2}{d}} \sin\frac{(r-r_s)}{d}\pi$$

2. Resistive modes resonating at q=2 surface: Usually only two unstable modes are found for m/n=2/1. Fig. 1(a) shows how the pressure gradient at the rational surface affect the two m/n=2/1 modes. It can be found that decreasing the p'_{rs} will stabilise the interchange mode when beta is still finite while the kink mode is not. The effects of shaping the current density and pressure profiles are studied in Fig. 1(b), where the growth rates of kink mode for different current profiles expressed in terms of the internal inductance are plotted as a function of the peaking factor of pressure ($p_0/<p>$). It is clearly seen that for the low $p_0/<p>$ (broad pressure profile), the growth rates decrease dramatically with the increasing internal inductance (gradually peaking the current density profile) while for the high $p_0/<p>$ (peaked pressure profile), the growth rate is relatively insensitive to the internal inductance. This may

be understood by the fact that peaking of the current density profile increases the magnetic shear near the edge that stabilises the large pressure gradient induced by broad pressure profiles. The result agrees well with the study of pressure profile effects on kink modes[6,7] and experiment results that obtained high beta value as well as improved confinement by using current ramp down techniques to create peaked current profile[3,4,5].

Fig. 2(a) shows the transition from kink mode to tearing mode[8,9]. Here in our case, it occurs for m/n=2/1 modes with small beta value. It can be found that with the decreasing β, the resistive scaling gradually changes from $\eta^{1/3}$ to $\eta^{3/5}$, which is the classical scaling of tearing mode in the limit of zero pressure. The growth rate as a function of resistivity using Δ' theory at zero beta has also been calculated (dashed-dotted line in Fig. 2(a)). It can be seen that the growth rates of the kink mode as a function of the resistivity at $\beta=10^{-4}$ agree with those from Δ' theory at zero beta. The growth rate of the interchange mode is shown in Fig. 2(b). The resistive scaling of the interchange mode is always $\eta^{1/3}$, independent of the beta values.

3. Resistive modes resonating at q=1 surface: Usually there exist several modes with different radial node numbers resonating at q=m/n=1 surfaces, the exact number of unstable m/n=1/1 modes depends on the values of beta and resistivity. Fig. 3(a) shows the growth rate of different m/n=1/1 modes as a function of beta and Suydam index. Seven different unstable modes are found resonating at the same surface when beta is 5%, their growth rates decrease with beta and Suydam index. When Suydam index reaches 0.6 (beta= 0.35%), only four modes are left. By scanning these modes over the resistivity, we found that the mode with one radial node and largest growth rate has an ideal mode scaling, η^0, whereas the other three modes scale with the resistivity as $\eta^{1/3}$ (interchange mode, see Fig. 3(b)).

4. Resistive modes resonating at q $\geq$ 3 surface: Generally the higher-m modes resonating at q $\geq$ 3 surfaces have a mode structure similar to that of m/n=2/1. The resistive scaling of the modes with m=6 is presented in Fig. 4(a). Both interchange and kink modes scale as $\eta^{1/3}$ and there is no transition from kink mode to tearing mode. This differs with m/n=2/1 modes that has a clear kink-tearing transition when the beta is small. Our interpretation of this result is that the modes with higher poloidal mode numbers usually are closer to the boundary compared to the m/n=2/1 modes, they are in a region with high pressure gradient. There is no kink-tearing transition even before these modes are stabilised. However, it is interesting to note that there exists another kind of transition: mutual transition between the kink mode and the interchange mode with the same poloidal mode number when the resistivity is reduced. When $\eta = 10^{-6}$, the mode with smaller growth rate has kink character while the one with larger growth rate has interchange character. With the decreasing resistivity, the growth rate of the kink mode grows while the growth rate of

interchange mode decreases. When η is around $2\sim3\times10^{-7}$, two modes are close to each other and have mutual transition, thus when $\eta < 2\times10^{-7}$, the mode with the larger growth rate has now kink character and the one with smaller growth rate has interchange character. Modes with m=5,4,3 have also this kind of mutual transition when the resistivity decreases, but they are not as clear as that of m=6 case.

We also study the effect of peaking the current density profile on these higher-m modes. Modes of m=6 with q_0 of 0.99 and 1.80 are plotted in Fig. 4(b). The unstable windows for both the kink and the interchange modes shrink with the increasing poloidal mode number and they are largely overlapped, which indicates the potential coupling of these higher-m modes. Again, there exist mutual transitions that are induced by peaking the current density profile. Increasing q_0 will make the higher-m modes shift to the lower internal inductance side. This means the m/n $\geq$ 3/1 modes can be stabilised for a relatively large q_0 together with a peaked current profile.

5. Summary: Stability analyses of internal resistive MHD modes resonating at the q=1,2 or higher surfaces in Tokamak are examined. For m/n=1/1 an ideal mode scaling as η^0 and several resistive interchange modes are found. For m/n=2/1, it is found that in addition to the usual kink mode whose resistive scaling undergoes a transition from $\eta^{1/3}$ to $\eta^{3/5}$ when beta is sufficiently low, there also exist resistive interchange modes which always scale as $\eta^{1/3}$. The resistive interchange mode can be stabilised with finite pressure gradients. Parameter studies on shaping the current density and pressure profiles indicate that broad pressure profiles as well as peaked current density profiles can stabilise the two most dangerous low n modes (m/n=1/1 ideal mode and m/n=2/1 kink mode). For higher-m modes, there are no kink-tearing transition but mutual transition between the kink mode and the interchange mode, which can be induced by reducing the resistivity or peaking of the current density profile. Relatively small increase in safety factor on axis plus peaking the current density profile will shift these higher-m modes to the low internal inductance side.

6. Reference:

[1]. E.J. Strait, Phys. Plasma, 1. 1415. 1994

[2]. J.R. Ferron et al, Phys. Fluids **B**5. 2532. 1903

[3] S. A. Sabbagh et al, Phys. Fluids **B**3. 2277. 1991

[4] L.L. Lao, Phys. Rev. Letters, 70. 3435. 1993

[5] J. Kesner, Phys. Fluids **B**5. 2525. 1993

[6]. W. Howl et al, Phys. Fluids **B**4. 1724. 1992

[7]. T.S. Taylor et al, Plasma Phys. and Controlled Fusion Research, 1990, Vol. I, p177

[8] L. A. Charlton et al, Phys. Fluids, 31. 347. 1988

[9] J. A. Holmes et al, Phys. Fluids **B**1 . 789. 1989

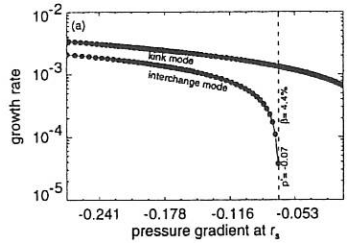

Fig. 1: (a) Growth rates of two m/n=2/1 modes vs. p'_{in}
(b) growth rate vs. $p_0/<p>$ with different l_i

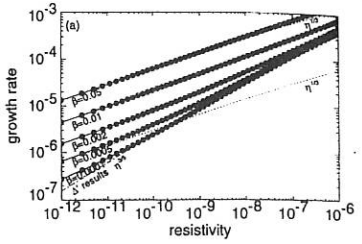

Fig. 2: (a) Scalings of kink mode with different β values, the dashed-dotted line indicates Δ' results. (b) scalings of interchange mode with different β.

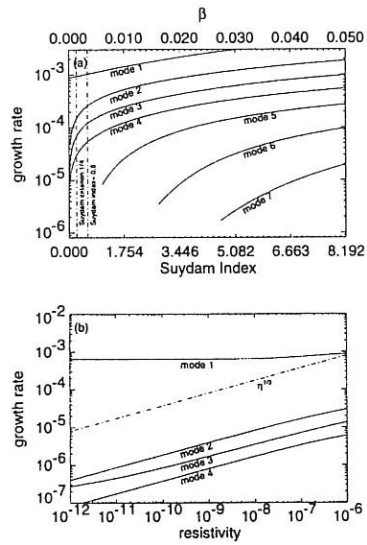

Fig. 3: (a) different m/n=1/1 modes as a function of beta and Suydam index. (b) scaling of four m/n=1/1 modes with $\beta=10^{-4}$ and $D_s=0.01785$.

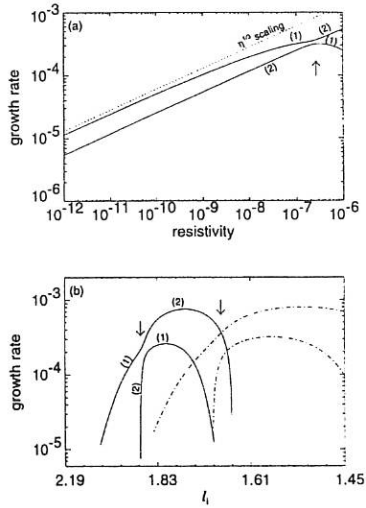

Fig. 4: (a) scaling of m/n=6/1: (1) indicates the kink character and (2) indicates interchange character, (b) growth rate of m/n=6/1 mode vs. l_i with q_0=0.99 and 1.80, the dashed-dotted line indicates q_0=1.80. The arrows indicate where the mutual transitions take place.

Nonlocal response of JET H-mode discharges to temperature perturbations induced by impurity injection

P.Galli[(1)], A.Cherubini, N.Deliyanakis, F.De Luca[(1)], M.Erba, R.Giannella, G.Gorini [(1)], A.Jacchia[(2)], H.J.Jäckel, P.Mantica[(2)], V.V.Parail, L.Porte, A.Taroni

JET Joint Undertaking, Abingdon, Oxon, OX14 3EA, United Kingdom
[(1)]Dipartimento di Fisica, Università degli Studi di Milano, 20133 Milano, Italy
[(2)]Istituto di Fisica del Plasma, Associazione EURATOM-ENEA-CNR, 20133 Milano, Italy

Small injections of metallic radiating impurities with laser blow-off (LBO) techniques are employed, in the framework of perturbed transport, in order to produce peripheral, well localised negative T_e perturbations (Cold Pulses, CP) propagating from the very edge inside the bulk plasma volume. This kind of experiments have been carried out so that "perturbative" electron heat diffusivity χ_e^p can be measured [1]. The results show some very interesting transport features: the propagation velocity of the CP is very high and difficult to reconcile with standard diffusive transport models, unless an unreasonably high degree of nonlinearity is introduced. A possible explanation in terms of the "nonlocal" variation of the transport coefficients has been proposed [2],[3].

In this paper the analysis, limited to ohmic discharges up till now, has been extended to CP in auxiliary heated (by NBI) H-mode plasmas. Nonlocal features are still present.

Experimental evidences

A set of 12 shots in which the LBO technique was combined with ECE measurements are examined: for 3 of them the LBO also triggers a type I ELM. A fast (compared to usual diffusive time scale) propagation of the cold front, which involves a large ($\rho \geq 0.5$) region of plasma column, is always observed. Such wide and fast modifications are similar to other experimental situations such as the L-H transition [4] and giant ELMs [5]. It seems natural to try and explain all of these observations in terms of nonlocal modifications of transport coefficients.

The time history of $< n_e >$, D_α, I_p, $< Z_{eff} >$ signals exhibit no significant perturbation at the injection time t_{LBO}; changes in n_e and Z_{eff} due to LBO are expected to be restricted to $\rho \geq 0.9$ [6]. Bolometric data show that at $t = t_{LBO}$ the total radiated power P_{rad} experiences a sharp enhancement whose range of values is wide for these discharges. Abel inverted p_{rad} profiles show that the cooling radiation is mainly concentrated outside $r/a > 0.8$ at the estimated value of the time t_{LBO}. These experimental observations suggest that the variation of T_e far into the

plasma core immediately after the LBO must be related to a mechanism acting on a time scale much shorter (≈1 ms) than that expected from energy and particle diffusion.

A χ_e with a global dependency (represented by the coefficient γ in the factorised expression $\chi_e = \gamma(\rho,t)\chi_{e0}$) has been shown [7] to be equivalent to an extra source term $\tilde{p}_\chi$ in the equation for the temperature perturbation $\tilde{T}_e$:

$$\tfrac{3}{2} n_{e0}\partial_t \tilde{T}_e - \nabla\cdot\left[n_{e0}\gamma(\rho,t)\chi_{e0}\nabla\tilde{T}_e\right] = \tilde{p}_e + \tilde{p}_\chi \qquad \text{with} \quad \tilde{p}_\chi = \nabla\cdot\{[\gamma(\rho,t)-1]n_{e0}\chi_{e0}\nabla T_{e0}\}$$

where $\tilde{p}_e$ is the perturbed power. Therefore it can be assumed that for a short time $t \cong t_{LBO}$ (when the diffusive term $\nabla\cdot\left[n_{e0}\gamma(\rho,t)\chi_{e0}\nabla\tilde{T}_e\right]$ can be neglected) and far from the inducing source (where $\tilde{p}_e \cong 0$) only $\tilde{p}_\chi$ is acting and is responsible of the above phenomenology.

Analysis technique and results

Under these assumptions, the intensity and the radial extent of such power source, $\tilde{p}_\chi$, can be estimated from ECE data by evaluating the jump in the time derivative of T_e, $\left(\partial_t \tilde{T}_e\right)_{t_{LBO}}$, at the instant of the laser blow off. This quantity is computed for each shot by a linear least-squares fitting of each ECE time trace over a short time before and after t_{LBO} and then evaluating $\left(\partial_t \tilde{T}_e\right)_{t_{LBO}} = \left(\partial_t T_e\right)_{t\to t_{LBO}^+} - \left(\partial_t T_e\right)_{t\to t_{LBO}^-}$. Fit intervals of about 4-5 ms are used, which are long enough to compute a statistically significant number of points within a linear approximation. Since the evaluation of $\partial_t \tilde{T}_e$ at $t = t_{LBO}$ involves a finite time interval, other transport mechanisms could influence the T_e time traces behaviour and bias the identification of non local effects. However for $t \le 5$ms all transport mechanisms are negligible. In addition it has to be expected that the assumption of a finite time interval for the evaluation of the time derivative induces a systematic smoothing in $\tilde{p}_\chi$ profiles. This has been tested by using numerically simulated cold pulses. It has been found that an interval of 4-5 ms is a good compromise.

Comparison between $\tilde{p}_\chi$ and corresponding $\tilde{p}_e = \Delta p_{rad}$ profiles shows (Fig.2) that the effects of the perturbing radiation on the plasma column at the injection time are indeed quantitatively much larger and broader than those expected from a purely local process. This confirms that *also in H-mode CP propagation has a non diffusive global character*: the scale length of the plasma response is $a/2$ or longer, the time scale is around 1-2 ms.

Out of 9 pure H-mode LBO-CPs, 8 of them present a $\tilde{p}_\chi$ effect whose intensity is comparable, though the value of the inducing ΔP_{rad} covers a wide range, from 1 to 20 MW. One example of has a more intense response and was obtained with a weak injection ($\Delta P_{rad} / P_{tot} \approx 0.07$). Normally the reaction is comparable to that obtained for O-mode CP [8], independently of the strength of the perturbation. The $\tilde{p}_\chi$ intensity appears fairly well correlated to the average T_e value at $t = t_{LBO}$. We found $< T_e > \cong 4.5$keV for the strong $\tilde{p}_\chi$ against $2.5 \le < T_e > \le 3.3$ keV for the others. The values of the total power P_{tot} are similar in all cases. The fact that stronger and broader $\tilde{p}_\chi$ effects arise during stages when, under the same auxiliary power input, higher T_e values are achieved (as in the case of the so called Hot-Ion H mode) could be an indication

that the state of the plasma confinement plays an important role in determining the characteristics the of nonlocal response.

Nonlocal transients and global confinement

The technique described above, due to its simplicity, can be easily extended to other T_e transients: in particular analysis of both spontaneous and LBO induced type I ELM CP has been pursued for the previously considered shots. This permitted one to compare nonlocal pulses with a different source within the same discharge. The strongest and broadest $\tilde{p}_\chi$ reactions (Fig.3) seem to be associated with ELMs occurring very close to (or in coincidence with) both an H and a Hot-ion H mode termination phase. During the high performance period of an Hot-Ion H mode the $\tilde{p}_\chi$ reaction to ELMs is still quite intense, comparable to the strongest LBO-CP example. In the Hot-Ion H modes considered so far, the $\tilde{p}_\chi$ reactions associated with LBO and with type I ELM instabilities occurring in the same discharges are barely distinguishable. On the other hand, in H mode phases far from termination the $\tilde{p}_\chi$ response to an ELM is found weaker, i.e. of the same order of most LBO CP, even for strong ELMs. These results suggest that the plasma is more unstable to boundary temperature perturbations in high performance than in low performance H-modes (Fig.4). This might indicate a possible link between the state of the confinement and the scale length of plasma transport, in the sense of a broader reaction to transients when confinement is better.

Conclusions

A simple technique analysis, based on the calculation of discontinuity in $\partial_t T_e$ at t_{LBO} from ECE data, shows that, in H modes, LBO-induced Cold Pulse propagation confirms nonlocal features. These features can be quantified by a power source term $\tilde{p}_\chi$ arising in the equation for $\tilde{T}_e$. The above procedure permits quantitative comparison to be made among $\tilde{p}_\chi$ due to different T_e perturbations. By correlating the results to the plasma state at $t = t_{LBO}$, we can associate larger $\tilde{p}_\chi$ reactions with better confinement regimes and, in particular, with the proximity to the H-mode termination phase. Nevertheless a larger database is needed in order to clarify this dependence in a more quantitative way.

[1] *J.O'Rourke et al, 35th APS Conf. (1993); W.Kissick et al., Nucl. Fus. 34 (1994) 349*

[2] *R.Giannella et al., Proc. 15th IAEA Conf. on Plasma Phys. and Contr. Nuclear Fusion Research (Seville, Spain, 1994), IAEA Vienna (1995), Vol.I, 289; De Angelis et al., 22nd EPS Conf., Bournemouth (1995)*

[3] *K.Gentle et al., Phys. Rew. Lett.; 74 (1995) 3620; W.Kissick et al., to appear in Nucl. Fus.*

[4] *J.G.Cordey et al., Plasma Phys. and Contr. Fusion, 36 Suppl. A (1994), 267*

[5] *V.V.Parail et al., Proc. 15th IAEA Conf. on Plasma Phys and Contr. Nuclear Fusion Research (Seville, Spain, 1994), IAEA Vienna (1995)Vol.I, 255*

[6] *R.Giannella et al., Nucl. Fus., 34 (1994) 1185*

[7] *J.G.Cordey et al., Nucl. Fus., 35 (1995) 505; A.Jacchia et al., Phys. Plasmas, 2 (1995) 4589*

[8] *G.Gorini et al., JET Report JET-R (95) 04, JET Joint Undertaking, Abingdon, UK (1995)*

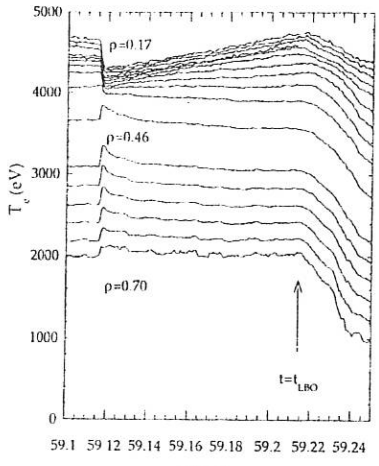

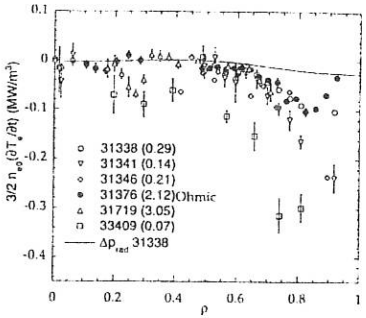

1. *Time evolution of T_e following Laser Blow Off in JET H mode shot #31719, corresponding to one of the most intense injections. The LBO is performed at t_{LBO}=59.2161 sec.*
2. *Spatial profiles of the term $\frac{3}{2} n_{e0} \partial_t \tilde{T}_e)_{t=t_{LBO}}$ for H-mode (white symbols) and Ohmic (black symbol) Cold Pulses. The $\Delta P_{rad} / P_{tot}$ values are reported near corresponding shot numbers. The enhancement in the radiated power deposition profile Δp_{rad} for one of them is also plotted.*

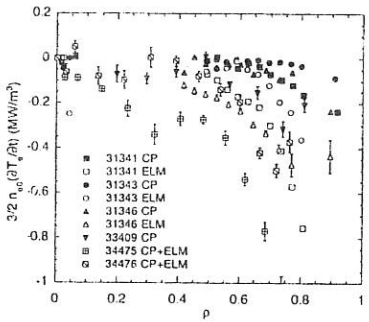

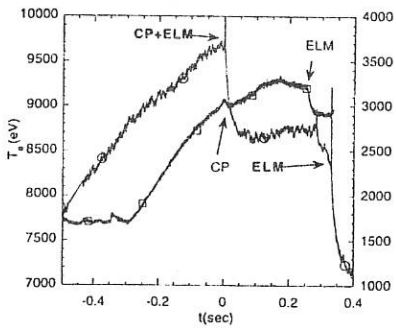

3. *The same quantity as in Fig.2 calculated for CPs due to type I ELM instability (white symbols). Few LBO-CPs are reported for sake of comparison (black symbols).*
4. *Examples of typical T_e evolution (measured at $\rho \equiv 0.55$) for an Hot-Ion H mode (open cyrcles, shot #34475) and for an H mode (open squares, #31343). Transients inducing strong $\tilde{p}_\chi$ responses are indicated in bold style. Total NBI power input is about 15 MW for both of two shots. Time has been rescaled so that t_{LBO}=0.*

BALLOONING INSTABILITIES IN THE SCRAPE-OFF-LAYER OF DIVERTED TOKAMAKS AS GIANT ELM PRECURSORS

R.A.M. Van der Linden, W. Kerner, O. Pogutse, B. Schunke.

Jet Joint Undertaking, Abingdon, Oxfordshire OX14 3EA, UK

Abstract

The linear stability of the SOL to ballooning modes is studied using the reduced MHD model and applying the ballooning approximation to the perturbations. Particular attention is focused on the role of the X-point in the stability analysis and on the potential role of SOL ballooning instabilities as precursors to giant ELMs.

INTRODUCTION

The edge region of tokamaks is a main factor determining the macroscopic behaviour and performance characteristics of the entire plasma. Instabilities in the Scrape-off-Layer (SOL) are believed to generate micro-turbulence leading to enhanced transverse transport. Thus, a quantitative analysis of the stability of the SOL is crucial for understanding phenomena like the L-H transition and ELMs, and for determining the dependencies of quantities like the SOL width on the discharge parameters. In this paper, the stability of the SOL with respect to ballooning modes is studied. Since SOL field lines are open, the periodicity constraint that complicates the ballooning mode representation inside the separatrix is replaced by *'line-tying'* boundary conditions at the target plates. In the ideal MHD model applied here these target boundary conditions might be expected to exert a significant *stabilising influence*. However, on flux surfaces close to the separatrix the X-point effectively shields the plasma from the target plates and removes the stabilising effect. Since the *'magnetic well'* is strongly stabilising *inside* the separatrix and pressure gradients are very large just *outside* the separatrix, the SOL region may become unstable first, acting as a trigger to the release of energy from inside the separatrix.

MODEL

We use orthogonal flux coordinates (ρ,ω,φ) with metric $ds^2 = h_\rho^2 d\rho^2 + h_\omega^2 d\omega^2 + R^2 d\varphi^2$ to describe the magnetic field geometry near the separatrix. Using the reduced MHD equations and the eikonal representation for the perturbations [1]:

$$f(t,\rho,\omega,\varphi) = \tilde{f}(\rho,\omega)\exp\left[\gamma t + in\int_{\omega_*}^{\omega} q(\rho,\omega')d\omega' - in\varphi\right],$$

with $nq >> 1$ yields the ballooning equation (here formulated in terms of the electric potential)

$$B_\varphi\left(\frac{B_\omega}{h_\omega B_\varphi}\frac{\partial}{\partial\omega}\right)\frac{1}{B_\varphi}\left(\frac{nq}{h_\omega}\right)^2(1+\zeta^2)\left(\frac{B_\omega}{h_\omega B_\varphi}\frac{\partial}{\partial\omega}\right)\tilde{\phi}-\gamma^2 c_A^{-2}\left(\frac{nq}{h_\omega}\right)^2(1+\zeta^2)\tilde{\phi}$$

$$-\frac{\mu_0}{RB_\varphi}\left(\frac{nq}{h_\omega}\right)^2\frac{1}{h_\rho}\left(\frac{1}{h_\rho}\frac{\partial}{\partial\rho}\frac{R}{B_\varphi}-\zeta\frac{1}{h_\omega}\frac{\partial}{\partial\omega}\frac{R}{B_\varphi}\right)\frac{dP_0}{d\rho}\tilde{\phi}=0,$$

where $q(\rho,\omega)=\dfrac{B_0 h_\omega}{B_\omega R}$ is the safety factor, and $\zeta(\rho,\omega,\omega_0)=\dfrac{h_\omega}{h_\rho}\dfrac{1}{q}\dfrac{\partial}{\partial\rho}\int_{\omega_0}^{\omega}q\,d\omega'$ is the shear.

We can apply the model to an experimental configuration, or use an analytical two-wire current model which allows high accuracy and makes it possible to separate individual effects. The metric coefficients and magnetic field in the (straight) two-wire model are given by:

$$h_\rho^2=h_\omega^2=h^2=\frac{y_0^2}{4}\frac{\exp(2\rho)}{\left[1-2\exp(\rho)\cos(\omega)+\exp(2\rho)\right]^{1/2}},$$

$$B_\omega(\rho,\omega)=\frac{B_{\omega 0}(\rho)}{h_\omega R},\qquad B_\varphi(\rho,\omega)=\frac{B_{\varphi 0}R_0}{R}.$$

The separatrix is located at $\rho=0$, while the X-point is given by $\omega=0,2\pi$. We define the dimensionless quantities

$$\tilde{\beta}=\frac{\mu_0}{B_{\varphi 0}^2}\frac{dp_0}{d\rho}\qquad\text{and}\qquad S_0=\frac{1}{q(\rho,\pi)}\frac{\partial}{\partial\rho}q(\rho,\pi).$$

Qualitatively, the results obtained for the experimental configuration and for the analytical model are very similar. This is illustrated in figures 1 and 2, where the (dimensionless) growth rate is plotted as a function of ω_0 for typical cases.

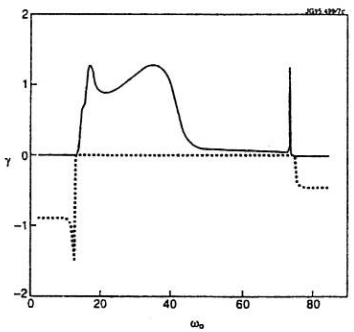

Fig.1: Growth rates for JET experimental configuration (pulse 31300).

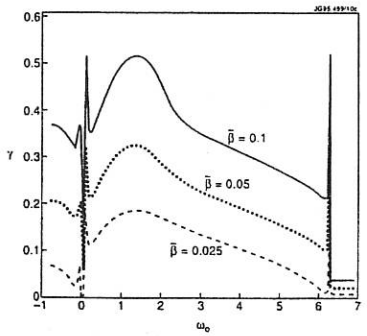

Fig.2: Growth rates for analytical model $(S_0=0)$.

The strong variation of the growth rates near the X-point reflects the strong variation of the equilibrium quantities. The characteristic feature that *identical* maximum growth rates are found at three points (one near the midplane and one on each side of the X-point) is due to the non-monotonic behaviour of $\int \frac{\partial q}{\partial \rho}$, as explained in detail in Kerner et al. (1996) [2].

STABILITY ANALYSIS OF THE EDGE REGION IN JET DISCHARGES

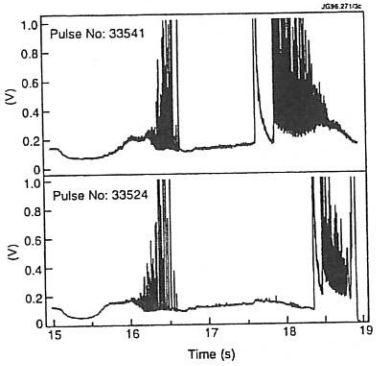

Fig. 3: Elm behaviour of two discharges with different shaping (D_α signal).

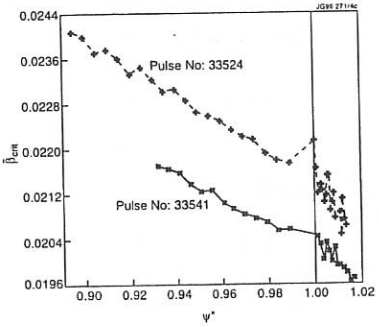

Fig. 4: Calculated $\tilde{\beta}_{crit}$ for these discharges

Experimentally it has been found that the duration of the ELM-free period can be increased by stronger shaping of the magnetic configuration, as shown in figure 3. This agrees with the higher critical gradient for the ballooning instability displayed in figure 4. It is also clear from figure 4 that $\tilde{\beta}_{crit}$ is lower in the SOL than inside the separatrix.

STABILITY ANALYSIS OF A TWO-WIRE MODEL OF THE SEPARATRIX REGION

In figure 5 the influence of shear on the marginal stability point $\tilde{\beta}_{crit}$ is shown. For small values of ρ we find the linear dependence $\tilde{\beta}_{crit} = a(S_0) + \rho b(S_0)$. Close to the separatrix shear is stabilising, but further out the dependence becomes non-monotonic. Thus the global effect of shear depends strongly on the natural mode width (e.g. due to FLR effect). Not shown here is that shear also affects the position where the most unstable solution is found. When the height of the X-point is varied (keeping the configuration fixed but increasing the distance of the target plates) it is found that close to the separatrix the height of the X-point has no significant effect on the critical gradient, i.e. the target plates are effectively shielded by the X-point (see Kerner et al. for more details). The eigenfunctions indicate that the perturbations of physical quantities (e.g. $\delta B_\rho \sim \frac{\partial^2 \phi}{\partial \omega^2}$, $\delta v_\rho \sim \frac{\partial \phi}{\partial \omega}$) are localised near the X-point.

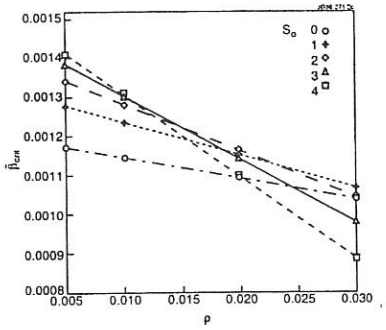

Fig. 5 Dependence of $\tilde{\beta}_{crit}$ on shear S_0.

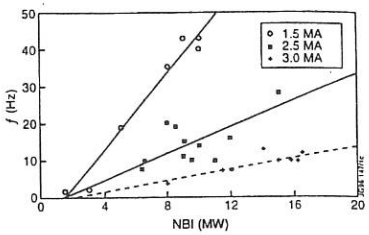

Fig. 6 Experimental dependence of ELM frequency on input power.

DISCUSSION

We have shown that the critical gradient for ideal ballooning modes in the SOL is lower than that just inside the separatrix. The X-point has a strong influence on the stability of the SOL (mainly by shielding the upstream plasma from the target plates), and in particular we have found that the perturbations of physical quantities are localised near the separatrix in the X-point region (some localisation near the midplane is also possible). The effect of shear is generally stabilising for modes that are strongly localised (i.e. with narrow mode width), but for larger mode widths shear may destabilise instead. The stability characteristics of the tokamak edge region are compatible with the ELM model proposed by Pogutse et al. [3]. In this model, the ballooning instability in the SOL is conjectured to act as precursor for giant ELMs. Because of the localisation the ballooning instability in the SOL destroys the magnetic X-point geometry and this makes hot plasma from inside the separatrix come into contact with the wall. The thus generated impurity influx then triggers the instability inside the separatrix (the main macroscopic event). Finally, the expelled plasma layers are diffusively refilled. This model leads to an estimate for the ELM frequency

$$f \propto \frac{P_{in} B_0}{I^3 \Delta_p^{1/2}}$$

As shown in figure 6, the predicted linear dependence on input power agrees with the experiment. An inverse dependence on input power is also obvious, but the exact scaling needs to be further investigated.

REFERENCES

[1] J. Connor, R. Hastie, and B. Taylor, Proc. R. Soc. (London). Ser. A365 (1979) 1.

[2] W. Kerner, O. Pogutse, R.A.M. Van der Linden and B. Schunke, submitted to Plasma Physics and Controlled Fusion.

[3] O. Pogutse, J.C. Cordey, W. Kerner, and B. Schunke, Proc. 22nd EPS Conf. on Controlled Fusion and Plasma Physics (Bournemouth, 1995), Vol III p.277.

LINEAR AND NONLINEAR DYNAMICS OF ALFVÉN EIGENMODES IN JET PLASMAS

D.Borba, J.Candy, A. Fasoli*, W. Kerner, D.Muir, S.Sharapov**

Jet Joint Undertaking, Abingdon, Oxfordshire OX14 3EA, U.K.
*CRPP, Assoc. EURATOM-Confederation Suisse EPFL , 1015 Lausanne, Switzerland
**Associação EURATOM/IST Av Rovisco Pais 1096 LISBOA PORTUGAL

ABSTRACT

The stability of Alfvén eigenmodes in JET is studied using a Hybrid Gyrokinetic MHD model which takes into account finite orbit effects, realistic plasma geometry and Alfvén waves fields including first order ion Larmor radius corrections. This analysis provides stability diagrams for global Alfvén eigenmodes in the presence of fusion products or energetic ions generated by auxiliary heating. The nonlinear evolution and saturation of the modes is studied using an Hamiltonian guiding center description of the particle motion in a perturbed magnetic field with a self consistent update of the amplitude and phase of the wave.

INTRODUCTION

The influence of energetic particles on the stability of Alfvén waves in the Joint European Torus (JET) is analysed using a three-step numerical procedure. First, the equilibria are reconstructed using the codes EFIT and HELENA. Secondly, linear properties of the toroidal Alfvén wave spectrum are determined by the MHD normal-mode code CASTOR (Complex Alfvén Spectrum in TORoidal geometry). The linear stability analysis includes the determination of the principal wave damping mechanisms, i.e. ion and electron Landau damping, radiative damping and collisional electron damping as well as the evaluation of the instability drive including effects due to large, non-standard (i.e potato) orbits characteristic of alpha particles and of radio-frequency-heated (RF) ions in the JET tokamak. Finally, the nonlinear mode evolution, including amplitude saturation and fast-particle redistribution/loss, is computed using the particle code FAC (Fast particle-Alfvén wave interaction Code).
JET discharges with a large fraction of RF and NBI generated ions are studied with distributions based on Fokker-Planck simulations using the codes PION (for RF ions) and PENCIL (for NBI ions). Possible scenarios for TAE excitation by alpha particles, as well as by NBI and/or RF-produced energetic ions, are studied in conditions relevant to JET DT experiments.

MODEL

Using the MHD equilibria reconstructed by EFIT and HELENA, the linear normal-mode analysis is performed by the spectral codes CSCAS and CASTOR. The linear MHD model (CASTOR-CR) includes

first order finite ion Larmor radius effects and the perturbed parallel electric field. The CASTOR-CR code solves the linearized MHD equations with the parallel resistivity obtained from kinetic theory:

$$\eta \approx 4\pi i\omega\rho_s^2\left(\frac{3}{4}+\frac{T_e}{T_i}\left(1-i\delta_e\right)\right).$$

The electron dissipation includes collisional damping δ_e due to a finite longitudinal electric field and collisional curvature damping obtained from a tabulated solution of the bounce-averaged electron kinetic equation. ρ_s is the ion sound Larmor radius, T_i, T_e are the ion and electron temperatures and ω frequency of the perturbation. The contribution of energetic ions is included perturbatively. The CASTOR-K code computes the first order perturbation on the eigenvalue due to the resonant interaction between the wave and the energetic ion population using a gyro-kinetic model. The resonant Landau damping from thermal particles is included in the same fashion.

$$\left(\omega_r+i\omega_i\right)^2 K=\delta W_{MHD}+\delta W_{hot}\ ,\ \frac{\gamma}{\omega}=\frac{\omega_i}{\omega_r}=\frac{\mathrm{Im}[\delta W_{hot}]}{2\omega_r^2 K}$$

K representes the kinetic energy of the perturbation, δW_{MHD}, represents the MHD part and δW_{hot} represents the contribution from energetic ions to the eigenvalue. CASTOR-K utilises the linear eigenfunction obtained by CASTOR-CR and decomposes the hot particle energy functional into poloidal bounce harmonics and integrates the resonant contribution over the particle phase-space $dP_\phi dEd\mu$ [3],

$$\delta W_{hot}=-\frac{2\pi^2}{\Omega m^2}\sum_\sigma\int dP_\phi dEd\mu\sum_{p=-\infty}^{\infty}\frac{\partial F}{\partial E}\frac{\tau_b|Y_p|^2\left(\omega-n_0\omega_.\right)}{\omega+n_0\omega_D+\left(n_0 q+p\right)\omega_b},\ Y_p=\oint\frac{d\tau}{\tau_b}\ L^{(1)}\ e^{ip\omega_b\tau}.$$

$L^{(1)}$ represents the perturbed Lagrangian of the unperturbed particle motion, ω_D, ω_d the precessional drift and bounce particle frequencies. The nonlinear dynamics is studied using the FAC code. The nonlinear interaction of a discrete spectrum of low-β fluid modes with a hot particle source is described by a Hamiltonian guiding center scheme for the particle motion in the presence of a field perturbation with a self consistent differential update of the phase and the amplitude of the wave. The time evolution of the perturbed distribution function δf is described as an initial value problem by a set of markers (quasi-particles).

$$\frac{d}{dt}\delta f_{hot}=-\frac{d}{dt}f_{hot}{}^0-\upsilon\delta f_{hot}$$

ANALYSIS OF JET DISCHARGES IN THE PRESENCE OF ALPHA PARTICLES

Due to a combination of the mode structure and the finite orbit effects the most unstable modes in JET in the presence of alpha particles $E = 3.5\ MeV$ are KTAE modes with n=5 to 8. The analysis shows that alpha particles have a strong destabilising effect $\gamma/\omega \approx 2\langle\beta_\alpha\rangle$. But due to the alpha particle pressures possible in JET tritium experiments $\langle\beta_\alpha\rangle \le 10^{-3}$ and the various damping mechanisms, these modes are expected to be marginally stable as shown in figure 2. The nonlinear simulations show that when the

KTAEs are found to be unstable the saturation amplitude scales as $\frac{\delta B}{B} \approx 0.5\left(\frac{\gamma}{\omega}\right)^2$ and therefore the saturation amplitude is small $\frac{\delta B}{B} \approx 10^{-5}$. For these amplitudes no significant anomalous alpha transport is expected. The computations are based on a typical JET high performance discharge with $n_e = 5 \times 10^{19} m^{-3}$, $B_0 = 3T$, $T_i \approx 10 \rightarrow 20 KeV$ and $T_e = 10 KeV$, using an alpha particle slowing down distribution. In the stability diagram the ratio between the alpha particle velocity and the Alfvén velocity on axis $\frac{V_\alpha}{V_A}$ is scanned by changing the plasma density.

INFLUENCE OF NBI AND RF HEATING

High performance JET discharges are characterized by a large auxiliary heating power in the form of NBI or/and RF. Due to the nature of the orbits of RF generated ions (trapped ions), it is more difficult to excite KTAE modes than TAE modes with RF heating. The interaction between TAE modes and RF is strongest when the RF resonant layer is localised at the low field side of the torus as shown in figure 4.
NBI injected ions have lower energy $E \leq 140 KeV$ than RF produced ions $E \geq 500 KeV$ and are expected to destabilise only high-n (n>10) TAE and KTAEs at high densities. For low-n (n<10) modes the beams should have a stabilising effect. Detailed calculations including the radiative damping of high-n modes, the ion Landau damping at high densities and the destabilising effect of large beam power on high-n TAE and KTAE modes are required in order to determine the stability boundaries.

CONCLUSIONS

The hybrid Gyro-Kinetic-MHD model developed provides detailed description of the interaction of energetic ions with global plasma waves taking into account: realistic geometry, finite particle orbit width including large non-standard orbits, realistic wave fields including first order ion Larmor radius corrections and linear and nonlinear evolution. Applications of the model to JET high performance discharges show that due to orbits effects RF ions do not have a strong influence on the KTAE modes. On the another hand neutral beam generated ions can destabilzize only high-n (n>10) TAE and KTAE modes at high densities. Alpha particles will have a strong destabilising effect only on low-n KTAE's modes due to finite orbit effects. As a consequence of the small alpha particle pressure and the various sources of damping low-n modes should be marginally stable in the JET tritium experiments.

REFERENCES

[1] H. L. Berk et al, Phys.Plasmas 2 (9), (1995) 3401
[2] A.Fasoli et al, Nuclear Fusion, Vol 35 No 12 (1995) 1485
[3] F. Porcelli et al, Phys. Plasmas 1 (3), March (1994) 470
[4] W. Kerner et al, Plasma Phys. Control Fusion 36 (1994) 991

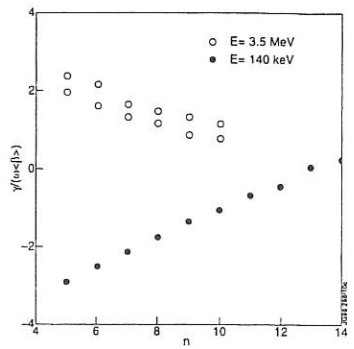

figure 1 Drive due to a slowing down distribution of alpha particles and NBI generated ions for KTAE modes as a function of the toroidal mode number.

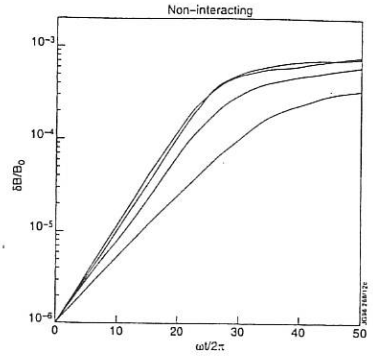

figure 3 Nonlinear evolution of unstable KTAE modes with n=5 to 8 in the presence of alpha particles. Each toroidal mode is simulated individually .

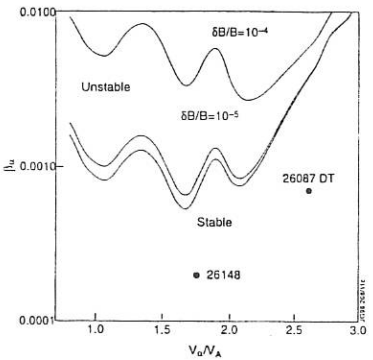

figure 2 Stability diagram for KTAE modes in JET high performance discharges for 1) the preliminary tritium experiment PTE1 #26148 and 2) a future 50% tritium discharge based on #26087.

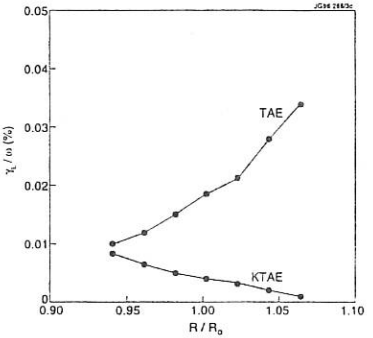

figure 4 Growth rate of TAE and KTAE modes as a function of the RF resonant layer position in the presence RF generated ions. Optimal excitation is achieved for TAE modes when the resonant layer localized in the low field side of the torus.

MHD RELATED TRANSPORT ANALYSIS IN JET

B. Balet, G. Huysmans, M.F.F. Nave[1], P. Smeulders and J.A. Wesson
JET Joint Undertaking, Abingdon, Oxfordshire, OX14 3EA
[1]Associaçao Euratom/IST, Institute Superior Technico, Lisbon, Portugal.

INTRODUCTION: The MHD activity observed during the JET hot ion H-modes, has been described in [1]. Three main types of MHD phenomena can be distinguished:

- Core modes such as sawteeth which cause substantial drops in the core temperatures.
- Outer Modes (OM) i.e. MHD oscillations (mainly n = 1, m = 3-5) with frequencies ~ 10kHz observed within the outer 20% of the plasma.
- Giant Edge Localised Modes (ELMs).

A selection of discharges (see Table I) has been analysed with the TRANSP code to clarify the effect of the MHD instabilities on the plasma transport. For that purpose an effective χ_{eff} is defined to quantify plasma losses:

$$\chi_{eff} = q_{loss}/(n_e \nabla T_e + n_i \nabla T_i)$$

χ_{eff} doesn't separate ion and electron loss channels and includes all loss terms (conduction, convection, CX losses etc).
A typical evolution of a hot ion H-mode pulse #34500, is shown in Fig. 1. The performance appears to be limited by MHD events. A saturation of the neutron yield (= 0.5 × R_{DD}), $T_e(0)$ and W_{DIA} coincides with the onset of an OM (seen in the magnetic coil signal between 12.63s and 13s). The increase in the D_α emission is correlated in time and shape to the OM. The OM is interupted by a small ELM. The plasma performance recovers until a giant ELM at t = 13.25s, which marks a drop in R_{DD} and W_{DIA}. Finally at t = 13.45s, a sawtooth combined with a giant ELM coincides with the irreversible decline of R_{DD}.

OUTER MODES: An increase of χ_{eff} near the edge, occurs at the time of the OM (see Fig. 1). However, it is not clear how they are related quantitatively. Fig. 2 shows the χ_{eff} profiles before (t = 12.55s), during (t = 12.8s) and after the OM (t = 13.2s) for #34500. During the OM, χ_{eff} ($\rho \geq 0.4$) increases by a factor 2-3. After the OM, χ_{eff} returns to values comparable to the pre-OM values. An interesting point to note is that the increase in χ_{eff} occurs over a large part of the plasma radius, even though the OM is located beyond the q = 3 surface, with displacements of 2-3 cm. However, the onset of the OM is followed by an increase in recycling, an influx of impurities and a cool front which reaches the core in ~ 20 ms (see [1]).
The increase of χ_{eff} over a larger part of the plasma radius reflects the increased loss associated with this cool front.

ELM AND SAWTOOTH: A typical evolution of χ_{eff} (ρ) is shown in Fig. 3 for #34500. χ_{eff} increases by up to 40% in the outer region at the time of an ELM (13.3s). It doesn't recover its previous value after the ELM and in fact increases further (13.4s), reaching values ~ 70% higher than 0.2 sec earler. At the time of a sawtooth combined with an ELM (13.45s) a large increase of χ_{eff} throughout the plasma radius occurs (by a factor 1.5 for $\rho < 0.8$ to 2.5 near the edge).

BALLOONING AND KINK LIMITS: The stability plot for external kink and ballooning for #34500 shows that the plasma edge is close to marginal stability for the external kink throughout the discharge (see Fig. 4). This is compatible with the observed OM. The edge pressure gradient increases along the n = 1 kink stability boundary up to the ballooning limit which is reached around the time of the maximum in R_{DD}, coincident with an ELM. This suggests that ELMs are related to ballooning modes possibly combined with external kink.

The same features are seen in #33648 and #33650, but not in the highest performance pulse #33643 whose edge remains in the stable region.

HIGH FREQUENCY MODES: A variety of high frequency coherent modes (f > 30 kHz) is observed growing throughout the H-mode phase. Some seem to be associated with a saturation of R_{DD}. Their frequencies are consistant with β-driven Alfvén eigenmodes (BAE with f ~ 60kHz) and toroidal Alfvén eigenmodes (TAE with f ~ 110-120 kHz). (see Fig. 5). The χ_{eff} profiles are not affected by these modes; this may indicate that it is mainly the fast ion population which is perturbed by the high frequency modes (causing a different beam deposition profile from the TRANSP calculated one).

NON-RECOVERY: In some circumstances, the plasma performance doesn't recover after the MHD event. This is the case for #33648 where the temperature profile T_e doesn't increase anymore once the OM has disappeared, contrary to #34500 (see Fig. 1) and despite the fact that both pulses show similar amplitudes and frequecies of the OM. The only difference is that, for #34500, the OM appears 0.63 sec after the onset of NBI, whereas it appears 1.25 sec after for #33648. The flattening of the beam deposition profile with time, due to the density build-up, is a feature of all the hot-ion H-modes (see Fig. 6), and in shot #33648 prevents the plasma core from reheating after the OM.

TERMINATION: The final loss of fusion performance is triggered in most cases by an OM and/or an ELM and in the highest performance pulses by a sawtooth and/or a giant ELM (see Fig. 1). This is accompanied by a large increase of P_{rad} and D_α, and by a sudden drop in R_{DD}, W_{DIA} and temperature. During this phase, $\chi_{eff}(\rho)$ increases by a factor 2-3, denoting huge thermal losses (see Fig. 3). After the terminating event, the plasma doesn't reheat (see $T_e(0)$ in Fig. 5) partly due to a decreasing NBI central heating (see Fig. 6) and to the fact that fast ions have been expelled out of the core region by the sawtooth.
The highest fusion performance #33643 doesn't show a change in W_{DIA} at the sawtooth as large as the comparable pulse #33650. (see Fig. 7). However for #33643, W_{DIA} keeps on falling after the sawtooth, suggesting a lasting change in the transport state of the plasma. This behaviour is discussed in more detail in [2].

DISCUSSION: The 3 classes of MHD instabilities (OM, ELM and sawtooth) have a clear effect in increasing the plasma energy losses. However this effect may be partly indirect. Sawteeth affect the fast ion distribution (and therefore the NBI heating profile). The OM and ELM, although localised in the outer part of the plasma, are accompanied by changes of the temperature profile over a wider region.
The precise loss mechanism associated with the MHD instabilities is unclear. Different interpretations have been put forward, each of them accounts for part of what is observed:

1) MHD is the direct cause of the degradation in transport.
2) MHD acts as a trigger to another state of the plasma transport, which partly remains once the MHD instabilities have disappeared.
3) MHD instabilities change the recycling conditions, causing a larger influx of neutrals and therefore increasing charge-exchange losses.

The investigation of the extent of these different processes is the aim of future studies.

CONCLUSIONS: The TRANSP analysis of individual MHD events: Outer Modes, Giant ELM and Sawtooth + ELM, shows the radial extent and the amplitudes of the loss processes, however the precise loss mechanism is not known.
The MHD instabilities have more severe consequences in the later stage of the heating phase because of decreased central heating by NBI, due to the density build-up.

REFERENCES:

[1] F. Nave, et al., 'An overview of MHD activity at the termination of JET hot ion H-modes', to be published in Nuclear Fusion.
[2] J. Wesson and B. Balet, 'Abrupt changes in confinement in the JET tokamak', submitted to Phys. Rev. Letters.

Table I:

Pulno	B (T)	I (MA)	P (MW)	β_N	H_{89P}	$<n_e>$ ($\times 10^{19}$ m-3)	q_{95}	κ	δ	W (MJ)	R_{DD} ($\times 10^{16}$ s^{-1})
33643	3.4	3.8	18.8	1.6	2.9	3.9	3.2	1.9	0.31	12.0	8.9
33648	3.4	3.0	16.5	1.6	2.6	3.6	3.9	1.9	0.32	8.9	5.3
33650	3.4	3.5	18.6	1.8	2.7	4.8	3.3	1.9	0.29	11.7	6.5
34500	2.7	3.1	16.0	1.9	2.5	4.0	3.3	1.9	0.32	9.0	4.0

Fig. 1: Time evolution of pulse #34500 showing the NBI power and the magnetic perturbation, χ_{eff} at $\rho = 0.25$ and $\rho = 0.9$ together with the ion neo-classical heat conductivity χ_{neo}(* 20) at the edge as calculated by TRANSP, D_α signal and total DD reaction rate R_{DD}, the central electron temperature $T_e(0)$, the plasma stored energy W_{DIA} and the line averaged electron density $\bar{n}_e$.

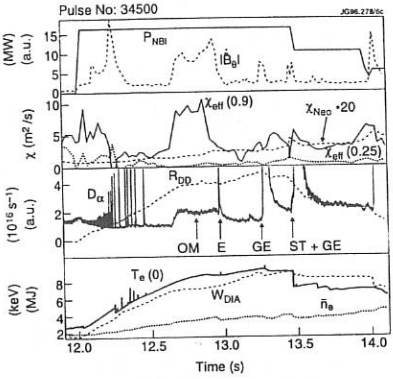

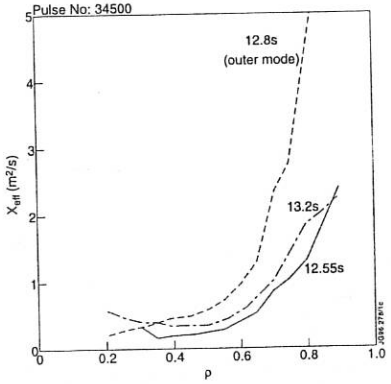

Fig. 2: χ_{eff} profiles before (t = 12.55s), during (t = 12.8s) and after (t = 13.2s) the OM for #34500.

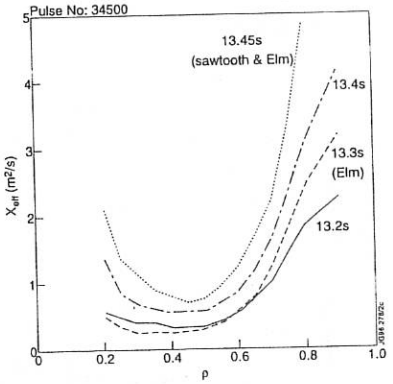

Fig. 3: χ_{eff} profiles for #34500 at different times.

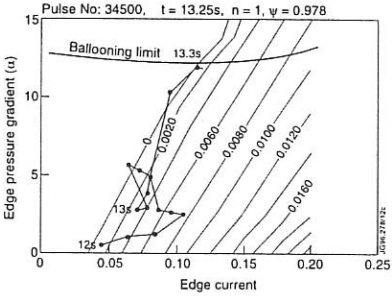

Fig. 4: Stability plot for the n = 1 kink and ballooning for #34500 at $\Psi = 0.978$.

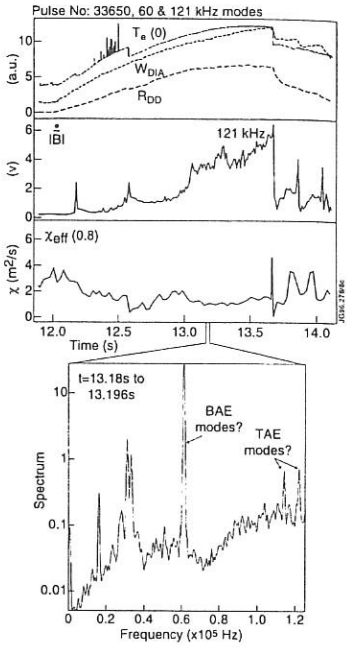

Fig. 5: Time evolution of pulse #33650 showing $T_e(0)$, W_{DIA} and R_{DD}, magnetic signals from comb filters at 121 kHz, χ_{eff} at $\rho = 0.8$ as calculated by TRANSP and spectrum versus frequency for t = 13.8 to 13.196s.

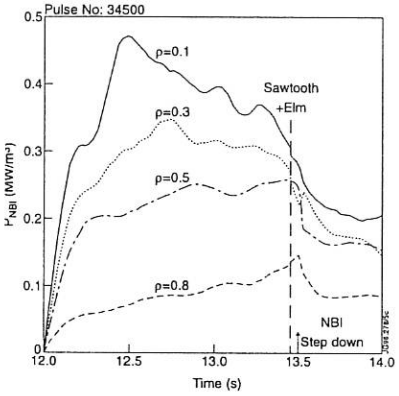

Fig. 6: Time evoultion of the absorbed NBI power density at different positions ρ for #34500.

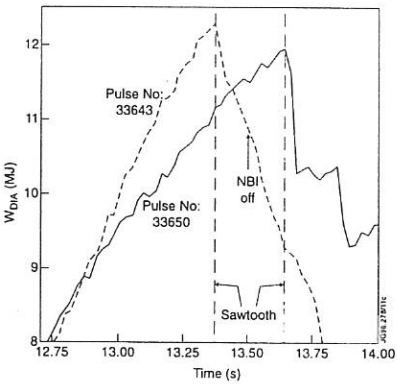

Fig. 7: Time evolution of W_{DIA} for pulses #33650 and #33643.

SIMULATIONS OF JET HOT-ION H-MODES WITH A PREDICTIVE CODE

H.P.L. de Esch, A. Cherubini, J.G. Cordey, M. Erba, T .T.C. Jones,
V.V. Parail, D. Stork and A. Taroni,
JET Joint Undertaking, Abingdon, Oxon, OX14 3EA, UK.

1. INTRODUCTION

The 1½-D predictive code PRETOR [1] has been modified to include, among other things, neutral beams [2]. PRETOR has been used to simulate the JET hot-ion H-mode. This mode is obtained by injecting high power neutral beams into a low density plasma. This results in a hot plasma ($T_i \approx 20$ keV, $T_e \approx 10$ keV) which exhibits almost linearly rising stored energy, plasma density and neutron yield, until a termination event limits the performance [3].
Simulations of hot-ion H-modes considering different levels of recycling, various beam energies and deuterium and tritium beams will be described in this paper. A limiting pressure gradient (based on ballooning modes) and a limiting edge current density (based on external kink modes) have been considered in the modelling and are discussed. The simulations point the way to possible improvements in performance.

2. DESCRIPTION OF THE PRETOR MODELLING

Recent additions to PRETOR include a mixed Bohm - gyro Bohm transport model for the bulk transport and a one poloidal Larmor radius wide neoclassical H-mode transport barrier at the plasma edge [4,5]. The following leading terms in the edge can be identified:

H-mode barrier width: $$\rho_\theta = 0.457\frac{\sqrt{AT_i}}{B_{pol}} \quad \text{(cm, keV, T)} \qquad (1)$$

Heat and particle diffusivity: $\chi_i = \chi_e = D \sim \dfrac{n_i(Z_{eff} - 0.7)}{\sqrt{T_i}B_{pol}^2}$ (m^2/s, 10^{19} m^{-3}, keV, T) (2)

Heat flux $$q_{heat} \sim \frac{n_i^2\,(Z_{eff} - 0.7)}{\sqrt{A}\,B_{pol}} \quad \text{does not depend on temperature} \qquad (3)$$

Due to (3) the stored energy of a hot-ion H-mode can grow almost linearly in time until heat losses proportional to n^2 and Z_{eff} become comparable to the input power.

3. SIMULATION OF THE HOT-ION H-MODES

JET's neutron yield record shot 33643 (3.75MA/3.4T) has been modelled, keeping the volume average density evolution ($\langle n_e \rangle(t)$) equal to the experiment: $d\langle n_e \rangle/dt = 1.29\ \phi_{nbi}$. Time traces for $\langle n_e \rangle$, Z_{eff}, total stored energy W_{tot} and D-D reaction rate R_{DD} are given in figure 1. Experimentally, the termination occurred at 13.38 seconds. This was simulated by increasing Z_{eff} at 13.38 seconds in line with the experimental Z_{eff} derived from charge exchange spectroscopy. An increase in Z_{eff} is modelled by puffing "carbon gas" into the edge of the discharge, so the *edge* Z_{eff} is even higher than the average Z_{eff} in figure 1, leading to a big increase in the heat loss (3) and irreversible termination of high performance. There are also successful simulations of a hot-ion H-mode at 1.7MA / 1.5T (34488)

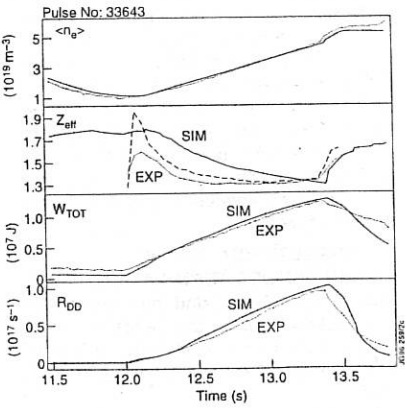

Fig. 1: Volume averaged density, Z_{eff}, Stored energy and D-D reaction rate for shot 33643. Simulation vs. Measurement

and shots where the beam power decreased stepwise after ½ or 1 second.

4. INFLUENCE OF THE RECYCLING

Plasma edge recycling of neutrals is quantified in this paper as the excess density rise over beam particle fuelling. It affects the performance because additional cold input gas must be heated. It also leads to higher density, increasing the particle/heat fluxes leaving the plasma (3) and reducing beam penetration. Improvements in performance are expected if excess edge fuelling can be reduced. Figure 2 shows two simulations of a plasma with the same equilibrium, power input and target density as 33643. One corresponds to the measured excess fuelling of 0.29, the other assumes no excess fuelling (every particle leaving the plasma is returned). No termination is assumed. It can be seen that stored energy and neutron yield reach much higher values for the low recycling case.

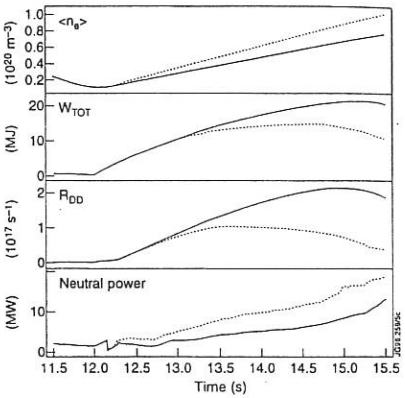

Fig. 2: Simulated density, Stored energy, D-D reaction rate and Power to heat neutrals: Solid lines: $d<n_e>/dt = \phi_{beam}$ dashed lines: $d<n_e>/dt = 1.29\ \phi_{beam}$

5. TARGET DENSITY PROFILE PEAKING

Two simulations were done using different values for the density in the plasma centre $n_e(0)$, but with identical volume average densities $<n_e>$ at the start of the H-mode at 12.15 seconds, to test the effects of target density profile peaking. Centrally deposited beam particles diffuse towards the edge where the H-mode barrier prevents most particles from leaving the plasma. The two simulations (figure 3), showing cases with a very peaked and flat density profile appear to reach the same density profile in less than a second: *core particle transport wins over beam fuelling*. Indeed, experiments with peaked target density profiles have never yielded significant benefits over modestly peaked target density profiles.

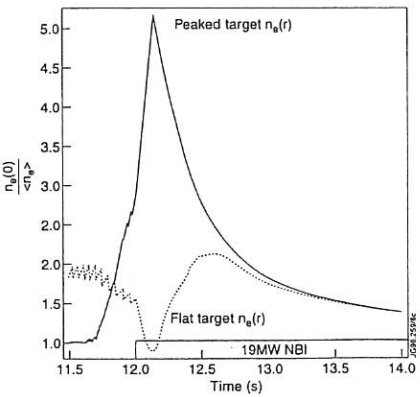

Fig. 3: Density profile peakedness ($n_e(0)/<n_e>$) evolution for two simulations: Solid line: Extremely peaked target density profile at the start of the H-mode. dashed line: Flat target density profile at the start of the H-mode.

6. PARAMETERISATION OF HOT ION H-MODE TERMINATION

Ballooning modes [6] and the external kink [7] impose a limit on the pedestal energy W_{ped} that can be sustained by the H-mode barrier. For the ballooning limit we have:

$$\frac{\nabla p}{\nabla p_{\max}} \sim \frac{W_{ped}/\rho_\theta}{B_{pol}^2} \sim \frac{W_{ped}}{B_{pol}\sqrt{AT_i}} \quad \Rightarrow \quad W_{ped} < Const\ B_{pol}\sqrt{AT_i} \qquad (4)$$

All quantities in (4) refer to the edge. The giant ELM terminating some hot ion H-modes is thought to be a ballooning limit [3,6]. The "outer mode", which occurs in other hot ion H-modes is thought to be related to the external kink [3]. For this mode, the fraction of edge current related to total current is the critical parameter. If the edge current arises solely from the bootstrap current one has, using a simple expression for the bootstrap current [8] and the H-mode barrier width given by (1):

$$\frac{I_{boot}^{edge}}{I_{tot}} \sim \frac{\rho_\theta j_{boot}^{edge}}{B_{pol}} \sim \frac{\rho_\theta (T_e + T_i) q \nabla n_e / B}{B_{pol}}$$

$$\sim \frac{W_{ped}}{B_{pol}^2} \Rightarrow W_{ped} < Const\ B_{pol}^2 \qquad (5)$$

The maximum pedestal energy achievable appears to be a function of the plasma current. The pedestal energy could conceivably be increased by driving an edge current in the opposite direction, e.g by *current rampdown.*

Simulations based on the present 33643 equilibrium; NBI power and target density are shown in figure 4, giving the D-D Reaction rate for various values of $d<n_e>/dt$ and termination assumptions. The terminations pose a significant limitation to performance.

With lower recycling, modest improvements in performance are possible. Larger improvements can only be obtained if the ballooning limit can be increased (e.g. by using a more favourable magnetic configuration) ***and*** by using current rampdowns to delay the external kink.

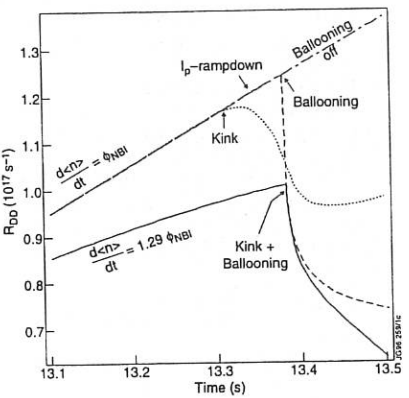

Fig. 4: Simulated D-D Reaction rates:
Solid line: *Benchmark for kink and ballooning.*
dotted and dashed lines:
dotted: Kink and ballooning enabled.
dashed: Current ramp to forestall kink
dot-dash: Ballooning switched off

7. DEPENDANCE ON BEAM INJECTION ENERGY

The mix of 13MW of 80 kV and 8 MW of 140 kV beams installed at JET is not suited for experiments on varying the beam energy in a hot ion H-mode, whilst keeping the total power constant. With PRETOR, however, we simulated 15 MW 80 kV NBI and 15MW 120 kV NBI cases (fig. 5). The high-energy beam case has a lower particle influx and reaches significantly higher stored energy and neutron yield than the low-energy beam case. Termination was by the "external kink" in the 120 kV beam case and by "ballooning" in the 80 kV beam case.

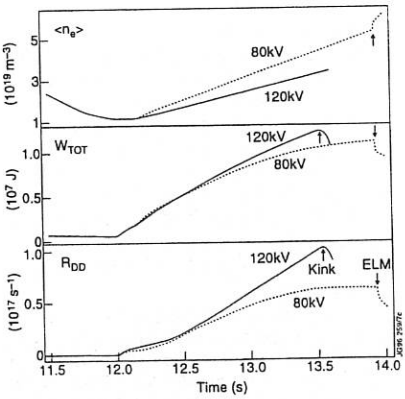

Fig. 5: Density, Stored energy and D-D Reaction rate for two 15 MW hot-ion H-mode simulations.
Solid line: 120 keV Beams (kink termination)
Dashed: 80 keV Beams (ballooning termination)

8. TRITIUM BEAMS

The present JET Experimental Programme includes a phase of DT plasma operation (Deuterium Tritium Experiment 1 - DTE1) to begin at the end of 1996. The tritium will

mainly be supplied with the high energy neutral beams at JET (E≈140-160 keV). The use of tritium beams has several effects on the hot ion H-mode:

- More power. Available beampower will rise from 21 MW to 24-26 MW.
- Lower beam fuelling per MW injected power. This also means that the tritium concentration in the plasma is expected to remain low (≈30%).
- More plasma ion heating from the tritium beams.
- Power from α-particle heating provides plasma heating without associated density rise.
- An isotope effect arises from the H-mode barrier width (1).

All these effects increase the fusion performance and stored energy. Figure 6 shows simulations with tritium beams in a 33643-like plasma. In all cases the same ballooning and kink termination limits were kept as for 33643. No current ramps are applied. Stored energy, D-T neutron yield ($P_{fus}=2.82\cdot10^{-12}\ R_{DT}$) and tritium concentration are shown for:

- 25 MW NBI, consisting of 12 MW 160 kV T-beams and 13 MW 80 kV D-beams.
- 19 MW NBI consisting of 10.5 MW 150 kV T-beams and 8.5 MW 80 kV D-beams.
- 19 MW NBI consisting of 7.5 MW 140 kV D-beams and 11.5 MW 80 kV D-beams.

From fig. 6, performance can be expected to be higher with the tritium beams, even without invoking improvements to recycling and MHD stability.

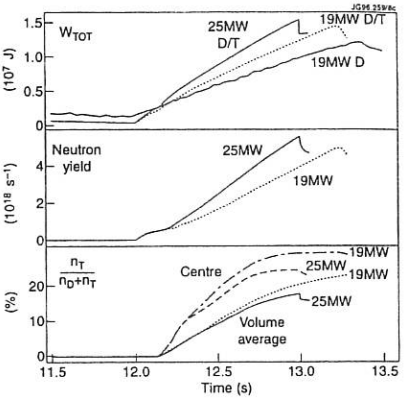

Fig. 6: Stored energy, D-T Neutron yield and tritium concentration for 25 MW D/T beams (solid lines) and 19 MW D/T beams. The experimentally measured stored energy using 19 MW deuterium beams is also indicated.

9. CONCLUSIONS

PRETOR has proven to be suitable for simulating a variety of JET hot ion H-mode discharges and the following experimental observations were successfully simulated:

- Low recycling is beneficial for high performance.
- A peaked target density profile will flatten quickly in the hot ion H-mode.
- The increase in edge Z_{eff} observed in most terminations causes it to be irreversible.

The following predictions have been made:

- Low recycling improves the ballooning stability at the edge.
- Current ramp-down can be used to improve the kink stability.
- Increasing the beam energy leads to higher performance.
- Tritium beams increase the plasma stored energy due to a variety of reasons (sect. 8).

REFERENCES

[1] D Boucher and P-H Rebut, Proc. IAEA Techn. Comm. meeting on Adv. in Simulation and Modelling of Thermonuclear Plasmas, Montreal, Canada, 1992. IAEA Vienna (1993) 142.
[2] H P L de Esch *et al*, Fusion Engineering and Design **26**(1995)589 *or* JET-P(93)103
[3] T T C Jones and the JET team, Plasma Phys. Control. Fusion **37**(1995)A359
[4] V Parail *et al*, JET-P(95)49, to be published in Plasma Phys. and Control. Fusion.
[5] A Cherubini *et al*, This conference.
[6] T C Hender *et al.*, Proc. 22nd Eur. Conf. on Contr. Fusion and Pl. Phys. (1995) **19C prt I p. 29**
[7] G T A. Huysmans *et al.*, 22nd Eur. Conf. on Contr. Fusion and Pl. Phys. (1995) **19C prt I p. 201**
[8] J Wesson, Tokamaks (page 95). Oxford, Clarendon Press, 1987

TRANSPORT MODELLING WITH A COMBINED CORE AND EDGE CODE

A.Taroni, A.Cherubini, G.Corrigan, H.Guo, G.K.McCormick, G.J.Radford, R.Simonini, J.Spence, E.Springmann

JET Joint Undertaking, Abingdon, OX14 3EA, United Kingdom

Introduction

Transport of energy and particles in Tokamaks is usually studied separately for the region inside the last closed flux surface (separatrix) and for the edge region. This implies that modelling of the plasma core is replaced by boundary conditions in edge transport codes and modelling of the plasma edge is replaced by boundary conditions in core transport codes.

However there are problems where such a splitting can be inadequate and it would be desirable to study transport in a global way, from the centre to the divertor targets. Examples of such problems are the L-H transition, ELMs, and other phenomena that appear to imply sudden modifications of transport coefficients over a wide plasma region correlated to modifications of the plasma edge [1].

On a longer time scale, of the order of the energy or particle confinement time, or even in steady state, transport studies in the plasma core can benefit from a global approach. This happens each time that particle and energy source or sink terms cannot be accurately measured or simulated without properly simulating the plasma edge. Examples are transport of hydrogen isotopes in all regimes and evaluation of charge exchange losses in the hot ion regime[2].

Numerical Approach

In developing the JET code for global transport studies we aimed to include all features routinely used in $1^1/_2$D core transport codes and 2D edge transport codes, such as sophisticated transport models for the plasma core, proper evaluation of power input terms, connection to existing data bases and well developed post-processors for the analysis of results and quantitative comparison with experiments. Another important requirement was the possibility to simulate transients on any time scale of interest without a big overhead in computer time.

Such considerations led us to couple the $1^1/_2$D core transport code JETTO to the EDGE2D/NIMBUS plasma/neutrals 2D transport code for the edge, by means of an adaptation of the so called fractional steps technique.

In essence the method reduces to enforcing continuity of density and temperatures (n, T_e and T_i), and of the corresponding total particle and energy fluxes (Φ, Q_e and Q_i) at a chosen interface, by imposing proper boundary conditions to each code at each time step. Namely, in JETTO:

$$n_J^n = n_E^{n-1} \quad , \quad T_{e,J}^n = T_{e,E}^{n-1} \quad , \quad T_{i,J}^n = T_{i,E}^{n-1} .$$

In EDGE2D/NIMBUS:

$$\Phi_E^n=\Phi_J^{n-1} \quad , \quad Q_{e,E}^n=Q_{e,J}^{n-1} \quad , \quad Q_{i,E}^n= Q_{i,J}^{n-1}.$$

Here the superscript n indicates the time step, while the subscripts E and J refer to the codes and poloidal averages of the quantities are used at the interface in EDGE2D/NIMBUS.

Continuity of neutral profiles and fluxes is also enforced in order to have a consistent evaluation of particle sources.

Other combinations of boundary conditions are possible and have been tested. The important point is that at the interface one code receives a variable or flux from the other and gives back the corresponding flux or variable. This procedure ensures continuity of all relevant quantities with sufficient accuracy by simply running both codes with time steps typical of EDGE2D/NIMBUS, avoiding extra iterations at each time step. As a result the coupled code is very robust and requires less than 10% additional computer time with respect to the stand alone EDGE2D/NIMBUS.

A series of tests showed that transients related to initial conditions not properly matching at the interface are washed out on a time scale shorter than the typical time τ_{sol} required by the Scrape Off Layer (SOL) to reach steady state in EDGE2D/NIMBUS runs ($\tau_{sol} \approx 30$ ms for typical JET discharges). The time evolution following these transients is consistent with the time scales expected from SOL and core physics. Moreover, large differences in the initial conditions of the SOL, which correspond to small differences in the initial conditions of the global problem, result in small differences at the interface and in the global solution after a time $\approx \tau_{sol}$. This is consistent with the overall problem being well posed and numerically stable. Therefore transients with a fast evolution (time scale $\leq \tau_{sol}$) require a pre-run of the coupled codes to obtain properly matching steady state or quasi-steady state (i.e. changing on a time scale of the order of the global confinement times) initial conditions. On the other hand transients on a time scale $> \tau_{sol}$ can be studied starting from initial conditions not accurately matching at the interface.

Very slow plasma evolution, on the time scale of the core energy or particle confinement time, and steady state situations can be studied assuming that the edge region follows a series of quasi steady states. These are obtained by running the coupled codes for relatively short time intervals ($\approx\tau_{sol}$) at chosen times during the evolution of the plasma core.

Example of Modelling with the Combined Code

As an example of the application of the combined code in a non stationary situation we present results of a simulation of the ohmic phase immediately following the X-point separatrix formation and preceding neutral beam injection in the JET shot 32919.

During this phase, lasting about half a second and normally preceding JET hot ion H-modes, the average plasma density $\langle n_e \rangle$ strongly decreases (fig. 1) supposedly due to particle absorption by the divertor targets.

In our simulation the particle absorption has been modelled by imposing a difference between the outgoing plasma flux and the influx of neutrals at the targets approximately equal to the rate of change dN/dt of the core plasma particle content N. The corresponding absorption rate

$\approx 1.4\ 10^{21}\ s^{-1}$ (out of $\approx 3.5\ 10^{22}\ s^{-1}$ ions reaching the divertor targets) is about ten times larger than the flux of neutrals to the divertor pump, as computed by NIMBUS.

This very crude model, which does not take into account the actual dynamics of the particle absorption nevertheless gives a reasonable simulation of the $<n_e>$ evolution (Fig. 1).

For the energy transport model in the core plasma (from the centre to the interface with the boundary region less than 5 mm inside the separatrix) we used a combined Bohm-gyro-Bohm model [1] including a 'non local' dependence of the Bohm-like term on $L_{T_{ea}}=<\nabla T_e/T_e>_{\rho>0.8}$. Results of this model are particularly sensitive to the electron temperature T_{ea} at the interface. This temperature is computed, not prescribed from experimental traces.

We also assumed an empirical effective particle diffusion coefficient D^{eff} which is of the order of the heat diffusivity χ in the central part of the discharge. However the ratio D^{eff}/χ needs to be decreased as the normalised minor radius ρ increases, in order to provide a reasonable simulation of the slope of the experimental density profile with the flux of neutrals across the interface computed by EDGE2D/NIMBUS ($\Phi_0 \approx 4\ 10^{21}\ s^{-1}$). This result could possibly be an indication of an inward particle flux term strongly increasing towards the plasma boundary.

The core boundary values resulting from the model have been used as constant transport coefficients in the region beyond the separatrix. However an explicit inward pinch velocity such that $V/D=15m^{-1}$ had to be added in this region for a proper simulation of the probe measurements reported in [3].

Simulated and experimental values of temperature and density profiles in the plasma core are given in Fig 2. Figs 3 and 4 show computed and experimental values of parallel ion saturation current and electron temperature at the external divertor target.

The power fluxes into the SOL are a result of the simulation ($P_e \approx 0.8MW$ and $P_i \approx 1.1MW$) and slowly diminish with time as $<n_e>$ decreases and the electron temperature increases. The density at the interface n_{ea} is also a result of the simulation and it appears to decrease with time together with $<n_e>$. However this implies a decreasing ion saturation current at the targets, which does not seem to be supported by probe measurements. This result might indicate that in this case D^{eff} should become larger as $<n_e>$ diminishes.

We conclude from the results obtained so far that the combined JETTO/EDGE2D/NIMBUS code is a powerful tool to simulate tokamak discharges in steady state and time dependent situations over the entire plasma cross section, from the centre to the divertor targets.

By eliminating ad hoc (and sometimes 'convenient') assumptions at the interface between core and boundary regions this code provides a very tough and complete test for transport models, including the effect on the boundary of transport assumptions in the core and viceversa.

References

[1] V.V.Parail et al., JET report JET-P(95)49, to appear in Plasma Physics and Controlled Fusion.

[2] A.Cherubini et al., This Conference.

[3] G.K.McCormick et al., 12th PSI Conference, St. Raphael, France, 20-24 May 1996.

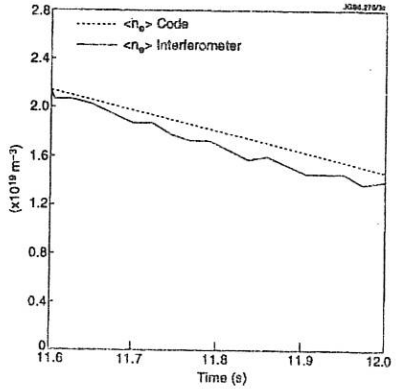

Fig. 1 Experimental and computed time evolution of the average density in JET pulse 32919 before NBI heating.

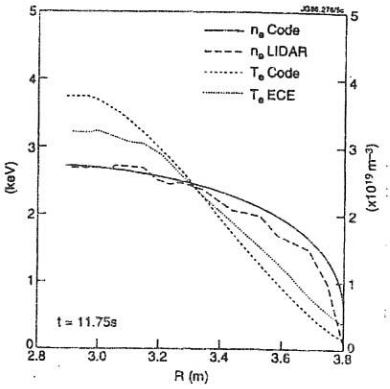

Fig. 2 Experimental and computed electron density and temperature profiles in the plasma core at t=11.75 s.

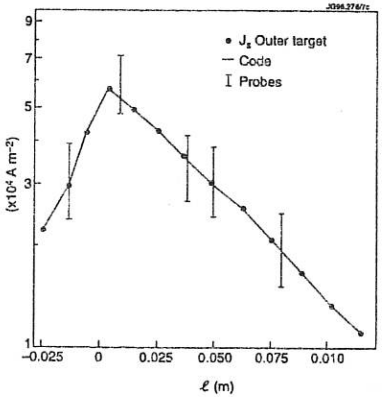

Fig. 3 Experimental and computed ion saturation current at the outer divertor target at t=11.75 s.

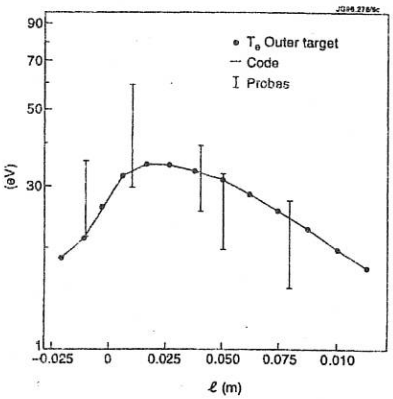

Fig. 4 Experimental and computed electron temperature at the outer divertor target at t=11.75 s.

FIRST MEASUREMENTS OF GAS BALANCE AND CHEMICAL COMPOSITION IN THE MK I PUMPED DIVERTOR PHASE OF JET USING THE GAS COLLECTION SYSTEM

A Rossi, G Saibene, P Kupschus
JET Joint Undertaking, Abingdon, Oxfordshire, OX14 3EA, UK

1.0. INTRODUCTION

Gas recovery measurements in Tokamaks give direct information both on the short and long term hydrogenic in-vessel wall retention; in particular, the determination of the deuterium vessel inventory is essential to extrapolate to D-T operations, as required for the forthcoming JET D-T campaign and for ITER. The measurement of the chemical species present in the gas released from the Tokamak wall provides data for the gas exhaust collection and reprocessing plant.
The new JET Gas Collection System (GCS) measures the time evolution, absolute amount and chemical composition of the gas released from the JET vacuum vessel in the following modes of operation:
1. Natural thermal wall outgassing, 2. After plasma pulses, 3. During divertor cryopump regeneration, and 4. During glow discharge cleaning.

This paper presents GCS measurements carried out during the 1994/95 JET campaign, and illustrates the effects of the introduction of the JET MARK I pumped divertor on the hydrogenic inventory of the machine.

2.0. THE NEW GAS COLLECTION SYSTEM FOR JET

The GCS measures the amount of gas (H, D, He and volatile impurities produced into the torus such as hydrocarbons of various stoicheiometry) released from the torus, in all conditions of operation of JET. Moreover, the GCS can analyse the composition of the gas released from the torus and allows on-line sampling for off-line chemical analysis.

During the 1994/95 JET campaign, gas recovery measurements and on line gas analysis were carried out. The short term gas recovery was measured and, at the same time, the gas composition was analysed with a high resolution quadrupole mass spectrometer.

3.0. EXPERIMENTAL RESULTS (MK I CAMPAIGN 1994/95)

3.0.1. Gas balance measurements and wall retention measurements

Measurements of the short term gas recovery were carried out during the 1994-95 Mark I Experimental Campaign (graphite and Inconel wall, with Be evaporated coating), both with carbon (CFC) and beryllium divertor tiles.
Figure 2 shows the percentage of gas recovered after non disruptive plasma pulses, when the divertor cryopump is not cooled down. The data are compared to previous JET results [1,2]

obtained with a first version of JET Gas Collection System. For the Mk I campaign, the average deuterium recovery varies from 30 to 60% of the input, depending on the total gas input, both for C and Be divertor tiles with T_{tile} = 50°C and T_{wall} = 250°C. These values are comparable to previous JET results for a Be coated machine, with walls at 250°C or 320°C. A detailed analysis of the dependence of the gas recovery on the wall temperature showed that at lower temperature less gas is recovered. This is consistent with the measured D inventory in the JET divertor tiles, determined by post mortem analysis [3]. The D inventory in the X-point tiles is greater than in 1991/92, even though the tile surface was a similar composition. It is believed that the factor that makes the difference is the lower temperature of the tiles.

In figure 3, the gas recovery is plotted as a function of the gas input, for pulses run with and without the cryopump, both for disruptive and non disruptive plasmas. The analysis of the gas released after non disruptive plasma pulses shows no appreciable difference between the case with C and Be divertor tiles. This is in agreement with the observation that no significant change in main plasma parameters and fuelling efficiency was observed between C and Be [4]. One reason why the gas release with C tiles is almost the same as with Be tiles can be that the near-surface layer of the exposed wall is, in both cases, a mixture of C and Be. Such a mixture is produced by the periodic conditioning (with Be evaporation and GDC) and by plasma-wall interactions.

When the cryopump is at LHe temperature (cryopump on), the gas released to the GCS is between 5 to 10 times lower than for pulses without cryopump.

For the cryopump off cases, an enhanced release of gas after disruption is observed. The gas recovered is higher than after non disruptive pulses. This is not the case when the cryopump is cooled at LHe temperature. This can be due to three concurrent causes:

1. The cryopump acts as a strong sink during plasma pulses and less fuel is retained into the walls. 2. The cryopump is pumping the excess gas after the disruption. 3. The wall is depleted in-between pulses more than when the cryopump is off because in the latter case the total pumping speed is lower.

The wall retention after 600 s from the plasma pulse is shown in figure 4. The two cases with and without cryopump are compared.

The net wall retention was calculated from the equation:

$$R_{wall} = Gas_{input} - [Gas_{out(GCS)} + K_{cryo} \times Gas_{out(GCS)}] - Gas_{cryo}$$

$$Gas_{cryo} = S_{cryo} \times \int P_{cryo}(t)\, dt$$

The estimated uncertainty in the calculation of R_{wall} is ± 50%.

$Gas_{out(GCS)}$ is the gas exhausted from the vessel and measured by the GCS. K_{cryo} represents the ratio between the gas pumped by the cryopump and the gas going to the GCS in a 600 s period after pulses. Gas_{cryo} is the amount of gas pumped by the cryopump during the discharge, P_{cryo} the pressure at the cryopump and S_{cryo} the cryopump pumping speed [5].

Globally, within the experimental errors, the increment to the net D wall inventory, after plasma pulses run with the divertor cryopump on, is close to zero for most of the discharges.

This result would explain why the amount of gas released from the machine after a disruption is not larger than the gas released after a non disruptive plasma (see figure 3). The apparent wall retention was calculated not including the cryopump effect during plasmas ($Gas_{cryo} = 0$). The apparent wall retention is much higher than the net wall retention, showing that the particle removal during the X-point phase of the pulse is dominant over the particle removal by thermal outgassing after the plasma.

The net wall retention at low input gas, for pulses with the cryopump on, is generally lower than for the cryopump off case. The discharges with highly negative wall retention (i.e. high wall depletion) at low gas input are identified to be ELMy H-mode, NBI fuelled with an extended X-point phase, during which the recycling gas is compressed into the divertor and efficiently removed by the cryopump. Net wall depletion occurs also at high gas inputs, for long high density L or H-mode plasmas, which are characterised by high neutral pressure in the divertor. This result is in agreement with the observation that the amount of gas pumped by the cryopump during pulses with ELMs or at high density can equal or exceed the gas input [5].

3.0.2. Gas balance measurements with nitrogen seeding

Nitrogen seeding was used at JET to obtain high radiation in the divertor region and consequent cooling of the plasma reaching the divertor target plates.

From the analysis of pulses run with the cryopump on, it is observed that the output gas (collected over a 600 s period) is further enriched in nitrogen, when compared to the gas input (mixture of nitrogen and deuterium). One explanation is that during the pulse more deuterium is pumped in proportion to nitrogen. This is, nevertheless, in contrast to the result that the composition of the gas in the divertor chamber during the plasma is the same as the input gas [6]. A possible explanation is that the thermal desorption rate after the pulse is higher for nitrogen than for deuterium. This needs further investigation.

4.0. CONCLUSIONS

1. When the divertor cryopump is off, the results of the gas balance and short term wall retention are in good agreement with results found in previous JET campaigns (1989-92) for a Beryllium coated machine, both for C and Be divertor targets tiles.
2. The cryopump reduces the wall retention after pulses. This implies a low D (and T) inventory, despite the large fuelling required to maintain a set plasma density when the cryopump is on.
3. It is observed that long ELMy H-mode pulses, run with low input gas and NBI heating, deplete the wall from the deuterium reservoir. Net wall depletion occurs also during long high density near detachment L-mode plasmas.
4. For pulses with nitrogen seeding the measured composition of the output gas is different from the input gas, and in particular is enriched in nitrogen.

References

[1] R Sartori et al., Journal of Nuclear Materials 176&177 (1990) 624-629.
[2] P Andrew & M Pick, Journal of Nuclear Materials 220-222 (1995) 601-605.
[3] P Coad et al., 14th PSI Conf., France, 1996 to be published in Journal of Nuclear Materials.
[4] D Campbell et al., 14th PSI Conf., France, 1996, to be published in Journal of Nuclear Materials.
[5] G Saibene et al., Europhysiscs Conf. Abstract, vol19c(IV), 1995 465-468.
[6] J Ehrenberg et al., 14th PSI Conf., France, 1996 to be published in Journal of Nuclear Materials.

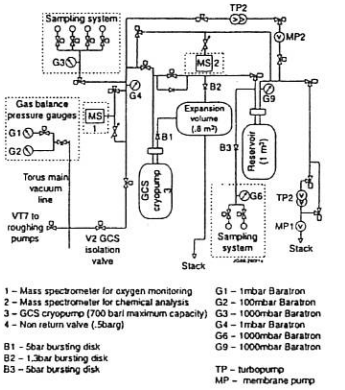

Fig.1 Layout of the JET New Gas Collection System

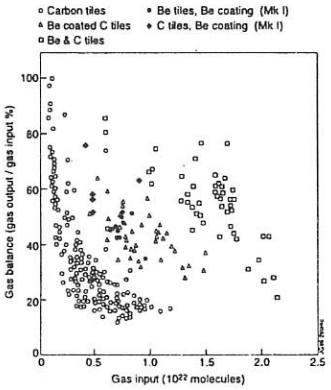

Fig. 2 JET data on the recovery of gas during a 600 s period after the discharge (T_{wall}=250°C and T_{wall}=320°C)

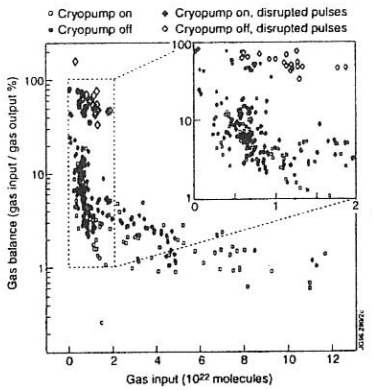

Fig. 3 JET data on the recovery of gas during a 600 s period after the plasma (T_{wall} = 250°C) during the JET MARK I campaign 1994/95. Comparison divertor cryopump on/off.

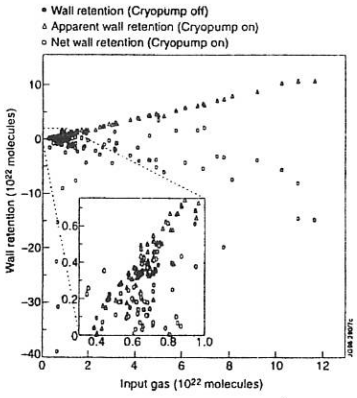

Fig. 4 JET data on the absolute wall retention after 600 s from the plasma pulse for non disruptive pulses. Comparison between divertor cryopump off (± 10%) and on case (± 50%).

Strong Asymmetries in Impurity Distributions of JET Plasmas

B. Alper, A.W. Edwards, R.Giannella, R.D. Gill, C.Ingesson,
M. Romanelli, J.Wesson, K-D.Zastrow
JET Joint Undertaking, Abingdon, Oxon. OX14 3EA, UK.

Introduction

A general feature observed during hot-ion H-mode discharges in JET has been a pronounced poloidal asymmetry in the soft X-ray (SXR) emission profiles with a distinct excess emission occurring on the outboard, low-field side. A tomographic reconstruction of one such plasma, using data from the new multi-camera SXR diagnostic[1] with 210 lines of sight and six independent views at one toroidal location, is shown in Figure 1. This figure clearly demonstrates this feature with a pronounced peak in the SXR emissivity beyond a major radius (R) of 3.5m. A similar phenomenon has been observed, in a less dramatic form in earlier JET plasmas [2], the effect being attributed to the centrifugal force on heavy (metal) impurities as a result of toroidal plasma rotation [3]. This feature is strongest at high toroidal velocities, which approach or even exceed the impurity ion thermal speed. These conditions occur in the hot-ion H-mode plasmas in which plasma rotation, driven by the neutral beams, reaches frequencies in excess of 18 kHz and where nickel impurities with temperatures in the range 10 - 15 keV are found. Also seen in Figure 1, in addition to this outboard peak, a second narrow peak is seen at, or close to, the magnetic axis. This is attributed to neo-classical diffusion of the metal impurities.

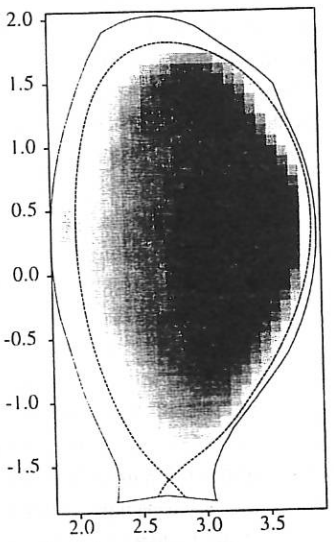

Figure 1. *SXR emission during the high performance phase of a hot-ion H-mode discharge 34425*

Laser Ablation of Nickel

The peak in SXR emission at large major radii, shown in Figure 1, is attributed to line emission from metal impurities. A more quantitative study of this effect has been possible with controlled injection of nickel by laser blow-off during high performance discharges. In one such case, shot 34476, the nickel injection was performed early in the high performance phase of a hot-ion H-

mode discharge. Figure 2 shows time traces of the concentration of nickel, together with its angular frequency and ion temperature from a high resolution X-ray crystal spectrometer. The rise in nickel concentration is clearly seen at the time of laser ablation and reaches 4 parts in 10^4 . The Ni^{26+} emission used in these measurements is also the dominant source of line emission contributing to the SXR diode data. At the time of peak nickel concentration (12.96s) the nickel temperature is 11 keV corresponding to $v_{thermal} \sim 1.3x10^5$ m/s with an angular frequency of 110 krad./s corresponding to $v_{rot.} \sim 4x10^5$ m/s (at a radius of 3.6m). Thus the rotational velocity of the nickel is more than a factor of 3 greater than the thermal velocity.

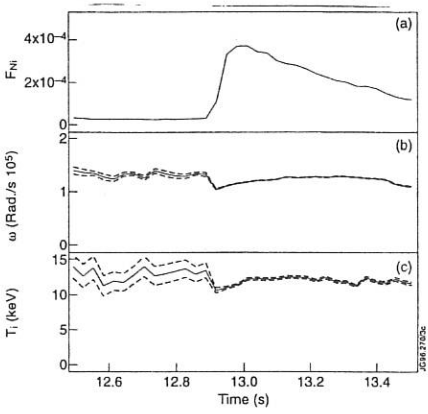

Figure 2. *(a) Ni concentration, (b) Ni^{26+} angular frequency and (c) the ion temperature of Ni^{26+} with errors for shot 34476.*

Tomographic reconstruction of the SXR emission during this event has been performed using a pixel technique developed initially by C. Fuchs for JET bolometer data. In Figure 3 the SXR emissivity along a horizontal line through the magnetic axis is shown for several time slices. The background emission at 12.91s has been subtracted. The inward progress of the nickel occurs very rapidly following the ablation over a period of about 10-15ms and then essentially stops. The last time slice, over 400ms later, shows the development of a secondary peak at the plasma axis (probably due to neo-classical diffusion) with a minimum in emission occurring between the two peaks. This two peaked structure also often develops late into a conventional hot-ion H-mode discharge (e.g. Figure 1). In Figure 3 the peak emission is centred on the outboard equator

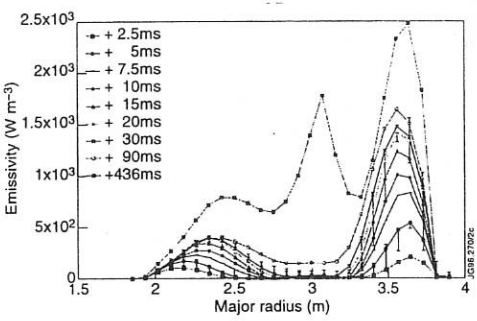

Figure 3 *Emissivity projected onto a horizontal line through the magnetic axis after subtraction of the first - pre-ablation time slice for shot 34476.*

at a major radius of ~3.6m; (the magnetic axis being at ~3.0m). Figures 4 shows a 3-dimensional view of SXR emission corresponding to the '+30ms' trace of Figure 3. Note that no up-down asymmetry is observed, unlike reference [3].

Theory of the Asymmetry

The asymmetry in the SXR emission distribution arises because the impurities take up the toroidal rotation of the plasma and the resulting 'centrifugal force' throws the impurity ions outwards. The behaviour is complicated by the electrostatic field which arises to maintain quasi-neutrality in the plasma. Nevertheless, it is possible to set up simple equations to describe the system and in the case of low impurity content, to solve for the poloidal distribution of each impurity species. The feature which makes this problem tractable is that the poloidal distribution of impurities on a flux surface depends only on the equation of pressure balance parallel to the magnetic field in the poloidal plane. The balance of forces, in the simple case of a trace species with charge Z in a hydrogenic plasma, arises from the pressure gradient, centrifugal force and electrostatic field in a magnetic surface (Ψ). This can be represented by

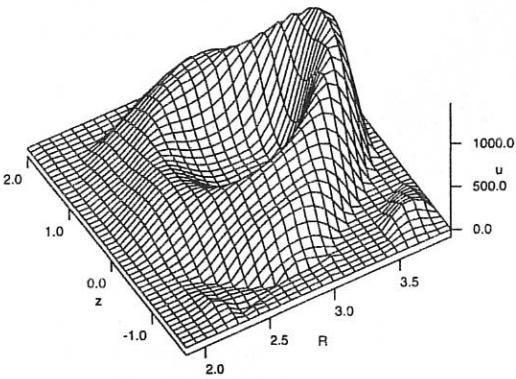

Figure 4 *Tomographic reconstruction 30ms after nickel injection with background emission subtracted.*

$$T_Z \frac{dn_Z}{dR} = n_Z \left(m_Z \omega^2 R - eZ \frac{d\phi}{dR} \right)$$

where the derivatives are taken at constant Ψ.

Solving the set of equations for a pure deuterium plasma with a small addition of impurity (s) yields the ratio of impurity concentration between the outboard-(o) and inboard-(i) sides

$$\frac{n_s^o}{n_s^i} = \exp\left\{ \frac{m_s \omega^2 (R_o^2 - R_i^2)}{2T_s} f \right\} \text{ where } f = \left(1 - \frac{T_e}{T_i + T_e} \frac{m_i}{m_z} Z_s \right).$$

At the radius of peak nickel emission for shot 34476, T_e is ~5.5 keV at 12.94s and taking $T_i=T_S$ a value for f ~0.7 is obtained. This yields a value for the ratio of concentrations of 5.5±1 :1. A further correction for the presence of other impurities in the plasma (carbon and beryllium) reduces this ratio by around 20%. (See [2] and references therein). Experimentally, from Figure 3 a value of 4±1 : 1 is found, in good agreement with theory.

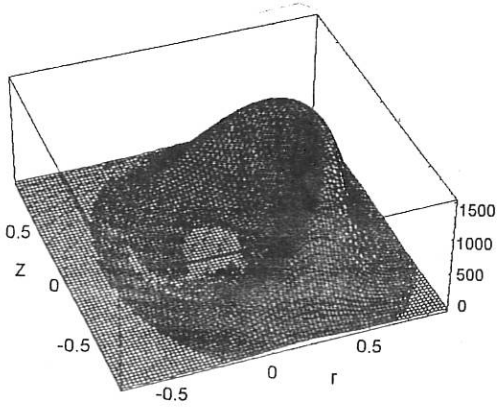

Figure 5 *Simulation of the poloidal distribution of the Ni emission for shot 34476. The outer equatorial intensity from Fig. 3 at +30ms was used as input and circular geometry assumed*

A numerical simulation of the poloidal distribution of the nickel emission has been carried out for one time slice using these equations. The outboard radial distribution through the magnetic axis was taken from the data at 12.94s. The model results are shown in Figure 5 and compare well to the data of Figure 4.

Summary and Conclusions

Strong in-out asymmetries are observed in the soft X-ray emission from JET hot-ion H-mode plasmas, a peak being observed on the outboard side. The key feature of the asymmetry can be explained by the effect of the centrifugal force on metal impurity ions in these rapidly rotating plasmas, where their rotational velocities exceed their thermal velocities by a factor of three. A simple model developed for the poloidal distribution produces quantitative agreement with data from a discharge in which there was laser ablation of nickel into the plasma. The radial distribution of impurity ions with a stationary peak at R~3.6m and the subsequent development of a secondary peak on axis is less well understood.

References

[1] Alper B. et al, 21st EPS Conference on Controlled Fusion and Plasma Physics, Montpellier, 1994, Vol.III p1305

[2] Giannella R. et al, 19th EPS Conference on Controlled Fusion and Plasma Physics, Innsbruck, 1992, Vol. I p279

[3] Smeulders P., Nuclear Fusion Vol.26 (1986) 267

Properties of Giant Elms

R.D. Gill, B. Alper, S. Ali-Arshad, A. Cheetham, N. Deliyanakis, A.W. Edwards,
G.M. Fishpool, I. Garcia-Cortez, L.C. Ingesson, J. Lingertat, L. Mayaux, O. Menicot,
R. Monk, L. Porte, F. Rochard, M. Romanelli, A. Rookes
JET Joint Undertaking, Abingdon, Oxon., UK

Elms are a persistent feature of tokamak configurations which include an X-point. Their phenomenological properties have been recently reviewed[1])but although their effects on tokamak plasma confinement and on the termination of high performance discharges are well known, many details of their structure and causes remain obscure. Several different sorts of elms have been classified, but this paper will confine itself to consideration of giant or type 1 elms. These elms cause the largest disturbance to the plasma and therefore give the best prospect of experimentally determining the detailed changes which occur as the elm progresses. A very detailed examination of the structure and time development of the elms has been made possible because of the development of the CATS data acquisition system[2]) which allows the simultaneous measurement at high time resolution (4μs) and synchronisation of the data from a number of diagnostics including ECE, reflectometry, soft

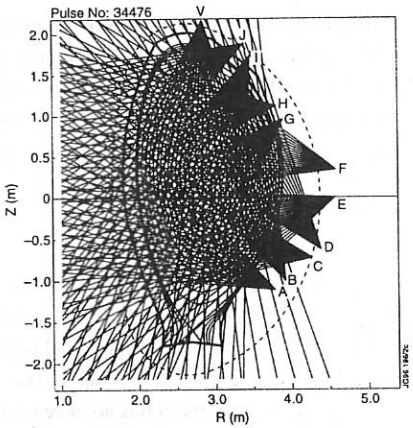

Fig. 1 The lines of sight of the individual detectors of the soft X-ray cameras are shown in relation to the JET divertor configuration.

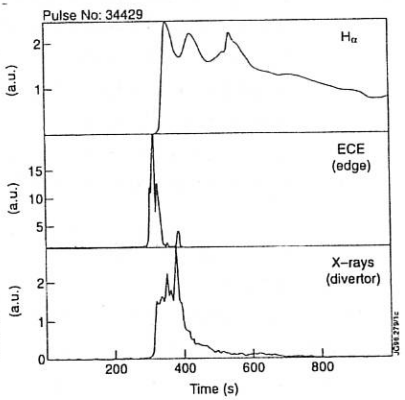

Fig. 2. The fast time development of a giant elm as seen on the ECE, a soft X-ray channel viewing the divertor and the H_α radiation.

X-rays, D_α, Langmuir probes, infrared camera and the magnetics including the diamagnetic loop. The high time resolution is essential for these investigations as the giant elm has a very fast onset with the fast diagnostics all responding within a few μs. Much of the very detailed information has come from the multicamera soft X-ray system[3]) which has 6 compact cameras (fig. 1) viewing the plasma from different directions in the same poloidal plane and a further vertical camera displaced toroidally by $3\pi/4$. Each camera consists of a pair of 35 element silicon diodes with each element 4 x 1mm. The detectors have been calibrated with an X-ray tube and view the plasma through common pinholes. Except for the vertical camera, alternate detector elements only are used. The lines of sight of the detector were determined using a HeNe laser to survey their positions.

The giant elms considered occur during neutral beam heated divertor discharges with P_{NI} = 17MW, B_ϕ = 3.1T, I = 3MA, elongation of 1.8, T_e = 11keV, $n_e = 10^{19}m^{-3}$ and lower hybrid heating. The elm is frequently associated with the termination of the period of good confinement in JET[4]) and has strong global effects on the plasma. In particular, it reduces the total plasma energy as measured by the diamagnetic loop by up to 7% (~ 0.6MJ) and this is reflected in a reduction of the electron temperature across the whole plasma profile. During the rapid part of the elm (fig. 2) the ECE measurement of T_e typically shows a pronounced very fast (40μs) spike many times the thermal value, with the largest enhancement at the plasma edge, followed by a dip to below the thermal level for a longer time. It is believed that the spike is due to the formation of a non-thermal electron distribution function following the partial mixing of hot and cold electrons. This modifies the emission and absorption of the cyclotron radiation[5]). The rapid onset of the spike is too fast for it to be caused by the formation of a group of non-thermal electrons with energy very much greater than T_e. The dip is probably due to the production at the edge of a high density region following the large particle influx which is inferred from the H_α measurements.

There do not seem to be precursors to the elms, although there is considerable activity seen by the mhd coils, particularly bursts of activity at 25-30 kHz probably with n = 3. Some of the giant elms occur during these bursts, but others do not, showing that they do not play an essential role in their initiation. This activity is not observed on the ECE or soft X-rays. The magnetics also show that the movement of the plasma caused by the elm is no more than 1-2 cms at the separatrix. The reflectometer observes a coherent mode at 25kHz at the plasma edge, possibly outside the separatrix. The mode stops at the elm and then becomes broad-banded activity. The plasma edge density is seen to increase.

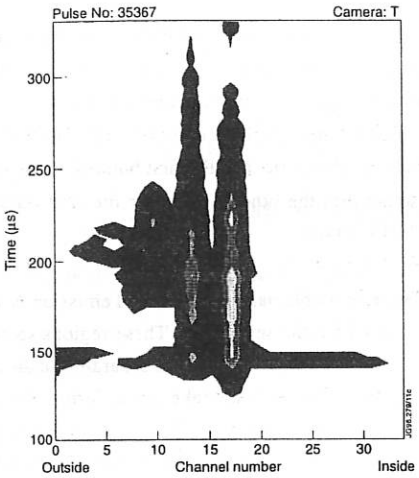

Fig. 3 Contour plot of soft X-ray data from the vertical camera during an elm. The background signal just before the elm has been subtracted from each channel. Complex time and spatial structure can be seen (left).

Fig. 4. Tomographic reconstruction showing the initial stages of the elms development. Again the background has been subtracted form all channels and the changes during the elm have been reconstructed (below).

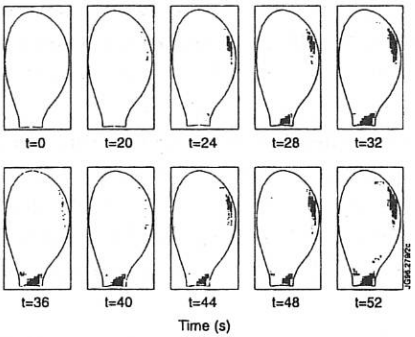

Data[6]) from Langmuir probes and an IR camera which views the divertor region shows strong movement of the divertor strike points with their separation increasing from ~ 30 to 45 cm during the elm, and this is confirmed by the X-ray measurements.

The most detailed information on the rapid development of the elm comes from the soft X-ray data. The view into the divertor from the vertical camera shows the main features (fig. 3) as (i) very rapid onset of emission (20μsec), (ii) very localized emission from four channels, (iii) time structure of ~ 30μsec within the total elm envelope of 250μsec. Two of the channels (15 and 18) may be identified with the divertor strike zones. This is confirmed by correlation of the position and time behaviour of the emission with the data from other

cameras also with a divertor view. X-ray emission from the divertor implies the presence of energetic electrons (> 500 eV) in this region. Calculations suggest that the observed intensity is consistent with the observed loss of plasma energy if the measured emission is caused by bremsstralung radiation of the former plasma electrons with the C divertor tiles. The toroidal camera shows that this emission is not toroidally symmetric, and the first burst of emission is sometimes at one poloidal position and sometimes the other. However the first burst of emission is coincident with the ECE and the H_α spikes.

The other X-ray spikes are somewhat more problematical. Enhanced emission is seen from several regions near the plasma edge but within the separatrix. These regions seem to coincide with the parts of the machine structure which are closest to the separatrix leading to the idea that enhanced impurity influx from these regions may take place during the elm. The structure of these regions of emission has been examined with a pixel tomography method developed by Ingesson which clearly shows (fig. 4) the different regions of enhanced emission. The tomography was carried out on data from which the background intensities before the elm had been subtracted so that the figure shows only the changes which take place during the elm. The very rapid increase in X-ray emission in the divertor is a very prominent feature.

In conclusion our results show that giant elms are very rapid events with a complex structure which are neither confined to the plasma edge nor localised in the divertor region. They do not have a unique precursor mode. A possible explanation for the observations is that currents in the divertor region lead to a movement and modification of the magnetic structure at the X-point. There is a clear need to develop a theoretical model of the elms which is able to explain these detailed observations.

REFERENCES

1. H. Zohm, Plasma Phys. Control Fusion, 38, (1996) 105.
2. A.W. Edwards *et al.*, APS Topical Conference on High Temperature Plasma Diagnostics. Rochester. 1994.
3. B. Alper *et al.*, EPS Conference on Controlled Fusion and Plasma Physics, Montpellier, (1994) 1304.
4. M.F.F. Nave *et al.*, Submitted to Nuclear Fusion.
5. J. Hastie, private communication.
6. H. Lingertat *et al,* Conference on Plasma Surface Interactions, St Raphael, 1996.

Monitoring of Detachment and the Edge using XUV Impurity Spectra from the Mark I Divertor Phase of JET

M G O'Mullane[1], I H Coffey[2], R Giannella

JET Joint Undertaking, Abingdon, Oxon., OX14 3EA, UK

[1]University College Cork, Ireland, [2]The Queen's University of Belfast, Northern Ireland

Introduction

The XUV spectrum of CV and CVI from the edge plasma in JET is rich in diagnostic potential. Impurities in the spectral range 20-40Å are monitored with an XUV grazing incidence spectrometer. It is possible to move the spectrometer so that it can view the inner wall at any angle. The spectra analysed here were taken with the spectrometer angled at it lowest position (see insert in Figure 3). Here the spectrometer views the SOL during the ramp-up phase of the discharge, typically for the first 5 seconds. When the X-point is formed the confined plasma is seen. During radiative divertor experiments the view is just above the radiating zone. If the plasma is going to detach from the strike plates it is reflected in the spectra, which can serve as an early indicator of detachment.

SOL Parameters in Ramp-up Phase

In the ramp-up phase of the plasma the spectrometer views the SOL exclusively. An unusual Lyman series and CV G-ratio (intercombination / resonance line ratio) are seen in *all* discharges (Figure 1). A 'distortion' in the Lyman series appears with the Lyman γ line prominent. There is also an inversion in the He-like system G ratio. In Figure 1 the top trace shows the pre-divertor JET limiter configuration spectra (# 13571). For the JET Mark I divertor configuration the middle trace shows a typical edge spectrum in the ramp-up phase (# 32595) and the lower trace shows a radial view through the main plasma (# 30763) in the X-point phase. The difference between the pre-divertor and Mark I divertor spectra is that no n>6 C VI Lyman series lines are now observed. These lines have been attributed to charge exchange with excited deuterium produced when there is contact between the limiter and the plasma [1]. Hence the neutral deuterium is formed by Frank-Condon dissociation at ~3eV

The emission seen by the spectrometer is a slice through a 3-D volume whose parameters vary in space and time (the fall-off lengths are ~cm). The model reduces the geometry to 0-D to elucidate the important atomic processes. The extreme values of the CV G-ratio can only be explained by emission from a strongly recombining plasma. A transient, recombining, model of the emission is used. Outfluxing C^{6+}, C^{5+} and C^{4+}, from the confined plasma, enters the SOL where ionisation equilibrium does not apply. The outfluxing carbon recombines with a competition between charge exchange and radiative recombination. The residence time of carbon in SOL is set by parallel transport, where $\tau = 2L_c/c_s$ (L_c = connection length, c_s = sound speed). The outfluxing mix is adjusted to match the Ly α /CV resonance line ratio, which is a measure of the ionisation balance. The system is allowed to evolve with the integration time set to 50ms to match the spectrometer's time resolution.

The emissivities of the driving processes (excitation, recombination and charge exchange) were calculated in a collisional-radiative code which forms part of ADAS [2] at JET. All possible transitions and excitation routes for $n \leq 5$ for CVI and $n \leq 4$ for CV were included. The atomic data is mostly taken from ADAS. The charge exchange cross sections are from [3,4]. These were extended by hand to lower energies. It must be noted that there is a severe lack of cross section data at such low thermal energies.

The residence time is estimated at ~4ms. It can be modified by effects such as thermal force in the SOL, but the calculated ratios are relatively insensitive to this parameter. The prominence of the Lyman γ line is conclusive evidence of charge exchange contributions. Figure 2 shows a comparison between calculated line ratios and observations. The model requires a n_{D^0}/n_e ratio of ~0.05, equivalent to a neutral density of $\sim 5 \times 10^{16} m^{-3}$. Neutral density fractions of 10^{-3} and above are necessary to explain the CV G ratio. Radiative and dielectronic recombination alone are not enough to account for the observations. The SOL temperature is estimated to fall in the range 50–90eV, which is consistent with all the calculated ratios.

Detachment Signature

The line-of-sight of the spectrometer passes just above the divertor radiation zone. The emission line ratio of the CV resonance line to the CVI Lyman α line is an early indicator of detachment (Figure 3). As the plasma approaches detachment this ratio rises. The CV G-ratio remains relatively constant as the plasma detaches. When the plasma is fully detached the region of cold plasma becomes localised at the X-point.

During the radiative divertor phase no CVI charge exchange lines are seen, indicating that the emission is from within the confined plasma. Hence a diffusive-ionisation balance equilibrium

model can be used (the neutral fraction is much lower in the confined plasma than in the SOL). The observed carbon G-ratio is ~0.7 compared with the equilibrium value of 0.45. The calculated G-ratio (figure 4) shows that in radiative divertor plasmas the plasma surrounding the X-point radiating zone is cooling as a result of the condensation in the divertor. The local temperature outside the X-point radiating zone, but from the confined plasma, cools to ~80–90eV from the 'normal' temperature of 300eV. G- ratio measurements further from the X-point show higher temperatures. This temperature gradient along the outer flux surfaces may be destabilising, possibly leading to radiative collapse of the plasma.

When a radiative divertor plasma detaches, the CV resonance to Lyman α line ratio begins a steady increase approximately 3.5s beforehand. Radiative divertor discharges which do not attain detachment do not exhibit this behaviour. Figure 4 shows this ratio calculated as a function of confinement time. The steady, monotonic, change in the line ratio as the plasma moves towards detachment is a measure of an increasing diffusion (because $\tau_p \propto a^2/D_\perp$) in the near-edge plasma. The poorer edge confinement may be caused by a degradation of the confinement mode.

Conclusion

It has been shown that the CV and CVI spectra can be used as diagnostics of the outer plasma region. In the SOL charge exchange with neutral deuterium is significant and amounts to ~0.05% of n_e. The temperature of the SOL is ~50-90eV. There is a lack of charge exchange cross section data at the low energies needed for this analysis. The near-edge XUV spectra provide a reproducible detachment signature. The condensation at the X-point sets up a temperature gradient along the flux surface. The ionisation balance is also affected. Enhanced diffusion or poorer edge confinement is evident well before the plasma fully detaches.

[1] M Mattioli *et al.*, Phys. Rev. A, **40**, p3886 (1989)
[2] H P Summers, Atomic Data and Analysis Structure (ADAS), JET IR(94)06
[3] N Shikamura *et al.*, Phys. Rev. A, **45**, p7876 (1992)
[4] M Kimura and C D Lin, Phys. Rev. A, **32**, p1357 (1985)

ACKNOWLEDGEMENT This work was partially funded by the UK Department of Trade and Industry and EURATOM.

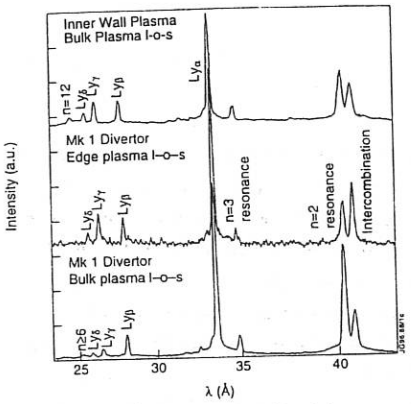

Figure 1 Comparison of observed C V and C VI spectra from the main and edge plasmas from different JET operational periods.

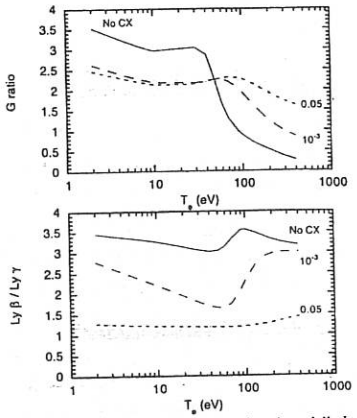

Figure 2 Comparison between observed and modelled line ratios. The spread of the observed ratio is indicated by a shaded region.

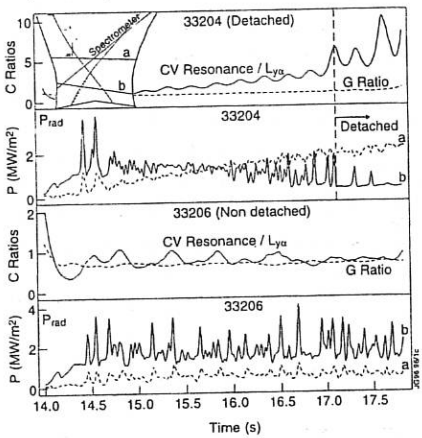

Figure 3 The spectroscopic detachment signature. The modulation of the ratios is due to divertor sweeping. Top shows a detached case with the non-detached on the bottom. Note that the G-ratios have similar values. a and b refer divertor bolometer LOS.

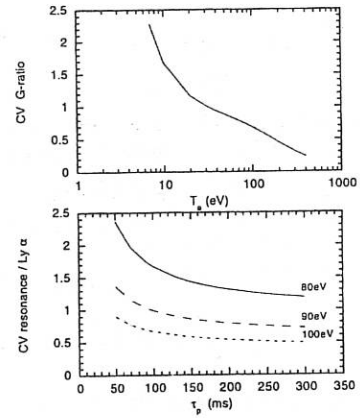

Figure 4 Top: Carbon G ratio in diffusive-ionisation balance equilibrium. The shaded region is the observed ratio. Bottom: C V resonance to C VI Lyman α emission line ratio as a function of confinement time.

Effects of density and plasma configuration on the divertor asymmetries

S Clement, A Chankin, S Davies, J Lingertat, R Monk, R Sartori and M Stamp.
JET Joint Undertaking, Abingdon, OXON, OX14 3EA, UK

1/ INTRODUCTION. Asymmetric power deposition with more power going to the outer divertor target is usually observed in single null divertor configurations and is expected from geometrical toroidal effects (higher area of outer magnetic surfaces) and higher anomalous transport towards the outer midplane. The additional effect of drift forces has been discussed in [1]. This paper presents the first results of an analysis of the asymmetries obtained in H-mode regimes. It is found that the magnetic configuration has a strong influence on the imbalance of power and particle fluxes in the divertor. The effects of gas fuelling are also discussed. Two regimes are distinguished: 1)hot ion mode regimes: these have high power (18 MW), central fuelling with the neutral beams (no gas fuelling) and result in a high temperature, poloidally isothermal scrape-off layer (SOL); one expects poloidal drifts to increase the asymmetries; 2) radiative divertor regimes: medium to high power (12MW), edge gas fuelling: these result in a high radiation fraction in the divertor region, and non-isothermal SOL, with possible extra radial drifts[1] which in turn may modify the particle and power exhaust ratios. Langmuir probe data implies high edge ion temperatures in low density hot ion modes. There is empirical evidence from other machines that high edge temperatures are associated with toroidal momentum [2] in the edge plasma. This effect has the correct sign to increase the density at inner divertor.

2/ HOT ION MODE: EFFECTS OF THE PLASMA CONFIGURATION. In general, the power flow towards the outer strike zone should be larger due to geometrical toroidal effects [3] (higher area of the outer magnetic surfaces: calculations yield a 23% higher outer pressure for JET toroidicity), higher $D_\perp$ towards outer mid-plane, and the Shafranov shift ([1] and references therein). Furthermore, in the low density/low recycling hot ion mode regime, one expects high and poloidally uniform edge temperatures to cause strong radial electric field and poloidal $E_r \times B$ drifts that should increase the asymmetry.

Higher power to the outer strike zone has been observed in most JET magnetic configurations (see[1] for ohmic and L-mode discharges). This was also evidenced by the fact hat most of the damage occurred on outer divertor tiles.

However, we have found that **high magnetic shear** configurations show a more even power distribution than the low shear equivalent discharges, and the power imbalance can even be reversed in favour of the inner strike zone. High confinement regimes have been found to depend on the magnetic configuration in DIII-D [4] and JET [5].

Fig 1 shows time traces for two discharges with I_p=3.8MA, B_t=3.4T . Discharge #32969 has a shear at q=95% SH_{95} =3.6, discharge 36677 has SH_{95} =5.0, at the time of the peak

neutron rate . It can be seen that the inner and outer strike zone peak temperatures are very similar in the higher shear case. The effect of shear (or more generally, of the shape of the plasma) has been studied for two series of discharges of hot ion modes: 1) the 20 best discharges of the campaign in terms of peak neutron production (plasma current 3MA $\leq I_p \leq$ 4MA, toroidal field B_t = 3.4T, input power P_{in} = 18MW NBI, shear values $3.1 \leq SH_{95} \leq 5$, no gas fuelling); 2) a series of 12 discharges of a configuration scan (I_p = 2.5MA, B_t = 2.5T, P_{in} = 10MW NBI, shear values $2.8 \leq SH_{95} \leq 4.2$, no gas fuelling, no tile temperature data available). All the discharges in the high performance dataset have moderate to high shear. The dataset includes two main types of configurations: the high flux expansion single null (moderate shear) and the double null type of discharge (high triangularity, high shear). All these discharges have low divertor densities and electron temperatures above 50eV, as measured by Langmuir probes. For the probe measurements the power accountancy is poor, indicating that the ions carry a higher fraction of power to the divertor than electrons. Good global power balance is found with the IR camera measurements. These discharges radiate below 10% of total input power, and show a constant and very weak D_α emission in the divertor during the ELM free period. It is observed that: 1) the ratio of outer to inner peak surface temperatures decreases with magnetic shear during the ELM- free H-modes (fig. 2); 2) the same trend is observed in the D_α ratio (fig3), as one would expect in a high temperature SOL, with no temperature gradients along the field lines; 3) the same effect on the temperature ratio is observed in the low confinement phase that follows the hot ion mode, although the temperature values are more scattered (movement of the strike points due to β changes).

Drifts alone cannot explain the higher power going to the inner strike zones at high shear for poloidally isothermal plasmas. Other possible explanations could be related to: 1) toroidal momentum: its effect is expected to be important at high edge temperatures; however high electron temperatures are measured in all the high performance dataset; unfortunately ion temperature data are not available to show if there is any effect of the plasma configuration. 2) fluctuations, observed to be different in the high and low field side; however, the position of the heat source does not seem to matter too much in isothermal SOLs; 3) thermoelectric currents in the SOL.

It has to be noted that the same trends are obtained by plotting the data against the triangularity of the plasma. The values of the triangularity are calculated with a greater accuracy than those of shear, because it is an edge parameter. However, there is a strong correlation between shear and triangularity in the dataset used. Finally, no correlation with the plasma current or with q was found.

3/ RADIATIVE DIVERTOR REGIMES: EFFECT OF DENSITY (GAS FUELLING).

When gas is injected in the divertor or the SOL, the resulting increase of the edge density will change the pattern of radiation in the divertor region. This is particularly important for radiative divertor regimes. In L-mode confinement regimes [1], the ratio of the power in

the outer and inner strike regions ranged from a factor ≈1.5 to values ≈3. In general, the asymmetries in the electron density, temperature and D_α fluxes appeared to be consistent with radial $E_\theta \times B$ drifts playing an increasingly important role as the density and hence the parallel temperature gradient was increased. However, the effect of increasing the divertor density on the power distribution was obscured by the onset of detachment occurring at the inner strike zone.

Two discharges at high power and far from detachment have been chosen to compare the effects of the density. The configuration is one of moderate shear (SH_{95}=3.3), and the power going to the target plates is very similar in the two cases. It can be seen (fig.4) that gas fuelling increases the density by a factor of two and brings the asymmetry factor in the divertor temperatures from 1.1 to 1.6 . The relative change in the radiated power in the divertor $Prad_{outer}/Prad_{inner}$ changes only from a value of 1 at low density to 0.85 at high density. This result is consistent with the development of a poloidal temperature gradient in the SOL as the density increases, giving rise to high radial $E_\theta \times B$ drifts.

4/ CONCLUSIONS. In the majority of the configurations used at JET more power flows to the outer than to the inner strike point, as expected from theoretical predictions; however in hot ion mode regimes (poloidally isothermal SOL) we observe a more even power distribution as the magnetic shear (or the triangularity) is increased. This effect is also observed in the particle flux to the divertor region. These observations are not accounted for by any classical drift. Toroidal momentum could play a role in the development of these asymmetries. However edge ion temperature data are needed to determine its importance.

The effect of gas fuelling on the power ratio is consistent with the development of a poloidal temperature gradient in the SOL as the density increases, giving rise to radial $E_\theta \times B$ drifts. The effect of the magnetic configuration on the power and particle distribution poses a problem for the design of a divertor for ITER. Codes based on edge and divertor parameters may need to have a model of the central plasma coupled to make reliable predictions.

The work of P J Lomas and Task Force H is gratefully acknowledged.

REFERENCES

1. A Chankin et al, Plasma Phys. Control. Fusion 36 (1994) 1853.
2. A Chankin and W Kerner, Nucl. Fusion 36 (1996) 563.
3. P J Harbour, Contrib. Plasma Phys 28 (1996) 417.
4. J Stambaugh and the DIII-D Team, Proc. of the 15th IAEA Conference on Plasma Physics and Controlled Nuclear Fusion (1994) 83.
5. PJ Lomas and the JET Team, as above, p.211.

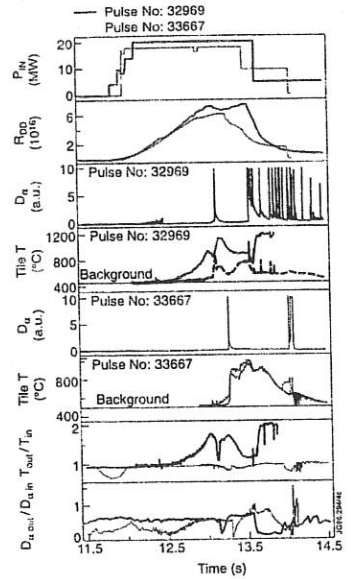

Figure 1 Time traces of the input power, radiated power, power going to the divertor target, central line density and the temperatures of the inner and outer strike zones for shots #35752(no gas fuelling) and #35752 (high gas fuelling).

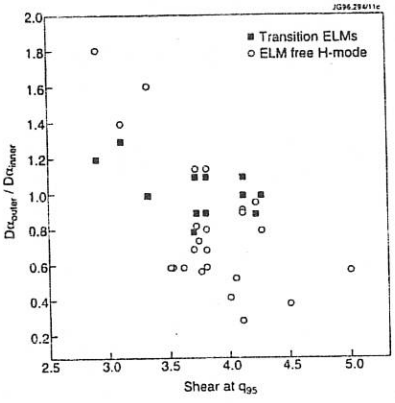

Figure 2 Ratio of the outer to inner strike zone total integrated particle fluxes versus shear at q_{95}.in ELM-free H-modes, and during the transition ELMs.

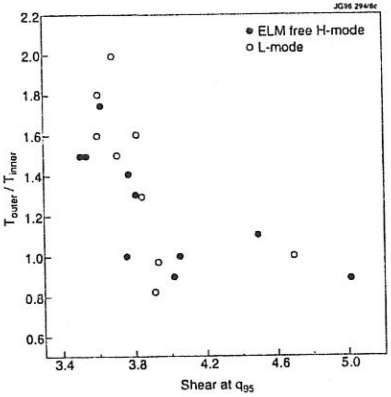

Figure 3 Ratio of the peak values of the outer to inner strike zone tile temperatures versus shear at q_{95} in .H-mode, ELM-free and L-mode.

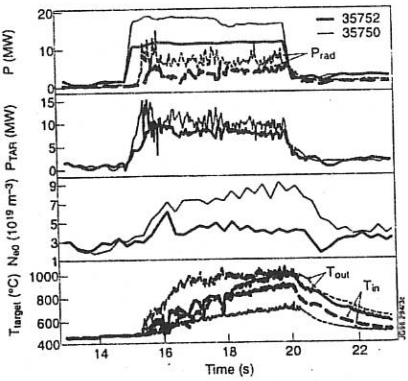

Figure 4 Time traces for shots #32969 and #33667: total input power, neutron reaction rate, D_α, peak tile temperatures in the inner and outer divertors, and the ratios of outer to inner values in temperature and D_α integrated photon fluxes.

Plasma movement at ELMs in JET

S. Ali-Arshad, A. Edwards, J. Lingertat, S. Puppin, J. Wesson
JET Joint Undertaking, Abingdon, Oxon. OX14 3EA, UK

Introduction

In JET giant ELMs can give rise to a sustained degradation of plasma confinement, and in some cases control of the vertical position of the plasma is lost following a giant ELM, leading to a major disruption. An example of such a case is given in fig. 1.

A variety of measurements suggest that during the ELM the scrape-off layer and bulk plasmas move rapidly. This paper presents these observations, and addresses implications for the vertical stability of the plasma.

Data analysis

Magnetic diagnostics show a short-lived perturbation appearing during the ELM, typically in the range 10-100 Gauss. The example in fig. 2 shows the amplitudes of the modes with toroidal mode number n=0,1,2,3, calculated from a toroidal array of coils at a poloidal position of θ~60°. The poloidal structure of the perturbation is shown in fig. 3 at two time slices. A dominant m=1 structure is seen. The amplitude of this structure is a factor of ~3 larger than the level of perturbation observed on each of the coils in the toroidal array at θ~60°, suggesting a principal mode with m=1, n=0. Thus during the ELM the plasma shifts downwards, reaching its lowest position in several hundred microseconds, and then it moves upwards reaching its highest position in about a millisecond. Interpretation of soft X-ray[3] data during ELMs is complicated by transient, highly local radiation sources. However, supporting evidence for the plasma movement is given by lines of sight not intercepting such sources. The position of the plasma current centroid, as determined from the current moment method, is shown in fig. 4. This supports the observation of a downward movement followed by an upward movement, and indicates the size of the movement is ±1cm. Fig. 4 also shows that during the downward movement little poloidal flux penetrates through the vessel. The plasma boundary displacement can therefore be calculated from flux compression between the plasma boundary and the wall: $\delta z_{down} \approx \Delta Z_0 \, \delta B_\theta / B_{\theta 0}$, where ΔZ_0 =initial plasma-wall distance, δB_θ = change in B_θ at top of vessel, $B_{\theta 0}$ = equilibrium field at top of vessel. The upward movement can also be estimated by this method, but is only accurate to a factor of ~2, due to partial flux penetration (see fig. 4). Such estimates give agreement with the centroid calculation, so that the perturbation might be approximated with a 'rigid body' displacement. In addition, this procedure allows

the movement to be determined from more abundant dB_θ/dt data. Fig. 5 shows such estimates for several ELMs plotted against the D_α light intensity. These suggest that larger ELMs can produce larger displacements, and that the upward overshoot is typically larger than the downward movement, by a factor of ~2.

Fig. 6 shows infra-red camera data on the divertor target before and during an ELM, showing an increase in the strike zone separation during the ELM. The change is too large to be a result of the bulk plasma movement described above, so the existence of SOL currents is suggested. This is supported by Langmuir probe measurements of SOL currents of order 10kA, intercepted by the divertor target during ELMs [1]. A toroidal current of order 10kA, transferred from the main plasma current is also predicted by consideration of spilling of hot electrons into the SOL during an ELM [2].

Interpretation

The vertical speed of the JET plasma is stabilised by a control system. A simplified model for this has been given [3], [4]. This has the form $I_p Z_p = \frac{C_1 V_R}{s(s-\gamma)} + \frac{C_2 f_z (s + 1/\tau_{eff})}{s-\gamma}$, Z_p = plasma current centroid vertical position; V_R = voltage to radial field coil, proportional to plasma speed, allowing for amplifier characteristic (±10kV max., 9 levels); γ = natural instability growth rate; τ_{eff} =effective radial field penetration time with divertor configuration; f_z =arbitrary vertical force applied to plasma. For an ELM with a 1:2cm down:up movement ratio, the model suggests a force waveform f_z as in fig. 7 (The plasma position is restored by a position control system on a time-scale of several milliseconds. This is not included in the simulation.) Scaling up this f_z waveform by a factor of ~3 produces a vertical instability in the model as shown in fig. 8. The forces on the plasma might arise from toroidal current transferred to the SOL during an ELM. Away from the X-point, to first order, this does not produce a force on the plasma. However, in the X-point region a downward force would be produced, as illustrated in fig. 9. If the SOL current then decays faster than the current recovers in the confined plasma, e.g. due to an impurity influx, an upward force could be generated due to the weaker poloidal field near the X-point compared with the top of the plasma.

Future Work

Further work is needed in diagnosing the SOL currents, understanding the resultant forces and the effect on the strike zones. The ELM database studied needs to be expanded, and

data from soft X-ray and infra-red cameras, Langmuir probes and magnetics need to be correlated. A multi-machine scaling study of the movement would be valuable to assess implications for ITER.

Acknowledgement: The authors would like to thank Dr. P. Noll for discussions on the vertical stabilisation system.

[1] J. Lingertat et. al., *Studies of giant ELM interaction with the divertor target in JET*, J. Nucl. Mater., to be published.

[2] J. Wesson, *SOL Current During ELM*, Private communication (1995).

[3] P. Noll and M. Garribba, *Review of Fast Radial Field Amplifier*, Private communication (1989).

[4] P. Noll, *A simplified model of the stabilisation system*, JET divisional note JDN/G(91)025, (1991).

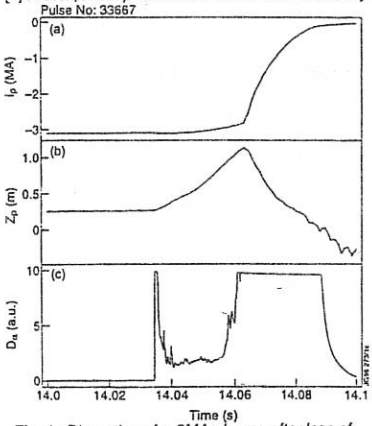

Fig. 1: *Disruption of a 3MA plasma after loss of vertical stability following a giant ELM*

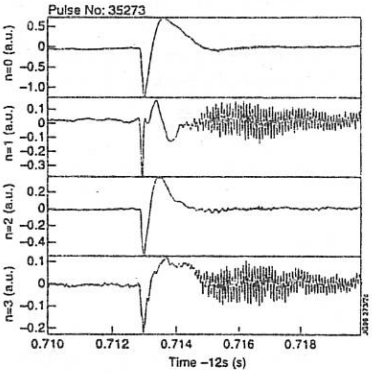

Fig. 2: *Amplitudes of dB_θ/dt, with toroidal mode numbers n=0,1,2,3 at a poloidal position of θ~60°.*

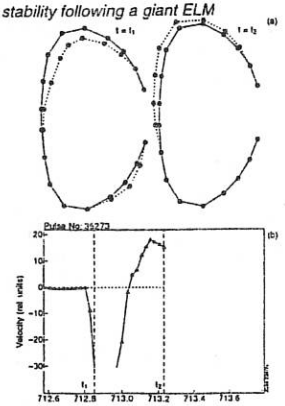

Fig. 3: (a) *dB_θ/dt perturbation at two times during an ELM (see (b)). On fast time-scales (<<3ms) this is proportional to the local normal plasma speed.*

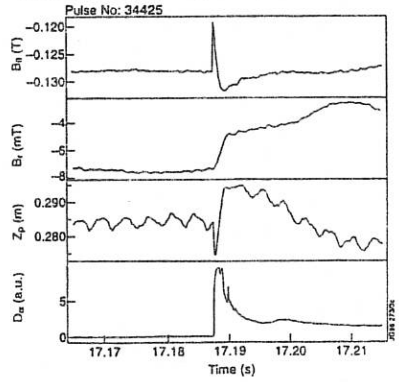

Fig. 4: *(a) Poloidal field and (b) radial field at top of vessel, and the plasma current centroid (c), at an ELM.*

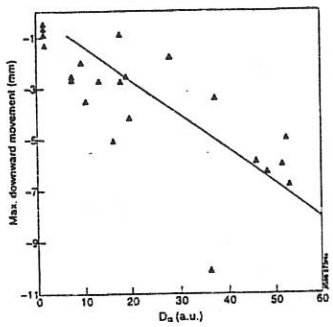

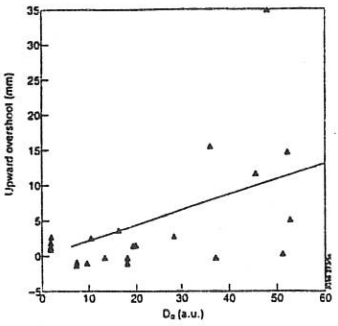

Fig. 5: *Plasma displacement estimated from poloidal flux compression. The upward movement is likely to be underestimated by a factor of ~2, due to partial flux penetration.*

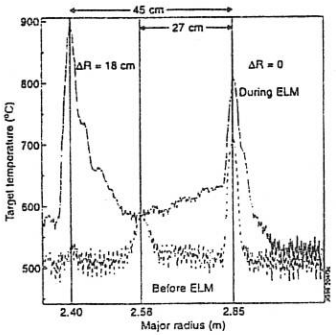

Fig. 6: *Infra-red camera view of the divertor target before and during and ELM.*

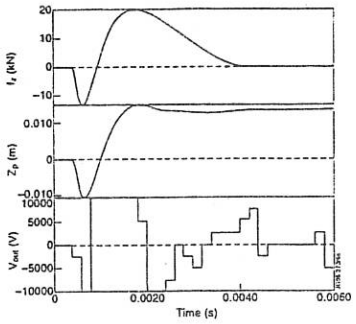

Fig. 7: *Force required for typical plasma movement at a giant ELM, for a 3MA plasma with γ=700s^{-1}.*

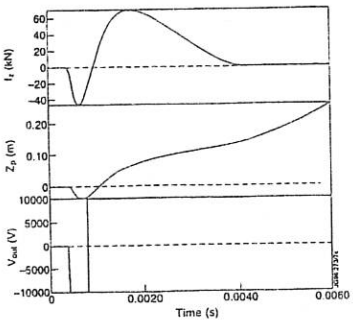

Fig. 8: *Vertical instability produced by amplifying the force waveform found in fig. 7 by a factor of ~3.*

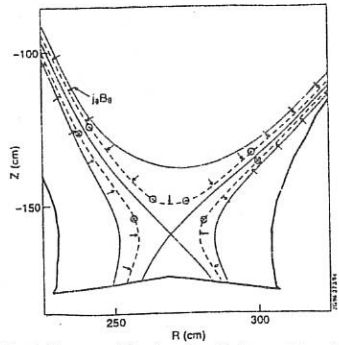

Fig. 9: *Forces arising from toroidal current transfer from edge confined plasma to the SOL*

Monte Carlo simulations of fast particle confinement during a sawtooth crash

L. C. Appel†, T. C. Hender†, G. T. A. Huysmans, F. Marcus, C. G. Gimblett† and S. D. Pinches‡

JET Joint Undertaking, Abingdon, Oxon, OX14 3EA, UK.
† UKAEA, Fusion, Culham Laboratory (Euratom/UKAEA Fusion Association), Abingdon, OX14 3DB, UK.
‡ Department of Theoretical Mechanics, The University of Nottingham, University Park, Nottingham, NG7 2RD, UK.

Introduction

The most common core instability affecting plasma performance is the sawtooth crash. Although the precise mechanism of this n=1, m=1 perturbation is not fully understood [1, 2, 3, 4], its effect on thermal plasmas, clearly visible from measurements of SXR and ECE, leads to a strong redistribution of thermal ions [5, 6, 7]. In contrast to the results for thermal plasmas, Marcus [8, 9] has used measurements of neutron flux to show that the spatial distribution of slowing down 1MeV tritons produced by D-D fusion is only weakly altered by the sawtooth crash. Understanding the nature of the interaction between the sawtooth and fast particles is crucially important, as in an ignited fusion reactor heated by alpha particles, the core heating efficiency will depend on their containment whilst they thermalize. In this paper we use the guiding centre code HAGIS [10] to study the behaviour of energetic particles during a sawtooth crash and make comparisons with experimental measurements.

Experimental evidence of fast particle redistribution

The clearest evidence showing the effect of a sawtooth crash on fast particles comes from measurement of neutron emission. Fusion in a deuterium plasma results either in the formation of a neutron (energy 2.5MeV) and a ^{3}He ion, or a proton and a triton with energy 1MeV. A secondary flux of neutrons with energy 14MeV can result from fusion of these tritons with deuterium. Although tritons are born with energy 1MeV, their reactivity peaks at 200keV (this is for a single triton fusing with a stationary deuteron).

Measurements of neutron emission in JET have been carried out using two fan-shaped multi-collimator cameras, with ten horizontal channels and nine vertical channels. The neutron detectors are designed to detect unscattered neutrons in each of two energy ranges, whilst filtering out the background gamma-ray radiation.

Discharge 26087 used 15MW of pure deuterium neutral beam injection to achieve the highest D-D neutron yield in JET at the time. The heating was applied from 12 to 14 secs after initiation of the discharge during which time the 2.5MeV global emission increased to peak just before a sawtooth crash at 13.47sec, apparent on SXR data. The 14MeV neutron emission, however, persisted for another 500msec as is evident from the radial cuts of 2-dimensional profiles for 2.5MeV and 14MeV neutrons shown in figure 1 [8]. Statistical analyses of similar but lower performance discharges indicate identical behaviour [9].

A useful insight can be gained from calculating the fractional beam-thermal contribution (F_{bt}) to the total yield of 2.5MeV neutrons at the time of the crash. This has been

computed for a number of discharges using TRANSP and figure 2 [9] shows plots of the emissivity profile widths on the mid-plane as a function of F_{bt}. Just before the crash, the profile width is an increasing function of F_{bt}. This is because as the density rises, the beam deposition profile broadens due to reduced penetration and, coincidently, the beam-beam contribution decreases because of the reduced beam density. Just after the crash, the emissivity profile width is approximately constant. Plotted on the same graph, the 14MeV neutron data from discharge 26087, appears consistent with the observations of 2.5MeV neutrons.

In summary, sawtooth crashes are observed to affect the flux of 2.5MeV neutrons strongly, but not the flux of 14MeV neutrons. These differences are most probably due to features of the hot particle distributions. Before the crash, the FWHM (full width at half maximum peak value) of the 2.5MeV neutrons is between 30% and 60% of the post-crash FWHM, whereas the FWHM of the 14MeV neutron flux increases by less then 10% during the crash. Plotting the beam-thermal contribution (obtained from TRANSP simulations) versus the FWHM pre- and post-crash indicates that the results from both neutron species are consistent.

HAGIS simulations

This section describes simulations that have been carried out to study the effect of a sawtooth crash on a population of energetic particles. The sawtooth behaviour is based on a model proposed by Gimblett and Hastie [4] in which a n=1,m=1 magnetic island grows until the pressure gradient at its separatrix triggers a 'crash' characterised by rapid stochastization of the central core. The post-crash equilibrium is reached by performing a Taylor-relaxation of the core region. In the simulations, an n=1, m=1 eigenmode computed by the linear resistive mhd code CASTOR [11] is increased from zero amplitude over a resistive growth time (100μsecs) until the plasma core is shifted by 25% of the minor radius at which point high (m,n) resistive interchange modes are triggered. Six high (m,n) modes with $n \lesssim 50$ are used each with a magnitude close to the (1,1) mode, chosen to induce stochasticity of the magnetic field lines in the core region. This was verified by computing a Poincaré plot, following field lines from within the q=1 region. The high(m,n) modes decay over 10μsecs whilst the (1,1) mode decays more slowly. The post-crash equilibrium at the end of the simulations is taken to be identical to the pre-crash equilibrium, close to the value predicted by Taylor-relaxation. The mode is taken to be stationary during the simulations.

We have used the HAGIS code to follow a population of 20000 tritons with energy 200keV and radial distribution of the form

$$f_o = (1 - \mathcal{R})^\gamma$$

where $\mathcal{R}$ is the average normalized poloidal flux surface at which each particle crosses the mid-plane. The initial particle conditions are obtained by first constructing a grid in ψ_p (poloidal flux), θ (poloidal angle) and E (energy) and integrating the distribution function in each grid cell. Values of the radial function $\mathcal{R}$ are obtained by expressing it as a function of the equilibrium constants of motion p_ζ, E, μ, (p_ζ is toroidal angular momentum and μ is the adiabatic invariant). From this, a cumulative probability function $g_{cpf}(i)$ ($i \equiv$ grid cell label) is computed describing the probability of particle occupancy. Since the function $g_{cpf}(i)$ is a monotonic function, the 'reciprocal' function $i(g_{cpf})$ is single-valued and can be readily calculated. Noting that the argument to this function lies between 0 and 1, we use a random number generator to obtain a set of initial particle conditions.

Simulations have been carried out for the cases of purely co-passing, counter-passing and trapped distribution functions where in the latter case, the magnetic field at the bounce tips is the value on the magnetic axis. Before considering the effect of the sawtooth, preliminary HAGIS simulations were carried out in the absence of helical magnetic perturbations to check that the particle distributions did not evolve in time. In the presence of the sawtooth, simulations predict a clear flattening of the radial profile in each of the three cases. This is illustrated for the case of a trapped distribution with profile index γ=8 shown in figure 3. The dominant effect on the profile is seen to be through the (1,1) mode. During the pre-crash phase, the growing (1,1) mode results in a peak electric potential of about 3kV. Resonant interaction of particles is observed. For each particle distribution, the equilibrium invariants p_ζ and E are not conserved and the originally mono-energetic particle distributions broaden. In addition, for co-passing particles there is an overall loss of energy to the wave whereas counter-passing particles experience an overall energy gain. By comparison, the effect of the high (n,m) modes during the crash phase is much less since the electric field is $\sim 1/n$ smaller.

The effect of the sawtooth crash on other radial distributions was deduced from the previous simulations which were obtained with γ=8 by appropriately weighting each particle i.e. for a particle i with initial $\mathcal{R}$= $\mathcal{R}_i$, the weighting is

$$w_i = \frac{f_o^*(\mathcal{R}_i)}{(1-\mathcal{R}_i)^8}$$

The profile coefficient γ was varied over a wide range and the number of particles close to the midplane ($|z| < 2$cm) plotted versus γ. The results, shown in figure 4, display the profile widths before and after the crash. The effect of the sawtooth on particle redistribution is greatest with an initially peaked profile. It is also clear that the final radial particle distribution is almost independent of the initial conditions. Both these effects are in agreement with experimental observations shown in figure 2.

Summary

The HAGIS code has been used to model experimental observations of fast particle redistribution during a sawtooth crash. Simulations carried out with purely co-passing, counter-passing and trapped 200keV particles predict that in each case the radial profiles are flattened. The effect is greatest with initially peaked profiles and the final profile width is almost independent of initial conditions. These results are in agreement with observations. In addition, the simulations predict resonant interaction of particles leading to a broadened energy distribution and an overall loss or gain of energy for the case of co-passing and counter-passing particle distributions.

Acknowledgements: The UKAEA authors were jointly funded by the UK Department of Trade and Industry and Euratom. The authors thank Mr. M.O'Brien for useful discussions.

References: [1] Aydemir et al.,Phys Fluids B **1**, 1989, 774. [2] Hastie, R.J., Phys Fluids, **30**, 1987, 1756. [3] Ottaviani et al.,JET pre-print JET-P(95)04. [4] Gimblett, C.G. and Hastie, R.J., Plasma Phys. Control. Fusion, **36**, 1994, 1439. [5] Pfeiffer, W.W., et al., Nuclear Fusion, **25**, 1985, 655 [6] Sadler, G., et al., Fusion Technology, **18**, 1990, 556. [7] Lovberg, J.A., et al., Phys Fluids B, **1**, 1989, 874. [8] Marcus, F.B. et al., Nuclear Fusion, **33**, 1993, 1325. [9] Marcus, F.B., et al., Nuclear Fusion, **34**, 1994, 687. [10] Appel, L.C., et al., Nuclear Fusion, **35**, 1995, 1697. [11] Kerner, W. at al., Proc 1993 EPS Lisbon, **1** paper I-46

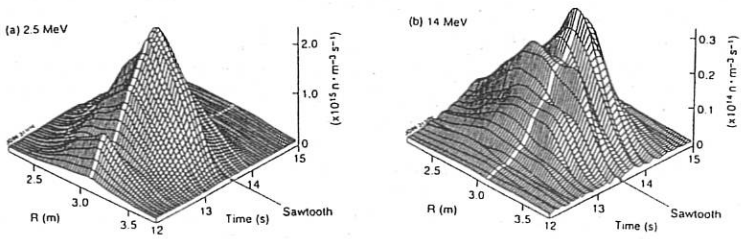

Figure 1. *One dimensional cuts of (a) 2.5MeV and (b) 14MeV neutron 2-D emissivity profiles, plotted as functions of time and radius along a major chord through the plasma midplane (z=0) for discharge No. 26087 during and after high power neutral beam heating [8].*

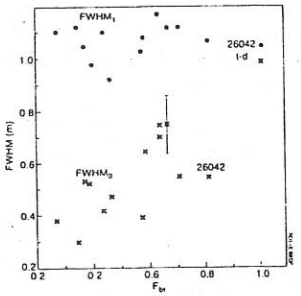

Figure 2. *FWHM emissivity profile in the midplane just before the ($FWHM_0$) (X) and just after the crash ($FWHM_1$) (•) versus F_{bt} of 2.5MeV neutron emissivity on-axis just before the sawtooth crash. The 14MeV neutron data from discharge 26087 is also shown [9].*

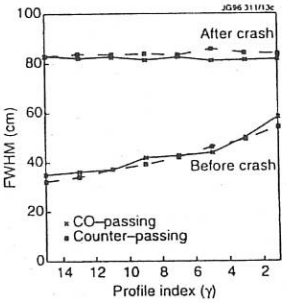

Figure 4. *FWHM profile of particles close to the mid-plane (|z| <2cm) before and after the crash (HAGIS simulation).*

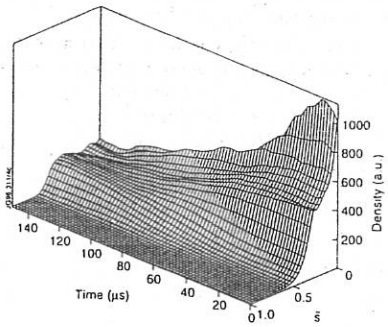

Figure 3. *Time-variation of radial profile density during a sawtooth crash for a distribution of trapped particles. The radial coordinate* $\bar{s} \equiv \sqrt{\psi_p/\psi_{p_{edge}}}$ (HAGIS simulation).

Effect of the error fields on plasma stability in JET and ITER.

P.Savrukhin[1], S.AliArshad, D.J.Campbell, G.D'Antona [2], M.De'Benedetti, A.M.Edwards[3], G.Fishpool, R.J.LaHaye[4], E.Lazzaro [2], A.Santagiustina, F.Sartori, A.Tanga

JET Joint Undertaking, Abingdon, Oxon., OX14 3EA, UK

[1] Russian Research Centre 'Kurchatov Institute', 123182, Russia; [2] Instituto di Fisica del Plasma, Euratom-ENEA-CNR, 20123, Milan, Italy; [3] Culham Laboratory, UKAEA Technology, Abingdon, OX14 3DB, UK; [4] General Atomic, San Diego, California, USA.

INTRODUCTION. Limitations of stable plasma operation due to magnetic field errors ('error' fields), arising from unavoidable misalignment of the tokamak magnetic configuration and non-symmetry of the in-vessel mechanical construction, are expected to give rise to significant problems in the design of future large tokamaks such as ITER. However, non-linear dynamic of the MHD perturbations observed in various experiments complicates predictions of the 'locked' modes in future tokamaks and prevents design of the reliable stabilisation techniques. To reveal physical mechanisms involved in the processes of mode 'locking' in regimes with plasma parameters approaching those in future reactors (relatively low level of impurities, high electron temperature and density at the plasma edge, relatively slow plasma rotation) dynamic of the MHD modes driven by the external helical magnetic field is analysed in ohmically and auxiliary heated plasma in JET pumped divertor configuration. External 'quasi-static' (DC) and rotating (AC) helical magnetic fields at JET are generated by system of four saddle-like coils (SC) placed inside vacuum vessel at the lower part of the torus [1]. Non-linear dynamic of the magnetic perturbations is compared with 'phenomenological' model in order to predict effect of the 'error' field on operation of the future tokamaks (ITER). Initial experiments with compensation of the error field and delay of the mode locking are analysed.

I. CONDITIONS OF THE 'LOCKED' MODES DESTABILISATION. Conditions of destabilisation of the MHD perturbations ('penetration' [2,3]) were studied in various plasmas at JET by application of DC and AC magnetic fields with increasing amplitude or sweeping frequency at the quasi stationary stage of the plasma discharges. Critical ('threshold') amplitude of the external magnetic field leading to destabilisation of MHD modes depends in a complicated way on the plasma parameters and geometry of the experiments. As in previous experiments [2,3], 'threshold' amplitude of the external DC field increases with the electron density in ohmically heated plasma (Fig.1a). 'Penetration' thresholds are smaller in plasma with low safety factor at the plasma edge (see also [4]). Increase of the 'penetration' thresholds in present experiments at JET with single null divertor (SND) in comparison with previous experiments with limiter configuration [4] can be associated with the reduction of the impurities (Z_{eff} <1.7) (see Fig.1b). Only small decay of the destabilisation threshold with auxiliary power was observed in experiments with RF heating (P_{rf} up to $10MW$), while application of the neutral beam injection leads to considerable increase of the 'thresholds' even at moderate auxiliary power (P_{nb}=2MW). Such increase is associated with fast rotation of the bulk plasma induced due to the toroidal momentum from the injected particles (see Fig.1c). Modification of the 'thresholds' in plasma with various toroidal magnetic field imbalance ('ripples') [1] is also correlated with different angular velocity of the bulk plasma rotation in respect to the external DC field (see Fig.1c).

Resonance dependence of the 'threshold' on the relative rotation of the external field and bulk plasma was also observed in the experiments with destabilisation of the rotating MHD modes by rotating external magnetic field (see Fig.1d). Magnetic AC fields with various

frequencies of rotation were applied in the experiments at similar plasma conditions in ohmically heated plasma [5].

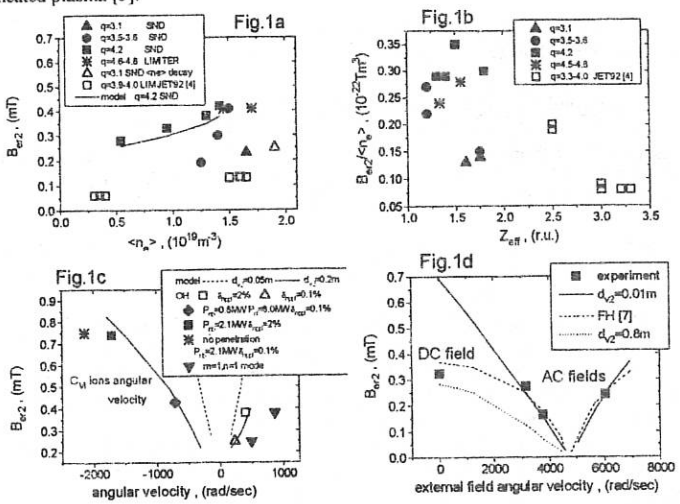

Fig.1. Locked modes 'thresholds' in JET

II. SIMULATION OF THE TEARING MODE DRIVEN BY THE EXTERNAL MAGNETIC FIELD. MHD perturbations driven by the externally applied magnetic field in JET are analysed with the use of single fluid 'phenomenological' MHD model [6] based on numerical studies of electromagnetic, inertial and viscous effects in rotated plasma, simultaneously with analysis of the magnetic field diffusion in viscous-resistive layer around the resonance surface [7,8]. Dynamic of the magnetic perturbations at the resonance surface entered two distinctive regimes [7] subject to the bulk plasma parameters and amplitude of the magnetic perturbations. In the non-linear regime [7] magnetic field perturbations are represented by single m=2,n=1 tearing mode rotating in the toroidal direction. Free boundary tearing mode stability parameter (Δ'_0) is calculated on the base of the current density profile determined from the magnetic equilibrium. Magnetic islands are entrained in incompressible 'phenomenological' viscous fluid [7] rotating in the toroidal direction. Parameters of the model were determined from the best fit to the experimentally observed behaviour of the MHD modes.

Model allows to describe experimentally observed 'thresholds' of the MHD modes driven by external magnetic field in various plasma conditions using the same set of free parameters [2,9]. Model also describes resonance frequency dependences of the driven MHD perturbations, growth of the 'threshold' with the electron density and dependence on power of the auxiliary heating and magnetic 'ripples'.

To clarify the predictions of locked modes dynamic in future tokamaks numerical model designed for analysis of the experiments at JET was used for simulation of the tearing modes stability in tokamaks DIII-D and Compass-C [2,3]. Analysis allows to establish the parameters of a phenomenological model for tokamaks of different size. Specified set of the 'free' parameters [9] is used for simulation of dynamic of the locked modes in tokamak ITER [10]. 'Penetration' threshold increases with frequency of rotation of the 'phenomenological' plasma fluid around the q=2 surface (see Fig.2a). For default set of the plasma parameters [2,9] 'threshold' becomes

higher than $B_{r2}/B_t(r=r_p)\approx 2\cdot 10^{-4}$ at frequency $\omega_{r2}(0)\approx 170Hz$ and 'reconnection' time scale $\tau_{rec2}=3.7$ sec ($\tau_{rec2}=\frac{2.1}{|\Delta'_0 r_{s2}|}\frac{\tau_H^{1/3}\tau_R^{5/6}}{\tau_V^{1/6}}$ [7]). However, present numerical simulations can not exclude very small 'penetration' threshold in ITER ($B_{r2}/B_t(r=r_p)\approx 2\cdot 10^{-5}$) if the 'reconnection' time is similar to one in present experiments in JET [$\tau_{rec2}=0.09$sec] (see also previous prediction [3,7]). Results of the analysis are summarised in Fig.2b using diagram introduced in [11].

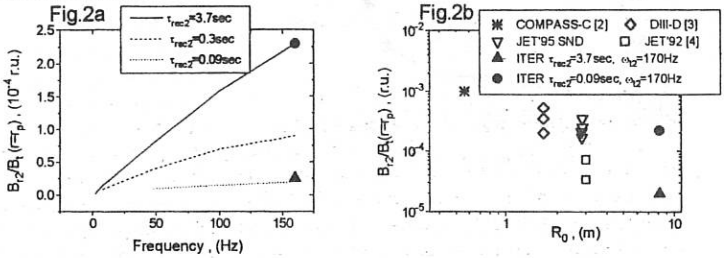

Fig.2. Simulations of the 'locked' modes thresholds in ITER.

III. PARTIAL COMPENSATION OF THE INTRINSIC ERROR FIELD AND DELAY OF THE MODE 'LOCKING'. Initial experiments were made in order to identify and partially compensate 'intrinsic' error field at JET. It was observed that in the similar plasma conditions destabilisation thresholds of the MHD modes differ up to 25% for different polarities of the currents in the saddle coils providing various angular orientation of the external field in respect to the 'intrinsic' error field (see Fig.3a.). This difference is equivalent to the 'error' field $B_{er2}\cong(0.75\div 1)\cdot 10^{-4}T$ at the 'equilibrium' q=2 surface ($R_0=2.90m$, $r_{s2}=0.7m$, $z=0.25m$, $k=1.4$), which is in agreement with results of numerical calculations [12].

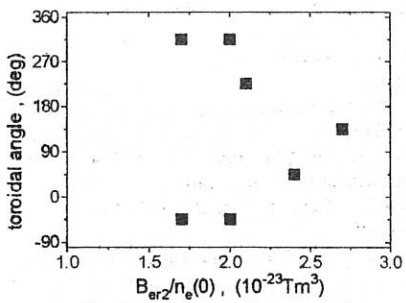

Fig.3a. Toroidal dependence of the locked modes 'threshold' in JET. Partial compensation of the 'intrinsic' error field is observed in the case at angular position around 135 degree.

Application of the rotating external magnetic field allows one to keep rotation of the MHD mode till at least two-three times larger amplitude of the magnetic perturbations than one of the 'natural' MHD mode (see Fig.3.b). Such enhancement is in agreement with the numerical simulations and demonstrates possibilities of application of the SC system for delay of the mode locking prior disruptions.

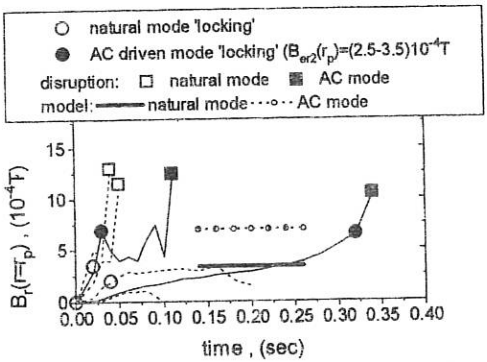

Fig.3b. Effect of the rotating external magnetic field on 'locking' of the m=2,n=1 modes in JET.

CONCLUSIONS. Application of the helical magnetic field perturbations in JET allowed to reveal conditions of destabilisation of the 'quasi-static' (locked) and rotating MHD modes in the reactor relevant plasma conditions. Non-linear dynamic model of the process is identified by comparison with numerical simulations. Numerical simulations predict a large variation of the 'threshold' of locked modes in future tokamaks ($B_{r2} / B_t \cong (0.1-3)\times 10^{-4}$) subject to the plasma parameters specified for the machines. The low 'threshold' value predicted for ITER under certain conditions will necessitate the use of active techniques for compensating error fields. Initial experiments demonstrated that partial compensation of the natural error field leads to increase of the locked modes 'threshold' up to 25%. Application of the rotating magnetic field allows to maintain rotation of the driven MHD modes up to two times larger amplitude of the magnetic perturbation than one of the 'naturally' destabilised modes and thus delay locking of the driven modes prior disruptions.

ACKNOWLEDGEMENTS. The authors would like to acknowledge fruitful discussions with many colleagues at JET and at AEA Culham Laboratory. We are grateful to P.Smeulders, P.Stott, and B.Tubbing for support of the experiments.

REFERENCES:

[1] Santagiustina,A., et al., (Proc. 22th Eur. Conf. Bournemouth, 1995), Vol.19C, IV-461.
[2] Morris,A.W., Carolan,P., Fitzpatrick,R., et al., Phys.Fluids 4 (1992) 413.
[3] LaHaye,R.S., Fitzpatrick,R., Hender,T.C., et al., Phys.Fluids B, 4 (1992) 2098.
[4] Fishpool,G.M., Haynes,P.S., Nucl.Fusion, 34 (1994) 109.
[5] M.DeBenedetti, et al, these proceedings.
[6] Savrukhin,P., et al. Transactions of Nuclear Science, 1996, A1.
[7] Fitzpatrick,R., Nucl. Fusion, 33 (1993) 1049.
[8] Lazzaro,E., et al., in Proc. of 15 Int. Conf. PPCNFR, 1994, IAEA-CN-60/D-P-II-6.
[9] Savrukhin,P.. S.AliArshad, D.J.Campbell, et al., To be published.
[10] ITER-JCT and Home Teams, Plasma Phys.Control.Fusion,27(1995) A19.
[11] The JET Team, Jet Report JET-R (95)05.
[12] Buttery,R.J., UKAEA report (1995), F/PL/WPA9.2a (unpublished).

IDENTIFICATION OF THE PHYSICAL MECHANISM OF LOW-M, N=1 MHD MODE CONTROL IN JET

M. De Benedetti[1], S. Ali Arshad, D. J. Campbell, G. D'Antona[2], A. M. Edwards[3], G. Fishpool, R. J. La Haye[4], E. Lazzaro[2], A. Santagiustina, F. Sartori, P. Savrukhin[5]

JET Joint Undertaking, Abingdon, Oxon, OX14 3EA, UK.

[1]Imperial College, London, SW7 2BZ, UK; [2]Istituto di Fisica del Plasma, Euratom-ENEA-CNR, 20123, Milan, Italy; [3]Culham Laboratory, UKAEA Technology, Abingdon, OX14 3DB, UK; [4]General Atomic, San Diego, California, USA; [5]Russian Research Centre 'Kurchatov Institute', 123182, Russia.

Introduction

Experiments have been performed in the JET pumped divertor to study the stability of plasmas in the presence of rotating applied fields and to investigate the possibility of stabilising disruptions by magnetic feedback control of the n=1 precursor mode.

Experimental Arrangement

The disruption feedback stabilisation system (DFSS) is based on a set of 4 saddle coils mounted inside the JET vacuum vessel, each consisting of 3 turns and covering approximately 90° toroidally and 60° poloidally (Fig. 1). Toroidally opposite pairs of saddle coils are coupled in an n=1 arrangement and each pair of coils is driven by an amplifier capable of operating in the range 0-1kHz at currents of up to 3kA, and in the range 1-10kHz at currents of up to 1/f kA/kHz. Low-m, n=1 rotating precursor modes are detected by a set of four pick-up coils, and a counteracting magnetic field is generated by the four saddle coils driven by the amplifiers with an appropriate amplitude and phase. A sophisticated digital controller, based on a set of six C40 processors, has been developed to integrate measurements from the magnetic pick-up coils and from Rogowski coils monitoring currents in the saddle coils. This controller, cycling at up to 200kHz, corrects the magnetic pick-up signals for known sources of error, such as the plasma response and vacuum vessel eddy currents, and calculates the amplitude and phase of the required currents in each pair of saddle coils.

Theoretical Basis

The theoretical framework on which the experiment is based is a modified version of Rutherford's theory for the growth of a magnetic island. The island time evolution is given by the well known equation: $\dot{w} = \eta\Delta'/\mu_0$. For the control to be effective we require that $k \geq r_s\Delta'/2m$, where k is the ratio of the island magnetic field and that produced by the feedback system at the resonant surface (gain of the loop)[1].

Experimental Details

A typical diverted equilibrium in JET has minor radius a=1.05m, vertical displacement Z_0=0.3m, elongation k=1.6, radius of the q=2 resonant surface r_s=0.75. A numerical code has been used to calculate the vacuum magnetic field components produced by JET saddle coils when the shape and position of the resonant surface is changed. m=2 magnetic fields on the resonant surface in the range $0.8 \div 2 \times 10^{-4}$ T are expected. Many different poloidal components are generated. Note that for

rotating fields, the interaction with the wall reduces the field amplitude by about 40% and changes their phases with respect to the DC field.

In addition, the presence of a plasma column changes the detected magnetic field at the wall. This so-called 'plasma response' (Fig. 2) is a strong function of the equilibrium parameters of the plasma. However, it is found that the response in JET is independent of the driving frequency of the external fields while it is linearly proportional to the amplitude of the saddle coil current. Observations are consistent with a simple theory based on the assumption that each surface reflects the magnetic field component with which it is resonant.

Production of Rotating Tearing Modes

Rotating tearing modes can be induced in the plasma by applying a rotating magnetic field. Such modes are locked to the external field frequency and reach an amplitude which is at least 3 times larger than naturally growing tearing modes before locking to the wall[4]. The threshold of mode generation is a function of the driving frequency and has a minimum around the natural frequency of the mode in the plasma, as expected on the basis of Hender-Fitzpatrick theory[2].

Feedback Control of Tearing Modes

Initial experiments on the feedback stabilisation of naturally growing tearing modes were performed during the MkI divertor campaign. The applied current during these experiments was, however, severely limited, to approximately 30% of the design value, to avoid the possibility of electromagnetic resonances causing damage to the saddle coils. This limitation will be substantially eased in the future due to strengthening of the saddle coils and to improvements in the saddle coil protection system.

The feedback control loop was initially closed in vacuum to investigate the intrinsic stability of the system. and oscillations (even at low loop gains) were seen at around 13kHz. This instability, which is due to the poor feedthrough compensation for high frequencies, can be prevented by filtering of the signals and by careful feedthrough compensation.

The loop was subsequently closed in the presence of naturally growing tearing modes which preceded density limit disruptions (Fig. 3). The controller generated fields with the correct phase and amplitude, indicating that the controller logic operated correctly and that the various corrections had been implemented properly. However, the magnetic islands usually grew too fast and locked before the precursor could be stabilised - it is not expected that the feedback control system will be powerful enough to suppress modes once they have grown to a sufficient amplitude for locking to the vessel wall (several Gauss in JET). A first estimation of the instability parameter Δ' and of the loop gain $2mk/r_s$ (Fig. 4) confirms that in the pulses studied an increased current capability, together with early detection of the growing islands, would be required to permit suppression of the precursor mode. Besides, with the present limitations in the system design, the modes were not controlled in speed and thus locking could not be prevented.

Modelling of Feedback Stabilisation Experiments

A numerical model[3] of the feedback control system, including a realistic model of the evolution of the internal mhd mode in the presence of externally applied fields, has been developed and detailed simulations of the control system have been performed. They reproduce with good accuracy the real behaviour of the system and can give useful information about the efficiency of the control. For

example, In shot 35221 the natural growth rate of a magnetic island changed abruptly when the feedback was switched on. Comparison of real signals with simulated ones suggests that, being the mode close to saturation, the feedback gain was actually big enough to completely stabilise the island .

Conclusions

Initial experiments with the disruption feedback stabilisation system in JET have allowed many aspects of the physics of magnetic island evolution in the presence of externally applied fields to be investigated. In addition, the operation of the control loop has been explored and phenomena such as the vacuum feedthrough and plasma response have been quantified. Analysis of these first experiments indicates that the control loop functioned correctly, but that limitations in the power capability of the system, related to the mechanical stresses in the saddle coils, prevented the system from stabilising disruption precursor modes. Simulations of the operation of the control loop using a numerical model have yielded insight into the physics of the control problem and should allow an understanding to be developed of the role of various processes in determining the behaviour of magnetic islands during feedback stabilisation experiments.

On the basis of the operating experience, the control system has been substantially upgraded in advance of the forthcoming experimental campaign. An improved protection system has now been installed which should permit the system to reach its full current capability of 3kA. In addition, improvements in the trigger logic of the controller should allow modes with an amplitude of only 20μT at the vessel wall to be detected, a substantial improvement over the present detection threshold of 50μT. As a final significant improvement, the upgraded controller will be able to control not only the mode amplitude but also its rotation frequency, and this will provide an important additional feature to increase the likelihood of achieving mode stabilisation. Overall, the disruption feedback stabilisation system should prove a powerful tool, not only in addressing the question of disruption control, but also in studying the physics of tearing mode evolution in tokamak plasmas.

References

1. Lazzaro E., Nave M.F., Phys. Fluids, **31** (1988) 1623.
2. Fitzpatrick R., Nuclear Fusion, **33** (1993) 1049.
3. Savrukhin P. et al., Numerical simulations of feedback control of coupled tearing modes at JET, Jet internal report JET-R(95)06.
4. Savrukhin P.et al., Effect of the error fields on plasma stability in JET and ITER, this conference.

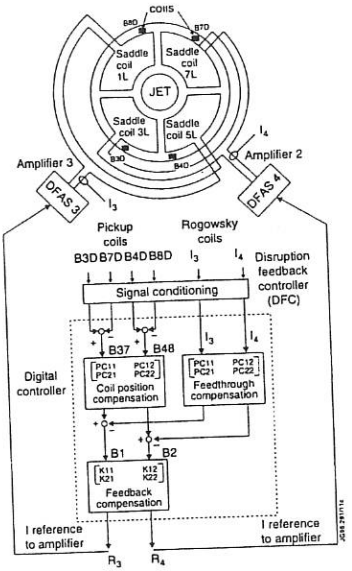

1. Scheme of the control system. Input signals from four pick-up coils and two Rogowsky coils are processed by a digital controller which drives two fast high-power amplifiers, each connected to a pair of saddle coils placed in the bottom of the vessel. The digital controller subtracts the feedthrough compensation from the detected signals and generates two reference signals proportional to the island magnetic field.

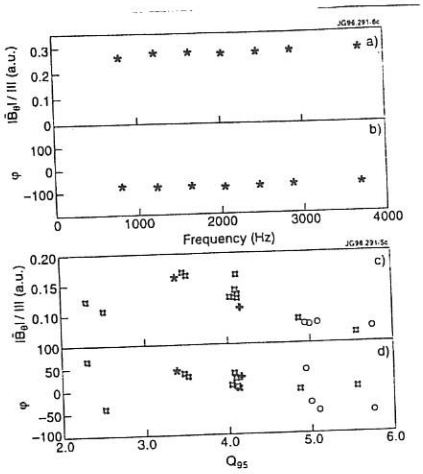

2. Measurements of the fast plasma response defined by the ratio of the reflected field measured at the outer limiter surface and the saddle coil current. a,b) Plot against the driving frequency: the response is independent on the frequency within the accuracy of the measurements. c,d) Phase and amplitude are plotted against the edge safety factor q(a). Points are scattered because the response is strongly dependent on the detailed equilibrium properties of the plasma.

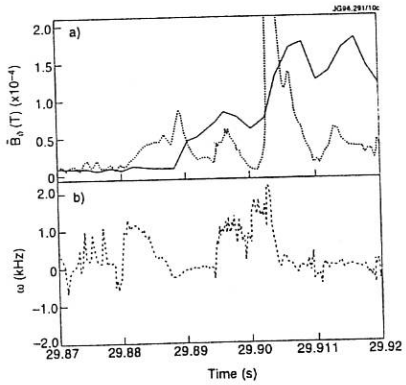

3. Feedback control in the presence of a magnetic island. a) $|\tilde{B}_\vartheta|$ at the wall (dotted), applied feedback field (solid). b) Estimated mode frequency ω. An island is present when ω is in the range 500-1500 Hz. The loop is closed at 29.89. The island grows too fast for the control loop.

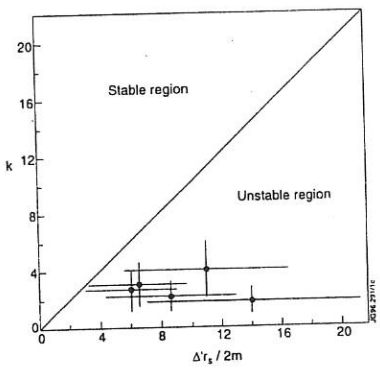

4. Stability parameters Δ' plotted vs. $2mk/r_s$ for a series of discharges in which intrinsic modes were observed. Large error bars are due to large uncertainties in the measurements of the resistivity and of the growth rates of the modes. There is no clear evidence of disruption stabilisation.

ICRH in Hot-Ion H-modes in JET

G.A.Cottrell, C.Gormezano, A.Howman, T.Jones, P.J.Lomas, F.Rimini, R.Sartori, G.Sips, D.F.H.Start

JET Joint Undertaking, Abingdon, Oxfordshire, OX14 3EA, U.K.

In JET the NBI-produced ELM-free hot-ion H-mode plasma has generated the highest DD fusion reaction rate (R_{DD}) and therefore represents one of the leading modes for high fusion performance in the next DT phase of operations. The work presented here examines the role of adding ICRH to hot-ion H-mode plasmas.

RF IN HOT-ION H-MODES

The plasma has triangularity $\delta \equiv 0.25$, expanded flux surfaces in the divertor and low recycling - conditions not optimised for ICRH coupling. Two discharges in Fig.1 had central ion temperatures $T_{i0} > 20$ keV and were pre-heated by similar LHCD powers to drive off-axis current, maintaining $q(0) > 1$, and suppress sawteeth prior to the main heating phase [1]. Pulse No. 34454 had both ICRF (6MW) and NBI (17MW) heating. ICRH was in the H-minority regime with near-axial resonance. The NBI-only reference (Pulse No. 34443), was heated with 16 MW. The discharges terminate by an ELM and sawtooth collapse. ICRH enhances R_{DD} as well as total plasma energy content - the latter is due to the increased heating power, an increased thermal confinement time, and the energy content of the ICRH fast ions. The fast ion content has been subtracted from the measured energy to estimate the thermal energy. The thermal confinement time was normalised to the ITERH93-P scaling law to derive the H-factor: $H = \tau_E/\tau_{93}$ where:

$$\tau_{93}\,(\mathrm{sec}) = 0.035\,(I_p/\mathrm{MA})^{1.08}\,(n/10^{19}\mathrm{m}^{-3})^{0.17}\,(B_T/\mathrm{T})^{0.32}\,(Q_L/\mathrm{MW})^{-0.67}(R/\mathrm{m})^{1.79}\varepsilon^{-0.11}\kappa^{0.66}M^{0.4}, \qquad (1)$$

and Q_L is the heat flux across the boundary. Fig. 2 shows the thermal H-factor is up to 30% larger during the combined heating case. The TRANSP code was used to analyse the improvement in global confinement. At t = 16.7s and in the interval ($0.3 < r/a < 0.7$), there are similar values of electron thermal diffusivity; $\chi_e \sim (0.5 \pm 0.25)$ m^2 s^{-1} for both pulses, values typical of those in JET hot-ion H-modes. Thus the enhancement in the global confinement found when ICRH was added cannot be explained by a change in χ_e. However the ICRF heating profile is more peaked than that of the NBI. About 85% of the total ICRH power is found within r/a = 0.4 whereas only 45% of the total NBI power is found in that region. We expect the more centrally condensed ICRH power deposition to increase the H-factor by only ~10% compared with the 30% measured increase. A model [2] which agrees with the experimental results is

based on a neo-classical boundary condition at the separatrix, representing an edge transport barrier and is derived assuming the energy loss is related to direct losses of trapped ions. Q_L (= kn_a^2) is independent of the edge plasma temperature and is constant for constant edge density and,

$$dW/dt = P - Q_L \qquad (2)$$

For constant n_a, and input power P, $W = W_0 + (P-Q_L)t$, where W_0 is the energy content at the time of barrier formation. Thus both W and τ_E [= W/(P-dW/dt)], increase linearly with time: $\tau_E = \tau_0 + (P/Q_L - 1)t$ where $\tau_0 = W_0/Q_L$. Since Q_L is constant, we see from Eq.(1) that τ_{93} is only weakly dependent on time through the density evolution and predict that H should increase approximately in proportion with time. Moreover dH/dt depends on applied power,

$$dH/dt = (1/\tau_{93})\,(P/Q_L - 1). \qquad (3)$$

In Pulse No. 34454, we estimate $Q_L \sim$ 10MW and calculate the fractional increase in dH/dt produced by ICRF finding the H-factor should increase ~1.4 times more rapidly than in Pulse No. 34443, in agreement with the observed ratio of ~1.3 of the slopes in Fig.2.

To exploit the potential benefit of this configuration, further optimisation is required. If we rate the performance of 3MA hot-ion H-modes in terms of R_{DD}, pulse No. 34454 ranks highly at 70% of the best performing 3MA discharge. This latter pulse was with NBI only and achieved its performance because the ELM-free period persisted for over twice as long. With lower recycling and improved stability [3], NBI can produce higher performance than in Pulse No. 34443. Adding ICRF/LHCD can certainly improve performance of the best NBI plasmas further, provided the ELM-free period is maintained, by optimising shear at the edge which normally decreases at low internal inductance.

HIGH ELECTRON TEMPERATURES

A record central electron temperature of T_{e0}= 15keV has been produced by RF + NBI heating in a hot ion H-mode (Fig.3). The H-mode was produced by 9MW of NBI which was progressively stepped down whilst the RF power was ramped up to 4MW. As a result, both the stored energy and the density reach stationary values during the H-phase. T_{e0} reached 15keV when $n_{e0} = 4 \times 10^{19}m^{-3}$ and T_{i0} = 12keV. H = 2.5 - 3 depending on whether the fast ion energy content is included. T_{e0} is plotted in Fig. 4 for hot ion and RF H-modes in 3MA triangular configurations and for RF-H-modes in 2.5MA discharges that simulate the JET "gas box" divertor configuration. For the hot ion cases, the data lie in the same region as those from pellet enhanced performance H-modes (PEP + H) and hot electron modes obtained in the 1991/92 experimental campaign. Fig. 4 also shows, for comparison, the scaling of T_{i0} with P_{NBI}/n_{e0}. Similar values of T_{e0} and T_{i0} are obtained for the same values of P/n_{e0} implying similar core values

of χ_e and χ_i. In 3MA, RF-only H-modes, T_{e0} increases linearly up to $P_{RF}/n_{e0} = 3 \times 10^{-19}$ m^3 MW. Above this, T_{e0} increases less rapidly possibly either due to fast ion orbit broadening of the electron heating profile or an adverse scaling of χ_e with temperature. A non-linear behaviour is evident in the 2.5MA "gas box" divertor data in which T_{e0} saturates at 9keV. TRANSP radial profiles of χ_e for the RF H-mode Pulse No. 34046 and the hot ion H-mode, Pulse No. 34242, at the time of maximum T_{e0} shows that, for the hot ion H-mode, χ_e is about half that in the RF H-mode. In the 2.5MA "gas box" divertor plasma with the highest P/n_{e0}, χ_e ($r/a = 0.3$) ~ 3m^2/s or about twice as large as that for the RF H-mode. For the hot ion H-mode χ_i ~1.5 χ_e. As T_e (and β_e) increase, the fraction of power absorbed by the electrons - by electron Landau damping + TTMP - also increases. This concentrates the power deposition in the core, ameliorating the orbit-broadening of the MeV fast ion heating profile. β_{e0} is a factor of two greater in the hot ion H-mode compared with the RF-only H-mode case. In Pulse No. 34242 the direct electron damping is 15% of the input power compared with 6% in Pulse No. 34046. A variation amongst the 3MA discharges was Pulse No. 35297 in which 5MW of ICRH with resonance ~ 0.3m on the high field side produced T_{e0} = 10keV at $n_{e0} = 2.7 \times 10^{19}$m^{-3}. This T_{e0} is higher than those obtained for the same P/n_{e0} with axial resonance in the 3MA RF-only H-modes (Fig. 4). TRANSP shows a core χ_e value similar to that for the hot ion H-mode and about half that for the RF-only H-mode.

SUMMARY AND CONCLUSIONS

The injection of fast waves into 3MA hot ion H-modes has increased the normalised thermal energy content by up to 30% compared with that achieved by beam heating alone. TRANSP analysis has established that there is no change in the thermal diffusivity. The enhancement is too large to be produced by the centrally localised nature of the ICRH alone, but is consistent with an interpretation in terms of an edge confinement barrier which maintains an energy loss independent of the plasma energy content. With this model, the H-factor increases with time at a rate which increases with the input power.

Central electron temperatures of ~ 15keV have been obtained in both RF-only and hot ion H-modes, close to the anticipated electron temperature in ITER at ignition, namely T_{e0} = 19keV. The temperature gradient and the electron toroidal beta are similar to the expected values in ITER, but the density in JET is three times lower. These data indicate that ICRH is an effective heating method - especially when its basic advantages - central heating independent of density and no fuelling at the edge - are fully exploited.

REFERENCES

[1] Ekedahl, A., et al. this conference

[2] Bak, P. et al, JET report JET-P(95)09, submitted to Nuclear Fusion.

[3] The JET Team, Plasma Physics and Controlled Fusion, 37 (1995) p. A359 - A370

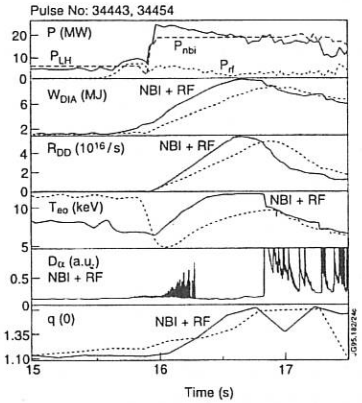

Fig.1. Parameters for two similar NBI hot ion H-mode plasmas (I_p = 3MA, B_T = 3.1T, q_{95} = 3.9) with (solid lines) and without ICRH (dashed lines)

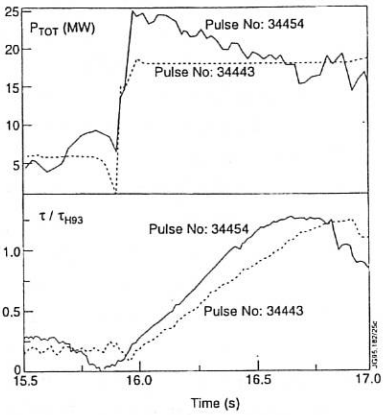

Fig.2. Upper: total power and lower: variation of normalised thermal H-factor for NBI and NBI+ICRH pulses hot ion H-mode plasmas of Fig.1.

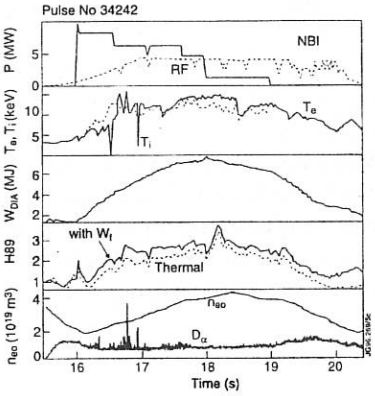

Fig.3. Variation of plasma parameters for a high central electron temperature discharge

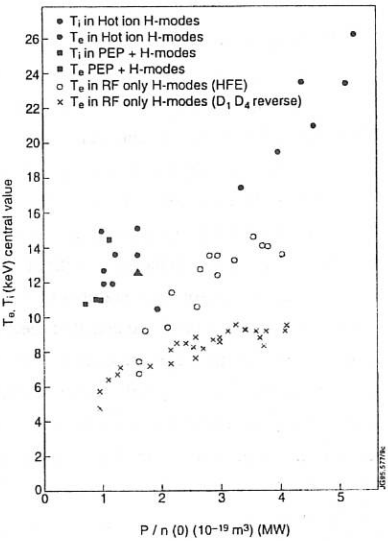

Fig.4. Central ion and electron temperatures versus applied power per particle: P/n.

A DESCRIPTION OF ELM-FREE H-MODES IN TERMS OF A NEOCLASSICAL EDGE BARRIER AND A 'MIXED' MODEL FOR ENERGY AND PARTICLE TRANSPORT

A. Cherubini, B.Balet, N. Deliyanakis, M. Erba, R.Giannella, N.C. Hawkes, V.V. Parail, L. Porte, A.Rookes, E. Springmann, A. Taroni

Jet Joint Undertaking, Abingdon, OX14 3EA, UK

INTRODUCTION:

High performance in JET ELM-free H modes appears to be related to the edge temperature, which can reach several *keV*'s, contributing up to half of the stored energy. A model to compute these edge values must then be given in order to predict plasma confinement. The existence of a neoclassical transport barrier was assumed in *[1]*: transport inside the separatrix is reduced to ion neoclassical values on a width scaling with the ion poloidal Larmor radius $\rho_{\theta i}$. In this work we extend that model to include plateau effects, and most importantly include particle transport, using the JETTO transport. Particle confinement and recycling conditions are shown to be crucial factors for energy confinement and the evolution of the discharge, as observed in experiments.

ENERGY TRANSPORT MODEL IN THE CORE PLASMA:

We use a 'mixed' transport model *[2]*, which combines a gyroBohm ($\chi_{gB} = c_{gB}\sqrt{T_e}\,\nabla T_e / B_T^2$) and a Bohm-like term ($\chi_B = c_B(\nabla P_e / n_e B_T) q^2 a^2 < \nabla T_e / T_e >_{\rho>0.8}$):

$\chi_e = \chi_B + \chi_{gB}$

$\chi_i = 2\chi_B + \chi_{gB} + \chi_{neo,i}$

This model can be used to describe both L and H modes, due to the non local dependence of the Bohm-like term on $L_{T_a}^{-1} \equiv < \nabla T_e / T_e >_{\rho>0.8}$, the electron temperature scalelength averaged in the outer 20% of the radius, excluding the transport barrier.

EDGE TRANSPORT BARRIER:

We assume that in H modes, free from ELMs or other MHD activity, all transport coefficients are reduced to ion neoclassical values, on a width $\sim\rho_{\theta i}$ inside the separatrix. In the banana regime, relevant to JET high performance shots, the heat loss from the edge then scales as: $Q_{neo} \sim n_a \chi_{i,neo} T_a / \rho_{\theta i} \sim Z_{eff}\, n_a^2 / I_p$, and particle losses as $\Gamma_{neo} \sim Q_{neo} / T_a$.

An important energy loss term is due to charge exchange with cold neutrals: $P_{CX} \sim \Gamma_0 T_a$, where Γ_0 is the neutral influx from the edge. We write $\Gamma_0 = \Gamma_{neo} + S^*$, with S^* taking into account any sources in addition to the 100% recycling. When S^* is small compared to the outgoing flux Γ_{neo}, then $P_{cx} \sim \Gamma_{neo} T_a$ and so total energy losses will retain the neoclassical scaling. Additional energy losses due to radiation P_{RAD} are included in the simulations, but are often negligible.

The scalings change when the edge approaches the plateau regime, when $\nu^* > 0.1$. The energy losses are not independent of T_a anymore: $Q \sim n_a T_a^2$, and a pedestal saturation is expected.

From the given scalings some conclusions can immediately be drawn.

a)The best confinement will require low edge density, and low recycling conditions (wall conditioning).

b) Steady state can be reached only in three ways: stepping down the input power P; increasing n_a up to $\sim\sqrt{P}$; elming or other additional energy losses (e.g. increased radiation).

c) While n_a remains low (i.e. heat loss $Q \sim n_a^2$ small compared to P), a situation of near thermal runaway is created, with $\dot{W} \sim P\text{-}Q$. Typically both W and T_a rise on a timescale faster than n_a, so the plasma hits a local β-limit (e.g. ELM, 'slow roll over', etc.) before reaching steady state. This is typically the case of JET high performance discharges.

In the JETTO code the transport barrier can be simulated in two ways. Either it can be taken into account explicitly, reducing all transport coefficients appropriately on a few mesh points close to the separatrix, or the neoclassical fluxes can be imposed as Neumann boundary conditions, thus solving the transport equations only up to the transport barrier. The two methods have been shown to be equivalent (see later), but the former allows coupling with SOL codes, as EDGE2D *[3]*, and thus further validation against SOL measurements.

Semipredictive simulations, i.e. imposing the density profile from measurements, have been initially used to check some of the dependencies predicted by the model. A series of discharges was performed scanning density and current and optimizing the configuration for edge measurements. All relevant plasma characteristics were successfully reproduced, even for shots with the edge approaching the plateau regime. These simulations support the dependencies of the model on current and collisionality, but given the importance of n_a, modelling of particle transport is required.

FULL ENERGY AND PARTICLE SIMULATIONS OF ELM FREE H MODES:

The NBI particle deposition profile is a very important ingredient in the analysis. This was obtained from the TRANSP Montecarlo package. The source profile of edge cold neutrals is computed by the code FRANTIC, with the total influx given by $\Gamma_0 = \Gamma_{neo} - S^-$. When simulating an experimental discharge, S^- can be imposed to reproduce the total particle content.

We describe the particle flow by using only an 'effective' diffusion term: $D_{eff} = f(\rho)\chi_e \chi_i / (\chi_e + \chi_i)$. The radial function $f(\rho)$ was chosen in one of the shots in order to reproduce the shape of the measured density profiles and the magnitude of Γ_0, and then kept constant in different shots. It turns out that in order to reproduce the experimental density profiles $f(\rho)$ must decrease from $f(0) \sim 1$ to $f(1) \sim 0.1$, though its exact form cannot be precisely determined (linear was used). This result can be interpreted as an indication for the existence of an inward pinch localized in the outer region of the plasma, in agreement with similar results from ohmic mode*[3]*.

All the main experimental measurements of hot-ion H modes have been satisfactorily reproduced, when S^- is given as above. Typical density and temperatures profiles computed for a very high performance shot are

given in *Fig.1,2*, together with experimental ones. Relevant time traces are given in *Fig.3*. The neutral flux Γ_0 grows up to ~2 $10^{21} s^{-1}$, in good agreement with the SOL modelling and measurements *[4]*.

To study the effect of recycling conditions we have scanned S^*, and run the simulations for a time longer than the experimental MHD-free period (usually <1.2 *s*). *Fig.4* shows the predicted time evolution for the stored energy, fusion reaction rate, and neutral influx: increasing S^* causes higher n_a and lower T_a, leading to an increase in Γ_{neo} (and so Q_{neo}) even bigger than S^* itself.

It is clear that low recycling is essential to high performance. Higher neutral influx will induce lower pedestal temperatures and increase transport everywhere, via $L_{T_a}^{-1}$. Natural saturation and even degradation of the high confinement phase is observed (*Fig 4*), because n_a grows in time ~linearly and so energy losses with $\sim r^2$, but the timescale on which saturation appear depends on recycling conditions, and it can be longer than the MHD free period.

The degradation of confinement can also be caused by an impurity influx: the increase in edge Z_{eff} enhances Γ_{neo}, and hence both Q_{neo} and P_{CX}, reducing pedestal and confinement (the increased radiation will also play a role). This effect can be used to simulate experimental confinement degradation ('slow roll over'), assuming a trigger event (MHD) to increase Z_{eff}.[5]

CONCLUSIONS:

The neoclassical transport barrier coupled with the 'mixed' transport model provides a reasonable description of the ELM-free H-mode. The scalings for energy and particle losses have been derived and tested in numerical simulations of experimental discharges.

Simulation of particle flows requires an 'effective' diffusion decreasing towards the edge, a possible indication for the existence of an inward pinch strongly growing in the outer region.

Energy and particle transport in hot ion discharges have been successfully simulated, including the prediction of pedestal values. High confinement is achieved when the energy losses through the barrier are small thus leading to high pedestal values, this in turn reduces the transport coefficients throughout the plasma.

The main energy losses are the predicted neoclassical heat losses and charge exchange with cold neutrals. Low recycling (wall conditioning) and low impurity content prove to be the main factors required to maintain the small energy losses necessary for high confinement.

REFERENCES

[1] M.Erba et al., proc. of 22nd EPS Conf. on Contr.Nucl.Fus.& Pl.Phys., Bournemouth,1996, pII-213

[2] V.Parail et al., JET-P(95)49, to be published in Pl. Phys. and Contr. Fus.

[3] A.Taroni et al., this conference.

[4] G.K.McCormick et al., 12th PSI Conference, St.Raphael, France, 20-24 May 1996.

[5] H. de Esch et al., this conference.

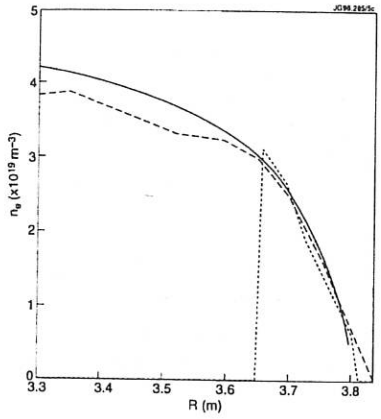

FIG.1 Computed (full line) density profile vs LIDAR(dashed) and reflectometry(dots), shot 33643, at t=53. Note no discontinuity in gradient at the barrier (R>3.75~m). Reflectometry provides reliable information close to the boundary.

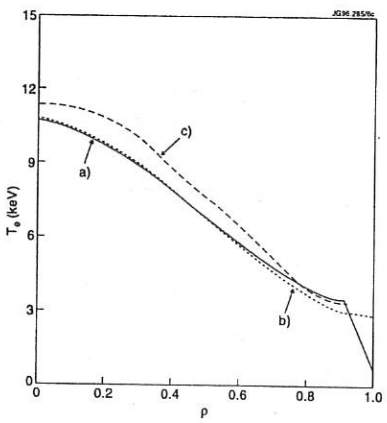

FIG.2 Profile comparison at t=53 of measured (LIDAR, trace **c**) and computed T_e profiles, shot 33643. Trace **a** is computed imposing the barrier explicitly: the change in slope is clearly visible. Trace **b** was computed with the barrier imposed as Neumann boundary condition.

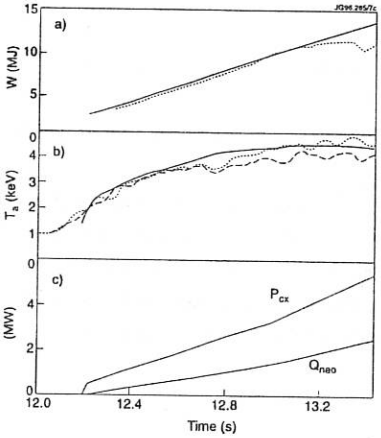

FIG.3 Measured and computed time traces for #33643. Note that experimentally the discharge suffers a 'slow roll over' at t~53.2, followed by a giant ELM. **a)** thermal energy (full line is simulated) **b)**Edge ion temperature. Full line is simulated, the others are from charge. **c)** Simulated heat losses: full line is total neoclassical losses Q_{neo}, dotted line is charge exchange losses to cold neutrals, P_{CX}. Note the importance of P_{CX}, that nonetheless remains proportional to Q_{neo}.

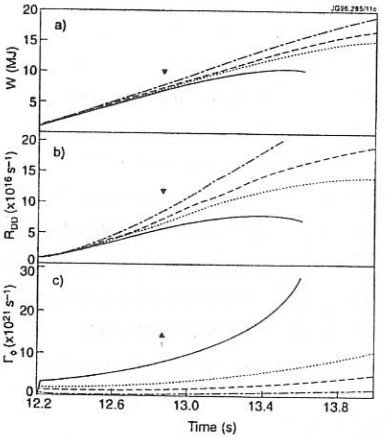

FIG.4 Scan in S^* =0,0.5,1,2 x10^{21}. **a)** energy content **b)** fusion reaction rate R_{DD} **c)** cold neutral influx from edge Γ_o. The arrow indicates increasing S^*.

Variation of Impurity Transport During ELMy H-modes in JET Plasmas

M G O'Mullane[1], H Chen[2], C Flewin[3], N C Hawkes[4], M von Hellermann, L Lauro-Taroni, N J Peacock[4]

JET Joint Undertaking, Abingdon, Oxon., OX14 3EA, UK

[1]University College Cork, Ireland, [2]Imperial College, London, UK, [3]University College, London, UK, [4]UKAEA Fusion, Culham, Abingdon, Oxon., UK (EURATOM-UKAEA Fusion Association)

Introduction

H-mode confinement is breached by Edge Localised Modes (ELMs) expelling particles and energy. One of the features of radiative divertor experiments is the appearance of giant ELMs followed by a series of smaller, grassy, ELMs. These 'compound' ELMs are then followed by a period of quiescent H-mode. The effect on impurity profiles of compound ELMs can be interpreted in terms of a time varying transport model. The effect of the ELMs is seen in the Ne^{10+} distribution inside the transport barrier [1]. During the H-phase an increase of the more highly stripped ions (e.g. Ne^{10+}), inside the transport barrier is accompanied by depletion of lower charge states (e.g. Ne^{5+}) outside the barrier and in the scrape-off layer. The build-up of ion pressure at the transport barrier during this phase is eventually terminated by the ELM. The JET charge exchange diagnostic of edge impurities has been absolutely calibrated. Its space resolution of ~1cm over the 10cm edge region is used to examine changes in the edge impurity profiles in detail. The time behaviour of the transport during ELMy H-mode and its variation as the ELM frequency increases are examined.

Charge Exchange Measurements of Impurity Density at the Plasma Edge

The JET edge charge exchange diagnostic (ECX) consists of two sets of opposing viewing chords positioned above and below the magnetic axis intersecting the neutral beams. The time resolution of the instrument is determined by photon statistics; with the large impurity densities of neon used in these experiments (~1.5% of n_e) the uncertainties are relatively low and the time resolution is 20ms or better. Interpretation of the measured intensities involves detailed consideration of the geometry and the neutral beam deposition characteristics.

The H-mode model is characterised by a narrow region of inward convection at the plasma edge – the transport barrier. The location of the barrier is determined by the change in slope of the ion density or ion pressure profiles. The T_i profile does not respond to the ELMs but the density gradient alters significantly [2]. The location of the barrier for an ELMy H-mode

discharge is not affected by giant ELMs. In general it remains located at ~7cm inboard of the last closed flux surface (LCFS), as calculated by the equilibrium reconstruction code.

Charge exchange measurements from the main plasma have shown that the light ($2<Z\leq10$) impurities do not accumulate on-axis in H-mode but are peaked at r/a~0.75-0.82 [3], with carbon and neon peaking at the same radius. The ECX measurements confirm the steep gradients at the outer part of the bulk measurements. The off-axis accumulation may be due to a centrifugal contribution to the convective transport as a result of the plasma rotation which is driven by the neutral beam torque. Phenomenologically this requires an outward convection in the model.

Time Dependent Transport Modelling

The SANCO 1.5-D impurity transport code has been used in all simulations. Particle transport is described by diffusive and convective terms with the flux of each ionisation stage given by coefficients which are a function of flux surface (Ψ) and time,

$$\Gamma_z = -D(\Psi,t)\nabla n_z + V(\Psi,t)n_z.$$

The transport functions (D,V) are changed until the transport is consistent with experiment. A limitation of the code is that it is not a closed description of the impurity evolution. The source function of the influx is based on a peripheral ion stage. SANCO uses experimentally measured T_e and n_e profiles. To follow the temperature evolution, fast ECE radiometric measurements of the electron temperature profile, with spatial resolution ≥1cm, at the edge, and temporal resolution ≥1ms, are employed. The density profiles are from LIDAR measurements.

The behaviour of intrinsic carbon shows the time evolution of the change in impurity profiles following the L-H transition and the build-up of impurities in quiescent H-mode. The transition is simulated by an abrupt change in transport at a time determined by the drop in Dα. The width and depth of the barrier were adjusted until there was agreement between the simulated and experimental C^{6+} ion densities (Figure 1). The simulations were constrained to match the absolute CIII emission. The experimental observations of a steady ramp-up of C^{6+} inside the transport barrier and a near constancy outside arise naturally from the simulations.

In ELM-free H-mode there are no gross disparities, in the time evolution of impurity emission, between the main vessel and the divertor. In ELMy H-mode the source of intrinsic impurities, such as carbon, becomes localised and the SANCO model of a symmetrical influx is no longer strictly applicable. In a radiative divertor discharge the gas puffing provides a steady source of impurities. The source term is based on the NeVII ($2s^2$ – 2s2p 465.22Å) line since NeVII radiates entirely in the SOL.

Compound ELMs are very suited to studying variations in the transport as they are well spaced. Figure 2 shows the time evolution of Ne^{10+} for a number of chords either side of the transport barrier (at R=3.68m, LCFS at 3.75m). The simulated radial profiles match the

experimental profiles across the barrier. In the model the transport is switched from H-mode at the onset of the ELM and remains so for the duration of the grassy ELMs. The transport coefficients used are shown in Figure 3. The simulations show that the convective transport barrier (~1-2cm wide) remains in place during ELMs and the degradation in confinement is from enhanced diffusion only. The increased diffusion is localised to a ~5cm zone inside the LCFS and extending into the SOL. The model predicts a threshold diffusion and a sensitivity to the height of the convective barrier. A diffusion greater than 1.0 m^2s^{-1} at the edge is sufficient to simulate the Ne^{10+} profiles. The barrier sets a minimum velocity for outfluxing impurities with $V(r=a) \sim 15 \pm 2$ m s^{-1}.

Time Independent Transport Modelling

With increasing ELM frequency the recovery of the H-mode phase is rapid and an average, or time independent, transport applies. The time variations in transport are smeared out for grassy ELMs and an average transport during the H-mode applies. A long impurity confinement time is one of the characteristics of H-mode. A series of laser ablation experiments were undertaken to measure the Z-dependence of particle confinement time in ELMy H-modes and in Ohmic plasmas. Figure 4 shows the decay times. There is a slight (~20%) increase in confinement in ELMy H-mode compared to ohmic discharges but this is significantly shorter than ELM-free H-mode where up to 4s has been observed. The confinement was found to be independent of Z.

Conclusions

A model of impurity transport during H-mode shows that the losses caused by compound ELMs are diffusive, suggesting a stochastic model of the ELM. The enhanced diffusion zone extends ~5cm inside the LCFS. Giant ELMs do not breach the convective barrier. Absolutely calibrated measurements of the impurity profiles at the edge have been simulated. The position of the transport barrier does not vary in time. With increasing ELM frequency the confinement degrades although the transport barrier remains. In general during discharges with grassy ELMs an average, time independent, transport is successful in modelling the spectroscopic observations. There is a modest increase in impurity confinement time for this type of H-mode over Ohmic plasmas.

[1] M G O'Mullane *et al.*, 22nd EPS Conference, III-121 (1995)

[2] N C Hawkes *et al.*, 22nd EPS Conference, III-261 (1995)

[3] M von Hellermann *et al.*, 22nd EPS Conference, II-9 (1995)

ACKNOWLEDGEMENT This work was partially funded by the UK Department of Trade and Industry and EURATOM.

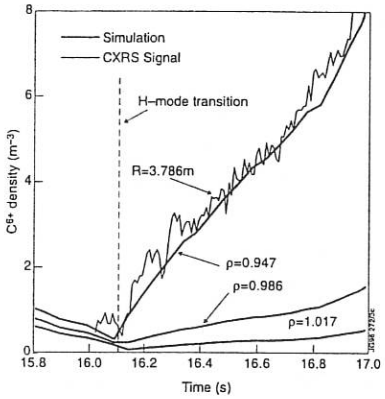

Figure 1 Time dependent transport simulation of fully stripped C^{6+} during the L-H transition. The near constancy of impurities in the SOL and the steady ramp-up inside the barrier are consequences of the switch in transport.

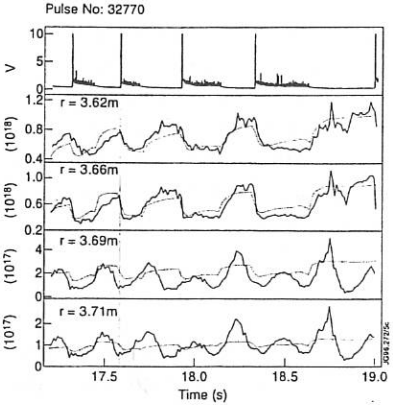

Figure 2 Time evolution of Ne^{10+} inside and outside the transport barrier. The difference between the simulations and measurements in the extreme outer chords arises from the plasma being swept across the divertor which introduces a periodic variation in the SOL position.

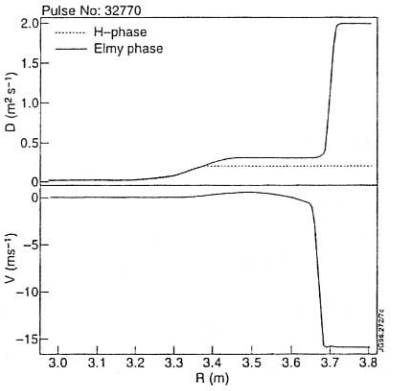

Figure 3 Transport profiles used in the simulation of Ne^{10+} ion profiles during ELMy H-mode. The barrier is at R=3.68m and the LCFS is at R=3.75m.

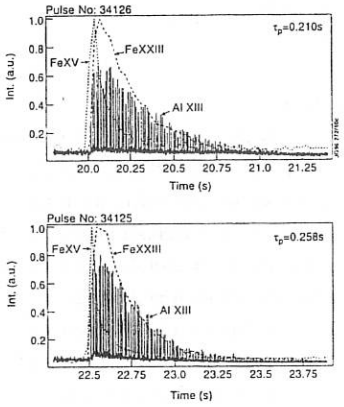

Figure 4 FeXXIII and AlXIII during ohmic (top) and ELMy H-mode (bottom). The aluminium is monitored with a scanning crystal spectrometer and the iron by a normal incidence VUV spectrometer.

Simulation Model for Runaway Electron Diffusion in the JET Tokamak

R.Martin-Solis, B.Esposito [1], R.Sanchez, F.B.Marcus [2]

Universidad Carlos III de Madrid, C/Butarque 15, Leganes, 28911-Madrid, Spain.
[1] Associazione Euratom-ENEA CRE, 00044-Frascati, Italy.
[2] JET Joint Undertaking, Abingdon, Oxfordshire, OX14 3EA, UK.

Abstract The radial transport of runaway electrons generated in JET low density ohmic discharges is analysed using a simple model that includes radial diffusion, collisional losses and electric field acceleration. It is shown that the time evolution of the runaway electron density is essentially diffusive, confirming previous estimates of the runaway radial transport coefficient, $D_r \sim 0.2\,\mathrm{m^2/s}$ $(r/a < 0.5)$, obtained using a diffusion model [1]. These results are employed, on the basis of existing theories of magnetic turbulent transport, to set limits on the level of the radial magnetic fluctuations in the plasma centre.

1. Experimental Data Runaway electrons have been detected during the start up phase of JET ohmic discharges by measuring the emitted perpendicular X-ray bremsstrahlung radiation using the collimated fast electron bremsstrahlung (FEB) monitor (with 10 horizontal and 9 vertical channels [2]), sensitive to X-rays in four energy windows from 133 - 400 keV. Discharge parameters were: $n_e \sim 0.5 - 1.5 \times 10^{19}\,\mathrm{m^{-3}}$, $I_p = 1 - 1.6\,\mathrm{MA}$ and $B_t \sim 2.75\,\mathrm{T}$. A typical time trace of the line integrated X-ray emission from the FEB vertical detectors (channels 15-19, energy window = 133 - 200 keV), is shown in Fig.1 for shot 29586. The signal from the central vertical chord (channel 15) starts at $t \sim 0.2\,\mathrm{s}$ after the beginning of the discharge, it increases up to a maximum at $t_{peak} \sim 1\,\mathrm{s}$ (t_{peak}: time of maximum signal in the central chord), and then it decays to almost level zero at $t \sim 4\,\mathrm{s}$. The most interesting feature of the FEB data is the different time evolution of the line integrated emission in different chords. The decay of the signal is slower for the outer channels, and the maximum in the measured X-ray emission is reached progressively at later times in the edge chords than in the central ones. The FEB data, converted to local X-ray emissivity, show that the emissivity radial profiles, initially peaked at time t_{peak}, tend to flatten at later times [1]. All these observations suggest an outward diffusion of fast electrons from the centre to the edge.

2. The Model The time evolution of the FEB signals are used to provide a measurement of an energy averaged fast electron radial diffusion coefficient. The radial transport of runaway electrons is modeled with a one-dimensional cylindrical spatial diffusion equation that includes collisional losses and electric field acceleration. The starting point of the analysis is the kinetic Fokker-Planck equation for the fast electron distribution function $f_e(r, p_{||}, p_\perp, t)$:

$$\frac{\partial f_e}{\partial t} = -eE_{||}\frac{\partial f_e}{\partial p_{||}} + C(f_e) + \frac{1}{r}\frac{\partial}{\partial r} r D_r \frac{\partial f_e}{\partial r} \qquad (1)$$

Here, D_r is the spatial diffusion coefficient, $E_{||}$ is the toroidal electric field, and e is the electron charge. The operator $C(f_e)$ is the relativistic high-velocity Coulomb collision operator [3]:

$$C(f_e) = \frac{\nu_0 p_e^3}{2}\left[\frac{1}{p^2}\frac{\partial}{\partial p}\left(\gamma^2 f_e + \gamma^3 \frac{p_e^2}{p}\frac{\partial f_e}{\partial p}\right) + \frac{\gamma}{p^3}\frac{1+Z_{eff}}{2}\frac{\partial}{\partial \mu}(1-\mu^2)\frac{\partial f_e}{\partial \mu}\right], \qquad (2)$$

where $p_e = (m_e k T_e)^{1/2}$, m_e is the electron mass, ν_0 is the collision frequency for thermal electrons, Z_{eff} is the effective ion charge, and $\ln\Lambda$ is the Coulomb logarithm; $p^2 = p_{||}^2 + p_{\perp}^2$, $\mu = p_{||}/p$, and $\gamma^2 = 1 + p^2/(m_e c)^2$.

Using the kinetic energy, $E = (\gamma - 1)m_e c^2$, as variable instead of the momentum p, and integrating (1) over μ, the kinetic equation for the energy distribution function, $N_E(r, E, t)$, is obtained:

$$\frac{\partial N_E}{\partial t} = \frac{1}{r}\frac{\partial}{\partial r} r D_r \frac{\partial N_E}{\partial r} - \frac{\partial}{\partial E}\left(eE_{||}\overline{\mu}v - \frac{\nu_0 p_e^3}{2m_e^2}\frac{1}{v}\right) N_E + \frac{\nu_0 p_e^5}{2m_e^3}\frac{\partial}{\partial E}\left[\gamma^2 \frac{\partial}{\partial E}\left(\frac{N_E}{\gamma^2 v}\right)\right] \qquad (3)$$

$N_E(E)\,dE$ is the electron density in the energy interval $(E, E + dE)$; v is the electron velocity, and $\overline{\mu}(E)$ is the average value of μ for electrons in the energy interval $(E, E + dE)$.

Eq. (3) for $N_E(r, E, t)$ is integrated over energy for electrons contributing to the FEB signal, from the low energy cut-off (ϵ_d = 133 keV) to infinity, to obtain a diffusion equation for the runaway electron density, $n_r(r, t) = \int_{\epsilon_d}^{\infty} N_E(E)\,dE$. The resulting equation is:

$$\frac{\partial n_r}{\partial t} = \frac{1}{r}\frac{\partial}{\partial r} r D_r \frac{\partial n_r}{\partial r} + \left(eE_{||}\overline{\mu}(\epsilon_d)v_d - \frac{\nu_0 p_e^3}{2m_e^2 v_d}\right) N_E(\epsilon_d) - \frac{\nu_0 p_e^5}{2m_e^3 v_d}\left\{\left(\frac{\partial N_E}{\partial E}\right)_{\epsilon_d} - \frac{N_E(\epsilon_d)}{\epsilon_d + m_e c^2}\left(1 + \frac{c^2}{v_d^2}\right)\right\} \qquad (4)$$

where v_d is the electron velocity at energy ϵ_d, and an average value of the diffusion coefficient D_r over energy is assumed. Eq. (4) shows that the fast electron density evolution is the result of three main contributions: *(i)* radial diffusion, *(ii)* a flux of electrons (number of electrons/m^3/s) in the energy space at energy ϵ_d due to electric field acceleration and collisional slowing down, and *(iii)* a flux of electrons at energy ϵ_d due to collisional diffusion in the energy space. Eq. (4) can be simplified by noting that, for fast particles, electric field acceleration and collisional energy transfer are more important than collisional diffusion [4], so that:

$$\frac{\partial n_r}{\partial t} \simeq \frac{1}{r}\frac{\partial}{\partial r} r D_r \frac{\partial n_r}{\partial r} + \phi(\epsilon_d) N_E(\epsilon_d), \qquad (5)$$

where $\phi(E, r) = eE_{||}\overline{\mu}(E)v - \frac{\nu_0 p_e^3}{2m_e^2 v}$, is the energy transfer rate of a test electron to the bulk plasma. Therefore, the effect of electric field acceleration and collisions on the evolution of the runaway density can be represented by a flux $\phi(\epsilon_d)N_E(\epsilon_d)$ at energy ϵ_d determined by single particle dynamics in the energy space. This flux of electrons at a certain time t will be given by electrons with energy E at time t_{peak} that have been accelerated to energy ϵ_d at time t following the single particle orbits obtained from:

$$\frac{dE}{dt} = eE_{||}v - \frac{\nu_0 p_e^3}{2m_e^2}\frac{1}{v} \qquad (6)$$

where $\mu \sim 1$ is assumed for runaway electrons. The single particle orbits for $r/a \sim 0.1$ and shot 29586 are shown in Fig.2: electrons are accelerated for energies greater than the runaway critical energy ϵ_c, and reach the energy cut-off ϵ_d in a short time scale ($\sim$ tens of milliseconds) in comparison with the one observed for the runaway electron evolution ($\sim$ seconds). This means that, unless a source of electrons is supplied at the critical energy ϵ_c, the electron flux at energy ϵ_d, $\phi(\epsilon_d)N_E(\epsilon_d)$, will be small in a short time, and the evolution of n_r, given by (5), will be dominated by the radial diffusive term. This source of electrons at the critical energy ϵ_c is given by the runaway production rate, Γ_r. The runaway production rate at $r/a \sim 0.1$, calculated

using ref.[5], is shown in Fig.3 for discharge 29586: Γ_r decreases very rapidly in comparison with the observed temporal evolution of the FEB signals. Therefore, from time t_{peak} onwards, the runaway density evolution will be essentially diffusive for most of the time. Simple modelling of $n_r(r,t)$, taking into account the fast runaway electron dynamics in the energy space, can be done by assuming that the instantaneous electron flux at ϵ_d, $\phi(\epsilon_d,t)\,N_E(\epsilon_d,t)$, is given by Γ_r. When substituting in Eq. (5), this yields:

$$\frac{\partial n_r}{\partial t} = \frac{1}{r}\frac{\partial}{\partial r} r D_r \frac{\partial n_r}{\partial r} + \Gamma_r(r,t) \qquad (7)$$

The results of the simulations for $n_r(r,t)$ are converted to local X-ray emissivity as explained in ref.[1] and integrated for each line of sight to obtain the line integrated emission to be compared with the experiment. In Fig.4, a comparison of the FEB data and the simulations for the central vertical chords 15-17 is shown for discharge 29586. The radial profile of D_r is assumed flat. Best agreement is found for $D_r \sim 0.2\,\mathrm{m^2/s}$. The deduced value of D_r is an averaged value for $r/a < 0.5$, and over the runaway electron energy.

3. Discussion Assuming that magnetic turbulence is responsible for the runaway electron transport, from D_r we can set limits on the level of the radial magnetic fluctuations (b_r/B_t). The radial diffusion coefficient due to magnetic turbulence can be written [6]: $D_r = \pi q R (b_r/B_t)^2 v_{\|} \Upsilon(E)$, where q is the safety factor, R the major radius, $v_{\|}$ is the runaway parallel velocity, and $\Upsilon(E)$ is the drift modification factor $(0 < \Upsilon(E) < 1)$, which gives the corrections to D_r due to orbit averaging, and decreases for increasing energy. For random phased turbulence, a sufficient fit to Υ is: $\Upsilon \sim \sigma/d_r$ [6], where σ is the correlation length of the turbulence and $d_r = m_e \gamma v_{\|} q/eB_t$ is the runaway drift. σ can be approximated by $1/m$, where m, the poloidal number, is given roughly by $m \simeq a/\rho_i$ (ρ_i is the ion Larmor radius). For the discharge considered above $T_i \sim 1\,\mathrm{keV}$, and $\sigma \sim 1.7\,\mathrm{mm}$. For the evaluation of the runaway drift, as the measured D_r is an averaged value over energy for electrons contributing to the FEB signal, an averaged value of d_r over the runaway electron energy must be considered. We do not have such estimate, but limits on d_r can be obtained by setting limits on the runaway electron energy. The lower limit is given by the cut-off energy, $\epsilon_d = 133\,\mathrm{keV}$, yielding $d_r \sim 0.95\,\mathrm{mm}$. The measured bremsstrahlung spectrum at time t_{peak} (see ref.[1]) allows to set an upper limit for the runaway energy: $\epsilon_{max}(t_{peak}) \sim 3\,\mathrm{MeV}$. The time evolution of ϵ_{max} can be calculated using (6): at $t \sim 4\,\mathrm{s}$, for $r/a < 0.5$, $\epsilon_{max} \sim 29\,\mathrm{MeV}$, and $d_r \sim 7\,\mathrm{cm}$. With these estimates for σ and d_r, we get $0.02 < \Upsilon(E) < 0.9$, and using the relation given before for D_r, we obtain for discharge 29586 and $r/a < 0.5$ ($D_r \sim 0.2\,\mathrm{m^2/s}$, $q = 2$, $R \sim 3\,\mathrm{m}$): $0.8 \times 10^{-5} < (b_r/B_t) < 4 \times 10^{-5}$.

The effect of stochastic magnetic fields on thermal electron transport can be evaluated considering the simple relation between runaway and electron thermal diffusivities: $D_r/\chi_e = \Upsilon(E) v_{\|}/v_e$ (v_e is the electron thermal velocity), which gives $D_r/\chi_e \sim (0.3 - 8)$ (discharge 29586), while the measured $D_r \sim 0.2\,\mathrm{m^2/s}$ and the value found for χ_e from power balance calculations, $\chi_e \sim 0.2 - 3\,\mathrm{m^2/s}$ $(r/a < 0.5)$, yields $D_r/\chi_e \sim (0.07 - 1)$. Therefore, the estimated values of (b_r/B_t) in the plasma centre could explain, within the experimental uncertainties, the measured thermal electron transport coefficient.

Acknowledgements: the first author thanks J.A.Cuesta for helpful discussions and A.J.Castro, J.Meneses for valuable assistance.

References

[1] B.Esposito, et al., Proc. 22nd Eur. Conf. Bournemouth, Vol. 19D, Part II-037 (1995).

[2] P.Froissard, PhD Thesis, Universite de Provence Aix-Marseille I (1992).

[3] P.T.Bonoli and R.C.Englade, Phys.Fluids **29**, 2937 (1986).

[4] N.J.Fisch, A.H.Boozer, Phys. Rev. Lett. **24**, 3245 (1981).

[5] R.Jaspers, et al., Nucl. Fusion **33**, 1775 (1993).

[6] J.R.Myra and P.J.Catto, Phys. Fluids B 4(1), 176, (1992).

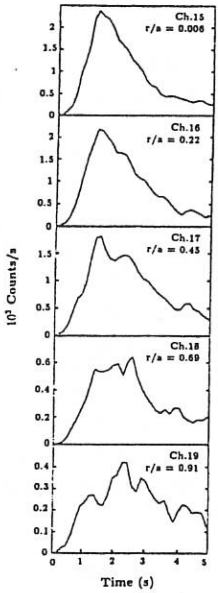

Fig.1: Line integrated count rate vs time of FEB vertical channels 15-19. Data are smoothed for clearness.

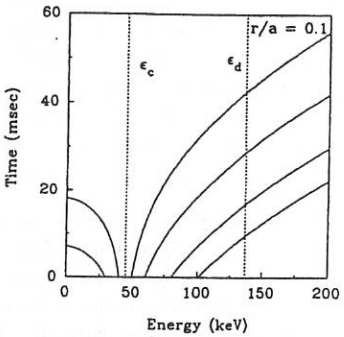

Fig.2: Single particle orbits of fast electrons for puls 29586 and $r/a = 0.1$; $t = 0$ corresponds to tim t_{peak}; ϵ_c is the runaway critical energy, and ϵ_d is th low energy cut-off, $\epsilon_d \sim 133\,keV$.

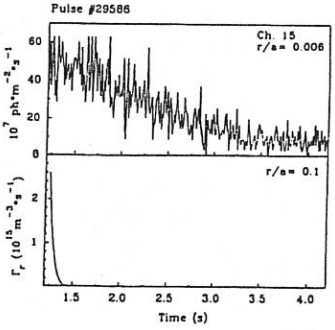

Fig.3: Time traces, from $t_{peak} \sim 1\,s$, of FEB channel 15 (top) and runaway production rate at $r/a = 0.1$ (bottom).

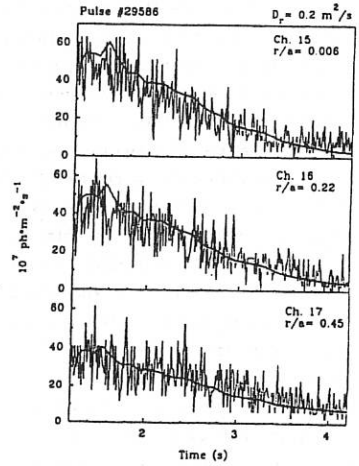

Fig.4: Comparison between measured and simulated time traces, using $D_r = 0.2\,m^2/s$, of line integrated X-ray emission for FEB channels 15,16,17.

NONDIMENSIONAL TRANSPORT EXPERIMENTS ON DIII–D AND PROJECTIONS TO AN IGNITION TOKAMAK*

C.C. Petty, T.C. Luce, B. Balet,† J.P. Christiansen,† J.G. Cordey†
General Atomics, P.O. Box 85608, San Diego, California 92186-9784 U.S.A.

The concept of nondimensional scaling of transport makes it possible to determine the required size for an ignition device based upon data from a single machine and illuminates the underlying physics of anomalous transport. The scaling of cross-field heat transport with the relative gyroradius ρ_*, the gyroradius normalized to the plasma minor radius, is of particular interest since ρ_* is the only nondimensional parameter which will vary significantly between present day machines and an ignition device. These nondimensional scaling experiments are based upon theoretical considerations[1,2] which indicate that the thermal heat diffusivity can be written in the form

$$\chi = \chi_B \rho_*^{x_\rho} F\left(\beta, \nu_*, q, R/a, \kappa, T_e/T_i, \ldots\right) \quad , \tag{1}$$

where $\chi_B = cT/eB$. As explained elsewhere,[3] $x_\rho = 1$ is called gyro-Bohm scaling, $x_\rho = 0$ is Bohm scaling, $x_\rho = -1/2$ is Goldston scaling, and $x_\rho = -1$ is stochastic scaling. The DIII–D results reported in this paper cover three important aspects of nondimensional scaling experiments: the testing the underlying assumption of the nondimensional scaling approach, the determination of the ρ_* scaling of heat transport for various plasma regimes, and the extrapolation of the energy confinement time to future ignition devices.

DIMENSIONALLY IDENTICAL H–MODE DISCHARGES

A basic assumption of the nondimensional scaling approach is that transport is dependent only upon local quantities. Therefore if two plasmas with different B and a are constructed which have the same values for all the nondimensional parameters (ρ_*, β, ν_*, q, R/a, κ, *etc.*), then it can be shown from Eq. (1) that the thermal energy confinement times normalized to the cyclotron frequencies (*i.e.*, $B\tau_{th}$) should also be the same for these two plasmas. Plasmas which have the same values for all the nondimensional parameters are referred to as dimensionally identical discharges.

Recently experiments on DIII–D and JET have compared the confinement of dimensionally identical discharges for the first time using plasmas with substantially different B and a. The JET discharge to be matched on DIII–D was selected from a previously published ρ_* scaling experiment (shot 35171 in Ref. 4). It is a stationary ELMing H–mode discharge with $\beta_N = 1.6$ and the same plasma shape as expected for ITER. Neutral beam injection (NBI) heating was utilized on both JET and DIII–D for these experiments.

The normalized plasma parameters for the DIII–D and JET H–mode discharges were well matched, as shown in Table I. The aspect ratio, elongation, and safety factor were the same to about 1%. In order to keep ρ_*, β_{th}, and ν_* fixed for these two discharges with different B and a, the quantities $Ba^{5/4}$, $W_{th}/a^{1/2}$, and $\bar{n}\,a^2$ were also held constant by adjusting the toroidal field, the injected power, and the density. The ELM frequencies (f_{ELM}) normalized to the thermal confinement times were similar although not identical for these two plasmas. Table I shows that the thermal confinement time (with the NBI power corrected for shine-through losses) normalized to the cyclotron frequency for the DIII–D and JET dimensionally identical H–mode discharges agreed to within 3%, which is well inside the experimental error bars. Thus plasmas which have identical values for the local dimensionless parameters have been shown to have identical

*Work supported by the U.S. Department of Energy under Contract No. DE-AC03-89ER51114.
†Permanent address: JET Joint Undertaking, United Kingdom.

normalized confinement, which demonstrates that nondimensional scaling is a valid approach to understanding transport processes.

Table I: Normalized parameters for JET (a = 0.97 m, B = 1.07 T) and DIII–D (a = 0.56 m, B = 2.09 T) dimensionally identical H–mode discharges.

Parameter	JET	DIII–D
R/a	2.96	2.98
κ	1.68	1.66
q_{95}	3.5	3.5
$Ba^{5/4}$	1.0	1.0
$W_{th}/a^{1/2}$	0.85	0.86
$\bar{n}a^2$	2.3	2.2
$f_{ELM}\tau_{th}$	5.0	7.0
$B\tau_{th}$	0.21	0.22

ρ_* SCALING OF HIGH-q H–MODES

Previous experiments on DIII–D which measured the ρ_* scaling of ions and electrons found that the ion ρ_* scaling varied according to the plasma regime. In H–mode plasmas with low safety factor (q_{95} = 3.8), the ion scaling was gyro-Bohm-like,[5] whereas in L–mode plasmas with the same safety factor, Bohm-like ion scaling was observed.[6] The ρ_* scaling for electrons was always found to be gyro-Bohm-like. Comparing the transport results for these H–mode and L–mode plasmas indicated a correlation between the ion ρ_* scaling and the density scale length,[6] *i.e.*, as the density profile became more peaked the ion ρ_* scaling varied from gyro-Bohm-like to Bohm-like.

Recent experiments on DIII–D have looked for a similar correlation between the ion ρ_* scaling and the safety factor scale length. This was motivated by the observation that the ion ρ_* scaling changed from Bohm-like to Goldston-like between low-q L–mode[6] and high-q L–mode[3] experiments. For this experiment, the ρ_* scaling of transport was measured on DIII–D in high safety factor (q_{95} = 7) ELMing H–mode discharges with flat density profiles (minimizing the influence of the density scale length) for comparison with the ρ_* scaling of the ITER-relevant low-q H–mode discharges previously studied.[5] The aspect ratio, elongation, T_e/T_i, and β_N were nearly the same for these two pairs of dimensionally similar discharges. The radial profiles of four important nondimensional parameters for the high-q H–mode discharges are shown in Fig. 1, demonstrating that the dimensionless quantities were held fixed as ρ_* was varied. The ratio of the ion thermal diffusivities for this ρ_* scan are shown in Fig. 2. The ion diffusivity had gyro-Bohm-like scaling in the inner half of the plasma, changing to Bohm-like scaling in the outer half of the plasma; this should be compared to gyro-Bohm-like scaling for the low-q H–mode. The safety factor scale length for the high-q ρ_* scan differs from the low-q ρ_* scan mainly in the outer half of the plasma since sawtooth activity enforces the same q profile in the inner region. Therefore, the change in the ion ρ_* scaling from gyro-Bohm-like to Bohm-like correlates with a shortening of the safety factor scale length. This indicates that a peaked current profile as well as a peaked density profile can lead to worse than gyro-Bohm scaling for the ions.

PROJECTIONS TO AN IGNITION TOKAMAK

The confinement properties of future magnetic fusion devices can be extrapolated from existing experiments using the scaling of heat transport with nondimensional parameters such as ρ_*. The ρ_* scaling of dimensionally similar discharges have been compared between DIII–D and JET for H–mode plasmas in order to test the extrapolation of heat transport to an ignition device. Using Eq. (1), the loss (transported) power for plasmas with different ρ_* but the same β, ν_*, *etc.*, can be shown to scale like $P_{loss} \propto \rho_*^{-5/2+x_\rho} a^{-3/4}$. The loss power projected along a dimensionally similar path for the ITER-relevant low-q H–mode plasmas on DIII–D which had gyro-Bohm-like scaling[5] is shown in Fig. 3. The favorable gyro-Bohm-like scaling extrapolates to a very low loss power (high confinement) for ITER.

As discussed in Ref. 6, however, this extrapolation from DIII–D to smaller ρ_* on ITER is complicated by the requirement that the loss power from core transport remain above the H–mode threshold power along the dimensionally similar path (in order for the plasma to remain in H–mode). Since the H–mode threshold power scales like $P_{thr} \propto \rho_*^{-3} a^{-3/4}$,[7] which is Goldston-like, the increase in the H–mode threshold power is

more rapid than the increase in loss power as $\rho_* \rightarrow 0$. Data from JET plasmas[4] (see Fig. 3) shows that when P_{loss} drops to the level of P_{thr} as ρ_* is decreased, the dimensionally similar path changes from gyro-Bohm-like scaling, which follows core transport, to Goldston-like scaling, which follows the H–mode threshold.

Choosing a scaling path at high beta (and low collisionality), along which the loss power remains above the H–mode threshold to the point of ignition, allows one to take full advantage of the gyro-Bohm-like scaling of heat transport in H–mode plasmas in the design of an ignition tokamak. An example of this is given in Fig. 3, where an ignition point along a dimensionally similar path at higher β than the ITER-relevant DIII–D and JET discharges is shown. If beta is increased by raising the temperature at fixed density, then the H–mode threshold powers are the same for the high β and low β paths. Since ignition takes place for P_{loss} slightly above P_{thr} along the high β path, there is enough power flow through the edge to sustain the H–mode condition. The parameters for this high β "compact-gB" ignition point are given in Table II; the reduced minor radius compared to ITER means a smaller extrapolation is needed from existing machines like DIII–D and JET and the density is lower relative to the Greenwald limit. The high H factor is a natural consequence of the favorable gyro-Bohm-like scaling of H–mode confinement.

The high value of β_N for the compact-gB scenario is a result of the low elongation and low triangularity of the assumed ITER shape. By utilizing a more highly shaped plasma, the normalized beta can be reduced without sacrificing performance. The parameters for such a "D" shaped H–mode plasma are given in Table II, where the ignition point was determined by the same procedure as for the compact-gB point shown in Fig. 3. It is noteworthy that the operating point for the compact-D scenario does not exceed either the Troyon beta limit or the Greenwald density limit.

CONCLUSIONS

Comparison of dimensionally identical H–mode discharges on DIII–D and JET found that the thermal confinement times normalized to the cyclotron frequencies were in good agreement,

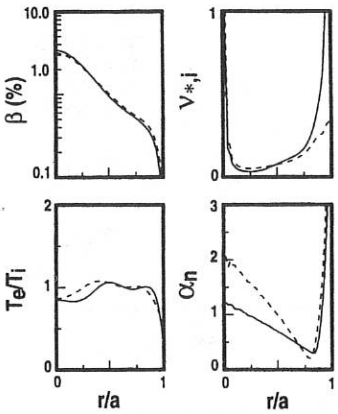

Fig. 1. Nondimensional parameters for the high-q H–mode ρ_* scan. The solid lines are for B = 2.1 T and the dashed lines are for B = 1.05 T. The quantity α is the power to which a parabolic radial dependence must be raised to get the local scale length.

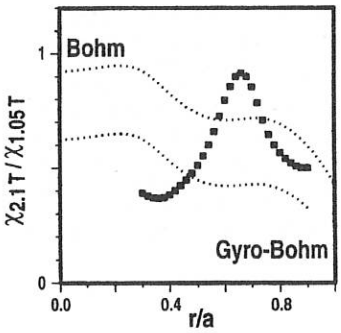

Fig. 2. Ratio of ion thermal diffusivities for the high-q H–mode discharges. The expected ratios for gyro-Bohm-like and Bohm-like scaling are also shown, postulating that $\chi_{gB} \propto T_i^{3/2}/B^2$ and $\chi_B \propto T_i/B$.

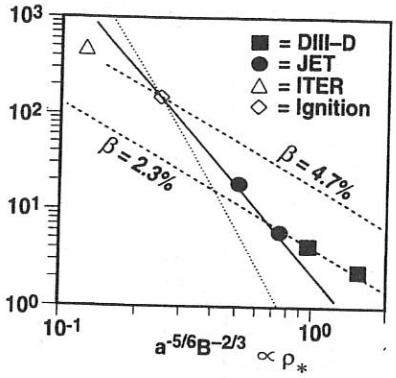

Fig. 3. Dimensionally similar paths for the loss power of DIII–D and JET H–mode discharges, the projected loss power for gyro-Bohm-like scaling at two values of β (dashed lines), H–mode threshold power (solid line), and the alpha loss power for the high β path (dotted line).

Table II: Projected parameters for gyro-Bohm ignition tokamaks with $R/a = 2.7$, $q_{95} = 3.8$, and $B_T = 5.7$ T.

Parameter	Compact-gB	Compact-D
R (m)	3.56	2.74
κ	1.68	2.1
δ	0.36	0.8
I (MA)	8.5	4.9
$\bar{n}$ (10^{20} m^{-3})	1.9	2.0
$\bar{n}/n_{GW}$	1.2	0.65
β_N	4.7	3.3
τ (s)	1.4	1.2
H	3.3	3.0
P_{fus} (MW)	660	490

indicating that transport is a function of only the local quantities and that Eq. (1) is a valid representation of the transport process. Other experiments on DIII–D showed that the ρ_* scaling for ions varied from gyro-Bohm-like for plasmas with broad density and current profiles to worse than Bohm-like for peaked density and current profiles. Finally, it was shown that the gyro-Bohm-like scaling of low-q H–mode plasmas can lead to an attractive compact ignition tokamak by choosing a high beta (low collisionality) path along which the loss power remains above the H–mode threshold power to the point of ignition.

[1]Kadomtsev, B.B., Sov. J. Plasma Phys. **1**, 295 (1975).
[2]Connor, J.W., and Taylor, J.B., Nucl. Fusion **17**, 1047 (1977).
[3]Petty, C.C., et al., Phys. Rev. Lett. **74**, 1763 (1995).
[4]Balet, B., et al., in the Proc. of the 22nd Euro. Conf. on Contr. Fusion and Plasma Physics, Bournemouth, (European Physical Society, Petit-Lancy, Switzerland, 1995) Vol. 19C, Part I, p. 9.
[5]Petty, C.C., et al., Phys. Plasmas **2**, 2342 (1995).
[6]T.C. Luce and C.C. Petty, in the Proc. of the 22nd Euro. Conf. on Contr. Fusion and Plasma Physics, Bournemouth, (European Physical Society, Petit-Lancy, Switzerland, 1995) Vol. 19C, Part III, p. 25.
[7]ITER H–mode Database Working Group, in the Proc. of the 21st Euro. Conf. on Contr. Fusion and Plasma Physics, Montpellier, (European Physical Society, Petit-Lancy, Switzerland, 1994) Vol. 18B, Part I, p. 334.

RESISTIVE INSTABILITIES IN ADVANCED NEGATIVE CENTRAL SHEAR TOKAMAKS WITH PEAKED PRESSURE PROFILES*

M.S. Chu, J.M. Greene, L.L. Lao, R.L. Miller, A. Bondeson,† O. Sauter,‡
B.W. Rice,¤ E.J. Strait, T.S. Taylor, and A.D. Turnbull
General Atomics, P.O. Box 85608, San Diego, California 92186-9784 U.S.A.

Negative central magnetic shear (NCS) is an operating regime[1-3] for advanced tokamaks which could lead to fusion reactors with higher performance and lower cost. In the NCS region, the plasma is in the second stable regime for ideal magnetohydrodynamic (MHD) ballooning modes. In Tokamak Fusion Test Reactor (TFTR) and DIII–D, the plasma also develops an internal transport barrier[4,5] that provides good central confinement, high central ion temperatures, and central peaking of the pressure profile — favorable for a high fusion rate,[5,6] record high neutron yield has been obtained in peaked pressure operations. In L–mode plasmas, *i.e.*, no edge pressure pedestal, these discharges typically terminated with hard disruptions. Despite the favorable ballooning mode stability cited above, localized MHD bursts are observed in plasmas with highly peaked pressure profile in DIII–D. These bursts limit the pressure peakedness $p(0)/\langle p\rangle$ [$p(0)$ is the pressure at the plasma center and $\langle p\rangle$ is the volume averaged pressure], and occur prior to the final disruption. In what follows, the scenario that leads to these bursts and the ensuing disruptions is analyzed through systematic computation of resistive MHD modes in NCS plasmas.

To investigate the parametric dependence of the resistive MHD modes in NCS configurations we generated a set of equilibria by using the TOQ equilibrium code[8] and corresponding to those obtained in DIII–D. The aspect ratio is fixed at 2.7, the elongation from 1.0 to 1.8, and the triangularity from 0.0 to 0.7. The q profile is specified by a spline with eight node points that include the magnetic axis, the minimum q location (at 1/4 of the total poloidal flux), and the location of 95% flux value. The value of q at 95% flux q_{95} is fixed at 5.1 with the value of $q_{\min}$ covering a range from 1.1 to 2.5. The value of $q_0 - q_{\min}$ ranges from -0.3 to 1 (a negative value of $q_0 - q_{\min}$ corresponds to normal q profile with the minimum value of q at the magnetic axis). The pressure profile is given by the form $p = p_0(1-\psi)^n$. With increasing value of the exponent n, the pressure profile becomes more peaked. The equilibria studied cover a range of $\beta_N = \beta(I_p/aB_0)^{-1}$ (% MA/mT) values between 0.5 and 5.0 (here $\beta = 2\mu_0\langle p\rangle/B_0^2$ is the ratio of plasma pressure to magnetic field pressure, I_p is plasma current, a the plasma minor radius, and B_0 the vacuum magnetic field) at the center of the last closed flux surface. Typical q and p profiles and the resultant flux plot is shown in Fig. 1.

*Work supported by the U.S. Department of Energy under Grant No. DE-FG03-95ER54309 and Contract W-7405-ENG-48, and in part by the Swiss National Science Foundation.
†Institute for Electromagnetic Field Theory, Chalmers University, Göteborg, Sweden.
‡CRPP/EPFL, Assoc. Euratom-Switzerland, Lausanne, Switzerland.
¤Lawrence Livermore National Laboratory, Livermore, California, U.S.A.

The localized stability criteria of these equilibria evaluated by TOQ are first examined. We found that these equilibria are stable to the ideal interchange even in the absence of magnetic shear ($D_I < -1/4$) and also stable to the ideal ballooning modes. However, the localized resistive interchange[9] is destabilized ($D_R > 0$) at sufficiently high β_N at fixed amount of shear reversal or sufficiently large shear reversal at fixed (but moderate) β_N. We note that these trends shown in this numerical evaluation of D_R are in agreement with the large aspect ratio analytic results for tokamaks with circular[10] and noncircular[11] cross-sections.

The stability analysis is performed by using the MARS code with the inclusion of the effect of a toroidal plasma flow.[10,11] The toroidal mode number n has been taken to be $n = 1$. An external ideally conducting wall is placed at 1.3 plasma radius. Two classes of modes have been found. The first is a localized mode, with the characteristics of an resistive interchange (see Fig. 2). They are destabilized beyond a critical β_{NC}. The growth rates of these localized modes have been found to be independent of the plasma rotation. With increasing plasma rotation, the mode has been found to rotate with the rotation speed of the inner singular surface with no change in its growth rate.

The second class of modes found is the global mode. It has the structure of a double tearing mode coupled to an external kink and an internal localized interchange. A typical mode structure is shown in Fig. 3 for $q_{min} = 1.5$ and $\beta_N = 2.5$. The main poloidal harmonics in this case is given by $m = 2$. Due to the existence of multiple resonance surfaces, there could exist multiple numbers of global modes with different growth rates, depending on different amounts of coupling to the sideband harmonics. In general, the mode with the largest growth rate has the least coupling to the sideband harmonic. The growth rate and coupling to the sidebands increase with increasing β_N. In contrast to the localized mode, the growth rate of this mode is very sensitive to the plasma shape and boundary condition such as the location of the external wall and the resistivity profile of the plasma. This mode is suppressed when the outer 50% of the plasma is assumed to be ideal. I this case, close to the critical β_{NC}, only the localized mode is found. This indicates that this mode could be stabilized by plasma rotation. Similarly, when the inner half of the plasma is assumed to be ideal, the growth rate of the global mode is reduced significantly. For this set of equilibria, the global mode has been found always less stable than the localized mode. These modes are stabilized by elongation with increasing triangularity and increased shear in edge q profile.

To assess the relevance of these two classes of modes to experimental observations, we compare first the stability boundary (β_{NC}) of the localized mode with the experimental data base for disruptions. They have been found to agree in their dependences on the value of q_{min}, and pressure peakness parameter. Since disruption follows the occurrence of MHD bursts, and the localized mode is relatively independent of the boundary conditions; these bursts, which are observed on the inner rational surfaces of these discharges, are identified as the resistive interchanges. Details of this comparison are given in Ref. 13.

Although many characteristics of the global mode, such as beta dependence, and the dependence on the pressure peakness parameter shows similarity to that found for the mode responsible for disruption, we need to compare the details of the predictions of the stability boundary of the global mode with that observed in experiment. For this purpose, evolution of the experimental equilibrium was reconstructed in detail by using EFIT[14] for shot 87009. The reconstructed equilibrium (at 1620 msec)is unstable to the localized mode at the time of MHD burst, but stable to the global mode. The reconstructed equilibrium at the slightly later time (at 1675 msec) prior to disruption is found to be unstable to both the local and the global mode with the global mode having a larger growth rate. The rotation frequency of the global mode is at the computed frequendy. Thus we identify the disruption mode with the computed global mode. We see that the DIII–D experiment is in a parameter space where these two modes are expected to interact strongly with each other. The localized mode regulates the pressure profile whereas the global mode leads to disruption.

We thus propose the following disruption scenario for NCS discharge in L–mode plasmas with peaked pressure profile. In these discharges, the plasma is kept stable to the global mode by plasma shaping and rotation until the resistive interchange stability criterion is violated. In this situation, the localized mode could become unstable. It may interact strongly with the global mode and eventually destabilizes it, leading to disruption. Broader pressure profiles and weaker shear reversal lead to stability at higher beta.

REFERENCES

[1]T.S. Taylor *et al.*, Plasma Phys. and Contr. Fusion **36**, b229 (1994).

[2]C. Kessel *et al.*, Phys. Rev. Lett. **72**, 1212 (1994).

[3]A.D. Turnbull *et al.*, Phys. Rev. Lett. **74**, 718 (1995).

[4]F.M. Levinton *et al.*, Phys. Rev. Lett. **75**, 4417 (1995).

[5]E.J. Strait *et al.*, Phys. Rev. Lett. **75**, 4421 (1995).

[6]L.L. Lao *et al.*, Phys. Plasmas 3, 1951 (1996)

[7]B.W. Rice, *et al.*, Phys. Plasmas 3, 1983 (1996)

[8]R.L. Miller and J.W. Van Dam, Nucl. Fusion **27**, 2101 (1987).

[9]A.H. Glasser, J.M. Greene, and J.L. Johnson, Phys. Fluids **19**, 567 (1976).

[10]A.H. Glasser, J.M. Greene, and J.L. Johnson, Phys. Fluids **18**, 875 (1975).

[11]A. Bondeson, G. Vlad, and H. Lutjens, Phys. Fluids B **4**, 1889 (1992).

[12]M.S. Chu, J.M. Greene, T.H. Jensen, R.L. Miller, A. Bondeson, R.W. Johnson, and M.E. Mauel, Phys. Plasmas **2**, 2236 (1995).

[13]M.S. Chu, J.M. Greene, L.L. Lao, R.L. Miller, A. Bondeson, O. Sauter, B.W. Rice, E.J. Strait, T.S. Taylor, and A.D. Turnbull, General Atomics Report GA-A22293 (1996), submitted to Phys. Rev. Lett.

[14]L.L. Lao *et al.*, Nucl. Fusion 30, 1035 (1990).

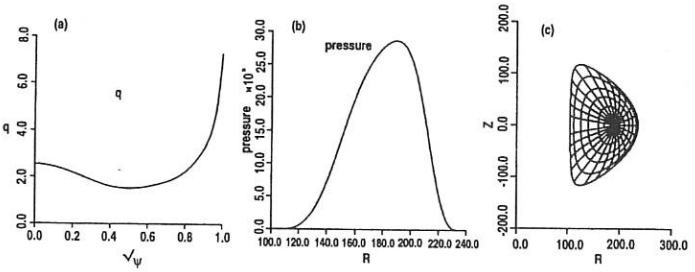

Fig. 1. Typical equilibrium profiles. (a) safety factor q; (b) pressure p; and (c) equilibrium flux plot for elongation = 1.8.

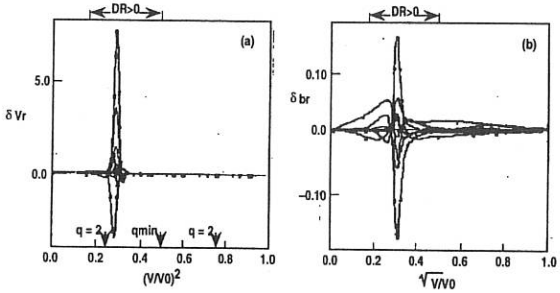

Fig. 2. Eigenfunction of localized mode (a) velocity perturbation, (b) magnetic field perturbation for $q_{\min} = 1.5$, $\beta_N = 3.3$.

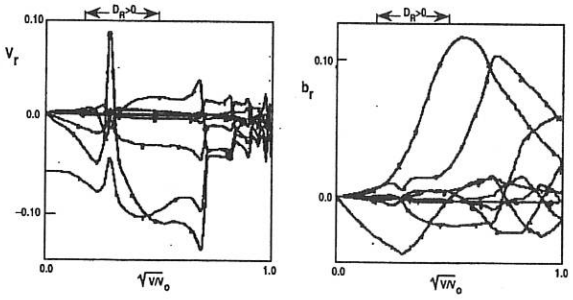

Fig. 3. Eigenfunction of global mode (a) velocity perturbation, (b) magnetic field perturbation for $q_{\min} = 1.5$, $\beta_N = 2.5$,

Characteristics of Ice Pellet Ablation and its Effect on Plasma Potential in the JIPP T-IIU Tokamak

K.N.Sato, H.Sakakita, I.Nomura, Y.Hamada, K.Ida, K.Narihara, K.Toi, T.Seki, K.Adachi, A.Ejiri, A.Fujisawa, S.Hidekuma, S.Hirokura, H.Iguchi, Y.Kano, Y.Kawasumi, M.Kojima, A.Nishizawa and Torus Exp. Group

National Institute for Fusion Science, Chikusa, Nagoya 464-01, Japan

1. Introduction

Ice pellet injection is one of the most important issues in the toroidal plasma research not only for profile control and confinement improvement, but also for the basic studies on the characteristics of toroidal plasmas[1~4].

A new pellet injection system, "the injection-angle controllable system", has been developed and installed to the JIPP T-IIU tokamak. By using this system, one can control the injection angle easily and continuously during an interval of two plasma shots in the course of an experiment, not moving the whole injector, and thus one can carry out various basic studies on toroidal plasmas by changing the pellet deposition profile actively and drastically. Details of the pellet ablation properties with various deposition positions (injection angles) have been studied by using this system and by multi-dimensional observations with two CCD cameras and a high speed framing photogragh. An interesting phenomenon has been obtained concerning the flow characteristics of the ablation cloud in the JIPP T-IIU plasmas[5].

A long helical ("tail-shaped") ablation light has been observed in the cases of on-axis and off-axis injection with the angle smaller than the certain value ($\theta \leqq 4°$). The direction of helical rotation ("tail") is independent to that of the total magnetic field lines of the torus. From the experiments of four conditions with the combination of two (CW and CCW) toroidal field directions and two plasma current directions, it is concluded that the "tail" seems to rotate, in most cases, to the electron diamagnetic direction poloidally, and to the opposite to the plasma current direction toroidally.

Spectroscopic measurements have been carried out in order to have informations on the parameters in the ablation cloud. From the results of analysis on the Stark broadening, it has been found that the typical cloud density is extremely high (in the range of 10^{15} - 10^{17} cm^{-3}). Consideration on various cross sections leads us to the conclusion that the "tail-shaped" phenomena may come from the situation of charge exchange equilibrium of hydrogen ions and neutrals at high density regime in the cloud. In addition, the result of the heavy ion beam probe (HIBP) measurements suggests that the phenomena may closely related to the plasma potential and the rotation.

2. Observation by the high speed framing photogragh

Experiments have been carried out by changing the injection angle poloidally from -6 to 6 degree, and this situation makes it possible for pellets to aim at from about r = -2a/3 to r =

2a/3 of the plasma. In the case of an injection angle (θ) larger than a certain value (θ ≥ 4°), a pellet penetrates straightly through the plasma with a trace of straight ablation cloud, which has been expected from usual theoretical consideration. On the other hand, a long helical shape ("tail") of ablation light has been observed in the cases of on-axis and off-axis injection with the angle smaller than the certain value (θ ≦4°).

In addition to the measurements by CCD cameras, the time-dependent flow characteristics of the ablation cloud have been observed by using the high speed framing photogragh. The cases of on-axis injection and of off-axis injection in the parallel direction to the ion diamagnetic drift in poloidal plane (so-called upward injection) are reported in the previous paper [5], however, the case of off-axis injection in the parallel direction to the electron diamagnetic drift (so-called downward injection) has been examined and is presented this time (Fig.1).

One of the important points in these phenomena is that the direction of "helical tail" is independent to that of the total magnetic field lines of the torus. In order to examine the tail direction, experiments have been carried out as to four conditions with the combination of two (CW and CCW) toroidal field directions and two plasma current directions. These results show that the tail seems to rotate to the electron diamagnetic direction poloidally, and to the opposite to the plasma current direction toroidally as to almost all conditions of injection angles. Only in the case of pellet-injection angle to be parallel to the electron diamagnetic direction in poloidal plane (i. e., in the case of so-called downward injection), it has been observed that the ablation cloud first rotates to the same direction with other cases, but at a certain time later it seems to decelerate and stay at the same location, or sometimes even flow back to the reverse direction as is seen in Fig.1. This tendency will be discussed in the Section 4 in connection with the plasma potential change after pellet injection.

3. Spectroscopy System and the Measurement of "Tail-Shaped" Cloud

In order to understand details of an ice pellet ablation structure, a new spectroscopy system has been developed to obtain the local parameters within the ablation cloud.

The system is shown in Fig.2, where the local electron density and temperature within the cloud can be obtained from the Stark broadening of Balmer Beta line, and from the line to continuum intensity ratio, respectively. The wavelength resolution of the system is 0.79 Å/pixel for a grating of 1200 grooves/mm (blaze wavelength is 5000 Å), but the actual resolution is a few Å because of a focus size of optics in the system. The temporal resolution in ideal case will be 3 μsec, because in a so-called Kinetic-Mode operation, charges stored on each array are sent to the upper array vertically with every 3 μsec (minimum exposure time). In the present preliminary experiment, however, the measurement has been done with time-accumulation mode (within 3 μsec x 64 = 192 μsec) as the first step.

A typical result is shown in Fig.3. Through the analysis by a multi-Lorentzian fitting method, it has been found that the typical cloud density is in the range of 10^{15} - 10^{17} cm^{-3}, and the typical temperature is in the range of 1 - 4 eV.

Based on these cloud parameters, the characteristic times for various processes such as charge exchange, elastic collision, excitation, ionization and recombination etc. are analized,

and listed in Table I. Consideration on various characteristic times leads us to the conclusion that, since the charge-exchange and elastic-collision times are greatly shorter than the ionization time in this region, the "tail-shaped" phenomena may come from the situation of charge exchange equilibrium of hydrogen ions and neutrals at extremely high density regime in the ablation cloud.

4. Potential Measurements and "Tail" Structure

The relation of ablation behaviour with plasma potential and rotation has also been studied. Potential measurements of pellet-injected plasmas by using heavy ion beam probe (HIBP) method have been carried out. Especially, the typical results of relative potential changes in two cases are compared. In the case of an injection angle to be parallel to the ion diamagnetic direction in poloidal plane (Fig.3(a) in Ref.[5]), the result shows that the direction of potential change is negative, and consequently the potential after the injection should be negative because it has been measured to be negative in usual ohmic plasmas without pellet injection. Thus, the direction of the "tail" structure in this case seems to be consistent (Fig.2(a) in Ref.[5]) to that of the plasma potential measured, if it is considered that the tail structure may be caused by the effect of the plasma potential and the rotation. The case of the injection angle to be parallel to the electron diamagnetic direction in poloidal plane has exhibited the opposite result, i.e. the direction of potential change is positive (Fig.3(b) in Ref.[5]), and this may be a cause of complicated behavior (tendency of deceleration of rotation) of ablation cloud, as is seen in Fig.1. Consequently, it is concluded from theoretical consideration that the "tail-shaped" behaviour of ablation cloud may be closely related to the plasma potential (E x B drift) and the rotation.

References

[1] TFR Group, *Nuclear Fusion* **27**, 1975 (1987)
[2] Weller A et al, *Physical Review Letters* **59**, 2303 (1987)
[3] Sato KN et al, *20th EPS Conference on Controlled Fusion and Plasma Physics* **17C**, I-239 (Lisboa, 1993)
[4] Sakamoto M et al, *Plasma Physics and Controlled Fusion* **33**, 583 (1991)
[5] Sakakita H et al, *22th EPS Conference on Controlled Fusion and Plasma Physics* **19C**, I-125 (Bournemouth, 1995)

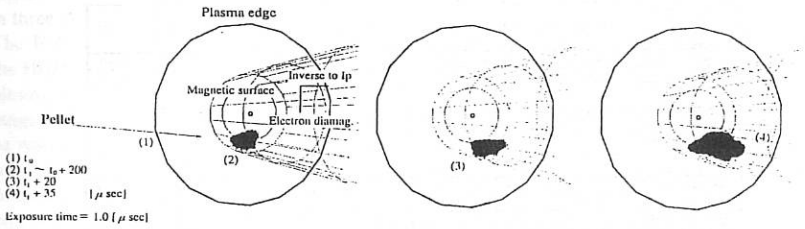

Fig.1: Time-resolved framing photographs of an ablation cloud in the case of off-axis injection in the parallel direction to the electron diamagnetic drift (so-called downward injection). The exposure time = 1.0 μsec. The viewing angle is essentially tangential, and wireframes show the geometrical configuration in the JIPP T-IIU tokamak.

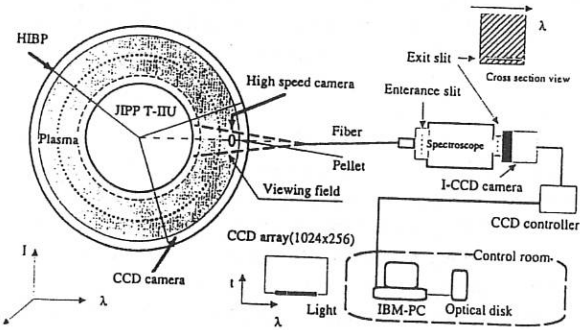

Fig.2: Spectroscopy system developed for obtaining the local parameters within the ablation cloud. The electron density and temperature within the cloud can be obtained from the Stark broadening of Balmer line, and from the line to continuum intensity ratio, respectively.

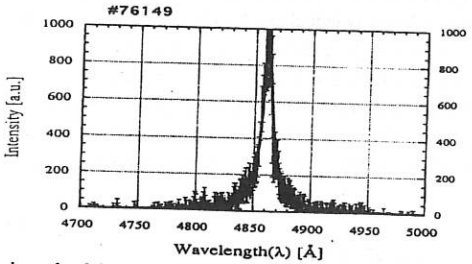

Fig.3: A typical result of the Stark broadening of Balmer line taken by the system in Fig.2. Through the analysis by a multi-Lorenzian fitting method, the typical cloud density has turned out to be in the range of 10^{15} - 10^{17} cm^{-3}, and the typical temperature is in the range of 1 - 4 eV.

Table I: List of the characteristic times for various processes.

· Characteristic times (sec) of charge exchange and elastic collision.

T_i [eV], n_i [cm^{-3}] / Reactions	300, 10^{13}	100, 10^{13}	2, 10^{17}	2, 10^{16}	2, 10^{15}	4, 10^{16}	20, 10^{16}	20, 10^{15}
Charge exchange	1.7×10^{-6}	2.0×10^{-6}	6.7×10^{-10}	6.7×10^{-9}	6.7×10^{-8}	5.0×10^{-9}	4.0×10^{-9}	4.0×10^{-8}
Elastic collision	1.7×10^{-6}	2.5×10^{-6}	2.5×10^{-9}	2.5×10^{-8}	2.5×10^{-7}	1.7×10^{-8}	7.1×10^{-9}	7.1×10^{-8}

· Characteristic times (sec) of excitation, ionization and recombination.

T_e [eV], n_e [cm^{-3}] / Reactions	500, 10^{13}	100, 10^{13}	2, 10^{17}	2, 10^{16}	2, 10^{15}	4, 10^{16}	20, 10^{16}	20, 10^{15}
Elastic collision(τ_{n-e})	- - -	1.4×10^{-6}	6.3×10^{-11}	6.3×10^{-10}	6.3×10^{-9}	5.3×10^{-10}	1.1×10^{-9}	1.1×10^{-8}
Excitation(1s→3d)	1.0×10^{-5}	1.0×10^{-5}	5.0×10^{-7}	5.0×10^{-6}	5.0×10^{-5}	3.3×10^{-7}	1.4×10^{-8}	1.4×10^{-7}
Excitation(1s→2p)	1.4×10^{-6}	1.1×10^{-6}	2.0×10^{-8}	2.0×10^{-7}	2.0×10^{-6}	1.4×10^{-8}	2.0×10^{-9}	2.0×10^{-8}
Excitation(2p→3d)	1.3×10^{-7}	6.7×10^{-8}	1.7×10^{-11}	1.7×10^{-10}	1.7×10^{-9}	6.7×10^{-11}	5.0×10^{-11}	5.0×10^{-10}
2p→Ionization	-	-	-	-	-	-	-	-
Ionization(e^-) (1keV H_b^+)	3.0×10^{-6} 10^{-4}	3.0×10^{-6}	1.0×10^{-7}	1.0×10^{-6}	1.0×10^{-4}	2.5×10^{-7}	6.7×10^{-9}	6.7×10^{-8}
3 body recombination	3.3×10^{7}	1.3×10^{7}	10^{-4}	10^{-3}	10^{-2}	3.3×10^{-3}	10^{-1}	1
Radiative recombination	3.0×10	1.4×10	3.0×10^{-3}	3.0×10^{-4}	3.0×10^{-5}	6.7×10^{-4}	3.3×10^{-3}	3.3×10^{-2}

Spherical Tokamak GLOBUS-M

V.E.Golant, V.K.Gusev, **V.B.Minaev**, A.N.Novokhatsky, K.A.Podushnikova, N.V.Sakharov, K.G.Shakhovetz, V.S.Uzlov
A.F.Ioffe Institute, 26, Politekhnicheskaya St., St.Petersburg 194021, Russia
V.A.Belyakov, A.A.Kavin, V.A.Korotkov, U.A.Kostzov, E.G.Kuzmin, V.F.Soikin
D.V.Efremov Institute, Metallostroy, 189631 St.Petersburg, Russia
E.A.Azizov, E.A.Kuznetzov, V.A.Yagnov
TRINITI, Troitsk, 142092, Russia
N.Ya.Dvorkin, I.N.Leikin, V.V.Mikov
Northern Plant, 10 Kolomjazhski Ave., 197348 St. Petersburg, Russia

ABSTRACT

Basic parameters of GLOBUS-M tokamak, which is under construction at Ioffe Phisico-Technical Institute are presented. GLOBUS-M is a spherical tokamak with high plasma current and RF auxiliary heating capable of creating limiter and X-point plasma magnetic configurations in a quasistationary discharge with a fully automatic feedback control of plasma position, shape and current. Characteristic features of the tokamak construction as well as the results of the last revision of some tokamak parts are described.

I. INTRODUCTION

GLOBUS-M is a small spherical tokamak [1, 2], designed to fit existing at Ioffe Institute power supplies after their reasonable upgrade. The GLOBUS-M experiment will investigate small aspect ratio highly elongated plasmas properties with emphasis on operational limits, plasma confinement, stability, equilibrium, density and beta limits. To achieve high beta regimes the auxiliary RF heating of plasma in three different frequency ranges is planed. The ICR heating at 7.5-8.0 MHz, 1 MW; the HHFW heating at 25-30 MHz, 0.5 MW; plasma heating in intermediate frequency range 2-10 GHz, 0.2-0.3 MW are going to be realized [3]. The plasma current, plasma column position and shape will be automatically controlled. The engineering experience gained in this project will serve for solving of design, construction, plasma control, and operational problems for future generation of spherical tokamaks.

The basic parameters of the tokamak are listed in Table 1, the vertical cross section is shown in Fig. 1. The vacuum vessel and the magnets will be designed, manufactured and assembled during a three year period (Apr. 1995 - March 1998) in frame of the contract sponsored by the International Science and

Table 1 GLOBUS-M Basic Parameters

Plasma major radius, R	0.36 m
Plasma minor radius, a	0.24 m
Aspect ratio, R/a	1.5
Plasma vertical elongation, k	1.5 - 2.2
Plasma triangularity, δ	~ 0.2
Plasma current I_p	0.3 MA
Toroidal magnetic field, B_T	0.5 T
Plasma shaping factor, $S=I_p q_\psi/aB_T$	25
Pulse length	0.3 sec
Auxiliary heating power	~ 1 MW
Weight of tokamak	~ 5 Ton

Technology Center (ISTC). After that the device will be installed in a new experimental machine hall at Ioffe Institute. At the moment the phase of the detail tokamak design is close to the end, and the manufacturing of the vacuum vessel and the magnet basic parts is started. The construction of the experimental machine hall will be completed this autumn.

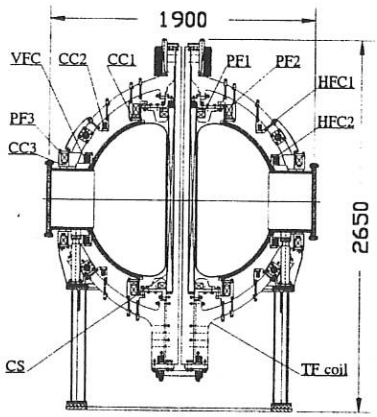

Fig. 1 GLOBUS-M vertical cross section

II. DESIGN PRINCIPLES

A. Poloidal Field Coils and Magnetic Equilibrium

Three pairs of poloidal field coils (PF1-PF3) are used for plasma shaping and plasma position monitoring. Three pairs of additional coils are used for "fast" vertical and horizontal feedback control (VFC, HFC). To simplify plasma breakdown and plasma shaping the compensation coils (CC) together with PF3 coil are used to compensate the central solenoid (CS) stray field. PF coil system of GLOBUS-M can provide equilibrium of differently shaped plasmas with high triangularity and elongation. The examples of simulated magnetic flux surfaces for plasma column with β_P=0.3 and l_i=0.7 are shown in Fig. 2

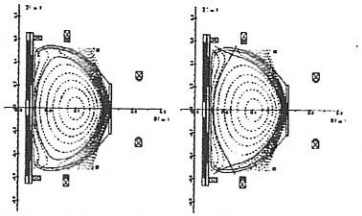

Fig. 2 Limiter and double X-point magnetic configurations.

B. Vacuum Vessel

An all welded stainless steel vacuum vessel (Fig. 3) has a "near-pure compression" shape to increase the vessel stability relatively to atmosphere pressure. It is supported through the rather thick equatorial plane ring, supplied with ports and manholes for plasma observation, heating and in-vessel components maintenance. 14 mm thickness of the equatorial plane ring provides more favorable conditions for plasma column vertical stability. The vacuum vessel has no insulation breaks or bellow inserts. The other basic parts of the vessel are the inner cylinder (2 mm thick), the upper and lower domes (3 mm thick) and intermediate cups of variable thickness. The vacuum vessel bakeout temperature is 200°C. The vessel parameters are listed in Table 2.

Table 2 Vacuum Vessel Main Parameters

Vacuum pressure	$< 2 \times 10^{-6}$ Pa
Horizontal axis of torus	0.536 m
Vertical axis of torus	1.094 m
Inner volume	1.1 m^3
Inner surface area	5.7 m^2
Weight	650 kg

To improve the device performance in future it is possible to provide a 3-fold changing of the inner cylinder with decreasing its diameter every time. This

procedure will allow to decrease the tokamak aspect ratio without significant changes in the basic vacuum vessel construction.

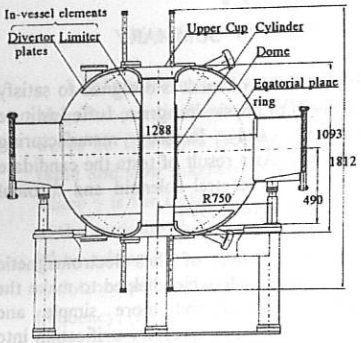

Fig. 3 Vacuum vessel basic parts

C. Toroidal Field Coils

There are 16 single turn toroidal field coils connected in series through the crossovers located at the machine bottom. The reverse turn is disposed on the both sides of crossovers for better compensation of stray field. Toroidal field coils basic parameters are listed in Table 3.

Table 3 Toroidal Field Coils Parameters

Number of coils	16
Toroidal field at R=0.36 m	0.5 T
Total central "rod" current	875 kA
Field ripple at R=0.36 m	1.6×10^{-4} %
Field ripple at R=0.6 m	0.99 %

The outer limbs of the toroidal field coils are the part of the tokamak support structure. They are used to support the poloidal field coils and should be stiff enough to withstand in-plane and out of plane forces.

The inner straight leg and the outer limb of TF coil are connected through the upper dismountable joint at the top of the machine (Fig. 4). For the convenience of the machine assembly the outer limb is made of two parts connected below the equatorial plane. To provide the necessary stiffness against TF coils toppling the outer limbs are embraced with the hoop closed intercoil structure below and above an equatorial plane. The inner leg is to be made from bronze or cold extruded copper. The outer limb is made from regular copper.

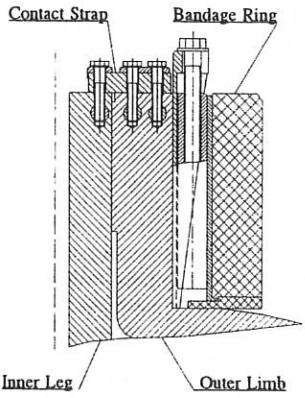

Fig. 4 TF coil top contact joint

D. Central Solenoid

The most critical component of GLOBUS-M electromagnetic system is the central core. The central core consists of the central solenoid [4] and the bundle of the TF coils inner straight legs of wedge shape inserted into the inner bore of the solenoid. To provide maximum possible magnetic flux the basic problems of the central solenoid development are to be solved:

- space restriction (the diameter of the vacuum vessel inner cylinder is 220 mm);
- compatibility with existing power supplies (thyrystor converters 70 kA, 450 V);
- conductor mechanical properties;
- winding procedure.

The basic solenoid parameters are listed in Table 4.

Table 4 Central Solenoid Main Parameters

Number of layers	2
Number of turns per layer	62
Conductor cross section	20×20 mm
Water cooling hole diameter	6 mm
Inner diameter	112 mm
Outer diameter	200 mm
Height of the coil	1313 mm
Length of the conductor	~ 66 m
Current in the conductor	± 70 kA
Axial magnetic field	8.3 T
Magnetic flux (double swing)	0.31 Wb
Design number of cycles	8×10^4

Strong cyclic loads, acting on the solenoid, require a high strength continuous conductor for its winding. After careful investigation of candidate materials, accompanied by static and cyclic mechanical tests, the conductor from silver bearing cold extruded copper alloy was selected (yield stress 270 MPa, ultimate tensile stress 330 MPa). The continuous hollow conductor with initial specially determined trapezoidal cross section will be manufactured in Finland at Outokumpu Oy Enterprise. At the moment the technology of manufacturing of sufficiently long conductor is developed and the tools for its extrusion are ready.

The 10 m length test piece of the conductor has been manufactured for winding and tests of the solenoid prototype. The coil of the full scale radius and decreased height (ten turns per layer) was wound and prepared for testing.

The design of the TF coils top contact joint (See Fig. 4) makes it possible a winding of the central solenoid separately on a bobbin or in-situ around the TF coils inner legs. The diameter of the TF center rod at the top does not exceed the diameter of the solenoid inner bore. Electric contacts are provided by a bandage ring, which press the outer limb to the inner leg and by horizontal straps. The final technology of the central solenoid winding will be determined after tests of the solenoid prototype.

IV. SUMMARY

GLOBUS-M tokamak is designed to satisfy the needs of physics program, Ioffe Institute facilities and Russia manufacturing capability. As a result of tests the candidate materials for central solenoid and toroidal field coils were chosen.

The modification of the electromagnetic system was made which helped to make the central solenoid coil more simple and reliable, introduce necessary unification into the PF coils construction and redesign the TF coils in order to reduce the toroidal field ripple near the outer plasma boundary. As a result the plasma dimensions were increased and the aspect ratio was decrease from the value 1.6 to the value 1.5.

REFERENCES

[1] V.A.Belyakov, V.A.Divavin, N.Ya.Dvorkin, et al., Ioffe Inst. Preprint 1629 (1994)

[2] V.E.Golant, V.K.Gusev, V.B.Minaev, et al., IEEE/NPSS 16th Symposium Fusion Technology, Vol. 2, pp. 1464-1467 (1996)

[3] A.R.Esterkin, E.Z.Gusakov, M.A.Irzak, et al., 22nd EPS Conf. on Controlled Fusion and Plasma Physics, Contr.Papers, Vol. 19C, Part IV, pp.389-392 (1995)

[4] V.K.Gusev, V.I.Nikolaev, K.A.Podushnikova, et al., IEEE/NPSS 16th Symposium Fusion Technology, Vol. 2, pp. 1460-1463 (1996)

COHERENT MAGNETOACOUSTIC CYCLOTRON INSTABILITY IN PLASMAS WITH HIGH ENERGY IONS

V.S.Belikov, Ya.I.Kolesnichenko, **O.A.Silivra**

Scientific Centre "Institute for Nuclear Research", Kyiv, 252650, Ukraine

1.Introduction. The present paper deals with the coherent destabilization of Fast Magnetoacoustic Waves (FMW) by superthermal ions, extending an analysis of earlier works on this topic (see e.g. overview [1] and the recent work [2]). It considers both rapid and slow magnetoacoustic instabilities i.e. instabilities with $\gamma > \tau_b^{-1}$ and $\gamma < \tau_b^{-1}$ where γ is the instability growth rate, τ_b is bounce/transit period of fast ions. The aims of the work are the following: (i) to generalize the analysis of the slow instability of Ref. [2] by taking into account the finite magnitude of $(\omega_{B_s} - \bar{\omega}_B)/\omega_{B_s}$ where ω_{B_s} is the ion cyclotron frequency at the magnetic axis and $\bar{\omega}_B$ is the bounce/transit-averaged cyclotron frequency; (ii) to develop a theory of the rapid instability allowing for the radial structure of the waves.

2.Slow coherent instability. We proceed from the dispersion equation describing FMW propagating across the magnetic field ($k_\parallel = 0$) in a tokamak plasma with fast ions [3]. This equation for $\omega = \omega_0 + \omega_1$, $\omega_0 = kv_A$, $\mid \omega_1 \mid \ll \omega_0$ yields

$$\varepsilon_{11}^{\alpha} + 2\frac{\omega_{pi}^2}{\omega_0^2}\frac{\omega_1}{\omega_0} = 0 \tag{1}$$

where $\varepsilon_{11}^{\alpha}$ is a flux surface averaged component of the dielectric permeability tensor associated with fast ions, ω_p is the plasma frequency. Eq.(1) implies that the number of fast ions is small ($n_\alpha/n \ll 1$) and the wave frequency satisfies the inequality $\omega_{Bi} \ll \omega \ll \omega_{Be}\sqrt{M_e/M}$, where ω_B is the cyclotron frequency, subscripts "e", "i" and "α" label species, M_e and M are the electron and ion mass, respectively.

For the time intervals exceeding the particle transit time we find $\varepsilon_{11}^{\alpha}$ as

$$\varepsilon_{11}^{\alpha} = -\frac{4\pi\omega_{p\alpha}^2}{\omega q r k^2}\sum_l I_l \tag{2}$$

where

$$I_l = \int_0^\infty EdE \int_1^\infty d\kappa^2 \frac{J_l^2(\xi)\hat{\Pi}F_\alpha}{(\Delta_l - a(\kappa^2))KQP^2} \tag{3}$$

$\hat{\Pi} = \partial/\partial E - SP/(2E)\partial/\partial\kappa^2$, $\xi = kv_\perp/\omega_{B\alpha}$, $v_\perp = (2E/P)^{1/2}$, $\Delta_l = (\omega - l\omega_{B_s})/(\epsilon l\omega_{B_s})$, $P = 1 + \epsilon(2\kappa^2 - 1)$, $S = 2\kappa^2 - 1 - \Delta_l$, $Q = (S(1-\Delta_l^2)/2\kappa^2)^{1/2}$, $E = v^2/2$, $\int F_\alpha d\vec{v} = 1$, F_α is a distribution function of fast ions, κ^2 is the trapping parameter, q is the tokamak safety factor, $\epsilon = r/R$, r is the radial coordinate, R is the large radius of the torus,

$$a(\kappa^2) \equiv \frac{\bar{\omega}_B - \omega_{B_s}}{\epsilon\omega_{B_s}} = 2\kappa^2\left(1 - E(1/\kappa^2)/K(1/\kappa^2)\right) - 1 \tag{4}$$

E and K are complete elliptic integrals.

Integrating by parts Eq.(3) we find

$$I_l = \frac{1}{2}\int_0^\infty dE \int_1^\infty d\kappa^2 \frac{F_\alpha}{\Delta_l - a(\kappa^2)} \left\{ f + \frac{\partial g}{\partial \kappa^2} + g\frac{\partial a/\partial \kappa^2}{\Delta_l - a(\kappa^2)} \right\} \tag{5}$$

where

$$f = \frac{1}{KQP}\left(\frac{1}{\epsilon}\frac{\partial J_l^2}{\partial \kappa^2} - \frac{2}{P}J_l^2\right), \quad g = \frac{SJ_l^2}{KQP} \tag{6}$$

One can see that Eq.(1) can be satisfied when denominator in Eq.(5) is small, which is the case for ω_0 determined by $\Delta_l(\omega_0) - a(\kappa^2) = 0$, i.e.

$$\omega_0 = l\bar{\omega}_B(\kappa) \tag{7}$$

For sufficient large κ Eq.(7) is transformed to $\omega_0 \cong l\omega_{B_s}$. Then the last term in Eq.(5) can be neglected and Eq.(1) is reduced to a quadratic equation with respect to ω_1, which implies that $\gamma \propto \sqrt{n_\alpha}$ [2].

When κ is not very large then Eq.(7) determines ω_0 dependent on κ. Therefore the real part of I_l (which is responsible for coherent instability) is not small provided F_α is close to $\delta(\kappa - \kappa_0)$. We take F_α as follows:

$$F_\alpha = \frac{\delta(v - v_\alpha)}{4\pi v_\alpha^2}\frac{1}{\sqrt{\pi}\theta}\exp\left(-\frac{(x - x_0)^2}{\theta^2}\right) \tag{8}$$

where $\theta \ll x_0$, $\theta \ll x_0 - 1$, $x = \kappa^2$. Expanding $f(x)$, $g(x)$ and $a(x)$ in the vicinity of x_0 and introducing $z = (\Delta_l - a_0)/(\theta a_0')$ we find ϵ_{11}^α for $z \gg 1$ as

$$\epsilon_{11}^\alpha = \frac{\omega_{p\alpha}^2}{2\omega_0 q r k^2 v_\alpha}\frac{g_0' - f_0 + 2g_0/(\theta z)}{\Delta_l - a_0} \tag{9}$$

where $\varphi_0 \equiv \varphi(x_0)$, $\varphi_0' \equiv \partial\varphi/\partial x$ at $x = x_0$. Due to Eq.(9) the Eq.(1) is cubic. In the simplest case of $\theta z \ll 1$ it yields

$$\frac{\gamma}{\omega_0} = \pm\frac{\sqrt{3}}{2}\left(\frac{\omega_{p\alpha}^2}{2\omega_{pi}^2}\frac{v_A}{v_\alpha}\frac{\epsilon a_0'}{kqR}\frac{SJ_l^2}{KQP}\right)^{1/3} \tag{10}$$

We observe that γ is proportional to $(n_\alpha)^{1/3}$, the instability being possible not only when $v_\alpha > v_A$ but also when $v_\alpha < v_A$.

Combining the used inequalities $\theta z \ll 1$ and $z \gg 1$ we arrive at the following restrictions on n_α:

$$n_1 < n_\alpha < n_2 \tag{11}$$

where n_1 and n_2 are determined by $\epsilon\theta a_0'\omega_0 = \omega_1(n_1)$ and $\epsilon a_0'\omega_0 = \omega_1(n_2)$.

3.Rapid coherent instability. Assuming that $k_\parallel = 0$, $\omega = \omega_0 + \omega_1$, $\omega_0 = kv_A$, $|\omega_1| \ll \omega_0$ we can write the equation for Fast Magnetoacoustic Eigenmodes (FME) in a plasma with fast ions as follows [4]:

$$(\hat{\Lambda} + \hat{\lambda})B = 0 \tag{12}$$

$\hat{\Lambda}$ and $\hat{\lambda}$ are integro-differential operands for the perturbed part of the magnetic field $B \equiv B_{\|}(r)$, $\hat{\lambda}$ is due to fast ions. The zero order solution of Eq.(12) is [5]:

$$B^{(0)}(r) \cong B_* \exp\left(-\frac{(r-r_*)^2}{L_W^2}\right), \qquad \omega_0^2 = \frac{m^2}{r^2} v_A^2\Big|_{r_*} + \delta\omega^2 \tag{13}$$

where $L_W \simeq \alpha r_*/\sqrt{m}$, $\alpha \simeq 1$, $B_* \equiv B(r_*)$.

We assume that the unperturbed magnetic field is homogeneous. Then

$$\omega_1 = \pm\left\{-\langle B^{(0)*}\hat{\lambda}_1 B^{(0)}\rangle / \langle B^{(0)*}\frac{\partial\hat{\Lambda}}{\partial\omega_0}B^{(0)}\rangle\right\}^{1/2} \tag{14}$$

where $\hat{\lambda}_1 = \omega_1\hat{\lambda}$, brackets mean the integration over the plasma volume. Eq.(14) takes into account that $\langle B^{(0)*}\hat{\lambda}B^{(0)}\rangle$ is proportional to $(\omega - l\omega_{B\alpha})^{-1}$. Calculating quadratic forms entering Eq.(14) we obtain

$$\omega_1 = \pm 2\pi i \frac{v_{A*}}{c}\left\{\frac{e_\alpha^2}{m_\alpha\omega_0^2}\frac{\int dr_c r_c \int dv_{\|}\int dv_\perp v_\perp^2 \frac{\partial F_\alpha}{\partial v_\perp} \mid G_l \mid^2}{\int dr r \mid B^{(0)} \mid^2}\right\}^{1/2} \tag{15}$$

where G_l describes the phase of wave particle interaction, $v_{A*} \equiv v_A(r_*)$, $r = r_c - \rho\sin\alpha$, $\rho = v_\perp/\omega_{B\alpha}$, r_c is guiding center radius.

One can see that in the limit case $\rho \ll L_W$ the dependence of $B^{(0)}$ on α can be neglected. In this case Eq.(15) yields an expression for ω_1 which corresponds to the local approximation and is known from the earlier works.

Let us assume now that ρ^2/L_W^2 is not very small but much less then l, and $l \gg 1$. Then we find:

$$G_l = i^{l+1}\frac{l^2}{\xi_c}\frac{m}{r_*}J_l(\xi_c)B^{(0)}(r_0)v_A^2(r_0) \tag{16}$$

where $r_0 = r_c - \rho\sin\alpha_0$, $\sin\alpha_0 = l/\xi_c$, $\xi_c \equiv \xi(r_c)$. The region which mainly contributes to the integral over dr_c in Eq.(15) is determined by $\mid r_* - r_c + \rho\sin\alpha_0 \mid /L_W \simeq 1$. In this region the argument of Bessel function changes by $\Delta\xi \simeq \xi L_W/r \simeq \rho/L_W$. This means that when $\rho \simeq L_W$ then Bessel function oscillates reducing the growth rate. Calculations below confirm this for $F_\alpha = (n_\alpha/2\pi v_\alpha)f_{\|}(v_{\|})\delta(v_\perp - v_\alpha)$. Assuming $\xi > l$ we find

$$\frac{\omega_1}{\omega} = \pm i\frac{\omega_{p\alpha}}{\omega_{pi}}\frac{v_A}{v_\alpha}\left\{\frac{1}{2\pi\xi}\left(1 - (-1)^l 2\bar{\xi}\cos 2\bar{\xi}\exp\{-\frac{\rho_\alpha^2}{2L_W^2}\}\right)\int dv_{\|}f_{\|}\right\}^{1/2} \tag{17}$$

where $\bar{\xi} = \xi_*(1 - \rho_\alpha/r_*\sin\alpha_0)$, $\xi_* = \xi(r_*)$, $\rho_\alpha \equiv \rho(v_\alpha)$.

Inhomogeneity of the magnetic field affects the considered instability in two ways.

First, it results in a restriction to the radial width of the region where the coherent wave-particles interaction is possible. This restriction follows from the necessity to satisfy

the condition $\mid \omega - l\omega_{B\alpha} \mid = \gamma \gg k_{\parallel} v_{\parallel}$. The magnetic shear ($\hat{s}$) leads to $k_{\parallel} \geq \hat{s} m \Delta r/(qrR)$, where Δr is the layer width around r_0 defined by $k_{\parallel}(r_0) = 0$. Therefore the inequality $\gamma \gg k_{\parallel} v_{\parallel}$ can be written as

$$\frac{\Delta r}{r} \ll \frac{\Gamma}{m\hat{s}} \tag{18}$$

Here $\Gamma \equiv \gamma/\omega_b$, $\Gamma \gg 1$ due to the used approach.

The second restriction arises because Eq.(15) neglects the toroidal drift term, which is justified when $\mid \omega - l\omega_{B\alpha} \mid \gg \omega_D$, where $\omega_D = \vec{k}\vec{v}_D$, $\vec{v}_D$ is the velocity of the toroidal drift of fast ions. We find:

$$lq \frac{(1+\chi^2)}{2\chi} \frac{v}{v_A} \frac{(k_r \sin\theta + k_\theta \cos\theta)}{k} \ll \Gamma \tag{19}$$

where θ is the poloidal angle. For $k_r \ll k_\theta$ this condition is rather severe near the the outer circumference of the torus ($\theta = 0$). Eq.(19) can be most easily satisfied near the vertical midplane ($\theta = \pm\pi/2$), especially for very large m (because $k_r/k_\theta \sim 1/\sqrt{m}$ [5]). But when m is large then the low shear is required in order to satisfy Eq.(18).

4.Conclusions. Our analysis has shown the following. First, unlike an existing point of view [3], the circulating fast ions can destabilize cyclotron waves in tokamaks through the coherent mechanism leading to slow instability ($\gamma < \tau_b^{-1}$) with $\gamma \propto (n_\alpha)^{1/2}$ or $\gamma \propto (n_\alpha)^{1/3}$. In the latter case the instability can arise even when $v_\alpha < v_A$ in contrast to the instability with $\gamma \propto (n_\alpha)^{1/2}$ when $v_\alpha > v_A$ is necessary. Destabilization takes place when distribution of fast ions over κ is strongly peaked and the number of fast ions is sufficiently small. The frequency of excited waves exceeds $l\omega_{Bs}$.

Second, the finite ratio of the fast ion Larmor radius to the width of the wave location decreases the growth rate of the rapid cyclotron-magnetoacoustic instability excited in a coherent way. But the reduction of γ is significant only when $\rho_\alpha/L_W > \sqrt{2}$. More strong restrictions for the fast coherent cyclotron instability are found to be associated with the magnetic shear and the finite velocity of the toroidal drift of fast ions. They in fact can prevent the excitation of the considered instability near outer circumference of the torus.

Third, the coherent mechanism of the influence of fast ions on the magnetoacoustic waves is hardly relevant to the ion cyclotron emission observed in tokamaks.

Acknowledgements. This work was supported in part by Grant No. UBB200 from the International Science Foundation and the Grant No. 09.02.02/107-94 of Ukrainian State Committee on Science and Technology.

REFERENCES

[1] Ya.I.Kolesnichenko, Nucl.Fusion **20** (1980) 727.

[2] V.S.Belikov, Ya.I.Kolesnichenko, O.A.Silivra, "Coherent cyclotron thermonuclear instability driven by circulating particles in tokamaks", Nucl.Fusion, (1996), in press.

[3] A.B.Mikhailovskij, in Reviews of Plasma Physics, N.Y., (1986) v.9, p.103.

[4] V.S.Belikov, Ya.I.Kolesnichenko, O.A.Silivra, Nucl.Fusion **35** (1995) 1603.

[5] B.Coppi, Phys.Lett., **A172** (1993) 439.

RESULTS OF 3D FOKKER-PLANCK SIMULATION OF RIPPLE -INDUCED LOSS OF ALPHA PARTICLES IN TFTR

V.Ya.Goloborod'ko, S.N.Reznik, **V.A.Yavorskij**
Institute for Nuclear Research of the National Academy of Sciences of Ukraine ,
Kiev, Ukraine

S.Zweben
Princeton Plasma Physics Laboratory, Princeton University, Princeton , New Jersey,
United States of America

1. INTRODUCTION

Toroidal magnetic field ripples are known to be the reason of one of the most important loss mechanisms of charged fusion products in tokamak-reactors. The DT experiments on TFTR have initiated a number of numerical investigations of this mechanism [1,2] in present-day fusion experiment [3].The main purpose of this report is carrying out of 3D Fokker-Planck simulation of ripple loss of alpha particles in DT experiments on TFTR. The approach of present work is alternative to Monte Carlo one used in Refs.[1,2]. It extends also 3D Fokker-Planck approach of Refs. [4,5] used for modeling of fusion product behavior in TFTR in axisymmetric limit. Calculations take into account ripple induced collisionless transport (stochastic diffusion [6] and convective loss of ripple-trapped ions [7]) as well as slowing down, pitch-angle scattering and first orbit loss of alphas. The distributions of escaped fusion products over the pitch angles are obtained. Dependence of alpha loss on plasma current is investigated. The distribution function of confined alphas is obtained. Comparison of numerical results with loss alpha measurements [1,3] and pellet charge exchange ones [8] is curried out. It is shown that simulation results are in satisfactory agreement with experimental ones.

2. RESULTS OF RIPPLE LOSS MODELING

We will approximate the TFTR magnetic field by the following expression $\mathbf{B} = \mathbf{B}^s + \mathbf{B}^r$, with $\mathbf{B}^s$ being model field of an axisymmetric magnetic toroidal configuration with nested circular flux surfaces [4] and $\mathbf{B}^r = \nabla U$ being the ripple perturbation, $U = (F\delta/N)\sin N\varphi$, F is the poloidal current outside the flux surface, N is the number of TF coils and δ is the ripple amplitude, which is modeled by [9]

$$\delta = \delta_0 I_0(N\eta), \quad \eta^2 = \left[(R_r - r)^2 + z^2\right] / (R_r r), \tag{1}$$

with $I_0(x)$ being modified Bessel function, $N = 20, R_r = 2.25\,m$ in accordance with Ref. [1]. For the radial dependencies of basic plasma parameters (plasma density, ion

and electron temperatures) and the alpha particle source we will use those used in Refs. [4,10]. As the transport coefficients of 3D Fokker-Planck equation,

$$\nabla_{\mathbf{c}}\left(\mathbf{d}-\tilde{\mathbf{D}}\nabla_{\mathbf{c}}\right)f = S(\mathbf{c}), \tag{2}$$

we will use $\mathbf{d}=\mathbf{d}^{s}$, $\tilde{\mathbf{D}}=\tilde{\mathbf{D}}^{s}+\tilde{\mathbf{D}}^{r}$, where $\tilde{\mathbf{D}}^{r}$ is ripple induced diffusion. In Eq.(2) $\mathbf{c}$ is 3D COM space [10]. Decrease of confinement domain of co-moving particles due to ripple convective loss is shown in Fig. 1. Fig. 2 demonstrates typical orbit of alpha particle lost due to ripple trapping in TFTR. For *MeV* alphas characteristic loss time corresponding to this mechanism, τ_c^r, is very short $\tau_c^r \le (5\div 10)a/v_d \approx (10\div 20)\tau_b \le 10^{-4}\div 10^{-5}s << \tau_s, \tau_\perp$ (here $\tau_s, \tau_\perp$ are collisional times of slowing down and pitch-angle scattering, respectively). Therefore ripple convective loss we will consider as a prompt one. For radial component of $\tilde{\mathbf{D}}^{r}$ in stochasticity domain we will use $\Delta^2/(2\tau_b)$, where

$$\Delta = \frac{q\rho_L\sqrt{\delta/2}}{\varepsilon}\begin{cases}(2\pi/\alpha)^{1/2}, & \alpha > 1\\ \alpha\ln(16e)/(\pi\alpha), & \alpha < 1\end{cases}, \tag{3}$$

is the magnitude of ripple induced drift of banana tips [6,11], $\alpha \equiv |\dot{=}|/(NqR\delta)$. Note that collisionless stochastic diffusion results in alpha loss with characteristic time $\tau_{st}^r \cong 2a^2\tau_b/\Delta^2 \le (10^3\div 10^4)\tau_b$ that satisfies the following condition $\tau_c^r << \tau_{st}^r << \tau_s, \tau_\perp$. Stochastic diffusion domain of 3.5 *MeV* alphas in 2 *MA* TFTR plasma with major plasma radius, R=2.52 *m*, is shown in Fig. 1. To take into account collisional ripple diffusion of banana trapped alphas we will use diffusion coefficients of axisymmetric limit enhanced by factor $M = 100$.

Fig. 3 represents dependence of ripple induced alpha loss in energy range $E/E_0 \le 0.5$ (here $E_0 = 3.5\,MeV$) and $R_0 = 2.52\,m$ on plasma current when collisional ripple diffusion of banana trapped alphas is neglected. One can see that maximum ripple induced diffusion loss take place at $I \cong 1.2\,MA$ and at $I \ge 2\,MA$ this loss mechanism dominate first-orbit one. These result are in qualitative agreement with results of Ref. [1]. Fig.4 shows the pitch-angle distribution of this loss at the midplane of TFTR. For $I = 1.6\,MA$ the peak in ripple diffusion loss take place at pitch angle of $62^0\div 64^0$ that also agrees with results of Ref. [1].

Pitch-angle and radial distributions of confined alphas are shown in Figs. 5, 6. Curves of Fig. 5 show distribution of 1.76 *MeV* alphas over the pitch angles at r/a=0.5 in equatorial plane. One can see strong effect of diffusion on distribution function in $-0.5 \le v_{\|}/v \le 0.2$ pitch-angle range. Finally curves 2 and 3 of Fig. 5 demonstrate effect of decrease of banana particle density due to ripple-induced transport. This effect was observed in PCX measurements [8] and Monte-Carlo modeling of alpha particle distribution function in TFTR DT discharges [2].

Aknowledgments

The research described in this publication was made possible in part by Grant # K6Z100 from the Joint Fund of the Government of Ukraine and International Science Foundation and was supported by the United States Department of Energy, under subcontract S-03691-K.

References

[1] R.L.BOIVIN, S.J.ZWEBEN, R.B.WHITE, Nucl. Fusion **33** (1993) 449.
[2] M.H.REDI et al., Nucl. Fusion **35** (1995) 1509.
[3] S.J.ZWEBEN, et al., Nucl. Fusion **35** (1995) 1445.
[4] V.Ya.GOLOBOROD'KO et al, Nucl. Fusion **35** (1995) 1523.
[5] M.R.O'BRIEN ET AL., Nucl. Fusion **35** (1995) 1537.
[6] R.J.GOLDSTON, et al., Phys. Rev. Lett. **72** (1974) 2895.
[7] A.V.GUREVICH, Ya.S.DIMANT, Problems of plasma theory, Ed. by B.B.Kadomtsev 16 (1987) 3.
[8] M.P.PETROV, et al., Nucl. Fusion **35** (1995) 1437.
[9] V.Ya.GOLOBOROD'KO et al, Proc. 10th Int. Conf. on Plasma Phys. and Contr. Nucl. Fus., IAEA, Vienna, 1985, v.2, 179.
[10] V.Ya.GOLOBOROD'KO et al, report a075, this conference.
[11] V.S.BELIKOV et al, Fusion Technology, **15** (1989) 1365.

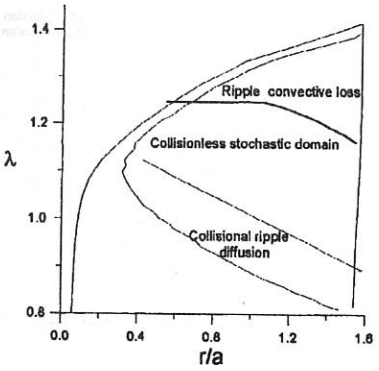

Fig.1. Alpha particle definition domain.

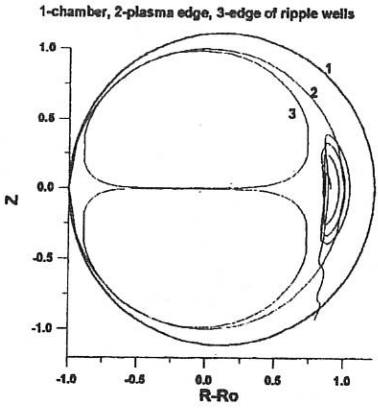

Fig.2. Typical orbit of alpha particle lost due to ripple trapping.

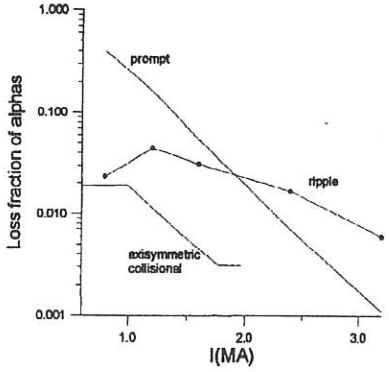

Fig.3. Loss fraction of alphas vs plasma current.

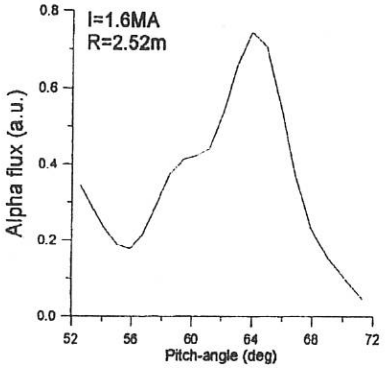

Fig.4. Typical pitch-angle distribution of alpha ripple loss at the midplane.

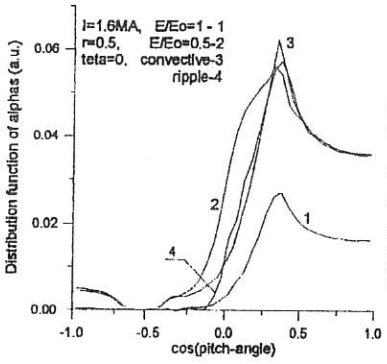

Fig.5. Pitch-angle distribution of confined alphas.

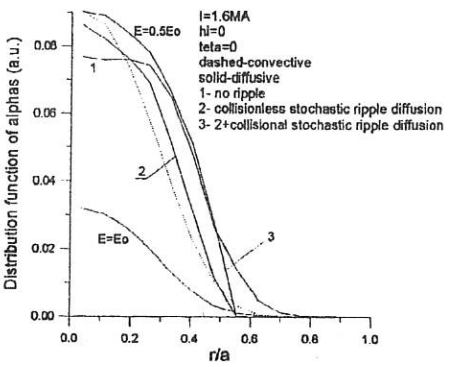

Fig.6. Radial distribution of confined alphas.

ON DISTRIBUTION FUNCTION OF FAST FUSION PRODUCTS IN TOKAMAK PLASMA

V.Ya.Goloborod'ko, S.N.Reznik, V.A.Yavorskij
Institute for Nuclear Research of the National Academy of Sciences of Ukraine , Kiev, Ukraine

ABSTRACT

Results of a 3D (in constants of motion space) Fokker-Planck simulation of distribution function of MeV fusion products in axisymmetric TFTR-like plasma are presented. The phase space distribution of confined fusion products is shown to be strongly anisotropic and non-uniform in radial coordinate (mainly for slowed down fusion products with small longitudinal energy). The influence of pitch-angle scattering on distribution function anisotropy is investigated. It is shown the strong influence of this scattering on distribution function in the regions of small pitch-angles ($v_{\parallel}/v \approx 0$) and those corresponding to separatrix between trapped and circulating fast ions in low current tokamak plasmas. A comparison of numerical results and theoretical predictions of distribution function anisotropy is carried out.

We will proceed from the 3D orbit-averaged Fokker-Planck equation for fast ions in COM space [1-5]

$$\partial f/\partial t + L_c f = S(\mathbf{c}), \tag{1}$$

where,

$$L_c = \frac{1}{\sqrt{g_c}} \sum_{k,l} \frac{\partial}{\partial c^k} \sqrt{g_c} \left(d_c^k + D_c^{kl} \frac{\partial}{\partial c^l} \right), \tag{2}$$

is 3D orbit-averaged Fokker-Planck operator in $\mathbf{c}$ space, $\sqrt{g_c}$ is Jacobian for $\mathbf{c}$-coordinate system, d_c^k and D_c^{kl} are orbit-averaged transport coefficients describing collisional diffusion and convection, S is fast particle source term. As the reference set of variables we will use the following one [2]

$$c^1 = v, \quad c^2 = \lambda, \quad c^3 = c^3(v, \lambda, J) \tag{3}$$

In (3) v is the particle velocity; $\lambda = (\mathbf{v} \times \mathbf{B})^2 B_0 / (v^2 B^3)$ is transverse adiabatic invariant; B_0 is magnetic field at magnetic axis; c^3 is "radial" coordinate; $J = \psi(\phi) - I v_{\parallel} / \omega$ is canonical angular momentum, $\omega = eB/(mc)$. We first consider convective approximation and neglect diffusion. Then taking into account that $d^2 = 0$ [1,2] and using as radial variable c^3 defined by characteristic equation

neglect diffusion. Then taking into account that $d^2 = 0$ [1,2] and using as radial variable c^3 defined by characteristic equation

$$\frac{dc^3}{dv} = \frac{d^3}{d^1}, \tag{4}$$

distribution function is determined by

$$\frac{\partial f}{\partial t} + \frac{1}{\sqrt{g}}\frac{\partial}{\partial v}\sqrt{g}d^1 f = \frac{\partial f}{\partial t} + \frac{1}{v^2}\frac{\partial}{\partial v}v^2 d^1 f = S(\mathbf{c}). \tag{5}$$

When obtaining Eq.(5) we take into account that for c^3 satisfying Eq.(4)

$$\mathrm{div}_c \mathbf{v} \equiv \sqrt{g^{-1}}\,\partial\left(\sqrt{g}v\right)\Big/\partial v = \mathrm{div}_v \mathbf{v} = 3. \tag{6}$$

Steady-state distribution of fast ions has the following form

$$f = -\frac{\int_v^\infty dv' v'^2 S\left(v', \lambda, c^3\right)}{v^2 d^1\left(v, \lambda, c^3\right)}. \tag{7}$$

We represent here results of numerical simulation of distribution function of fast alphas $(E > E_0/2)$ in TFTR-like [7] axisymmetric DT discharge with $I = 1.6MA$. We will use model magnetic configuration with shifted circular flux surfaces. For the radial dependencies of basic plasma parameters (plasma density, ion and electron temperatures) we choose following expressions

$$\frac{n(x)}{n(0)} = 0.72\left(1-x^2\right)^6 + 0.24\left(1-x^2\right)^{0.3} + 0.04; \quad T_\beta(x) = \left(T_{\beta 0} - T_{\beta a}\right)\left(1-x^2\right)^2 + T_{\beta a}, \tag{8}$$

where $x = \rho/a$, ρ is flux surface radius, $T_{e0} = 35KeV, T_{i0} = 15KeV, T_{ea} = 2KeV, T_{ia} = 1KeV$. As the alpha particle source we will use

$$S(\mathbf{r}, v) = S_0\left(1-x^2\right)^8 \delta(v - v_0). \tag{9}$$

All the rest required physical quantities and parameters correspond to that of given in Ref.[6].

To simplify the problem we will investigate steady state distribution of alphas and will neglect speed diffusion (in energy range under consideration it is negligibly small). Hence we will treat slowing-down and pitch-angle scattering, including the large banana-width effect in TFTR-like plasma (see Refs. [4,5,7]).

Distribution function of fast alphas was obtained by integration of Eq. (1) using alternative direction implicit method. Fig.1 represents pitch-angle distributions of alphas at

different points of plasma cross section. Curves of this figure demonstrate strong pitch-angle dependence of distribution function of alpha particles in low current tokamak plasma. To clarify the role of pitch-angle scattering in this figure it is shown also distribution function of alphas in convective approximation ($D^{\vartheta\vartheta} = 0$, see Eq. (7)). Distribution function in convective approximation is in good agreement with results of Rfs.[2,6,7].

Spatial distributions of alphas with fixed pitch angles and v are shown in Fig. 2. One can see that in plasma center radial profiles of alphas are monotonic, while in convective approximation f is strongly non-monotonic in the vicinity of flux surfaces corresponding to separatrix. Note, that we do not obtain nonmonotonic radial profiles of alphas in the central region of plasma, predicted for the cases with strong radial peaking of alpha particle source in Ref. [8]. Finally, Fig. 3 represents alpha particle distribution function in TFTR-like plasma with I=3.2 MA. Comparison of distribution function of alphas at 1.6MA and 3.2MA discharges demonstrates the weakens of diffusive transport processes on confined fast fusion products.

Comparing convective distribution function with 3D boundary value solutions we conclude that pitch-angle scattering can play an important role in forming of fusion product distribution function (at least in the range of small pitch-angles and vicinities of loss-cone boundaries and separatrix between trapped and circulating orbits). Of course with current increase this role weakens.

The research described in this publication was made possible in part by Grant # K6Z100 from the Joint Fund of the Government of Ukraine and International Science Foundation.

REFERENCES

[1] ROME, J.A., PENG, Y-K.M., Nucl. Fusion **19** (1979) 1193.

[2] HIVELY, L.M., MILEY, G.H., ROME, J.A., Nucl. Fusion **21** (1981) 1431.

[3] GOLOBOROD'KO, V.Ya., KOLESNICHENKO, Ya.I., YAVORSKIJ, V.A., Nucl.Fusion **23** (1983) 399.

[4] V.Ya.GOLOBOROD'KO et al, Nucl. Fusion **35** (1995) 1523.

[5] M.R.O'BRIEN ET AL., Nucl. Fusion **35** (1995) 1537.

[6] BUDNY, R.V., BELL, M.G.,BIGLARI, H., et al., Nucl. Fusion **32** (1992) 429.

[7] GORELENKOV, N.N., PUTVINSKIJ, S.V., Fizika Plazmy **15** (1989) 145.

[8]KOLESNICHENKO, Ya.I., LISAK, M., LUTSENKO, V.V., WISING,F., Plasma Phys. Control. Fusion **37** (1995) 363.

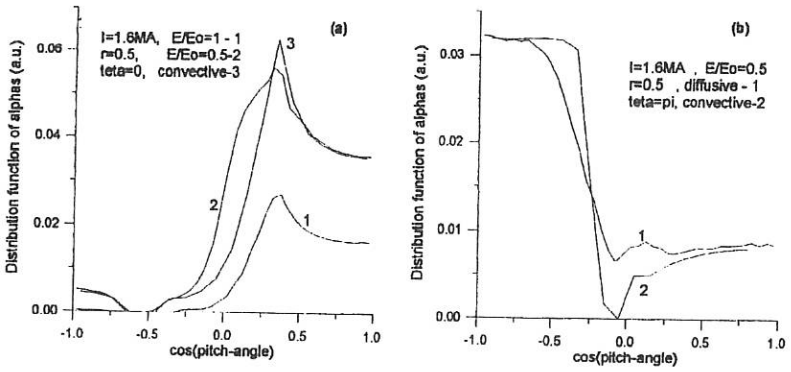

Fig.1. Pitch-angle distribution of alpha particles

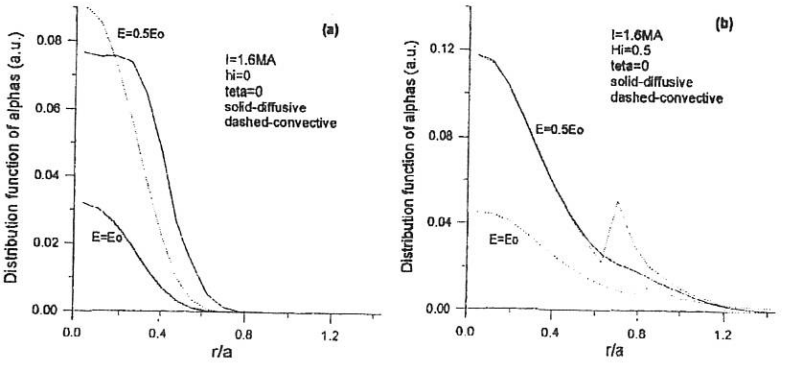

Fig.2. Radial profiles of alpha distribution function

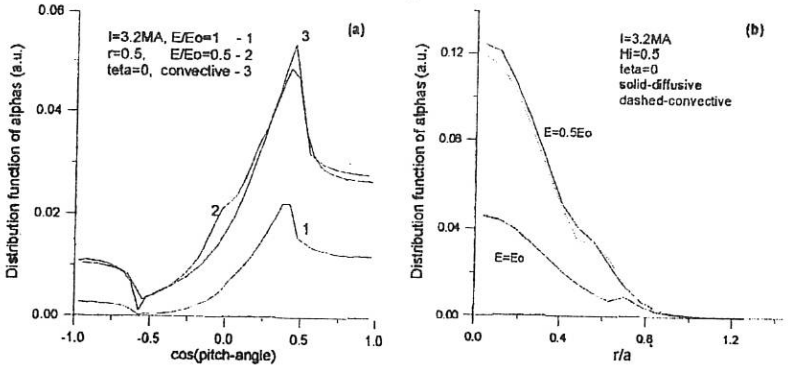

Fig.3. Alpha particle distribution function at I=3.2MA

Investigation of the Current-Kinetic Instability in the T-10 Tokamak

V.I.Poznyak, A.A.Bagdasarov, V.V.Piterskii, A.N.Yakovets
Russian Research Centre "Kurchatov Institute". Nuclear Fusion Institute
Moscow, Russian Federation

Plasma-wave processes were investigated in different regimes in the T-10 tokamak (n_e= 0.5-4x10^{13}cm^{-3}, I=100-400KA, B=14-28KGs). The purpose of investigations was to check the hypothesis about the key role of the potential plasma oscillations in the plasma self-organising processes [1,2]. Earlier, the authors of work [3] suggested the model of instability of rare uniform plasma with the flux of runaway electrons. But the later theoretical investigations [4] showed that the decision of the using kinetic equation is a stable distribution function with Cherenkov's and Doppler's plateau. We think that a consideration of such problems is efficient only for a nonuniform plasma with certain initial and boundary conditions.

Fig.1 shows a example of stationary nonuniform distribution function on longitudinal velocities of electrons. It was suggested that the local shape of distribution function is similar to the quasylinear decision [3,4]. Empirical distributions on perpendicular velocities were selected with taking into account real experimental data [2]. The working parameters of calculations are $\alpha=E_z/E_D$ and $\beta=\omega_{pe}/\omega_{be}$.Here. E_z=const. The beginning of Cherenkov's area coincides with the critical velocity $C=v_e\alpha^{-1/2}$ (v_e - thermal velocity). Doppler's mode is provided with the area $u>D=C/\beta$. The classical collisions are took into account in body part $u<C$. We note some essential pequliarities of such distribution. The part of accelerated electrons, them current and noise energy decrease under β increase because of the increment $\gamma_D\sim\omega_{pe}\beta$. Registration of suprathermal electrons is being more difficult. The flux of accelerated electrons $\Gamma\sim e^{-\alpha/4}$. them current and noise energy increase with α, but distribution function is compressed in the longitudinal direction owing to the reverse impact of the electron plasma waves. The corresponding dependence of the average direct velocity (local current density) on α is shown in Fig.2. In the region $\alpha>\alpha_2$, the current density is a fallen down function. A transition over the point $\alpha\sim\alpha_2$ leads to an

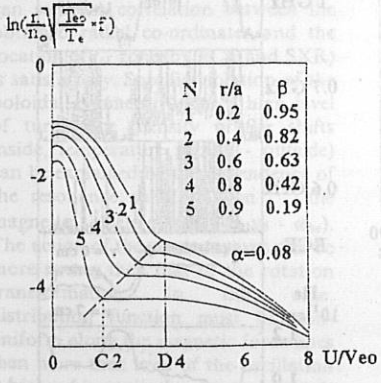

Fig.1. Space - dependent stationary electron distribution function normalised by the central values of the parameters.

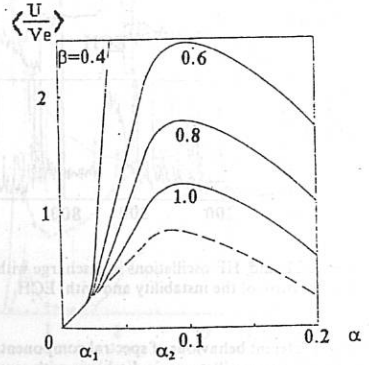

Fig.2. The average direct velocity versus β. The dotted line - main body part.

instability in consequence of the positive feedback between current and electric field E_z. The determinate modification of E_z is secured by the electrodynamic compression of the current channel (pinch-effect). It is essential what the plasma pinch velocity v_r is connected with runaway phenomenon by positive feedback ($v_r \sim E_z B_\vartheta / cB_z$, $E_z \sim v_r B_\vartheta / c$; $j \sim (c/r)d(rB_\vartheta)/dr$, $dj/dt \sim e<u>\Gamma \sim e\nu_{col}<u>\exp(-\alpha/4)$).

The oscillations of high amplitude can be realised if them spectrum is enough narrow (high coherent), that is, certain spectral components must have some advantages (principle of natural selection). We assume that plasma in the vicinity of the resonance magnetic surfaces q= 1,2,3..., where a magnetic flux function has the pequliarities [5], possesses such property. A regular structure of magnetic field allows to arise to the intensive coherent waves. The oscillations with the natural plasma frequencies of the corresponding zones are intensified in a direction of the resonance particles gradient. Most property of the oblique Langmuir waves is transport of the longitudinal momentum across the magnetic field. Under $\alpha \geq \alpha_2$, plasma flows out the excitation area, which is surrounded with the resonance surface r_{sm}, to the absorbing area (outside r_{sm}) with a drift velocity of more cold plasma component. Energy of the electric field is pass to the oscillations. Oscillations are damped under the realisation of the uniform space distribution inside the resonance magnetic surface r_{sm}. The corresponding heuristic formula for the period of the volume oscillations or duration of the breakdown

$\tau_{inst}[ms] \approx 0.2\, r_{sm}\, R[m]\, B_z[T]\, \{\min(T_e, T_i)\}^{-1}[KeV^{-1}]$

coincides satisfactory with the real experimental values for different installations.

Fig.3 shows some characteristics of the discharge with different development of the instability. Measurements of the plasma noises were fulfilled in region band 0.5-7.5GHz [1]. All investigated discharges are accompanied by the intensive splashes of the HF oscillations in the beginning of current (1-st time window), when we deal with a cold plasma cloud and

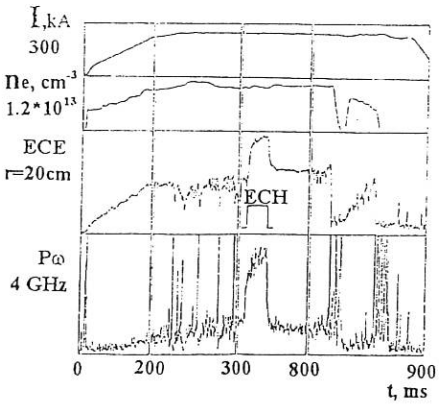

Fig.3. ECE and HF oscillations in discharge with different form of the instability and with ECH.

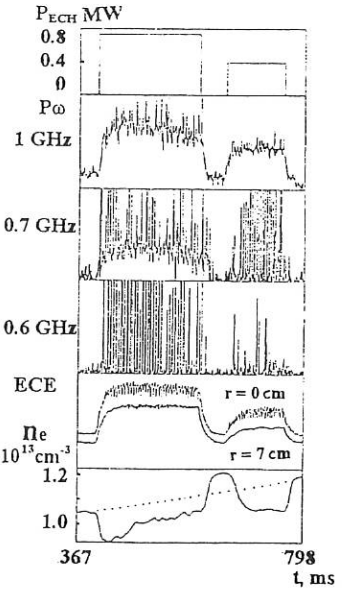

Fig.4. Different behaviour of spectral components of the plasma oscillations in discharge with saw-tooth oscillations under ECH. →

flux of accelerating electrons. The instability is finished by the establishment of an quasi-stationary spectrum. Fluctuations have a chaotic character and grow with plasma current. Before the ELM-like instability on q=3 (2-nd window), ECE and HF signals are being regular. HF signal is enhanced shortly before the breakdown mainly in low frequency region, but diminish in high frequency region. The instabilities are stopped under ECH (3-rd window), but a total intensity of the oscillation increasesseveral times. The disruptive form of the instability on q=2 is shown in 4-st window. As result, temperature and density drop very fast and disruption transforms spontaneously in the fan instability, when body plasma is cold, energy and current are concentrated in a runaway component. The characteristic energy region of tail for any kind of discharge is relatively narrow and soft (15-30KeV, by ECE and SXR).

Fig.4 shows the regime with saw-tooth oscillations. Average density increases monotonously without ECH. Under ECH, the modulation of it is determined by a rebuilding of the density profile. HF signal in a high frequency region has a noise-like shape. Under the successive reduction of frequency (or the rise of density under fixed frequency), the sharp splashes are appeared in the moment of each breakdown. This splashes can reach several order of value close to low frequency boundary of HF mode.

Fig.5 shows spectra of oscillation under OH, ECH and in the instability. The semibreadth of spectrum $\Delta\omega_s$ is essentially narrow then ω_{pe}. For the low frequency maximum, $\Delta\omega_m << \Delta\omega_s$. Its position shifts to the left then more, then the amplitude modulation of ECE is more deep. We believe that this maximum is the result of the non-linear scattering of the intensive Langmuir waves on electrons and ions and its stationary frequency corresponds to the ion plasma frequency ω_{pi}. Thus, we can find the space location of zone which plays the role of the carrier trigger generator. Fig.6A was obtained due to many frequency measurements in the regimes with quasistationary density before and in ECH. The horizontal lines show a probable interval of frequency of the stable maximum. Fig.6B illustrates two moments under ECH with increasing average density when the noise part of spectrum is appeared in the band of receivers with fixed frequencies. It can see that correlation between the obtained radial co-ordinates and the location of r_{s1} zone (by ECE and SXR) is satisfactory. Specific violation of the poloidal symmetry under a high level of turbulence (density profile shifts inside, temperature profile - outside) can be explained by the dependence of the resonance conditions on the magnetic field ($\omega_k = k_\psi v_\psi - \omega_{be}$). The action of the plasma waves can be more strong then that of the rotation transformation. In this case, distribution function must be non-uniform along the magnetic force lines then more then level of the oscillation is higher (in particular, for instability). It should to add that such almost ideal picture for q=1 mode can be

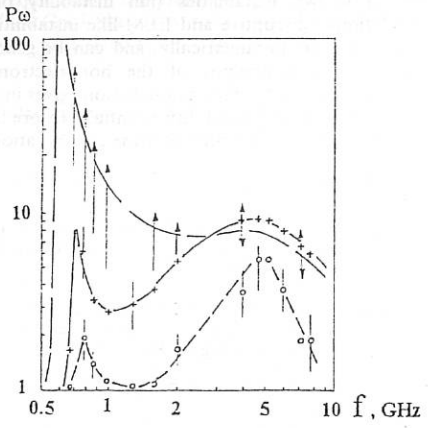

Fig.5. Spectra of the electron (Langmuir) oscillations for stable OH, ECH and in the instability q=1.

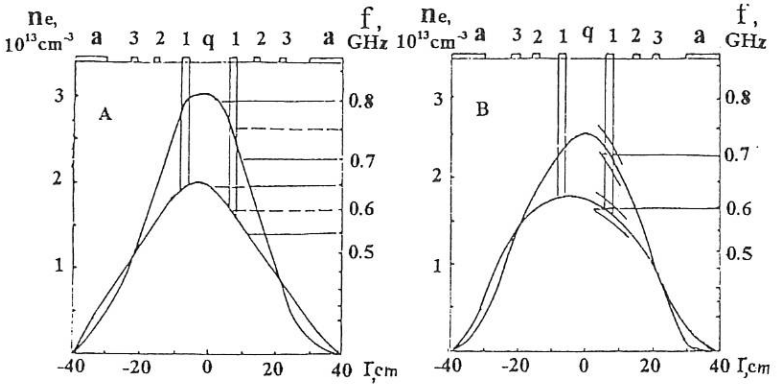

Fig.6. The determination of the space boundary conditions for mode q=1.

essentially complicated by the processes of another kind (radiation, ionisation, charge exchange), which are very important for more high mode number. Apparently, the impurity flux from wall and limiter plays the most important role for ELM-like instability. This flux is appeared as result of the plasma diffusion under action of the plasma oscillation. In such case, electric field on the plasma periphery can increase that leads to forming of the high energy electron tail. We have qualitative data that this is possible, but it is necessary more detail measurements.

The comparison of the theoretical and experimental data gives ground to assume that several known instabilities (fan instability of strong magnetised plasma, saw-tooth oscillations, disruptive and ELM-like instabilities) differ by the beginning and boundary conditions, i.e. parametrically, and can be generalised by the unit term - **current kinetic instability**. The analysis of the hot electron behaviour together with the spectral measurements of the plasma oscillations gives in some cases the possibility to obtain certain signs of the coming instability essentially before the time of breakdown.

Autors are very grateful for the collaboration with T-10 Team.

REFERENCES

1. V.I.Poznyak, A.A.Bagdasarov, V.V.Piterskii, A.N.Yakovets, V.I.Bodnarchuk, D.B.Evdokimov, Yu.D.Pavlov, Proc. in Intern. Conf. on Plasma Phys. and Contr. Fusion, Seville, 1994, IAEA, Vienna, 1995, v.2, p.169.

2. V.I.Poznyak, A.A.Bagdasarov, V.V.Piterskii, A.N.Yakovets, V.I.Bodnarchuk, D.B.Evdokimov, Yu.D.Pavlov, Proc. of the Ninth Joint Workshop on ECE and ECH, Borrego Springs, California, 1995, World Scientific Publishing Co. Pte., p.137.

3. V.V.Parail. O.P.Pogutse, Sov. Plasma Physics, 1976,v.22, p.228.

4. Muskietti L., Appert K., Vaclavik K., Appl. Phys., 2512 (1982) 1187.

5. Coppy B., Pegoraro F., Pozzoli R., Rewoldt G., Nucl. Fusion, 162 (1976).

Shear Flow Steady State of Tokamak Plasma with Anisotropic Pressure

V. I. Ilgisonis, V. P. Pastukhov

Russian Research Centre "Kurchatov Institute", 123182 Moscow, Russia

Introduction

Conventional equilibrium theory of plasma confined in tokamak deals usually with isotropic plasma models that is traditionally motivated by high frequencies of particle collisions. However, present day tokamaks operate with high ion temperature plasmas ($T_i \geq 10KeV$) under powerful auxiliary heating. Under such conditions a role of Coulomb collisions for plasma isotropization reduces significantly. Additionally, the most advanced regimes of tokamak operation recently developed in DIII-D and TFTR devices [1, 2] reveal fast plasma rotation with velocity of order of ion sound velocity in a plasma core. Such a fast plasma rotation awakes the necessity of adequate plasma behavior description during time scales less than typical isotropization time.

The effects of plasma anisotropy [3, 4] and plasma flows [5] were early separately considered to study plasma equilibrium in tokamak. In this report we take into account both these effects together. The specifics of plasma flows is a sensitivity (contrary to static equilibria!) to the pressure dynamic model. Indeed, in a static case the macroscopic equilibrium equation can be derived directly from kinetics under the only assumption on small Larmor radii. The details of chosen model for pressure evolution (ideal MHD adiabate, Chew-Goldberger-Low (CGL) double adiabates, or something else) are not important for force balance. In a case of rotating plasma stationary flow structure must hit in *all* the steady state equations, but not the force balance only. This requirement is able to restrict the stationary flow structure and/or the permissible distribution of stationary plasma parameters. That is why we have chosen CGL adiabates [6] as an acceptable model of pressure tensor evolution, which looks rather simple to be proceeded, but incorporates all the most important features of anisotropic plasma behavior. We have found that similar to [7] the presence of stationary plasma flows results from the hidden symmetry inherent in the CGL equations in toroidal topology. The general flow structure is revealed, and the generalized Grad-Shafranov equation, which covers the analogous one for static case [3] as well as Kerner's and Tokuda's one for isotropic plasma [5], is derived.

General relations

Macroscopic evolution of ideal plasma with mass velocity $\mathbf{V}$ obeys the following equation of motion:

$$\rho\,\partial_t \mathbf{V} + \rho\,(\mathbf{V}\nabla)\mathbf{V} + \nabla\cdot\mathsf{P} + [\mathbf{B}\times\mathrm{curl}\,\mathbf{B}] = 0\,, \tag{1}$$

where density ρ obeys the continuity equation

$$\partial_t \rho + \mathrm{div}\rho\mathbf{V} = 0\,, \tag{2}$$

and magnetic field $\mathbf{B}$ is supposed to be frozen in plasma:

$$\partial_t \mathbf{B} = \mathrm{curl}\,[\mathbf{V}\times\mathbf{B}] \quad (\mathrm{div}\mathbf{B}\equiv 0)\,. \tag{3}$$

We shall consider the diagonal pressure tensor P : $P_{ij} = p_\perp\delta_{ij} + (p_\parallel - p_\perp)B_iB_j/B^2$, whose components satisfy CGL adiabates:

$$d_t s_\parallel = d_t s_\perp = 0\,, \tag{4}$$

where functions $s_{\parallel,\perp}$: $s_\parallel = p_\parallel B^2/\rho^3$; $s_\perp = p_\perp/(\rho B)$; and d_t means the substantional time derivative: $d_t = \partial_t + (\mathbf{V}\nabla)$.

The equation set (1 -4) is complete and represents the macroscopic plasma dynamics for a CGL pressure model. Steady state configuration should be found from (1-4) by setting $\partial_t \to 0$.

Below we shall consider the systems with nested magnetic surfaces only. For such systems a general magnetic field is suitable to be represented in terms of coordinates $\{\psi, \theta, \zeta\}$:

$$\mathbf{B} = [\nabla\psi \times (q\nabla\theta - \nabla\zeta)] , \tag{5}$$

where ψ labels the magnetic surface, and angle-like coordinates θ and ζ are measured in the poloidal and toroidal directions correspondingly. The dimensionless quantity $q = q(\psi)$ has just the same sense as a "safety factor" in tokamak.

The representation (5) for a magnetic field allows easily to find the general structure of stationary velocity field from the Eqs. (3), (2) via "basic flows" [7]:

$$\mathbf{V} = \kappa\mathbf{u} + \eta\mathbf{v} . \tag{6}$$

Here $\kappa = \kappa(\psi)$ and $\eta = \eta(\psi)$ are arbitrary surface functions; $\mathbf{u} = \mathbf{B}/\rho$; $\mathbf{v} = \mathbf{e}_\zeta - R^*\mathbf{u}$; $\mathbf{e}_\zeta$ is a co-variant unit vector in the toroidal direction

$$\mathbf{e}_\zeta = J^{-1}[\nabla\psi \times \nabla\theta] ;$$

and the function $R^*(\psi, \theta, \zeta)$ is introduced to satisfy (2) as a particular solution of the equation

$$\mathbf{B}\nabla R^* = J\partial_\zeta\left(\frac{\rho}{J}\right) . \tag{7}$$

For irrational magnetic surfaces such a solution of (7) always exists; the related problem for rational surfaces was briefly discussed in [7]. For axisymmetric systems $\partial_\zeta \equiv 0$, and R^* can be chosen to be equal to zero.

The general shear flow structure (6) is consistent in stationary case with CGL-adiabates (4) if

$$s_{\|,\perp} = s_{\|,\perp}(\psi) . \tag{8}$$

The condition (8) generalizes as the conventional static equilibrium requirement $p = p(\psi)$ as the result $s \equiv p\rho^{-\gamma} = s(\psi)$ obtained for shear flows in frames of ideal MHD[7] (γ is adiabatic exponent). The break-down of the requirement (8) results in the narrowing of the class of permissible stationary flows. E. g., in axisymmetric case $\mathbf{V}\nabla s_{\|,\perp} = V^\theta\partial_\theta s_{\|,\perp} = 0$, that gives immediately $V^\theta \equiv 0$ (or $\kappa \equiv 0$) when $\partial_\theta s_{\|,\perp} \neq 0$. Therefore, if pressure distribution in tokamak doesn't satisfy (8), only toroidal stationary flows may appear. To avoid that narrowing we shall consider below a general case (8) only.

The obtained shear flow structure (6) satisfies the stationary equations (2-4) for any configuration with nested magnetic surfaces. In particular, $\operatorname{div}\rho\mathbf{V} = 0$, $\operatorname{curl}[\mathbf{V} \times \mathbf{B}] = -\operatorname{curl}(\eta\nabla\psi) = 0$, and the flow lines are lying on the magnetic surfaces. The magnetic surfaces should be calculated from $\nabla\psi$-component of the force balance equation (1), which can be rewritten in the form similar to the Grad's one [3]:

$$\rho\nabla\frac{V^2}{2} + \nabla p_\| - (1-\sigma)\nabla\frac{B^2}{2} = [\operatorname{curl}\sigma\mathbf{B} \times \mathbf{B}] - \rho[\operatorname{curl}\mathbf{V} \times \mathbf{V}] . \tag{9}$$

Two other components of vector equation (9) give the additional solvability conditions, which can be revealed for a general 3D-case. Multiplying (9) by $\mathbf{B}$ and $\mathbf{V}$ we find immediately the needed requirements in a divergent form:

$$\operatorname{div}\left(\frac{\mathbf{B}}{\rho}\left(\rho\frac{V^2}{2} + \frac{3}{2}p_\| + p_\perp\right) + [\mathbf{V} \times [\mathbf{V} \times \mathbf{B}]]\right) = 0 , \tag{10}$$

$$\operatorname{div}\left(\mathbf{V}\left(\rho\frac{V^2}{2} + \frac{3}{2}p_\| + p_\perp\right) + \sigma[\mathbf{B} \times [\mathbf{V} \times \mathbf{B}]]\right) = 0 .$$

Using (6, 7), the conditions (10) can be rewritten as

$$\mathbf{B}\nabla\left(\frac{\kappa-\eta R^*}{\rho}\mathbf{VB}-\frac{V^2}{2}+\frac{3p_\parallel+2p_\perp}{2\rho}\right) = -J\eta\mathbf{e}_\zeta\nabla\frac{\mathbf{VB}}{J}\,, \tag{11}$$

$$\mathbf{B}\nabla\left((\kappa-\eta R^*)\left(\frac{V^2}{2}+\frac{3p_\parallel+2p_\perp}{2\rho}+\frac{\sigma}{\rho}B^2\right)-\sigma\mathbf{VB}\right) = -J\eta\mathbf{e}_\zeta\nabla\left(\frac{\rho V^2+3p_\parallel+2p_\perp}{2J}+\sigma B^2/J\right).$$

The direct transition to the static equilibrium ($\kappa, \eta = 0$) in formulas (11) is not appropriate, because those formulas only result in the requirement for the quantity $(3p_\parallel + 2p_\perp)/2\rho$ be a surface function. Indeed, such a requirement follows from the longitudinal equilibrium equation

$$\mathbf{B}\nabla p_\parallel - \frac{1-\sigma}{2}\mathbf{B}\nabla B^2 = 0$$

under the conditions (8). However, there is no reason to satisfy (8) without plasma flows. Therefore, the presence of flows is able to reduce an arbitrariness in steady state distributions of plasma parameters. It should be noted again that all the considerations in this section do not invoke any assumption on geometrical symmetry of the configuration considered, but are based on the prescribed topology of nested magnetic surfaces.

Axisymmetric steady state

To compute a steady state for axisymmetric system, we work in the conventional cylindrical coordinates r, ζ, z with corresponding orthogonal basis $\mathbf{e}_r$, $\mathbf{e}_\zeta$, $\mathbf{e}_z$: $|\mathbf{e}_r| = |\mathbf{e}_z| = r^{-1}|\mathbf{e}_\zeta| = 1$. The magnetic field (5) in these coordinates has a form:

$$\mathbf{B} = \frac{1}{r}\left(\mathbf{e}_r\partial_z\psi + \mathbf{e}_\zeta\frac{I}{r} - \mathbf{e}_z\partial_r\psi\right)\,, \tag{12}$$

where poloidal current $I = qJr^2$ is introduced instead of q. However, in presence of shear flows poloidal current I does not appear to be a surface function. The toroidal coordinate ζ is presumed to be ignorable due to axial symmetry, i.e.

$$\partial_\zeta a = \mathbf{e}_\zeta\nabla a = 0 \tag{13}$$

for any stationary physical quantity a. The following useful expressions can be easily derived using (12):

$$\begin{aligned} B^2 &= \frac{1}{r^2}\left(|\nabla\psi|^2 + I^2\right)\,, \\ \mathbf{VB} &= \frac{\kappa}{\rho}B^2 + \eta I\,, \\ \mathbf{V}^2 &= \left(\frac{\kappa B}{\rho}\right)^2 + \eta^2r^2 + \frac{2\kappa\eta}{\rho}I = \left(\frac{\kappa|\nabla\psi|}{\rho r}\right)^2 + \left(\frac{\kappa I}{\rho r}+\eta r\right)^2\,. \end{aligned} \tag{14}$$

Let us consider the requirements (11) closer. Due to axisymmetry (13) the right sides in (11) equal zero identically, and the quantities under gradients in the left sides have to be surface functions. Using (14) we can write explicitly:

$$H(\psi) = \frac{\kappa}{2\rho^2r^2}(|\nabla\psi|^2 + I^2) - \frac{1}{2}\eta^2r^2 + \frac{3p_\parallel+2p_\perp}{2\rho}\,, \tag{15}$$

$$F(\psi) = I\left(\sigma - \frac{\kappa^2}{\rho}\right) - \eta\kappa r^2\,. \tag{16}$$

For chosen flow velocity parameters κ and η the relations (15, 16) restrict the admissible distributions of ρ and I to provide H and F be surface functions. When the relations (15, 16) are satisfied, the only ψ-component remains in Eq. (9) that looks as follows:

$$\frac{1}{r^2}\left(\sigma-\frac{\kappa^2}{\rho}\right)\Delta^*\psi-\frac{\kappa}{r^2}\nabla\psi\,\nabla\frac{\kappa}{\rho}+\eta\eta'\rho r^2+\frac{F'I}{r^2}+\frac{\kappa\kappa'}{\rho}\left(\frac{I}{r}\right)^2+\frac{\nabla\psi\,\nabla\sigma}{r^2}+ \qquad (17)$$

$$\rho H'-p_\perp\frac{s'_\perp}{s_\perp}-\frac{1}{2}p_\parallel\frac{s'_\parallel}{s_\parallel}=0\,.$$

Here the usual notation

$$\Delta^*\psi=r\,\frac{\partial}{\partial r}\left(\frac{1}{r}\frac{\partial\psi}{\partial r}\right)+\frac{\partial^2\psi}{\partial z^2}$$

was introduced. This formula generalizes the Grad-Shafranov equation for a flowing anisotropic plasma and together with (15, 16) provides the complete set of steady state equations for axisymmetric configuration. Equation (17) allows a formal transition to isotropic case analyzed in Ref. [5] by putting simply $\sigma\to 1$, $p_{\parallel,\perp}\to s\,\rho^\gamma$, $\gamma=5/3$. Without flows ($\kappa=0,\eta=0$) this formula gives the static anisotropic equilibrium [3, 4] (with above given remarks concerning the relation (8)).

To demonstrate these transition let us note that the quantity

$$Z=\rho H'-p_\perp\frac{s'_\perp}{s_\perp}-\frac{1}{2}p_\parallel\frac{s'_\parallel}{s_\parallel}$$

in Eq. (17) can be rewritten in terms of partial ψ-derivatives:

$$Z=\left(\frac{\kappa}{\rho}+\sigma-1\right)\partial_\psi\frac{B^2}{2}+\partial_\psi p_\parallel+\frac{\rho B^2}{2}\partial_\psi\left(\frac{\kappa}{\rho^2}\right)-\frac{\rho}{2}\partial_\psi\left(\eta^2r^2\right)\,. \qquad (18)$$

All the above mentioned transitions should be done using a form (18) rather then (17). In particular, without flows the form (18) gives immediately:

$$Z\Big|_{\kappa,\eta\to 0}\to(\sigma-1)\,\partial_\psi\frac{B^2}{2}+\partial_\psi p_\parallel\,,$$

that provides the correct form for Eq. (17). If we go then to an isotropic case, Eq. (17) (accounting Eq. (18).) results precisely in canonical Grad-Shafranov equation. The only addition following from (8, 15) is the reasonable requirement for ρ to be a surface function while there is no such a requirement in conventional theory of static equilibria.

Thus, the equation set (15-17) covers indeed all the important particular cases [4, 5].

This work was supported in parts by INTAS grant 94-3802 and Russian Foundation for Basic Research (project 94-02-03443-a).

References

[1] F.M.Levinton, M.C.Zarnstorff, S.H.Batha, M.Bell, R.E.Bell, et all. Phys. Rev. Lett., **75**(24), 4417 (1995).

[2] E.J.Strait, L.L.Lao, M.E.Mauel, B.W.Rice, T.S.Taylor, et all. Phys. Rev. Lett., **75**(24), 4421 (1995).

[3] H.Grad.Phys.Fluids, **10**, 137 (1967).

[4] L.E.Zakharov, V.D.Shafranov. In: *Review of Plasma Physics*, Vol. 11, edited by B.B.Kadomtsev (Consultants Bureu, N.Y., 1985).

[5] W.Kerner, S.Tokuda. Z. Naturforsch., **42a**, 1154 (1987).

[6] G.F.Chew, M.L.Golberger, and F.E.Low. Proc.Roy.Soc. London **A236**, 112 (1956).

[7] V.I.Ilgisonis, V.P.Pastukhov. Plasma Phys. Reports, **22**(3), 228 (1996).

Numerical simulations of density fluctuations in T-10 SOL

Soldatov S.V.,Vershkov V.A.
RRC "Kurchatov Institute ",Institute of Nuclear Fusion, Moscow, 123182, Russia.

Several turbulence types were identified in T-10 experiments in core and SOL [1, 2, 3]. The present work is devoted to numerical modeling of turbulence structure in the SOL obtained by means of multipin Langmuir probe. In principle the reconstruction of the whole spatial and time evolution of the turbulence from measurement at several fixed spatial positions is difficult and even not correct in the case of small propagation velocities of fluctuations. Usually only two spatial points, separated in poloidal direction were registered. Thus only restricted number of parameters such as the form of the signals, Fourier, cross-phase and coherency spectra, auto- and cross-correlation functions were available to characterize the turbulence. As the direct reconstruction of the spatial turbulence structure was not possible, so the numerical model was developed. The best fitting criteria were the coincidence of all mentioned above parameters in experimental and model data. The final goal of modeling is to determine spatial and temporal characteristics of different turbulence types in order to compare them with theory. The turbulence model was developed on the base of probe measurements due to the fact, that interpretation of probes data much more certain, then reflectometry.

It is supposed, that the fluctuations may be described by the stochastic space distribution of local density enhancements. The perturbations have spatially distribution as Gauss function with a half-width Δ , which may vary randomly in the range +/- δ and move in poloidal direction with the phase velocity V. The fluctuations rise and decay (life time) exponentially with times τ_1 and τ_2. The Gaussian and oscillating spatial distributions are possible according to expression:

$$n(x_p, x_1, t) = \exp\{-(x_0 - x_1)^2/\Delta^2\} \times \{b + a\cos(2\pi\gamma(x_0 - x_1)/\Delta\} \times$$
$$\times \{\exp-[(t-t_0)/\tau_2]^{\alpha} - \exp-[(t-t_0)/\tau_1]^{\alpha}\},$$

where $x_1 = x_0 + V*t$; x_p- probe position; x_0- initial position of perturbation; x_1 - position of enhancement at time t; γ - spatial period of oscillation; α - the parameter which control the time evolution; parameters a and b determine the relative contributions of aperiodic and oscillating parts.

The local density enhancements are introduced with time period T to the computational field randomly in time and space. Each local enhancement is treated during certain time, when it decays to negligible level. The probes positions are chosen inside the computational field. The code generates the time realizations of density evolution at two probe positions with the time step of 1 μs. Thus the form of code

output exactly simulate experimental data and can be processed with the same procedures as experimental data.

The comparison of experimental and simulated turbulence characteristics for the two cases of "broad band" turbulence [1, 2] is presented in Fig. 1 a and b. This type of turbulence is typical for all plasma column and characterized by very broad amplitude spectrum, flat coherence spectrum and low coherence value. The autocorrelation function are very narrow about 1.5 - 3 μs. The experimental data for both figures were taken in one discharge during density build up phase and after switching off the gas valve. The experimental and the simulated data were obtained with the probes distance of 0.6 cm. The Fourier amplitude spectrum, cross-phase, coherence spectrum and autocorrelation function are presented. The model parameters for the Fig. 1 a was: Δ= 0.2 cm ; τ_1 = 1.1 μs ; τ_2= 6 μs ; V = 1.75×10E5 cm/s ; α = 5. For the second case those parameters were: Δ= 0.15 cm; τ_1 = 2 μs; τ_2= 2.1 μs; V = 2.35×10E5 cm/s ; α = 1. It is seen that in both cases the computer model well simulates experimental data. It must be underlined that it is possible to reproduce very broad amplitude and coherence spectra together with the autocorrelation functions with one waveform of single turbulence event. The poloidal velocities from the slope of cross-phase correspond well to the code input value. The simulations show that the gas puff significantly influence the properties of "broad band" leading to the increase of spatial localization Δ.

The comparison of experiment with the code for the case of "edge" turbulence [2] is presented in Fig. 1 c. Those fluctuations are typical for the cold SOL regions and look like aperiodic relaxations with rising time 2 - 10 μs and decay time about 100 μs. The spatial dimensions are about 3 - 5 cm. The most important peculiarity of the "edge" turbulence is the value of coherence of 0.5 as it is seen in Fig. 1 c. Such low coherence value for the probes separation 0.6 cm is absolutely inconsistent with the perturbation width 3 cm and life time 100 μs in the frame of simple computer model, discussed above. Special model have been developed to simulate this turbulence. It is supposed that local enhancement of 3 - 5 cm contains stochastic turbulence of smaller scale inside. It looks like a turbulent envelope moving poloidally. The low coherence results from low life time of this small scale turbulence. It is seen that results of such model are in good agreement with experiment. The small fraction of "broad band" was also added. The parameters of the model are as follows: Δ of envelopes equal to 1.75 cm; Δ_2 for secondary turbulence is equal to 0.5 cm and their life time 15 μs. The velocity was 0.3×10E5 cm/s. Good agreement with experiment supports the idea of complex nature of "edge" turbulence. The case of mixture of the "edge" turbulence with the "broad band" is illustrated by Fig. 1 d and 2. Figure 1 d presents the comparison of the experiment and the model for the probes distance 0.6 cm. Simple model was used

for simulation of two types of turbulence. The model parameters for "edge" turbulence were : Δ= 2 cm ; τ_1 = 15 μs ; τ_2= 30 μs ; V = 1.8×10E5 cm/s . For the "broad band" case those parameters were: Δ= 0.2 cm ; τ_1 = 1.0 μs ; τ_2= 5.5 μs; α=6; V = 1.8 ×10E5 cm/s. The results are presented in Fig.2 a and b for probes distance 0.6, 1.2 and 1.8 cm. The coherence disappears uniformly in experiment and model at 1.2 and 1.8 cm distance over all frequencies except the lowest. High coherence at distance 1.8 cm, proves big dimensions and long life time of the "edge" turbulence.

The case of "high frequency quasi-coherent" turbulence [1, 2, 3] is shown in Fig. 1 e. This turbulence type is always observed together with the "broad band" and some fraction of "edge" turbulence. The "HF quasi-coherent" turbulence is characterized by the maximum at 30 kHz in amplitude and coherence spectra. It was modeled by stochastic bursts of oscillations at this frequency. The parameters of HF quasi-coherent turbulence are: Δ= 2 cm; τ_1 = 15 μs ; τ_2= 20 μs ; V = 1.0×0E5 cm/s ; γ = 0.65. The "edge" turbulence parameters in the model were : Δ= 1.5 cm ; τ_1 = 10 μs ; τ_2= 50 μs ; V = 0.4×10E5 cm/s and for the "broad band": Δ= 0.25 cm ; τ_1 = 2.3 μs ; τ_2= 2.8 μs ; V = 1.2×10E5 cm/s . The agreement with experiment is good. The presented results illustrate the typical case when all three turbulence type have different velocities. Figure 1 f shows the experimental and model results for the correlation reflectometry in core plasma. These data were simulated by means of "HF quasi-coherent" and "broad band" turbulence. This result is just qualitative due to the difficulties in interpretation of reflectometry data.

In summary it is possible to conclude that the simple model may satisfactory simulate "HF quasi-coherent" and "broad band" turbulence, while more complex model is needed for the "edge" turbulence. The question about unumbiguity of such interpretation must be addressed in future.

This work was supported by Russian Foundation for Fundamental Researches, the Grants Nos 94-02-06521-a and 96-02-18807.

References.

1. Vershkov V.A., 22th EPS Conf., Bournemouth (1995), V 19C, part IV, p.5

2. Vershkov V.A et al, to be publ. in Proc. of 12th PSI Conf.,Saint Raphael (1995) France.

3. Vershkov V.A. Soldatov S. V., this Conference.

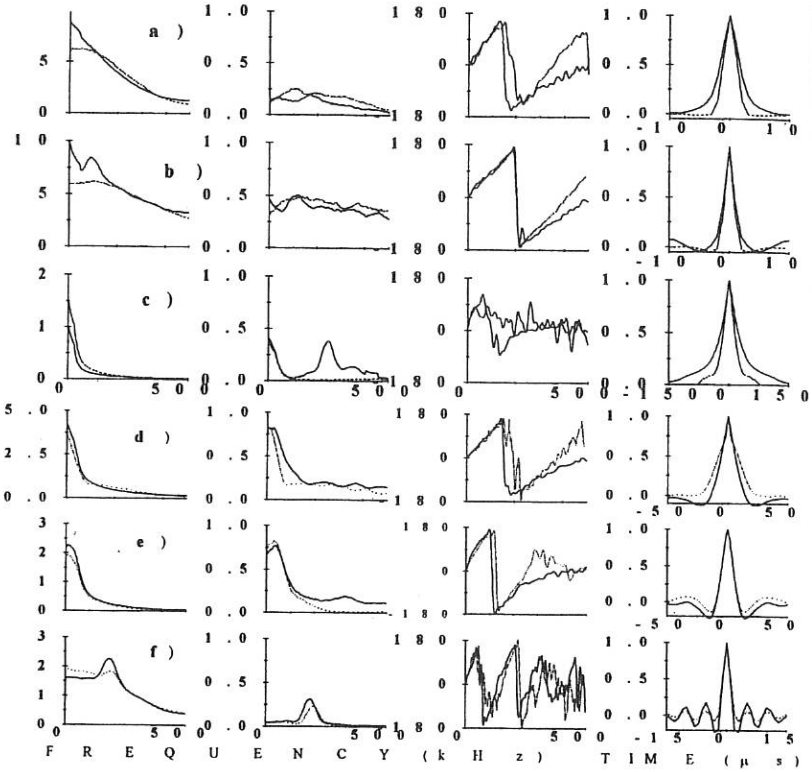

Fig.1 Comparision of experimental (solid) and model (dotted) results. From left to right: amplitude spectrum, cohernce spectrum; cross-phase and autocorrelation function. a) "broad band" turbulence during gas puff; b) "broad band" turbulence after gas puff; c) "edge turbulence"; d) the summ of "edge" and "broad" turbulence; e) "quasi-coherent " turbulence; f) "quasi-coherent " turbulence for reflectometer case.

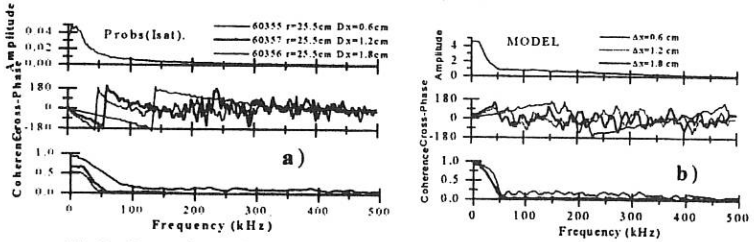

Fig.2. Comparison of the experimental and model results for three different probes distance. a) experiment; b) model

Investigation of three types of core small scale density fluctuations, identified in T-10 experiments

V.A.Vershkov, **S.V.Soldatov.**

Nuclear Fusion Institute RRC "Kurchatov Institute", 123182, Moscow , Russia.

Three types of small scale density turbulence were identified in the core plasma in previous T-10 experiments with correlation reflectometer [1, 2, 3]. Experiments with multipin Langmuir probes were carried out [5, 6] to verify reflectometry results. This report summarize the properties of core turbulence.

The T-10 experimental setup and diagnostics described in [3, 5]. The probes and reflectometry register simultaneously two poloidally separated channels at 1 MHz sampling rate for 0.5 s. The OH and ECRH discharges were investigated.

Figure 1 f presents the typical data of two poloidally separated reflectometry channels reflected at r=18 cm in the core plasma. The Fourier amplitude of the first signal, the coherency spectrum of two signals and the autocorrelation function of the first one are shown. Three turbulence types may be distinguished. They are associated with maximums at zero and 170 kHz frequencies and the low coherent broad frequency band (10 - 500 kHz) forming background of both maximums, which were referred to in [3] as Low Frequency (LF) and High Frequency (HF) quasi-coherent turbulence and "broad band" turbulence respectively. In contrary to the HF quasi-coherent turbulence "broad band" and LF turbulence encounter significant difficulties in interpretation. In fact the broad spectrum with Fourier amplitude ~1/F was predicted in [4] as the universal spectrum of the reflected phase fluctuations at high turbulence level and LF maximum may result from the stochastic phase jumps at the moments, when interference of several reflected beams gives zero total amplitude. The probes data were used to clarify those problems. The ion saturation current of two probes spaced poloidally 0.6 cm apart was measured at five radial positions. In Fig. 1 b one can see the appearance of "broad band" turbulence with high frequency tail and low, but constant, coherency value alongside with "edge" low frequency fluctuations [6]. The dashed line proves a low poloidal coherence at the increased poloidal separation of the probes (1.2 cm). The case of practically pure fluctuations of that type may be seen in Fig. 1 d. The "HF quasi-coherent" bursts of oscillation appear in Fig. 1 c at r=25.5 cm as a maximum at 40 kHz. It's evolution with decrease in radius can be seen in Fig. 1 d, e, f for r=23.5 cm, the rail limiter probe and correlation reflectometry in plasma core. The maximum position is shifted to 100 , 120 and 150 kHz for the three cases, respectively. Figures 1 d,e,c also show the appearance of the "LF core" turbulence which corresponds to the maximum near zero frequency. Thus all three

core turbulence types were observed in the hottest part of the SOL by means of Langmuir probes. The computer model of turbulence types is presented in [7]. The properties of the three core turbulence will be discussed bellow.

"Broad band" turbulence - The "broad band" turbulence was found to be the most universal instability, as it exists over whole plasma column. It is characterized by very broad and practically constant amplitude Fourier and coherency spectra. The value of poloidal and radial correlation length is about 0.5 cm in core. The estimations give the value $k_{pol} \times \rho_i \sim 1$ in the cold and hot parts of the SOL and in core plasma. This turbulence is highly asymmetric poloidally [6]. It rotate in ion diamagnetic drift direction with respect to plasma [6], thus indicating possible ion origin. The "broad band" is sensitive to the gas influx, but it seems governs by the local plasma parameters. There are no observations of quick variations of that turbulence in response to the fast change of an edge conditions. The ITG instability is considered now, as the physical mechanism of the "broad band" turbulence.

"HF quasi-coherent" turbulence - The time evolution of that turbulence is analyzed in Fig. 2. The traces a - e are the Fourier amplitudes of autocorrelation function of one of the reflectometer channel. The autocorrelation functions were taken with the intervals of 0.5 ms for time realizations of 1 ms. The Fig. 2 f show the Fourier amplitude of time averaged autocorrelation function. The Fig. 2 g and h present the time averaged cross-phase and coherence. The presence of a quasi-monochromatic oscillations are clearly seen for each 0.5 ms realizations. The values of their frequencies vary in time from 110 to 160 kHz in random way, resulting in appearance of the maximum in spectra at 125 kHz in Fourier of average autocorrelation function and coherence. The poloidal phase velocity of oscillations from the slope of cross-phase equals to 2.7x 10E5 cm/s, which gives the wavelength about 2.0 cm and $m \approx 45$, $n \approx 30$. The radial correlation length is also 2-3 cm. Thus two physical mechanisms may be distinguished: the existing of unknown driving force over frequency range of 110 - 160 kHz and realization of that drive in random excitation of high rational modes. The exited wavelength is sensitive to the impurity composition and it decreases after Ne puffing [3]. The amplitude and the number of oscillations in the bursts decreases during working gas puff. The decrease of the oscillation number in the bursts evidenced the increase of dissipation. Thus the amplitude decrease may be explained by the relatively more strong increase of the dissipation due to toroidal modes coupling with respect to excitation rate. The HF turbulence rotates together with plasma [1, 7]. The HF quasi-coherent turbulence is sensitive to the edge conditions [3] and may be involved in "nonlocal" transport.

"LF core" turbulence - This type of turbulence is the most difficult in interpretation due to the existing of quick stochastic small density jumps and the

absence of rotation typical in core plasma. The first reflectometry measurements with the registration of the phase derivative show the excitation LF quasi-coherent modes, as it is seen in Fig. 1 d and e, alongside with the stochastic spikes. In order to exclude the specific reflectometry technical origin of such spikes, experiments with direct phase recording and probes measurements were made. Figure 3 a show the ion saturation current trace in the cold SOL region. It is clearly seen specific relaxation type "edge" turbulence [6] together with the burst of oscillations. The latter were considered in [6] as the edge localized "Alfven Frequency Modes" (AFM) observed in TFTR [8]. The time traces of the probe ion saturation current in the hot SOL (Fig. 3 b), the tip limiter probe (Fig. 3 c) and core reflectometry measurements with phase converter (Fig. 3 d) also show the presence of stochastic jumps. It is important that typical time of the jumps for all four cases about 2-5 μs, which is near to the period of ARM equal to 4 μs in cold SOL (Fig. 3 a) and 2 μs (Fig. 3 c). Thus the experiment proves the reality of the jumps. It may also indicate the involvement of MHD processes in this phenomenon. The typical feature of LF Core turbulence in the central part of discharge is the absence of rotation. It is clearly seen from the constancy of cross-phase in Fig. 4 a, taken at the r=12 cm. In contrary at r=17 cm it begins to rotate with the same velocity as "HF qusi-coherent" turbulence (Fig. 4 b). The estimated poloidal wavelength about 18 cm for 30 kHz at r=17 cm, but such estimations not possible in the central case.

This work was supported of Russian Foundation for Fundamental Researches, the Grants Nos 94-02-06521-a and 96-02-18807.

REFERENCES

1. V.Vershkov et al, 15th IAEA Conf., Plasma Phys. and Contr. Nucl. Fus., 1995, V 2, p.65.

2. Vershkov V.A., et al, 21th EPS Conference , Montpellier, 1994, V 18B, part 3. p. 1192.

3.V.Vershkov, 22th EPS Conf.,Bournemouth 1995, V 19C, part IV, p. 5.

4. Nazikian R., Mazzucato E., Rev. Sci. Instr. V 66, No 1, Part II, (1995) 392.

5.Vershkov V.A., et al, 21th EPS Conference , Montpellier, 1994, V 18B, part 2. p. 886.

6. Vershkov V.A., et al, to be publ. in Proc. of 12th PSI Conf., Saint Raphael, France, 1996.

7. Soldatov S.V.,et al, this Conference.

8. Z. Chang et al, Nuclear Fusion, V 35 (1995) 1469.

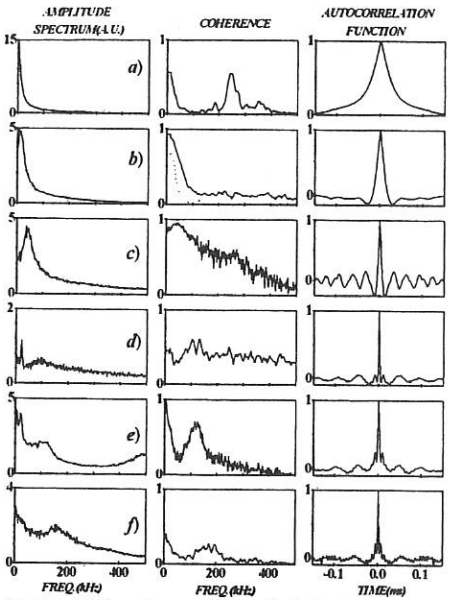

Fig.4. Radial dependences of the amplitude Fourier and coherency spectra and the autocorrelation function: (a) probe at R=30.5cm; b) probe at R=27.8cm; (c) probe at R=25.5cm; (d) probe at R=23.5cm; (e) probes at the rail limiter tip; (f) correlation reflectometry at R=18cm.

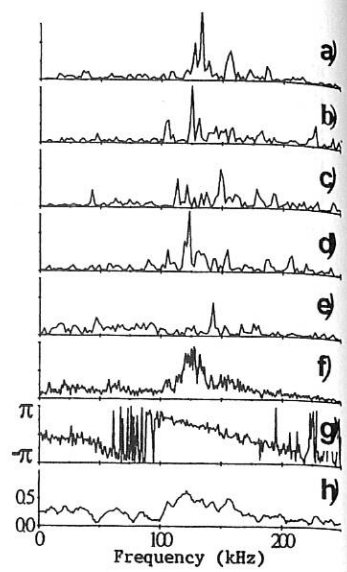

Fig2 Time evolution of the HF quasi-coherent turbulence; a)-e) - Fourier spectra of autocorrelation function, taken each 0.5 ms; f) - Fourier spectrum of the time averaged autocorrelation function; g) - averaged cross-phase; h) - averaged coherence.

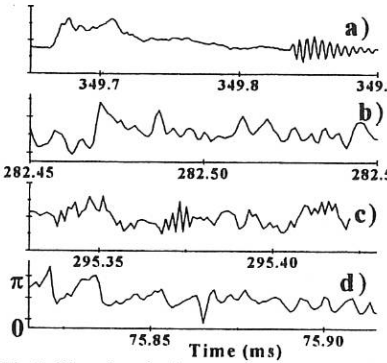

Fig.3. The signals time traces. Ion saturation currents for probes at r=30.5 cm (a);r= 23.5 cm (b); rail limiter probe (c); reflectometry phase converter (d).

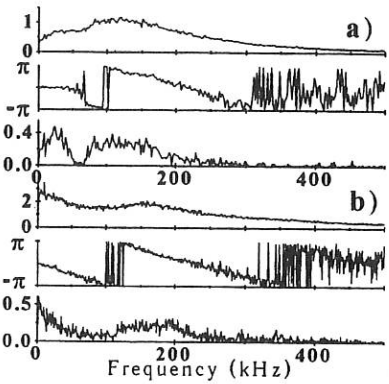

Fig. 4. The amplitude. coherence spectra and cross-phase for reflectometer. a)reflection from 12 cm; b) - from 17 cm.

ON THE MODELS OF HEAT TRANSPORT IN A TURBULENT MAGNETIZED PLASMA

Yu.V.Gott, E.I.Yurchenko

RRC "Kurchatov Institute", Moscow, Russia

Models representing various types of turbulent transport in the plasma confined by an external magnetic field are complex sets of non-linear differential equations in partial derivatives in a real space and in a phase one. The complexity of these model sets of equations applied to production of heat transport coefficients and to prediction of the energy confinement time in toroidal magnetic traps at present makes it necessary to use the methods of the similarity theory for a theoretical analysis. Examples of utilizing these methods for a number of turbulent models are represented in [1-3].

In a given paper, we shall investigate the properties of the heat transport models in a turbulent magnetized plasma, dependent on the main decisive parameters: ρ/a, β, d/a, λ/a. Here ρ and d are the Larmor and Debye radii, β is the plasma pressure to the magnetic field pressure ratio, λ is the particle range respective to the Coulomb collisions, a is the characteristic plasma size.

Since we consider four main dimensionless parameters, the total number of transport models is determined by the number of all the possible combinations out of four different elements, being equal 16. In [1-3] eight kinetic models and two MHD ones were analyzed.

In this paper, using algebraic equations representing physical conditions of collisionality, quasi-neutrality, electrostaticity and magnetohydrodynamicity, the similarity criteria for eight MHD-models have been produced. The magnetohydrodynamicity condition was first proposed in [4]. Satisfying this condition the transport coefficients do not depend on the Larmor radius.

For conveniency of comparison with the experimental data, let us write the ion diffusivity coefficient in the form:

$$\chi \sim n^{-p} \cdot T^{-q} \cdot B^{-r+1} \cdot a^{-s+2} \qquad (1)$$

where n and T are the plasma density and temperature, B is the magnetic field magnitude. The indices p,q,r,s are chosen so that the results of papers [1-4] could be used.

For an initial four-parametric model the ion diffusivity coefficient can be represented as

$$\chi_H \sim a \cdot v_T \cdot \left(\frac{\rho}{a}\right)^R \cdot \beta^\alpha \cdot \left(\frac{d}{a}\right)^K \cdot \left(\frac{\lambda}{a}\right)^\nu \qquad (2)$$

where v_T is the thermal velocity. Indices R, α, K и ν are found from the comparison between the expressions (1) , (2). The condition of going to zero for the indices of parameters λ/a, β, d/a, ρ/a in the expression (2) are the conditions of plasma collisionality, quasi-neutrality, electrostaticity and magnetohydrodynamicity, respectively.

$$\nu = 2p + r - s = 0 \tag{3}$$

$$\alpha = -3p - q - \frac{3}{2}r + s = 0 \tag{4}$$

$$K = -8p - 2q - 5r + 4s = 0 \tag{5}$$

$$R = 6p + 2q + 4r - 2s - 1 = 0 \tag{6}$$

The form (2) of an expression for χ_H allows one to produce the equations for the indices p,q,r,s and the concrete relationships for the model coefficients χ_j for all the simpler models without an analysis of the corresponding sets of equations with all possible combinations of conditions $\nu = 0$, $\alpha = 0$, $K = 0$, $R = 0$ only, in accordance with the diagram, Fig.1. It is of interest to note that in such a way one can produce the transport coefficients of MHD models for which the corresponding sets of non-linear differential equations neither studied, nor even written.

As an example of implementing the similarity methods and turbulent transport models, given in Fig.1, let us obtain the expressions for the ion diffusivity coefficients in the Enhanced Reversed Shear mode (ERS) at the TFTR [5].

Physical processes resulting in the ERS-mode emergence are unknown at present. However, with the help of the methods of the similarity and of the invariance principle [1-3], even in this case, one can select a suitable model - having analysed various turbulent models - representing the ion heat transport and find the limitations to the transport coefficient dependencies on the main plasma parameters.

One of the ERS-mode features is that the ion diffusivity and diffusion coefficients in the vicinity to the magnetic axis of the tokamak are smaller by a few orders of magnitude than the corresponding neoclassical values. The modified ion diffusivity coefficient [6] is only a few times smaller than the standard neoclassical values, therefore it cannot explain the existing transport.

An analysis of the experimental data at our disposal on the Standard Supershot (SS) mode and on the ERS one allows one to make the following conclusions:

1. The turbulent mode at which the ion diffusivity coefficient is inversely-proportional it the ion temperature and to the magnetic field magnitude is realised in the vicinity to the tokamak centre in the SS-mode.
2. The mode at which the ion diffusivity is proportional to the root square of the electron temperature and inversely-proportional to the magnetic field magnitude is set in the vicinity to the plasma boundary. Such a turbulence was previously observed in the L-modes in the vicinity to the centre in a number of tokamaks [3].
3. Under ERS, at a power of heating exceeding the threshold one, the turbulence in the central region is suppressed.

The informational-physical technique proposed in [2] allows one to show that the ion diffusivity coefficient in both modes can be represented by Vlasov's G three parametric nonquasineutral electromagnetic model.

Within the framework of that model, the ion diffusivity coefficient in the vicinity to the facility centre has the form :

$$\chi_1 \sim \rho_e \cdot \nu_i \cdot \left(\frac{\rho_e}{d}\right)^4 \cdot \beta_i^{-3/2} \cdot \beta_e^{-1/2} \cdot \left(\frac{m_e}{m_i}\right)^{3/2} \tag{7}$$

or in the form convenient for calculations :

$$\chi_1 = \frac{670}{T_i \cdot B \cdot A_i^{3/2}} \cdot \frac{<n>}{n_o} \cdot \sqrt{\frac{r}{a} \cdot \left(1 - 0.6 \cdot \left(\frac{r}{a}\right)^2\right)} \qquad (8)$$

In the vicinity to the plasma boundary, one has

$$\chi_2 \sim \rho_e \cdot v_e \cdot \frac{\rho_e}{d} \cdot \left(\frac{\rho_e}{a}\right)^{1/4} \cdot \beta_e^{-5/8} \qquad (9)$$

or

$$\chi_2 = \frac{760 \cdot \sqrt{T_e}}{B \cdot \sqrt{A_i}} \cdot \frac{<n>}{n_o} \cdot \left(\frac{r}{a}\right)^4 \cdot \left[1 - 0.75 \cdot \left(\frac{r}{a}\right)^3\right] \qquad (10)$$

where ρ_e и d are the electron Larmor radius and Debye one , v_i and v_e are the thermal velocities of ions and electrons, β_i and β_e are the ion and electron plasma component pressure to the magnetic field pressure ratio, a is the minor tokamak radius, T_i and T_e are the ion and electron plasma temperature, A_i is the atomic mass of ion, n_o is the plasma column centre density, <> means an averagening over the plasma volume.

In the SS-mode the ion diffusivity coefficient for the whole plasma column is represented by the relationship

$$\chi_{SS} = \chi_1 + \chi_2 \qquad (11)$$

The ERS-mode differs from the SS-one by the fact that the ion diffusivity coefficient is determined in the main by processes occurring outside the central region, being represented by the relationship :

$$\chi_{ERS} = \chi_2 \cdot f \qquad (12)$$

where $f = \exp(-\exp(-z))$, $z = (t - t_o) \cdot \sigma^{-1}$, $t = r/a$, $\sigma = 0.05$, $t_o \approx 0.35$ - normalised t-radius, where the derivative of the safety factor respect to the radius (q') is equal zero.

The comparison between the experimental ion diffusivity coefficients (solid line) and the calculated ones with relationships (11) and (12) (•, ×) are given in Fig.2 for the SS-mode (before transition) and for the ERS-one (after transition). In this Fig. one can see that the proposed relationships well represent the radial dependence of the ion diffusivity coefficient for both modes under consideration.

1. Connor J.W., Plasma Physics and Controlled Fusion, 1988, v.30, p.619
2. Gott Yu.V., Yurchenko E.I., Plasma Physics Reports, 1994, v.20, p.853
3. Gott Yu.V., Yurchenko E.I., Plasma Physics Reports, 1996, v.22, p.13
4. Gott Yu.V., Yurchenko E.I., 22nd EPS Conf. on Contr.Fus. and Plasma Phys., 1995, v.19C, pt.IV, p.221
5. Levinton F.M., Zarnstorff M.C.,Batha S.H., et al, Phys.Rev.Letters, 1995, v.75, p.4417
6. Gott Yu.V., Yurchenko E.I., On effect of finite plasma pressure on the neoclassical ion heat transport, this conference

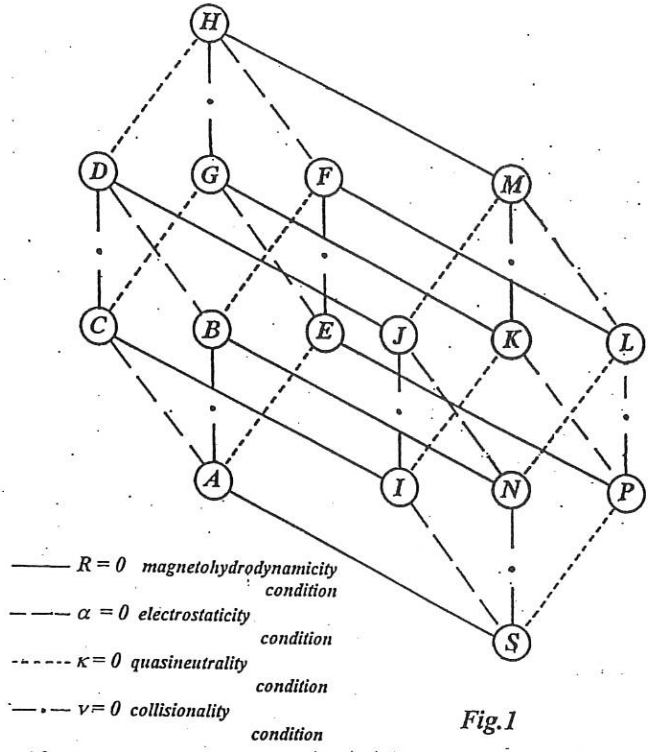
H
D
G
F
M
C
B
E
J
K
L
A
I
N
P
S
R = 0 magnetohydrodynamicity condition
α = 0 electrostaticity condition
κ = 0 quasineutrality condition
ν = 0 collisionality condition

Fig.1

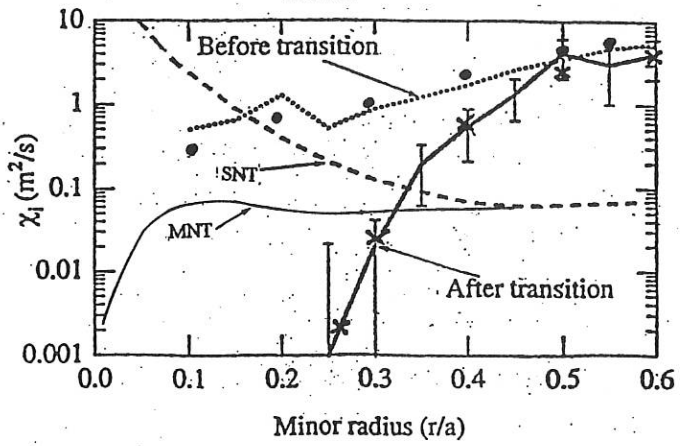
10
1
0.1
0.01
0.001
0.0
0.1
0.2
0.3
0.4
0.5
0.6
Before transition
SNT
MNT
After transition
χi (m²/s)
Minor radius (r/a)

Fig.2

NEOCLASSICAL ION HEAT TRANSPORT IN A PLASMA WITH HIGH GRADIENTS IN PARAMETERS

Yu.V.Gott

RRC "Kurchatov Institute", Moscow, Russia

All the relationships used at present for representing neoclassical transport in the tokamak plasmas have been produced under assumption that the characteristic gradient dimensions are much greater than the maximal width of the banana trajectories. In that case the heat and particle fluxes in the plasma are proportional to the gradients of temperature and dencity.

Under real conditions these assumptions are not alwais satisfied, and therefore it is of interest to produce relationships representing neoclassical transport in a plasma with large gradients of parameters.

The distribution function produced by Kovrizhnykh [1] in the τ (Krook) - approximation [1] does not include limitations to the rate of changes in the plasma parameters along the radius, and therefore it can be used for solution of a given problem.

The first attemt of finding an effect of banana trajectory width on the neoclasical heat transport done in [2,3] has shown that an increase in the banana trajectory width at the fixed characteristic plasma temperature and density gradients results in a non-linear increase in the heat fluxes.

In this paper the radial plasma temperature and density dependences are taken in the form :

$$T_i(r/a) = T_o \cdot (1-(r/a)^2)^{\alpha} \qquad (1)$$

$$n(r/a) = n_o \cdot (1-(r/a)^2)^{\beta} \qquad (2)$$

where a is the minor tokamak radius, T_o and n_o are the ion temperature and the density at the plasma column centre. A change in the temperature gradient size $L_T = \left(d\ln T_i/dr\right)^{-1}$ and in the density one $L_n = \left(d\ln n/dr\right)^{-1}$ has been done due to a change in the parameters α and β. Neoclassical walues were taken as maximal widths of banana trajectories, Δ .

The calculations have been done by the numerical method in a banana range of collisional frequencies with help of method published in [2,3]. The results of calculations are approximated by analytical relationships.

It was shown that the ratio of the ion diffusivity coefficient χ to the neoclassical coefficient χ_{NC} can be represented in the form :

$$\chi / \chi_{NC} = \frac{1 + 2Z_T + 6Z_T^4 + 6(Z_T Z_n)^{1.5}}{1 + 1.5Z_n^{1.4}} \qquad (3)$$

Thus the ion diffusivity coefficient in the complicate nonlinear way depends on $Z_T = \Delta / L_T$ and on $Z_n = \Delta / L_n$.

One can see that when the ratio of the maximal banana trajectory width to the size of density gradient approachs to unity the ratio χ / χ_{NC} is 2-2.5 times reduced, and when the ratio of the maximal banana trajectory width to the size of temperature gradient approachs to unity the ratio χ / χ_{NC} , is almost eight time increased. At the tendency of these quantities to be equal unity simultaneously, the ion diffusivity coefficient is 10-20 times increased (See Fig.1).

In the neoclassical theory, the total energy flux Q is related with the heat flux q and with the convective energy flux ΓT by the relationship $Q = q + y\Gamma T$, where Γ is the diffusion coefficient. The quantity y depends on the frequency of collisions and it is changed in the range from 1.33 in the banana range to 3 in the Pfirsh-Schlüter range.

In the case under consideration, the ratio y / y_{NC} has the form :

$$y / y_{NC} = \frac{1 + 0.26Z_n^{1.65} + 3(Z_n Z_T)^{1.5}}{1 + 0.16Z_T + Z_n Z_T^5} \qquad (4)$$

One can see that in the banana range y depends on L_T, L_n and their combination, being varied from 1.33 up to ~3 (See Fig.2).

So if one wants to reduce the heat losses through the ion channel due to neoclassical processes, it is necessary to increase the plasma density gradient size and to reduce its ion temperature one.

1. Kovrizhnykh L.M., Fizika plasmy, 1982, v.9, p.1105

2. Gott Yu.V., Yurchenko E.I., Plasma Physics Reports, 1994, v.20, p.853

3. Gott Yu.V., Yurchenko E.I., Plasma Physics Reports, 1996, v.22, p.13

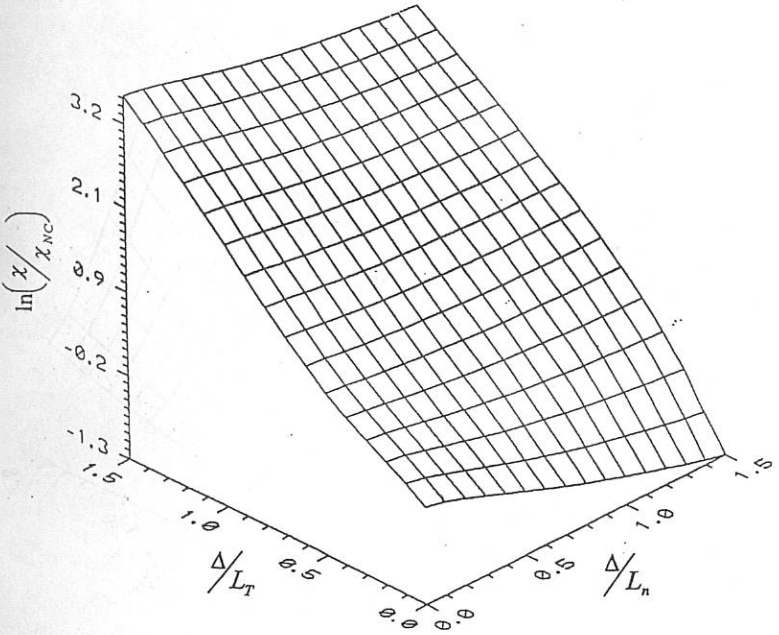

Fig.1

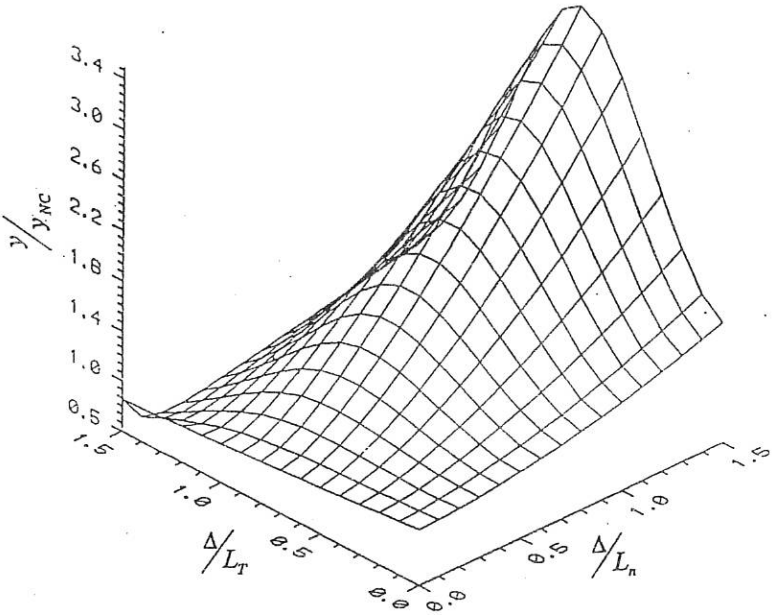

Fig.2

TEMPORAL EVOLUTION OF CHROMIUM LINE EMISSION DURING ARGON PUFFING IN T-10

V.A. Rantsev-Kartinov, V.A. Shurygin
RRC "Kurchatov Institute", INF, Moscow, Russia

1. Introduction

The assumption of coronal equilibrium and empirical so-called anomalous diffusion coefficients are commonly used to model the impurity radiation in tokamak plasmas. However, it is necessary to take into account the effects of suprathermal electrons and neutrals on the impurity radiation [1, 2]. These effects can result in appreciable increasing ionization, excitation and recombination rates especially during the nonstationary processes in the plasma periphery. It is in these regions the underestimate of rate coefficients is an equivalent to the overestimate of impurity diffusion. Taking into account these effects one can obtain the reducing of the model diffusion coefficients [3] and provide the calculation of x-ray spectra time evolution in startup phase and during a major disruption [4] generally without using of adjustable anomalous diffusion coefficients. Similarly, the electron-impact excitation of resonance lines with transition energy $\Delta E_\gamma / T_e >> 1$ for plasmas with $n_e \sim 10^{13}$ cm^{-3} and $T_e < 1$ keV appears to be under strong effect of suprathermal electrons [1].

Experiments in tokamaks have shown how the population of suprathermal electrons can be changed by puffing in some gas from almost complete suppression of their production up to regimes in which the majority of the current are carried by runaways [5, 6]. Hence, in these cases one would expect that the intensities of resonance lines with $\Delta E_\gamma / T_e >> 1$ are governed by population of suprathermal electrons. For example, when a large fraction of them is lost rapidly after gas puffing.

This paper presents time-resolved observations of resonance line emission (2p-1s - transitions) for Li- , Be-, B-like states of Cr ions with temporal resolution of about 1 ms (and $\lambda / \Delta\lambda \approx 10^3$) during pulse puffing argon in the T-10 tokamak. The founded differences in time evolutions of continuum and line chromium emission allow one to assign the observed radiation processes to the class of nonlocal transport effects [7] although our interpretation deals with the effects of suprathermal electrons on impurity radiation but not with traditional anomalous diffusion.

2. Experiment

The experiments were carried out in the T-10 tokamak ($n_e = 2 \cdot 10^{13}$ cm^{-3}, plasma current 220 kA, minor radius 34 cm, magnetic field 1.5 T). The horizontally scanning crystal spectrometer [8] was used on a shot-to-shot basis along the central chord of T-10. Four channels of the spectrometer were used simultaneously to record three resonance (2p-1s - transitions) lines of Li- (λ=2.202 Å), Be- (λ=2.214 Å) and B-like (λ=2.228 Å) charge states of chromium and continuum emission (close to λ=2.0 Å). The data collected during several tens of shots in T-10 were averaged and then measured background signal was subtracted. The final estimated error of intensity determination was about 10-15%. The duration of pulse puffing argon at 400 ms of the discharge was 1 ms. The K_α radiation ($E_\gamma(K_\alpha) \approx 3.0$ keV) from the plasma core and the electron temperature $T_e(t)$ have shown the delay time close to 40 ms (see Fig.1). All of the signals from chromium lines decayed immediately after the argon puffing without any delay time (it was at least lesser than 1 ms, see Fig. 2) while continuum signal

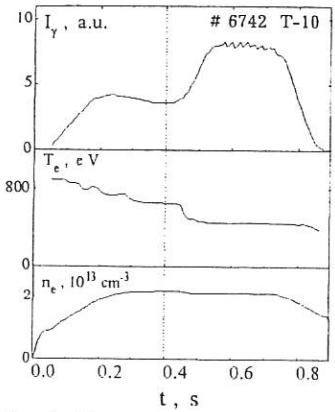

Fig. 1. Time traces of plasma density, temperature and x-ray emission of the argon K_α line measured along central chord in T-10.

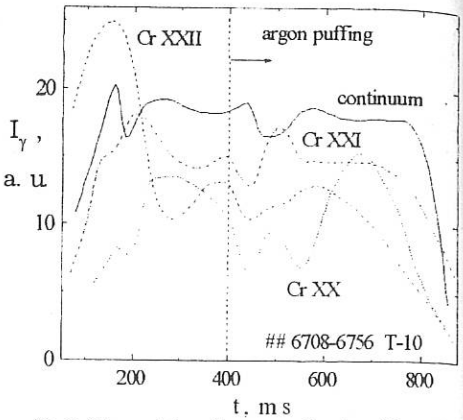

Fig. 2. Time evolution of resonance line intensities and continuum emission in discharges with the argon puffing at 400 ms.

even slightly increased during the first 40 ms after puffing. In contrast to this line intensity decaying following the argon puffing, the time evolution of their ratios shown in Fig. 3 reveals distinct correlation with the time evolution of continuum signal.

3. Interpretation and modelling

According to the estimate [1], the interpretation of resonance line intensity based only on the effect of thermal part of plasma electrons can lead to the error comparable with measured intensity if $E_D / E = 4\pi e^3 n_e \Lambda / E T_e \leq 7 \Delta E_\gamma / T_e$, where E and E_D are the electric and critical Dricer's fields respectively, e is the electron charge, Λ is the Coulomb logarithm. It means that for the T-10 conditions with $E_D / E \cong$ 10-20 and $T_e \cong$ 0.4-0.8 keV the nonthermal effects could be neglected only in the part of the x-ray spectrum where $E_\gamma \approx \Delta E_\gamma < 3$ keV. In the case of interested lines $\Delta E_\gamma / T_e \approx$ 8-12 with $\Delta E_\gamma \cong$5.65 keV. Averaging over the real non-Maxwellian electron distribution one can obtain that nonthermal contribution to the excitation rate could be decisive being proportional to the relative population of suprathermal electrons α_{zth}. From the other side, the intensity ratios for resonance lines are determined by ionization balance effects

$$I_w^{i+1} / I_w^i \sim n_{i+1} / n_i \,. \qquad (1)$$

The resulting balance due to effects of suprathermal electrons and neutrals on the charge state distribution [1, 2] can provide the ratios (1) even close to corona equilibrium but only for some states with fulfilled quasi-stationary conditions of coupled balance equations [4]. However, beside T_e the ratios (1) are functions of relative populations of neutrals $\xi_n = n_n / n_e$ and suprathermal electrons α_{zth} as follows

$$\frac{n_i}{n_{i+1}} = \frac{R_{i+1}^{rad} + \xi_n \cdot R_{i+1}^{cx} + R_{i+1}^{d}}{(1-\alpha_{zth}) \cdot \langle \sigma_i \upsilon_{th} \rangle + \alpha_{zth} \cdot \langle \sigma_i \upsilon_{zth} \rangle} \,. \qquad (2)$$

All ionization $\langle \sigma_i \upsilon_{th} \rangle$ and recombination rate coefficients (R_{i+1}^{rad}, $\xi_n \cdot R_{i+1}^{cx}$, R_{i+1}^{d} are radiative, charge exchange and dielectronic respectively) were calculated by the formulas from Ref. [9]. In particular,

$$\xi_n \cdot R^{cx}_{i+1} \approx 2.6 \cdot 10^{-7} \cdot Z_{i+1} \cdot \frac{n_n \upsilon_n}{n_e \upsilon_0} \quad , \qquad (3)$$

where R^{cx}_{i+1} in $cm^3\ s^{-1}$, υ_n is the velocity of neutrals, υ_0=2.2·10^8 cm s^{-1} , Z_{i+1} is the ionic charge. The parameter $\delta_{cx}=(n_n \cdot \upsilon_n)/(n_e \cdot \upsilon_0)$ from (3) varies in wide limits over the plasma cross section and/or in nonstationary processes such as a major disruption [10].

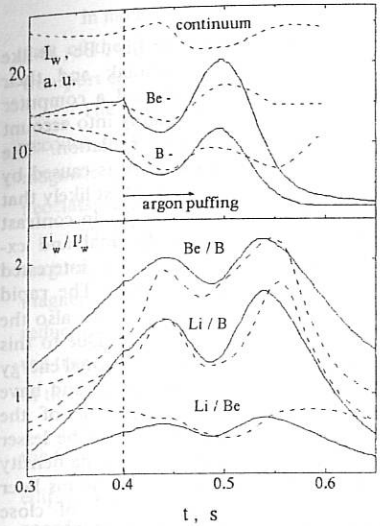

Fig. 3. Experimental (dashed) and calculated (solid) line intensities and their ratios during argon puffing.

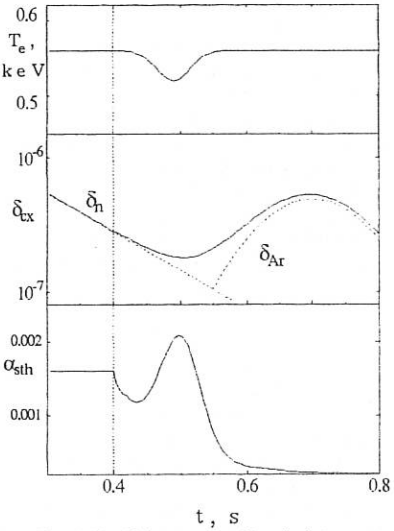

Fig. 4. Model functions used in calculations.

As follows from our calculations, the effects of suprathermal electrons on the ionization balance of Li-, Be- and B-like chromium states at T_e = 0.4-0.8 keV can be neglected if α_{sth} ($T_{sth} \approx 3$ keV) < 0.05. Hence, while the time evolution of I_w^i is determined by $\alpha_{sth}(t)$ (note that $\Delta E_\gamma / T_e \approx$ 8-12), the resonance line ratios I_w^i / I_w^j depend on $T_e(t)$ and $\delta_n(t)$. The results of modelling and their comparison with experimental data are shown in Fig.3. The model functions for $T_e(t)$, $\delta_{cx}(t) = \delta_n(t) + \delta_{Ar}(t)$ and $\alpha_{sth}(t)$ used in (1)-(3) are shown in Fig.4. According to the model, the changes observed on $I_w^i(t)$ during the first 150 ms after the argon puffing are related mainly to the time evolution of plasma electron energy distribution function. The time evolution of $\alpha_{sth}(t)$ was adjusted as followed from the time behaviour of Be-like state intensity in Fig.2. Moreover, similar time evolution of hard x-ray signals caused by runaway electron bombardment of the limiter have been observed on the PLT tokamak during gas puffing experiments [11]. The sharp α_{sth} decrease immediately after puffing does not affect the time evolution of ratios I_w^i / I_w^j as shown in Fig. 3. According to the model, the argon incoming changes the charge exchange recombination rate appreciably only in 150 ms after puffing and, finally, results in decrease in the ratios I_w^i / I_w^j for Be / B, Li / B and Li / Be states. Thus, the average charge of impurities decreases only in 150 ms after gas puffing.

It could be assumed that the α_{zth} increase in 40 ms after puffing deals with the secondary generation of runaway population [12]. In this time interval some part of incoming argon works as a source of secondary generated runaways. This assumption corresponds to the increase in I_w^i and probably in hard x-ray signals caused by runaway electrons as observed in PLT [11]. Moreover, the time of the Coulomb collisions between the runaways and the particles of argon is about 30 ms [12].

4. Conclusions

The time-resolved measurements of resonance line emission for Li- , Be-, B-like states of Cr ions during pulse puffing argon in the T-10 tokamak and their interpretation were presented. To interpret the data, we have developed a computer code that calculates the emission of chromium lines and their ratios taking into account the effects of suprathermal electrons and neutrals on impurity radiation. The calculations has shown that the time evolution of line intensities in T-10 is caused by the time behaviour of nonthermal part of electron energy distribution. Most likely that the plasma periphery gives the main contribution to the line intensities [8]. In contrast to the line intensities, the behaviour of line ratios are driven by thermal and cx-recombination effects. The change of the cx recombination rate for interested chromium charge states begins only in 150 ms after the argon puffing. The rapid decrease in α_{zth} immediately after puffing as it follows from the model means also the decrease in the part of plasma current that carried by runaway electrons. Due to this plasma current redistribution one would assume rather small increase in thermal energy of plasma electrons that observed also on the continuum signal (see Fig. 2) and have been interpreted as nonlocal transport effect in Ref. [7]. The time scale of the suprathermal population redistribution over the plasma cross section could be lesser than 1 ms at least [13]. At the onset of puffing, the peripheral changes in plasma density and temperature result in a suppression of runaway tail generation. Then, 40 ms later the secondary runaway electron generation becomes significant because of close collisions between fast tail electrons and electrons bounded on the shells of the argon ions. These electrons gain a considerable transverse momentum $p_\perp / p_{//} >> 1$ [12].

The time-resolved observations of line intensities during gas puffing can be useful to study nonstationary phenomena in tokamak plasmas and to analyze the effects of nonthermal electrons, charge-exchange and associated profile distributions on the line intensities of K_α - spectra of plasma impurities.

References

[1] Marchenko V.S., Yakovlenko S.I. Sov.J.Plasma Phys. **5**, 331 (1979).
[2] Krupin V.A., Marchenko V.S., Yakovlenko S.I. *JETP Letters*. **29**, 218 (1979).
[3] Gontis V.G., Lisitsa V.S. Sov.J.Plasma Phys. **11** (1985).
[4] Shurygin V.A. Proc. 22nd EPS Conf. Bournemouth. V.19 C. P. IV-013, (1995).
[5] Vlasenkov V.S. et al. Nucl. Fusion. **13**, 509 (1973).
[6] Swain D.W., Zweben S.J. Nucl. Fusion. **20**, 711 (1980).
[7] Gentle K.W. et al. Proc. 22nd EPS Conf. Bournemouth. V.19 C. P. I-005, (1995).
[8] Morozov D.Kh., Rantsev-Kartinov V.A. Plasma Phys.Rep. **20**, (1994).
[9] Gervids V.I. et al. Issues of plasma theory. Vol.12. Energoizdat (1982) (in Russian).
[10] Bortnikov A.V. et al. Plasma Phys. Rep. **21**, 634 (1995).
[11] Strachan J.D. et al. Nucl. Fusion. **22**,1145 (1982).
[12] Besedin N.T., Pankratov I.M. Nucl. Fusion. **26**, 807 (1986).
[13] Rodríguez-Rodrigo L. et al. Nucl.Fusion. **34**, 649 (1994).

EFFECT OF A FINITE PLASMA PRESSURE ON THE NEOCLASSICAL ION HEAT TRANSPORT

Yu.V.Gott, E.I.Yurchenko
RRC "Kurchatov Institute", Moscow, Russia

In modern tokamaks [1] the ion diffusivity and diffusion coefficients in the central part of the plasma column can be a few tens-times smaller than the corresponding transport coefficients predicted by the Standard Neoclassical Theory (SNT).

The SNT of transport in tokamaks has been developed without taking into account of the plasma pressure, assuming that the particle displacement from the magnetic surface is much smaller than the radius of this surface. In this connection, the neoclassical theory turns out to be unjust in the vicinity to the plasma column centre.

The due to regard for the finite plasma pressure results in a distortion in the magnetic surface configuration in the vicinity to the magnetic axis and in the toroidal magnetic field in the region occupied by plasma. One can assure himself that a reduction in the magnetic field - related with the plasma diamagnetism - does not affect the transport, but the ellipticity - related with the plasma pressure - results in reduction in the transport coefficients.

Let us consider the tokamaks with elliptic magnetic surfaces, presenting them in the form $r(\theta)^2(1 + e\cdot\cos 2\theta) = r^2\cdot(1 + e)$ and compare the transport through elliptic and circular cross-sections, equally long. Making transition to the rounded coordinate system ρ_o, θ let us find the relationship between the minor ellipse semiaxe r and a new radial variable :

$$\rho_o = r\cdot\{0.5\cdot[1.5\cdot(1+K) - \sqrt{K}]\} \qquad (1)$$

where $e=(K^2 - 1)/(K^2 + 1)$, K is the ratio of the ellipse semiaxes.

The trajectory of particle motion in the rounded coordinate system is represented by the set of equations of trapped particle motion :

$$\int_{\rho_*}^{\rho_o}\frac{\rho' d\rho'}{q} = \frac{R}{\Omega}\cdot(v_{\text{II}} - v_{\text{II}}^*) \qquad (2)$$

$$\rho_*\cdot\frac{d\theta_*}{dt} = \frac{\rho_*}{q\cdot R}v_{\text{II}}^* - v_d\cdot\cos\theta_* = 0 \qquad (3)$$

where q is the safety factor, Ω is the gyrofrequency, R is the major tokamak radius, v_{II} is the parallel to magnetic field component of velocity, v_d is the drift velocity, ρ_* and θ_* are the return point coordinates of trapped particles.

Considering the value of q as constant along the particle trajectory one can obtain from Eq.(2),(3) the dimensionless equation describes the trajectory of trapped particles :

$$x^2 - x_*^2 = \pm\left(\sqrt{x\cdot\cos\theta - x_*\cdot\cos\theta_* + \nu^2} - \nu\right) \qquad (4)$$

where $\varsigma = 2\cdot\rho\cdot q/(R\cdot\sqrt{E})$, $\nu = |\cos\theta_*|/(4\cdot x_*)$, $r = x\cdot\varsigma^{2/3}$, $E = 0.5\cdot[1.5\cdot(K+1) - \sqrt{K}]$

An analysis of these equations shows that when the particle turn-back point is located in the range of angles $0<\theta_*<\pi/2$, the trapped particles exist upon any magnetic surface, at $x_* \to 0$. Under condition $\pi/2 < \theta_* < \pi$ a limitation to the minimal radius of a magnetic surface emerges, where the particles still can be trapped

$$x_* \geq x_m = 2.02\cdot\left(|\cos\theta_*|/4\right)^{1/3} \qquad (5)$$

The treatment of the numerical solution results of Eq.(4) allows one to produce approximate expression representing the trajectories of trapped particle motion in the form convenient for flux calculation in the tokamak plasma.

For a positive branch of the trajectory we have :

$$\delta_+ = \sqrt{\cos\theta - \cos\theta_*}/(1 + 2\cdot\sqrt{x_*}) \qquad (6)$$

For a negative one we have:

$$\delta_- = x_*\cdot\sqrt{\cos\theta - \cos\theta_*}/(1 + 2\cdot x_*^{3/2}) \qquad (7)$$

where δ is the deviation of a particle from the surface with the radius x_*. In this case, x_* should satisfy the limitation (5).

The equation for calculation of the ellipticity of magnetic surfaces - dependent on the plasma pressure and the boundary plasma surface configuration [3] - can be written in form :

$$r^2\cdot e'' + (5 - 2\cdot S)\cdot r\cdot e' - S\cdot e = 3\cdot[\alpha\cdot\Delta' - (2 - S)\cdot\Delta'^2] \qquad (8)$$

where the prime designates the derivatives with respect to r, $S = r\cdot q'/q$ is the magnetic field shear, $\alpha = -8\cdot\pi\cdot p'\cdot R\cdot q^2/B^2$ is the relative plasma pressure gradient, Δ is the Shafranov's shift.

Since we are mainly interested in the processes in the vicinity to the magnetic axis, we shall solve Eq.(8) for the almost uniform current, i.e. at a small value of S for plasma column with equivalent radius a. For $p = p_o\cdot(1 - r^2/a^2)^n$ the solution found by expansion technique with respect to the degrees of deviation from the magnetic axis has the form :

$$e = e_a\cdot\frac{1 + S''\cdot r^2/12}{1 + S''\cdot a^2/12} + \frac{n^2\cdot\beta^2\cdot q^4}{2}\cdot\frac{R^2\cdot(1 - r^2/a^2)}{a^2\cdot(1 + S''\cdot a^2/12)} \qquad (9)$$

where e_a is the ellipticity of the boundary plasma column surface, $\beta = 4\cdot\pi\cdot p_o/B^2$ is the thermal/magnetic energy ratio.

One can see that the maximal ellipticity is reached in the vicinity to the magnetic axes and its value depends on the sign of a shear. At the negative shear the ellipticity is greater than that at the positive one.

For calculation the modified neoclassical ion diffusivity coefficient χ we have used the method described in [2] and the ion distribution function found in the τ (Krook) - approximation in [4]. Using the expressions (6),(7),(9) it is possible to write

$$\chi = C \cdot \frac{\chi_{NC}}{E^3} \int_0^{\pi/2} \cos^2\psi \cdot d\psi \int_0^1 \frac{\kappa^2 \cdot d\kappa^2}{\sqrt{1-\kappa^2 \cdot \sin^2\psi}} \int_0^\infty \Theta(\omega) \cdot \frac{x_*^{5/2}}{x_+^o} \cdot \left(\frac{\delta_+}{x_+} + \frac{\delta_-}{x_-} \right) \cdot d\omega \qquad (10)$$

where $\chi_{NC} = 0.17 \cdot A^{7/2} \cdot \varsigma_T^2 \cdot \left(r/a \right)^{-3/2} \cdot a^2 \cdot \tau_{ii}^{-1}$ is the neoclassical ion diffusivity coefficient through circular surface of the radius r, $A = R/a$ is the tokamak aspect ratio, τ_{ii} is the time of particle scattering within the angle $\pi/2$, $\varsigma_T = 2 \cdot \rho(T) \cdot q/R$, T is the particle temperature, $x_\pm = x_* \pm \delta_\pm$, x_+^o is the magnitude of x_+ at $\theta = 0$, ω is the ratio of particle energy to the T, $2\kappa^2 = 1 - \cos\theta_*$, $\sin\psi = \kappa \cdot \sin(\theta/2)$, other quantities are determined in [2].

Having done the numerical integration of the expression (10), one can produce the dependence of χ on the radius :

$$\chi = \chi_{NC} \cdot \frac{(r/a)^2}{E^3 \cdot [(r/a)^2 + 0.20 \cdot A^2 \cdot (\varsigma_T / \sqrt{E})^{2/3}]} \qquad (11)$$

From (11) one can see that, in difference from SNT, the modified ion diffusivity coefficient tends to zero, when the radius of magnetic surface under consideration tends to zero too. An increase in plasma pressure results in a rise in ellipticity, thus reducing the transport coefficient.

The ion diffusivity coefficient dependencies in SNT (curve 1) and modified one for the quantity $\xi = A^{3/2} \cdot \varsigma_T = 0.1$ - typical value for the DIII-D tokamak (curve 2) and for $\xi = 0.2$ (TFTR) (curve 3) are given in Figure. Solid curves are calculated with help of relationship (11) for $K = 1$, dash curves are calculated for $K = 2$. One can see that the modified diffusivity coefficient trends to zero when approaching the plasma column centre, in difference from SNT where it tends to infinity.

We consider as a pleasant duty to express our gratitude to V.Merezhkin who has attracted our attention to a given problem.

1. *Levinton F.M., Zarnstorf M.C., Batha S.H., et al, Phys.Rev.Letters, 1995, v.75, p.4417,*
2. *Gott Yu.V., Yurchenko E.I., Fizika plasmy, 1987, v.13, p.131*
3. *Shafranov V.D., Yurchenko E.I., Plasma Phys. and Contr.Nucl.Fus.Res., 1971, v.2, p.519*
4. *Kovrizhnykh L.M., Fizika plasmy, 1982, v.9, p.1105*

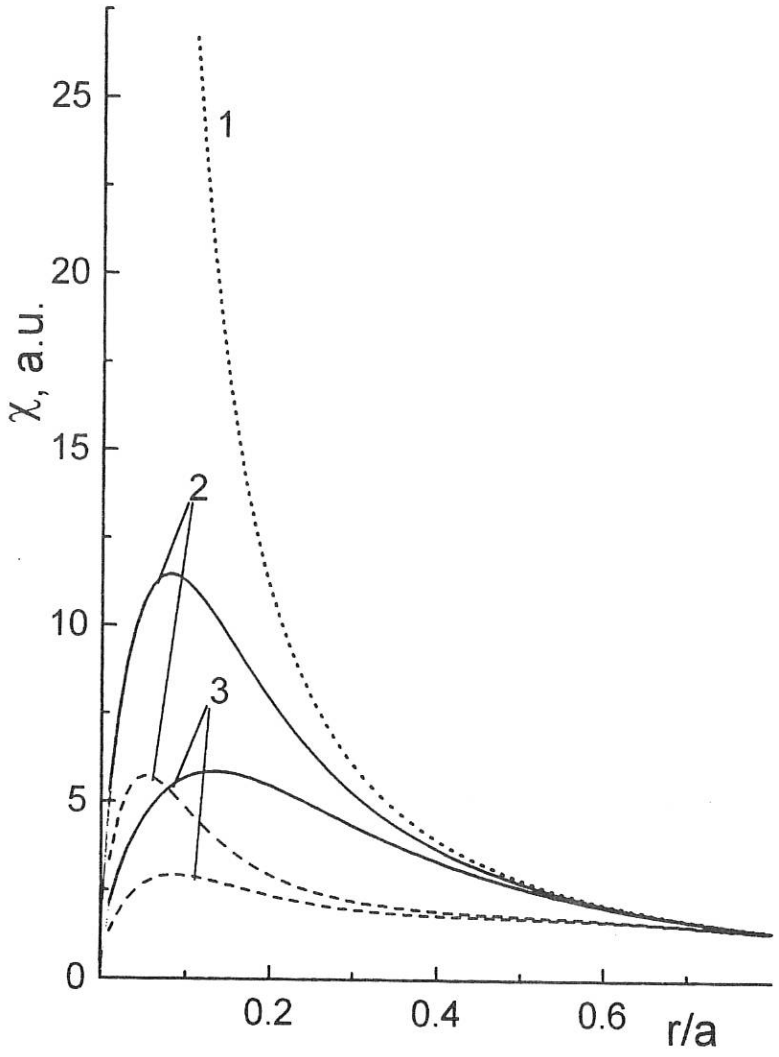
25
20
15
10
5
0
χ, a.u.
1
2
3
0.2
0.4
0.6
r/a

FAST PROCESSES WITHIN THE CANONICAL PROFILES TRANSPORT MODEL

Yu.N. Dnestrovskij, S.V. Cherkasov, Yu.V. Esipchuk, S.E. Lysenko, K.N. Tarasyan, S.V. Tsaun

Russian Research Centre "Kurchatov Institute", Moscow, Russia

The Canonical Profiles Transport Model (CPTM) is reconsidered. The new equation for the evolution of canonical profiles and corresponding boundary conditions are proposed. The model is used for the description of fast transient processes in the TFTR and JET with cooling of the plasma edge.

1. INTRODUCTION

Recent experiments confirmed that the energy transport in tokamaks is determined not only by the slow diffusion time, but also by some collection of fast times. Most spectacular are experiments with cooling of the plasma edge by injection of impurities [1-3] or gas puffing, and with heating of the plasma edge by fast current ramp up [4]. In these experiments the central electron temperature changes at $\tau_d \approx 1$-3 ms after strong action at the edge, and the absolute increase of the central temperature $\Delta T_e(0)$ is about 100-300 eV. The time delay of the response, τ_d is 1-2 orders of magnitude less than the energy confinement time τ_E, and 2-3 orders less than the skin time of the current redistribution, τ_s.

In this Report we attempt to describe the experiments [1-4] using the Canonical Profiles Transport Model (CPTM) [5]. We revise the basic ideas of the model, and include an additional equation with a fast time $\tau_c \propto \tau_d$. This equation describes the evolution of the canonical profiles. The main point of the modified model is a revision of the boundary conditions for the canonical profiles. As a result, the canonical profiles become depending on the profile of the real electron temperature $T_e(r)$ near the edge. The change of the $T_e(r)$ profile near the edge leads to fast redistribution of the canonical profile over the whole plasma cross section, and, as a consequence, to visible changes of the heat diffusivities χ_e and χ_i. The resulting model is self consistent. We use it for description of the JET and TFTR experiments [3-4].

2. THE MODEL DEVELOPMENT

We assume that the form of the canonical profiles is determined by the minimum of the free energy functional and by conservation of the total plasma current [6]. Then using the Maxwell equation $j=\frac{cB_0}{4\pi R}\frac{1}{r}\frac{\partial}{\partial r}\left(r^2\mu\right)$, where $\mu=1/q$, and assuming that $j(\mu)/j_0=p(\mu)/p_0$, where $j_0=j(\mu_0)$, $p_0=p(\mu_0)$, $\mu_0=\mu(r=0)$, and eliminating j and p, we obtain an Euler equation for the canonical profile $\mu(r)$

$$\frac{d\Phi}{dr}=\frac{d}{dr}\frac{B_0}{cR}\left[(r^2/\mu')\frac{d}{dr}(\mu^2+\lambda_2\frac{d\mu}{d(r^2)})\right]=0 \qquad (1)$$

where $\lambda_2=\frac{4cR}{B_0}[\lambda_1+(p_0/((\gamma-1)j_0)]$, $\mu'=d\mu/dr$, λ_1 is a Lagrange multiplier, other notations are standard. The regular solutions of (1), $\mu_c=\mu_c(r)$, satisfy to a more simple equation of second order

$$d\Psi/dr=0,\quad \Psi=\mu_c^2+\lambda_2\frac{d\mu_c}{d(r^2)} \tag{2}$$

containing the parameter λ_2. Therefore, for the selection of a unique solution we need three boundary conditions. In [6] the following conditions were used

$$\mu_{ca}=\mu_c(a)=2IR/(ca^2B_0)\qquad \mu_c(0)=\mu_0,\quad \mu_c(r)\to 0 \text{ at } r\to\infty \tag{3}$$

and the simple analytical (Kadomtsev) solution was obtained

$$\mu_c=\mu_c^K=\frac{\mu_0}{1+r^2/a_j^2},\quad a_j=a(\mu_a/(\mu_0-\mu_a))^{1/2} \tag{4}$$

Solutions (4) were used in paper [5] with $\mu_0=1$. However, the boundary conditions (4) raise many questions. What is μ_0? Why does the plasma "know," what is happening beyond the chamber? To resolve these questions, we suppose that the evolution of canonical profiles is described by the time dependent equation

$$\tau_c\frac{d\mu_c}{dt}=\frac{d\Psi}{dr} \tag{5}$$

where τ_c is the characteristic time of evolution, which is small in comparison with the energy confinement time τ_E ($\tau_c<<\tau_E$). We suppose also that in the Ohmic (OH) and L modes the boundary conditions for Eq. (5) have the form

$$\mu_c(a)=\mu_a=2IR/(ca^2B_0)\ ,\quad \mu_c'(a,t)=\mu'(a,t),\quad \mu_c''(a,t)=\mu''(a,t) \tag{6}$$

where $\mu(r,t)$ is the solution of the equation for the poloidal magnetic field. Hence

$$\lambda_2=a^2\mu_a\lambda,\quad \lambda=\frac{4}{1-a\mu_a''/\mu_a'} \tag{7}$$

The electron temperature and conductivity at the plasma edge are small, therefore for the estimation of the λ value we can use the steady state equation for diffusion of the poloidal magnetic field $\frac{d}{dr}\left(\frac{1}{r\sigma}\frac{d}{dr}(r^2\mu)\right)=0$, where σ is the plasma conductivity. Hence

$$\lambda=\frac{1}{1-\frac{a\sigma_a'}{4\sigma_a}\left(1+2\frac{\mu_a}{a\mu_a'}\right)}=\frac{1}{1+\frac{a\sigma_a'U}{8\pi R(\bar{j}-j_a)}} \tag{8}$$

where $U=2\pi Rj_a/\sigma_a$, is the loop voltage, $\bar{j}=I/(\pi a^2)$ is the average current density, $a\sigma'_a/4\sigma_a\propto(3/8)a(T_e'/T_e)_a-(1/4)a(Z'/Z)_a$. As a result, the parameter λ depends on the current density, the logarithmic derivatives of the temperature and Z_{eff} at the edge.

The second term in the denominator of (9), containing the product σ'_aU, is very sensitive to the scenario of the plasma edge cooling. During the cooling the value of σ'_a decreases as the

electron temperature profile becomes more flat, and simultaneously U rises. Their product can either to decrease or to rise. As a consequence, the proposed model can describe both the heating of the plasma core (experiments on TEXT and TFTR), and its cooling (JET) during the edge cooling. Using the expansion of $\mu_c(r,t)$ in the plasma centre and the conformity principle [5], we obtain the following expression for $T_{ec,ic}(r)$.

$$T_{ec}(r)/T_{ec}(0)=T_{ic}(r)/T_{ic}(0)=(\mu_C^K(r)/\mu_C^K(0))^{G_0(\lambda)} \qquad (9)$$

where $G_0(\lambda)=(\lambda_0-1)/\lambda-1$, λ_0 is the steady state value of λ.

3. SIMULATION OF TFTR AND JET EXPERIMENTS

At first we simulated the steady state OH regimes described in [2,3] and obtained the value $\lambda_0=1.29$ for the TFTR shot #31889 and $\lambda_0=1.32$ for JET shot #31736.
The second step is the choice of scenario for the description of the edge cooling. In the TFTR [2] the pellet is small and the increase of radiation power P_{rad} is not large. Furthermore, for the limiter OH shots the boundary electron temperature $T_e(a)$ in the steady state is low (we assume 50 eV), and it is natural to propose that this temperature remains unchanged during the transient stage after the pellet ablation.

The scenario of $P_{rad}(t)$ and $T_e(a,t)$ for transient process in TFTR is shown in Fig. 1. We proposed also that the radiation power is localized in the region $0.85<r/a<1$. The flattening of $T_e(r)$ near by the boundary leads to peaking of a canonical profile and, as a consequence, to peaking of $T_e(r)$. In Fig. 2 we compare the behavior of $T_e(r,t)$ in the calculations and experiment for the two spatial points: $r/a=0.16$ and 0.22. The maximum values of the temperature deviations δT_e vs the radius are shown in Fig.3. The experimental points are marked by black circles. The points of δT_e sign change are close one to another. The absolute values of δT_e^{exp} and δT_e^{calc} in the plasma core are also similar. The divergence of these values at $r/a\approx 0.7$-0.8 can be explained by the influence of unablated pellet fragments in the experiment.
In the JET experiment [3] the pellet is large, and P_{rad} rises in a factor of 5. The value of $T_e^{exp}(0.92a)$ quickly diminishes from 170 eV to 20 eV. So, the scenario here is quite different. Fig.4 shows the chosen JET scenarios for P_{rad} and $T_e(a,t)$. The temporal evolution of $T_e(r,t)$ for two points is shown in Fig.5. Fig.6 shows the radial variation of maximum of δT_e. In this case plasma is cooled everywhere.

As a conclusion, the developed transport model allows to describe the fast transient processes. The experiments in the TFTR and JET with opposite signs of the electron temperature deviations were simulated. The model predict the similar behavior of the ion temperature.

This research was supported in part by the UKAEA contract GQ 11001.

References

[1] Gentle, K.W., et al., Phys. Rev. Lett., **74** (1995) 3620.
[2] Kissik, M.V., Callen, J.D., Fredrickson E.D., et al., submitted in Nucl. Fusion.
[3] De Angelis, R., Deliyanakis,N., De Luca, F., et al, in Control. Fusion and Plasma Phys. (Proc. 22nd Eur. Conf., Bournemouth, 1995) Part 1, p. .
[4] Gentle, K.W., Cima, G., Phillips P.E., et al., in Control. Fusion and Plasma Phys. (Proc. 22nd Eur. Conf., Bournemouth, 1995) Part 1, p. 5.
[5] Dnestrovskij, Yu.N., Lysenko, S.E., Tarasyan, K.N., Nucl. Fusion, **39** (1995) 1047.
[6] Kadomtsev, B.B., Sov. J. Plasma Phys., **13** (1987) 11.

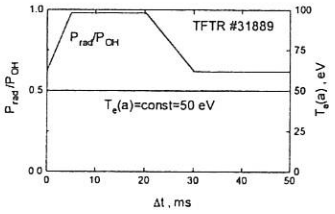

Fig. 1. Scenario of the electron temperature and radiated power variation after impurity injection in the TFTR.

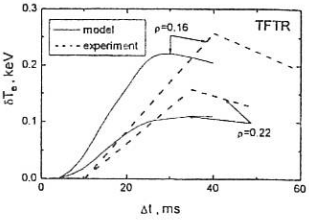

Fig. 2. The temporal evolution of the electron temperature at two spatial points in the TFTR.

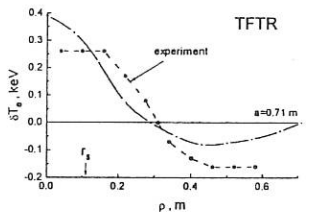

Fig. 3. Radial variation of the maximal temperature deviations in the TFTR.

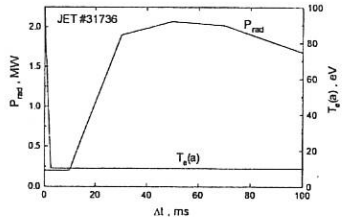

Fig. 4. Scenario of the electron temperature and radiated power variation after impurity injection in the JET.

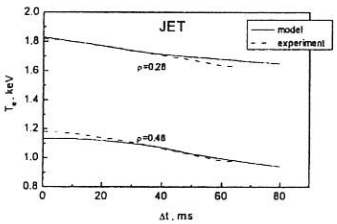

Fig. 5. The time evolution of the electron temperature at two spatial points in JET.

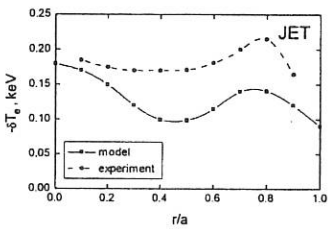

Fig. 6. Radial variation of the maximal temperature deviations in the JET

NEUTRAL ATOM DISTRIBUTION FUNCTION BEHAVIOUR IN NON-MAXWELLIAN PLASMA

N. T. Besedin

Institute of Plasma Physics, National Science Center "Kharkov Institute of Physics and Technology", 310108 Kharkov, Ukraine

1. INTRODUCTION

Neutral atom distribution function in plasma has been studied for the case when the ion distribution function f_i is highly anisotropic. For the isotropic one the problem was considered earlier [1, 2]. In the present paper Boltzmann kinetic equation has been solved numerically by iterative method. The maximum values of plasma parameters in calculations are the following: plasma density $n = 10^{14}$ cm^{-3}, electron temperature $T_e = 5$ keV, ion temperature (in the plasma regions where function f_i is Maxwellian) $T_i = 5$ keV. The ion distribution function anisotropy is described by simple model function.

2. THE KINETIC EQUATION

Directing z-axis normally to the plasma boundary and using the cylindrical coordinates v_z, v_ρ, θ in the velocity space the kinetic equation for the neutral atom distribution function $f(z, v_z, v_\rho, \theta)$ can be written in the form

$$v_z \frac{\partial f(z,v_z,v_\rho,\theta)}{\partial z} = -f(z,v_z,v_\rho,\theta)\sum_{j=1}^{3} S_j(z,v_z,v_\rho,\theta) +$$

$$+ f_i(z,v_z,v_\rho,\theta)\Big[\int_0^\infty dv'_\rho\, v'_\rho \int_{-\infty}^{+\infty} dv'_z \int_0^{2\pi} d\theta'\, f(z,v'_z,v'_\rho,\theta')\sigma_1(g)g + S_4(z,v_z,v_\rho,\theta)\Big], \quad (1)$$

where $S_j(z,v_z,v_\rho,\theta) = \int_0^\infty dv'_\rho\, v'_\rho \int_{-\infty}^{+\infty} dv'_z \int_0^{2\pi} d\theta'\, f_j(z,v'_z,v'_\rho,\theta')\sigma_j(g)g$, (j=1,2,3,4),

$$g = \sqrt{(v'_z - v_z)^2 + v'^2_\rho + v_\rho^2 - 2v'_\rho v_\rho \cos(\theta - \theta')}\,,\ f_1 = f_3 = f_i,\ f_2 = f_4 = f_e\,.$$

The cross-sections $\sigma_1, \sigma_2, \sigma_3, \sigma_4$ in Eq. (1) describe the processes of charge exchange, ionization by electron impact and by proton impact and recombination respectively [1].

The dimensionless quantities are used in Eq. (1). The width of the plasma layer z_0 (in cm), the scale factor for the particle density n_0 (in cm^{-3}) and the characteristic temperature T_0 (in eV) are used as the main scale parameters. The scales of cross-sections, velocity and distribution functions are determined in the following way: $\sigma_0 = \pi^{3/2}/(n_0 z_0)$, $v_0 = (1.6021\cdot 10^{-12}\cdot 2\cdot T_0/m_i)^{1/2}$, ($m_i$ is ion mass), $f_0 = n_0/(\pi^{3/2} v_0^3)$.

Function $f(z, v_z, v_\rho, \theta)$ satisfies to the symmetric boundary conditions

$$f^+(0,v_z,v_\rho,\theta) = f_w + Rf^-(0,-v_z,v_\rho,\theta),\quad f^-(1,v_z,v_\rho,\theta) = f_w + Rf^+(1,-v_z,v_\rho,\theta) \qquad (2)$$

Here, $f^+ = f$ for $v_z > 0$ and $f^- = f$ for $v_z < 0$, f_w is the distribution function of low energy atoms, R is the reflection coefficient.

Using expressions (2) the solution of Eq. (1) is obtained by iterations.

$$\text{For } v_z < 0 \quad f^-_{k+1}(z,v_z,v_\rho,\theta) = [f_w + Rf^+_k(1,-v_z,v_\rho,\theta)]\exp[-\frac{1}{v_z}\int_1^z \sum_{j=1}^3 S_j(u,v_z,v_\rho,\theta)du] -$$

$$-\frac{1}{v_z}\int_z^1 dz'\ f_i(z',v_z,v_\rho,\theta)[\int_0^\infty dv'_\rho\, v'_\rho \int_{-\infty}^{+\infty} dv'_z \int_0^{2\pi} d\theta'\ f_k(z',v'_z,v'_\rho,\theta')\sigma_1(g)g + S_4(z',v_z,v_\rho,\theta)] \times$$

$$\times \exp[-\frac{1}{v_z}\int_{z'}^z \sum_{j=1}^3 S(u,v_z,v_\rho,\theta)du]\,. \qquad (3)$$

$$\text{For } v_z > 0 \quad f^+_{k+1}(z,v_z,v_\rho,\theta) = [f_w + Rf^-_k(0,-v_z,v_\rho,\theta)]\exp[-\frac{1}{v_z}\int_0^z \sum_{j=1}^3 S_j(u,v_z,v_\rho,\theta)du] +$$

$$+\frac{1}{v_z}\int_0^z dz'\ f_i(z',v_z,v_\rho,\theta)[\int_0^\infty dv'_\rho\, v'_\rho \int_{-\infty}^{+\infty} dv'_z \int_0^{2\pi} d\theta'\ f_k(z',v'_z,v'_\rho,\theta')\sigma_1(g)g + S_4(z',v_z,v_\rho,\theta)] \times$$

$$\times \exp[-\frac{1}{v_z}\int_{z'}^z \sum_{j=1}^3 S(u,v_z,v_\rho,\theta)du] \qquad \text{(k is the iteration number)} \qquad (4)$$

The iterative processes starts from $f_1(z,v_z,v_\rho,\theta) = 0$

3. NUMERICAL RESULTS

Three cases are considered in this paper. In the first case the plasma region with anisotropic ion distribution function is $0.15<z<0.85$. In the second case it is $0.4<z<0.6$. In the third case it is given by $0.15<z<0.4$ and $0.6<z<0.85$. For the other z values function f_i is modeled by Maxwellian using ion temperature profile $T_i(z)$ coinciding with $T_e(z)$.

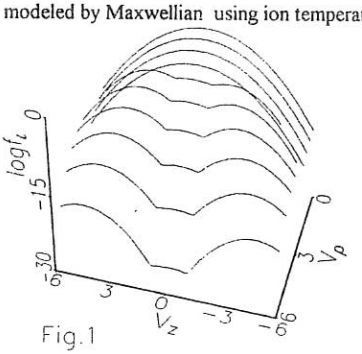

Fig.1

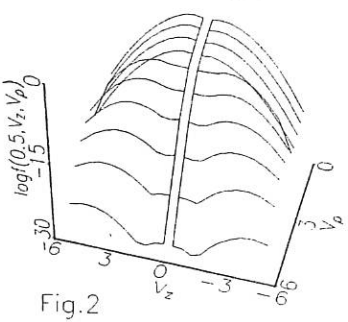

Fig.2

Anisotropic function f_i is modeled by the function shown in Fig.1. This function coincides with Maxwellian for $v_\rho < 2$ and has two characteristic high energy tails for $v_\rho > 2$. Such tails may appear during plasma heating [3]. For the real experimental conditions the anisotropic ion distributions may be calculated using RF heating or NB injection codes.

Assuming plasma density and electron temperature profiles n(r) and $T_e(r)$ as cubic parabolic ones electron distribution function f_e is modeled by Maxwellian in the whole plasma volume. In the plasma center $T_e(0.5) = T_0$ ($T_0 = 5000$ eV), $n(0.5) = 100 n_0$. At the plasma edge $T_e(0) = T_e(1) = 5$ eV, $n(0) = n(1) = n_0$. The $n_0 z_0$ value is equal to $13 \cdot 10^{13}$ cm^{-2}, that at $z_0 = 130$ cm and $n_0 = 10^{12}$ cm^{-3} corresponds to the parameters of the W7-X project. The calculations were performed for distribution functions independent on the angular variable θ. In the real experimental conditions the ion distribution anisotropy varies with θ. In the present calculations R=0.5.

In the first case function $f(z, v_z, v_\rho)$ in the plasma center and at the plasma edge is shown in Figs. 2, 3 respectively. Comparison of Fig. 2 with Fig.1 shows that function $f(z, v_z, v_\rho)$ and function f_i have much in common. Function $f(z, v_z, v_\rho)$ is tail-distributed too.

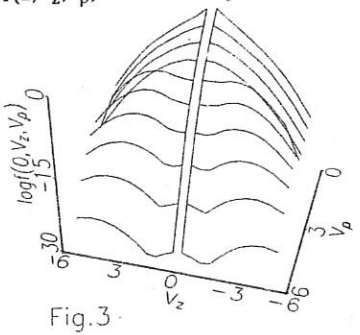

Fig.3

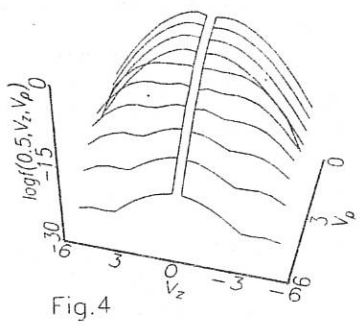

Fig.4

Function $f(z, v_z, v_\rho)$ which corresponds to the second case as in the plasma center (Fig. 4) so at the plasma edge (Fig. 5) has an additional hill at $v_z = 0$. This hill is caused by broader as compared with the first case plasma region where function f_i is Maxwellian. Comparison of Fig.3 with Fig. 2 and of Fig. 5 with Fig. 4 shows that $f(z, v_z, v_\rho)$ varies with z only for the small velocity values and is practically independent on z at $(v_z^2 + v_\rho^2)^{1/2} > 2$. The variation of low energy part of neutrals distribution function is caused by the cold atoms penetrating into plasma.

In the third case function $f(z, v_z, v_\rho)$ in the plasma center (Fig. 6) coincides very good with the one in Fig. 4, though in comparison with the second case function f_i is Maxwellian in the region $0.4 < z < 0.6$. Identical distributions of neutrals correspond to the different local values

of ion distribution function, Function $f(z, v_z, v_\rho)$ at the plasma edge in the third case (not shown in this paper) coincides with the one in Fig. 5

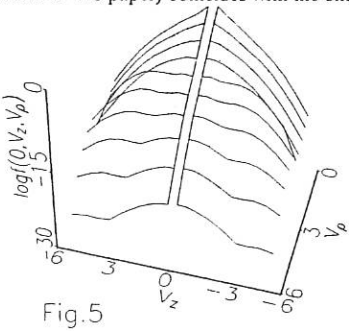

Fig.5

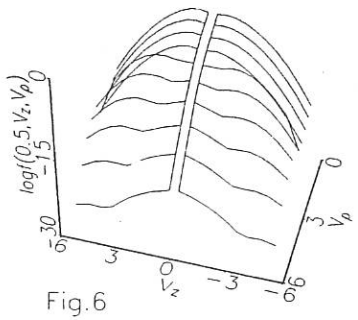

Fig.6

4. CONCLUSIONS

High energy part of neutral atom distribution function is almost the same in the whole plasma volume. The outgoing neutral atoms possess in themselves information about the ion velocity distributions in the most hot regions of plasma. The determination of the local ion distributions from measurements of the neutral energy distribution may be very difficult problem.

An accurate description of neutral atom distribution function is of primary importance for interpretation of diagnostic measurements. The numerical code described here can be used for this purposes. For a long time the following energy dependence of the neutral particle flux is used for interpretation of the diagnostic results. [4-6].

$$F(E_0) \propto \int_0^L n n_a \sigma_1(g) g E_0^{1/2} \exp(-E_0/T_i) \exp(-\int_0^x ds/\lambda_{tot}) / T_i^{3/2} dx \qquad (5)$$

Here, n_a is neutral atom density, L is a chord length.

Note that expression (5) may be obtained from expression (3) using the total mean free path λ_{tot} value and assuming functions $f_{i,e}$ of Maxwellian and $\sigma_1(g)g = \text{const}$. As it was shown in Ref. [1], the last assumption brings the significant errors to the neutrals density and distribution function.

The calculations have shown that the influence of the reflection coefficient value on the neutral distribution function relief is small.

The code developed here facilitates the calculation of neutral atom distribution function both for a two-dimensional velocity space and for a three-dimensional one.

References

[1] N.T .Besedin. Sov. Journ. of Plasma Phys. **16** (1990), p.257
[2] N.T. Besedin et al. XX Int. Conf. on Phenomena in Ionized Gases. Pisa, 1991 V.**2**, p.365
[3] C.H. Chang, P.Colestock. Phys. Fluids **B 2** (2) 1990, p.310
[4] M.H.Hughes, D.E.Post. Journal of computation physics **28** (1978), p.43
[5] J.Stolber et al. 22 EPS Conference. on Contr. Fus. and Plasma. Phys. (1995) Part III, p.249
[6] N.Rust et al. 22 EPS Conference. on Contr. Fus. and Plasma. Phys. (1995) Part III, p.137.

RUNAWAY ELECTRONS SECONDARY GENERATION

I. M. Pankratov, N. T. Besedin
Institute of Plasma Physics, National Science Center "Kharkov Institute of Physics and Technology", 310108 Kharkov, Ukraine

1. INTRODUCTION

In present tokamaks with longer discharges in low density regimes the energy of runaway electrons reaches up to tens of MeV and even more. Due to close collisions these high energy electrons may kick thermal electrons in the runaway region [1]. The knocked-out electrons have a significant transverse momentum $p_\perp >> p_\parallel$ ($p_\perp$ and $p_\parallel$ are transverse and parallel momenta of runaways with respect to the magnetic field **B**). The inequality of

$$p_\perp > p_{\perp cr}, \qquad p_{\perp cr} = \sqrt[4]{12}\,p_{cr}/3 \tag{1}$$

determines the runaway region of the knocked-out electrons [2], $p_{cr}^2 = 4\pi e^3 mnL(2+z_{eff})E^{-1}$, e and m are the charge and the rest mass of the electron, n is the bulk plasma density, L is the Coulomb logarithm, z_{eff} is the effective ion charge number, E is the inductive electric field.

The avalanche-like process of the runaways generation arises with the avalanching time

$$t_0 = 1/cn\sigma(W_{\perp cr}) = \sqrt{12}mcL(2+z_{eff})/9eE. \tag{2}$$

This process of the secondary generation of the runaway electrons was experimentally demonstrated in the TEXTOR tokamak [3], that is why the present calculations were carried out for the TEXTOR experimental conditions

$$n=0.85\cdot10^{19}\,m^{-3},\ E=0.08V/m,\ L=12,\ z_{eff}=2,\ B=2.25\ T. \tag{3}$$

We assumed the maximum energy of runaways to be 25 MeV, and electrons with higher value of the energy were not taken into account.

2. RUNAWAY ELECTRON DISTRIBUION FUNCTION

The present analysis is performed on the basis of the integral of close collisions [2]

$$I(p_\parallel,p_\perp,t) = 4ncr_0^2\left[\frac{p_\parallel+p_{\parallel1}}{\sqrt{(p_\parallel+p_{\parallel1})^2+m^2c^2}}-\frac{p_{\parallel1}}{\sqrt{p_1^2+m^2c^2}}\right]^{-1}\frac{p_{\parallel1}^4}{p_\perp^4}\frac{m^2c^2}{(p_\parallel+p_{\parallel1})^4}\overline{F(p_\parallel+p_{\parallel1},t)}, \tag{4}$$

$$p_{\parallel1} = p_\parallel\frac{p_\perp^2}{p_\parallel^2-\left(\sqrt{p^2+m^2c^2}-mc\right)^2},\quad \overline{F(p_\parallel+p_{\parallel1},t)} = \theta\left(\frac{eEt}{p_\parallel+p_{\parallel1}}-1\right)+2\pi\int_0^\infty p_\perp dp_\perp F(p_\parallel+p_{\parallel1},p_\perp,t)$$

$$\theta(x)=1 \text{ for } x\ge0,\quad \theta(x)=0 \text{ for } x<0,\quad r_0=e^2/mc^2.$$

The drag force [2] and radiation losses [4] are taken into account $\left(\Gamma=\sqrt{1+p^2/m^2c^2}\right)$

$$\frac{dp_\parallel}{dt} = eE\left(1-\frac{p_{cr}^2p_\parallel}{\left(p_\parallel^2+p_\perp^2\right)^{3/2}}\right)-\frac{2}{3}r_0^2B^2\frac{p_\parallel}{mc\Gamma}\left(\frac{p_\perp}{mc}\right)^2. \tag{5}$$

The runaway electron distribution function formed as a result of close collisions can be written as follows

$$F(p_{\parallel},p_{\perp},t)\approx\int_0^{\infty}p'_{\perp}\,dp'_{\perp}\,f(p_{\parallel},p'_{\perp},t)\{(2D_{\perp}\Delta t)^{-1}I_0(p_{\perp}p'_{\perp}/2D_{\perp}\Delta t)\exp\left[-\left(p_{\perp}^2+p'^2_{\perp}\right)/4D_{\perp}\Delta t\right]\}. \quad (6)$$

Here $f(p_{\parallel},p_{\perp},t)$ is the secondary generation distribution function without including the diffusive spreading , and the term in the braces describes (for a certain value of $p_{\parallel}$) the transverse momentum diffusive spreading of the distribution function due to distant collisions of secondary runaways with the bulk plasma particles

$$St_{\perp}\{F\}=\frac{1}{p_{\perp}}\frac{\partial}{\partial p_{\perp}}\left(p_{\perp}D_{\perp}\frac{\partial F}{\partial p_{\perp}}\right), \quad D_{\perp}=2\pi e^4 nmL\left(1+z_{eff}\right)p_{\parallel}^2\Gamma p^{-3}, \quad (7)$$

$I_0(x)$ is the modified Bessel function, Δt is the time interval during which the knocked-out electron changes its parallel momentum from $p_{\parallel}\cong p_{cr}/\sqrt[4]{27}$ to a certain value of $p_{\parallel}$. Eq. (7) is obtained from the relativistic Landau collision term [5].

The relief function $f(p_{\parallel},p_{\perp},t)$ and its fragment in the region $p\sim p_{cr}$ at t=2s are shown in Figs.1 and 2 respectively. At this moment the distribution function does not relax to the stationary state yet. The projection on the plane $(p_{\parallel},p_{\perp})$ of the first line in relief $f(p_{\parallel},p_{\perp},t)$ is indicated by the triangle. The knocked-out electrons are arranged on elongated ellipses, major axes of which are equal to momenta of the energetic incident electrons. A part of the ellipsis for the incident electron with $\max(p_{\parallel})$=50mc is indicated in Fig. 2 by the circle. The birth of secondary generation electrons takes place mainly near this curve, where $p_{\perp}\sim p_{\perp cr}$.The radiation losses of electrons with $p_{\perp}\sim p_{\perp cr}$ are not too large.

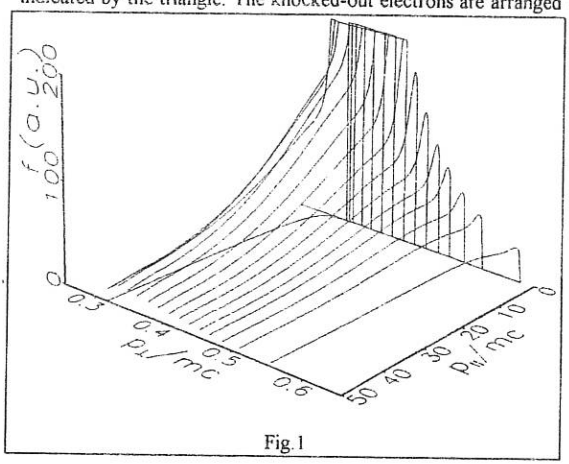

Fig.1

The curve where $\left(p_{\parallel}^2+p_{\perp}^2\right)^{3/2}=p_{\parallel}p_{cr}^2$ is indicated by the square. The maximum value of the transverse momentum in this curve is $p_{\perp cr}=\sqrt[4]{12}\,p_{cr}/3$ at $p_{\parallel max}=p_{cr}/\sqrt[4]{27}$ .The region where $\left(p_{\parallel}^2+p_{\perp}^2\right)^{3/2}<p_{\parallel}p_{cr}^2$ is the barrier for the knocked-out electrons. Therefore, we have the regime of continuos acceleration if the energy of knocked-out electrons W is

$$W>W_{\perp cr}\ ,\quad W_{\perp cr}=p_{\perp cr}^2/2m\ . \quad (8)$$

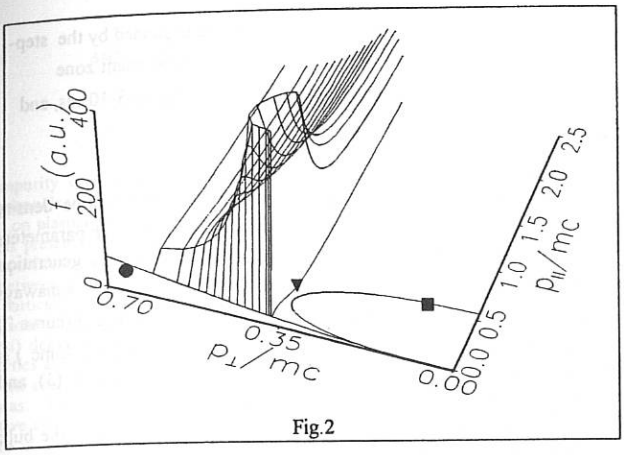

Fig.2

In the figures $p_{\perp cr} = 0.35mc$, in accordance with (3).

The function $f(p_{||}, p_\perp, t)$ is not in equilibrium with respect to the transverse momenta $(\partial f / \partial p_\perp > 0)$. From Eq. (6) we obtain that the region of $\Delta p_{||}, p_{||} \sim p_{cr} / \sqrt[4]{27}$ always exists, for which $\Delta t(\Delta p_{||}) < p_{\perp cr}^2 / 2D_\perp$.

Hence in this region $\Delta p_{||}$ $F(p_{||}, p_\perp, t)$ is not in equilibrium with respect to the transverse and parallel momenta $(\partial F / \partial p_{\perp,||} > 0)$. For the parameters (3) $D_\perp \approx 5.4 m^2 c^2 \cdot s^{-1}$ and $\Delta p_{||} \sim 0.1 mc$ in accordance with $\Delta t < 1.3 \cdot 10^{-2} s$.

Therefore, the observed intense infrared radiation in TEXTOR [3] is the result of instability of the runaway electrons distribution function which is not in equilibrium with respect to the transverse and parallel momenta.

3. FAST CHANGE IN THE INFRARED RADIATION

If during the shot z_{eff} suddenly increases , the barrier, where $\left(p_{||}^2 + p_\perp^2\right)^{3/2} < p_{||} p_{cr}^2$, also increases at this moment. Just from this moment we have a new condition $p_\perp > p_{\perp cr2}$ $(p_{\perp cr2} > p_{\perp cr1})$, and a strong reconstruction in the relief $F(p_{||}, p_\perp, t)$ starts in the region $p \sim p_{cr}$. In the relief of $F(p_{||}, p_\perp, t)$ for $p_\perp < p_{\perp cr2}$, $p_{||} > p_{cr2} / \sqrt[4]{27}$ a zone with $\partial F / \partial p_{||} > 0$ will be formed, which moves in accordance with Eq. (5). The region, where $\partial F / \partial p_\perp > 0$, will be removed to a higher value of $p_\perp$. The essential increase in the instability zone leads to the fast change in the infrared radiation. This fast phenomenon was named as Fast Pitch Angle Scattering Event [6].

In general, if $p_{\perp cr} \propto \sqrt{n(2 + z_{eff}) / E}$ is changed stepwise or in some other way, this results in a change of the instability condition. The fast change in the infrared radiation will be observed.

In the case of instability at frequency $\omega = 2\omega_{e0}$, $N_{||} = 0$ (signal of the ECE channel), the resonant condition $\omega = l\omega_{e0} / \Gamma$ ($\omega_{e0} = eB / mc$, $N_{||}$ is the parallel refraction index) for runaway electrons is fulfilled on the circles $p_{||}^2 + p_\perp^2 = p_l^2$, where $p_l = mc\sqrt{(l/2)^2 - 1}$, $l = 5/2, 3, 7/2, 4....$ Hence the distance between two neighbouring resonant values of $p_{||}$ is $\Delta p_{||} \approx (0.25 - 0.3)mc$.

A stepwise increase of the ECE signal during the fast event [6] may be explained by the step-by-step addition of new groups of resonant runaway electrons, when the rezonant zone increases. In accordance with Eq. (5) for $\Delta p_{\parallel} \approx (0.25-0.3)mc$, Δt is equal to (5-10)ms, and that is in a good agreement with the experiment in TEXTOR.

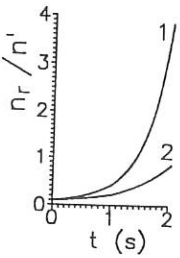

Fig. 3

4. RUNAWAY DENSITY BEHAVIOUR

In Fig. 3 (curve 1) the time dependence of the relative density n_r / n' of secondary generation runaways is presented for parameters (3) (n' is the density of runaways without the secondary generation process). For a given value W_{max} the density of secondary runaways strongly depends on the local z_{eff} value. For example, in Fig. 3 (curve 2) the time dependence of n_r / n' for the case $z_{eff} \approx 4.6$ ($p_{\perp cr} = 0.45mc$) is presented, the remaining parameters being the same as in (3) and $W_{max} = 25MeV$.

Earlier it was shown that the electron density value of the bulk plasma influences the secondary runaways density [7].

For the value of $t_{eff}(t)$, where $n_r / n' = \exp[t / t_{eff}(t)]$, (9)

from Fig. 3 for $p_{\perp cr} = 0,35mc$ (curve 1) we obtain $t_{eff} \approx 0.7s$ at t=1s and $t_{eff} \approx 0.56s$ at t=2s. From Eq. (2) we have $t_0 \approx 0.55s$. For the case $p_{\perp cr} = 0.45mc$ (curve 2) we obtain $t_{eff} \approx 1.3s$ at t=1s and $t_{eff} \approx 0.95s$ at t=2s. Eq. (2) leads to $t_0 \approx 0.9s$ for this case.

5. THE ROLE OF SECONDARY GENERATION DURING A DISRUPTION

As it follows from Eq. (2), the avalanching time t_0 during the disruption in TEXTOR ($n=(0.5-1)10^{20} m^{-3}$, E=30 V/m, $z_{eff} \approx 3$) is $t_0 \approx 1.8ms$. This t_0 is lower than the L / R -time (4.5ms). In Ref.[8], where the role of secondary generation during disruption was investigated, the time $t_0 = (2 + z_{eff})mcL / eE$ was used instead of expression (2). This inaccuracy may change the conclusion about the role of the secondary generation process during disruptions.

6. CONCLUSION

It is shown that a series of the phenomena observed in the runaways secondary generation experiment in TEXTOR can be explained by the peculiarity of the runaway distribution function in the region $p \sim p_{cr}$.

ACKNOWLEDGEMENTS: The authors thank K.H.Finken and R.Jaspers for the information about runaway electrons experiment in TEXTOR.

References

[1] Yu. A. Sokolov, Zh. Ehksp. Teor. Fiz.. Pis'ma -Red **29** (1979) 244.
[2] N. T. Besedin, I. M. Pankratov, Nucl. Fusion **26** (1986) 807.
[3] R. Jaspers et al., Nucl. Fusion **33** (1993) 1775.
[4] L.D.Landau,E.M.Lifshitz,The Classical Theory of Fields,Moscow,Nauka,1967(in Russian).
[5] E.M.Lifshitz,L.P.Pitaevskij, The Physical Kinetics, Moscow,Nauka,1979 (in Russian).
[6] R.Jaspers, PhD Thesis,Tech. Univ.Eindhoven, Netherland, 1995.
[7] N.T.Besedin et al.,Sov. J. Plasma Phys. **12** (1986) 436.
[8] R.Jaspers et al.,Nucl. Fusion **36** (1996) 367.

CHARACTERIZATION OF CORE IMPURITY TRANSPORT AND ACCUMULATION IN VARIOUS OPERATING REGIMES IN DIII-D*

M.R. Wade,† D.G. Whyte,Δ R.D. Wood,◊ and W.P. West
General Atomics, P.O. Box 85608, San Diego, California 92186-9784 USA

Impurity contaminants in the core plasma of future burning devices such as the International Thermonuclear Experimental Reactor (ITER) are inevitable and will undoubtedly have a deleterious effect on plasma performance. Unfortunately, because of the limited amount of information available, the models presently being used to predict ITER performance simply assume a flat concentration profile for all impurities with an ad hoc concentration chosen for each impurity. In an attempt to start closing the gap between present experimental data and these models, experiments have been conducted on DIII-D with particular emphasis placed on 1) characterizing the buildup of intrinsic impurities in the plasma core in various confinement and divertor regimes, 2) measuring the steady-state impurity (both intrinsic and seeded) density profiles in various operating regimes, and 3) determining whether impurity transport properties are dependent on the charge (or mass) of the impurity. The primary focus of these studies has been on characterizing impurity buildup in a wide variety of operating conditions in ELMing H-mode plasmas. However, enhanced confinement regimes such as ELM-free H-mode, VH-mode, and the negative central shear (NCS) regime offer the potential of a more attractive reactor scenario. Since the degree of impurity accumulation will have a significant impact on the attractiveness of these regimes, studies have also been conducted to characterize impurity buildup in these regimes.

In the present configuration of DIII-D in which graphite tiles cover ~90% of the plasma facing surface, spectroscopic surveys show carbon to be the dominant impurity with the core carbon concentration typically between 1%-3% of the electron density. These studies are made possible by the ability to accurately measure carbon density profiles on DIII-D using active charge-exchange recombination (CER) spectroscopy.[1] In most DIII-D plasmas, carbon is fully stripped over the majority of the plasma cross section, and therefore the total inventory of carbon can be computed directly, thereby alleviating uncertainties associated with transport modeling that is generally required to determine the charge-state distribution.

Impurity Behavior in L-mode and ELMing H-Mode Plasmas

In both L-mode and ELMing H-mode plasmas, the carbon inventory reaches steady-state shortly after the onset of the mode, provided other plasma parameters (e.g., injected power, magnetic equilibrium, plasma density, etc.) are maintained constant. This is similar to previously reported observations of high-Z impurity behavior in DIII-D.[2] The steady-state carbon concentration (relative to the electron density) profile is flat in both L-mode and ELMing H-mode. Presently, analysis is in progress to provide a complete survey of carbon buildup in a variety of operating conditions in L-mode and ELMing H-mode plasmas. Although this survey is incomplete, several interesting phenomena have been observed to date. Of particular interest to ITER are data from power scans and radiative divertor discharges which suggest that the core carbon content is not necessarily directly related to the heat/particle flux incident on the divertor target. Table 1 summarizes data of interest from a set of attached divertor, ELMing H-mode discharges in which the injected beam power was systematically increased from 3 MW to 9 MW. As expected, the increase in beam power resulted in a concomitant increase in the total conducted power to the divertor target. One would expect that such an increase in the heat flux would result in an increase in target erosion and carbon influx to the divertor plasma. This expectation is verified by inference of the divertor carbon density from measurements via a SPRED UV instrument viewing the divertor plasma which indicate that the carbon density increases by a factor of 2 as the power is increased from 3 to 9 MW. However, measurements of the core carbon content via CER show the content decreases as the input power is increased. Such a trend suggests that the divertor and

*Work supported by the U.S. Department of Energy under Contract Nos. DE-AC03-89ER51114, DE-AC05-96OR22464, and W-7405-ENG-48.
†Oak Ridge National Laboratory, Oak Ridge, Tennessee.
ΔINRS — Energie et Materiaux, Varennes, Quebec, Canada.
◊Lawrence Livermore National Laboratory, Livermore, California.

SOL plasma becomes more efficient in screening impurities from the core plasma as the input power is increased. One possible mechanism for this improvement is an increase in the ELM frequency as the input power is increased. Since previous studies have shown that ELMs are effective in sweeping impurities out of the edge plasma , it is likely that an increased frequency of ELMs leads to better screening of impurities. The data shown in Table 1 is consistent with this hypothesis as the ELM frequency increases in these discharges from 40 Hz to 150 Hz as the input power is increased. However, since there are several other possible mechanisms for this improvement (e.g., improved ionization potential of the divertor plasma, increased particle flow toward divertor target thereby entraining the impurities, better, etc.), detailed modeling (including modeling of the carbon sources) is requited to determine the primary mechanism responsible for this trend.

Table 1. Selected Parameters During an Input Power Scan

Input power (MW)	8.9	6.2	3.1
Line-averaged density ($\times 10^{19}$ m^{-3})	6.0	6.0	6.2
Separatrix density ($\times 10^{19}$ m^{-3})	2.0	1.8	2.0
Separatrix temperature (eV)	90	80	75
Total heat flux to divertor (MW)	3.9	3.1	1.6
ELM frequency (Hz)	150	140	40
Core carbon content ($\times 10^{19}$ particles)	1.0	1.2	1.8
Carbon concentration at $\rho = 0.7$ (%)	0.9	0.95	1.5

Over the past several years, several modes of operations have been demonstrated on DIII–D in which the peak heat flux to the divertor target has been reduced by a factor of 5 through controlled gas injection of either deuterium, neon, or nitrogen.[3,4] Given this large reduction in heat flux to the divertor target, one might expect a similar decrease in the core carbon content. Because the formation of radiative divertor conditions in DIII–D are accompanied by increases in the plasma density, systematic comparisons between the detached and attached cases are difficult. The comparisons made here take advantage of the fact that gas injection to form radiative divertor conditions generally begins subsequent to the high-power phase and H–mode formation. This allows measurement of the evolution of the carbon content from the attached divertor phase into the heat flux reduction phase. Such analysis shows that in the deuterium injection case the core inventory of carbon to be ~20% larger while the fuel dilution due to carbon remains essentially the same due to a similar increase in the plasma electron density. In the neon injection case, a large reduction (~ a factor of 2) in the core carbon inventory and fuel dilution due is observed even though the additional neon radiation in the core reduces the ELM frequency from ~60 Hz to 10 Hz. However, because of the additional influx of neon impurities, the core Z_{eff} increases substantially from 1.5 to 3.0. In the nitrogen injection cases, the core inventory of carbon increases by approximately 50% and the fuel dilution due to carbon increases by ~25%. The difference between Ne injection and either D_2 or N_2 injection suggests chemical sputtering of carbon in the deuterium and nitrogen cases may play an important role in the total carbon sputtering rate, but further studies (including detailed modeling) are required to determine the predominant mechanisms in these cases.[5]

Impurity Behavior in Enhanced Confinement Regimes

In enhanced confinement regimes such as ELM-free H–mode, VH–mode,[6] and NCS discharges,[7] the carbon inventory evolution is somewhat more complicated. In ELM-free H–mode plasmas, the carbon inventory increases monotonically throughout the ELM-free phase. The carbon density and concentration increases over the entire profile at equal rates until late in the discharge when central accumulation occurs. This central accumulation leads to increased radiation and eventually to loss of H–mode confinement. This observation is consistent with previous observations on DIII–D and other tokamaks with regard to impurity accumulation in ELM-free H–mode plasmas. In VH–mode plasmas, the total carbon content in VH–mode plasmas is observed to increase approximately linearly with time throughout the entire VH–mode phase (see Fig. 1). In some cases, the electron source rate from this influx (9×10^{20} s^{-1}) exceeds the beam source rate by a factor of ~2–3. In contrast to the ELM-free H–mode results, this influx of carbon primarily accumulates in the plasma periphery (near $\rho = 0.8$), resulting in carbon concentration profiles that get progressively more hollow throughout the VH–mode phase. Typically, this leads to an edge Z_{eff} (computed assuming carbon to the only impurity) near 4.0 (~6.0 in some extreme cases) while the plasma core remains relatively clean with $Z_{eff} \sim 1.5$. Since the carbon density profile does not reach equilibrium during the short extent of the VH–mode phase, it is not possible to determine *a priori* from this data whether such a hollow profile is inherent to the VH–mode or

is primarily due to the transient nature of the measurement. Transport studies designed to elucidate the intrinsic transport properties of VH–mode as well as L–mode and ELMing H–mode are described in more detail in Section III.

The carbon behavior in NCS discharges appears to be dependent on whether the edge plasma exhibits an L–mode or H–mode character. The evolution of a typical NCS discharge is shown in Fig. 2. As is typical of NCS plasmas, the target plasma is produced by the application of an early beam during the plasma current ramp-up phase. In this particular discharge, the edge plasma exhibits an L–mode character (shallow gradients in density and temperature) from the initiation of beam injection to 2.25 s. At 1.9 s, the input power is raised to 8.0 MW and a transport barrier forms in the core plasma near ρ = 0.4 as evidenced by a rapid increase in the core ion temperature. The carbon density in the core plasma is also observed to increase during this phase while the edge carbon density remains nearly constant. The simultaneous increase in the core electron density and the impurity density results in a carbon concentration (and Z_{eff}) that changes little during this phase. Also, it is observed that the carbon inventory increases only slightly throughout the L–mode phase. At ~2.25 s, the edge plasma undergoes a transition and begins to exhibit an H–mode character (sharp gradients in density and temperature). Subsequent to this transition, the carbon inventory increases linearly throughout the remainder ELM-free portion of this phase. As in the VH–mode case, this carbon influx primarily accumulates in the plasma edge with impurity concentrations on the order of 6%–10% quickly achieved while the core plasma remains relatively clean (f_C < 3%). Discharges in which NCS has been maintained simultaneously with ELMs exhibit a clamping and subsequent decrease in the carbon concentration once ELMs begin, similar to what is observed in ELMing H–mode plasmas.

From this set of data, it is clear that enhanced confinement regimes with edge plasmas which exhibit an H-mode edge (ELM-free H–mode, VH–mode, and NCS H–mode) are susceptible to impurity buildup to the extent that calls into question their suitability for a reactor. Clearly, some means of controlling impurity buildup is required. In the case of ELM-free H–mode and NCS H–mode, ELMs have been

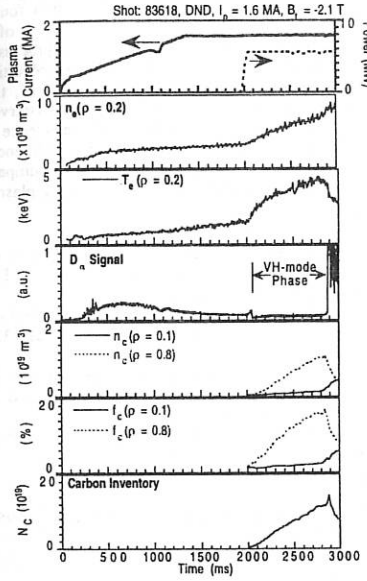

Fig. 1. Selected waveforms for a VH–mode discharge.

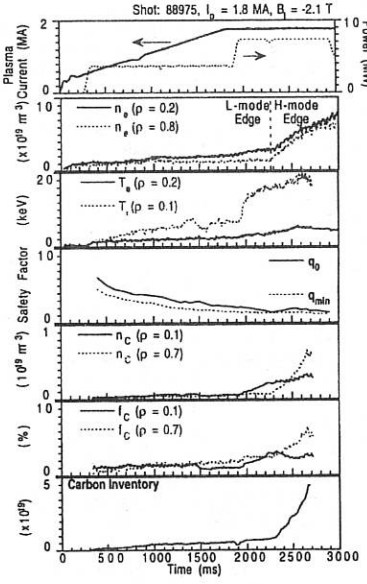

Fig. 2. Selected waveforms for a NCS discharge.

From this set of data, it is clear that enhanced confinement regimes with edge plasmas which exhibit an H-mode edge (ELM-free H–mode, VH–mode, and NCS H–mode) are susceptible to impurity buildup to the extent that calls into question their suitability for a reactor. Clearly, some means of controlling impurity buildup is required. In the case of ELM-free H–mode and NCS H–mode, ELMs have been shown to be effective in reducing the rate of carbon buildup. In this regard, the benefit of ELMs in controlling the impurity levels in these confinement regimes likely outweighs the loss in energy confinement associated with the ELMs.

Low-Z Impurity Transport

As discussed above, distinct differences in the measured steady-state profiles of various low-Z impurities have been observed as the confinement mode changes. In L–mode and in ELMing H–mode plasmas, the concentration profiles of helium, neon, and carbon are all similar to the electron density profile. However, in VH–mode plasmas, the helium density profile continues to mimic the electron density whereas the carbon and neon profiles are distinctly hollow. To address these obvious differences in transport behavior of low-Z impurities, experiments to determine the transport coefficients (namely, particle diffusivity and convective velocity) have been carried out by introducing perturbative gas puffs of helium, nitrogen, and neon in L–mode, ELMing H–mode, and VH–mode plasmas. The evolution of impurity density profile subsequent to the gas puff is followed using the DIII–D CER system with a time resolution of 5 ms. To deduce transport coefficients, the impurity particle flux Γ_Z is determined from the continuity equation. Assuming the impurity flux is be made up of diffusive and convective flows, the relevant transport coefficients (namely, the diffusivity D_Z and the convective velocity V_Z) are determined by using a linear regression analysis of the normalized flux Γ_Z/n_Z and the normalized density gradient $\nabla n_Z/n_Z$.[8,9] The results of such analysis are shown in Fig. 3, where the diffusivity and pinch velocity for helium and neon is compared for both L–mode and VH–mode plasmas. It is found that in L–mode plasmas, the transport of helium and neon is essentially the same. The lack of a Z-dependence in L–mode plasmas suggests that impurity transport is dominated by anomalous processes in this regime. However, in VH–mode plasmas, there is a substantial difference in the transport properties of helium and neon. Although the diffusivity for both helium and neon are nearly the same, the convective velocity is nearly equal and opposite in magnitude in the two cases. This observed Z-dependence is suggestive of neoclassical-like impurity transport, in which a strong Z-dependence is expected. Note that the L–mode and VH–mode regimes are also characterized by substantial differences in plasma rotation. Work is in progress to compare this data to neoclassical predictions including plasma rotation effects.

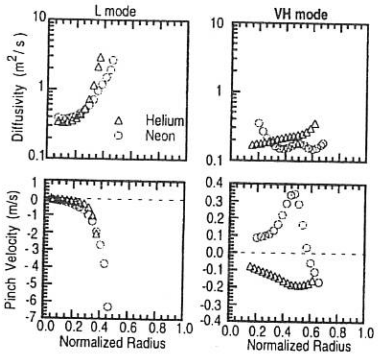

Fig. 3. Comparison of the transport coefficients for helium (Δ) and neon (o) in L–mode and VH–mode.

[1] Gohil, P.. et al., in Proc. of the 14th Symp. on Fusion Engineering, San Diego, California (IEEE, New York, 1992), Vol. 2, p. 1199.

[2] Perry, M.E., et al., Nucl. Fusion **31**, 1859 (1991).

[3] Allen, S.A., et al., J. Nucl. Mater. **220-222**, 336 (1995).

[4] Petrie, T.W., "Radiative Divertor Experiments in DIII-D with Deuterium Injection," submitted to Nucl. Fusion (1996).

[5] Kallenbach, A., et al., Nucl. Fusion **34**, 1557 (1994).

[6] Jackson, G.L., et al., Phys. Rev. Lett. **67**, 3098 (1991).

[7] Strait, E.J., et al., Phys. Rev. Lett. **75**, 4421 (1995).

[8] Wade, M.R., *et al.*, Phys. Plasmas **2**, 2357 (1995).

[9] Synakowski, E.J., et al., Phys. Fluids B **5**, 2215 (1993).

MAGNETIC AND THERMAL ENERGY FLOW DURING DISRUPTIONS IN DIII–D*

A.W. Hyatt, R.L.Lee, J.W.Cuthbertson,† D.A. Humpreys, A.G. Kellman, C.J. Lasnier,Δ
P.L. Taylor, and the DIII–D Team

General Atomics, P.O. Box 85608, San Diego, California 92186-9784 USA

We present results from disruption experiments where we measure magnetic energy flow across a closed surface surrounding the plasma using a Poynting flux analysis to measure the electromagnetic power, bolometers to measure radiation power and IR scanners to measure radiation and particle heat conduction to the divertor. The initial and final stored energies within the volume are found using the full equilibrium reconstruction code EFIT. From this analysis we calculate an energy balance and find that we can account for all energy deposited on the first wall and the divertor to within about 10%.

INTRODUCTION

A disruption is an abrupt termination of a tokamak discharge, usually caused by a loss of MHD stability, in which the magnetic and thermal energy stored in the tokamak is rapidly lost. Disruptions in an ITER-scale fusion device are projected to distribute in excess of 1 GJ of thermal and 1 GJ of magnetic energies to in-vessel tokamak components on a time scale of milliseconds. The energy flow magnitude, the spatial distribution, the time scale and the loss mechanism taken to the various in-vessel components are critical issues for any large tokamak and resolution of these issues will have a significant impact on the engineering costs.and the lifetime and reliability of the components.

We have begun dedicated disruption experiments on the DIII–D tokamak[1] to address these issues. DIII–D has a large complement of disruption relevant diagnostics, including fast core and divertor Thomson scattering, toroidal and poloidal arrays of halo current monitors, fast ECE, fast Xuv spectrometry, several IR scanners viewing different internal wall locations, and multichannel bolometry that covers the inner chamber. The DIII–D tokamak has a robust internal mechanical structure to withstand a disruption's electromechanical forces. Conditioning of the vessel and carbon first wall, including baking to 350°C, boronization, and inter-shot helium glow cleaning provides immediate recovery from high power disruptions.

This paper describes an effort to address the disruption energy flow/energy balance issues by measuring the magnetic, radiative and conductive power fluxes. We use the MHD equilibrium reconstruction code EFIT[2] coupled with a Poynting flux analysis[3] at a surface nested just within the conducting vacuum wall, multichannel bolometry, and two toroidally separated infrared (IR) scanners with full radial view of the divertor floor.

ENERGY FLOW ANALYSIS METHOD

In the paper we are concerned with energy flows and energy balance within the first wall defined surface. Of particular interest is the flow of energy in or out of the surface, specifically through radiation, conduction and electromagnetic energy flow. We begin by applying conservation of energy,

$$\frac{\partial W_{TOT}}{\partial t} + \int_{surface} S_{TOT} \cdot \hat{n}\, dA = 0 \quad , \tag{1}$$

where $W_{TOT} = W_M + W_{TH}$, $W_M = \int dV(\mathbf{B}\cdot\mathbf{H} + \mathbf{E}\cdot\mathbf{D})$, W_{TH} is the plasma thermal energy, $W_M = W_{MT} + W_{MP}$ and W_{MP}, W_{MT} are the poloidal and toroidal magnetic field energies respectively. The contribution of the $\mathbf{E}\cdot\mathbf{D}$ term is small and can be neglected. $S_{TOT} = S_{AUX} + S_{EM} + S_{COND} + S_{RAD}$ where S_{AUX} is the input auxiliary heating flux, $S_{EM} = (\mathbf{E}\times\mathbf{H})$ is the Poynting flux of electromagnetic energy across the surface, S_{COND} is the thermal energy conducted across the surface, and S_{RAD} is the

*Work supported by the U.S. Department of Energy under Contract No.s DE-AC03-89ER51114 and W-7405-ENG-48 and Grant No. DE-FG03-05ER-54294.

†University of California, San Diego, California.

ΔLawrence Livermore National Laboratory, Livermore, California

energy radiated across the surface. Power balance can be written in terms of two coupled equations:

$$dW_{TH}/dt = P_{OHM} - P_{AUX} - P_{RAD} - P_{COND} \quad (2)$$

and

$$dW_M/dt = - P_{EM} - P_{OHM} \quad (3)$$

Here P_{OHM}, P_{AUX}, P_{RAD}, P_{COND} and P_{EM} are the surface integrals of S_{AUX}, S_{RAD}, S_{COND} and S_{EM}, and $P_{OHM} = \int \mathbf{J}\cdot\mathbf{E}\ dV$ is the conversion of electromagnetic energy to thermal energy.

For DIII–D we choose a closed toroidally symmetric surface just inside the vacuum vessel surface, but outside the first wall, as shown in Fig. 1. This surface passes through a set of 31 magnetic probes so that H_p is measured directly on the surface. The Poynting flux in an axisymmetric system consists of two components: $(\mathbf{E}\times\mathbf{H})\cdot\hat{\mathbf{n}}dA = (E_pH_\phi - E_\phi H_p)dA$, where $\hat{\mathbf{n}}$ points outwards from surface A, ϕ is in the toroidal direction, and $\mathbf{p} = \phi\times\hat{\mathbf{n}}$. Then $P_{EM} = P_{EMT} + P_{EMP}$, where P_{EMT} is due to E_pH_ϕ and P_{EMP} is due to $E_\phi H_p$. A full time-dependent reconstruction with the code EFIT provides $RE_\phi = -2\pi\partial\varphi/\partial t$ on the surface, where R is the major radius, and hence one component of the Poynting flux at the surface is unambiguously measured. EFIT also calculates the time dependent W_M and W_{TH}. The local value of the toroidal electric field is known, but only the average poloidal electric field. The average poloidal electric field $\langle E_p\rangle = L^{-1}\,\partial\Phi/\partial t$, where L is the poloidal length of the surface and Φ is the enclosed toroidal flux. $\partial\Phi/\partial t$ is approximately measured by a diamagnetic flux loop just outside the vessel wall. It can be shown that in the tokamak if the change in toroidal field is small, i.e. $B_T = B_{T0}(1+\delta)$ with $\delta << 1$, then to lowest order $dW_{MT}/dt + P_{EMT} \approx 0$. Then the change in toroidal field energy, ΔW_{MT}, passes through the surface as $\int dt P_{EMT}$. This near equality is confirmed by specific example in the next section.

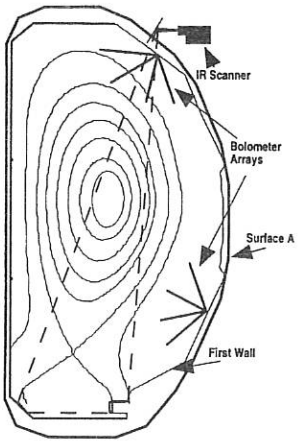

Fig. 1 A cross sectional view of DIII–D showing the poloidal locations and tokamak views of the IR scanners and bolometer arrays. The outermost line denotes Surface A. The line labeled First Wall denotes the plasma facing carbon armor surface. Not shown is the vacuum vessel inner wall which lies just outside Surface A.

Using the full equilibrium reconstruction from EFIT gives an accurate representation of the time dependent Poynting flux. However, robust equilibria are not yet available throughout the entire disruption process; progress is still being made on improving the robustness of solutions during disruptions. We can still estimate the total amount of electromagnetic energy crossing the surface. We note, following Hosogane[4] that the poloidal field coil cage defines a highly conducting boundary; see Fig 1. During the time of the disruption, the electromagnetic energy flux crossing this boundary is very small, so that the electromagnetic energy flux across the surface just inside the vacuum vessel is approximately equal to the net change in electromagnetic energy in the annulus between the poloidal coils and surface A. We term this assumption the "coil cage assumption" and use it in the following energy flow calculations to carry the analysis past the point where EFIT does not converge well.

P_{COND} is measured using Inframetrics 525 IR scanners at 8 kHz.[5] The scanners view a radial chord spanning the lower divertor floor at two toroidal locations 105 degrees apart. Each scanner has about 5 ms dead time every 16.7 ms and cannot be externally synchronized, so any given disruption may have incomplete coverage. A one dimensional model is used to convert measured temperatures to heat flux.[6] Where there is toroidal asymmetry in the calculated heat flux a simple average is used. Toroidal asymmetries of deposited energies (Max/Average) of up to 1.6 have been observed.

P_{RAD} is measured using two poloidally separated 24 channel metal foil resistor bolometer arrays.[7] The total power is calculated using the sum of all channels' line averaged power and by geometrically constraining the radiating volume with EFIT reconstructed boundaries. The last reconstructed EFIT boundary is assumed for times after successful EFIT reconstruction stops. This assumption should have only a small effect on the total radiated energy.

With use of the Poynting flux, all of the components of the energy flux in Eqs. (2) and (3) except P_{OHM} and P_{AUX} are determined. P_{OHM} need not be explicitly determined for an accurate energy flux accounting, since it simply transfers energy from the magnetic to the thermal within the surface. Only neutral beam heated discharges are considered here, and P_{AUX} is determined from the measured accelerating voltages and neutral currents.

EXPERIMENTAL RESULTS

Three types of disruptions are analyzed: #84356, a high beta disruption precipitated by exceeding the expected MHD high beta stability limit; shot #81168, a disruption precipitated by an argon gas puff induced radiative collapse, and #88824, a Vertical Displacement Event (VDE), precipitated by disabling the vertical feedback controls. The evolution of 84356 is shown in Fig. 2. For reasons discussed above we omit W_{MT} and P_{EMT} in the following analysis. We choose t_0 at 2200 ms, and t_{end} at 2240 ms, when the plasma current has vanished. At t_0 EFIT calculates a total energy $W(t_0) = W_{TH}(t_0) + W_{MP}(t_0) = 1.01$ MJ + 1.33 MJ = 2.34 MJ. From a central soft x-ray signal we see that there is a large initial dump of thermal energy at 2212 ms which is followed by the thermal quench (TQ) at 2222 ms. The EFIT reconstruction at $t_{TQ} = 2223$ ms shows that W_{TH} has dropped to nearly zero. The energy remaining is then measured to be $W(t_{TQ}) = W(t_0) - \int(P_{AUX}+P_{EMP}+P_{COND}+P_{RAD})dt = 1.41$ MJ. Over this interval $\int dt\, P_{AUX}$ has input 0.40 MJ of thermal energy, and $\int dt\, P_{EMP}$ has input 0.06 MJ of magnetic energy. The bolometers measure $\int dt\, P_{RAD} = 0.70$ MJ radiatively flowing out of the volume, and the IR scanners measure $\int dt\, P_{COND} = 0.69$ MJ conducted out calculated from the 0.83 MJ thermal flux measured by the IR scanners minus the 0.14 MJ of energy radiated to the divertor measured by bolometry tomography. At t_{TQ} EFIT calculates $W_{TH} \approx 0$ and $W_{MP} = 1.44$ MJ. If we define an energy balance $EB = \int(P_{AUX}+P_{EMP}+P_{COND}+P_{RAD})dt/[W(t_0)-W(t_{end})]$ and express EB as a percentage, then at the thermal quench EB = 103%, i.e. the net energy flow is accounted for to within 3%. This measure of energy balance is attractive in that all the measured flows are in the numerator, and only end point EFIT reconstructions are in the denominator. Measurement errors are estimated to be ±10% for the bolometers and the IR scanners, and ±5% for EFIT. We employ the coil cage assumption to carry the analysis to t_{end}. This implies a total of about 0.47 MJ of magnetic energy input during the disruption. Then the measured net energy flow leaves 0.26 MJ in the volume at t_{end} while EFIT calculates 0.17 MJ of vacuum magnetic energy for an overall EB = 96%.

From P_{EMT} determined experimentally from diamagnetic loop measurements, we find $\int dt P_{EMT} = 0.3$ MJ flowing out of the vessel over the span of the disruption. The change in the toroidal magnetic energy calculated by EFIT, $\Delta W_{MT} = -0.3$ MJ, as expected. So to within the accuracy of the measurement all of the diamagnetic energy within the surface flows electromagnetically through the surface and is not converted to thermal energy which might appear on the first wall.

Analyses for all three cases are summarized in Table 1. In the second row we see that the net energy flow is accounted for to within 10% or better for the first two cases; for the VDE the overall energy flow is 22% too large. We believe the over counting is due to the relatively low level of pre-disruption energy. The third row displays the pre-disruption energies and the measured total magnetic and thermal energy inputs. In the cases shown there is a net flow of electromagnetic energy, ΔW_{EMP}, into the vessel

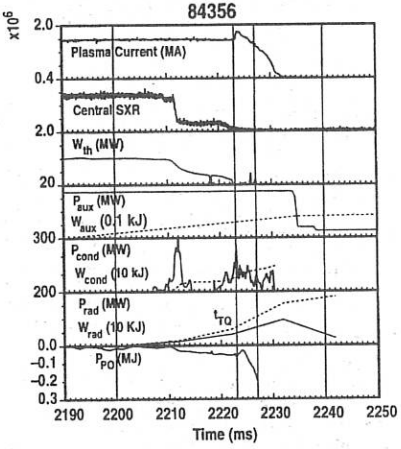

Fig. 2. Time history of the disruption. The central soft xray signal shows the initial thermal collapse followed by the thermal quench at 2223 ms. The vertical lines are t_0, t_{TQ}, t_{EFIT}, t_{end} from left to right. P_{AUX}, P_{COND} and P_{RAD} are shown as solid lines with the integrated power as dashed. W_{EMP} is the net energy flow out of the surface due to P_{EMP}. Note W_{EMP} is negative; magnetic energy flows into the plasma chamber during the disruption.

TABLE I

Discharge Type Current, Field	81168 Radiative Collapse 1.5 MA, 2.1 T	84356 High Beta 1.5 MA, 1.2 T	88824 VDE 1.0 MA, 1.0 T
EB at TQ EB overall	110% 111%	103% 96%	102% 122%
$W_{TH}(t_0)$ $W_{MP}(t_0)$ ΔW_{EMP} ΔW_{AUX}	1.17 1.53 0.50 0.41	1.01 1.33 0.47 0.54	0.53 0.64 0.19 0.11
$W_{COND}/W(t_0)$ $W_{RAD}/W(t_0)$	0.67/2.70 = 25% 2.88/2.70 = 107%	1.16/2.34 = 50% 1.75/2.34 = 75%	0.68/1.17 = 58% 0.90/1.17 = 77%
$W_{FW}(t_{TQ})/W(t_0)$ $W_{FW}(t_{end})/W(t_0)$	2.18/2.70 = 81% 3.55/2.70 = 132%	1.39/2.34 = 59% 2.91/2.34 = 124%	0.71/1.17 = 61% 1.58/1.17 = 135%

$W(t_0) = W_{TH}(t_0) + W_{MP}(t_0)$, the initial stored energy at t_0, in MJ
$W_{FW}(t)$ = energy deposited on inner walls & divertor, in MJ, at time t
W_{COND} = total energy conducted to divertor, in MJ
W_{RAD} = total energy radiated to first wall, in MJ
ΔW_{EMP} = total magnetic energy input from P_{EMP}, in MJ
ΔW_{AUX} = total thermal energy input from P_{AUX}, in MJ

during the disruption which is approximately 30% of the pre-disruption magnetic energy stored within the vacuum vessel. The fourth row displays the measured conducted and radiated energy flows normalized to $W(t_0)$, the total pre-disruption energy. Radiation dominates, and for the radiative collapse case it strongly dominates; the extra radiation comes at the expense of conducted power. The radiative collapse case conducts about half of its pre-disruption thermal energy to the divertor, while the other cases conduct more than 100%. The fifth row displays the total net energy that flows to the first wall, W_{FW}, similarly normalized, at t_{TQ} and t_{end}. We see that in all cases ~130% of W_0, the total pre-disruption energy, eventually flows to the walls. This is due in part to ΔW_{EMP}, the total electromagnetic energy inflow during the disruption, and to ΔW_{AUX}, the total thermal energy inflow from P_{AUX}. Presumably ΔW_{AUX} can be significantly decreased if auxiliary heating is terminated earlier in the disruption, but ΔW_{EMP} is not likely to decrease.

DISCUSSION

The Poynting flux analysis described here provides a precise method to measure magnetic energy flow into and out of the vacuum vessel volume. It may also prove beneficial for similar energy flow measurements to the vacuum vessel itself, and to structure outside the vacuum vessel. The energy balance based upon it give a total accounting of energy flows to roughly 10%. Analysis indicates that net electromagnetic energy flows into the plasma during disruptions where it is converted to thermal energy and deposited on the first wall. In DIII-D the assumption that the relevant volume for calculating the stored magnetic energy is defined by the poloidal field coils gives a good overall energy balance, and this is likely more or less true for any tokamak with a resistive vessel depending on the details of the coil cage. Projections which assume that only the stored magnetic energy associated with the plasma internal inductance, l_i, will be deposited in a disruption will be too low; in DIII-D by a factor of 2. The data indicates that unless mitigation efforts are employed over 100% of the pre-disruption thermal energy will be conducted to the divertor. Finally, the data indicates that the plasma diamagnetic energy is not converted to heat which may be conducted or radiated to the first wall.

[1]Taylor, P.L, et al., Phys. Rev. Lett. **76**, (1996).916; Evans, T.E., et al., "Non-Axsymmetric Halo Currents With and Without "Killer" Pellets During Disruptive Instabilities in DIII-D," to be published in J Nucl. Mater.
[2]L.L. Lao, et al., Nucl. Fusion **25**, (1985) 1611.
[3]Ejima, et al., Nucl. Fusion **22**, (1982) 1313.
[4]Hosogane, JAERI-M 90-066.
[5]Lee, R.L., et al., "Thermal Deposition Analysis During Disruptions on DIII-D Using Infrared Scanners," Proc. 16th Symp. on Fusion Engineering., (Institute of Electrical and Electronics Engineers, Inc. Piscataway, New Jersey) to be published.
[6]Hill, D.N., Ellis, R., Fergusen, S.W., Perkins, D.E., Rev. Sci. Instrum. **59**, (1988) 1878.
[7]Leonard, A.W., et al., Rev. Sci. Instum. **66**, (1995) 1201.

TRANSPORT IN HIGH PERFORMANCE WEAK AND NEGATIVE CENTRAL SHEAR DISCHARGES IN DIII-D*

C.M. Greenfield, D.P. Schissel, B.W. Stallard,† E.A. Lazarus,# G.A. Navratil,§ R.V. Budny,‡ K.H. Burrell, T.A. Casper,† J.C. DeBoo, E.J. Doyle,Δ R.D. Durst,◊ R.J. Fonck,◊ R.J. Groebner, L.L. Lao, D.C. McCune,‡ M. Murakami,# C.C. Petty, C.L. Rettig,Δ B.W. Rice,† T.L. Rhodes,Δ H.E. St. John, T.S. Taylor, K.L. Tritz,◊ M.R. Wade,# and D. Whyte¶

General Atomics, PO Box 85608, San Diego, CA 92186-9784, USA

In recent experiments in the DIII–D tokamak, the previously reported enhanced performance regime with negative central magnetic shear (NCS)[1,2] has been extended to further improve fusion performance. This was done by using controlled L–H transitions to further broaden the pressure profile, thereby delaying the onset of MHD activity which would lead to the termination of the high performance phase.[3] Such discharges have achieved record parameters for DIII-D, including D–D fusion power up to 28 kW and stored energy in excess of 4 MJ.

Discharge Evolution

As in the earlier discharges, the core magnetic shear is reversed by use of low power neutral beam injection during the plasma current ramp. This has the effect of heating the core region, thereby "freezing in" the hollow current density profile peaked off-axis. By varying the early beam power, we can alter the degree of inversion of the current profile.

These discharges frequently undergo a transition to a regime of high performance. This transition typically involves formation of an internal transport barrier, developing in the region of negative central shear, as indicated by peaking of the ion temperature and rotation velocity (and with sufficient power, the electron density and temperature) profiles. These L–mode plasmas with peaked profiles have exhibited high fusion performance in DIII-D, but are frequently unstable, often resulting in disruption at relatively low normalized beta.

In recent experiments (Fig. 1), a double–null divertor configuration was biased toward the top of the vessel, in order to direct the ∇B drift away from the primary (upper) X–point and suppress the L–H transition.[4] Shortly before the plasma would otherwise reach the stability limit, the plasma is shifted downwards to make the lower null the controlling null, thereby reducing the H–mode power threshold and triggering a transition to H–mode. This has the effect of broadening the profiles (Fig. 2), and delaying the onset of detrimental MHD activity.

With these broadened profiles, the plasma continues to evolve, with increasing confinement time, beta and reactivity, until the regime of high performance terminates with MHD activity similar to the VH–mode termination.[5] During these experiments, such a procedure resulted in record performance in DIII-D.

Transport

The recent discharges (Fig. 1) were typically produced using somewhat lower beam power during the early phase, resulting in current profiles with weak negative (or neutral) shear (WNS).[6] Although local magnetic shear in the core is much weaker than in the NCS regime, the region with low shear extends over more of the plasma (to $\rho \leq 0.7$ instead of $\rho \leq 0.5$).

*Work supported by the U.S. Department of Energy under Contract Nos. DE-AC03-89ER51114, W-7405-ENG-48, DE-AC05-96OR22464, and Grant Nos. DE-FG03-85ER53266, and DE-FG02-89ER53297.

†Oak Ridge National Laboratory, Oak Ridge, Tennessee, USA.
§Columbia University, New York, New York, USA.
‡ Princeton Plasma Physics Laboratory, Princeton, NJ, USA.
¶Lawrence Livermore National Laboratory, Livermore, California, USA.
ΔUniversity of California, Los Angeles, California, USA.
◊University of Wisconsin, Madison, Wisconsin, USA.
¶INRS — Energie et Materiaux, Varennes, Quebec, Canada.

At the internal transport barrier formation, fluctuation diagnostics including beam emission spectroscopy (BES)[7] and far infrared (FIR)[8] scattering indicate reductions in turbulence to below the minimum detectable level ($\tilde{n}/n \leq 0.1\%$, Fig. 3) in regions of weak or negative magnetic shear. This effect is seen regardless of the strength of the magnetic shear in this region, as long as the shear is not strongly positive. The volume in which the transport barrier develops is typically larger for WNS than NCS plasmas. At the H–mode transition, this region extends to cover the entire plasma.

A pair of discharges was selected for detailed transport analysis, each with I_P=2.1 MA, B_T = 2.1 T and P_{NBI} = 20.5 MW (during the full power phase of the discharge). The main difference between these two discharges is that one (87937) had weak central magnetic shear (WNS, P_{NBI} = 3.5 MW in the early phase) and the other (87953) negative central shear (NCS, P_{NBI} = 5.5 MW in the early phase) at the time of application of full beam power (Fig. 2). The NCS discharge clearly reaches stability limits earlier in its evolution, limiting the peak performance achieved in the discharge.[6] Prior to the termination of the high performance phase in the NCS discharge, the two behave similarly, with nearly identical evolution. We will focus on a comparison of transport analysis between the two discharges.

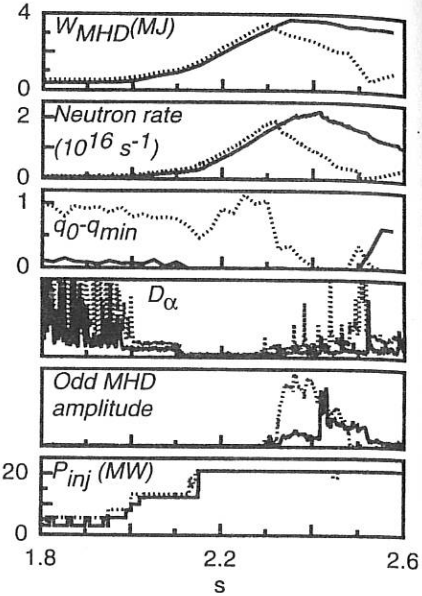

Fig. 1. Time traces for a pair of high performance discharges with weak (87937, solid lines) and negative (87953, dotted lines) magnetic shear and a controlled L–H mode transition. The high power neutral beams are applied at 2.0 s, with an L–H transition occurring at 2.106 s following a downward shift of the plasma.

During the L–mode phase, the formation of an internal transport barrier becomes evident in the ion temperature profiles (Fig. 2). After an L–H transition at 2.106 s, the identifiable transport barrier vanishes, with steep gradients now extending over the entire ion temperature profile. During this period, the second largest term in the core power balance (Fig. 4) after the applied heating power is dW/dt. In other words, the plasma core at this time acts as an integrator of the applied power. As a result, there is little power available to be diffusively conducted away from the core. In both discharges, these calculations suggest ion diffusivities consistently below Chang–Hinton neoclassical (Fig. 5). This implies that diffusive transport is not an important term in the core power balance in these discharges during H–mode.

Based on the transport analysis, during the H–mode phase, these discharges behave essentially the same. The difference between NCS and WNS discharges appears to be mainly in stability, with the NCS discharge reaching peak values ~100 ms sooner and at lower levels of β_N and reactivity.

High Performance

The discharges exhibit levels of fusion performance (D-D reactivity) a factor of 4 above the highest seen in DIII–D VH–modes,[9] and a factor of 3 above the highest observed in DIII–D NCS discharges prior to the introduction of the controlled L–H transition as a profile control "knob" (Table 1).

We used the TRANSP[10] code to simulate the discharge with the highest Q_{DD} (87977, I_P = 2.25 MA, B_T = 2.1 T and P_{NBI} =17.75 MW, $S_N = 2.2 \times 10^{16}$ s^{-1}, Q_{DD}=1.46 × 10^{-3} in conditions where a portion of the deuterium injected by the neutral beams is replaced by tritium. In this numerical experiment, the density, temperature and impurity rotation profiles are all held fixed in the DT plasma as measured in the DD plasma. No correction is made for differences in transport due to isotope effects, other than the poorer penetration of the tritium neutral beams.

Under conditions where TRANSP computes roughly equal amounts of deuterium and tritium in the plasma core, we calculate a power multiplier (P_{DT}/P_{DD}) of 220. Applying this to Q_{DD} = 1.46 × 10^{-3} measured in the best discharge yields $Q_{DD}^{equivalent} \approx 0.32$. We note that this multiplier is higher than published predicted multipliers for TFTR Supershots made using a similar procedure.[11] This is not unreasonable given the differences between the DIII–D NCS/WNS and Supershot regimes. The higher central ion temperatures in Supershots (~35 keV vs. ≤20 keV in NCS/WNS) result in a considerably lower ratio $\langle\sigma v\rangle_{DT}/\langle\sigma v\rangle_{DD}$ (by about 25% on axis), and therefore of the thermonuclear reactivity multiplier. The higher neutral beam voltages in TFTR (110 kV vs. 80 kV in DIII–D) lead to a reduction of about 10% in the ratio σ_{DT}/σ_{DD} and therefore of the beam–plasma reactivity multiplier.

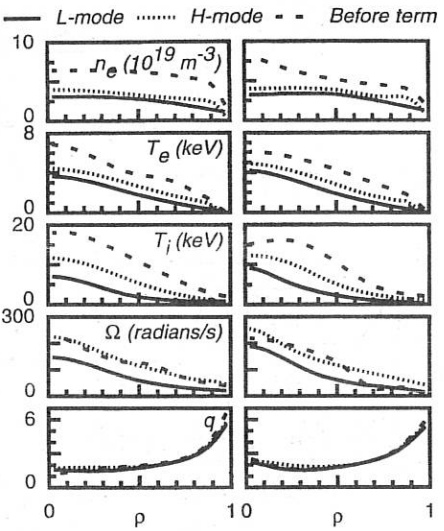

Fig. 2. Profile evolution of two similar discharges with weak (87937, left) and negative (87953, right) magnetic shear. Profiles shown in L–mode (2.05 s), H–mode (2.15 s) and prior to the termination of high performance (2.3 s for 87953 and 2.4 s for 87937).

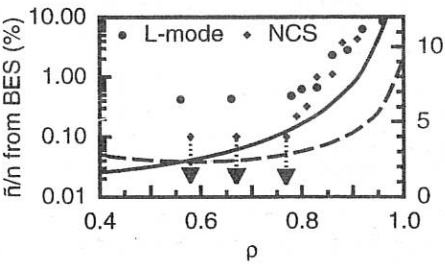

Fig. 3. Data from BES indicates that turbulence is suppressed by even weak shear in the current profile as compared to standard L–mode.

Summary

The high performance obtained in NCS and WNS plasmas in DIII–D has been further enhanced by application of controlled L–H transitions as a means of profile control. These discharges exhibit characteristics of a transport barrier (steep gradients, suppressed turbulence and low calculated energy flows) extending over nearly the entire plasma resulting in DIII–D record levels of fusion reactivity.The crude profile control employed gives a hint of the possibilities open to us in future experiments where we expect to have more toolsavailable, including radio frequency power (fast wave and electron cyclotron), density control via the pumped high triangularity divertor and pellet injection (deuterium and lithium).

Table 1. Highest parameters achieved in H–mode NCS/WNS plasmas in DIII–D (not simultaneously achieved)

Neutron rate S_N	2.4×10^{16} s^{-1}
Fusion power P_{DD}	28 kW
Fusion power efficiency Q_{DD}	1.46×10^{-3}
Equivalent DT efficiency Q_{DT}	0.32
Stored energy W_{MHD}	4.4 MJ
β_N	4.3
Confinement time τ_E	0.5 s (at P_{NBI} =17.75 MW)
Normalized confinement time H	4.8

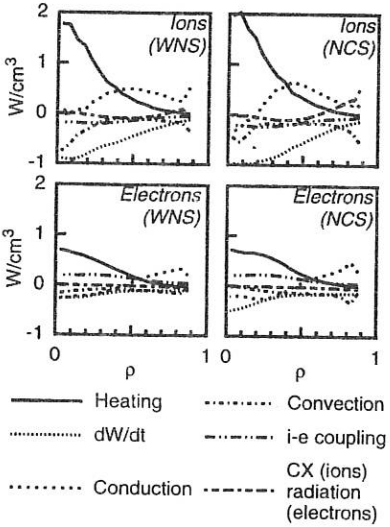

Fig. 4. Power balance for both discharges during H-mode phase (2.150 s).

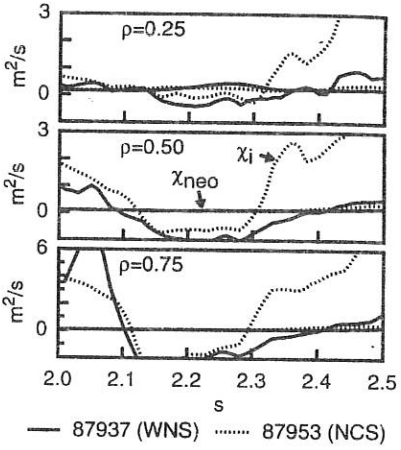

Fig. 5. Ion diffusivities vs. time for ρ= 0.25, 0.50 and 0.75 in both discharges.

[1]Strait, E. J., et al., Phys. Rev. Lett. **75**, 4421 (1995).

[2]Rice, B.W., et al., Phys. Plasmas **3**, 1983 (1996).

[3]Lazarus, E.A., et al.,"Higher Fusion Power Gain With Pressure Profile Control in Strongly Shaped DIII–D Tokamak Plasmas," submitted to Phys. Rev. Lett.

[4]Carlstrom, T.N., et al., Plasma Phys. Contr. Fusion **36**, A147 (1994).

[5]Lazarus, E.A., et al., Plasma Phys. and Contr. Nucl. Fusion Research (Proc. 15th Intnl Conf., Seville, 1994), paper IAEA–CN–60/A5–1 (1995).

[6]Lao, L.L., et al., Phys. Fluids **3**, 1951 (1996).

[7]Durst, R.D., et al., Bull. Am. Phys. Soc. **40**, 1790 (1995).

[8]Rettig,, C.L., et al., Rev. Sci. Instrum. **61**, 3010 (1990).

[9]Greenfield, C.M., et al, Plasma Phys. Contr. Fusion **25**, B263 (1993).

[10]Goldston, R.J., et al, J. Comput. Phys. **43**, 61 (1981).

[11]Budny, R.V., et al., Nucl. Fusion **32**, 429 (1992).

Modeling of current profile evolution and equilibria in negative central shear discharges in the DIII-D experiment.*

T. A. Casper, J. Crotinger, W. Meyer, J. Moller, L. D. Pearlstein,
B. Rice, and B. Stallard
Lawrence Livermore National Laboratory
P.O. Box 808, Livermore, CA 94550 USA
L. Lao and T. Taylor
General Atomics
P.O. Box 85608, San Diego, CA 92186 USA

1.0 Abstract

Recent DIII-D advanced tokamak experiments with negative central shear (NCS) have resulted in operation at high normalized β, $\beta_N=\beta/(I/aB)$, to 4.2, confinement enhancement factors to H=4 ($H=\tau_E/\tau_{ITER\text{-}89P}$), and record neutron rates for DIII-D to $2.4x10^{16}$ neutrons/sec. These data were obtained during high triangularity, single and double null diverted operation with peaked (L-mode) and broad (H-mode) pressure profiles. We are modeling the spatial and temporal current profile evolution for these discharges using Corsica, a predictive 1-1/2 D equilibrium and transport code. Current profile evolution is self-consistently determined by including current diffusion resulting from current drive due to early neutral beam injection during the ohmic current ramp-up phase of the discharge and the bootstrap current drive associated with pressure profile evolution.

1.0 Introduction

The prospect for achieving high performance discharges in reduced size advanced tokamaks has stimulated much of the current interest in negative central shear (NCS) experiments. Recent studies[1,2] have indicated that NCS is a leading candidate scenario for operation in steady state due to improved stability to high-n ballooning modes and bootstrap current density aligned with the total current profile and it has been proposed as an advanced confinement scenario in ITER[3]. We are applying Corsica to model DIII-D discharges to explore techniques to improve and sustain these discharges, ultimately leading to steady-state.

Corsica[4] is a comprehensive, predictive toroidal plasma simulation code being developed for design and simulation of existing experiments and of future experiments such as ITER or other advanced tokamaks and alternatives. Corsica is currently running with the combined capabilities of 1D tokamak transport codes and 2D free-boundary equilibrium and edge modeling codes. It is being

---

*Work supported by U.S. DoE under LLNL Contract W-7405-ENG-48 and GA contract DE-AC03-89ER51114

used to model ITER ohmic operation and to assess feedback control capabilities and power requirements. Previous DIII-D L-mode simulations have compared favorably with the EFIT analysis code for high β_p operation and for the low pressure phase of NCS discharges. We are now extending this modeling to high performance phases of NCS and weak shear discharges in DIII-D.

2.0 Simulation methodology

We are presently simulating the temporal evolution of the current profiles to develop an understanding and validation of the models for forming and sustaining the high performance NCS configuration. At this time, we use experimental measurements of the density and temperature profiles rather than model the particle and energy transport. We take as input the measured electron and impurity densities and the electron and ion temperatures and infer the ion density and effective charge (Z_{eff}) from quasi-neutrality using carbon as the main impurity. We initialize the equilibrium by choosing the pressure (p') and current (ff') parameterizations used in fitting data with EFIT. A free boundary calculation provides a starting equilibrium with forced convergence to the plasma current and fitted values of the poloidal field coil currents to account for currents in structures. This prescription allows us to directly compare with the EFIT results and boundary shapes produced in this manner are in generally good agreement. The simulated discharge is evolved from this initial state using a fixed boundary equilibrium calculation while simultaneously accounting for current diffusion.

In previous simulations, an approximate particle orbit model resulted in too little neutral beam current drive on axis. We have replaced this portion of our neutral beam injection code with an orbit following calculation for the Monte Carlo simulation of neutral beam current drive. The injection process is now tightly coupled to the local equilibrium flux surfaces with current drive determined from the residence time of particles in flux zones. By evaluating the trapped, passing, and lost particle distributions we infer the direct current drive from passing beam particle orbits and the bootstrap contribution due to the trapped injected ions.

3.0 Simulation Results

We have begun our modeling with two different high performance discharges. Shot 84682 is a double null, negative central shear discharge with peaked pressure profiles[5]. Confinement factors up to H~2.5 were obtained while maintaining the pressure profile with an L-mode edge which allows for good penetration of the neutral beams. The inverted q-profile is achieved by early neutral beam injection during the ohmic current ramp-up phase of the experiment. Ion temperatures in excess of 15 KeV were obtained with peaked density profiles, $n(0)/\langle n\rangle \sim 2.2$. A second case, shot 88964, is a single null, weak central shear discharge with H-mode-like pressure profiles giving a broader deposition profile for the neutral beam injection. The weak shear is formed at reduced neutral beam injection power during the ohmic ramp. This DIII-D shape is representative of the JET and ITER advanced tokamak scenarios.

In Figure 1, we show the plasma current and neutral beam injection histories for these two shots along with the simulation time interval. We model the neutral beam injection as two aggregate sources having the proper geometry for the two beamline orientations on DIII-D and step the average power in time consistent with the experimental variations. Corsica is run in time dependent

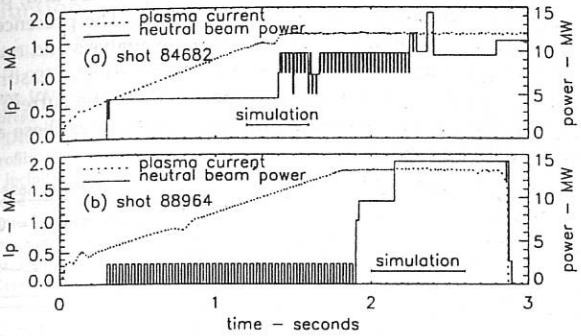

Figure 1. Time history of plasma current and neutral beam power injected.

mode to simulate the evolution of the equilibrium associated with the current diffusion process and obtain spatial-temporal profiles of plasma parameters. We show profiles of the total, ohmic, bootstrap, neutral beam driven current densities in Figure 2 at times near the peak stored energy. As indicated in Figure 3a for the NCS simulation (84682), we obtain good agreement between the simulated q-profile evolution and EFIT analysis outside of ρ=0.2 (ρ = √[normalized toroidal flux]), where we note good agreement with the minimum value of q and of q95 . Inside ρ=0.2, the current drive due to neutral

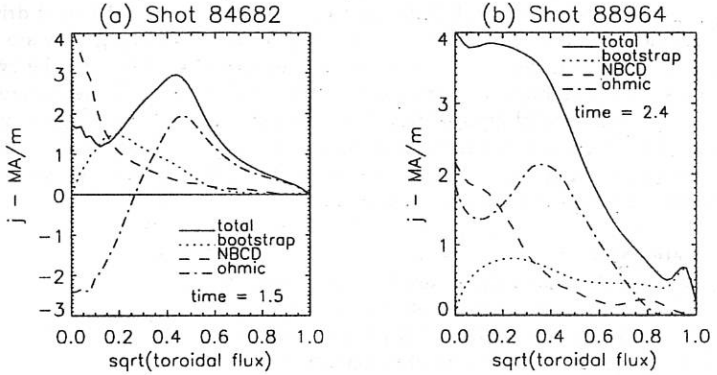

Figure 2. Current density profiles at times near peak stored energy

beam injection dominates the total current and forces the simulation q_0 to drop below that inferred from the EFIT reconstruction. For the weak shear simulation case, Figure 3b, there is agreement over most of the profile during the entire simulation as indicated at times t=2.0 and 2.6 s. However, the predicted q-profile evolution does not show the weak bump near ρ~0.35 that arises in the EFIT analysis during the times when the density and temperature and, presumably, the ensuing current distribution are rapidly changing. The presence of this bump is critically dependent on fit parameters used in the analysis and on reconstruction constraints such as the motional Stark effect measurement of the local magnetic field. We are investigating the details of the current drive associated with the neutral beam injection which dominates these and all high performance discharges in DIII-D.

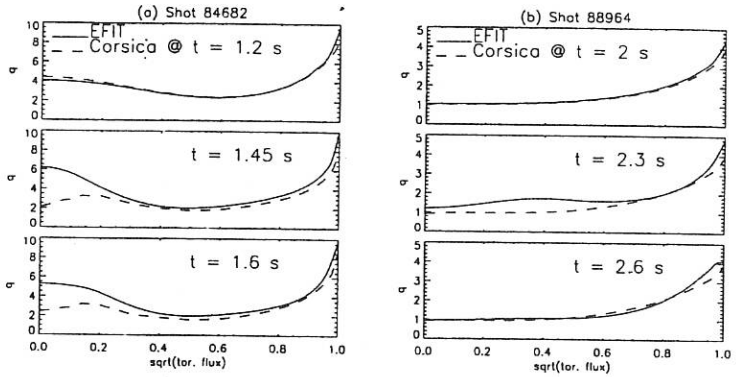

Figure 3. Simulation q-profiles with data fits from EFIT for comparison.

In summary, the initial results at simulating the formation of high performance discharges in DIII-D using our new neutral beam current drive calculation in a fully predictive simulation code are encouraging. We are able to simulate the characteristics of the current profile formation during the evolution of these complex, high performance discharges and we are in general agreement with the experimental data fitting. Discrepancies due to the peaking of the neutral beam current drive near the magnetic axis are a concern and we are investigating the details of these differences. In future simulations, we will be incorporating the use transport models.

5.0 References

1. Turnbull, A.D., et.al. Phys. Rev. Lett. **74**, 718 (1995).
2. Kessel, C., et. al. Phys. Rev. Lett. **72**, 1212 (1995)
3. Nevins, W. M., et. al. **IAEA-CN-60/E-P5**, 543, Seville, 1994.
4. J. Crotinger, et. al. Bull. Am. Phys. Soc. **38** 2016 (1993).
5. B. W. Rice, et. al., Phys. Plasmas **3**, 1983 (1996).

Thermal Transport Coefficient for Ohmic and ICRF Plasmas in Alcator C-Mod

W. Daughton. B. Coppi. F. Bombarda[†]. L. Sugiyama
Massachusetts Institute of Technology. Cambridge. MA 02139
[†]Associazione Euratom-ENEA sulla Fusione. Frascati. 00044 Italy

1 Introduction .

The observed similarity in the global thermal confinement between the ohmic and ICRF heated L-mode plasmas [1],[2],[3] opens the possibility that thermal transport in the Alcator C-Mod machine may be described by one transport coefficient for both regimes. A modified form of a transport coefficient previously reported [4] has been used to simulate both ohmic and ICRF discharges over a wide range of parameters. Detailed simulations carried out by means of the BALDUR code reproduce the observed temperature profiles, loop voltage and energy confinement time of the Alcator C-Mod discharges. The coefficient D_e^{th} includes the constraint of profile consistency and is inspired by the properties of the so-called electron and ion "ubiquitous" modes [5]. Thus D_e^{th} includes a significant dependence on the electron pressure gradient. The resulting confinement time improves with the plasma current, in agreement with the observations, and contains only a weak dependence on density. A total of nearly two dozen ohmic and ICRF Alcator C-Mod discharges have been fit over the range of parameter space available using this transport coefficient.

2 Thermal Transport Coefficient

Consider a toroidal geometry where ξ is the square root of the normalized toroidal flux and ϕ, and θ are the toroidal and poloidal angles. We assume that the electron thermal conductivity is the main form of power loss and write the surface averaged electron energy equation as

$$\langle \nabla \cdot \vec{q}_e \rangle = \langle S_H \rangle, \tag{1}$$

where $\vec{q}_e$ is the heat flux and S_H is the heating power per unit volume. The surface average is defined by

$$\langle A \rangle = \frac{1}{V'} \int A \sqrt{g} d\theta d\phi, \tag{2}$$

where $g \equiv |\nabla\xi \times \nabla\phi \cdot \nabla\theta|^{-1}$ is the Jacobian and

$$V' = \frac{\partial V}{\partial \xi} = \int \sqrt{g} d\theta d\phi.$$

The divergence theorem is used to write

$$\langle \nabla \cdot \vec{q}_e \rangle = \frac{d}{dV} \int \vec{q}_e \cdot \nabla\xi \sqrt{g} d\theta d\phi, \tag{3}$$

where V is the volume within the flux surface labeled by ξ. Substituting this into equation (1) gives

$$\frac{1}{V'} \frac{\partial}{\partial \xi} (V' \langle \vec{q}_e \cdot \nabla\xi \rangle) = \langle S_H \rangle. \tag{4}$$

If we assume that the electron thermal transport coefficient D_e^{th} is a function of the flux surface variable, we can write the heat flux as

$$\langle \vec{q}_e \cdot \nabla\xi \rangle = -n D_e^{th} \frac{\partial T_e}{\partial \xi} \langle |\nabla\xi|^2 \rangle. \tag{5}$$

Integrating over ξ from the magnetic axis to a given flux surface and solving for D_e^{th} gives,

$$D_e^{th} = -\frac{P_H}{n \frac{\partial T_e}{\partial \xi} V' \langle |\nabla\xi|^2 \rangle} \tag{6}$$

where

$$P_H = \int_0^{\xi} V''\langle S_H\rangle d\xi.$$

is the heating power. In addition, we consider the temperature profile to be represented by

$$T_e = T_{e_0}\, exp\left(\frac{-\alpha(\xi)V'(\xi)}{V_a}\right) \quad . \tag{7}$$

where T_{e_0} is a constant and V_a is the total plasma volume. Then equation (6) becomes

$$D_e^{th} = \frac{P_H V_a}{nT_e \frac{d(\alpha V')}{dV'}\langle|\nabla V'|^2\rangle} \tag{8}$$

In order to derive a transport coefficient which is dependent only on the local and global plasma parameters, it is desirable to relate the heating power to the global plasma parameters. We observe that a key difference between ohmic and ICRF discharges is that β_p is roughly constant for ohmic discharges but increases when there is a significant fraction of ICRF heating as shown in figure 1. Motivated by the

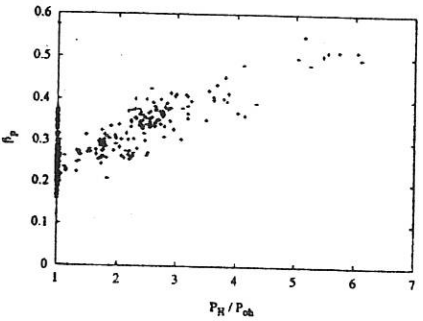

Figure 1: Experimental values of β_p verses P_H/P_{oh} where P_{oh} is the ohmic heating.

properties of the "ubiquitous" modes[4] we assume that the underlying collective modes responsible for the energy transport are driven by the electron pressure gradient and consider the parameter

$$\beta_{p_e} = \frac{8\pi p_{e_0}}{\langle B_\theta^2\rangle}, \qquad p_{e_0} = \left(\frac{dp_e}{d\xi}\langle\,|\nabla\xi|\,\rangle\right)_{max} a, \tag{9}$$

where a is the half width of the flux surface with maximum $dp_e/d\xi$. We draw inspiration from the transport coefficient suggested by Coppi et al.[4] for ohmic plasmas and we take

$$P_H = C_e \beta_{p_e} I_\phi(\xi)\frac{d}{dV'}\left[\alpha(\xi)V'(\xi)\right]\frac{T_e(\xi)}{e}\left(\omega_{pi}d_e^2\frac{\nu_{ei}}{V_{the}^2}\right)^{1/3}\left[\frac{Z_*}{A_i}\right]^{1/2} \tag{10}$$

where C_e is a constant numerical coefficient, I_ϕ is the toroidal current within a flux surface. $d_e \equiv c/\omega_{pe}$. A_i is the mass number of the main ion population, $Z_* = A_i\sum_j n_j Z_i^2/(n_e A_j)$, and $[\,]$ represents a volume average and the quantities appearing in the braces are all functions of the flux surface. We note that since

$$T_e(\xi)\left(\omega_{pi}d_e^2\frac{\nu_{ei}}{V_{the}^2}\right)^{1/3} \propto [n(\xi)T_e(\xi)]^{1/6}\,.$$

is a weak function of ξ we may conclude that equation (10) gives a relationship between $\alpha(\xi)$ and $P_H(\xi)/I_\phi(\xi)$. In particular

$$\alpha(\xi) \propto \frac{1}{V(\xi)}\int^{\xi} d\xi \frac{P_H(\xi)}{I_\phi(\xi)}V'. \tag{11}$$

This implies that in the case of ohmic heating where $P_H(\xi) \propto I_o(\xi)$. as the loop voltage is constant over the plasma column. $\alpha(\xi)$ is about constant. Then D_e^{th} takes the form

$$D_e^{th} = C_e \left(\omega_{pi} d_e^2 \frac{\nu_{ee}}{V_{the}^2} \right)^{1/3} \frac{I}{en} \frac{V_o}{\langle \nabla V^2 \rangle} \beta_{p*} \left[\frac{Z_*}{A_i} \right]^{1/2} . \qquad (12)$$

where C_e is found to be $C_e \approx 0.11$.

For a plasma with a circular cross section and assuming that the profiles and radiative losses remain constant, equation (12) implies that the energy confinement time should increase with current and decrease very weakly with heating power, $\tau_E \sim I^{6/7}/P_H^{1/7}$. In reality, the profiles and radiative losses do vary and the scaling for the energy confinement time resulting from the simulations cannot be deduced in a simple way by the adopted form of D_e^{th}.

3 Transport Simulation

The simulation was carried out with the 1 1/2D transport code BALDUR. The electron thermal transport, that is considered to be the dominant one, was described by equation (12) while the ion thermal transport was assumed neoclassical as was the electrical resistivity. The density profile was held fixed to match the experiment and the particle transport was set to zero. The simulation was performed with an up-down symmetric plasma shape while the actual configurations had a bottom null point. The fraction of ICRF heating going to the electron and ion channels was estimated by first running a Fokker Planck simulation to determine the distribution function of the minority species and the collisional transfer to the electrons and ions. Typically 80 percent of the energy was collisionally transfered to the electron population. For high current discharges with sawteeth, a simple model was used with sawtooth period set to match experiment. The geometric parameters and boundary conditions were set to match a particular Alcator C-Mod discharge at equilibrium and the transport simulation with arbitrary initial conditions was was run forward in time until an equilibrium was reached. Table 1 and 2 give the plasma parameters for the ohmic and ICRF discharges which have been simulated. Agreement between the simulation and experiment for the energy confinement time, loop voltage and stored energies is quite good. Figures 2 and 3 show simulated electron temperature profiles and experimental ECE temperature profiles for selected discharges.

In conclusion, detailed transport simulations indicate that the coefficient can reproduce the temperature profiles, energy confinement time, and loop voltage for both ohmic and ICRF discharges. The coefficient is simple to derive, contains only one numerical coefficient and captures key elements of the physics.

Acknowledgments

The authors gratefully acknowledge the Alcator C-Mod group for its collaboration and for providing the data. This work was supported in part by the U.S. Department of Energy.

References

[1] F. Bombarda. B. Coppi, W. Daughton, L. Sugiyama et al., *Proceedings of the 22nd EPS Conf. on Controlled Fusion and Plasma Physics*, 1995

[2] M. Greenwald, R. Boivin, P. Bonoli et al.,*Physics of Plasmas 2.* **6** 2305 (1995)

[3] I.H Hutchinson, Plasma Phys. Control. Fusion **36** 143 (1994)

[4] B. Coppi, L. Sugiyma, M. Greenwad, W. Daughton, *Proc. of the* 21st *EPS Conf. on Contr. Fusion and Plasma Phys.*, Montpellier, **18B III** 520 (1994)

[5] B. Coppi and G. Rewoldt, *Phys. Rev. Letters* **33** 1320 (1974). B. Coppi and F. Pegoraro, *Nucl. Fusion* **17**, 963 (1977).

Table 1: Experimental Parameters of Ohmic Discharges. (* are hydrogen discharges)

shot	I_p (MA)	$\overline{n}_e$ 10^{14} $(cm)^{-3}$	P_{oh} (MW)	P_{rad} (MW)	Z_{eff}
930818011*	0.376	0.829	0.50	0.22	1.76
930818022*	0.376	0.684	0.51	0.24	2.14
940603018	0.410	0.88	0.52	0.37	1.42
931021022	0.565	1.06	0.52	0.13	1.0
931008014	0.608	0.939	0.61	0.19	1.29
931006015	0.676	0.781	0.70	0.21	1.6
940603012	0.786	1.33	1.1	0.68	1.21
931013013	0.800	1.75	1.1	0.21	1.0
931021010	0.850	1.15	0.93	0.21	1.24
931012007	0.992	1.45	1.29	0.27	1.0

Table 2: Experimental Parameters of ICRF Discharges

shot	I_p (MA)	$\overline{n}_e$ 10^{14} $(cm)^{-3}$	P_{rf} (MW)	P_{oh} (MW)	P_{rad} (MW)	Z_{eff}
950302010	1.01	1.55	0.78	1.29	1.37	2.6
950301016	0.64	1.43	0.90	0.62	0.88	1.3
950406036	1.01	2.34	1.24	1.38	1.46	1.9
950208028	0.85	1.62	1.33	0.89	1.15	1.6
950303010	1.02	2.72	1.41	1.36	1.18	1.7
940616025	0.44	0.91	1.48	0.32	0.78	1.9
940602019	0.82	1.51	1.66	0.86	1.07	1.5
950301025	0.64	1.29	2.2	0.48	2.00	3.5
950407016	1.01	1.72	2.88	1.28	3.49	3.0
950118033	0.82	1.00	3.42	0.96	3.40	2.4

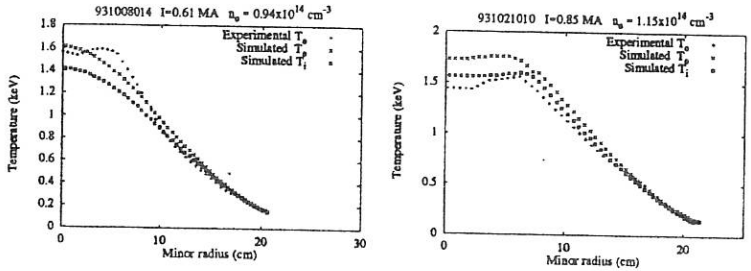

Figure 2: Comparison of simulated and experimental ECE temperature profiles for selected Ohmic discharges

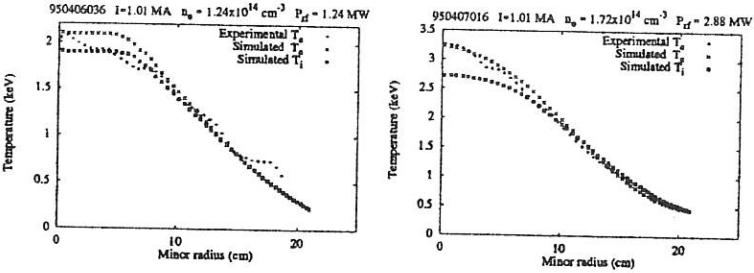

Figure 3: Comparison of simulated and experimental ECE temperature profiles for selected ICRF discharges.

Rationale for Ignition Experiments and the Ignitor Program

F. Bombarda†, B. Coppi, P. Detragiache‡
Massachusetts Institute of Technology, Cambridge, MA 02139 U.S.A.
†Associazione Euratom-ENEA sulla Fusione, Frascati, 00044 Italy
‡ ENEA, Torino, 10129

1. Introduction

"Ignition, or near-ignition, is the first requirement for a fusion reactor. Unless reproducible plasma conditions close to ignition can be achieved, work on other aspects of a reactor will be without meaning. Achievement of near ignition conditions, together with the exploration of alpha particle and burning-plasma physics, would be truly impressive research achievements and would signal a major advance toward an economically viable fusion reactor" [1]. In addition, it has been recognized that "...the initial model (experiment) need not resemble the one that is later commercialized; much of what would be learned in a tokamak ignition experiment would be applicable both to more advanced tokamak approaches and to other confinement concept" [2]. These ideas that have been expressed in recent analyses of, and debates on fusion research have in fact guided the Ignitor program since its inception, when the value of pursuing ignition had not been fully recognized on one hand, and the problem of reaching ignition in any type of confinement configuration was commonly underestimated on the other.

2. Physics of Ignition

Ignition in a D-T plasma is defined as the condition at which the heating power of the fusion α-particles equals the total of all energy loss. Thus a relationship between the confinement product, $n\tau$, and the plasma temperature can be established. For reason of confinement, the considered plasma current in practice is the highest compatible with the applied toroidal magnetic field, corresponding to low values of the edge safety factor q_a ($q_a \simeq 3.3$ is the lower limit that we consider). A high current also provides the poloidal field needed to keep β_{pol} sufficiently low as a form of protection against the onset of $m^0=1$ and coupled $m^0=2$ modes, since at ignition the central pressure is relatively high. Reversed shear configurations would allow higher values of q_a ($q_a \sim 6$), therefore lower currents, but in this case the toroidal field B_T should be sufficiently high to produce the desired plasma currents, because there is a

limitation on plasma size and on the minimum value of B_p that is acceptable. Experimentally it is seen that the peak electron density correlates with the average current density. In fact, high field, compact machines have repeatedly reached $n_0 \equiv 10^{21}$ m^{-3}.

There are other features of ignition regimes to consider: i) the slowing down time of α-particles is less than the energy replacement time $\tau_{sd}^{\alpha} < \tau_E$, ii) the electron temperature $T_e \geq T_i$ to ensure energy transfer from electrons to ions, iii) the high degree of plasma purity (numerical simulations indicate that, in practice, Z_{eff} should not exceed 1.6). Thus the objective of ignition can be pursued at present by compact, high field, high density, experiments igniting at relatively low temperatures using normal conducting magnets. Furthermore, relatively low dimensions and low ignition temperatures involve small values of the collisional current equilibration time $\tau_I \propto a^2 T^{3/2}$ (a is the plasma minor radius). Ignitor is expected to reach full ignition at $T_0 \sim 12$ keV and $n_0 \sim 10^{21}$ m^{-3} and to produce approximately 20 MW of α-particle heating.

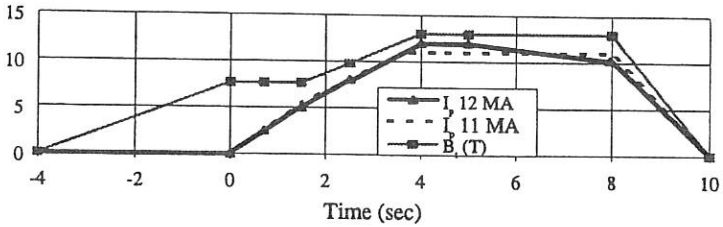

Fig.1 Toroidal field and plasma current time evolution for the 12 and 11 MA scenarios

3. The Ignitor-Ult Experiment

The choice of machine parameters (Table 1) has been guided by these main principles: i) to reach D-T burn conditions under realistic assumptions on the expected degree of energy confinement, in particular by exploiting ohmic heating to the maximum possible extent, thus limiting the role of injected heating to that of a backup; ii) to operate over a wide range of plasma parameters; iii) to attain significant ratios of the plasma duration time to the plasma intrinsic times by adopting supercooled magnets (He-gas with initial temperatures of 30 K); iv) to make full use of the adopted ICRH system to extend the machine operating conditions.

The time evolution of the plasma current I_p and toroidal field B_T are shown in Fig. 1; ignition regimes are expected to be reached shortly after the end of the current ramp [3], during which the magnetic field, density and plasma size are all simultaneously increased. The dynamic nature of the path to ignition should be stressed here: the loop voltage is not constant over the minor radius, but it has a hollow profile, thus allowing a strong rate of ohmic heating, in spite of the fact that the temperature is high at the center of the plasma column as the current is grown adding "skin layers" in the outer region. For the 12 MA maximum parameter scenario, the current is gently decreased 1 sec after reaching its top value to increase the edge q and "freeze" in the current density profile (at 11 MA I_p can be held flat), but the plasma should remain in ignited conditions until the toroidal field is turned down at 8 sec (see Fig. 1). Thus the burning phase is over 200 times longer than the α-particles slowing down time.

Major radius R_0 (m)	1.32
Minor radii a × b (m^2)	0.47 × 0.86
Aspect ratio	2.8
Elongation κ	1.85
Triangularity δ	0.43
Vacuum toroidal field B_T (T)	13
Toroidal current I_p (MA)	12
Poloidal current I_θ (MA)	<9
Paramagnetic field (T) produced by I_θ	1.5
Mean poloidal field $\overline{B}_p = I_p/(5\sqrt{ab})$ (T)	3.75
Confinement strength $S_c = \overline{B}_p I_p$ (MN/m)	45
Av. toroidal current density $\langle J_\phi \rangle$ (MA/m^2)	9.3
Maximum poloidal field $\overline{B}_{PM}$ (T) ($R<R_0$)	6.5
Magnetic flux swing (Vs)	37
Flattop (s)	4 @ 13T
Edge magnetic safety factor q_ψ	3.3 @ 12 MA
Plasma volume V_0 (m^3)	≅10
Plasma surface S_0 (m^2)	≅36
Additional heating power P_{ICRF} (MW)	18

Table 1. Ignitor reference parameters.

The detailed engineering design has been carried out by members of the Ansaldo, FIAT, and ABB industrial groups. The main components of the machines are shown in Fig. 2. Full scale prototypes of all the key components of the machine have been constructed. These include 1/12th of the plasma chamber, including the major access port, one module of the toroidal magnet, one C-clamp (the main structural element outside the toroidal field coil), the innermost element of the central solenoid, and a section of the machine tensioning system. Advanced technological processes to be used in the construction of the machine have been developed and successfully tested. The ongoing phase involves the construction of the full central post and solenoid and the full completion of 1/12th of the machine, including a fully tiled sector of

the plasma chamber, with C or Mo as first wall material. The high values of the density that characterize the main regimes of operation of Ignitor involve correspondingly relatively low values of the temperature at the edge, and Z_{eff} naturally close to unity. This observation as well as engineering considerations have led to the decision of not using a divertor. The average surface power density in Ignitor is also low (~0.5 MW/m^2), similar, for example, to the values presently obtained by the Alcator C-Mod machine.

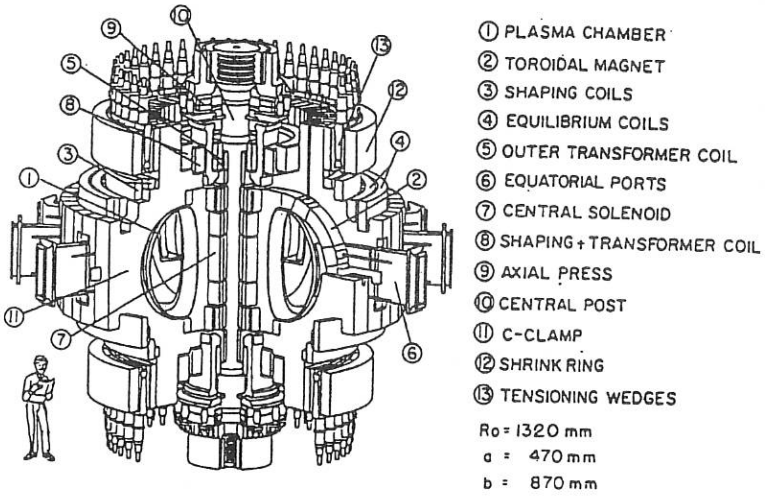

Fig. 2: The Ignitor machine: main components

We are grateful to all of our collegues participating in the Ignitor Program for their contributions. This work was supported by ENEA of Italy and in part by the U.S. Department of Energy as well as the CNR of Italy.

References

[1] A. Sessler and T. Stix, *Physics Today* **49** 21 (1996)

[2] PCAST Report of the Fusion Review Panel (O.S.T.P., White House, 1995)

[3] Coppi B., Nassi M., Sugiyama L.E., *Physica Scripta* **45** 112 (1992)

Global Stability and Operational Regimes of Ignition Experiments

P. Detraglache[1], F. Bombarda[1], B. Coppi[2], A. H. Glasser[3], S. Migliuolo[2]

[1] Associazione Euratom-ENEA sulla Fusione, Italy
[2] Massachusetts Institute of Technology, Cambridge, MA
[3] Los Alamos National Laboratory, Los Alamos, NM

One of the primary requirements of an ignition experiment is stability against pressure-driven global internal modes which may degrade energy confinement or cause disruptions of the plasma in toroidal magnetic confinement systems. Among these are the internal m=1 modes, that are believed to be responsible for the sawtooth oscillations of the central plasma pressurre. Large scale sawteeth can hinder or even prevent ignition, by mixing the central portion of the plasma column with the colder surrounding regions, and spoiling the confinement of fusion products. The necessity of avoiding them puts rather stringent conditions on the design of ignition experiments such as Ignitor [1] and ITER [2]. It should be noted that, while the two devices have similar aspect ratio, Ignitor will benefit from significantly lower values of β-poloidal and from a programmed equilibrium [1] which will keep $q_0 \geq 1$ up until ignition and then increase q_a, the edge safety factor, by decreasing the current.

Our stability calculations are carried out in a (ψ, θ, ϕ) coordinate system where ψ is the normalized poloidal flux $(0 \leq \psi \leq 1)$ and the equilibrium is parametrized as follows:

$$p(\psi) = p_0 (1 - \psi^{\alpha_F})^{\alpha_p} \text{ and } q(\psi) = q_0 + (q_a - q_0)\psi^{\alpha_q} \quad (1)$$

with (unless otherwise stated): $\alpha_F=1$, $\alpha_p=3/2$, $\alpha_q=3$, while $q_0 = 0.85$ and $q_a = 3.0$. These profiles are similar to those constructed by equilibrium codes, following prescriptions from PRETOR simulations for the ITER design [2]. We note, in particular that these profiles have relatively low magnetic shear, resulting in a mean radius of the q =1 surface lying at $\rho_1 \simeq a/2$. The pressure profile is rather peaked, with central-to-average ratio $p_0 / \bar{p} \simeq 3.3 - 3.4$

The stability of global n=m=1 internal modes is studied, for equilibria [1], with a conducting wall placed at ρ/a=1.1 in order to avoid so-called external modes which are largely caused by the presence of a finite gradient in the current density at the plasma edge, which may be a numerical artifact. We recall [3] that internal n=1 modes become unstable in configurations with finite magnetic shear once the value of the parameter $\beta_{p1} = (2\mu_0/B_{p1}^2)[\langle p \rangle_1 - p_1]$ exceeds a critical value that depends on profiles of the pressure and magnetic shear and on the geometry of the plasma cross section. The subscript 1 refers to the q= 1 surface and < > denotes an average over the corresponding volume. Our computations will make use of the more directly available parameter, $\beta_{p0} = (2\mu_0 p_0 / \bar{B}_p^2)$ where $\bar{B}_p = 2\mu_0 I_p / \oint dl$. For Ignitor, we find $\bar{B}_p$=3.5T and β_{p0}=0.79, while the corresponding values for ITER are $\bar{B}_p$=1.14T, β_{p0}=2.32. We also construct a simple parameter of merit that takes into account the magnitude of the q=1 volume:

$$M_Q = \frac{q_E}{\beta_p^0} = \frac{I_M I_p}{20\pi R_0^2 p_0} = \frac{B_T I_p}{4\pi R_0 p_0} \qquad (2)$$

where q_E is the engineering safety factor and I_M is the total current in the toroidal magnet (here B_T is in T, I_p is in MA, R in m and p in MPa). Taking the empirical relationship, $r_1 / a \approx 1 / q_E$, we find that M_Q=2.35 for as typical set of Ignitor parameters, while for the reference parameters of ITER, M_Q=0.95. Fig. 1 presents the normalized growth rates relevant to ITER; two curves are shown corresponding to α_q=2,3 while α_F=1 and α_p=3/2. Clearly increasing magnetic shear improves stability, but not nearly enough to avoid a strongly growing macroscopic mode at the nominal operative pressure ($\beta_{p0} \approx 2.72$). In this context, we mention that these growth rates are substantial, much larger than the local diamagnetic frequency, and hence rule out any possibility of stabilization by finite diamagnetic frequency effects. We have also looked at effects due to fast particles, i.e. fusion α-particles, and found no stabilization is likely from them either. It is important to realize that, although the m=1 harmonic dominates the poloidal spectrum of this mode, toroidicity couples it to other harmonics, notably the m=2 component. For the ITER reference configuration this means that the mode influences the plasma up to the q=2 surface, namely $\rho_2 / a \approx 3 / 4$.

Figure 1

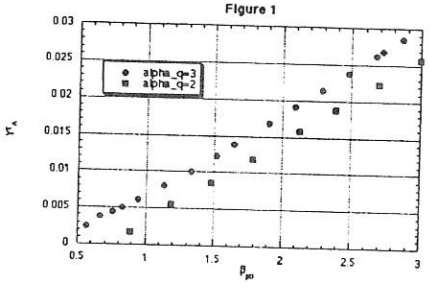

Since these modes are pressure-driven, one expects flatter profiles to improve stability. We have varied the parameter α_F and found that, generally, one must nearly flatten the pressure within the q=1 volume in order to achieve stabilization: $\alpha_F \geq 5$.

Recent experiments in TFTR and DIII-D have indicated the good confinement and stability properties of high-q, reversed shear configurations (typically q_a=6 and q_{min}>1). We have briefly considered them for ITER, constructing a model equilibrium with the pressure given by Eq. (1), with α_F=1 and α_p=3/2, while the q-profile matched that measured in the high-power TFTR supershot 84011. We find that high-nq ballooning modes will be unstable over a large portion of the plasma (roughly $0.35 \leq \psi \leq 0.8$) unless the pressure profile is also modified so as to place the largest pressure gradient at a radius smaller than that where magnetic shear reverses.

These results raise the question of the extent of validity of the ideal-MHD analysis. One can expect that the orderings implied in the small amplitude expansion of linear theory will fail when the gradient in the perturbed pressure (or, equivalently, the density) becomes comparable to the equilibrium pressure gradient. Referring to the case of m=1 modes and

denoting by ξ the radial component of the perturbation displacement and by δ the width of the transition layer, centered about the q=1 surface, the condition for breakdown of the approximation becomes:

$$\xi > \delta \Leftrightarrow \gamma\tau_A < \xi / r_1 \qquad (3)$$

In other words, as one approaches marginal stability, the layer (whose width in the ideal-MHD limit is $\delta = \gamma\tau_A$, with τ_A the characteristic poloidal Alfven time) becomes thinner and a smaller linear displacement is sufficient to result in a macroscopically large perturbed pressure (or density) gradient. Hence, we may define a "practical" point of marginal stability, $\gamma\tau_A = c_m$ where the constant c_m can be chosen appropriately, e.g. 1-5%.

Alcator C-Mod offers a rich variety of sawteeth varying from simple sawteeth in Ohmic plasmas to long duration "monsters" in discharges with high-power ion cyclotron heating and including compound sawteeth. A common thread runs through all these phenomena: they all appear to be related to resistive internal modes. Calibrated temperature traces from the ECE polychromator suggest that the amplitude of the precursor oscillation seen before the crash increases with radius from the center to the q=1 radius, a feature that is characteristic of modes involving magnetic reconnection at the q=1 surface. This is confirmed by a simple calculation in which the radial displacement, $\xi \approx -\delta T_{max} / (dT / dr)$, is shown to increase with r.

Figure 2

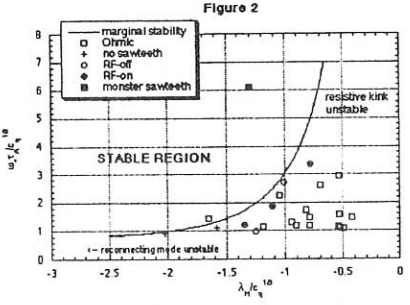

A synopsis of our analysis is presented in Fig. 2, where the Alcator C-Mod data is plotted in $\lambda_H - \omega_* \tau_A$ space, with λ_H being the ideal MHD instability parameter [4] proportional to $-\delta W_{MHD}$ and ω_* is the diamagnetic frequency (where we assume equal ion and electron temperatures). It should be noted that one point (the highest one in the figure) corresponds to a "monster" which occurred in a shot with 2.4MW of ICRH in an H-mode plasma. This "data point" actually includes the effect of energetic minority ions, whose kinetic response, λ_K, stabilizes [5] the ideal mode: $\lambda_H \rightarrow \lambda_H + \lambda_K < 0 < \lambda_H$ and lies in the stable region. We speculate that, as in JET, the sawtooth-free period of the "monster" is terminated, by a crash, as a result of the expansion of the q=1 radius. This increase in r_1/R reduces the stabilizing kinetic response relative to the ideal-MHD term [6].

Considering that ignition can only be attained with relatively high pressures, typically $p_0 \approx 1 - 4\text{MPa}$, the avoidance of global internal n=1 modes is of crucial importance. The path to be taken is suggested by the factor of merit M_{Q_2} given in (2), and indicates the need

for high poloidal and toroidal components of the magnetic field. The reference parameters of Ignitor are $B_T = 13T$, $p_0 = 2.4\ 10^{22} keV / m^3$, $I_p = 12MA$, $R_0 = 1.32m$, $a = 0.47m$ while for ITER $B_T = 5.7T$, $p_0 = 7.5\ 10^{21} keV / m^3$, $I_p = 21MA$, $R_0 = 8.14m$, $a = 2.80m$. We note that it is possible to obtain small or altogether non-existent $q<1$ volumes, under slowly transient conditions, by programming the current evolution [1]. In the case of Ignitor the rise in size of the $q=1$ volume is limited by a decrease of the plasma current after Ohmic ignition is achieved at 12 MA so that q_a is gradually raised toward 5. Another option considered for Ignitor is to operate with a constant maximum plasma current $I_p \approx 11MA$ so that $q_a \approx 3.6$. Alternatively, one may consider operating in the so-called "enhanced reversed shear" scenarios of, e.g., TFTR, though care must be taken to simultaneously program the pressure profile (as well as the current profile) so as to avoid ballooning modes. Of course, these profiles with non-monotonic $q(r)$ are themselves transients. In addition, high currents are needed for confinement even in this regime, thus requiring the adoption of relatively high toroidal fields.

Acknowledgments

The authors thank J. Freidberg, J. Kesner, J. Manickam, F. Porcelli, J. Ramos, and L. Zakharov for guidance and support. This work has been supported in part by the U.S. Department of Energy and ENEA of Italy.

References

[1] B. Coppi, L. Sugiyama and M. Nassi, *Physica Scripta* **4 5**, 112 (1992).

[2] M. N. Rosenbluth, et al., in *Plasma Physics and Controlled Fusion Research 1994* (I.A.E.A., Vienna, 1995).

[3] M. N. Bussac, R. Pellat, D. Edery, and J. L. Soule, *Phys. Rev. Lett.* **3 5**, 1638 (1975).

[4] B. Coppi, R. Galvao, R. Pellat, M. N. Rosenbluth, and P. H. Rutherford, *Sov. J. Plasma Phys.* **2**, 533 (1976).

[5] B. Coppi, P. Detragiache, S. Migliuolo, F. Pegoraro, and F. Porcelli, *Phys. Rev. Lett.* **6 3**, 2733 (1989).

[6] B. Coppi, S. Migliuolo, F. Pegoraro and F. Porcelli, *Phys. Fluids* **B 2**, 927 (1990).

Transport Simulations of Tokamak Parameter Scans Using the Weiland Ion Temperature Gradient Model

Arnold H. Kritz, Jon E. Kinsey, Glenn Bateman, Jan Weiland†, Aaron J. Redd
Lehigh University, Physics Department, 16 Memorial Drive East, Bethlehem, PA 18015
† Chalmers University of Technology, Göteborg, Sweden

Abstract. Using a fixed combination of theoretically derived transport models in the BALDUR transport code, we predict the evolution of temperature and density profiles in tokamaks. Our model has been successfully benchmarked against a wide variety of discharges from different tokamaks including L-mode scans in current, heating power, density, normalized gyro-radius (ρ_*), collisionality (ν_*) and β. Recent work has focused on studying DIII-D and JET H-mode scans in normalized gyro-radius, density, heating power, and elongation. The transport model in these simulations combines the Weiland ion temperature gradient and trapped electron mode model together with the Guzdar-Drake drift-resistive ballooning mode model.

1. Introduction

We use a fixed combination of theoretically derived transport models in BALDUR transport code to predict the evolution of temperature and density profiles in tokamaks [1, 2, 3, 4]. This model has been extensively tested and benchmarked against a wide variety of experimental data from many different tokamaks. These discharges include L-mode scans in current, heating power, density, normalized gyro-radius (ρ_*), collisionality (ν_*) and β, and 20 discharges from the ITER Profile Database including DIII-D and JET H-mode scans in gyro-radius, density, heating power, and elongation. In Fig. 1 the total stored energy predicted in the simulations of the L- and H-mode scans are compared against the reported experimental values. Here, the solid line indicates a perfect fit to the data. We find that the relative root mean square deviation (rms error), defined by $\sigma = \sqrt{\frac{1}{N}\sum_{i=1}^{N}\left[(W_{\mathrm{sim}_i} - W_{\mathrm{exp}_i})/(W_{\mathrm{exp}_i})\right]^2}$, is 11.4%.

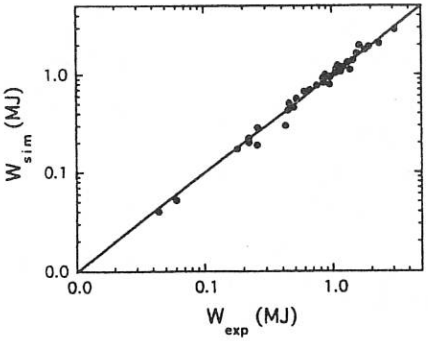

Figure 1. Predicted total stored plasma energy versus experiment data for L- and H-mode scans from TFTR, DIII-D, and JET.

2. Transport Model

The transport model employed takes the basic form of previously used *Multi-mode* models [4, 5] in that a linear combination of neoclassical theory, electrostatic drift waves, and ballooning modes is used to predict the radial transport of particles and energy in the plasma core. The model presently used to predict the transport associated with the trapped electron (TEM) and ion temperature gradient (ITG) modes is the Weiland formulation as derived in Ref. [3, 6] with finite beta effects and parallel ion motion included [7]. The other relevant piece of our core transport model is the Guzdar-Drake model [8] for the drift-resistive ballooning mode. When used in conjunction with the Weiland ITG formulation, it was recently found that the nominal Guzdar-Drake model yielded significantly improved results compared with those obtained using the nominal Carreras-Diamond prescription previously used. With this transport model, we achieve the correct current scaling while maintaining a scaling with density and heating power consistent with the ITER-89P L-mode confinement scaling [2].

3. Results for Parameter Scans

In addition to the other parameter scans, time-dependent transport simulations have been carried out for ten dimensionally similar neutral beam (NBI) and radiofrequency (RF) heated L-mode discharges from TFTR, DIII-D, and JET [1]. We find that our fundamentally gyro-Bohm transport model ($\chi \propto B_T^{-1}$) produces an observed non gyro-Bohm behavior due to imperfections in achieving "true" dimensionless similarity between discharges [1]. This results from changes in the neutral penetration depth as the normalized gyro-radius is varied, thus altering the collisionality and normalized pressure gradient is such a way that they are not held constant near the plasma edge.

While the profiles tend to be robust to changes in the transport, the scaling of the effective diffusivities is sensitive to variations in collisionality and temperature gradients. Thus, small deviations in dimensionless parameters within uncertainty in the experimental data can cause a gyro-Bohm transport model to appear to deviate from its intrinsic scaling. Typical temperature profile results are shown in Fig. 2 for TFTR low ρ_* discharge, #50911, plotted as a function of major radius.

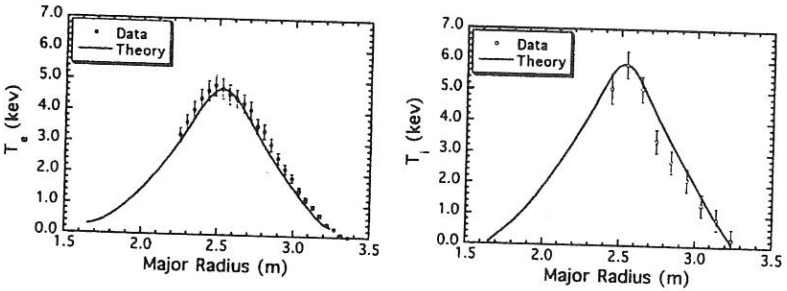

Figure 2. Electron and ion temperature profiles for the low ρ_* discharge TFTR #50911 at 3.93 seconds.

For sawtoothing discharges, it is important to model the sawtooth period and phasing accurately as a function of time when comparing the predicted profiles with experimental data at a given diagnostic time. We use either soft x-ray data or the evolution of the central electron temperature to prescribe the period and phasing in our simulations. Fig. 3 shows the predicted central electron temperature (solid line) plotted against the TRANSP analyzed experimental data (dashed line) for a TFTR discharge included in the ITER Profile Database. In this particular case, the temperature difference between the top and bottom of the sawtooth crashes is relatively large illustrating the possible impact of sawteeth activity on time-dependent modeling.

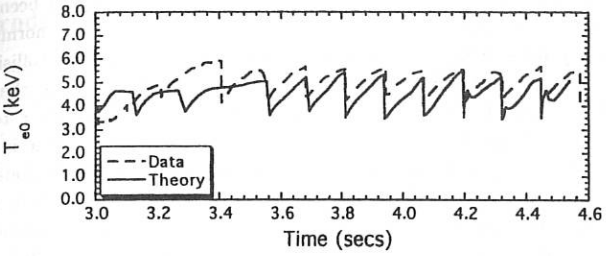

Figure 3. Time evolution of the central electron temperature for L-mode discharge TFTR #45950.

Recently, we have applied the same transport model and methodology to H-mode discharges in the ITER Profile Database, but enforcing the boundary conditions for density and temperature at the top of the density pedestal. For the seven DIII-D H-mode discharges comprising scans in gyro-radius, density, power, and elongation along with the three JET H-mode gyro-radius discharges we find a relative rms error of 7.9% for the total stored energy. Fig. 4 shows the time evolution of the total stored energy for one of the JET H-mode discharges.

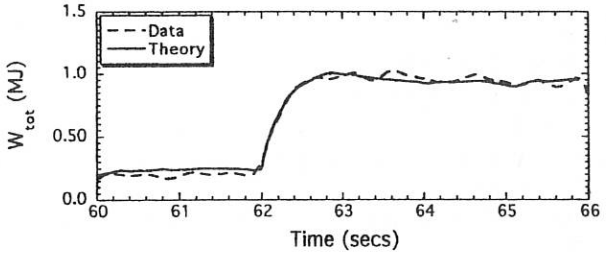

Figure 4. Time evolution of the total stored energy for the dimensionally similar H-mode discharge JET #35171.

For the 10 H-mode profiles, the average rms error relative to the maximum is 7.3% for n_e, 5.3% for T_e, and 5.6% for T_i. Here, the relative rms deviation between the simulated profile and the experimental data is defined as $\sigma_i^{\rm rel} = \sqrt{\sum_{j=1}^{J_i} \epsilon_{ij}^2 / J_i} / X_{\rm max}^{\rm exp}$ where J_i is the

number of data points on i^{th} profile, X_{max}^{exp} is the maximum experimental value for the i^{th} profile, $\epsilon_{ij} = X_i^{exp} - X_i^{sim}$ is the residual for any given j^{th} measurement on the i^{th} profile.

4. Conclusion

A benchmarked *Multi-mode* transport model based upon the Weiland ion temperature gradient and Guzdar-Drake drift-resistive ballooning formulations has been applied to numerous L- and H-mode discharges. These discharges include scans in normalized gyro-radius (ρ_*), plasma current, heating power, electron density, elongation, collisionality (ν_*) and β. Sensitivity studies indicate that L-mode profiles are robust to changes in the effective diffusivities, but the overall scaling of the transport is sensitive to variations in the shapes of the profiles. In particular, the resistive ballooning mode is sensitive to changes in collisionality and normalized pressure gradient while the ITG mode is sensitive to variations in the temperature gradient. While our transport model is purely gyro-Bohm, it yields surprisingly promising results for the dimensionally similar L-mode discharges from TFTR, DIII-D, and JET. For all the L- and H-mode scans studied, we find an rms deviation of less than 8.0% (relative to the maximum) for the predicted density and temperature profiles compared with experimental data. Moreover, for the total stored energy, the relative rms error is 11.4%.

5. References

[1] J. Kinsey and G. Bateman, "Theory-Based Transport Modeling of the Gyro-radius Experiments," to appear in Phys. Plasmas, September, 1996.

[2] J. Kinsey, G. Bateman, A. Kritz, and A. Redd, Phys. Plasmas, February 1996.

[3] G. Bateman, J. Weiland, H. Nordman, J. Kinsey, and C. Singer, Physica Scripta **51**, 591 (1995).

[4] J. Kinsey, C. Singer, T. Djemil, D. Cox, and G. Bateman, Phys. Plasmas **2**, 811 (1995); Physica Scripta **52**, 428 (1995).

[5] G. Bateman, Phys. Fluids B **4**, 634 (1992).

[6] H. Nordman, J. Weiland, and A. Jarmén, Nucl. Fusion **30**, 983 (1990).

[7] J. Weiland and A. Hirose, Nucl. Fusion **32**, 151 (1992); J. Nilsson and J. Weiland, Nucl. Fusion **34**, 803 (1994).

[8] P. N. Guzdar, J. F. Drake, D. McCarthy, A. B. Hassam, and C. S. Liu Phys. Fluids B **5**, 3712 (1993).

Self - sustainment of magnetic islands

J.H. Chatenet, J.F. Luciani and X. Garbet *

C.Ph.T., Ecole Polytechnique, 91128 Palaiseau Cedex, France

* Association Euratom-CEA
CEN Cadarache, 13108 St Paul lez Durance Cedex, France

Introduction

The stability of magnetic islands has been extensively studied in connection with the problems of anomalous transport and MHD stability in tokamaks. There exist in particular several analytical calculations. An important result [1,2] is that diamagnetism is destabilizing when the island width w is smaller than an ion Larmor radius ρ_i, although any small perturbation is stable (linear stability). This leads to the conclusion that islands could be self-sustained [1,2] for a large enough beta. This paper presents a numerical study of such islands, in slab geometry with a two-fluid model (Braginskii equations). The island width is smaller than ρ_i and the electron temperature gradient is much larger than the density gradient.

The model

The equilibrium magnetic field is $\mathbf{B} = B_0 \mathbf{e}_z + \nabla A_{eq} \times \mathbf{e}_z$; $A_{eq} = \frac{1}{2}\frac{B_0}{L_s} x^2$, where x is the radial distance to a resonant surface. Equilibrium profiles (electron temperature and density) are linear. The plasma is then perturbed by an electromagnetic mode. As $\rho_e < w < \rho_i$, we must treat the electron and ion responses separately.

The electron response is given by the Braginskii equations :

$$\begin{cases} \partial_t n_e + \mathbf{v}_E \cdot \nabla n_e + \nabla_{//}(j_z / e) = D_\perp \left\{ \nabla_\perp^2 \left(n_e + n_0 \frac{eU}{T_0} \right) + \alpha \frac{n_0}{T_0} \nabla_\perp^2 T_e \right\} \\ \partial_t A_z + \frac{T_0}{n_0 e} \nabla_{//} \left(n_e + n_0 \frac{eU}{T_0} + \kappa \frac{n_0}{T_0} T_e \right) = -\eta_{//} (j_z - j_{eq}) \\ \partial_t T_e + \mathbf{v}_E \cdot \nabla T_e + \kappa \frac{2T_0}{3n_0} \nabla_{//}(j_z / e) = \\ \qquad = \frac{2}{3} D_\perp \left\{ \alpha \frac{T_0}{n_0} \nabla_\perp^2 \left(n_e + n_0 \frac{eU}{T_0} \right) + \alpha' \nabla_\perp^2 T \right\} + \frac{2}{3} \chi_{//} \nabla_{//}^2 T_e \end{cases}$$

where χ=1.05, κ=1.71, α=–0.5, α'=2.66 and $D_\perp = \frac{1}{2} v_e \rho_e^2$.

The island size being smaller than a gyroradius, the ion response is adiabatic

$$\frac{\tilde{n}_i}{n_0} = +\frac{1}{\tau}\frac{e\tilde{U}}{T_0},$$

where τ is the ratio of the ion temperature to the electron temperature. The self-consistency is ensured by quasi-neutrality condition $n_i=n_e$ and the Ampère law $\nabla_\perp^2 A_z = -\mu_0 j_z$.

In the following, we consider α, α' and $D_\perp$ as free parameters in order to model the perpendicular particle and heat transport by plasma turbulence.

We define $\beta_p^* = \frac{4\mu_0 n_0 T_0}{B_0^2}\left(\frac{L_S}{L_{Te}}\right)^2$ and the operator $[F,G] = \frac{1}{B_0}\vec{\nabla}F \times \vec{\nabla}G.\vec{e}_z$.

Normalizing properly the density, temperature, current, electric potential and vector potential (noted N,T,J,U,A), we obtain the system :

$$\begin{cases} \partial_t N + [U,N] + \frac{4}{\beta_p^*}[J,A] = D_\perp \nabla_\perp^2 (N + U + \alpha T) \\ \partial_t A + [N + U + \kappa T, A] = -\frac{4\eta}{\beta_p^*}(J - J_{eq}) \\ \partial_t T + [U,T] + \frac{8\kappa}{3\beta_p^*}[J,A] = \frac{2}{3} D_\perp \nabla_\perp^2 (\alpha(N+U) + \alpha' T) + \chi[[T,A],A] \\ U = \tau(N - N_{eq}) \\ -\nabla_\perp^2 A = J \end{cases}$$

Theoretical results

Two types of modes can be linearly excited: small-scale η_e modes and collisional microtearing modes. η_e modes [6] can grow if $\eta_e = d\ln T_e / d\ln n_e > \eta_{ec} \simeq 1.75$. However, they are stabilized at τ=0. Collisional microtearing [3,4] can be unstable above a β_p^* threshold. For the present system, and under the constant A assumption, it can be shown analytically that damping occurs. A numerical study, where the constant A approximation is relaxed, confirms this result.

In the studies of the nonlinear regime, it is usually assumed that there exists a quasistationary island with a width larger than the linear value and constant A. Regarding diamagnetism and perpendicular diffusion as perturbations, the above system can be expanded. The detailed calculation is given for instance in [5]. Cancelling the current in quadrature of phase (perpendicular diffusion) determines the rotation frequency and yields $\Omega = \alpha + 1/\eta_e$. Diamagnetism is destabilizing for $\Omega > 1/\eta_e$ or $\Omega < -\tau/\eta_e$, equivalent to $\alpha > 0$ or $\alpha < -(1+\tau)/\eta_e$ with the above expression for the rotation frequency.

Numerical results

We have simulated the full time evolution of one island at τ=0 and infinite η_e. In this case, theory predicts no linear instability and nonlinear self-sustainment. One reads the evolution of the amplitude on the curve A(x=0) as a function of time. Comparing three locations in y, one can deduce the rotation. From our numerical results three conclusions follow.

It has been verified that the frequency of the mode is governed by perpendicular diffusion. Without diffusion, the island does not rotate.

Varying α from -1 to +1, the theoretical dispersion relation $\Omega = \alpha + 1/\eta_e$ gives the correct trend, but the slope is found to be a factor two lower (see fig. 4).

So far as stability is concerned, more significant differences are met. If α>-1, the island is damped (see fig. 1). The island shrinks into the O-point surrounded by a current sheath and the X-point degenerates in a long flat plateau. For α=-1, the island is self-sustained (see fig. 2). On the section passing through the O-point, diamagnetic effects appear as a dip in the current profile near the boundary of the island (see fig. 3). Far from the island, we recover the linear current.

During its evolution, the island leaves rapidly the domain of validity of the constant-A approximation. This could explain the discrepancy between theory and the observed behavior. However, the detailed mechanism of damping remains to be understood.

Conclusion

In the present work, we exhibit cases of non linearly self-sustained islands, whereas they are linearly stable. The drive is diamagnetic. However, this situation is not generic. The island shrinks in most cases, even for a range of parameter where it is predicted to be self-sustained. The reason is yet unexplained.

References :

[1] Samain A., Plasma Phys. Contr. Fusion **26**, 731 (1984).

[2] Smolyakov A.I., Plasma Phys. Contr. Fusion **35**, 657 (1993).

[3] Drake J.F. and Lee Y.C., Phys. Fluids **20**, 1341 (1977).

[4] Garbet X., Mourgues F. and Samain A., Plasma Phys Contr. Fusion **32**, 917 (1990).

[5] Zabiego M. and Garbet X., Phys Plasmas **1**, 1890 (1994).

[6] Lee Y.C., Dong J.Q., Guzdar P.N and Liu C.S., Phys. Fluids **30**, 1331.

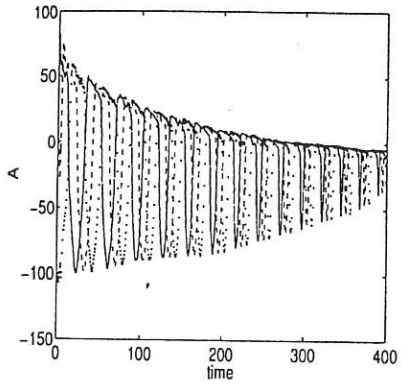

Figure 1 : Amplitude of the vector potential as a function of time at x=0 and y=0 (solid curve), $y=\pi/2$ (dashed curve) and $y=\pi$ (dotted curve).

Parameters are $k_y=0.025$, $\tau=0$, $D_\perp=0.6$, $\beta_p^*=10$, $\eta_e=\infty$ and $\alpha=1$. The rotation frequency is $\Omega = +0.2$.

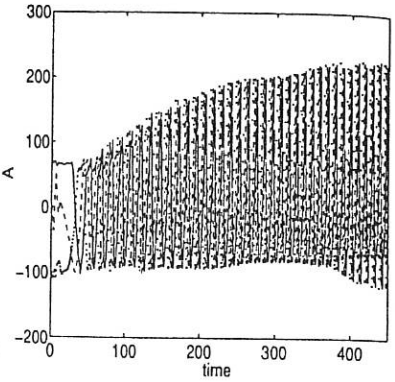

Figure 2 : Amplitude of the vector potential as a function of time at x=0, and y=0 (solid curve), $y=\pi/2$ (dashed curve) and $y=\pi$ (dotted curve).

Parameters are $k_y=0.025$, $\tau=0$, $D_\perp=0.6$, $\beta_p^*=10$, $\eta_e=\infty$ and $\alpha=-1$. The rotation frequency is $\Omega=-0.5$.

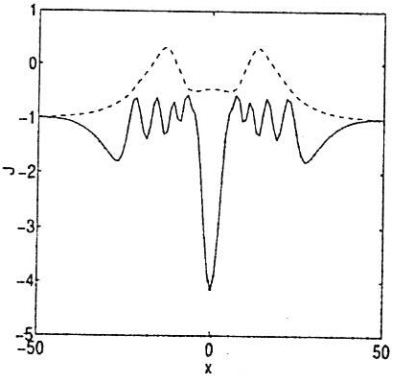

Figure 3 : Radial profiles of the current J at the O-point (solid curve) and X-point (broken curve). Same parameters as in Fig.2.

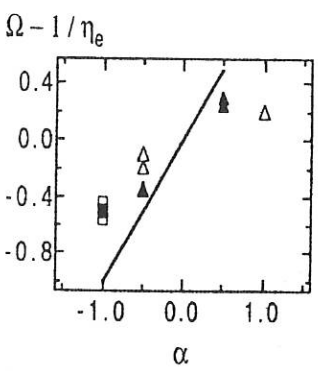

Figure 4 : $\Omega - 1/\eta_e$ as a function of α. The cases where the island is damped are indicated by open triangles ($\beta_p^*=10$) or full triangles ($\beta_p^*=20$). The self-sustained cases are marked by open squares ($\beta_p^*=10$) or full square ($\beta_p^*=20$). The theoretical relation $\Omega - 1/\eta_e = \alpha$ (solid curve) is also shown.

Nonlinear and stochastic interaction between TAE and alpha particles

L. Krlín, P. Pavlo and I. Malijevský
Institute of Plasma Physics, Acad. Sci., CR,
182 00, P.O. Box 17, Prague 8, Czech Republic

1 Introduction

There is an increasing interest in the interaction of the toroidicity-induced Alfvén eigenmodes (TAE) with thermonuclear alpha particles. In the intrinsic stochasticity regime, this interaction can result in a strong radial diffusion of particles, which might negatively influence the energy output from the tokamak - reactor. This interaction has been discussed in papers [1,2]. Our contribution is aimed at a more detailed study of this interaction in the intermediate regime between the passing and trapped particles ones.

2 Hamiltonian formalism

For the study of a rather complicated behaviour of particles (both untrapped an trapped) under the effect of RF fields, the use of a suitably chosen canonical formalism is effective. Our approach is based on the use of the non-orthogonal coordinate system, determined by the Euler potential [3] (for which, one of the set of coordinate curves is formed by magnetic field lines), and on our previous study [4] and application in [5]. After having determined, by the usual canonical procedure, the conjugated generalized momenta [6], we have found a Hamiltonian, describing in a convenient form the motion of particles in the tokamak magnetic field and in RF fields. Finally, introducing into the coordinate system three types of angles (the angles of the cyclotron, poloidal and toroidal rotations) we have obtained a simplified form of the interaction Hamiltonian (see [7]) for an alpha particle

$$\begin{aligned} H &= \omega_{c0} P_1 [1 - \frac{r(P_2)}{R_0} \cos\tilde{\beta}] + \frac{P_3^2}{2m_\alpha} [1 - 2\frac{r(P_2)}{R_0} \cos\tilde{\beta}] + \\ &+ \frac{1}{m_p} \sqrt{2e_\alpha P_2 B_0}\, \frac{\delta B}{B_0} \, [v_{alf} - \frac{1}{m_\alpha}(P_3 + \frac{P_2}{qR_0})] \times \\ &\times \cos(n_t \frac{Q_3}{R_0} - m_p \tilde{\beta} - \omega t). \end{aligned} \tag{1}$$

The meaning of the canonical coordinates in (1) is the following: $P_1 = \frac{e_\alpha B_c}{2}\rho_c^2$, $P_2 = \frac{1}{2}e_\alpha B_0 r^2$, $P_3^2(1 - 2\frac{r}{R_0}\cos\tilde{\beta}) = m_\alpha^2 v_\parallel^2$, $Q_1 = \omega_{c0}t$, $\tilde{\beta} = \theta = Q_2 + \frac{Q_3}{qR_0}$. $Q_3 = R_0\phi$, $r =$

$\sqrt{\frac{2P_\zeta}{e_\alpha B_0}}$. Here, R_0, a are the major and minor radii of the tokamak, $\omega_{c0} = \frac{e_\alpha B_0}{m_\alpha}$ is the cyclotron frequency on the tokamak axis and q is the safety factor. θ and ϕ are the poloidal and toroidal angles, respectively, and e_α is the charge and m_α is the mass of an alpha particle. Parameters δB, m_p, ω, v_{alf} are the parameters of the considered toroidicity-induced Alfvén eigenmode; δB is the perturbation of the magnetic field, caused by TAE. TAE is represented by its scalar potential Φ_{rf} and the parallel component of the vector potential, $A_{\|,rf}$. The usual assumption $E_{\|,rf} = \delta B_{\|,rf} = 0$ allowed the expression of both potentials by means of δB. Parameters n_t, m_p are the toroidal and poloidal wave numbers, respectively, ω is the angular frequency of TAE and v_{alf} is the Alfvén velocity. The toroidal magnetic field B_T has been taken, as usually, as $B_T = \frac{B_0}{1+\frac{r}{R_0}\cos\theta}$.

It is well known that the banana motion is characterized by ist oscillations in the poloidal and toroidal direction, as well as by its precession velocity. It is supposed that the banana bounce frequency $\omega_B \approx \frac{v}{qR_0}\sqrt{\frac{r_c}{2R_0}}$, satisfies $\omega_B \ll \omega_{c0}$. In this case it is possible to neglect any resonance effects on the cyclotron frequency, and to take average of the Hamiltonian over Q_1. This is the reason why the Hamiltonian (1) is cyclic in Q_1.

3 Numerical results

For the numerical discussion, we use the following set of ITER parameters [8]: $R_0 = 7.75m, a = 2.8m, B_0 = 6T, n_0 = 1.4 \times 10^{20}m^{-3}, \alpha_n = 0.26, \frac{n_D}{n_T} = 0.4, \Delta q = 2$. Here, the radial profile of the density $n(r)$ is defined as $n(r) = n_0(1-(\frac{r}{a})^2)^{\alpha_n}$, and the radial profile of q is chosen as $q_r = 1 + \Delta q(\frac{r}{a})^2$.

The results of the numerical discussion is presented in the form of the Poincaré plots. The surface of section is defined by the conditions $\tilde{\beta} = 0$ and $r = r_{max}$. The parallel axis represents the phase $\eta = n_t\frac{Q_3}{R_0} - m_p\tilde{\beta} - \omega t$, the perpendicular axis the parallel component of the particle velocity, $v_\|$, both taken at the moment the phase line crosses the surface of section. The initial values were chosen as $\omega = 3.41 \times 10^5 s^{-1}, n_t = 3, m_p = 3, \frac{r}{a} = 0.5$. We choose the energy of particles 3.52 MeV.

Fig. 1 presents the Poincaré plot for both types of particles, untrapped and trapped, for $\frac{\delta B}{B_0} = 10^{-5}$. The separatrix is in the region $v_\| \approx 6.8 \times 10^6 ms^{-1}$; trapping appears in the lower half of the picture. Fig. 2 shows the same for the same parameters, but for $\frac{\delta B}{B_0} = 5 \times 10^{-4}$. Fig. 2 already presents a stochastic region. This is seen in the next pictures. Fig. 3 shows the radial excursions of particles in the banana regime for two close parallel velocities, $v_\| = 5.25; 5.5 \times 10^6 ms^{-1}$. (These points are defined the conditions $\tilde{\beta} = 0, r = r_{max}$, and are connected by straight lines). These excursions are impressive (in the region of a half meter). Fig. 4 presents a typical maximum radial particle's excursions in the region close to the passing-trapping boundary. Here we choose $\frac{r}{a} = 0.9$, $\frac{\delta B}{B} = 5 \times 10^{-4}$ and other parameters the same as in the foregoing. Starting with $v_\| = 7.5 \times 10^6 ms^{-1}$, the particle jumps stochastically between the banana and passing regime. Here the particle travels between $r_{max} \approx 2.7m$ and $r_{min} \approx 1.9m$. We have found nonnegligible stochastic radial excursion also for particles with the energy 350 keV; this can perhaps help with the ash extraction.

Since we have considered only a single TAE mode, the stochasticity regime appears only in a limited region. A global stochasticity can be expected in the case of several TAE modes, however, if their relative spatial displacement is of the order of the characteristic

radial excursions for single mode interaction.

According to recent proposal of Fisch and Rax [9], the radial diffusion of alpha particles, induced by the stochastic interaction with lower hybrid waves (LHW), is generically coupled with the transfer between LHW energy and alpha particles *perpendicular* energy. It can be easily shown that a similar effect appears also in the case of the stochastic interaction of alpha particles with Alfén waves. Considering the resonant condition (for simplicity, for passing particles) $p\omega_2 + q\omega_3 - \omega = 0$, where ω_2 represents the basis frequency of the motion of a particle in the poloidal direction and ω_3 the basic frequency of the motion in the toroidal direction, the following integral can be obtained: $P_2 = \frac{p}{q}P_3 + const.$. Here, the symbolics of the Hamiltonian (1) was used, together with the analogical procedure in [10]. Consequently, there exists a transfer of energy between the wave and the *parallel* energy of a particle, accompanying its radial diffusion. The significance of this effect requires a further study.

4 Conclusion

We have found that the stochastic interaction of TAE with alpha particles in the regime close to passing/trapped boundary results in large radial excursions of particles for usually considered wave amplitudes. Deeper in the passing or trapped regimes, particles move radially rather quasiperiodically. The stochasticity appears not only for thermonuclear energies, but also for rather low energies of the ash regime. Our results need to be discussed for a broader regime of parameters and for several simultaneously acting modes. Finally, the effect of these losses on the global reactor efficiency needs to be estimated (for this, see e.g. [11]).

Acknowledgement. The authors thank Dr. R. Klíma for valuable discussions.

[1] C.T. Hsu, D.J. Sigmar, Phys. Fluids B 4 (1992) 1492, 1506.
[2] H.L. Berk et al., Phys. Fluids B 5 (1993) 1506.
[3] D.P. Stern, Amer. J. Phys. 38 (1970) 494.
[4] L. Krlín, P. Pavlo et al., Plasma Physics and Contrl. Fusion 29 (1987) 1653.
[5] Z. Gášek, L. Krlín, Z. Tlučhoř, Phys. Lett. A 135 (1989) 284.
[6] R. Klíma, Czech. J. Phys. B 15 (1965) 473.
[7] I. Malijevský, Diploma work, Charles University, Prague, 1995.
[8] K. Tomabechi et al., Nucl. Fusion 31 (1991) 1135.
[9] N.J. Fisch, J.M. Rax, Phys. Rev. Lett. 69 (1992) 612.
[10] L. Krlín, P. Pavlo, Nucl. Fusion 34 (1994) 1517.
[11] G. Kamelander, Ya.I. Kolesnichenko et al., Nucl. Fusion 35 (1995) 1679.

Figure captions

Fig.1. Poincaré plot for $\omega = 3.41 \times 10^5 s^{-1}, n_t = m_p = 3, \frac{r}{a} = 0.5, \frac{\delta B}{B_0} = 10^{-5}$.

Fig.2. Poincaré plot for the same parameters, as in Fig.1, but for $\frac{\delta B}{B_0} = 5 \times 10^{-4}$.

Fig.3. The change of the maximal radial excursion of particles with $v_{||,0} = 5.25; 5.5 \times 10^6 ms^{-1}$ and for other parameters as in Fig.2.

Fig.4. Particle's maximal radial excursions for parameters of Fig. 2, but for $\frac{r}{a} = 0.9$ and for $v_{||,0} = 7.5 \times 10^6 ms^{-1}$.

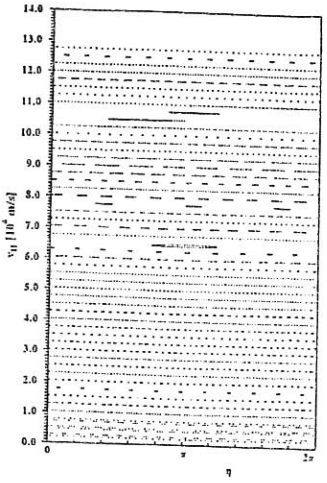

Fig. 1

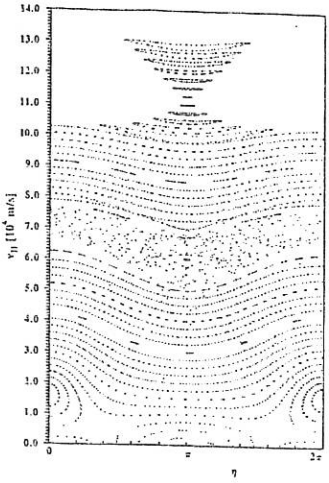

Fig. 2

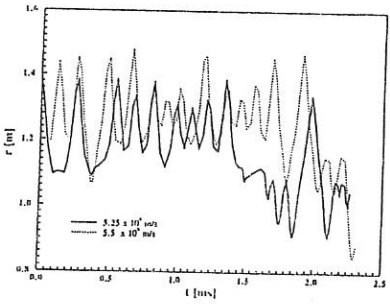

Fig. 3

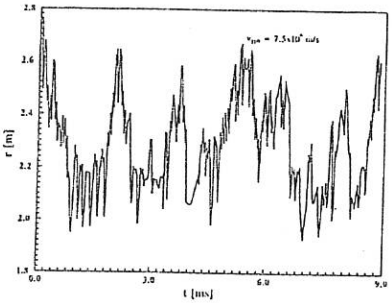

Fig. 4

EVOLUTION OF EDGE PLASMA PARAMETERS DURING L-H TRANSITION IN T-11M

E.A. Azizov, A.M. Belov, V.P. Budaev*, A.P. Chernobai, S.G. Maltsev, S.V. Mirnov

TRINITI, 142092 Troitsk, Moscow Region, Russia

*Institute for High Temperature RAS, Scientific Station, Bishkek , 720049, Kyrghyzstan

INTRODUCTION

Enhanced confinement modes have been observed as in auxiliary also in ohmic heated tokamaks and physics of these regimes is not well understood. The role of edge microturbulence suppression and electrical fields across L-H transition is considered as important aspect of the reduction of anomalous transport [see f.e. 1,2]. However, the mechanisms that produce the changes are not yet understood. There are conceptions [3] that consider the tokamak turbulence to consist of a few types of turbulences having got different physical nature, frequency and wave number spectra. The types react differently on dynamic changes of the discharge condition, impurity and working gas puff, intensity of every type depends on small radius. The aim of this study is to analyze T-11M experimental data edge turbulence in respect of types of the edge turbulence observed and link of the turbulence fractal properties with transport ones.

EXPERIMENTAL RESULTS AND DISCUSSION

Edge microturbulence changes across L-H transition in T-11M [4] were studied by movable Langmuir probes in the shadow of rail limiter (ECRH antenna) positioned at r=19 cm. Ohmic H-mode was induced typically into a plasma with $2\text{-}4\times10^{13}$ cm^{-3} line-averaged density, a plasma current of 86 kA, and toroidal magnetic field of 1.14 T. Probes were located at outerboard of tokamak midplane and allowed to measure the edge plasma time-averaged parameters and fluctuations (with bandwidth $1<f<500$ kHz) of density n (determined from the measured probe ion saturation current I_{sat}), floating potentials φ_{fl}, electron temperature T_e. Two poloidal spaced probes allow poloidal electric field E_p to be estimated from difference in φ_{fl} (assuming T_e is time invariant). The inferred turbulent particle flux $\Gamma_r=<nE_p>/B$, where <> denotes a time average over 1 ms. Fluctuations in I_{sat} (fig. 1) over the radial region extended from r=24 to 20.5 cm like "events" measured on T-10 [5] and ASDEX [6]. In the hotter region spectra become broader (fig. 2). These observations are in qualitative correlation with the drift ballooning resistive model [7]. For both L- and H-mode the coherency between I_{sat} and E_p is 0.4-0.6 in frequency range < 150 kHz for both L- and H-mode (fig. 3) and phase angle between . I_{sat} and E_p is in range $[-\pi, -\pi/2]$ and does not change significant.

At the L-H transition the edge plasma density decreases by approximately 20-25% in the shadow of rail limiter (fig. 5a). Density fluctuation level dropped from 0.35 in L-mode up to 0.2 in H-mode. Poloidal electric field does not change significantly in L-H transition, r.m.s. of E_p drops. Turbulent driven

flux is reduced by the factor 2-3 in H-mode and did not returned to L-values after edge reached equilibrium in H-mode. This reduction caused mainly by decorrelation in edge turbulence (fig. 5b). The correlative properties of the microturbulence observed are formed by the fractal structure of the edge turbulence strange attractor. Probe data have been processed by fractal analysis, that allows observe a catastrophic change in turbulence fractal structure across L-H transition and compare turbulence properties in these two confinement modes. The dimensionality of T-11M edge turbulence in L-mode was typically 3.5 (fig. 3a). Low value of the dimensionality in L-mode shows relatively higher order in comparison with H-mode turbulence (fig. 4a), where the turbulence dimensionality was about 5 (fig.5a). Higher disorder of edge turbulence in improved confinement mode is observed also in TEXTOR [8]. This change in the turbulence structure causes the decorrelation in modes of edge turbulence and leads to the reductions in anomalous turbulent transport. Spectra of Lyapunov exponents, that characterize intensity of the turbulence modes, have shown the number of coupled modes to be about 6 (Fig. 4b). This result correlates with the T-10 turbulence fractal features observed near the wall [9]. Across the L-H transition the number of T-11M edge turbulence modes is not appeared to change.

CONCLUSIONS

The probe measurements of the time-averaged and fluctuating plasma and electric field over a radial region in the shadow (SOL) of the rail limiter installed at r=19 cm are presented. At the L-H transition the normalized density fluctuation level is reduced by approximately 20%, density and potential fluctuations are decorrelated over an extended region. Decorrelation are caused by changes in fractal structure and by higher disorder of turbulence strange attractor in H-mode. The higher disorder results in the reduction of the turbulent particle cross-field transport by the factor 2-3 in this region. The measurements in the poloidal rotation shear region near LCFS are needed to be taken for detailed studying the role of fractal properties in the transport barrier formation in H-mode.

References

1. K.H. Burrell et a. Phys. Plasmas.1 (5), p.1536, (1994).
2. G.R. Tynan et a. Phys. Plasmas.1 (10), p.3301, (1994).
3. V A Vershkov. 22nd EPS Conf Contr Fusion Plasma Phys. Bournemouth,1995,19C,IY,005. Fonk R. Report at APS Meeting, St. Lois (1993).
4. V.B. Lasarev, S.V. Mirnov, A.P. Chernobay e.a. IAEA-CN-60/A2/4-p-6, 1994.
5. V.A.Vershkov e.a.21st EPS Conf Contr Fus. Plasma Phys., Montpellier, V18B,II,886 (1994).
6. M. Endler, L. Gianon, 20th EPS Conf Contr Fusion. Lisbon 193,v17C,pt 2, p583-586(1993).
7. M.V.Ossipenko e. a. 21st EPS Conf Contr Fusion PlasmaPhys,Montpellier,V18B,II,600(1994).
8. V Budaev et al. Plasma Phys. Contr. Fusion, 35, 429 (1993).
9.V.P. Budaev e.a.22st EPS Conf Contr Fusion Plasma Phys, Bournemouth, V18B,II,886(1995).

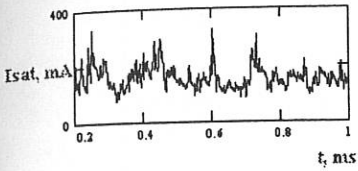

Fig.1 Time trace of I_{sat}, L-mode, r_p=21 cm.

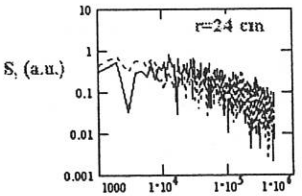

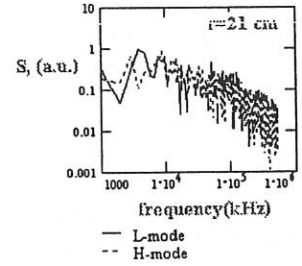

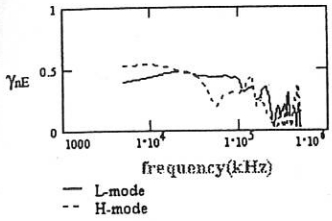

Fig. 3. Coherence between n and E_p fluctuatins for the L- and H-mode cases.

Fig. 2 Ion saturation current spectra for two radial probe positions.

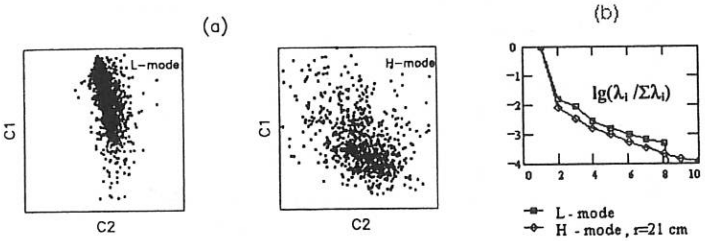

Fig. 4. Changes in fractal feature of edge turbulence across the L-H transition: (a) Poincare plots of the attractor into plane spanned by two of the eigenvectors, we took C1 and C2 as example, other combination of vectors with low index gives similar results. (b) Lyapunov eigenvalues λ_i spectra of the edge turbulence. There exist higher disorder in H-mode edge turbulence in respect with L-mode.

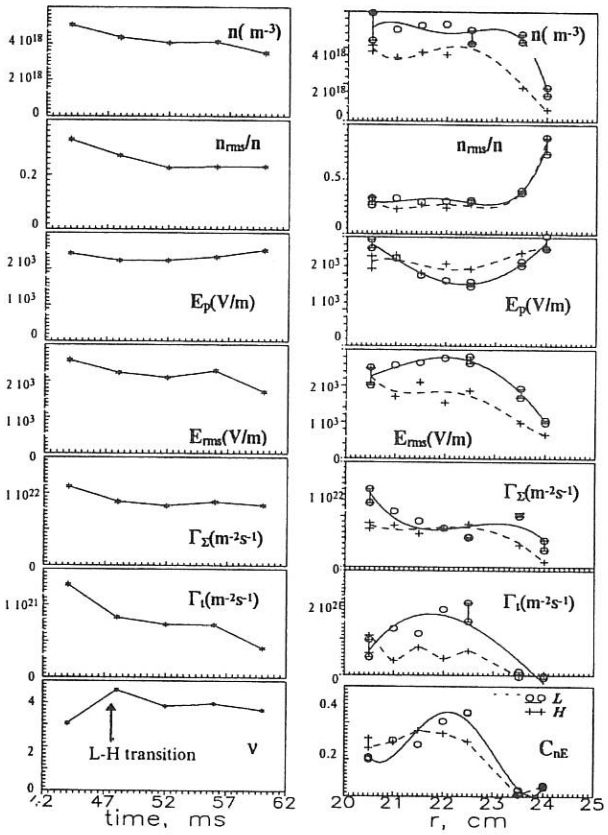

Fig. 5 (a) Time evolution across the L-H transition at r=21 cm and (b) radial profiles for L- and H-modes of fluctuation level n_{rms}/n and time-averaged edge density n , time averaged E_p and r.m.s. E_{rms} of poloidal electric field, turbulent $\Gamma_t=<nv>$ and total particle flux $\Gamma_\Sigma=\Gamma_t+<n><v>$, cross-correlation coefficient of n E_p fluctuations $C_{nE}(t=0)$ and fractal dimensionality ν of edge turbulence attractor.Rail limiter positioned at r=19 cm.

POST-CRASH RELAXATION OF THE SPACE AND VELOCITY DISTRIBUTIONS OF FAST IONS

Ya.I. Kolesnichenko, V.V. Lutsenko, **Yu.V. Yakovenko**

Scientific Centre "Institute for Nuclear Research", Kyiv, 252650, Ukraine

1. Experimental [1] and theoretical [2,3] studies of radial redistribution of fast ions during crashes of sawtooth oscillations have shown that the redistribution depends on the particle energy and the pitch angle. Thus, the post-crash velocity distribution differs from the pre-crash one, being anisotropic even when the pre-crash state is isotropic. Furthermore, according to the most widespread opinion, the sawtooth crash is associated with the $m = n = 1$ instability. That is why the spatial structure of the ion flux as well as the post-crash spatial distribution of fast ions are likely to be non-axisymmetric. The aim of the present work is to study post-crash collisional relaxation of the fast-ion distribution function (f) to the axisymmetric and isotropic state.

2. According to Refs. [1–3], the radial profile of the distribution function of the toroidally trapped ions of MeV energies almost does not change during crashes. In contrast to that, the circulating ions are well redistributed [2,3]. Therefore, the fast ion population, which is peaked in the plasma centre before a crash, becomes enriched with trapped ions near the magnetic axis and dominated by the circulating ones at $r \lesssim r_{mix}$ (r_{mix} is the sawtooth mixing radius) after the crash, see Fig.1.

There are two factors that contribute to relaxation to the isotropic state. They are the pitch-angle scattering and replacement of the anisotropic population as a result of isotropic production of ions and the particle slowing-down. As the width of the trapped particle region is $\Delta v_{\|}/v \sim \sqrt{\epsilon}$ (where $\epsilon = r/R$, R is the major radius of the torus, and $v_{\|}$ is the particle velocity along the magnetic field, B), the effective time of the pitch-angle scattering is $\tau_1 \sim \tau_\perp \epsilon_{mix}$, where $\tau_\perp$ is the perpendicular scattering time, $\epsilon_{mix} \equiv r_{mix}/R$. The time of the replacement in a steady state is the ion slowing-down time, τ_s. Thus, the anisotropy relaxation time can be estimated as follows:

$$\tau_{rel} \simeq min\,(\tau_s, \tau_\perp \epsilon_{mix}) \qquad (1)$$

For instance, for plasma parameters $T = 10\text{keV}$, $n = 3 \times 10^{13}\text{cm}^{-3}$, $\epsilon_{mix} = 0.1$ we obtain $\tau_{rel} \simeq 1.5\text{s}$ for 1-MeV tritons, the relaxation being dominated by pitch-angle scattering. For 3.5-MeV α-particles $\tau_{rel} \simeq 1\text{s}$, being determined by slowing down. In both cases τ_{rel} may well exceed the sawtooth period. Thus, the sawtooth-induced anisotropy may persist throughout the sawtooth cycle.

3. If a crash is associated with the magnetic reconnection uniting the flux surfaces with different particle densities (this is the case in e.g. the Kadomtsev model) then the particle distribution along the flux surfaces will be inhomogeneous (having the helical $m = n = 1$ structure) immediately after a crash, see Fig. 2(a). Such inhomogeneous

distributions were observed in numerical simulations [3]. One can expect that a similar state would follow from any model where the redistribution of particles is associated with the $m = n = 1$ instability. Below we investigate relaxation from such a state to the axisymmetric one assuming that the magnetic configuration is axisymmetric after the crash.

We proceed from the following kinetic equation:

$$\frac{\partial f}{\partial t} + \dot{\omega}\frac{\partial f}{\partial \omega} = \frac{1}{\tau_b}\frac{\partial}{\partial \lambda}\left(\tau_b D_\lambda \frac{\partial f}{\partial \lambda}\right) \tag{2}$$

where $\omega \equiv \theta - \varphi$, θ and φ are the poloidal and toroidal co-ordinates, respectively,

$$\dot{\omega} = \dot{\omega}(v, \lambda, r) \equiv (q^{-1} - 1)\left\langle \frac{v_\parallel}{R} \right\rangle + \Omega_D, \tag{3}$$

$D_\lambda = 2\langle v_\parallel^2 v_\perp^2 (1 + \epsilon\cos\theta)^2\rangle / (\tau_\perp v^4)$, $\lambda \equiv v_\perp^2 B_0 / |v|^2 B$, $B_0 \equiv B(r = 0)$, τ_b is the bounce/transit period, $v_\perp$ is the particle velocity across the magnetic field, Ω_D is the toroidal precession frequency, and angular brackets denote bounce averaging. The LHS of Eq. (2) represents the collisionless bounce-averaged kinetic equation obtained in Ref. [4] and simplified here for the considered case of an axisymmetric magnetic configuration. The RHS is the bounce-averaged collisional term written in assumption that the pitch-angle scattering dominates. Collisions play an important role because without them the inhomogeneity would persist infinitely long for each group of particles with fixed v and λ, rotating along the flux surface with the particles.

To solve Eq. (2), we take advantage of the fact that $\tau_\perp$ is large as compared to $\dot{\omega}^{-1}$ and find at first the solution of Eq. (2) with the zero RHS as follows:

$$f = f(\omega - \dot{\omega}t, v, \lambda, r) = \sum_j f_j(v, \lambda, r)\exp[ij(\omega - \dot{\omega}t)] \tag{4}$$

where f_j are arbitrary functions. Now we apply the method of variation of arbitrary constant in order to find the solution of the full equation (2). Taking f_j as functions of time and keeping only the highest-order terms in $\dot{\omega}^{-1}$, we obtain:

$$f_j = f_{j0}\exp\left[-\frac{1}{3}j^2\left(\frac{\partial\dot{\omega}}{\partial\lambda}\right)^2 D_\lambda t^3\right]. \tag{5}$$

Hence, the characteristic time of homogenization of f is determined by the damping time of the first harmonic ($j = 1$) and equals to:

$$\tau_{hom} = \left[\frac{1}{3}\left(\frac{\partial\dot{\omega}}{\partial\lambda}\right)^2 D_\lambda\right]^{-1/3} \sim \tau_\perp^{1/3}\dot{\omega}^{-2/3} \tag{6}$$

One can see that τ_{hom} is much less than typical characteristic times associated with collisions. The mechanism of the homogenization can be qualitatively explained as follows. Fast toroidal rotation with the rate depending on the pitch angle changes the fast ion

distribution, decreasing characteristic scales in the velocity space as shown in Fig. 2, which enhances the effect of diffusion. The characteristic length of the inhomogeneity in the λ direction after the time interval τ can be estimated as $\delta\lambda \sim (\tau\dot{\omega})^{-1}$. The collisional relaxation time can be found from the equation $\tau \sim (\delta\lambda)^2/D_\lambda$, which immediately gives the estimate of Eq. (6).

As $\dot{\omega}$ is mainly determined by the longitudinal motion for the well circulating ions and by the toroidal precession for the trapped ions, Eq. (6) yields for these groups of ions:

$$\tau^c_{hom} = \left[\frac{1}{6\tau_\perp}\left(1-\chi^2\right)\frac{v^2\left(q^{-1}-1\right)^2}{R^2}\right]^{-1/3}, \qquad \tau^t_{hom} = \left[\frac{1}{8\tau_\perp}\epsilon F(\kappa)\left(\frac{G'(\kappa)v^2}{2\kappa k r^2\omega_B}\right)^2\right]^{-1/3}. \quad (7)$$

where $\chi = v_\parallel/v$, $\kappa^2 \equiv [1-\lambda(1-\epsilon)]/(2\lambda\epsilon)$ is the trapping parameter, $G(\kappa) \equiv 1 - 2E(\kappa)/K(\kappa) \sim 1$, $F(\kappa) \equiv 2[E(\kappa)-(1-\kappa^2)K(\kappa)]/K(\kappa) \sim 1$, $K(\kappa)$ and $E(\kappa)$ are the complete elliptic integrals, k is the ellipticity of the cross section, and $\omega_B \equiv eB/mc$ is the cyclotron frequency.

Thus, τ_{hom} weakly depends on the ion energy ($\tau^t_{hom} \propto v^{-1/3}$, $\tau^c_{hom} \propto v^{1/3}$). It is much less than characteristic collisional times but typically exceeds the crash duration (10^{-4}s).

Let us find what time resolution is required to observe the considered inhomogeneity experimentally. This time is determined by the rotation period of the inhomogeneity along the torus, which, in turn, is determined by the particle rotation. The motion of particles across a $m = n = 1$ helical perturbation is described by Eq. (3). The rotation period of the well circulating and trapped ions is given by:

$$\tau^c_{rot} = \frac{2\pi}{\dot{\omega}} = \frac{2\pi R}{v\chi\left|q^{-1}-1\right|}, \qquad \tau^t_{rot} = \frac{2\pi}{\dot{\omega}} = \frac{4\pi k r R\omega_{B0}}{v^2 G(\kappa)} \quad (8)$$

For instance, for 140-keV deuterium ions located at $r = 0.3$m in JET Eq. (8) yields $\tau^t_{rot} = 1.8\times10^{-4}\text{s}\cdot G^{-1}(\kappa)$, $\tau^c_{rot} = 5.4\times10^{-4}\text{s}\cdot\left|q^{-1}-1\right|^{-1}\chi^{-1}$. As τ^c_{rot} strongly grows when q approaches unity, a possibility arises to measure $q(r)$ by measuring the rotation period. Note that a short pulse of neutral beam injection is also suitable for this purpose. To implement this possibility, one has to have diagnostic equipment able to observe fast ions with time resolution not exceeding τ^c_{rot}. Eq. (8) shows that $\tau^c_{rot} \sim 10^{-4}$s for $\left|q^{-1}-1\right| \sim 0.1$, which is typical at the plasma centre. In the case when there is a region of low shear near the $q = 1$ surface [5,6], $\left|q^{-1}-1\right| \sim 0.01$, τ^c_{rot} as well as τ^c_{hom} is greater being as large as $\gtrsim 10^{-3}$s.

4. We have shown that the collisional relaxation time of the crash-induced anisotropy of the fast ion velocity distribution may well exceed the sawtooth period so that the pre-crash pitch-angle distribution in general depends on the previous sawteeth. This anisotropy may affect plasma stability, which should be investigated in the future.

Concerning the relaxation of the crash-induced axial asymmetry of the fast ion spatial distribution, the mechanism of the relaxation was found to be the pitch-angle diffusion enhanced by the dependence of the toroidal rotation on the pitch-angle. The resulting relaxation time is much less than the characteristic times of collisions.

As the toroidal rotation of circulating ions depends on q, the spatial asymmetry may be used for diagnostics of $q(r)$.

Acknowledgement. This work was supported in part by Research Contract No. 8924/R0 of International Atomic Energy Agency.

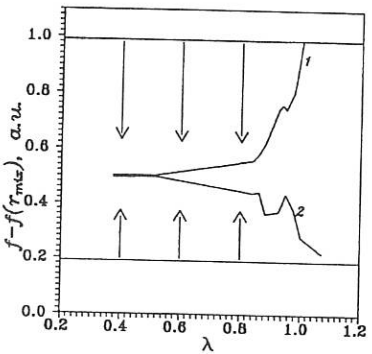

Fig.1.

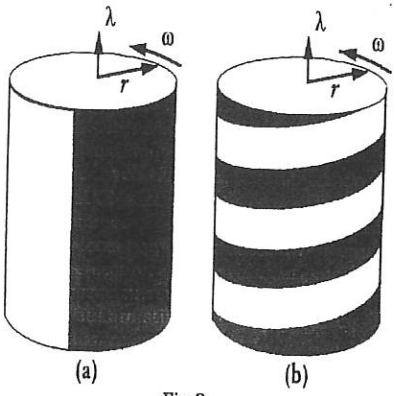

Fig.2.

Fig.1. Crash induced transition from the isotropic to anisotropic distribution function $f(\lambda)$ at $r \approx 0$ (curve 1) and $r \approx r_{mix}$ (curve 2). The post-crash distribution is taken from numerical simulations of Ref. [3].

Fig.2. Formation of a small-scale structure because of non-uniform rotation of particles in the ω direction. (a) $f(\lambda, \omega)$ at a flux surface immediately after a crash; (b) the same function after several rotation periods. Black and white colours correspond to high and low values of f, respectively.

REFERENCES

[1] Jarvis, O.N., et al., Preprint JET-P(95)37, p.137.

[2] Kolesnichenko, Ya.I., Yakovenko, Yu.V.,Report at the IV IAEA TC Mtg on Alpha Particles in Fusion Research (Princeton, April 1995); Nucl. Fusion **36** (1996) 159.

[3] Kolesnichenko, Ya.I., Lutsenko V.V., Yakovenko, Yu.V., Kamelander, G., poster a110, this conference.

[4] Kolesnichenko, Ya.I., Yakovenko, Yu.V., Nucl. Fusion **35** (1995) 1579.

[5] Soltwisch, H., et al., Plasma Physics and Controlled Nuclear Fusion Research (Proc. 11th Int. Conf. Kyoto, 1986), Vol. 1, IAEA, Vienna (1987) 263.

[6] Gill, R.D., Edwards, A.W., Weller, A., Nucl. Fusion **29** (1989) 821.

EFFECT OF SAWTOOTH CRASHES ON FAST IONS WITH VARIOUS ENERGIES AND PITCH ANGLES

Ya.I. Kolesnichenko, **V.V. Lutsenko,** Yu.V. Yakovenko
Scientific Centre "Institute for Nuclear Research", Kyiv, 252650, Ukraine

G. Kamelander
Austrian Research Centre Seibersdorf, A-2444, Austria

1. Introduction. Experiments on tokamaks indicate that crashes of sawtooth oscillations affect particles with various energies and pitch-angles in different ways [1]. This peculiarity was predicted theoretically in Ref. [2], where the physical picture of the sawtooth-induced transport of fast ions was elucidated. According to Ref. [2], the particle redistribution is associated with the electric field, $\vec{E}$, arising from evolution of the magnetic configuration during the crash. It was shown in Ref. [2] that the $\vec{E} \times \vec{B}$ drift drives the particle redistribution, and the resulting effect is determined by the competition of this drift, the toroidal precession, and the longitudinal motion. Basing on approach of Ref. [2], a kinetic equation suitable for numerical treatment was derived in Ref. [3]. However, till now no quantitative results on the redistribution of ions with taking into account the toroidal drift have been obtained. The purpose of the present work is to make the first step in this direction, generalizing the kinetic equation of Ref. [3] and finding the solution of this equation numerically.

2. Kinetic model of fast ion transport. We proceed from the following bounce-averaged kinetic equation for the distribution function of fast ions (f), which generalizes the equation of Ref. [3]:

$$\frac{\partial f}{\partial t} + \dot{r}\frac{\partial f}{\partial r} + \dot{\omega}\frac{\partial f}{\partial \omega} + \dot{\mathcal{E}}\frac{\partial f}{\partial \mathcal{E}} = 0 \tag{1}$$

Here $\omega \equiv \theta - \varphi$; r, θ and φ are the radial, poloidal and toroidal co-ordinates associated with the unperturbed magnetic flux surfaces, respectively; and $\mathcal{E}$ is the particle energy. The coefficients $\dot{r}$, $\dot{\omega}$ and $\dot{\mathcal{E}}$ and are given by:

$$\dot{r} = -\frac{R}{B\sqrt{g}}\left\langle\frac{v_\parallel}{R}\right\rangle\frac{\partial \Psi}{\partial \omega} - \frac{cR}{B\sqrt{g}}\frac{\partial \Phi}{\partial \omega} \tag{2}$$

$$\dot{\omega} = \frac{R}{B\sqrt{g}}\left\langle\frac{v_\parallel}{R}\right\rangle\frac{\partial \Psi}{\partial r} + \frac{cR}{B\sqrt{g}}\frac{\partial \Phi}{\partial r} + \Omega_D \tag{3}$$

$$\dot{\mathcal{E}} = -e\frac{\partial \Phi}{\partial \omega}\Omega_D \tag{4}$$

where angular brackets denote bounce averaging, Φ is the electric potential associated with the instability, Ψ is the helical magnetic flux, $R = R_0 + r\cos\theta$ is the distance to

the axis of the symmetry, R_0 is the radius of the unperturbed magnetic axis, $\sqrt{g}$ is the metric tensor determinant of the co-ordinate system, and Ω_D is the toroidal precession frequency. In this work the analytical expressions for $\Psi(r,\omega,t)$ and $\Phi(r,\omega,t)$ modelling the Kadomtsev-type crash and suggested in Ref. [2] are used. The proposed expressions for Ψ and Φ contain an arbitrary function $\alpha(t)$ which determines relative rate of the change of the magnetic configuration at different stages of the crash. Note that considering Ψ and Φ as given functions implies that there is a strong polarization current which almost compensates for the current arising from different redistribution of the fast ions and the bulk plasma.

Eq. (1) differs from the corresponding equation of Ref. [3] by the presence of the term associated with the particle acceleration by the electric field of the $m = n = 1$ instability driving the crash, $\dot{\mathcal{E}}\partial f/\partial\mathcal{E}$. Using Eq. (4) and the relations $\nabla\Phi \sim Br_{mix}/(c\tau_{cr})$, $\Omega_D \lesssim v^2/(2\omega_B R_0 r)$, one can show that the energy change during the crash is rather small, $\Delta\mathcal{E} \lesssim \mathcal{E}r_{mix}/R_0$, where r_{mix} is the sawtooth mixing radius, ω_B is the ion cyclotron frequency, and τ_{cr} is the crash duration. Nevertheless, the $\dot{\mathcal{E}}$ term plays an important role. Indeed, as $v_\parallel = v\sqrt{1-\lambda R_0/R}$ ($\lambda \equiv \mu B_0/\mathcal{E}$, $B_0 \equiv B(r=0)$, and μ is the particle magnetic moment), the turning point of a trapped particle is $R_t = \lambda R_0$, which implies that the particle cannot move into the region $r < R_t - R_0$ when $R_t > R_0$. The energy change leads to $\Delta R_t = R_0\Delta\lambda$, removing the restriction on the particle approach to the plasma centre.

The characteristics of Eq. (1) are the solutions of Eqs. (2)-(4), which determine the bounce-averaged particle trajectories in the electromagnetic field evolving during the crash. Our analysis shows that during the crash the particle bounce/transit orbits may undergo transformations, which can be of three kinds. First, an orbit of a trapped particle may split into two orbits of circulating particles, which means that the particle may become either a co- or a counter-circulating one. Second, two circulating orbits may merge into a trapped particle orbit. Third, $\sigma \equiv \mathrm{sgn}(v_\parallel)$ of a circulating particle may change. The last possibility means the reflection of a circulating particle, which occurs at the boundary between trapped and circulating particles, $r = R_0(1-\lambda) = R_0 - R_t$. An example of orbit transformations is shown in Fig.1. The described orbit transformations are taken into account by means of setting the appropriate boundary conditions at $r = R_0 - R_t$ when solving Eq. (1).

3. Results of calculations. Eq. (1) was solved numerically for the parabolic profile of the pre-crash safety factor, $q(r)$, and a given pre-crash distribution function, $f^-(r,\mu,\sigma)$, which is justified when $\partial f/\partial\ln\mathcal{E} \ll [f(r=0) - f(r=r_{mix})]R_0/r_{mix}$. As a result, the distribution function of fast ions immediately after the crash, $f^+(r,\omega,\mathcal{E},\mu,\sigma)$, was obtained. Calculations were carried for both circulating and trapped α-particles with energies from 280 keV to few megaelectronvolts in a JET-like tokamak ($r_{mix}/R_0 = 0.13$, $B_0 = 3.5$ T, $q(0) = 0.8$, and the ellipticity of the cross-section $k = 1.5$). The results are presented in Figs. 2-4. Note that they are valid also for deutrons of twice less energy.

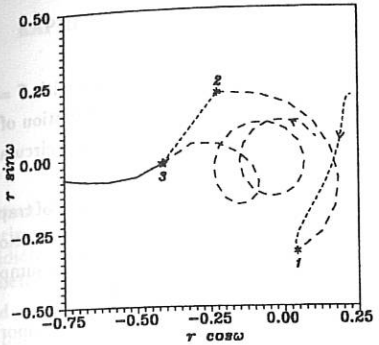

Fig.1.

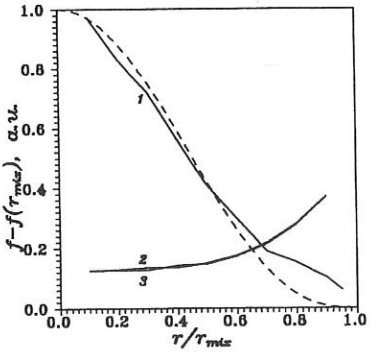

Fig.2.

Fig.1. Orbit transformations during particle motion in an evolving electromagnetic configuration. The arrows show the direction of bounce-averaged motion. Solid, dashed and dotted lines correspond to trapped, co- and counter-circulating particle orbits, respectively. 1 and 2, the points of reflection where $v_\parallel$ changes the sign; 3, the point where two orbits of circulating particles merge. Calculations are carried out for 2.8-MeV α-particles.
Fig.2. The redistribution of trapped and circulating α-particles with $\mathcal{E} = 2.8$ MeV. Dashed line, f^-; solid lines, f^+. 1, trapped particles with $\lambda = 1$; 2 and 3, co- and counter-circulating particles with $\lambda = 0.875$.

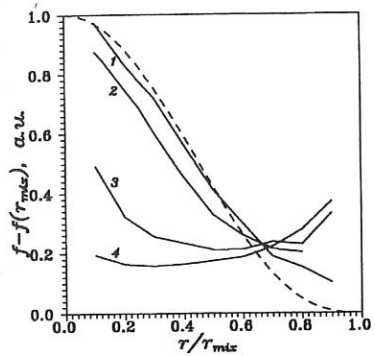

Fig.3.

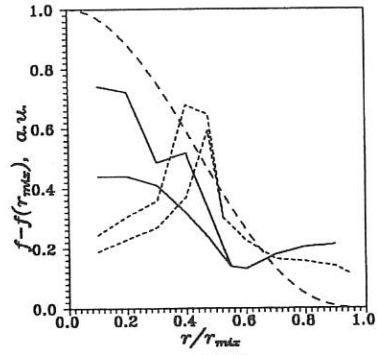

Fig.4.

Fig.3. The redistribution of trapped α-particles with $\lambda = 1$ and various energies. Dashed line, f^-; solid lines, f^+. 1, $\mathcal{E} = 2.8$ MeV; 2, $\mathcal{E} = 1.4$ MeV; 3, $\mathcal{E} = 0.56$ MeV; 4, $\mathcal{E} = 0.28$ MeV.

Fig.4. Post-crash radial profiles for two different laws of time evolution of magnetic configuration. Solid line, f^+ for $\alpha(t)$ as in Figs.2,3; dotted line, f^+ for $\alpha(t)$ corresponding to faster plasma flow at the plasma centre; dashed line, f^-.

Fig.2 shows very different behaviour of trapped and circulating particles with $\mathcal{E} = 2.8$ MeV. We conclude that the toroidal precession almost prevents the redistribution of the trapped particles with the energy in the MeV range. On the other hand, the circulating particles are strongly redistributed.

Fig.3 demonstrates that the influence of the precession on the redistribution of trapped ions is small at energies below 300 keV. This justifies the modelling of redistribution of neutron emission in NBI JET experiments, which was carried in Ref. [4] in the assumption that particles follow the evolving flux surfaces.

It follows from Fig.4 that in the intermediate case, when the precession is important but does not dominate, the particle behaviour depends on dynamics of the crash even for the same kind of crash (in the considered example different redistributions take place in the framework of the Kadomtsev model). The redistribution is stronger in the region where the plasma flow is faster. Because of this, different post-crash distributions are possible for particles with the same pre-crash characteristics.

4. Conclusions. Our calculations confirm qualitative results of Ref. [2] that the trapped and circulating particles are affected by the crash in a different way, this difference growing with the particle energy. In particular, the calculations show that the trapped fast ions in the MeV range are not sensitive to the crash whereas the trapped particles of lower energies and the circulating particles are strongly redistributed during the crash. The weak redistribution of the trapped particles of MeV energies is consistent with the experimental data [1].

On the other hand, it is found that the character of the temporal evolution of the magnetic configuration during the crash is an additional factor affecting the redistribution of well trapped ions of intermediate energies or marginally trapped and circulating ions of high energies for which the effect of the toroidal precession is noticeable but does not completely decorrelate the phase of the wave-particle interaction.

Acknowledgement. This work was supported in part by Research Contract No. 8924/R0 of International Atomic Energy Agency. Two of the authors (V.L. and Y.Y.) would like to acknowledge the hospitality of Austrian Research Centre Seibersdorf.

REFERENCES

[1] Jarvis, O.N., et al., Preprint JET-P(95)37, p.137.

[2] Kolesnichenko, Ya.I., Yakovenko, Yu.V., Report at the IV IAEA TC Mtg on Alpha Particles in Fusion Research (Princeton, April 1995); Nucl. Fusion **36** (1996) 159.

[3] Kolesnichenko, Ya.I., Yakovenko, Yu.V., Nucl. Fusion **35** (1995) 1579.

[4] Anderson, D., et al., Nucl. Fusion **34** (1994) 217.

RAPID CYCLOTRON INSTABILITIES IN PLASMAS WITH FAST IONS

Ya.I.Kolesnichenko
Scientific Center "Institute for Nuclear Research", Kyiv, Ukraine
D.Anderson, M.Lisak
Chalmers University of Technology, Göteborg, Sweden

Abstract. The key mechanism in the origin of Ion Cyclotron Emission (ICE) in tokamak experiments, as the present general but preliminary analysis has shown, is the toroidicity affected cyclotron resonance interaction between superthermal ions and Fast Magnetoacoustic Waves (FMW) with very small parallel wave numbers ($k_\parallel$). It is also found that the dependence of the growth rate (γ) of cyclotron-magnetoacoustic instability on the fast ion density (n_α) is, in general, complicated, and in fact γ may even decrease with n_α.

1.Introduction. The present work considers rapid instabilities with growth rates exceeding the bounce frequency of the fast ions. Its analysis is based on the following dispersion equation for FMW:

$$1-\frac{\omega^2}{k^2 v_A^2}=\frac{\omega^2}{\omega_{pi}^2}\left(\epsilon_{11}^T+\epsilon_{11}^\alpha\right) \qquad (1)$$

Here v_A is the Alfven velocity, ω_{pi} is the plasma frequency of the bulk ions, ϵ_{11}^T is a thermal correction to a component of the permeability tensor of the bulk ions and ϵ_{11}^α is a contribution to the permeability ϵ_{11} due to fast ions.

2.Instabilities involving the Hermitian part of ϵ_{ij}^α. In this section we demonstrate that despite the fact that the number of fast ions is small, the Hermitian part of ϵ_{ij} can affect the character of the solutions of Eq.(1). Let us assume the magnetic field to be homogeneous and take the distribution function of the fast ions as $f_\alpha = f_1(v_\parallel)f_2(v_\perp)$ where $f_1=\exp\left(-v_\parallel^2/v_1^2\right)/\left(\sqrt{\pi}v_1\right)$, $f=\delta(v_\perp-v_2)/(2\pi v_2)$. Such a choice enables us in the simplest way to make qualitative conclusions regarding instabilities excited due to non-monotonic energy dependence and/or velocity anisotropy of the fast ion distribution. Writing $\omega=\omega_0(1+y)$ with $\omega_0=kv_A$, $|y|<<1$ and taking $k=l\omega_B/v_A$, we can approximate Eq.(1) as

$$y^2=\sigma_1+\sigma_2\hat{Z}(\alpha y) \qquad (2)$$

where

$$\sigma_1=\frac{l^2 I_l(a_i)\exp\{-a_i\}}{2a_i},\quad \sigma_2=\frac{n_\alpha}{n}\frac{l^2}{2}\frac{1}{\xi_2}\frac{\partial f_i^2}{\partial\xi_2},\quad \hat{Z}(z)=-i\sqrt{\pi}z\exp(-z^2)\left[1+\frac{2i}{\sqrt{\pi}}\int_0^z\exp\left(t^2\right)dt\right]$$

$J_l = J_l(\xi_2)$ is the Bessel function, $\xi_2 = kv_2 / \omega_B$, $I_l = I_l(a_i)$ is the modified Bessel function, $a = k^2\rho_i^2$, $\rho_i = v_{Ti} / \omega_B$, $\alpha = \omega_0 / (k_\parallel v_1)$.

In the limit $\alpha|y| >> 1$ $\left(k_\parallel \to 0\right)$, the resonant wave-particle interaction is negligible and Eq.(2) has a simple solution:

$$y = \pm\sqrt{\sigma_1 + \sigma_2} \tag{3}$$

It follows from Eq.(3) that fast ions will affect the gap between the wave branches when $\sigma_1 + \sigma_2 > 0$ and they will lead to instability with $\gamma \sim \sqrt{n_\alpha}$ for $\sigma_2 < 0, |\sigma_1| << |\sigma_2|$. A "coherent" instability of this kind excited by α-particles with $f_\alpha \sim \delta(v - v_\alpha)$ has been considered in earlier works (see overview [1]).

On the other hand, when $\alpha|y| << 1$, resonant wave-particle interaction plays an important role. In this case one usually neglects the real part of the RHS of Eq.(2), which leads to a growth rate proportional to n_α. Here we will show that completely different dependences of γ on n_α are possible under certain circumstances, and that even when γ is proportional to n_α, the solution differs from the one obtained by neglecting the real part of the RHS of Eq.(2).

Assuming $\alpha^2|\sigma_2| << 1$ and $\sigma_2 < 0$ we find:

$$y = i\frac{\sqrt{\pi}}{2}\alpha|\sigma_2| \pm \sqrt{\sigma_1 - \frac{\pi}{4}\alpha^2\sigma_2^2} \tag{4}$$

From (4), we conclude that γ increases with n_α, but $\gamma \sim n_\alpha$ takes place only when the expression under the square root is positive. In this case, waves with the frequencies $\omega_0 \pm \delta\omega$ are excited simultaneously. However, we note that $\delta\omega$ is very small ($\delta\omega \le \sqrt{\sigma_1}\omega_0$, and $\sigma_1 < 10^{-6}$ for $l > 3$ in JET) and therefore excitation of these waves would be seen as single lines in the ICE spectrum. Besides, when $k \ne l\omega_B / v_A$ and $|\omega_0 - l\omega_B| >> \sqrt{\sigma_1}$ then σ_1 and $\mathrm{Re}\,\hat{Z}$ can be neglected in Eq.(2) which leads to an increase of the numerical coefficient of γ by a factor of two as compared to Eq.(4). However, α decreases with $|\omega_0 - l\omega_B|$, which means that the waves with $|\omega - l\omega_B| << \omega$ are most strongly destabilized.

When $\sigma_2 < 0$, $\alpha^2|\sigma_2| >> 1$ we obtain:

$$y = \frac{\sqrt{\pi}}{4\alpha}\left(i \pm \sqrt{\frac{8\sigma_1}{\pi|\sigma_2|} - 1}\right). \tag{5}$$

This shows that the growth rate does not depend on n_α if $8\sigma_1 \geq \pi|\sigma_2|$ but this is valid only in a narrow region Δn_α where $8\sigma_1 \sim \pi|\sigma_2|$ (otherwise the condition $\alpha|y| << 1$ is violated).

The described instabilities are excited due to the non-monotonic energy dependence of f_α which provides $\sigma_2 < 0$. When $\sigma_2 > 0$ the instability can arise due to anisotropy of $f_\alpha(\mathbf{v})$. Then the instability may be driven by ions with $v_\alpha < v_A$, which is not possible for the instabilities associated with $\sigma_2 < 0$. For $\alpha^2\sigma_2 >> 1$, $\sigma_2 > 0$ we find:

$$\frac{\gamma}{\omega} = \frac{\sqrt{\pi}}{4\alpha}\left(1 + \sqrt{1 + \frac{8\sigma_1}{\pi\sigma_2}}\right). \tag{6}$$

Eq.(6) is consistent with the condition $\alpha|y| << 1$ provided that $8\sigma_1 << \pi\sigma_2$.

The unusual dependences of γ on n_α described by Eqs.(5),(6), i.e. $d\gamma / dn_\alpha \leq 0$, agree with the observations in the TFTR experiments where the intensity of ICE does not necesserily follow the increase of the production of neutrons [2]. However, we cannot claim that Eqs.(5), (6) are applicable to TFTR experiments as we do not model the specific TFTR conditions and we disregarded the effect of toroidicity on the instability.

3. Instability driven by the toroidicity affected cyclotron resonance. When $\Delta\omega / \omega$ $(\Delta\omega = \omega - l\omega_B)$ is small but well exceeds the minimum distance between the wave branches near the l^{th} cyclotron harmonic, then ϵ_{11}^T and Re ϵ_{11}^α can be neglected in Eq.(1) and we obtain:

$$\frac{\gamma}{\omega} = \frac{n_\alpha}{n}\frac{\pi^2 l^2 \omega_B^2}{k^2}\int dv J_l^2(\xi)\frac{\left[\omega v\frac{\partial f_\alpha}{\partial v} + \left(\frac{\omega - l\omega_B}{\chi} - \omega\chi\right)\frac{\partial f_\alpha}{\partial \chi}\right]_{\chi_r}}{|\partial\Omega / \partial\chi|} \tag{7}$$

Here $\xi = kv_\perp / \omega_B$, χ_r is the magnitude of the pitch-angle $\chi = v_\parallel / v$ determined by the resonance condition

$$\Omega \equiv \Delta\omega - k_\parallel v_\parallel - \omega_D = 0 \tag{8}$$

$\omega_D = -mv_D / r$, m is the poloidal wave number, v_D is the toroidal drift velocity. Eqs.(7),(8) allows for the results of the eigenmode analysis that the edge localized FMW are characterized by $k_r << k$ [4] and that they are localized not only radially but also poloidally near the outer circumference of the torus [5].

We conclude from Eq.(7) that $\gamma(\omega)$ has a maximum when $\Delta\omega = \omega_D$. It exceeds γ for $\Delta\omega >> \omega_D$ (the case of Refs.[1-3]) by a factor of $\chi_r^{-2}\nu$ where $\chi_r^{-2} >> 1$ and

$\nu \equiv \Delta\omega / \omega_D >> 1$, as well as γ for $\Delta\omega << \omega_D$ (the case of Ref.[4]) by a factor of χ_r^{-2}. This conclusion is general as it is only based on an analysis of the dependence of $|\partial\Omega / \partial\chi|_{\chi_r}$ on $\Delta\omega$ in Eq.(7) and does not involve any assumption on the form of $f_\alpha(v)$. Moreover, it provides an explanation of the splitting into doublets of the spectral lines of ICE observed on JET. Indeed, destabilization of waves with $\omega = l\omega_B + |\omega_D|$ and $\omega = l\omega_B - |\omega_D|$, for which the growth rate is maximum, implies a formation of doublets lines with the width $\delta = 2|\omega_D|$. The only important parameter of the fast ions which affects the relative width of the doublets (δ / ω) is their energy. This explains why the observed doublet width in experiments with a deuterium plasma, where 3 MeV protons were produced, is approximately the same as in a DT plasma containing 3.5 MeV alpha particles. The ratio δ / ω can be estimated to be 0.6-0.7 for JET, in agreement with experimental results [6].

The discrete character of the wave numbers breaks the symmetric dependence of γ on ω around $l\omega_B$. Because of this, the magnitude of δ changes and the peaks within doublet spectral lines of ICE usually have different intensities. Furthermore, the discrete wave numbers make simultaneous excitation of waves with $\omega > l\omega_B$ and $\omega < l\omega_B$ impossible for $l = 1,2$, which explains why spectral lines corresponding to $l = 1,2$ are single in JET experiments.

The toroidicity affected cyclotron resonance leads to an instability growth rate that well exceeds the bounce/transit frequency of the fast ions even if n_α / n is very small (less then 10^{-4}) as is the case in experimental conditions. This growth rate provides a broadening of the resonance which is sufficient to make spectral lines merge into a continuum in the high frequency range, $l > 8$, again in agreement with experiments.

Acknowledgements. One of the authors (Ya.K) would like to acknowledge the hospitality of Chalmers University and the research support by the ISF during 1995.

[1] Ya.I.Kolesnichenko, Nuclear Fusion, **20** (1980) 727.
[2] S.Caufmann, et al., Nuclear Fusion, **35** (1995) 1597.
[3] R.O.Dendy et al., Phys. Plasmas, **1** (1994) 1918.
[4] B.Coppi, Phys.Lett., **A172** (1993) 439.
[5] N.N.Gorelenkov, C.Z.Cheng, Phys. Plasmas, **2** (1995).
[6] G.A.Cottrell, et al., Nuclear Fusion, **33** (1993) 1365.

Analyses of Electron and Ion Transport Properties in JT-60U H-mode Plasmas with Improved Core Confinement

H. Shirai, T. Takizuka, M. Sato, Y. Koide, T. Hirayama
Japan Atomic Energy Research Institute, Naka Fusion Research Establishment
Naka-machi, Naka-gun, Ibaraki-ken 311-01 JAPAN

1. Introduction

H-mode plasmas with good energy confinement (H factor ≥ 2) have been obtained in JT-60U. These plasmas called "high T_i H-mode plasmas" [1] or "high β_p H-mode plasmas" [2] have a feature of improved core confinement (ICC) with high $T_i(0)$ and $T_i(0)/T_e(0) > 2$ in addition to the edge transport barrier. In the previous work we clarified the time evolution of the improvement of thermal energy confinement (TH factor, in Sec. 2) at L-H and H-L transitions [3]. At the L-H transition TH factor increases much faster than thermal energy confinement time, τ_E^{th}, and keeps increasing with a time scale of τ_E^{th} in the successive H phase. At the H-L transition, on the other hand, TH factor decreases much faster than τ_E^{th} and remains at small value during the L phase. We have also clarified that the effective thermal diffusivity, χ_{eff}, which is evaluated by adding both the electron and the ion heat flux, changes over a wide plasma region simultaneously at L-H and H-L transitions.

We proceed the previous work and examine the characteristics of the relative change of the electron and ion thermal diffusivity, $\delta\chi_e/\chi_e$ and $\delta\chi_i/\chi_i$, at H-L transition in JT-60U ICC H-mode plasmas with different plasma current. We also study the relative change of the particle diffusivity, $\delta D/D$.

2. Numerical Method

Profiles of χ_e and χ_i are calculated from the profile data of n_e, T_e, T_i, P_{rad}, P_{abs} and so forth by using 1.5 dimensional tokamak transport analysis code, TOPICS. An Orbit Following Monte Carlo (OFMC) code is used to evaluate the NBI power deposition profile in order to take into account the large ripple loss rate of beam ions. We added the convection heat flow to the conduction heat flow when evaluating χ_e and χ_i. We also added the particle diffusion term and the pinch term at the estimation of D. Thus obtained χ and D values just before and after the H-L transition provide their relative changes as $\delta\chi/\chi = 2\,(\chi(\mathrm{L})-\chi(\mathrm{H}))\,/\,(\chi(\mathrm{L})+\chi(\mathrm{H}))$ and $\delta D/D = 2\,(D(\mathrm{L})-D(\mathrm{H}))\,/\,(D(\mathrm{L})+D(\mathrm{H}))$. We represent χ and D values at $r/a = 0.6$ for the estimation of $\delta\chi/\chi$ and $\delta D/D$. In order to make clear the difference in transport properties, we study the transition from ELM free H phase (not ELMy H phase) to the L phase.

We evaluate the change of thermal confinement improvement at the H-L transition together with the local transport properties. The scaling of the thermal stored energy, W_{th}, in JT-60 ohmically heated plasmas and NBI heated L-mode plasmas is given as follows [4],

$$W_{th}^{scaling}(\mathrm{MJ}) = 0.026\, M_i^{0.3}\, \kappa^{0.87}\, R^{1.44}(\mathrm{m})\, a^{0.93}(\mathrm{m})\, B_t^{0.39}(\mathrm{T})\, I_p^{0.5}(\mathrm{MA})\, \bar{n}_e^{0.5}(10^{19}\mathrm{m}^{-3})\, P_{net}^{0.33}(\mathrm{MW})\,.$$

When W_{th} varies in time, we put $P_{net} = P_{abs} - dW_{th}/dt$. Here we define the "TH factor" (Thermal H factor) by $W_{th}^{exp}/W_{th}^{scaling}$. The relative change of TH factor at the H-L transition is also defined by δTH/TH = 2 (TH(H)–TH(L)) / (TH(H)+TH(L)). Since the improvement of core confinement does not fully vanish even in the L phase, TH(L) is larger than unity, which is different from the 'usual' L-mode plasmas. This ICC gradually decreases during the L phase in the time scale larger than τ_E^{th}.

3. Results

We have analyzed seven discharges in the parameter range of I_p=1.6~3.5 MA, B_t=3.9~4.2 T, q_{eff}=3.2~5.7, P_{NBI}^{inj}=21~31 MW, R=3.2~3.4 m, a=0.82~0.90 m, V=65~72 m^3, $\bar{n}_e$= 1.8~3.5 $\times 10^{19}$ m^{-3}, $T_e(0)$=6.2~8.5 keV and $T_i(0)$=15~30 keV. The deposition profile of NBI is rather broad. None of these shots has internal transport barrier (ITB).

Figure 1 shows the waveform of shot E21440 (I_p=1.6 MA, B_t=3.9 T, q_{eff}=5.6, R=3.4 m, a=0.82 m, κ=1.58, V=67 m^3). The line integrated electron density, $n_e L$ (L is about 2.4 m), the injected NBI power, P_{inj}, the net power, P_{net}, the stored energy measured by diamagnetic loop, W_{dia}, the D_α from the divertor region, $D_{\alpha div}$, and the TH factor are shown. L-H and H-L transitions appear alternately. Both W_{dia} and $n_e L$ begin to increase at the L-H transition and decrease at the H-L transition. Just before and after the H-L transitions at t = 8.15 s, TH factor drops from 1.57 to 1.16.

Figure 2 shows the profiles of n_e, T_e and T_i at t=8.13 s, just before the H-L transition. The n_e profile is fairly flat, which is common for all analyzed shots. In the plasma core region, T_i profile is peaked, while T_e profile is almost parabolic and does not have clear central peaking. More than 70 % of NBI power is absorbed by ions in this shot. The local T_e and T_i values over the wide region ($0.4 \le r/a \le 0.8$) also begin to change at the transitions.

Figure 3 shows the profiles of χ_e and χ_i in the H phase (thick line) and the L phase (thin line). At the H-L transition, χ_e increases over the whole plasma. The increase of χ_i in the region $r/a \ge 0.5$ is remarkable, but is very small in the plasma core region, because T_i in the central region is not sensitive to H-L transition for this case. At the H-L transition, D also increases over the whole plasma. The value of $\delta D/D$ at r/a = 0.6 is about 0.34.

Figure 4 shows the relation between I_p and δTH/TH, where the dependence cannot be seen. We also found that $\delta\chi_e/\chi_e$, $\delta\chi_i/\chi_i$ and $\delta\chi_{eff}/\chi_{eff}$ do not have I_p dependence, either.

Figure 5 shows the δTH/TH dependence of $\delta\chi_e/\chi_e$, $\delta\chi_i/\chi_i$ and $\delta\chi_{eff}/\chi_{eff}$. We evaluate $\delta\chi/\chi$ at r/a = 0.6. An interesting point is that δTH/TH dependence of $\delta\chi_e/\chi_e$ and $\delta\chi_i/\chi_i$ is different. The $\delta\chi_e/\chi_e$ becomes large (0.5~0.6) from small δTH/TH value (=0.15) and does not increase too much with δTH/TH. On the other hand, $\delta\chi_i/\chi_i$ increase with δTH/TH. In the discharge of the largest δTH/TH value (=0.35), $\delta\chi_i/\chi_i$ becomes the same level as $\delta\chi_e/\chi_e$ and χ_i decreases over the whole plasma region at the H-L transition. As for the effective thermal diffusivity, $\delta\chi_{eff}/\chi_{eff}$ behaves like $\delta\chi_i/\chi_i$. The improvement of total thermal confinement depends on the reduction of ion heat transport.

The relation between $\delta D/D$ and $\delta\chi/\chi$ are shown in Fig. 6. It is found that there is no clear correlation between them. Two shots have negative $\delta D/D$ value at the H-L transitions, although $\delta\chi/\chi$ values are positive. In these shots $\bar{n}_e$ keeps increasing after the H-L transition although the NBI power remains constant and no gas puffing is done. Since D estimated here includes both the diffusion term and the pinch term, it is necessary to examine the roles of both terms separately at the H-L transitions. This is an important future subject to clarify the relation between the heat transport and the particle transport.

4. Summary and Discussion

The relative change of the electron and ion thermal diffusivity, $\delta\chi_e/\chi_e$ and $\delta\chi_i/\chi_i$, and that for the improvement of thermal energy confinement, δTH/TH, at the H-L transition has been studied in JT-60U H-mode plasmas with I_p = 1.6~3.5 MA and $B_t \simeq$ 4.0 T. As for $\delta\chi_e/\chi_e$, it is large (0.5~0.6) even for small δTH/TH value (=0.15) and changes very little with the increase of δTH/TH. On the other hand, $\delta\chi_i/\chi_i$ increases with δTH/TH. The improvement of total thermal confinement in H phase is dominated by the reduction of ion heat transport. The relative change of the effective particle diffusivity, $\delta D/D$, is independent of δTH/TH.

In the discharge with the largest $\delta\chi_i/\chi_i$ value, both the toroidal and poloidal rotation shear profile change drastically at the H-L transition. In the discharge with lower $\delta\chi_i/\chi_i$ value, the change in the rotation shear is much smaller. Detailed study on the correlation between the ion heat transport reduction in the H phase and plasma rotation is necessary. In the high β_p H-mode plasmas with ITB, the rotation shear profile accross the ITB [5] and the time evolution of χ_e, χ_i profiles behave differently accross ITB [6]. We will clarify the transport characteristics of high β_p H-mode plasmas and compare the results with this presentation in order to make more clear physical picture of transport phenomena in H-mode plasmas.

Acknowledgments Authors are grateful to Drs. S. Ishida, Y. Kamada and T. Fukuda for fruitful discussion and suggestions. They are indebted to members of JT-60 team for their collaboration.

References

[1] M. Kikuchi, H. Shirai, T. Takizuka, Y. Kamada, et al., *Proc. 14th Conf. on Plasma Physics and Controlled Nucl. Fusion Research, Würzburg, 1992*, Vol. 1 (1993) 189.

[2] S. Ishida, M. Matsuoka, M. Kikuchi, S. Tsuji, et al., ibid. Vol. 1, (1993) 219.

[3] H. Shirai, T. Takizuka, Y. Koide, Y. Kamada, S. Ishida, et al, *in Proc. IAEA Technical Committee Meeting on H-mode Physics (Princeton, 1995).*

[4] H. Shirai T. Takizuka, O. Naito, M. Sato, et. al, J. Phys. Soc. Jpn **64** (1995) 4209.

[5] Y. Koide, M. Kikuchi, M. Mori, S. Tsuji, et al., Phys. Rev. Lett. **72** (1994) 3662.

[6] H. Shirai, T. Takizuka, M. Kikuchi, M. Mori, et al., *Proc. 15th Conf. on Plasma Physics and Controlled Nucl. Fusion Research, (Seville, 1994)*, Vol. 1 (1995) 355.

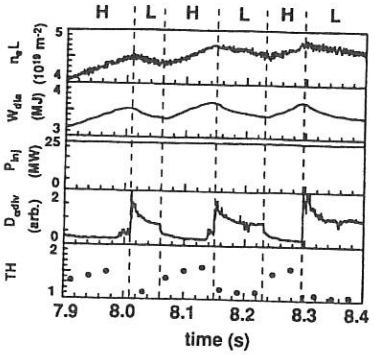

Fig. 1 Waveforms of shot E21440.

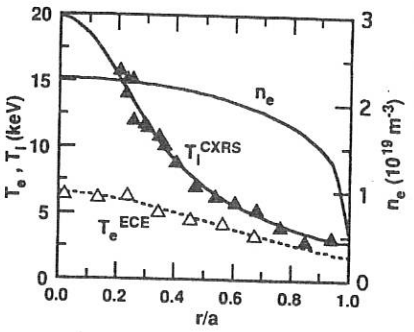

Fig. 2 Profiles of n_e, T_e and T_i in shot E21440 during H phase.

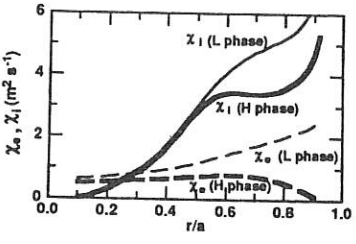

Fig. 3 Profiles of χ_e and χ_i in shot E21440 in H phase and L phase.

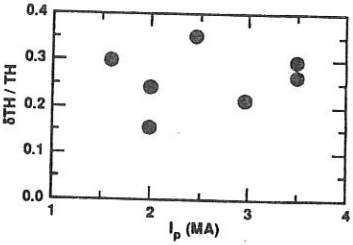

Fig. 4 Relation between I_p and $\delta TH/TH$.

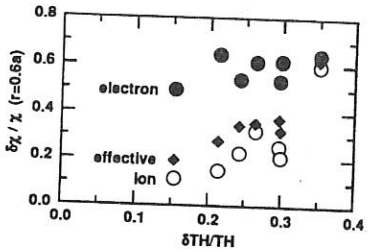

Fig. 5 $\delta TH/TH$ dependence of $\delta\chi/\chi$.

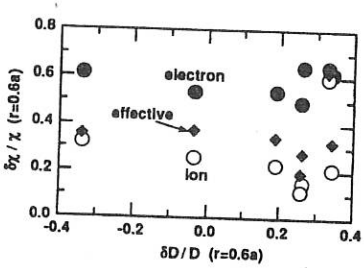

Fig. 6 Relation between $\delta D/D$ and $\delta\chi/\chi$.

Relation of the Toroidal Current to the Radial Plasma Flux in Tokamaks. Possible Manifestation of This Relation in L-H Transition in the TUMAN-3 Device.

S.G. Kalmykov
A.F.Ioffe Physical-Technical Institute, St. Petersburg, Russia

1. On the nature of the relation. Conventional neoclassical Ohm's law is well known to be not adequate to real experimental situation because in the experiments radial transport fluxes are anomalous and exceed the quantities given by the neoclassical theory by the order of magnitude and more. The disagreement causes repetitive Ohm's law examinations and attempts of revision. In several recent works [1,2,3] a formulation of Ohm's law for tokamaks

$$j_{\parallel} = \sigma_{Sp}(E_{\parallel} + V_r B_p/c), \tag{1}$$

alternative to the conventional one, is proposed to be considered. It implies that there is a relation between the parallel plasma current, $j_{\parallel}$, and the radial plasma flux velocity, V_r. In frames of the MHD approximation, this formulation takes place when a sign dependent poloidal force, F_p, exists [4]. Its parallel component induces an additional current and the transversal one results in radial plasma flux. Then the additional, "plasma flux driven", current may be expressed in terms of the plasma flux velocity as $j_{pfd} = \sigma_{Sp} V_r B_p/c$.

Two situations are known when the Ohm's law formulation (1) does work. One of them is magnetic plasma compression [5]. There the poloidal electric field is induced by the toroidal magnetic field increasing in time: $E_p = -r(dB_t/dt)/2c$, and V_r is the plasma compression velocity, $V_r = -r(dB_t/dt)/(2B_t)$. The standard neoclassical theory is another case [1,6]. Here $F_p = -\nabla_\theta\, p_i - en\, \partial\phi/\partial\theta + ...$ (θ is poloidal angle) originates from poloidal variations of plasma pressure and potential induced by the $gradB$ drift. Then the Ohm law (1) is quite equivalent to commonly used

$$j_{\parallel} = \sigma_{neo} E_{\parallel} + j_{bs} \tag{2}$$

if neoclassical $V_{r,neo} = V_{Ware} + V_{dif,neo}$ is substituted as V_r. Basing on formulae of the neoclassical theory (e.g. [7]), it may easily be shown that $(\sigma_{neo} - \sigma_{Sp})E_{\parallel} = j_{Ware} = \sigma_{Sp} V_{Ware} B_p/c$ because the Ware pinch velocity, V_{Ware}, is proportional to $E_{\parallel}$, $j_{bs} = j_{dif,neo} = \sigma_{Sp} V_{dif,neo} B_p/c$, and finally

$$j_{\parallel} = \sigma_{Sp} E_{\parallel} + j_{Ware} + j_{dif,neo} \tag{3}$$

So far as the anomalous transport is concerned, it is necessary to stress that this is the poloidal direction of the force F_p that defines the Ohm's law form (1). Some turbulencies

which distort the magnetic configuration (ergodization, "magnetic flutter", magnetic islands, etc.), contribute sufficiently to the radial transport by means of plasma flow parallel to the magnetic field lines. Instabilities of a different kind, similar to the flute instability, produce the radial particle flux owing to a fluctuating electric field exactly perpendicular to the magnetic one. These both will induce no additional current. But if the averaged turbulent electric vector has both parallel and perpendicular components, such an instability has to maintain the additional current proportional to the velocity of the anomalous radial plasma flux. Besides, one can imagine a kind of turbulency which distorts the plasma potential through a weak intervention into the ambipolar flux, then the proportionality between j_{pfd} and V_r may also occur. *Thus, in spite of a distinct comprehension is hardly attainable, the possible relation between the toroidal current and the radial plasma flux should be studied to obtain an adequate Ohm's law form for the tokamak practice.*

2. Plasma influx and countercurrent in pellet injection experiments on the tokamak T-10. In experiments on off-central injection of small low-Z (LiD or H_2) pellets into plasmas of T-10 (Moscow, Kurchatov Institute) an enigmatic post-injection approximately twofold increase in the loop voltage was observed [2,3]. It could be explained conventionally neither by weak and transient plasma conductivity decrease nor by accompanying changes in the poloidal magnetic flux. In contrast to the temperature, the profile of the plasma density exhibited stronger variations what suggested that a plasma influx arose, at least, in an inner part of the discharge $r/a \leq 2/3$. The influx velocities were derived from the experimental particle balance; they were found to be about -50cm/s at the middle of the minor radius. By analogy with the Ohm law (3) the influx has been assumed to be responsible for generation of a countercurrent. Then the loop voltage had to be increased to maintain the plasma current flattop. Numerical loop voltage simulation based on Ohm's law (1), where the plasma conductivity was deduced from experimental data on the plasma parameters and V_r was the experimental plasma velocity, has been performed. The good agreement of the calculated waveform with the experimental one has validated the hypothesis. Attempt to understand whether the anomalous diffusion outflux was related to an additional toroidal current failed because the outflux velocities were substantial only at the plasma periphery where their influence on the loop voltage was negligible, within the 20% accuracy of the analysis, due to low conductivity.

3. Analysis of TUMAN-3 ohmic H-mode. It has been speculated in [3] that dramatic alteration in the plasma potential value and even in its sign characteristic of the $L \rightarrow H$ transition should suggest noticeable variations in j_{pfd} as well. Really, a loop voltage excess has been observed during the early phase of the ohmic H-mode in TUMAN-3 tokamak (St.-Petersburg, Russia) (Fig. 1) [8]. To explain it, the authors of the paper assumed a rather substantial electron temperature drop in a boundary zone of the plasma column where the measurements were not performed (Fig. 2, dashed curve). However, a pronounced plasma influx has been reported there to arise just after the $L \rightarrow H$ transition. In Fig. 3 of the present work the plasma flux velocities are displayed. They have been derived from the experimental data in [8] on evolution of the electron concentration and of the ionization rates. By analogy with the above discussed case, the influx has been supposed to be related to the voltage excess.

A new loop voltage simulation has been carried out taking into account the plasma velocities. Calculation made for the stage before the transition has shown that the neoclassical correction to the conductivity (i.e. j_{Ware}) contributed some half to the loop voltage whereas the anomalous diffusion outflux influence might be only insignificant. Ohm's law in form

$$j_{\|} = \sigma_{Sp} E_{\|} + j_{pinch} + j_{bs} \tag{4}$$

was used in the simulation. Here j_{bs} is the neoclassical bootstrap current [7] and $j_{pinch} = \sigma_{Sp} V_{pinch} B_p / c$.

In the quasi stationary stage before the transition the actual pinch velocity, V_{pinch}, was anticipated to be equal to the Ware pinch one. During the transitory period the pinch velocity should be obtained from the total plasma flux (Fig. 3) by subtracting that of the anomalous diffusion. Minimum and maximum estimations of V_{pinch} were made, respectively, at $V_{dif} = 0$ and when assuming V_{dif} to keep the same value as before the transition. In Fig. 4 an intermediate V_{pinch} value is shown (dashed curves). It has been calculated in the belief that the diffusion, in accordance with data of [8], was less than before the transition by a factor of 3. The solid line ($t = 27.0$ms) represents $V_{pinch} = V_{Ware}$ just before the transition. It is seen that during the transient process the actual pinch velocity exceeded its neoclassical value by a factor of 2 to 3 returning back to it at the end of the non-stationary phase.

To calculate σ_{Sp}, electron temperature profiles (Fig. 2, solid lines), based on reported in [8] Thomson scattering data, were used. Current ramp up stage of the discharge was included into the simulation to account for the skin effect persisting at the current flattop. Sawteeth were also modelled.

Comparison of the simulated loop voltage with the experimental one is shown in Fig. 1. Curve 1 reproduces the experimental waveform. Curve 2 is the result of the simulation using the standard neoclassical Ohm's law (2). It is clear that the voltage behaviour cannot be explained in the conventional way if the hypothesis on the substantial transient temperature drop at the plasma column surface is not used. The loop voltage simulated with use of Ohm's law (4) and with taking into account the effect of V_{pinch} (curve 3) demonstrates quantitative agreement between modelled and experimental waveforms.

4. Conclusions. Thus, in two different experiments, where transient processes were provoked by two quite different mechanisms, plasma influxes arose in the opposite to the density gradient direction. In the both cases the same relation exists between these pinches and the parallel current, similar to that in the neoclassical theory.

Earlier, in different non-stationary processes, the plasma influxes were also observed (e.g. [9]). That time this pinch had been termed as "anomalous pinch". However the factor of the excess above the neoclassical level was always not so high, about 2 to 5. Perhaps, the actual pinch has, nevertheless, a classical nature but a "dynamic" version of the neoclassical theory is needed to describe non-stationary processes.

References

[1] Segre, S.E., Zanza, V., Nucl. Fusion **32** (1992) 1005.
[2] Kalmykov, S.G., et al., Nucl. Fusion **35** (1995) 795.
[3] Kalmykov, S.G., Sergeev, V.Yu., Controlled Fusion and Plasma Phys. (Proc. 22nd

EPS Conf., Bournemouth, 1995), Vol.19C, Part II (EPS, Geneva, 1995), p.II-081.
[4] Rozhanskii, V.A., State Tech. Univ., St.-Petersburg, Russia, personal comm., 1995.
[5] Goncharov, S.G., et al., in Plasma Phys. and Contr. Nucl. Fusion Res. 1984 (Proc. 10th Int. Conf., London, 1984), IAEA, Vienna, 1985, v.1, p.155.
[6] Kim, J.-S., Greene, J.M., Plasma Phys. Control. Fusion **31** (1989) 1069.
[7] Hinton, F.L., Hazeltine, R.D., Rev. Mod. Phys. **48** (1976) 239.
[8] Andrejko, M.V., et al., in Plasma Phys. and Contr. Nucl. Fusion Res. 1992 (Proc. 14th Int. Conf., Würzburg, 1992), IAEA, Vienna, 1993, v.1, p.485.
[9] Dnestrovskii, Yu.N., et al., Sov. J. of Plasma Phys. **10** (1984) 137.

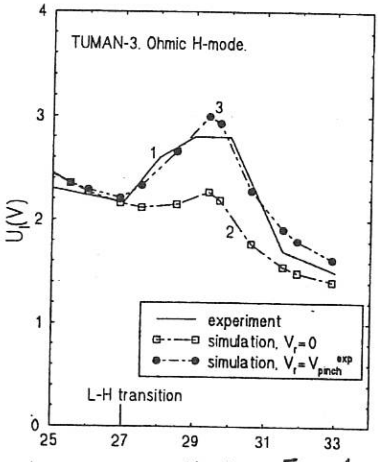

Fig. 1

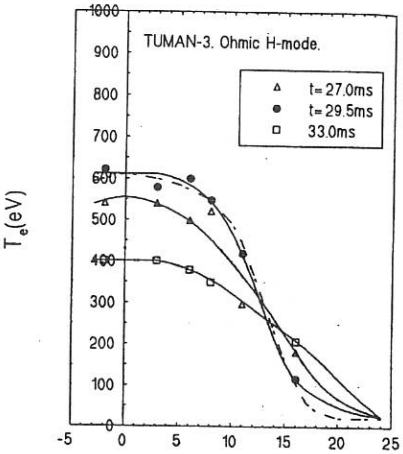

Fig. 2

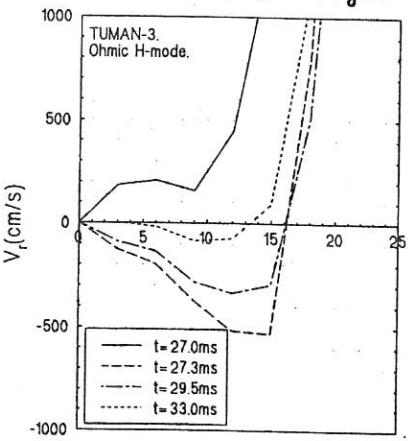

Fig. 3

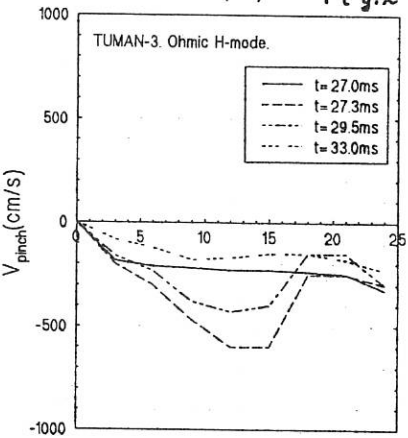

Fig. 4

Profile dependent signature of the linear MHD spectrum

H.A. Holties[1], A. Fasoli[2], J.P. Goedbloed[1],
G.T.A. Huysmans[3], W. Kerner[3]

[1]FOM Instituut voor Plasmafysica Rijnhuizen, Nieuwegein, The Netherlands
[2]CRPP-EPFL, Lausanne, Switzerland
[3]JET Joint Undertaking, Abingdon, Oxfordshire, United Kingdom

1 INTRODUCTION

The steady state version of the CASTOR code (Complex Alfvén Spectrum in TORoidal geometry) [1] has been developed to study the stable part of the magnetohydrodynamic (MHD) spectrum of toroidal plasmas. In this paper the influence of equilibrium parameters on the Alfvén spectrum is studied. The goal of this study is to solve the inverse problem: identification of the plasma profiles, and especially the safety factor profile, using measurements of MHD waves. This new kind of spectroscopy has been called MHD spectroscopy [2].

The determination of plasma parameters from measurements of the magnetohydrodynamic (MHD) spectrum has become a subject of interest because this spectrum is sensitive to the safety factor profile. This profile is essential for determining the MHD stability of plasmas, but it is difficult to measure accurately, especially in the center of the plasma.

2 THE SAFETY FACTOR ON AXIS

For specific values of the central safety factor, the TAE gap closes due to the coupling parameter (the local inverse aspect ratio ϵ) being zero on axis. For a pressureless JET-like equilibrium the $n = -1$ continuum and gap frequency ranges are shown in figure 1 as a function of q on axis. The general behavior is generic for plasma equilibria in toroidal geometry. When q on axis has the value 1.5 (or more general: when $q(0) = (m + 1/2)/n$), the TAE gap on axis is closed. In this case there can no longer be undamped global modes in the TAE frequency range. The observation of TAE modes during phases where the central safety factor profile goes through a change can thus provide a diagnostic for the safety factor on axis.

When the central shear is sufficiently small two TAE modes can exist for each value of the toroidal mode number. One has a frequency near the top of the gap. The other mode has a frequency closer to the bottom of the gap. They are localized in the central region of the plasma and are therefore called core-localized TAE's [3, 4]. As the central q value approaches the value $(m + 1/2)/n$, the frequencies of the two modes will coalesce. The two modes only exist when $q(0) \leq (m + 1/2)/n$. For larger values the corresponding TAE-gap is no longer existent in the plasma. The (dis-)appearance of these core-localized modes thus provides a good diagnostic for the central q value.

Knowledge of $q(0)$ is important, for example, for predicting the onset of sawtooth crashes. An accurate diagnostic can help operating a plasma close to, but on the stable side of, sawtooth stability limits. However, this parameter is difficult to measure directly

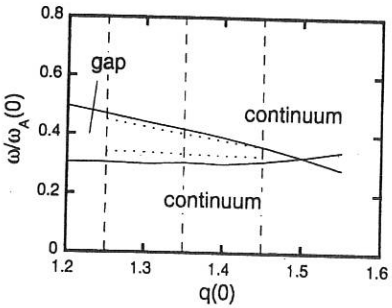

Figure 1: *Continuum frequency ranges as a function of q on axis. The $n = -1$ TAE-gap is closed for $q(0) = 1.5$. The dotted lines correspond to the TAE frequencies.*

and it is usually not known within an error margin of 10%. The measurement of core-localized TAE's could lead to much more accurate values of $q(0)$ for those moments when the TAE gap closes.

3 MULTIPLE GAE SPECTRUM

In this section we will study the spectrum of MHD waves in a high beta plasma with reversed shear. The cross section is circular and $\epsilon = 0.34$. The normalized pressure gradient $dP/d\Psi = 1 - \Psi$, where Ψ is the normalized poloidal flux. The poloidal beta is equal to 1.25. In figure 2 we show the antenna loading of this equilibrium, for $n = -1$ excitation, as a function of the excitation frequency. There is a large resonance peak, at the normalized frequency $\omega/\omega_A(0) = 0.415$, belonging to a TAE that is continuum damped because of its coupling to a continuum branch at $s = 0.6$. A sequence of sharp (undamped) resonance peaks occurs starting from the frequency $\omega/\omega_A(0) = 0.49$ upwards. The modes are apparently clustering at a continuum branch with a maximum. The high beta causes the Alfvén and sound continua to be strongly coupled, so that it is difficult to distinguish which is the most important component in this branch. There is one dominant poloidal harmonic in the modes, suggesting that they are of the Global Alfvén Eigenmode (GAE) type. They are localized near, but away from, the plasma center, where the continuum branch has a local maximum. The component in the perturbation normal to the magnetic field is larger than the tangential component, indicating that the discrete waves are of the Alfvénic (as opposed to slow magnetosonic) type.

GAE's are usually found to be strongly continuum damped in tokamaks because of coupling to the Alfvén continuum wave, due to toroidal effects. The multiple GAE's found here are not necessarily continuum damped because they can appear in the TAE gap where strong coupling between poloidal harmonics creates a frequency range free of Alfvénic continuum modes.

4 VERY LOW SHEAR PLASMAS

In plasmas with very low shear, the existence of an enlarged spectrum of ideal TAE's has been predicted from analytical theory [5]. It is found that for small values of $\epsilon(r)/\hat{s}(r)$, two

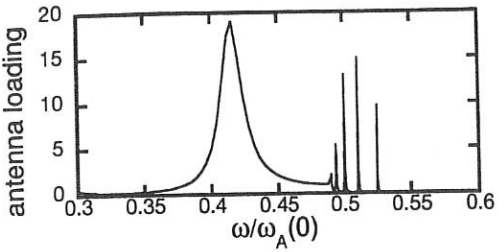

Figure 2: *Antenna loading as a function of the normalized excitation frequency for a high beta reversed shear plasma;* $n = -1$, $\eta = 10^{-7}$.

TAE modes can exist inside a single TAE gap. One comes from the top of the toroidicity induced gap and the other comes from the bottom of the gap. These correspond to the two core-localized modes studied in section 2. When the parameter $\epsilon(r)/\hat{s}(r)$ is increased, new modes appear near the top and the bottom of the TAE gap. Each new mode has one more radial node in the amplitude of its harmonics than the previous mode.

Multiple TAE's are of special interest for tokamaks with a very tight aspect ratio. A small aspect ratio tokamak experiment is planned at the university of Texas. This experiment (USTX [6]) will have an inverse aspect ratio of 0.7 and might be used to study the spectrum of multiple low shear TAE's. The minor radius of the plasma is approximately 50 cm, the toroidal field is about 0.5 tesla. In this section we will study a plasma relevant to the USTX experiment. The elongation is 1.7, the triangularity is 0.19, the plasma beta is 12%, the plasma self induction l_i is 0.57, and the plasma current is 1.125 MA. We have chosen the current density profile to be non-monotonic to make the safety factor profile flat in the plasma center with a high plasma beta value.

We have calculated the $n = -4$ MHD spectrum, with q on axis equal to 1.05, so that the TAE gap closest to the plasma center is the $m = 4, m' = 5$ gap at the flux surface where $q = 1.125$. On this flux surface, the flux parameter is $s = 0.45$, giving a local inverse aspect ratio of approximately 0.32. The shear parameter $\hat{s}$ is 0.12, so that $\epsilon(s)/\hat{s}(s) = 2.6$.

To assess the possibility of exciting multiple TAE modes with an external antenna we have used the stationary state version of CASTOR described in Ref. [1]. Figure 3 shows the result of the simulation of an excitation experiment for the USTX plasma modeled here. The antenna loading curve for the frequency range close to the top of the TAE gap has been calculated using $\eta = 10^{-6}$ for the plasma resistivity. The resonance peaks in the curve indicate the existence of global modes.

All the modes are localized in the region of the $(m, m') = (4,5)$ TAE gap. The $m = 4$ and $m = 5$ poloidal harmonics are the ones with the largest contribution to these modes. They have opposite sign, which indicates that the modes are localized on the high field side of the plasma. The number of nodes increases when the mode is closer to the continuum. As with the multiple GAE modes in the previous section, the multiple TAE modes can be used for MHD spectroscopy. The localization, frequency, and number of modes can be used to determine local values of the density, the q profile, and the magnetic shear in the plasma core, respectively.

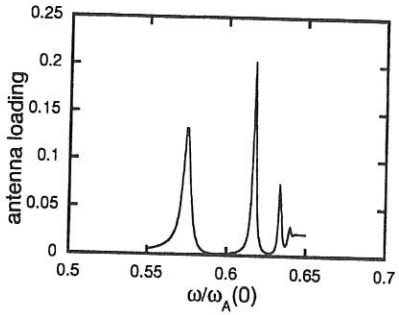

Figure 3: *Antenna loading spectrum near the top of the TAE gap for a USTX-like plasma equilibrium. The resonance peaks correspond to the spectrum of multiple core localized TAE's.*

5 CONCLUSIONS

The relation between the spectrum of MHD waves and plasma parameters has been studied. An important result is that detecting the existence and frequency of core-localized TAE's can lead to an accurate diagnostic of the central q value. We find that core localized modes appear with the opening of the TAE gap in the center of the plasma, which is directly correlated with q on axis. Experimental indications from JET and TFTR for the existence of core localized TAE's are consistent with the numerical calculations.

We have shown the existence of multiple discrete modes that are related to the safety factor profile. A multiple spectrum of undamped Global Alfvén Eigenmodes can appear in plasmas with an inverted safety factor profile and high β values.

For a low aspect ratio USTX-like plasma we have calculated the multiple Toroidicity induced Alfvén Eigenmode spectrum. The spectra can be used in the context of MHD spectroscopy since their characteristics (frequency, frequency spacing, localization, number of modes) depend on the details of the plasma equilibrium profiles. This will be explored in future studies.

REFERENCES

[1] G.T.A. Huysmans, W. Kerner, D. Borba, H.A. Holties, J.P. Goedbloed, *Phys. Plasmas* **2**, 1605 (1995).

[2] J.P. Goedbloed, H.A. Holties, S. Poedts, G.T.A. Huysmans, W. Kerner, *Plasma Phys. Control. Fusion* **35**, B277 (1993).

[3] G.Y. Fu, *Phys. Plasmas* **2**, 1029 (1995).

[4] H.L. Berk, J.W. van Dam, D. Borba, J. Candy, G.T.A. Huysmans, S. Sharapov, *Phys. Plasmas* **2**, 3401 (1995).

[5] J. Candy, B.N. Breizman, J.W. Van Dam, T. Ozeki, *submitted to Phys. Lett.*

[6] E. Solano, B.N. Breizman, *private communications.*

MHD STABILITY ANALYSIS OF THE KT-2 PLASMA

S. Poedts [1], A. De Ploey [2], J.P. Goedbloed [1], B.G. Hong [3], and S.K. Kim [3]

[1] FOM-Institute for Plasma physics, Nieuwegein, The Netherlands
[2] Centre for Plasma Astrophysics, Leuven, Belgium
[3] Korean Atomic Energy Research Institute, Yusong, Taejon, Korea

Abstract

The stability of the KT-2 tokamak plasma has been analyzed in the framework of ideal and resistive linearized magnetohydrodynamics (MHD). KT-2 is a Korean tokamak project which involves a large aspect-ratio divertor tokamak with up-down symmetric plasma cross-section [1]. Three numerical codes have been used for this purpose, viz. CASTOR [2] for the study of kink modes and infernal modes, HBT [3] for the ballooning stability analysis and the calculation of equilibria, and HELENA [4] as an interface between HBT and CASTOR. First, equilibria with monotonic q-profiles are investigated. Starting from four ballooning stable 'reference equilibria' with ever broader pressure profiles, the effects of the shape of the poloidal plasma cross-section (ellipticity and triangularity), the aspect ratio, and the total plasma current on the ballooning and ideal and resistive external kink instabilities are studied. Also, 'advanced tokamak scenarios' have been investigated for typical KT-2 parameters. A local profile optimization study is performed for a lower total current, viz. $I_p = 300\,\mathrm{kA}$, and a magnetic field of 2 T. Next, the stability of the marginally ballooning stable equilibria with respect to so-called 'infernal modes' is analysed [5].

1 Monotonic q-profiles

Four marginally ballooning stable equilibria have been determined characterized by ever broader pressure profiles and different current density profiles and by the parameter values: aspect ratio $\epsilon^{-1} = 5.6$, ellipticity $b/a = 1.8$, triangularity $\tau = 0.6$, plasma current $I_p = 500\,\mathrm{kA}$, and magnetic field $B_0 = 3\,\mathrm{T}$. These are typical parameter values for the KT-2 tokamak.

The four reference equilibria are 'marginally' ballooning stable in the sense that an increase of the pressure yields at least one ballooning unstable magnetic surface. The effect of the ellipticity and triangularity of the poloidal cross-section of the plasma, and of the aspect ratio and the total plasma current on the β limits has been investigated for these four equilibria. Fig. 1, e.g., shows the effect of the ellipticity on the normalized plasma beta, $g_N \equiv 100\,\beta\,a[m]B_0[T]/(\mu_0 I_p[A])$, and the poloidal beta, β_p. From this plot it is clear that g_N is close to optimal for $b/a = 1.8$, for all four reference equilibria.

The marginal poloidal plasma beta, β_{pmax}, increases monotonically with increasing ellipticity. The optimal value for the triangularity turns out to be 0.6 for all four reference equilibria. The aspect ratio was varied from 4.0 to 6.0. An increase of the aspect ratio reduces the bending of the magnetic surfaces so that the plasma becomes less susceptible to ballooning instabilities. The relative change of β_{max} in the aspect ratio scan was roughly the same for the four reference equilibria, viz. about 8%. The total plasma current was varied from 300 kA to 550 kA. The marginal plasma beta, β_{max}, increases monotonically with the plasma current. However, the marginal poloidal plasma beta, β_{pmax}, *decreases almost linearly* with increasing plasma current.

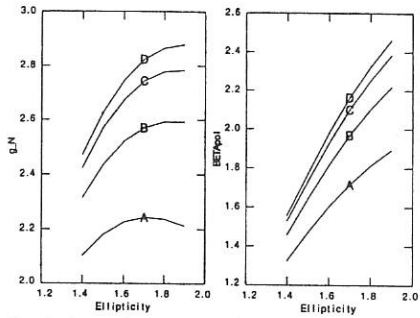

Figure 1: The normalized plasma beta, g_N, and poloidal beta, β_p, versus the ellipticity of the plasma cross-section for four reference equilibria with ever broader pressure profiles (A $\rightarrow$ D) and with $\epsilon^{-1} = R_0/a = 5.6$, $B = 3\,\mathrm{T}$ and $I_p = 500\,\mathrm{kA}$. The triangularity of the cross-section is 0.6.

The four ballooning stable 'reference equilibria' are unstable with respect to ideal external kink modes. The calculations show that $q_1 \propto 1/I_p$ plays a key-role for the growth rate of the kink instability. The reference equilibria have $q_1 \approx 4.8$. By lowering I_p somewhat, we can get $q_1 > 5$. This proves to be sufficient to stabilize equilibria A and B. The kinks of equilibria C and D, i.e. the most unstable equilibria with the highest current gradient at the edge, are not stabilized, but their growth rate becomes lower. Figure 2 summarizes the result of the calculations. The equilibrium with the highest β, which is still stable for external kinks, is attained from equilibrium B with $I_p = 477\,\mathrm{kA}$, where $q_1 = 5.05$, $\beta = 1.9\%$, $g = 3.03$, $g_N = 2.41$, and $q_0 = 1.34$. The findings for the $n = -2$ instability are similar to those for the $n = -1$ instability.

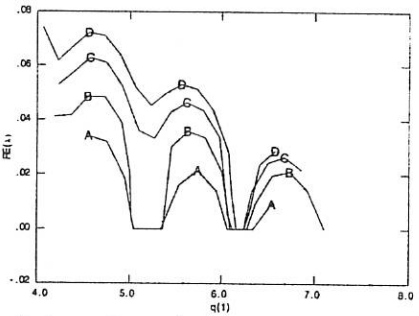

Figure 2: The normalized growth rate ($\mathrm{Re}(\lambda) \equiv \mathrm{Re}\,(i\omega/\tau_A)$ with τ_A the Alfvén transit time) of the $n = -1$ ideal external kink as a function of q_1, i.e. q at the plasma boundary, for four 'reference equilibria' (the labels on the curves refer to the equilibrium), where q_1 was varied by changing the total current I_p.

The influence of the different plasma shape parameters, i.e. triangularity, ellipticity and the aspect ratio, has been investigated. The variation of the triangularity and the ellipticity of the plasma cross-section offers a possibility to stabilize the external kink

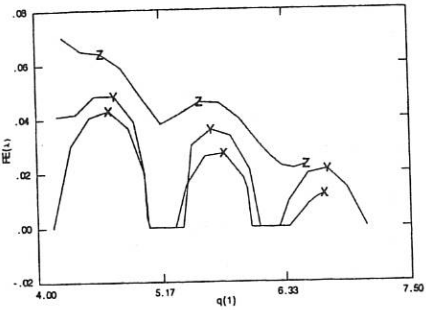

Figure 3: The normalized growth rate for equilibrium B of the $n = -1$ ideal external kink as a function of q_1, where q_1 was varied by changing the total current I_p. Labels X, Y, Z indicate the value for the inverse aspect ratio, i.e. $\epsilon = 0.17$, $\epsilon = 0.1786$ and $\epsilon = 0.19$, respectively.

for some of the reference equilibria, because of the impact of these parameters on q_1. The effect of total current was calculated for different values of the inverse aspect ratio. Figure 3 compares the reference value of $\epsilon = 0.1786$ with $\epsilon = 0.17$ and $\epsilon = 0.19$ for equilibrium B. It is remarkable that the external kink in this equilibrium B can not be stabilized for $\epsilon = 0.19$. The 'stability window' at $q_1 > 6$ is wider for $\epsilon = 0.17$. Some analogy can be found with the calculations of the ballooning stability, where a higher β_{max} is found for ϵ below the reference value ($\epsilon = 0.1786, \epsilon^{-1} = 5.6$).

The growth rates of the resistive external kink modes calculated are higher but very sensitive to the value of η. Calculations show a $\eta^{1/2}$ scaling with growth rates from 1.14×10^{-1} for $\eta = 10^{-4}$ to 2.63×10^{-3} for $\eta = 10^{-7}$. At realistic tokamak values for η, i.e. $10^{-7} - 10^{-8}$, the resistive external kink modes have growth rates of the order 10^{-3}.

2 Advanced tokamak scenarios for KT-2

For the study of 'advanced tokamak scenarios' for KT-2 the total current is lowered to $I_p = 300\,\mathrm{kA}$ corresponding to $B = 2\,\mathrm{T}$. A local optimization procedure for the pressure profile for a fixed average current density profile (we took a typical profile from profile control experiments at JET, yielding an inverted q-profile) yielded a marginally ballooning stable equilibrium for the profiles displayed in Fig. 4.

Here 'optimal' means 'marginally ballooning stable'. If the marginal ballooning stable pressure profile is increased locally, e.g. at one specific $\bar{\psi}$-value, that magnetic surface becomes immediately ballooning unstable. Also, when the plasma beta is increased, e.g. by increasing the horizontal shift of the magnetic axis, all magnetic surfaces become ballooning unstable at once. The marginally stable equilibrium obtained has a plasma beta of 3.425% and $\beta_p = 4.086$. This corresponds to quite high Troyon factors, viz. $g_N = 4.540$ and $g \equiv a[m]B_0[T]/I_p[MA]\,\beta = 5.705$.

We have looked for infernal modes for the marginally ballooning stable equilibria discussed above. Infernal modes require a high spatial resolution. In particular the number of Fourier modes is typically quite high. Hence, we first did a convergence study for the number of Fourier modes with CASTOR. The instability we found turns out to

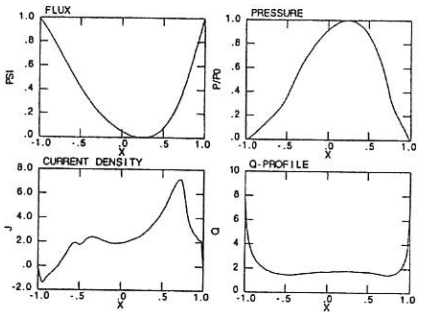

Figure 4: The $\bar{\psi}$, $\bar{P}(\bar{\psi})$, $J_\phi(\bar{\psi})$, and $q(\bar{\psi})$-profile for the 'optimal' equilibrium with a marginally stable pressure profile.

be an external mode. This is exemplified by shifting the wall towards the plasma surface which results in a decrease of the growth rate of the instability.

3 Main conclusions

The stability of the KT-2 tokamak plasma has been analysed in the framework of linearized resistive MHD. The cross-section shape parameters $\tau = 0.6$ (triangularity) and $b/a = 1.8$ (ellipticity) are close to optimal for this large aspect ratio tokamak ($R_0/a = 5.6$). Current control offers a tool to maintain stable equilibria. For stability with respect to external kink modes this requires that the safety factor profile, and in particular q_1, is fixed before the plasma is heated. The highest value of the Troyon factor g_N obtained in the kink stability analysis for monotonic q-profiles is 2.79 ($\beta = 2.34\%$). A profile optimization study for 'advanced tokamak scenarios' with inverted q-profiles yielded a marginal ballooning stable equilibrium with $\beta_p = 4.230$ and $\beta = 3.542\%$ corresponding to quite high Troyon factors: $g_N = 4.697$ and $g = 5.902$. For this optimal equilibrium we found 'infernal' modes with large growth rates for $\tau < 0.6$. For $\tau = 0.6$ the growth rates are much lower and stability windows are found in a scan of the total plasma current.

References

[1] Concept definition of KT-2, a large-aspect-ratio divertor tokamak with FWCD, Korea Atomic Energy Research Institute, KAERI/TR-472/94.

[2] G.T.A. Huysmans, J.P. Goedbloed, and W. Kerner, *Phys.Fluids* **B**, **5**, 1993, 1545, "Free boundary resistive modes in tokamaks".

[3] G.T.A. Huysmans, R.M.O. Galvão, and J.P. Goedbloed, *Rijnhuizen Report 90-194*, 1990, "Documentation of the high beta stability codes HBT and HBTAS at JET".

[4] G.T.A. Huysmans, J.P. Goedbloed, and W. Kerner, *Proc. CP90 Conf. on Comp. Phys. Proc.*, World Scientific Publ. Co., 1991, 371, "Isoparametric Bicubic Hermite Elements for Solution of the Grad-Shafranov Equation".

[5] S. Poedts, A. De Ploey, and J.P. Goedbloed, *Rijnhuizen Report 96-227*, "MHD stability analysis of the KT-2 tokamak plasma".

Development of double double-tearing modes in reversed shear tokamak plasmas

M.R. de Baar, G.M.D. Hogeweij, N.J. Lopes Cardozo, A. Montvai, A.A.M. Oomens, F.C. Schüller and RTP-team

FOM-Instituut voor Plasmafysica "Rijnhuizen", Association Euratom-FOM, P.O.Box 1207, 3430 BE Nieuwegein, The Netherlands

Abstract
In the Rijnhuizen Tokamak Project (RTP) steady-state hollow electron temperature (T_e) profiles have been sustained with strong off-axis electron cyclotron heating (ECH). The hollow T_e profile leads to a hollow current density profile. In the transition to the hollow profiles a bifurcation in confinement is observed. Discharges in the good confinement branch often exhibit strong MHD activity. Sawtooth-like oscillations of T_e at half radius are observed with a typical period of 1 ms. The amplitude of these oscillations is modulated by a more global sawtooth oscillation with a period of 10 ms. These oscillations are understood in terms of the double-tearing mode at the q=3 and q=4 surfaces, respectively.

1. Introduction

Tokamak plasmas with reversed magnetic shear have gained the interest of the fusion community in view of their good confinement [1, 2] In RTP ($R_0 = 0.72\,\mathrm{m}$, $a = 0.164\,\mathrm{m}$, $B_\phi \leq 2.4\,\mathrm{T}$, $I_p \leq 150\,\mathrm{kA}$), hollow T_e profiles can be made reproducibly by off-axis ECH in high density ($ne(0) > 5 \times 10^{19}\mathrm{m}^{-3}$) discharges [3]. Power from a 110 GHz gyrotron is injected in the horizontal mid plane, from the low field side. In these experiments the deposition radius (r_{dep}) was chosen around 0.5a. The absorbed power is 350 kW, which is 5 times the Ohmic input power P_Ω. The steady state hollow T_e profile leads to a hollow current profile and reversed shear. Within the region of reversed shear the effective electron heat diffusivity is very small. Preliminary experiments indicate that the low net heat flux is the result of a balance between the inward flux driven by ∇T_e, and an outward flux driven by other gradients. In this paper we discuss the transition from peaked to hollow T_e-profiles, and present an analysis of MHD activity that is associated with the double-valued q-profile. Measurements have been carried out with a 19-channel interferometer-polarimeter, a 20-channel radiometer, a bolometer and a 118-point single shot Thomson scattering system.

2. Results

Fig. 1 shows a series of Thomson scattering T_e-profiles. At $t = 150\,\mathrm{ms}$ ECH is switched on. First a rapid increase of $T_e(r > 0.5\,a)$ is observed. As a consequence, the current diffuses outwards. The central current density decreases, and with it, the Ohmic power density in the centre of the plasma. For sufficiently high n_e, the electron-ion energy exchange can now beat the Ohmic input, leading to a hollow T_e profile. Typically after 50 ms a new equilibrium is reached. Interestingly, this new equilibrium can be in one of two classes with distinctly different confinement.

Fig. 2 shows the evolution of $T_e(0)$ for 6 near identical discharges Although the discharges all start from nearly the same state, they develop into two branches. The subtlety of the bifurcation is exemplified by one discharge, which hesitates and then crosses over from the low branch to the high branch.

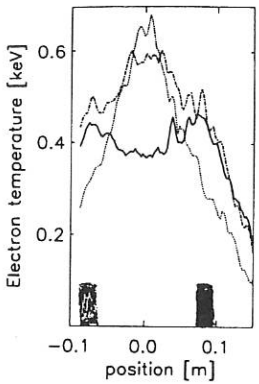

Figure 1: *Evolution of* $T_e(r)$ *measured with Thomson scattering. Shown are profiles measured at t= 149 ms (dotted), t=155 ms (dash-dotted), and t=190 ms (full) respectively. The bars indicate the EC deposition*

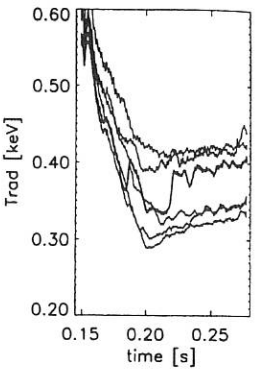

Figure 2: *The evolution of* $T_e(0)$ *in 6 discharges showing the bifurcation of confinement. The subtlety of the bifurcation is exemplified by one discharge that crosses from the low branch to the high branch.*

Discharges with hollow T_e profiles sometimes show vigorous MHD activity. However, this is only observed in discharges in the high confinement branch. It appears that two reconnection processes occur simultaneously, one acting as an envelope of the other. Fig. 3 shows the $T_e(t)$ of two discharges. For one of them $T_e(0)$ shows sudden increases (at t = 191, , 201; , 213, , 224 and 253 ms) followed by slow relaxations. The increase is 'fast', occurring typically within 400 μs whereas the decrease is a process of 10 ms. Fig. 5 shows the T_e profiles just before and just after the crash. The increase of $T_e(0)$ coincides with a decrease of T_e at r_{dep}. The crash flattens the T_e profile over the whole central part of the plasma. After the crash, $T_e(r_{dep})$ increases until the next crash occurs, forming sharp off-axis maxima ('rabbit ears') on the T_e-profile.

Fig. 4 shows 2 ECE channels corresponding to r = 22 and 69 mm, respectively. While the central channel shows only the 10 ms reconnection sequence discussed above, the off-axis channel shows an extra oscillation with a period of 1 ms. This fast oscillation starts with a large amplitude and spreads out over about 6 cm, and gradually decreases in amplitude while contracting to about 2 cm. Note that the 1 ms oscillation is modulated by the 10 ms oscillation. Fig. 6 shows T_e profiles just before and just after the crash of the fast oscillation, showing that this MHD event affects only a small part of the plasma around r_{dep}, chopping off the rabbit ears.

Finally, in one discharge it is observed that the frequency of the fast oscillation suddenly doubles.

3. Interpretation and discussion

In reversed shear profiles, double tearing modes [4] can develop at rational values of the $q = \frac{m}{n}$ in which m and n are the poloidal and toroidal mode number, respectively. These double tearing modes can short-circuit the plasma between the two radii with identical

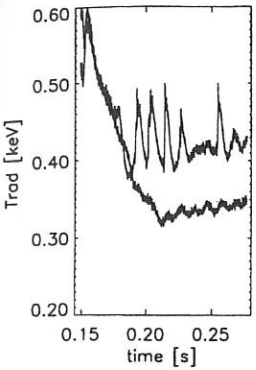

Figure 3: *Central temperature for two discharges. The quiescent evolution of the a discharge on the low branch of confinement is shown for reference. On the high branch sudden increases in* $T_e(0)$ *can be indentified.*

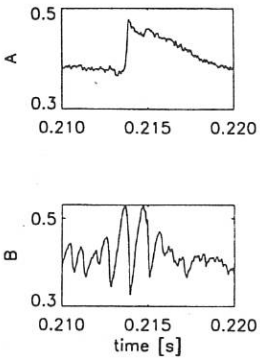

Figure 4: *The radiation temperature at* r_{dep} *shows a fast oscillation which is modulated by the slow oscillation seen on the central temperature.*

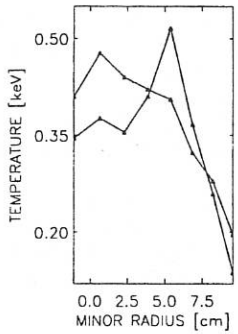

Figure 5: T_e *profiles just before and after a crash of the slow oscillation. This crash affects the entire plasma column .*

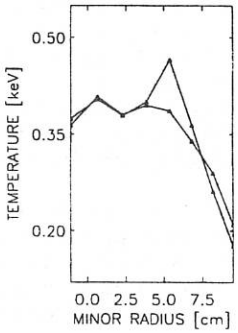

Figure 6: T_e *profiles just before and just after a crash of the fast oscillation. This crash affects only a small part of the plasma.*

rational q on either side of the off-axis minimum in the q-profile. This diminishes all gradients in T_e and n_e and redistributes the current density convectively. Frequency analysis of the precursor proves the toroidal mode number n to be 1. In fig. 7 $q_c(r)$ just before the big crash and right after a minor crash is shown. Exactly at r_{dep} a pronounced minimum formed, that touches q = 3. The q-profile has been derived from Thomson $T_e(r)$. The high collisionality and the negligible bootstrap current imply that Spitzer resistivity $\sigma \propto T_e(r)^{3/2}$ can be applied. There are two possible rational values of q: q = 3 and q = 4.

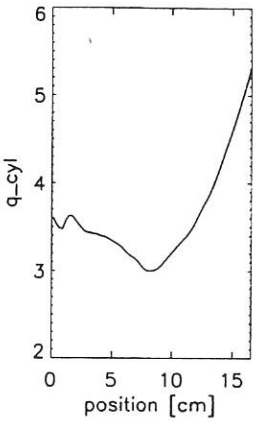

Figure 7: *Safety-factor just before the big crash. Note that at* r_{dep} *the profiles touches* $q = 3$.

We interpret the fast crash as a double tearing mode involving the q=3 surfaces alone, while the slow crash as a double double tearing mode involving both the q=4 and q=3 surfaces. During the fast crash, only a small part of the plasma column is short-circuited. During the sequence of fast crashes the central q-value gradually increases. This process leads to a q-profile in which there are q=3 and q=4 surfaces located, on either side of a region of almost zero shear, with q just below 3. This is the q-profile that is measured just before a big crash. After the big crash the central q is below 4 and the cycle starts again.

The bifurcation in confinement is mainly caused by a different heat conductivity in the region outside r_{dep}. The only macroscopic plasma parameter correlating with the two regimes that we have been able to identify is r_{dep}: in the discharges with good confinement the deposition is about 1 cm further out. It is at present not clear why such a clear distinction between two different modes of confinement should occur.

Acknowledgements
This work was performed under the Euratom-FOM association agreement with financial support from NWO and Euratom.

References

[1] B.W. Rice *et al*, Observations of enhanced core confinement in negative magnetic shear discharges with an L-mode edge on DIII-D, (1995), GA-A22129
[2] X. Litaudon *et al*, Stationary magnetic shear reversal during lower hybrid experiments in Tore Supra, (1996), EUR-CEA-FC 1565
[3] G.M.D. Hogeweij et al, Phys.Rev.Lett. **76** (1996) 632.
[4] D. Biskamp, Nonlinear Magnetohydrodynamics, Cambridge University Press, (1993) 273

Influence of magnetic Reynolds number on internal disruptions in the RTP tokamak

C.P. Tanzi, F.C. Schüller, A. Frank * and the RTP team

FOM-Instituut voor Plasmafysica 'Rijnhuizen', Association Euratom-FOM,
P.O.Box 1207, 3430 BE Nieuwegein, The Netherlands

* IOFAN General Physics Institute
117942 Moscow, Vavilov street, 38, Russian Federation

Introduction, motivation

In RTP, as shown in [1], the $m = 1$ precursor phase of internal disruptions can display a behaviour suggesting that it can be driven by either ideal MHD or magnetic reconnection. This paper investigates the assumption that the relative importance of resistivity might determine whether the $m = 1$ precursor displays an ideal or a resistive development. A measure of the relative importance of resistivity is the magnetic Reynolds number. In order to study its effect on the character of the $m = 1$ precursor, a series of dedicated discharges in which the magnetic Reynolds number S was systematically varied has been analyzed by means of the method introduced in [1, 2], where an MHD invariant, the enthalpy H, is calculated from tomographic reconstructions of the Soft X-Ray (SXR) system on RTP.

A scan in S has been made, by varying the magnetic field, the density and the temperature. This scan was done in a single day in order to minimize the change of impurity content of the plasma, and hence its effect on the resistivity. Constraints over the range of variation of these parameters are both set by the characteristics of the SXR system (which defines an upper limit to the density, to avoid saturation), and by the physics of ohmic heating (a higher density corresponds to a lower electron temperature). It follows that these parameters cannot be varied independently, and not over a large interval. The main plasma parameters of these discharges are given in Table 1, together with the duration of each sawtooth oscillation. In order to keep the magnetic field configuration and current density profile shape as constant as possible, the q_a value (≈ 3.4) and the pressure profile shape were kept fixed within the operational constraints. The variable parameters left are therefore the magnetic Reynolds number S and the absolute value of the central pressure. These are the two quantities that are expected to be of direct influence on the $m = 1$ instability.

Description of experiment

The value of S can be calculated in terms of easily accessible experimental values:

$$S = \frac{\tau_M}{\tau_A} = \frac{\mu_0 L^2 v_A}{\mu_0 R \eta_1}$$

where L is the radius of the $q = 1$ surface and η_1 is the average resistivity inside the $q = 1$ radius ($\eta_1 = \mu_0 V_{loop}/4\pi B_0$). For the toroidal Alfvén velocity the value on axis is considered, assuming that minority impurities do not play a role:

$$v_A = 2.18 \times 10^{16} B_0[T] \sqrt{m_p/m_i n_i [10^{19}\,\mathrm{cm}^{-3}]}\,.$$

By keeping $q_a \approx 3.4$ constant, all the discharges of this series had the $q = 1$ radius at ≈ 5 cm with $R_0 = 72$ cm. It then follows

$$S = 1.74 \times 10^5 \frac{B_0^2[T]}{V_{loop}[V]\sqrt{n_e[10^{19}\mathrm{cm}^{-3}]}\sqrt{m_i/m_p Z_i}} .$$

For ohmically heated discharges in RTP the loop voltage V_{loop} is always ≈ 2 V. Therefore it is possible to vary S by varying the magnetic field B, the electron density n_e and the majority ion species. In Table 1 examples of these three possibilities are given. They lead to a variation of S between 0.8 and 2.3×10^5. Within the operational constraints of RTP it was not possible to obtain a wider range in ohmically heated discharges. However, with 400 kW of ECR heating at the second harmonic electron resonance frequency, the loop voltage could be reduced by a factor two, thereby reaching the highest S value of this series, 3.5×10^5.

Table 1. Main plasma parameters of analyzed discharges.

	heating method	B (T)	$T_e(0)$ eV	$n_e(0)$ $10^{19}\,\mathrm{m}^{-3}$	$p_e(0)$ (kPa)	V_{loop} (V)	S	duration (ms)
#21.042	H (ohmic)	2.05	900	2.8	4.0	1.9	2.3×10^5	0.5
#21.052	H (ohmic)	1.495	560	4.6	4.2	1.8	1.0×10^5	1.2
#22.042	He (ohmic)	2.04	830	6.4	8.7	2.5	0.8×10^5	1.5
#21.044	H (ECRH)	2.05	1400	4.3	10.0	1.0	3.5×10^5	0.6

As it can be seen from this table the absolute central electron pressure varied within a factor 2.5. The inclusion of the ion pressure to obtain the total pressure can be made by multiplying the electron cyclotron pressure with roughly a factor 1.5. It has been checked if indeed the pressure profile shape has been preserved. Figures 1 and 2 show that the pressure profile shapes were indeed identical for all cases. Also the inversion radius of all four cases indicated that the $q = 1$ radius was kept constant at ≈ 5 cm.

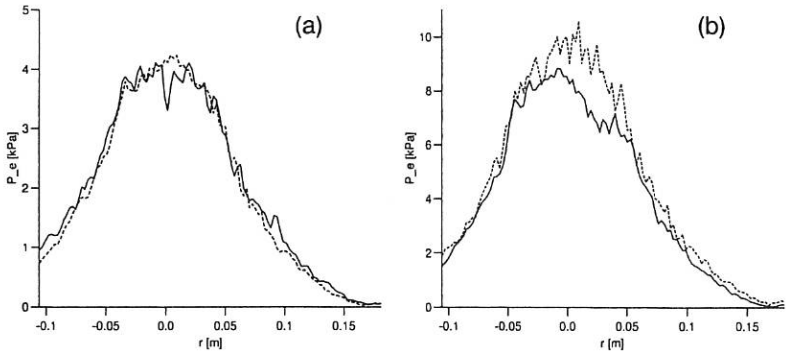

Fig. 1 *Electron pressure profile measured by Thomson scattering at 200 ms of (a) two H plasmas with different S values (# 21.052, $S = 1 \times 10^5$, dotted line, and # 21.042, $S = 2.3 \times 10^5$, solid line). (b) the He plasma (# 22.042, $S = 0.8 \times 10^5$, solid line) and a H plasma with ECRH (# 21.044, $S = 3.5 \times 10^5$, dotted line).*

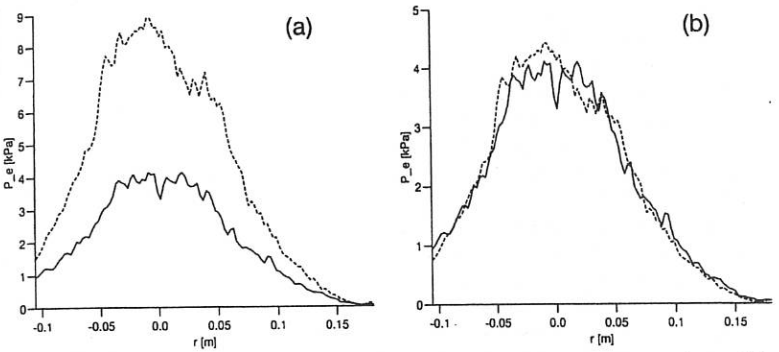

Fig. 2 *(a) Electron pressure profile measured by Thomson scattering at 200 ms, of one of the H plasmas of Fig. 1 (# 21.042), solid line, and a He plasma (# 22.042), dotted line. (b) same as (a), normalized to* $P_e(0)$ *of (# 21.042).*

Discussion of results

In Fig. 3 the uncalibrated brightness of the channel of the side camera of the SXR system (tangent to the $q = 1$ radius) are given in sequence of increasing S value for the four cases of Table 1. From raw data it is already apparent that the precursor behaviour at low S values is much more pronounced and appears as a regular oscillation whilst at high values the precursor is irregular. The pressure difference is seemingly not relevant as there are considerable pressure differences between the discharges of Table 1 (Figs. 1 and 2).

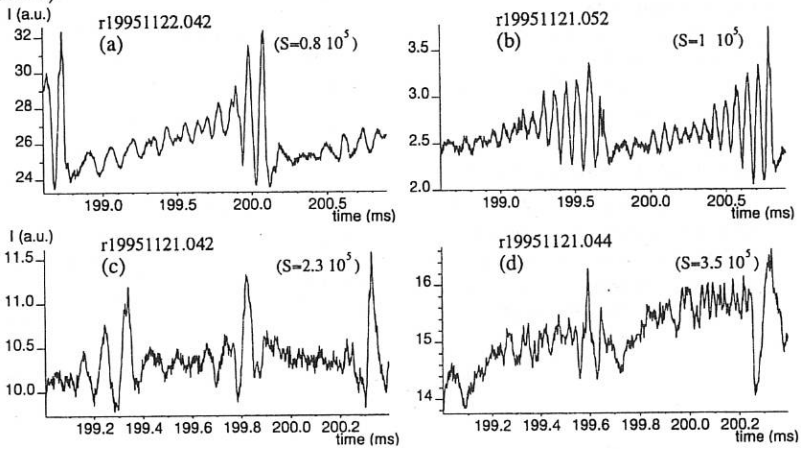

Fig. 3 *Signals of SXR detector a07 (impact parameter* $p = 3$ *cm) for different discharges.*

Subsequently, the enthalpy H has been calculated from the tomograms, as described in [2], in order to detect reconnection. From this four cases only the one with the lowest S number showed evidence of magnetic reconnection before the sawtooth crash. The discharge with the highest S value shows no reconnection before the crash. Also in this aspect the absolute pressure value does not appear to have a large influence. The analysis of other cases than the ones given in Table 1 yields a similar pattern: resistive ohmic discharges with low S tend to show $m = 1$ with reconnection whilst ECRH heated discharges with high S values tend to behave according to an ideal MHD model. However these cases have all different $q = 1$ radii and profile shapes. Therefore more statistics should be gained before a firm conclusion on the role of S can be drawn.

A different but interesting observation, which might be related to the difference between reconnection and ideal MHD behaviour, can be made from the sawtooth duration column in Table 1. There appears to exist an inverse proportionality between S and this duration. This might indicate that the early development of the islands by reconnection in the sawtooth rise phase diminishes the tension in the magnetic configuration such that it takes longer to reach the sawtooth crash. Also this aspect deserves more analysis in the future.

Conclusions

Measurements have been conducted to determine the influence of resistivity on the development of the sawtooth instability. With increasing values of the magnetic Reynolds number S, in the range $0.8 - 3.5 \times 10^5$, the $m = 1$ precursor instability of the sawtooth crash changes from a magnetic reconnection behaviour towards ideal MHD behaviour. This transition does not seem to be influenced by the absolute pressure value. With increasing value of S the duration of the sawtooth diminishes. Firmer conclusions could be drawn in the future if a similar analysis is done on a larger class of sawtooth crashes.

Acknowledgments

Egbert Westerhof is acknowledged for very useful discussions. This work was performed under the Euratom-FOM association agreement with financial support from NWO and EURATOM and with support from an INTAS agreement.

References

[1] C.P. Tanzi, Ph.D. Thesis, Utrecht, 1996

[2] C.P. Tanzi and H.J. de Blank, "New method to analyse internal disruptions with tomographic reconstructions", submitted to Physics of Plasmas, and C.P. Tanzi, H.J. de Blank and the RTP team, "Estimate of magnetic reconnection in sawtoothing RTP plasmas by means of soft x-ray tomography", Proc. of the 22nd EPS Conf. on Contr. Fusion and Plasma Phys. (Bournemouth, 1995), Part II-029.

MODIFICATION OF PLASMA CONFINEMENT USING RESONANT HELICAL FIELD ON IR-T1 TOKAMAK

A. ABBASPOUR, M.GHORANNEVISS, and M.MASNAVI

Plasma Physics Research Centre of (I.A.U.)
P. O. BOX: 14835-159, Tehran, Iran.
Tel: 0098-21-4404198, Fax: 0098-21-260099

ABSTRACT

Effects of programmed resonant helical fields (RHFs) were studied during discharge of the IR-T1 Tokamak. Sawtooth and Mirnov oscillations are observed and their characteristics are analyzed. Also, the intensity of visible line emissions from oxygen (OII), carbon (CIII)-impurities and (Hα) have been measured with and without RHF. Diagnostic methods included soft X-ray (SXR), visible spectrometer and magnetic probes.

I.INTRODUCTION

IR-T1 is a small air core transformer tokamak without a copper shell and divertor. The major and minor radii of tokamak are 45 and 12.5 cm, respectively. The plasma parameters in our experiments were: Ip=15-40 kA, Vloop≈2.6-8 V, Bt = 6- 9kG, ne=(0.7 -3.0)× 10^{13} cm^{-3} ,Te(0)= 150-250 eV, t discharge =18-23 ms, Zeff <2 and safety factor q=2-4. The ordinary diagnostics are soft x-ray (SXR) detectors, electron cyclotron emission (ECE), visible spectrometer, HCN far infrared (FIR) laser interferometer and electromagnetic measurement systems .

Weak external helical fields can act as local resonant disturbances in a tokamak plasma. Such fields can therefore be used as "active magnetic probes" in the study of magnetohydrodynamic (MHD) instabilities in tokamak plasmas. For this purpose, ℓ=2 and ℓ=3 helical windings have been installed on the IR- T1. In these experiments the resonant helical fields (RHFs) are weak, the total current through the ℓ=2 and ℓ=3 helical winding is between 120-350 A, compared with a plasma current of 15-40 kA, and the magnitudes of the RHFs are normally about (0.5-0.01%) of that of the poloidal field (Bθ) around the resonant surface. The pulse length and the magnitude of the helical windings could be programmed.

II. DESCRIPTION OF INSTRUMENT

In these experiments, The main diagnostics used for the MHD studies are; an array Au-Si detector, a visible spectrometer and Mirnov probes located at different toroidal positions .The raw data were sent to a data acquisition computer through a common A/D CAMAC system and then analysed by a central computer.

A. Soft x-ray system

The soft x-ray measurement system for IR-T1 includes a detection chamber, an array silicon surface-barrier detector (SBD), an electrical discharge filter circuit, and a data collection system. An array SBD is located at a place facing the center of the vacuum chamber; the end detectors are capable of detecting soft x-ray signals from different parts other than the center of the chamber. The detector array, which is placed at horizontal location, consists of 23 silicon barrier diodes.

B. Visible spectrometer

The profiles of visible line emissions from the OII (λ=4416 Å,configuration:$2p^2 3s$-$2p^2 3p$) and CIII(λ=4647 Å,configuration:2s3s-2s3p)- impurities and Hα(λ=6563 Å) line are determined using visible spectrometer, in which there is a two-lens image system in front of the spectrometer entrance slit and a multichannel optical fiber attached to its exit slit. The detectors in the system are photomultipliers.

C. Helical Windings

There are helical windings with optimized geometry installed closely outside the vacuum chamber (ℓ=2 ,ℓ=3). The radii of these two helical windings are 22 and 23 cm, respectively.

III. RESULTS

Fig. (1-a) shows variation of plasma current versus time while Fig.(1-b) is the signal of Mirnov coil at (θ=0). We observe that the amplitude of Mirnov coil signal at flat top (8-15 ms) is smaller than the rise and the fall priod of plasma current. This can be attributed to high poloidal field fluctuation[1,2].

Fig.(2-a and b) show a 20% decrease in the amplitude of Mirnov coil when the RHF is on. The expanded profiles of three chanels of Mirnov coils at three angles(θ = 0, θ = 45 and θ = 90) with RHF show a phase shift in signals, which disappear after RHF is applied(Fig.3-a and b).

A very intersting point is that a weak RHF could significantly influence sawtooth processes and thereby change the global thermal properties of the plasma.The ℓ = 2 RHF (Iℓ ≈300-350 A) could increases the amplitude and ramp-up of sawtooth oscillation (Fig.4). This amplification correlates with an improvement in plasma confinement, such as a decrease of the thermal conductivity, and an improvement in particle confinement. The fluctuations in the SXR emission from the hot plasma core are mainly due to two processes, i.e. the m=1/n=1 oscillation and the m=0/n=0 sawtooth oscillation. On IR-T1, there are two kinds of discharges with different SXR signals. For the first kind there is only a 19-25 kHz oscillation, and for the second kind there is very clear sawtooth oscillation in the SXR signals[3,4,5,6,7].

Fig.(5) shows the signals of the soft x-ray array versus time with (a) ℓ=3, (b) ℓ=2 and (c) without RHFs, respectively. From the soft x - ray signals it has been found that the amplitude and the frequency of the sawtooth also be influenced by so weak ℓ = 2 or ℓ = 3 current. The RHFs are effective only when their magnitudes are chosen to be near critical values; when the RHF is too low, there are no observable changes in any of the diagnostic signals. For the ℓ=3 current (120-160 A) seems enlarge the sawtooth and ℓ=2 current suppress it.The periods prolong from 200μs-300μs. The crash time of the sawtooth is 35μs- 45μs[8].

The spectral visible line emissions of the light impurity ion were investigated in the IR-T1. Figures (6-a,b), (7-a,b) and (8-a,b) shows the measurement results of visible line emissions of OII, CIII-impurities and Hα with and without RHF (ℓ=2), which the plasma pulse duration being slightly different for each shot. The visible line emissions of light impurities (OII and CIII) and Hα held a plateau while RHF was on for 3 to 17 ms. The visible line emissions from both oxygen and carbon impurities was about 1/3-1/2 of its original values. The line emissions of OII and CIII-impurities increased over the whole plasma. We noticed that, the Hα radiation behaved differently from OII and CIII-impurities during the RHF period, it rose in the first 1-3 ms and immediately decayed to its original value[9].

IV. CONCLUSION

When we apply the resonant helical field (RHF) the amplitude of this Mirnov signals is decreased and the phase shift between the signals at different angles disappeared.The stability properties of the discharge are improved by RHFs and also by the suppression of mode signal at soft x-ray (SXR) diodes. The ℓ= 2 RHF ($l\ell \approx$300-350 A) could amplify the sawtooth oscillation but changes the period a little and also, suppresses m = 1 fluctuations.

This RHF could increase the amplitude, and ramp-up of sawtooth oscilation. This amplification correlates with an improvement in plasma confinement, such as a decrease of the thermal conductivity, and improvement in particle confinement. For the ℓ=3 ($l\ell \approx$120-200 A),it seems that the sawtooth enlarges and ℓ=2 current suppress it. RHF (ℓ=2) enhanced the impurities line (e.g. OII and CIII) emissions but, The Hα radiation did not be enhanced by RHF.

REFERENCES

[1]Equipe TFR, *Nuclear Fusion*, Vol.18, No.5, pp 647-730,1978.

[2]Huchinson, I.H., *Principles of Diagnostics*, Chapter 2, 1981.

[3]Chen Jiayu, *Nuclear Fusion*, Vol. 30, No.11, pp 2271-2284,1990.

[4]Huang rong, Xie Jikang, *Academia Sinica, ASIPP*/126, pp1-10, Jan.1991.

[5]Xie Jikang, *modification of Sawtooth behavior using RHF on HT-6B Tokamak*, proc. 14th Euro. conf. Madrid, Vol. 11D part 1 , 221, 1987.

[6]Xie Jikang and et al, *plasma physics and controlled nuclear fusion research*, Vol.1, IAEA-CN-47/A-V-6,1986.

[7]Zhaoa Qingchu, *plasma physics and controlled nuclear fusion research*, Vol.1, 1985.

[8]HT-6B Group, Institute of Plasma Physics, Academia Sinica, Hefei, *12th Europ. Conf. Budapest*, 1985.

[9]Y.P. Huo, *Small plasma physics experiments II*, ICTP Trieste, IAEA, pp52 - 89, May 15 - June 9,1989.

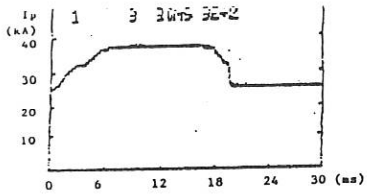

Fig.(2-a):Plasma current with (RHF).

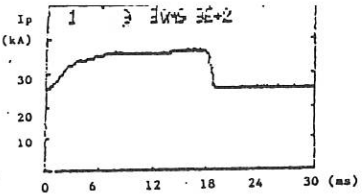

Fig.(1-a):Plasma current without(RHF).

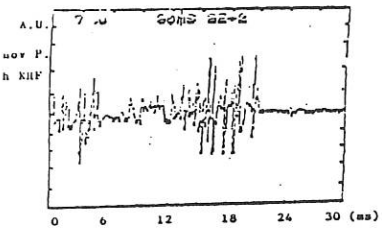

Fig.(2-b):Mirnov signal with (RHF).

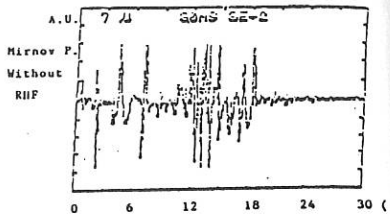

Fig.(1-b):Mirnov signal at (θ=0) without (RHF).

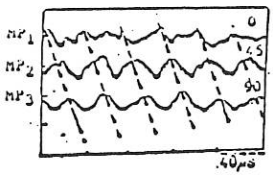

Fig.(3-a):Expanded profiles of MP without (RHF).

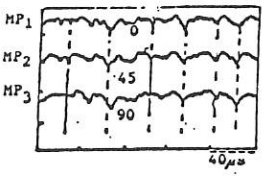

Fig.(3-b):Expanded profiles of MP with (RHF).

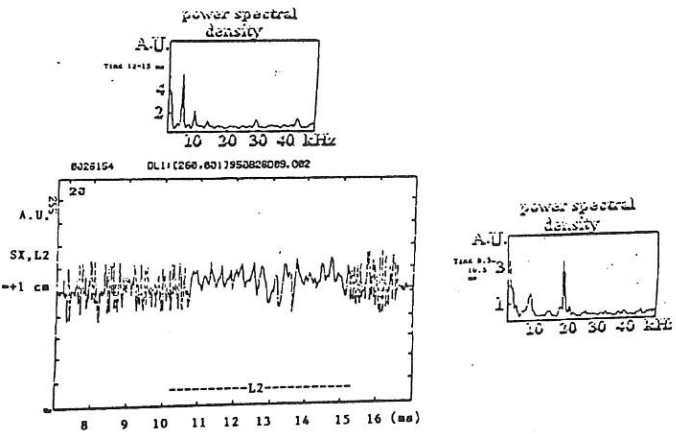

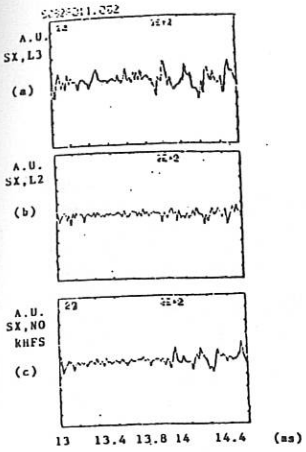

g.(5):Sawtooth behavior with RHFs,curves from he top are SXR at +3 cm,(a) with ℓ=3, (b) ℓ=2 and (c) without RHFs.

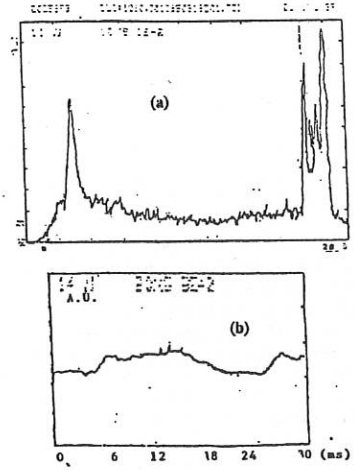

Fig.(6):Line emission signals of OII (+3.56 cm) (a) without and (b)with ℓ

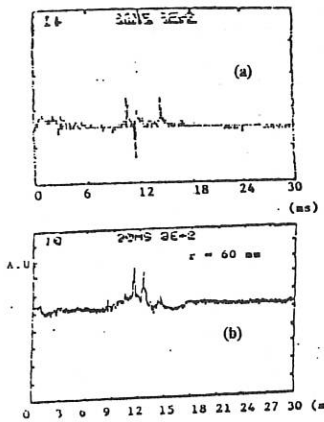

Fig.(7):Visible line emissions CIII (+3.56 cm) (a) with and (b) without ℓ=2.

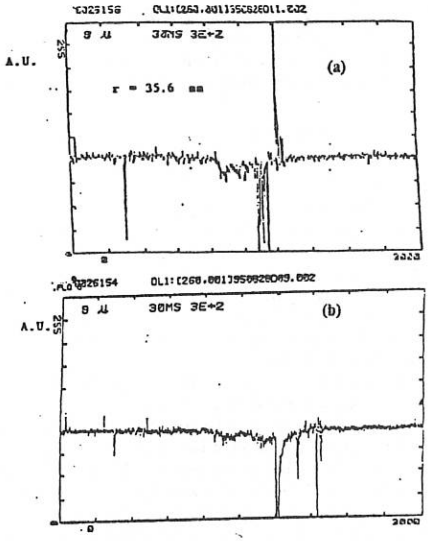

Fig.(8):Visible line emissions Hα(+3.56 cm) (a)with and (b)without ℓ = 2

Pellet disturbed plasmas in the RTP Tokamak

J. de Kloe, J. Lok, M. N. A. Beurskens, J. F. M. van Gelder,
B. de Groot, G. M. D. Hogeweij, A.A.M. Oomens, and the RTP Team
FOM-Instituut voor Plasmafysica 'Rijnhuizen', Association Euratom-FOM,
P.O. Box 1207; 3430 BE Nieuwegein, The Netherlands

Introduction

On RTP we have the possibility to measure temperature, density and pressure profiles with high spatial accuracy using our Thomson scattering (TS) setup. This gives unique opportunities to gain more insight on the process of pellet ablation and the reaction of the plasma to pellet injection.

In this paper we concentrate on one outstanding problem: precooling. The process of pellet ablation is often assumed to be adiabatic (the kinetic energy content of the plasma remains constant) and local (the flux surfaces not crossed by the pellet trajectory remain unperturbed). Experimentally violations of these assumptions are reported [2, 5, 6, 8, 10], and known as the precooling effect, i.e. a cold front propagates radially through the plasma with a velocity larger than the pellet speed. Several types of precooling have been reported. First a small but very fast cooling of the plasma centre when the pellet is still at the edge. Second a very sudden large drop of temperature in the plasmacenter when the pellet reaches a certain position outside q=1. Third a cooling front moving faster than the pellet after it has crossed the q=1 surface. We try to determine wich type of precooling occurs in RTP using various diagnostics like the ECE radiometer and TS.

If ECE observations are used, one has to be very careful in interpreting the signals as temperatures, since other effects, like refraction, could play an important role. This is investigated by a comparison of ECE profiles with high temporal resolution (2 μs), as measured by an antenna viewing from the low field side (LFS) and one viewing from the high field side (HFS), and TS profiles with high spatial resolution (1% of the plasma minor radius). It is shown that in these experiments an apparent precooling phenomenon is caused by a small region in the plasma in which the EC-cut-off density is exceeded (i.e. $\omega^+ > 2\omega_{ce}$). Furthermore that for small pellets a precooling of the second kind, i.e. a sudden drop of the temperature in the plasma center, as seen in ref. [5], at least outside the q=1 surface, does not occur. For large pellets TS profiles show precooling only when the pellet is inside the q=1 surface [3].

Experimental setup

The measurements in RTP have been done under the conditions: $R_0 = 0.72$ m, $a = 0.164$ m, $I_{pl} = 80 - 120$ kA, $B_T = 1.5 - 2.2$ T, central density $n_e = 1.5 - 5.0 \times 10^{19}\mathrm{m}^{-3}$, central temperature $T_e = 0.6 - 0.9$ keV, edge safety factor $q_a = 3.6 - 7.3$, H_2 plasmas and boronized vessel. The pellet injector was built by the Risø National Laboratory [9]. The pellet velocity and time of arrival are measured with two optical detectors when the pellet is in free flight. The pellet mass is measured using a microwave resonance cavity. The emitted H_α radiation is measured with a photomultiplier, and used to estimate the ablation rate. Earlier results of experiments with this equipment have been reported in [3] and [7]. For this investigation H_2 pellets with a particle content of 0.5×10^{19} atoms, which is comparable to the particle content of the plasma, and $v_p \approx 1000$ m/s have been used. The pellets have been injected in the stationary phase of an ohmic discharge and the effects were observed with the following diagnostics: a TS setup, which yields T_e, n_e, and p_e at 118 points along a vertical chord through the plasma center, with a spatial resolution of 1.7-2.5 mm at one point in time [1]. The laser of the TS system can be fired during the ablation process on a pre-programmed position of the pellet. In this way the reaction of the plasma to the pellet can be scanned. The radiation temperature ($T_{e,rad}$) of the plasma is measured with an ECE radiometer (2nd harmonic X-mode, 20 channels, time resolution 2 μs, spatial resolution 7-16 mm in the radial direction, spacing between 2 subsequent channels about 20 mm in the plasma center) [4]. The $T_{e,rad}$ profile is measured along a horizontal chord either from the LFS or the HFS of the plasma. The density profile is measured with an interferometer viewing vertically through the plasma along 19 chords (time resolution 16 μs). The toroidal angle between the pellet injector and the ECE-radiometer (LFS and HFS), the TS setup and the interferometer is 30°, 60°, and 120°, respectively, all in the electron drift direction.

Measurements

The $T_{e,rad}$ profiles observed from the LFS with the radiometer are plotted in Fig.1a. The instants at which the pellet is at the limiter radius and the magnetic axis are indicated by arrows and vertical dashed lines. The projection of the pellet trajectory on the flux surfaces is indicated by the diagonal dashed lines. The pellet penetrated 14 cm into the plasma, thus up to r = 2.4 cm. A sudden drop in this signal is seen when the pellet is halfway the plasma at r≈9 cm. After that, the plasma seems to be very cold for a while (less than 50 eV), except for 2 channels on the HFS.

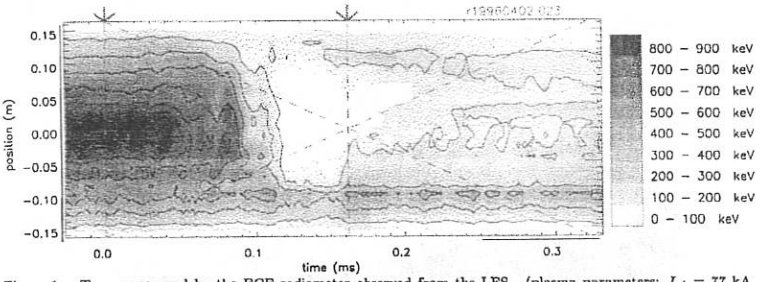

Figure 1a: $T_{e,rad}$ measured by the ECE radiometer observed from the LFS . (plasma parameters: I_{pl} = 77 kA, B_T = 2.2 T, $T_{e,0}$ = 0.9 keV, $n_{e,0} = 2.4 \times 10^{19} m^{-3}$, q_a = 5.4) The arrows indicate when the pellet passes the limiter radius and the magnetic axis (ignoring its lifetime). The projection of the pellet trajectory is indicated by the oblique dashed lines. The time is set to zero when the pellet passes the limiter.

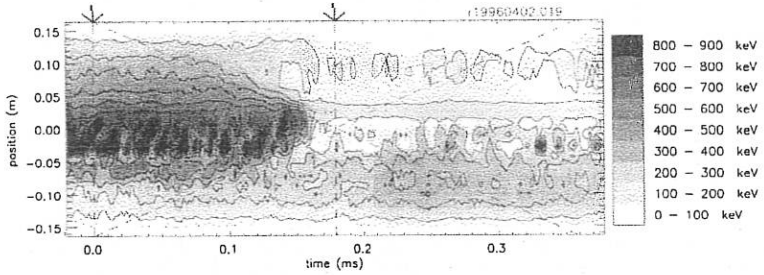

Figure 1b: As Figure 1a for a similar discharge, but now the plasma is observed from the HFS.

$T_{e,rad}$ profiles as observed from the HFS for similar pellet and plasma parameters are plotted in Fig.1b. In this case the sudden drop in the signal when the pellet is halfway the plasma is not seen. There could be a precooling effect inside the q=1 surface (between -3 and 3 cm) but the ECE measurements do not resolve this because of the limited spatial resolution.

During the short interval ($\leq 400\mu s$) of the ablation itself, a series of TS profiles under similar conditions was measured. An example of these profiles is plotted in Fig.2. Here the horizontal bars indicate the flux surfaces crossed by the pellet. When these profiles for a series of successive pellet positions in the plasma are plotted as a function of time, Fig.3 is obtained. The diamonds indicate the positions where a Thomson profile was taken.

Interpretation

On first sight the sudden drop in $T_{e,rad}$ in Fig.1a cannot be accounted for by too high a density cutting off the ECE-signals because the maximum increase in density as seen on the TS profiles or on the interferometer profiles is not large enough. However, if these $T_{e,rad}$ profiles are compared with $T_{e,rad}$ profiles measured from the HFS in Fig.1b, it is clear that $T_{e,rad}$ only drops for those

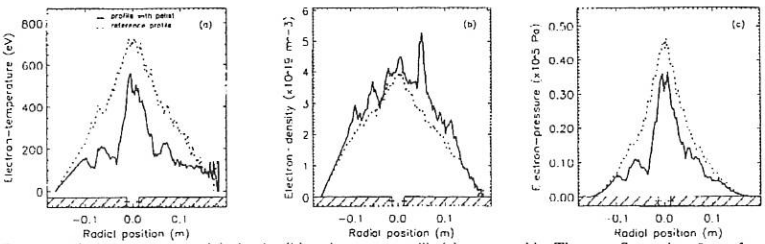

Figure 2: Plasma temperature (a), density (b) and pressure profile (c), measured by Thomson Scattering, 2 μs after the end of pellet ablation. The penetration depth is up to r=3.0 cm. The left part of the profiles between -0.1 and -0.164 m is an extrapolation and not measured. (Note that the centers of these profiles do not exactly correspond to the magnetic axis due to a Shafranov shift of about 1 cm)

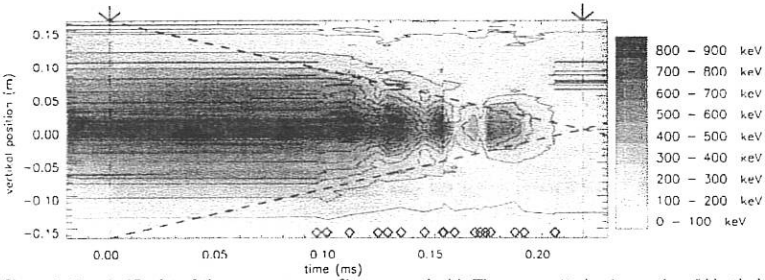

Figure 3: Pseudo-2D plot of the temperature profiles measured with Thomson scattering in a series of identical discharges. The diamonds indicate the time at wich the profiles were taken. Plotted in between are values obtained from a linear fit.

flux surfaces that have been crossed by the pellet trajectory. The TS temperature scan (Fig.3) confirms the $T_{e,rad}$ profiles as measured by the HFS ECE during the ablation. The irregularities inside q=1 in Fig.3 are most probably caused by the not quite reproducible plasma and pellet parameters from shot to shot, which makes it difficult to conclude something about precooling.

The first 200 μs after the end of the ablation the central temperature is of the order of 200 eV according to the TS measurement, which is in contradiction with the LFS ECE measurements. For the LFS measurement most channels are affected by cut-off. For the HFS-ECE measurement the channels between -0.05 and -0.15 m seem to give the right temperature, indicating that the density perturbations affect mainly the LFS of the measured chord.

The density perturbation at the position of the radiometer antennae is estimated to explain this cut-off. It is assumed that the ablatant travels along the magnetic field lines, that the ablation cloud has a poloidal extension in the order of 1 cm, and that the ablatant is uniformly distributed over the flux-tube between the pellet trajectory and a shock front. Furthermore the H_α signal is assumed to be proportional to the ablation rate. For a small pellet with 0.5×10^{19} atoms, the maximum electron density perturbation at the poloidal cross-section of the radiometer is $\approx 2 \times 10^{21} \mathrm{m}^{-3}$ when the ablatant passes this cross-section for the first time. After the ablatant has travelled around the torus once, the material is spread over a roughly 10 times larger volume, so the second time the perturbation passes the poloidal cross-section of the radiometer it has a density of $\approx 2 \times 10^{20} \mathrm{m}^{-3}$. This density is large enough for all channels of the radiometer to go in cut-off. This effect is shown in Fig.4. Shown in Fig. 4a are 2 measured profiles and 1 artificial density profile with a high peak at the edge, which are used to calculate the cut-off frequencies shown in Fig. 4b. The dashed line indicates $2\omega_{ce}(r)$ which determines the position of the $T_{e,rad}$ measurement.

If the geometry is such that the ablatant passes the viewing line of the radiometer antenna within 1 or 2 toroidal turns (which is the case in our tokamak for the LFS antenna, but not for the HFS antenna), then cut-off can be expected. However, it should be noted that when larger pellets

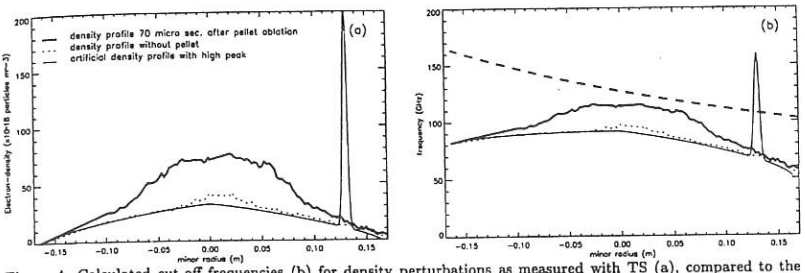

Figure 4: Calculated cut-off frequencies (b) for density perturbations as measured with TS (a), compared to the expected cut-off due to a local peaking of the density.

are used the cut-off effect can cause problems after much more than a few toroidal rotations, so the geometry should always carefully be considered.

Due to the geometry in the RTP setup it is impossible in the case of relatively small pellets to see the high density peak at the outer part of the plasma with the TS setup, since it takes several toroidal rotations of the ablatant to get into the viewing line of TS.

The reason that these short density perturbations are usually not seen on interferometer profiles is twofold:

- these measurements are in most tokamaks often taken relatively long after pellet injection ($300-400\mu s$), which gives the local perturbation time to spread over the whole flux-surface;
- interferometers measure line-integrated densities. For RTP a very localised perturbation, for example a peak of $\approx 1 \times 10^{20} m^{-3}$ with a width of only 1 cm, on a profile with central density of $\approx 5 \times 10^{19} m^{-3}$ would give a change in the interferometer signal of no more than 5 % .

If we accept the HFS measurement as shown in Fig.1b to be true temperatures we can say that strong precooling at least outside the q=1 surface does not occur. Due to the noise in these signals we can not draw conclusions on a small precooling in the center when the pellet is still in the outer regions of the plasma.

ECE measurements for larger pellets ($\approx 2 \times 10^{19}$ atoms) give the same results, except that the cut-off at the LFS antenna occurs even earlier (when the pellet has only penetrated 2 to 3 cm). Some TS profiles for larger pellets are available, and these show precooling when the pellet is inside the q=1 surface [3]. A systematic scan of the ablation process for these pellets with the TS setup will be the subject of future studies.

Acknowledgement

This work was performed under the Euratom-FOM association agreement, with financial support from NWO and Euratom.

References

[1] C. J. Barth et al., Rev. Sci. Instrum. 63 (10) 1992, p. 4947-4949.
[2] A. D. Cheetham et al., 14th EPS conf., Madrid 1987, Vol. 11D, part 1, p.205-208
[3] D. F. da Cruz et al., Phys. Rev. Letters, 75 (20), 1995, p.3685-3688
[4] J. F. M. van Gelder et al., Rev. Sci. instrum. 66 (1), 1995, p.416-418
[5] W. Liu et al., Nucl. Fusion, 34 (3), 1994, p.337-347
[6] S. L. Milora et al., Nucl. Fusion, 35 (6), 1995, p.657-754, chapter 4.2
[7] A. A. M. Oomens et al., proc. 22nd EPS conf. 1995, Bournemouth, Vol. 19C, part 1, p.129-131
[8] M. Sakamoto et al., Plasma Phys. and Contr. Fusion, 33 (6), 1991, p.583-594
[9] H. Sørensen et al., Proc. 17th symp. on Fusion Technology 1992, Rome 1992, Vol. 1, p.647-650
[10] TFR group, Nucl. Fusion, 27 (12), 1987, p.1975-1999, chapter 3.

FEEDBACK CONTROL OF THE CURRENT PROFILE ON TORE SUPRA

T. Wijnands, G. Martin, D. Van Houtte, P. Froissard, X. Litaudon, M. Tareb

Association EURATOM-CEA
Département des Recherches sur la Fusion Contrôlée
Centre d'Etudes Cadarache, 13108 Saint Paul-lez-Durance, France

1. Introduction

The TORE SUPRA (TS) tokamak (circular limiter plasmas with major radius R<2.40 m, minor radius a<0.79 m) is especially designed for long pulse operation in which plasmas have been sustained for up to 2 minutes. During long pulse operation, the plasma current is partially or fully driven by Lower Hybrid (LH) waves. During steady state operation, the flux on the plasma boundary is constant (V_{loop}=0) so that no ohmic power flows from the transformer to the plasma.
A new plasma control system [1] has allowed to operate TS in a steady state scenario in which two separate feedback loops are used simultaneously : one to control the flux on the plasma boundary (ϕ_{plasma}) by varying the voltage on the ohmic power supply (V_{OH}) and the other to control the plasma current (I_p) by a variation of the LH power (P_{LH}) .

$$P_{LH} = \alpha \Delta I_p$$
$$V_{OH} = \beta \Delta \phi_{plasma} \qquad (1.1)$$

With this scenario, TORE SUPRA has sustained steady state plasmas for up to 70 seconds [2] (figure 1) operating at B_t=3.9 T, $\langle n_e \rangle$ = 1.7 $10^{19} m^{-3}$, I_p=0.65 MA while the average LH power is about 3 MW.
However, control of the flux on the plasma boundary and the total plasma current alone is not always sufficient to access and sustain a steady state plasma.
First, 'sawtooth like' MHD instabilities located in the plasma core [3] can cause a sudden decrease of the plasma pressure (Te_0 crash form 9 to 5 keV) and the formation of magnetic islands. The reduction of current drive efficiency can then terminate the pulse. Particular ohmic initial conditions in combination with pre-selected values of the parallel index of the LH waves ($n_{//}$) have been used to cope successfully with this problem.
Second, in the fully non inductive driven phase, the current density profile can change in shape and the plasma can access to a regime of Enhanced Performance ($H_{RLW}=W_e/W_{e\text{-}RLW}$=1.3-1.8). This 'hot electron mode' is characterised by a sharp increase of the electron temperature in the centre of the plasma (from typically Te_0=5 to 9 KeV) together with a flattening of the q-profile ($q_0 \approx 1.5$ while q_a=7) and a high internal inductance l_i (l_i=1.6-1.8). However, unforeseen events like influx of impurities, bad coupling of the LH power or variations of the plasma density can change the current profile shape again and terminate the phase of Enhanced Performance. Thus, in order to make a long pulse in a LH driven steady state Enhanced Performance mode, it is required to have a control of the current profile.
Therefore, the steady state operating scenario has been extended with a feedback control of the global shape of the current density profile by changing the phasing between two adjacent modules of the LH grill :

$$\delta\phi = \gamma \Delta l_i \qquad (1.2)$$

The current profile is characterised by its internal inductance l_i, defined as $l_i = \langle B_\theta^2 \rangle / B_\theta^2$ and derived in real time from the magnetic measurements. The suprathermal contribution to the total presure is <5% so that l_i has only an error of a few per cent. The Δl_i represents the difference

between the desired and measured value of l_i : $\Delta l_i = l_i^{ref} - l_i$. The phasing $\Delta\phi$ between two adjacent modules of the LH grill results in a variation of the parallel index (n//) of the launched LH waves. The feedback loop varies the phasing between the modules of the LH grill with respect to a fixed, preset value so that $\Delta\phi = \Delta\phi^{fixed} + \delta\phi$. The $\delta\phi$ are limited to $|\delta\phi| \leq 45°$ in order to avoid bad coupling of the LH power.

2. The role of n// in Steady State

When TORE SUPRA is operated at reduced plasma density and current (B_t=4T I_p=0.75 MA and $\langle n_e \rangle$=1.6 $10^{19}m^{-3}$), the LH waves are only weakly damped and travel many times around the torus before being damped out. In this so called 'multi-pass regime', the rays become sufficiently stochastic to fill up the phase space accessible to them [4]
Thus, in order to control the location of the LH power deposition in a steady state discharge, we have to change the shape of the domain in which the LH waves propagate. At constant current and constant electron density, this can be achieved in two different ways : i) variation of the n// of the launched LH wave spectrum ii) variation of the q-profile.
Both experiment and theory have shown that the q-profile has a strong influence on the localisation of the absorption of the LH power : peaked current profiles tend to have a central deposition of the LH power, while flat or even hollow current profiles have an off axis power deposition. On the other hand, in the theoretical case of a fixed plasma equilibrium, the variation of n// from 1.4 to 2.2 will change the wave propagation domain only weakly, since the ray behaviour in a mutli-pass regime is stochastic.
In the steady state experiments presented here, these two effects are always coupled. Therefore one has to realise that the LH current drive efficiency changes with n//. This was experimentally confirmed by operating at different (but fixed) n// at V_{loop}=0 and I_p=0.8 MA using scenario (1.1). Figure 2 a shows that current drive efficiency varies as $(n//)^{-1}$. This is different from the theoretical predictions about the current drive efficiency in a simple single pass regime where the current drive efficiency varies as $(n//)^{-2}$.
Thus, in our experiments, a variation of the launched wave spectrum (n//) results in a variation of the total LH power. The variation of the plasma pressure and the magnetic equilibrium fields change the wave propagation domain as well as the location of the absorbed LH Power. Then, the current profile will change its shape. From a large number of steady state equilibria at B_t=4T I_p=0.75 MA and $\langle n_e \rangle$=1.6 $10^{19}m^{-3}$ it is observed that the internal inductance l_i varies with the n// of the launched LH waves (figure 2 b) : increasing n// leads to an increase of l_i.
The variation of the wave propagation domain with n// and the q-profile is also observed during the transition of the plasma from an ohmic to a steady state phase. In the ohmic phase, the current profile is characterised by an $l_i \approx 1.4$ while $q_o \approx 1.1$ (I_p=1 MA, q_a=5), while purely LH driven plasmas at I_p=0.8 MA have current profiles with $l_i > 1.6$ and $q_o > 1.2$ and q_a=7 (figure 3). Thus, as soon as the loop voltage is fixed to zero, the current density profile starts to change its shape towards a pure LH current profile. If $q_o > 1.5$ during the transition, magnetic reconnection events are systematically observed in the plasma core. This can be avoided by ramping the plasma current down prior to application of any LHCD. Then, only LHCD at n//=1.6-1.8 leads to sufficient peaking the q profile so that $q_o < 1.5$ (figure 4). This is again in contradiction with the simple condition of Electron Landau Damping (ELD) $n//T_e^{1/2}[keV] > 6.5$ in a single pass regime which would lead to much more pronounced flattening of the q-profile.

3. Feedback control of l_i with n// in Steady State

Real time variations of n// have allowed for experiments with feedback control of the current density profile in steady state plasmas for the first time on TS. Figure 5 shows a steady state discharge in which the plasma current, the flux on the plasma boundary and the internal inductance are controlled simultaneously. The flux on the plasma boundary is constant from 5 seconds onwards (i.e. V_{loop}=0). Initially, there is no LHCD present, so that a resistive L/R decay of the plasma current begins. In this process the current profile is peaked, which is visible as a rapid increase of the internal inductance. Peaking of the current density profile is required in

order to get smooth access to the steady state regime (see section 2). At 5.5 seconds, LHCD is switched on and the feedback control regulates the LH power in order to keep the plasma current constant at I_p=0.75 MA. With the variation of the current profile the plasma enters a regime of Enhanced Performance in which $H_{RLW}=W_e/W_{e\text{-}RLW}=1.4$.

The pre-programmed value of the phasing between the LH modules in this shot is set to $\Delta\phi^{fixed} = -40°$ (i.e. n//=1.7). Initially, the measured l_i is below its reference value (dotted line, bottom figure) so that the feedback (1.2) responds by increasing $\Delta\phi$ (increase of n//). Then, at 16 seconds, l_i is required to vary in a stepwise manner from l_i=1.70 to 1.50. The feedback loop reacts with a rapid decrease of $\Delta\phi$ thereby briefly saturating at $\Delta\phi$ =-85°. The rapid decrease of $\Delta\phi$ leads to increase of the current drive efficiency so that the LH power is reduced in order to keep the plasma current constant. The variations of $\Delta\phi$ also results in a decrease of the plasma pressure and the central electron temperature, measured by the ECE radiometer.

Directly after the variation of $\Delta\phi$, at 16 seconds, the current profile starts to change its shape. The internal inductance is slowly reduced to $l_i \approx 1.55$ while q_o (interfero-polarimeter) is increased. A new steady state equilibrium is reached about 10 seconds later. The $\Delta\phi \approx -60°$ (n//≈1.5) while $l_i \approx 1.55$ and $q_o \approx 1.45$. A small decrease of the enhanced energy confinement is observed.

In this example, there is a finite difference between the desired and the measured internal inductance. This partly due to the use of pure proportional control, but also due to the fact that the variety of profile shapes in a steady state discharge with LH current drive alone is limited. Too much flattening of the q-profile for example, leads systematically to the onset of magnetic reconnection events in the plasma core if $q_o > 1.5$ (q_a=7) (see next section).

Conclusion

At reduced plasma current and density, the shape of the current profile has been controlled successfully by varying the n// of the LH waves. The variation of the q-profile has probably a large influence on the location of the LH power deposition. At $q_a \approx 7$, a physical limit to the shape of the q-profiles has been observed, formulated as $q_o < 1.5$. Further increase of q_o leads systematically to the onset of 'sawtooth like' MHD activity in the plasma core. Further experiments have to be carried out at other plasma currents and densities. Electron Cyclotron heating and on line determination of q_o are foreseen for the 1997 campaign.

References :

[1] WIJNANDS, T., MARTIN, G., EUR-CEA-FC-1573, January 1996.
[2] WIJNANDS, T., MARTIN, G., to be published in Nuclear Fusion (1996).
[3] TURLUR, S., *et al.*, Contr. Fusion & Pl. Heating (Proc. 22nd EPS Bournemouth, 1995)
[4] LITAUDON, X., *et al.*, to be published in Pl. Phys. and Contr. Fusion, 1996.

Figure 1 (top left) : 70 seconds long pulse steady state operation with LHCD.

Figure 2a (top right top) : Experimentally observed Current drive efficiency in steady state discharges.

Figure 2b (top right bottom) : Experimental observed variations of l_i (average values, deduced from a large number of steady state experiments) as a funcyion of n//.

Figure 3 (middle left) : Current profiles in a pure ohmic and a fully LH driven plasma.

Figure 4 (middle right) : Transition from ohmic to steady state : n//=1.7 and no ramp down (diamonds) gives MHD acitivity, similar to ramp down and n//= 1.9 (triangles, squares). Only ramp down with n//=1.7 keeps $q_o < 1.5$ and provides MHD stable access to steady state (closed circles).

Figure 5 (bottom) : Feedback control of the internal inductance l_i in a steady state LH driven plasma through real time control of the n// of the launched LH waves. At 16 seconds, the reference curve for l_i (dotted line) is varied from 1.7 to 1.5.

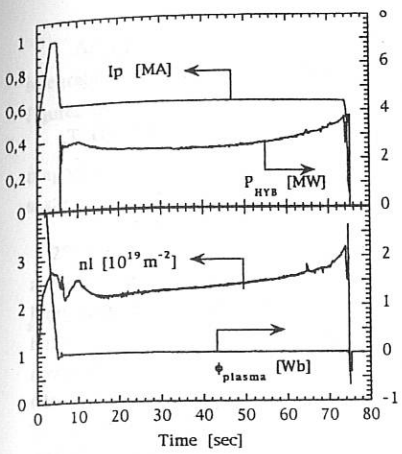
Ip [MA]
P HYB [MW]
nl [10^19 m^-2]
φ plasma [Wb]
Time [sec]

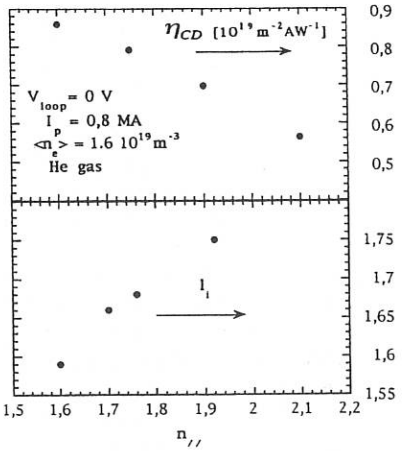
η CD [10^19 m^-2 AW^-1]
V loop = 0 V
I p = 0,8 MA
<n e> = 1.6 10^19 m^-3
He gas
l i
n //

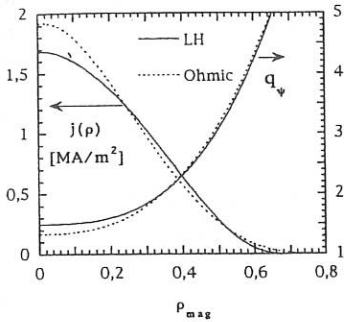
LH
Ohmic
q ψ
j(ρ)
[MA/m^2]
ρ mag

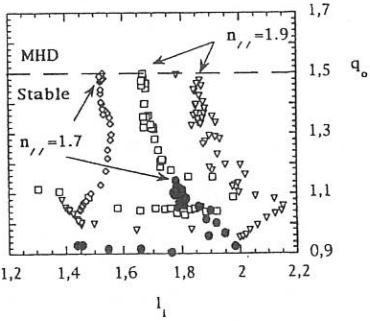
MHD
Stable
n // =1.9
n // =1.7
q o
l i

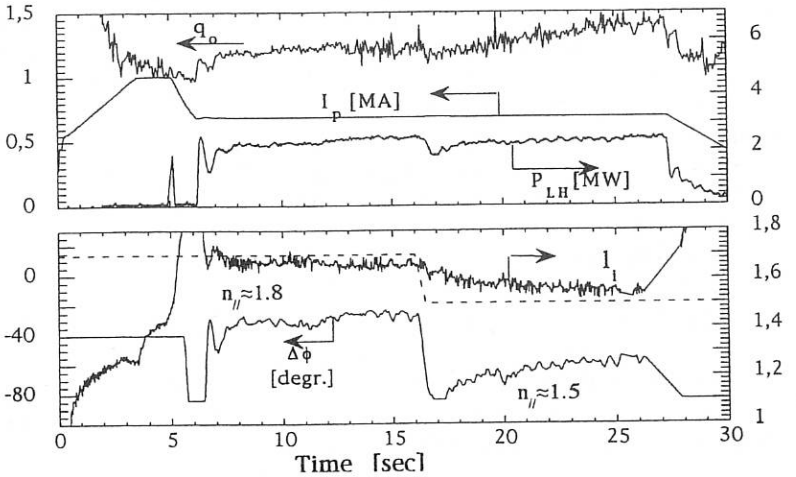
q o
I p [MA]
P LH [MW]
l i
n // ≈1.8
Δφ
[degr.]
n // ≈1.5
Time [sec]

Parametric Analysis of Internal Magnetic Fluctuations in the TORE SUPRA Tokamak

COLAS L., ZOU X.L., PAUME M., CHAREAU J. M., GUIZIOU L., HOANG G. T., GRÉSILLON D.*
Association Euratom-CEA sur la fusion contrôlée, C.E. Cadarache, 13108 Saint Paul lez Durance France
* Laboratoire PMI, École Polytechnique, 91128 Palaiseau - France

Internal small-scale magnetic turbulence is a serious candidate to explain the anomalous heat transport in tokamaks. This turbulence was measured on Tore Supra with an original diagnostic: Cross Polarisation Scattering (CPS) [1]. Measured fluctuation levels were found compatible with observed electron heat diffusivities. Strong correlation was observed between the CPS signal increase and global confinement degradation during radio frequency (RF) heating. In this paper the magnetic fluctuation behaviour is analysed over a wide range of plasma current, density and RF power. A scan of plasma density or magnetic field is used to move the CPS measurement location from $r/a = 0.3$ to $r/a = 0.75$. A fluctuation radial profile is thus obtained by these two different means. In L-mode discharges, the relation between magnetic fluctuations, temperature profiles and local heat diffusivities is investigated. With all measurements, we attempted to find a simple local driving parameter for the turbulence in a large domain of plasma conditions.

1°) Description of the CPS diagnostic and operating conditions.

The cross-polarisation scattering (CPS) diagnostic relies on the eigenmode change of a probing polarised microwave beam scattered by magnetic fluctuations [1,2], close to a cut-off layer for the incident wave. Two scattering scenarios can be chosen, $O + \tilde{B} \rightarrow X$ or $X + \tilde{B} \rightarrow O$, depending on which eigenmode is reflected in the plasma. Both theoretical considerations [3-5] and experimental indications [1] suggest that the CPS process is strongly amplified in the cut-off region, which provides a spatial localisation in that area for the scattered signal. The working frequency is 60 GHz ($k_0 \approx 12.57$ cm^{-1}), and the fluctuation wavenumber selected by the Bragg resonance condition at the cut-off layer is $\tilde{k}_{r_c} = k_0$; $\tilde{k}_\theta \approx 0$. The data acquisition system of the diagnostic includes :

- a 4 MHz heterodyne detection, providing turbulence spectra at selected times.
- a signal S_{300}, monitoring the component at 300 kHz (± 10 kHz) of the scattered spectrum.

The magnetic fluctuation spectral component at $\tilde{k}_{r_c}$ is evaluated from the S_{300} signal through several steps:

- The CPS power is proportional to S_{300}, once a Doppler effect is corrected. This Doppler shift is due to the poloïdal plasma rotation at the cut-off position.
- Using a 1D scattering model defined in [1], the CPS source term at $\tilde{k}_{r_c}$ is then deduced from the CPS power. In this model the measured CPS power is proportional to a scattering volume size defined by L_n, the density gradient length at the cut-off layer.

An estimate for $(\delta B/B)^2$ values (±100%) is infered from the CPS source term by integrating over a k-spectrum assimilated to a square box ($\Delta k_r = \Delta k_\theta = \tilde{k}_r$). The errorbars in all figures account for the dispersion of S_{300}, and for the uncertainty on L_n.

Without special mention, typical plasma conditions in these experiments were : toroïdal magnetic field $B_0 = 3.7$ T, major radius $R = 2.32$ m, minor radius $a = 0.75$ m, helium gas, scattering scenario $O + \tilde{B} \rightarrow X$.

2°) Radial profile of magnetic fluctuations.

A set of ohmic shots was carried out with three current plateaus (I_p= 0.7, 1.0 and 1.3MA) at fixed volume average density $\langle n_e \rangle$. $\langle n_e \rangle$ was scanned shot by shot from 2.2×10^{19} to 5.2×10^{19}m^{-3}. Thus the O-mode cut-off layer location (determined by a local density $n_e = 4.47\times10^{19}$ m^{-3}) was shifted from $r/a = 0.3$ to $r/a = 0.75$. In this density domain the energy confinement time is found constant, i.e. we are in the SOC regime.

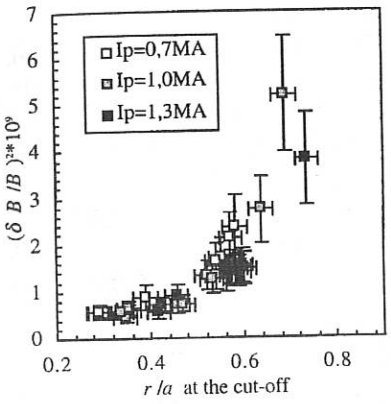

Fig.1 : *Magnetic turbulence profile derived from O→X measurements.*

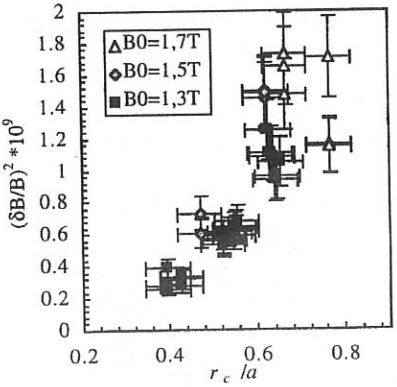

Fig.2 : *Radial variation obtained in experiments with X→O configuration.*

Within instrumental errorbars, the measured turbulence levels show no clear dependence on I_p, and strongly increase with $\langle n_e \rangle$. This behaviour can be attributed *a priori* to a radial variation of $(\delta B/B)^2$ for different locations of the cut-off, or to a parametric dependence on $\langle n_e \rangle$. In the first case a fluctuation radial profile in the gradient region can be derived from cut-off positions. Figure 1

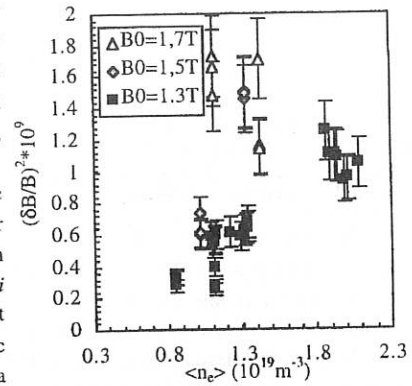

Fig. 3 : *fluctuation levels in X→O experiments, versus $\langle n_e \rangle$ for several B_0.*

shows that $(\delta B/B)^2$ is a growing function of r/a , with an 9-fold increase between r/a = 0.3 and r/a = 0.7.

To discriminate between radial and parametric dependence, experiments were conducted at low $\langle n_e \rangle$ and B_0 with the X→O CPS scenario. The incident X-mode cut-off layer was moved either by sweeping B_0 or $\langle n_e \rangle$. The results are shown on the figure 2. Note that whatever B_0, observed radial variations have similar features, which are consistent with that reported in the figure 1. Interpreting the X→O results in terms of a parametric dependence on B_0 or $\langle n_e \rangle$ is more difficult, since turbulence levels are sensitive to small parameters changes (see Figure 3). These indications lead to attribute the major variation of the observed $(\delta B/B)^2$ to the fluctuation radial profile.

3°) Magnetic fluctuations and transport in L-mode.

A series of experiments was carried out with Ion Cyclotron Resonance Heating (ICRH, minority heating scenario) and Lower Hybrid (LH) waves heating. The plasma conditions are: I_p = 1.3MA, $\langle n_e \rangle = 3.5\times10^{19}$ m^{-3}. The additional power was scanned from 1 to 3 MW with four 1 second steps. Density profiles remained unchanged throughout the shots, and thus also L_n and the cut-off position (r/a = 0.55).

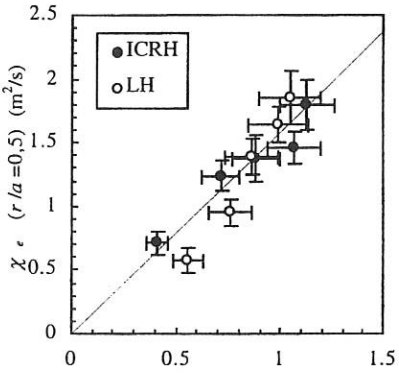

Fig. 4. *Heat diffusivities determined by transport analysis, compared to those expected from magnetic fluctuations.*

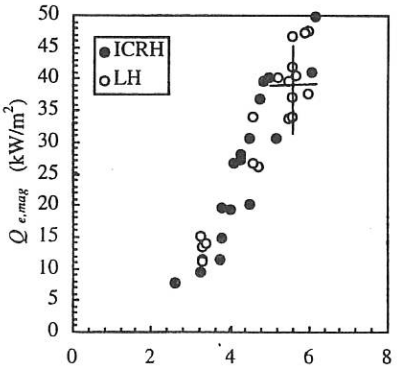

Fig. 5 : *Quasilinear estimate of fluctuation induced heat fluxes $Q_e=n_e\chi_e\nabla T_e$, versus ∇T_e at the cut-off layer.*

In these experiments, $(\delta B/B)^2$ measured at the gradient region strongly rises with the additional heating power. This increase can be attributed to a steepening of the temperature profile, which was the only plasma feature significantly modified by RF application. Correlation can be found between $(\delta B/B)^2$ and either ∇T_e or $\nabla T_e/T_e$ at the cut-off. In the same time, the additional heating causes an increase of the local electron heat diffusivity χ_e at half radius, that can be explained by a temperature profile peaking. On the figure 4, χ_e determined from profile analysis [6] is plotted versus diffusivities expected from magnetic turbulence levels

through the non-collisionnal quasilinear formula [7]: $\chi_e^{mag} = \pi q R \nu_{th} (\delta B / B)^2$. Note that both diffusivities have similar behaviours with additional heatings and the same order of magnitude. A factor of 1.5 is found between χ_e^{mag} and actual χ_e. This difference can be originated in the uncertainty of various parameters in the expression of χ_e^{mag} : the correlation length πqR, $(\delta B/B)^2$ measured for one component at $k = \tilde{k}_r$, etc. As illustrated on the figure 5, the local heat flux calculated from magnetic turbulence depends linearly on ∇T_e with a critical gradient close to that observed in transport studies [6].

4°) Discussion and conclusions.

Three major observations can be drawn from these experiments :

- Sweeping the cut-off layer positions has allowed to estimate, by two different means, a radial profile of magnetic fluctuation. The profiles obtained in the two cases have compatible shapes : $(\delta B/B)^2$ strongly increases radially towards r/a=0.7.
- A large increase of the turbulence levels is observed with additional heating, that can be linked to the deterioration of local and global confinements in L-mode. The magnetic turbulence-induced heat fluxes estimated by the non-collisionnal quasi-linear formula exhibit a linear dependence on ∇T_e, with a threshold. This critical gradient is very close to that obtained by local transport analysis.
- If the turbulence is assumed to be local, all experimental results obtained in this paper should reflect the variation of a local plasma parameter at the cut-off position. This parameter should increase radially, and be weakly dependent on I_p in the SOC regime. It should also involve the local shape of the temperature profile. Several simple plasma parameters were tested over the whole O→X database. Among these parameters, a good correlation is found with either the temperature gradient length L_{Te} (see fig.6) or the pressure gradient length L_P. Empirical relations show a threshold, which is to be linked to the critical gradient observed in RF-heated discharges.

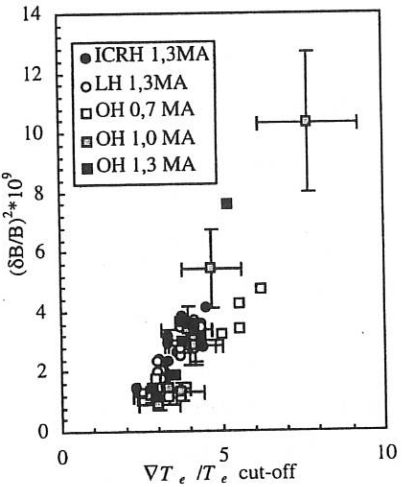

Fig.6. *Compilation of all the O→X results as a function of L_{Te} at the cut-off.*

[1] : Zou X.L. *& Al.* : *Physical Review Letter* **75** vol. 6 (1995) p.1090
[2] : Lehner T., Rax J.-M. & Zou X.L. : *Europhys. Letter* **8** (8) 1989 p.759
[3] : Zou X.L., Laurent L. & Rax J.-M. : *Plasma Phys. Control. Fusion* **33** 903
[4] : Bruskin L.G., Mase A. & Tamano T. : *Plasma Phys. Control. Fusion* **36** 681
[5] : Bruskin L.G., Mase A. & Tamano T. : *Plasma Phys. Control. Fusion* **37** 255
[6] : Devynck P. *& Al.* : *Proc. 22nd EPS Conference, Bournemouth* (1995) *IV-101*
[7] : Rechester A.B. & Rosenbluth M.N. : *Phys. Rev. Letter* **40** (38) 1978

GLOBAL ENERGY CONFINEMENT TIME SCALING DERIVED FROM THE LOCAL REBUT-LALLIA-WATKINS TRANSPORT MODEL

J. Johner, J. Villar Colomé
Association Euratom-CEA sur la Fusion
CEA Cadarache, 13108 Saint-Paul-lez-Durance, FRANCE.

1. Introduction

The Rebut-Lallia-Watkins (RLW) local transport model [1] is implemented in the PRETOR transport code [2]. This transport model is characterized by a critical temperature $\nabla T_{e,crit}$ above which the thermal diffusivity is independent of the temperature (except through a gradient length dependence). Such a model is known to result in a global energy confinement time with an offset-linear dependence with respect to the total heating power.

Comparison of PRETOR calculations of the energy confinement time with the offset-linear RLW scaling for the global confinement time [3] exhibits quantitative and sometimes qualitative disagreement.

Starting from the steady state local transport formulation for both electrons and ions, we show that, assuming a constant T_e/T_i ratio, and a flat Z_{eff} profile, transport for $|\nabla T_e| \gg \nabla T_{e,crit}$ can be described by a single fluid equation. Taking the local RLW expressions for anomalous electron diffusivity and for the χ_i/χ_e ratio, and for given density and external heating profiles, the incremental global energy confinement time expression may be analytically derived except for a universal function $C_\tau(A, \alpha_n, \alpha_P)$ where A is the torus aspect ratio and α_n, α_P the peaking factors for the density and the heating profiles, respectively.

An analytical expression is also derived for the offset thermal energy content assuming that it corresponds to the energy content of the critical temperature profile.

2. The one fluid transport equation for $|\nabla T_e| \gg \nabla T_{e,crit}$

Summing the steady state radial transport equations for electrons and N ion species supposed to have the same temperature T_i and same thermal diffusivity χ_i, and using the following RLW assumption valid for $|\nabla T_e| \gg \nabla T_{e,crit}$

$$\frac{\chi_i}{\chi_e} = C_{\chi_{ie}} \frac{2T_e}{T_e + T_i} \frac{1}{(1+Z_{eff})^{1/2}} \frac{n_e}{n_{ion}}$$

where $n_{ion} = \sum_{j=1}^{N} n_j$ and $C_{\chi_{ie}}$ is a constant, we obtain the following one fluid transport equation for a large aspect ratio circular plasma

$$-\frac{1}{r}\frac{d}{dr}\left(r n_e k \chi \frac{dT_e}{dr}\right) = p_{ext} \tag{1}$$

where p_{ext} is the total external power density and χ is an effective thermal diffusivity defined as

$$\chi = \left[1 + \frac{C_{\chi_{ie}}}{(1+Z_{eff})^{1/2}} \frac{2\theta_{ie}}{1+\theta_{ie}}\right] \chi_e \qquad \text{with} \qquad \theta_{ie} = \frac{T_i}{T_e}$$

For $|\nabla T_e| \gg \nabla T_{e,crit}$, the RLW electron diffusivity is

$$\chi_e \simeq C_{\chi_{e,RLW}} \left(1 - \sqrt{\frac{\rho}{A}}\right) \left|\frac{1}{T_e}\frac{dT_e}{d\rho} + \frac{2}{n_e}\frac{dn_e}{d\rho}\right| \frac{q^2}{\left|\frac{dq}{d\rho}\right|} \left(\frac{T_e}{T_i}\right)^{1/2} \frac{(1+Z_{eff})^{1/2}}{B_t R^{1/2}} \quad \text{with } \rho = r/a$$

Supposing that T_e/T_i and Z_{eff} are approximately constant, assuming the following modelisation for the electron density and the external heating power profiles

$$n_e(\rho) = n_{e0}\left(1-\rho^2\right)^{\alpha_n} \qquad , \qquad p_{ext} = p_{ext,0}\left(1-\rho^2\right)^{\alpha_P}$$

where the 0 subscript is used for central values, and supposing a Spitzer like resistivity $\eta = \eta_0 Z_{eff}/T_e^{3/2}$, the q profile at equilibrium (radially constant electric field) may be computed as a function of T_e and Eq. (1) for decreasing temperature profiles may be written as

$$\frac{\rho^2}{1-(1-\rho^2)^{1+\alpha_P}}\left(1-\sqrt{\frac{\rho}{A}}\right)n_e^*\left(\frac{1}{T_1}\frac{dT_1}{d\rho}+2\frac{n_e^{*\prime}}{n_e^*}\right)\frac{dT_1}{d\rho}-\frac{1}{\rho^2}\int_0^\rho T_1^{3/2}(\rho')2\rho' d\rho' - T_1^{3/2}(\rho)=0 \quad (2)$$

where T_1 is a normalized temperature, $n_e^* = n_e/n_{e0}$, and the prime denotes differentiation with respect to ρ.

The above integral equation for T_1 is only a function of A, α_n, α_P. It may be shown to be equivalent to a second order differential equation for $y_1 = T_1^{1/2}$. However, for the form of the density profile that we consider and the zero edge temperature condition, this equation for y_1 may be shown to exhibit a numerical singularity for $\rho = 1$. This problem is solved by introducing the variable $u = 1-(1-\rho)^{1-\alpha_n/2}$. The resulting equation for $y_1(u)$ is regular. Its solution is obtained by a Runge-Kutta shooting integration of the differential equation obtained for the function $\beta(u)$ defined by the relation $y_1(u) = (1-u)\beta(u)$ and which can be shown to have a finite value and a zero slope for $u = 1$.

3. Expression for the incremental energy confinement time

From the above model, the incremental electron energy confinement time $\tau_{Einc}^{(e)}$ may be shown to be

$$\tau_{Einc}^{(e)} = \frac{\mu_0}{4\pi}\frac{1}{C_{\chi_{e,RLW}}}C_\tau(A,\alpha_n,\alpha_P)\frac{\theta_{ie}^{1/2}}{(1+Z_{eff})^{1/2}+C_{\chi_{ie}}\frac{2\theta_{ie}}{1+\theta_{ie}}}I_p R^{3/2} \quad (3)$$

with

$$C_\tau(A,\alpha_n,\alpha_P) = \frac{3}{T_{10}^{1/2}}\frac{\int_0^1 n_e^*(\rho)T_e^*(\rho)2\rho d\rho}{\int_0^1 T_e^{*3/2}(\rho)2\rho d\rho} \quad (4)$$

where T_{10} and $T_e^*(\rho)$ are given by the numerical solution of Eq. (2). The following fit is proposed for C_τ

$$C_\tau(A,\alpha_n,\alpha_P) \simeq \frac{1-\frac{\alpha}{\sqrt{3}}}{1-\frac{\alpha}{\sqrt{A}}}C_\tau(A=3,\alpha_n,\alpha_P) \quad (5)$$

with

$$C_\tau(A=3,\alpha_n,\alpha_P) = \begin{pmatrix} 1 & \alpha_n & \alpha_n^2 & \alpha_n^3 \end{pmatrix}\begin{pmatrix} 0.3290 & 0.2313 & -0.0316 \\ 0.0366 & -0.1607 & -0.0007 \\ -0.3371 & 0.4856 & -0.0195 \\ 0.1016 & -0.4064 & 0.0542 \end{pmatrix}\begin{pmatrix} 1 \\ \alpha_P \\ \alpha_P^2 \end{pmatrix}$$

The fit for $C_\tau(A=3,\alpha_n,\alpha_P)$ gives a maximum error of 4% in the range of values $\alpha_n = 0 \div 1$ and $\alpha_P = 0 \div 1.5$. For the aspect ratios in the range $A = 2.6 \div 5$, the fit for $C_\tau(A,\alpha_n,\alpha_P)$ with $\alpha = 0.65797$ gives a maximum error of 10% for $A = 5$.

The above expression is to be compared with the incremental part of the global RLW confinement time expression, i.e. (SI units):

$$\tau_{Einc,RLW}^{(e)} = 1.2\times 10^{-8}\frac{1}{Z_{eff}^{1/2}}I_p R^{1/2}a \quad (6)$$

Comparing Eq. (3) and Eq. (6), we see that the plasma current dependence is the same. In contrast, the detailed dimension dependence as well as the Z_{eff} dependences are different. Moreover, the global RLW scaling exhibits no dependence on T_i/T_e, α_n and α_P.

4. Comparison with the PRETOR code

In order to check the validity of our scaling [Eq. (3)], we compare the values obtained for the incremental energy confinement time τ_{Einc} in the case $T_e \simeq T_i$ (giving $\tau_{Einc} \simeq 2\tau_{Einc}^{(e)}$), as calculated by the PRETOR code [with $\nabla T_{e,crit} = 0$, $C_{\chi_{te}} = 2$, $C_{\chi_{e,RLW}} = 2$, $Z_{eff} = 1$, $T_e(a) = T_i(a) \simeq 0$], using our scaling with the exact value of C_τ [as given by Eq. (4)], or the approximate fit proposed above, and using the global RLW scaling. Fig. 1 shows the variation with the aspect ratio, Fig. 2 the variation with the external heating peaking parameter α_P. Comparison of the electron energy confinement time when varying the plasma effective charge is presented in Fig. 3 .

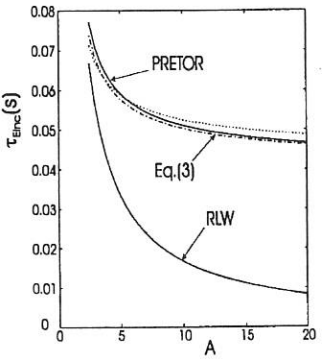

Fig. 1: Comparison of the incremental confinement time given by PRETOR (full line), our scaling [Eq. (3)] with the exact value for C_τ (dash-dotted line) or the proposed fit (dotted line), and the global RLW scaling (R=10 m, B_t=6 T, I_p=0.22 MA, Z_{eff}=1, $\theta_{ie} \simeq$1, α_n=0, α_P=0, variation of A obtained by varying a).

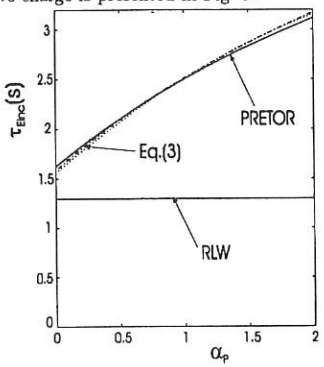

Fig. 2: Comparison of the incremental confinement time given by PRETOR (full line), our scaling [Eq. (3)] with the exact value for C_τ (dash-dotted line) or the proposed fit (dotted line), and the global RLW scaling (R=9 m, a=3 m, B_t=6 T, I_p=6 MA, Z_{eff}=1, $\theta_{ie} \simeq$1, α_n=0).

We see that our scaling reproduces the A, α_P as well as the Z_{eff} dependences given by the code and that it is numerically accurate.

5. Expression for the offset thermal energy content

Supposing that the offset thermal energy content is approximately given by the energy content corresponding to the temperature profile for which $|\nabla T_e| = \nabla T_{e,crit}$ at each point, and taking the RLW expression for $\nabla T_{e,crit}$

$$\nabla T_{e,crit} = C_{\nabla T_{e,crit}} \frac{1}{q} \left(\frac{\eta j B_t^3}{n_e T_e^{1/2}} \right)^{1/2}$$

the equation for the critical temperature profile may be shown to be

$$n_e^{*1/2} T_2^{1/4} \frac{dT_2}{d\rho} + \frac{1}{\rho^2} \int_0^\rho T_2^{3/2}(\rho') 2\rho' d\rho' = 0$$

where T_2 is a normalized temperature. The corresponding electron energy content is

$$W_{th0}^{(e)} = \frac{3}{2^{1/2}} \pi^{5/4} \mu_0^{1/2} k \eta_0^{1/4} C_{\nabla T_{e,crit}}^{1/2} C_{W_0}(\alpha_n)\, Z_{eff}^{1/4} I_p^{3/4} (\overline{n})^{3/4} B_t^{1/4} R^{3/2} a \qquad (7)$$

where

$$C_{W_0}(\alpha_n) = \frac{1}{T_{20}^{1/8}} \frac{\int_0^1 n_e^*(\rho) T_e^*(\rho) 2\rho d\rho}{\left[\int_0^1 n_e^*(\rho) d\rho \int_0^1 T_e^{*3/2}(\rho) 2\rho d\rho \right]^{3/4}}$$

The following fit, with an error below 1% in the range $\alpha_n = 0 \div 1.5$, is proposed for $C_{W_0}(\alpha_n)$

$$C_{W_0}(\alpha_n) \simeq 0.7730 + 0.2635\alpha_n - 0.2492\alpha_n^2 + 0.1326\alpha_n^3$$

The above expression for $W_{th0}^{(e)}$ is to be compared with the offset energy content given in the global RLW scaling, i.e. (SI units):

$$W_{th0,RLW}^{(e)} = 2.6 \times 10^{-13.25} Z_{eff}^{1/4} I_p^{1/2} (\overline{n})^{3/4} B_t^{1/2} R^{11/12} a^{11/6}$$

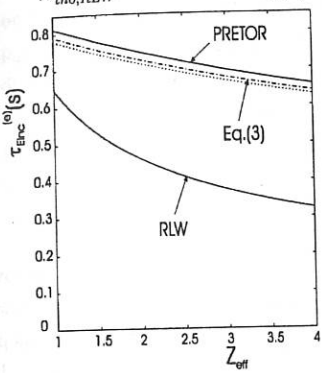

Fig. 3: Comparison of the incremental electron energy confinement time given by PRETOR (full line), our scaling [Eq. (3)] with the exact value for C_τ (dash-dotted line) or the proposed fit (dotted line), and the global RLW scaling (R=9 m, a=3 m, B_t=6 T, I_p=6 MA, $\theta_{ie} \simeq 1$, α_n=0, α_P=0).

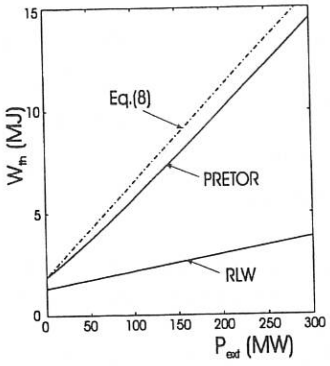

Fig. 4: Comparison of the energy content given by PRETOR (full line), our scaling [Eq. (8)], and the global RLW scaling (R=10 m, a=0.5 m, B_t=6 T, I_p=0.22 MA, $\theta_{ie} \simeq 1$, α_n=0, α_P=0).

Fig. (4) compares the total energy content as calculated by PRETOR, with the expression

$$W_{th}^{(e)} = W_{th0}^{(e)} + \tau_{Einc}^{(e)} P_{ext} \tag{8}$$

with $W_{th0}^{(e)}$ given by Eq. (7) and $\tau_{Einc}^{(e)}$ given by Eq. (3). We see that Eq. (7) describes the offset energy content with a very good precision. For large P_{ext}, the incremental energy confinement time is well described by Eq. (3).

6. Conclusion

Semi-analytical expressions have been derived from the local RLW transport model for the incremental electron energy confinement time ($\tau_{Einc}^{(e)}$) and the offset electron thermal energy content ($W_{th0}^{(e)}$) for circular plasmas. Comparison with the global RLW scaling shows important differences namely in dimension and profile dependences. With respect to the results of the PRETOR code, our scaling shows for arbitrary parameters much better agreement than the global RLW expression.

Effect of elongation and finite edge temperature will be considered in a subsequent paper.

References

[1] P.H. REBUT, P.P. LALLIA, and M.L. WATKINS, *Plas. Phys. & Contr. Nucl. Fus. Res.* (IAEA-CN-50/D-4-1), **2**, 63 (1989).

[2] D. BOUCHER, PhD Thesis, École Polytechnique de Paris (09/09/1992).

[3] N.A. UCKAN, "*ITER Physics Design Guidelines: 1989*", p. 36, IAEA, Vienna, 1990.

Scaling laws of turbulence in tokamaks

X. Garbet

Association Euratom-CEA sur la Fusion, Bat. 513,

CE Cadarache,13108 St Paul lez Durance, France

R.E. Waltz

General Atomics, P.O. Box 85608,

San Diego, California 92186-9784

I.Introduction

Several experimental studies of dimensionless confinement scaling laws are now available. As expected from usual turbulence theories, the scaling of the electron thermal diffusivity is gyroBohm, i.e. $\chi \equiv {}^{T}/_{eB}\, \rho_*^{\alpha}$, with α=1, where ρ_* is the ion Larmor radius ρ_s normalized to the minor radius a, T is the temperature and B the magnetic field [1]. In contrast, the ion scaling is found to vary from the Goldston regime (α=-0.5) through Bohm (α=0), up to gyroBohm (α=1), depending on plasma parameters. Several explanations have been proposed to explain this behavior. One of them relies on shear flow stabilization [2]. This effect can be understood as follows. Electric and diamagnetic shear stabilization induces a decrease of the growth rate γ, which is given by the relation $\gamma=\gamma_0-d/dr(V_*+V_E)$, where γ_0 scales as c_s/a (c_s is the ion thermal speed), and $d/dr(V_*+V_E)$ scales as $\rho_* c_s/a$ (V_* is the diamagnetic drift and V_E is the electric drift which is diamagnetic when there is no external momentum sources). Assuming that the correlation length scales as an ion Larmor radius ρ_s, a random walk argument leads to a diffusivity $\chi \equiv {}^{T}/_{eB}\, \rho_*(1-\alpha_*\rho_*)$. The latter scaling exhibits all possible coefficients α. Numerical simulations of Ion Temperature Gradient (ITG) turbulence confirm this picture, which holds when the temperature gradient is close to the threshold and ρ_* is large enough. In particular, the departure from gyroBohm scaling comes mainly from the breaking of the correlation time scaling, whereas the scaling of correlation lengths is gyroBohm. The purpose of the present study is to give some insight on this issue by analysing the turbulence signal with a Singular Value Decomposition. It is shown in particular that the principal spatial components are close to linear modes, called global modes, when a breaking of gyroBohm scaling is observed.

II. The model

The code which is used is based on a simplified model, which captures the main features of ITG turbulence [2]. Writing the relative density, pressure and potential fluctuations as

$\delta n/n(r)=(\rho_{s0}/a)\bar{n}$, $\delta p/p(r)=(\rho_{s0}/a)\bar{p}$, and $e\delta\phi/T(0)=(\rho_{s0}/a)\bar{\phi}$, each field is developed as a Fourier series, namely

$$[\bar{n},\bar{p},\bar{\phi}](r,\theta,\varphi,t)=\sum_{k=(m,n)}[n,p,\phi]_k(r-r_k,t)\exp\{i(m\theta+n\varphi)\} \qquad (1)$$

Throughout we use the time unit a/c_{s0}, where $c_{s0}=(T_e(0)/m_i)^{1/2}$ is the ion acoustic speed on the magnetic axis, the levels of fluctuation are normalized to $\rho^*=\rho_{s0}/a$, where $\rho_{s0}=m_ic_{s0}/eB$ is the central ion gyroradius on the magnetic axis. The parallel ion motion dynamics is expected to determine the radial structure of the poloidal and toroidal Fourier harmonics (m,n) through the magnetic shear. Here, these radial shapes are predetermined with a fixed model detailed below and thus the fast parallel ion motion is ignored. The moment equations for the gyrocenter density N_k and pressure P_k are given by

$$\frac{dN_k}{dt}=-i\varpi_k^*\left[(\hat{1}-\hat{\eta})\phi_{1k}+\hat{\eta}\phi_{2k}\right]+i(\varpi_D\phi_{12})_k+i\tau(\varpi_D P)_k \qquad (2)$$

$$\frac{dP_k}{dt}=-i\varpi_k^*\left[\hat{1}\phi_{1k}+\hat{\eta}\phi_{2k}\right]+\Gamma i\left(\varpi_D\phi_{12}\right)_k+\Gamma i\tau(\varpi_D P)_k+x_0\Gamma i\tau(\varpi_D(P-N))_k$$

where $N_k=\left[n_k+\tau\left(\phi_k-\phi_{1k}\right)/\hat{T}\right]$, and $P_k=\left\{p_k+\tau\left[\phi_k-(1/3)\phi_{1k}-(2/3)\phi_{2k}\right]/\hat{T}\right\}$ are related to the physical density n_k and pressure p_k, and ϕ_{1k}, ϕ_{2k} and $\phi_{12k}=(\phi_{1k}+\phi_{2k})/2$ are gyroaveraged potentials. Using the Padé approximates for the modified Bessel functions these are adequately represented by $\phi_{vk}=(1+b)^{-v}\phi_k$ where $b=\tau\rho_s^2k_\perp^2$, $\tau=T_i/T_e$, and $\rho_s(r)$ is the local ion Larmor radius and $\hat{T}$ is the electron temperature normed to the central temperature. The radius ranges between 0 and a, and $\varpi_k^*=\rho_{s0}m/\hat{r}$, $\hat{1}=(a/L_n)(r)$, and $\hat{\eta}=(a/L_{Ti})(r)$. The quasi-neutrality imposes $n_k=(\lambda\phi_k-i\delta_k\phi)/\hat{T}$ to represent the electron dynamics. The time derivative is defined as

$$\frac{d}{dt}=\frac{\partial}{\partial t}+i(m/\hat{r})v_E+\tilde{v}_E.\nabla-\mu_0-\mu_1\rho_s^2(m/\hat{r})^2-\mu_2\rho_s^4(m/\hat{r})^4 \qquad (3)$$

where v_E is the local ExB drift, μ_0, μ_1, and μ_2 are model damping parameters, the non linear ExB convection term is $\tilde{v}_E\cdot\nabla$.

Each (m,n) Fourier component is characterized by a combination of even and odd radial shapes W_k. These shapes are Gaussians centered on the resonant surface $r=r_{m,n}$. Their width w scale as the local gyroradius. For the n=0 radial modes, we have taken the radial functions to be given by sinusoidal forms. Details can be found in the reference [2].

III. Signal analysis

The SVD allows to decompose any signal $P_k(t)$ under the form

$$P_k(t)=\sum_{j=1}^{\min(k_{max},t_{max})}\lambda_jT_{kj}C_j(t) \qquad (4)$$

where the vectors T_j and C_j are sometimes called *topos* and *chronos* and constitute two sets of orthonormal functions [3]. The cases which have been chosen here correspond to $\rho_*=0.02$,

0.01, and 0.005. Ion thermal diffusivities normalized to the gyroBohm value ρ_*T/eB are found to be different (Fig.1). It is therefore clear that the scaling is not gyroBohm.

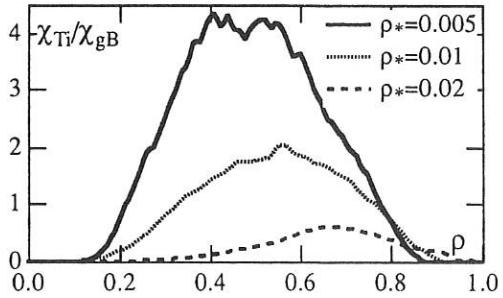

Fig.1: Ion thermal diffusivity normalized to the gyroBohm value $\chi_{gB}=\rho_*T/eB$

Figs.2 show the first topos and the first global eigenmodes for $n\rho_*=0.12$. It appears that these are close for large ρ_*, and different for small ρ_*. In practice, it is found that the correlation time normalized to a/c_{s0} depends on ρ_*, i.e. the simulation is dominated by long-lived global modes for small ρ_*. On the contrary, the scaling of the correlation lengths is mainly gyroBohm [2].

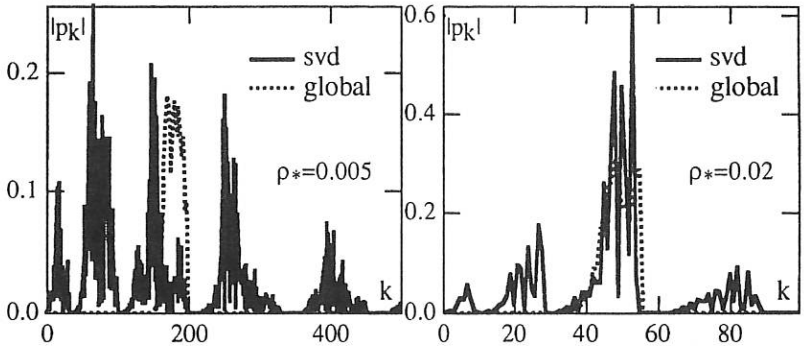

Fig.2: Comparison of the first topos (j=1)with the most unstable global mode $n\rho_*=0.12$

It may be surprising to find a correlation length which scales as a gyroradius whereas the spatial structure of the principal components is close to the linear global modes. This may be understood as follows. Let us assume that the topos are global modes, corresponding to a given toroidal number n and associated to even shape functions. The index k will now label the poloidal number. From numerical results, these global modes are of the form $\exp\{-k^2d^2/L^2+ik\theta_j\}$, where L scales as $\sqrt{\rho_s}$ (L>>w) and θ_j is the ballooning angle. A spatial correlation function is defined as $C(x)=\int P(0,t)P(x,t)dt \,/\, \int P^2(0,t)dt$ with

$$P(x,t)=\sum_j \lambda_j C_j(t) P_j(x) \quad ; \quad P_j(x)=\sum_k T_{kj} W_k(x)=\exp\left\{-\frac{x^2}{L^2}+i\frac{x\theta_j}{d}-\frac{w^2\theta_j^2}{4d^2}\right\} \qquad (5)$$

where d=1/nq' is the distance between two adjacent resonant surfaces and w is the width of the gaussian radial shapes $W_k(x)$.The correlation function is given by

$$C(x)=\exp\left\{-\frac{x^2}{L^2}\right\}\frac{\sum_j \lambda_j^2 \exp\left\{-\frac{w^2\theta_j^2}{2d^2}+i\frac{x\theta_j}{d}\right\}}{\sum_j \lambda_j^2 \exp\left\{-\frac{w^2\theta_j^2}{2d^2}\right\}} \qquad (6)$$

Two cases are possible. If only one global mode is excited, the correlation length is given by $L\equiv\sqrt{\rho_s}$. If a broad spectrum of λ_j is excited, and if θ_j varies smoothly with j, the expression (6) shows that C(x) is close to $\exp\{-x^2/2w^2\}$, i.e. the correlation length is given by $w\equiv\rho_s$. Fig.3 shows that the λ_j spectrum is flat, corresponding to a gyroBohm correlation length. Exceptions can be found when the temperature gradient is very close to the threshold and for large values of ρ_*. It can be seen indeed on Fig.3 that the eigenvalue spectrum is more peaked for a large ρ_*. On the other hand, the correlation time is clearly given by the function $C_j(t)$ which exhibits the largest characteristic time.

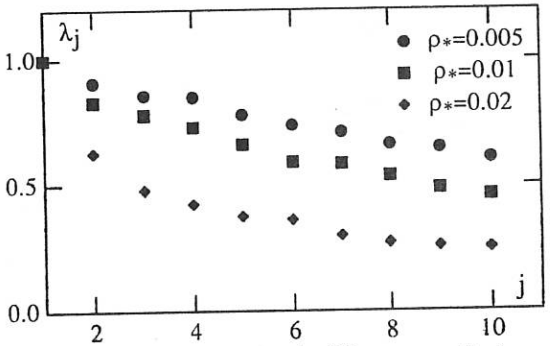

Fig.3: First 10 SVD eigenvalues for different gyroradii.

IV. Conclusion

A SVD analysis shows that global modes are present when a breaking of gyroBohm scaling is observed. These modes are long-lived structures, leading to a breaking of the correlation time scaling. The fact that several global modes are usually excited explains why the correlation lengths still scale as the ion gyroradius.

References

[1] C. C. Petty, T. C. Luce, et al. Phys. Rev. Lett. **74**, 1763 (1995).

[2] X. Garbet, R.E. Waltz, Phys. Pasmas **3**, 1898 (1996).

[3] N. Aubry, R. Guyonnet, and R. Lima, J. Stat. Phys. **64**, 683 (1991).

Diffusion processes in stochastic magnetic fields

M. Vlad, F. Spineanu, J. H. Misguich and R. Balescu[◇]

Association Euratom-CEA sur la Fusion, DRFC,
Centre d'Etudes de Cadarache, F-13108 Saint-Paul-lez-Durance, France

[◇]Association Euratom-Etat Belge sur la Fusion, Université Libre de Bruxelles, Belgium

A detailed study of the evolution of colliding particles in a stochastic magnetic field is presented. We analyse the effects on the effective diffusion coefficient produced: (a) by particle collisions, (b) by the stochastic drifts determined by the gradients of the magnetic field which are always present along a stochastic magnetic line, (c) by the macroscopic flows of the plasma (perpendicular and parallel to the confining magnetic field) and (d) by the time variation of the stochastic magnetic field. The study is based on analytical treatments of the Langevin-type equation that describes the guiding center approximation of particle motion.

The equations for the guiding centre trajectories are:

$$\frac{d}{dt}\underline{x}_\perp(t) = \underline{b}(\underline{x},t)\,\eta_\parallel(t) + \underline{\eta}_\perp(t) + \underline{v}_D(\underline{x}) + \underline{u}_\perp, \qquad \frac{d}{dt}z(t) = \eta_\parallel(t) + u_\parallel \tag{1}$$

where $B_0\underline{b}$ is a small stochastic component of the magnetic field which is perpendicular to the confining magnetic field $B_0\underline{e}_z$. Here $\underline{x}_\perp(t) = (x,y)$, $\eta_\parallel(t), \underline{\eta}_\perp(t)$ are the parallel and resp. the perpendicular collisional velocities, $\underline{v}_D(\underline{x})$ is the magnetic drift velocity that can be approximated as $v_{D_x} \cong -(V_T^2/\Omega)\partial b_y/\partial z$, $v_{D_y} \cong (V_T^2/\Omega)\partial b_x/\partial z$ (V_T is the thermal velocity and Ω is the gyration frequency). $u_\parallel$, $\underline{u}_\perp$ are the components of a deterministic (average) velocity which can be produced by an electric field perpendicular to the confining magnetic field or by any other flow of the plasma.

The following statistical properties of the collisional velocity are considered. $\eta_\parallel(t), \underline{\eta}_\perp(t)$ have zero average and are modelled by a Gaussian coloured noise:

$$\left\langle \eta_\parallel(t)\eta_\parallel(t')\right\rangle = \chi_\parallel \nu R, \qquad \left\langle \eta_\perp^i(t)\eta_\perp^i(t')\right\rangle = \chi_\perp \nu R \tag{2}$$

where $R \equiv \exp(-\nu|t-t'|)$, ν is the collision frequency of the plasma, $\chi_\parallel = V_T^2/(2\nu)$ is the (classical) parallel diffusion coefficient, $\chi_\perp = V_T^2\nu/(2\Omega^2)$ is the cross-field diffusion coefficient and $i = x, y$. The statistical properties of the stochastic magnetic field are modelled by means of the vector potential $\Psi(\underline{x},t)$ which is a Gaussian random field, spatially homogeneous, isotropic in the (x,y) plane and stationary. Its Eulerian autocorrelation function is taken as:

$$\langle \Psi(\underline{x}+\underline{r}, t+\tau)\,\Psi(\underline{x},t)\rangle = \beta^2\lambda_\perp^2 \exp\left[-\frac{r_z^2}{2\lambda_\parallel^2} - \frac{r_\perp^2}{2\lambda_\perp^2}\right] \exp\left[-\frac{|\tau|}{\tau_c}\right] \tag{3}$$

where β is the amplitude of the stochastic field, $\lambda_\parallel, \lambda_\perp$ are the correlation lengths along and resp. perpendicular to the unperturbed confining field and τ_c is the correlation time. The

effect of the nonlinearity is described by the parameter $\alpha \equiv \beta\lambda_\parallel/\lambda_\perp$. Our calculations apply to the quasilinear regime $\alpha < 1$.

Two methods are developed for dealing with the Langevin equations (1). The first [6, 7] is an exact method and applies when the stochastic perpendicular velocities determined by collisions and magnetic drifts can be neglected ($\underline{\eta}_\perp = 0$ and $\underline{v}_D = 0$ in Eq.(1)). In these conditions it is possible to determine the Lagrangian correlation of the perpendicular velocity $\underline{v} \equiv \underline{b}\eta_\parallel$ determined by particle motion along perturbed field lines:

$$L_{v_y}(t) = \frac{\beta^2\lambda_\parallel}{l_\parallel}\left[\chi_\parallel \nu R - \frac{\varphi^2}{l_\parallel^2} + u_\parallel^2\left(1+\frac{\varphi t}{l_\parallel^2}\right)^2\right]\exp\left[-\frac{u_\parallel^2 t^2}{2l_\parallel^2} - \frac{u_\perp^2 t^2}{2l_\perp^2} - \nu t\right] \tag{4}$$

$$L_{v_x}(t) = L_{v_y}(t)\left[1 - \frac{u_\perp^2 t^2}{l_\perp^2}\right] \tag{5}$$

where $l_\parallel^2 = \lambda_\parallel^2 + \left\langle (z(t) - u_\parallel t)^2\right\rangle$ and $\varphi(t) = \chi_\parallel(1 - \exp(-\nu t))$. The particle mean square displacement (MSD) $\Gamma(t) \equiv \left\langle \left(x(t) - \langle x(t)\rangle_{b\eta_\parallel}\right)^2\right\rangle_{b\eta_\parallel}$ and the time dependent diffusion coefficient are calculated as integrals of this function.

The second method [4, 6] is used for estimating the effects of the perpendicular collisional velocity and/or of the curvature drift velocity. The moments of the modification of the trajectory due to these small stochastic velocities are obtained in the quasilinear and Markovian approximation and the decorrelation time t_d is calculated. Finally, a random walk estimation of the diffusion coefficient is performed: $D \cong \lambda_\perp^2/(2t_d)$

The following results were obtained:

First, a time independent stochastic magnetic field is considered.

(a) Our calculations [4] confirm the well known results of Kadomtsev-Pogutse [2] and Rechester-Rosenbluth [1] which describe **collisional particles** in stochastic magnetic fields (only $\underline{b}$, $\eta_\parallel$, $\eta_\perp \neq 0$ in Eqs(1)). We also obtain a new form of the diffusion coefficient, valid in the weakly collisional domain.

(b) The effect of the **magnetic drifts,** determined by the gradients of the stochastic magnetic field, consists in an intrinsic particle-field line decorrelation [6] which leads to diffusion even in the absence of $\underline{\eta}_\perp$. We determine a new effective diffusion coefficient produced by this mechanism. A general graph [5] which describes the physical domains corresponding to the validity of various transport regimes determined by the three stochastic processes $\underline{b}$, $\underline{\eta}$ and $\underline{v}_D$ is obtained. The diffusion coefficients and their validity ranges can be represented in terms of two dimensionless parameters $n \equiv (\lambda_\perp^2\nu)/(4D_m V_T)$ and $p \equiv (\rho_L^2\nu)/(4D_m V_T)$ where $D_m = \sqrt{\pi/2}\beta^2\lambda_\parallel$ is the diffusion coefficient of the magnetic lines.

(c) The influence of a **macroscopic flow** of the plasma (produced e.g. by a radial electric field) is determined. We show that such an average motion commonly found in experiments, superposed on the stochastic velocity of the collisional particle motion in a stochastic magnetic field, can produce a strong increase of the effective diffusion coefficient [7]. The effect is important in both Kadomtsev-Pogutse and Rechester-Rosenbluth diffusion regimes and, when the average velocity is large enough, the diffusion coefficient becomes

independent on the collisionality regime. Analytical approximations for $D_i(u_\parallel, u_\perp)$, $i = x, y$ are obtained:

$$D\left(u_\parallel, 0\right) \cong 5Du_\parallel \quad for\ u_\parallel \ll V_T, \tag{6}$$

$$D_y\left(0, u_\perp\right) = D_m\sqrt{\frac{1}{\pi}\frac{\chi_\parallel u_\perp}{\lambda_\perp}}, \quad D_x(0, u_\perp) = 1.5D_y\left(0, u_\perp\right) \quad for\ u_\perp \ll \frac{\lambda_\perp}{\lambda_\parallel}V_T. \tag{7}$$

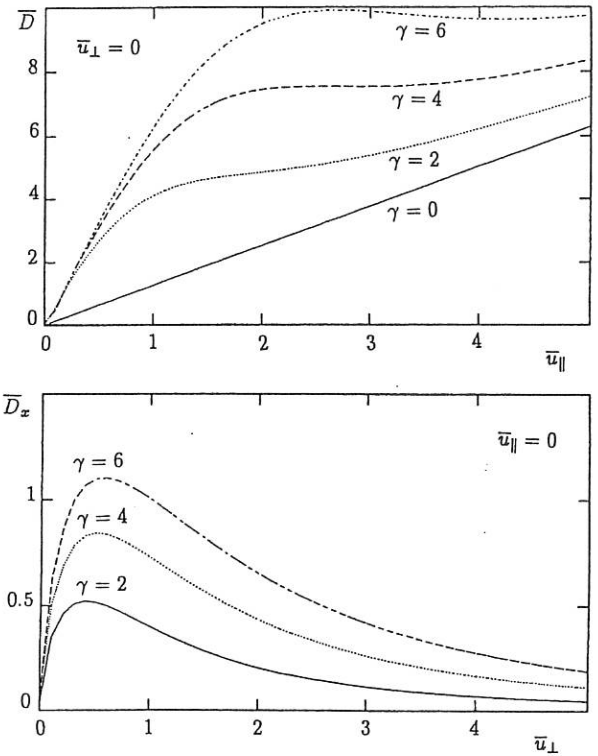

Fig.1. The dependence of the normalised diffusion coefficient $\overline{D}_i \equiv D_i/(\beta^2\lambda_\parallel^2\nu)$ on the flow velocities $\overline{u}_\perp \equiv u_\perp/(\lambda_\perp\nu)$ and $\overline{u}_\parallel \equiv u_\parallel/(\lambda_\parallel\nu)$.

(d) The last part of this work deals with **time dependent** stochastic magnetic fields. We determine the diffusion coefficient as a function of $\omega \equiv 1/\tau_c$. It shows a maximum, significantly larger than the diffusion coefficient in a time independent case, which is located around the inverse of the collision frequency. $D(\omega)$ can be approximated as:

- in the strong collisional regime $\gamma \equiv (\lambda_{mfp}/\lambda_\parallel) \ll 1$:

$$D(\omega) = \begin{cases} \sqrt{\frac{\pi}{2}}\beta^2\lambda_\parallel\sqrt{\chi_\parallel\omega} & \frac{\omega}{\nu} \ll \gamma \\ \beta^2\chi_\parallel\left(1-\sqrt{\frac{\gamma}{2}}\right) & \gamma \ll \frac{\omega}{\nu} \ll 1 \\ \frac{1}{2}\beta^2\frac{V_T^2}{\omega} & 1 \ll \frac{\omega}{\nu} \end{cases} \tag{8}$$

- in the weakly collisional regime $\gamma \gg 1$:

$$D(\omega) = \begin{cases} \sqrt{\frac{\pi}{2}}\beta^2\lambda_\parallel\sqrt{\chi_\parallel\omega} & \frac{\omega}{\nu} \ll 1 \\ \frac{1}{\sqrt{2}}\beta^2\lambda_\parallel V_T\left(1-\left(\frac{2}{\gamma}\right)^{1/4}+\left(\frac{1}{\gamma}\right)^{1/2}\right) & 1 \ll \frac{\omega}{\nu} \ll \sqrt{\gamma} \\ \frac{1}{2}\beta^2\frac{V_T^2}{\omega} & \sqrt{\gamma} \ll \frac{\omega}{\nu} \end{cases} \tag{9}$$

in agreement with [8]. We have also shown that the collisional stochastic velocity $\eta_\perp$ has not a significant effect on the effective diffusion coefficient at large frequencies.

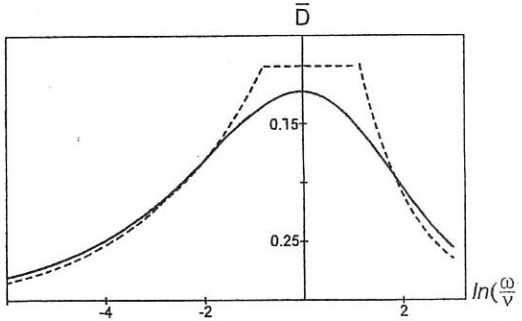

Fig.2. The normalized particle diffusion coefficient $\overline{D} \equiv D(\omega)/D_{\max}$; continuous line: the result from Eq.(4), dashed line: the approximation (9); ($\gamma = 20$)

The general conclusion of our study is that the effective diffusion of the particles in a stochastic magnetic field can be strongly influenced by plasma flows or by a time variation of the stochastic magnetic field. A significant increase of the diffusion coefficient can arise due to the coupling of these factors to the collisional particle motion along the perturbed magnetic lines.

[1] A.B. Rechester and M.N. Rosenbluth, Phys.Rev.Lett.40 (1978) 38.
[2] B.B. Kadomtsev and O.P. Pogutse, in Plasma Phys. Controlled Nucl. Fusion Res., Proc. 7th Int. Conf. (Innsbruck, 1978), Vol. I, p.649 (IAEA,Vienna).
[3] M.B. Isichenko, Plasma Phys. Control. Fusion 33 (1991) 795.
[4] Hai-Da Wang, M. Vlad, E. Vanden Eijnden, F. Spineanu, J.H. Misguich, R. Balescu, Phys. Rev. E 51 (1995) 4844.
[5] J.H. Misguich, M. Vlad, F. Spineanu, R. Balescu, Comments Plasma Physics. 17 (1995) 45.
[6] M. Vlad, F. Spineanu, J.H. Misguich, R. Balescu, Phys. Rev. E 53 (1996) 5302.
[7] M. Vlad, F. Spineanu, J.H. Misguich, R. Balescu, Phys. Rev. E 54 (1996), in print.
[8] J.H. Misguich, M. Vlad, F. Spineanu, R. Balescu, Report EUR-CEA-FC 1556 (1995).

Similarity Experiments in Tore Supra

Zou X.L., Laviron C., Colas L., Paume M., Clairet F., Devynck P., Garbet X.,Leclert G.*, Moreau P., Brégeon R., Gil C., Hoang G.T., Litaudon X., Maget P., N'guyen F, Ségui J.L.

Association Euratom-CEA sur la fusion contrôlée, C.E.Cadarache,
13108 Saint Paul lez Durance France
* Laboratoire de Physique des Milieux Ionisés, URA CNRS 835,
Université Henri Poincaré, Nancy I, BP 239, 54506 Vandœuvre Cedex, France

1) Introduction

A new experimental approach using dimensional analysis has recently been made in tokamak plasmas for a better understanding of transport mechanisms as well as prediction of the performance of future tokamaks[1]. In this method, all non dimensional parameters governing the plasma are kept constant, except the normalized Larmor radius ρ^* ($=\sqrt{2m_eT_e}/(q_eBa)$). In L regimes, four non dimensional parameters are fixed : the aspect ratio R/a, the safety factor q, the toroidal beta number β_T ($=nT/(B^2/2\mu_o)$), and the collisionality ν^* (= const $(R/a)^{3/2}q_aRn_e/T_e^2$). From this analysis, the heat diffusivity can be written as [3]:

$$\chi^L = \chi^B(\rho^*)^\alpha F(R/a,q,\nu^*,\beta_T) \propto B^{-(1+2\alpha)/3}a^{(2-5\alpha)/6} \quad (1)$$

where χ^B (= T/B) is the Bohm transport coefficient. Gyro-Bohm, Bohm, and Goldston transport correspond respectively to $\alpha = 1$, $\alpha = 0$ and $\alpha = -1/2$. To characterize a similarity state in ohmic (OH) plasmas, a better choice is to replace β_T by the Hugill number H [2] ($H = 5a^2n_e/I_p$). Similar scaling can be defined for OH plasmas:

$$\chi^{OH} = \chi^B(\rho^*)^\alpha F(R/a,q,\nu^*,H) \propto B^{-(1+3\alpha)/4}a^{-\alpha} \quad (2)$$

In this case, gyro-Bohm, Bohm, B-independent transport correspond to $\alpha = 1$, $\alpha = 0$ and $\alpha = -1/3$. In this paper, results of heat transport from global and local analysis in Tore Supra are presented, as well as the density fluctuations.

2) Global Analysis of Transport

To investigate the similarity physics of transport in Tore Supra, two series of experiments, corresponding to two different magnetic fields (B=3.76T, 1.71T), have been performed. For all considered discharges, the plasma is Helium gas, and the plasma position remains unchanged: the minor radius a is 0.75 m, and the major radius R is 2.32 m.

2.1) L regime

Tables I and II show the engineer and non dimensional parameters for shots 16276 and 17833 in their L phase. For B varying from 1.71 T to 3.76 T, I_p, n_{eo}, P_{add} are chosen so as to maintain constant q, β_T, and ν^*, while ρ^* varies from 1.24×10^{-4} to 7.68×10^{-5}. Two heating methods are used in these experiments: ICRH, which is only efficient in a high magnetic field range (high density in this case), and lower hybrid (LH) wave heating, which is more efficient in low density regimes. The global (effective) heat diffusivity χ_{eff} is evaluated from the energy confinement time τ_{Dia} (diamagnetic measurement) with $\chi_{eff} = a^2/\tau_{Dia}$. χ_{eff} includes both electron and ion effects. In global analysis, the central temperature and central density are used in the

expression of β_T, and ν^*, and q is given by the edge value $q_a = 5a^2B/(RI_p)$. From the evolution of χ_{eff}/χ^B in table II, and using Eq.(1), a value of $\alpha \approx 0.7$ is obtained. This means that the effective transport in L regimes is rather gyro-Bohm.

Shot	B (T)	Ip (MA)	n_{e0} ($10^{19}m^{-3}$)	Heating	P_{add} (MW)	T_{e0} (keV)	τ_{Dia} (sec)
16276	***3.76***	1.32	6.2	ICRH	3.25	4.1	0.152
17833	***1.71***	0.60	2.2	LH	0.9	2.2	0.089
Ratio	0.45	0.45	0.35		0.28	0.54	0.585

Table I. Engineer parameters of shots 16276 and 17833 in their L phase.

Shot	R/a	q_a	β_T (10^{-3})	ν^*	ρ^* (10^{-4})	χ^B	$\chi_{eff} = a^2/\tau_{Dia}$	χ_{eff}/χ^B
16276	3.04	3.57	7.06	17.0	0.77	1.06	3.83	3.60
17833	3.08	3.50	6.37	19.0	1.2	1.29	6.37	4.95
Ratio	1.01	0.99	0.90	1.12	***1.6***	1.22	1.66	1.38

Table II. Non dimensional parameters of shots 16276 and 17833 in their L phase.

2.2) OH regime (SOC)

In dimensional analysis for ohmic plasmas, β_T should be substituted by the Hugill number H as indicated in [2]. Tables III and IV show the engineer and non dimensional parameters of shots 16276 and 17825 in their OH phase. For the same B variation as in §2.1, q, H, and ν^* remain nearly constant (see Tab.IV), while ρ^* varies from 1.0×10^{-4} to 5.7×10^{-5}. Note that both plasmas (H≈14) are in the saturation ohmic confinement regime (SOC) [2]. From table IV, α is found to be $\alpha \approx -0.03$, hence the effective transport in this OH regime is Bohm.

Shot	B (T)	Ip (MA)	n_{e0} ($10^{19}m^{-3}$)	Heating	P_{OH} (MW)	T_{e0} (keV)	τ_{Dia} (sec)
16276	***3.76***	1.32	6.2	OH	1.29	2.23	0.223
17825	***1.71***	0.60	2.8	OH	0.52	1.45	0.17
Ratio	0.45	0.45	0.45		0.39	0.65	0.762

Table III. Engineer parameters of shots 16276 and 17825 in their OH phase.

Shot	R/a	q_a	H	ν^*	ρ^* (10^{-4})	χ^B	$\chi_{eff} = a^2/\tau_{Dia}$	χ_{eff}/χ^B
16276	3.04	3.58	14.3	57.4	0.57	0.59	2.61	4.4
17825	3.08	3.53	13.6	59.3	1.0	0.85	3.68	4.32
Ratio	1.01	0.99	0.95	1.03	***1.8***	1.44	1.41	0.98

Table IV. Non dimensional parameters of shots 16276 and 17825 in their OH phase.

3) Local Analysis of Transport

In §2, the difference between ions and electrons, and the radial feature of transport are not considered. In this section, a local transport analysis is performed with a numerical code LOCO [4]. To run this code, the following input values are required: the electron temperature profile $T_e(r)$, the electron density profile $n_e(r)$, the current profile J(r), the additional heating power profile $P_{add}(r)$ and Z_{eff}. T_e is measured by three diagnostics: Thomson scattering,

Michelson interferometry, and heterodyne radiometry. n_e is measured by FIR inteferometry and reflectometry. J is measured by polarimetry. Z_{eff} is measured by Bremsstrahlung spectroscopy. For Helium plasma as in our case, the neutron flux is not large enough to allow the ion temperature measurement. Thus in the LOCO code, it is necessary to impose a scaling for the ion transport. This scaling is in turn controlled by the energy balance, i.e. the total kinetic energy W_{kin} (= W_e + W_i) is compared to W_{dia}. W_e is obtained from profile measurements, W_i from the numerical code, and W_{dia} from diamagnetic measurements. It is observed that gyro-Bohm scaling for ion transport can not satisfy the energy balance condition for all analysed discharges, contrary to Goldston scaling. This demonstrates indirectly that ion transport is rather Goldston than gyro-Bohm in the considered discharges.

3.1) L regime

The discharges considered in this section are the same as those in §2.1. Fig.1-2 display the radial profiles of ν^*, β_e. These parameters are kept nearly constant in the whole profile, when B varies from 1.71 T to 3.76 T. The injected power deposition in both cases is located inside the region defined by $\rho \leq 0.3$. In Fig.3, we can see that the electron transport is rather gyro-Bohm, as well as the effective transport. This confirms the results of global analysis.

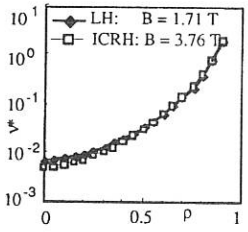

Fig.1 ν^* profile

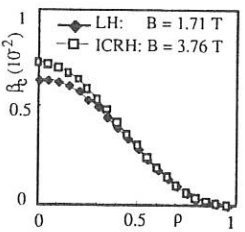

Fig.2 β_T profile

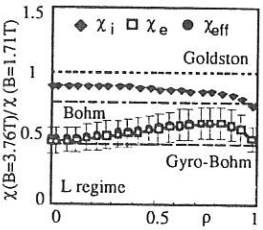

Fig.3 Heat diffusivity ratio.

3.2) OH regime

The discharges considered in this section are the same as those in §2.2. Fig.4-5 display the profiles of ν^*, q, H. Compared to the previous section, only the density ratio is different for the two considered discharges. The density is now chosen to keep H constant instead of β_T. In OH plasmas, contrary to L regimes, the electron transport is now rather Bohm (see Fig.6), and so is the effective transport. This result is compatible with that obtained by global analysis.

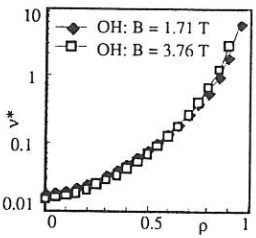

Fig.4 ν^* profile

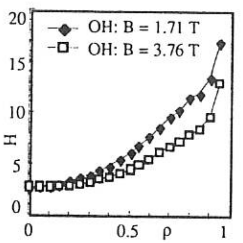

Fig.5 H profile

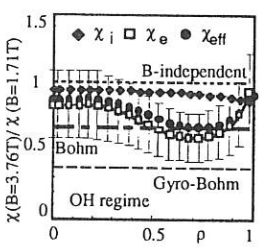

Fig.6 Heat diffusivity ratio.

4) Fluctuation Analysis

Density fluctuations are measured by CO2 laser coherent scattering [5] in order to establish an eventual relation with the local transport. Fig.7 displays the two power spectra of $\tilde{n}/n$ relative to two magnetic fields in L regime. The poloidal wavenumber of fluctuations probed is $k_\theta = 5\ cm^{-1}$. The scattering volume is located in a region from $\rho \approx 0.6$ to $\rho \approx 0.9$. For B = 3.76 and 1.71T, the fluctuation levels are respectively $\tilde{n}/n \approx 0.22$ and ≈ 0.15 [a.u.]. In OH regimes described in §2.2, the density fluctuation levels are respectively $\tilde{n}/n \approx 0.18$, $\tilde{n}/n \approx 0.17$ for the same B. From these values, a dependence on ρ^* of one component of $\tilde{n}/n$ at a given $k_\theta = 5\ cm^{-1}$ can be deduced: $\tilde{n}/n|_{k_\theta} \approx (\rho^*)^{-0.8}$ in L regimes, $\tilde{n}/n|_{k_\theta} \approx (\rho^*)^0$ in OH regimes. On the other hand, the mixing length theory can directly link $\tilde{n}/n$ to ρ^* as $\tilde{n}/n = 1/(<k_\theta>L) = \rho^* f(k_\theta \rho^*)$. This scaling can lead to a gyro-Bohm transport. For one measured k_θ-component of fluctuation and due to the Fourier transform, it yields: $\tilde{n}/n|_{k_\theta} = (\rho^*)^2 f(k_\theta \rho^*)$. The function f can be determined empirically by noting that the experimental fluctuation k-spectrum follows a Kolmogorov scaling [6]: $(\tilde{n}/n|_{k_\theta})^2 \approx k_\theta^{-3}$. Hence the ρ^*-scaling of $\tilde{n}/n$ is: $\tilde{n}/n|_{k_\theta} \approx k_\theta^{-3/2} (\rho^*)^{1/2}$. For these experiments, the measured density fluctuations and the internal transport do not follow the same trend. Two explanations are possible. Either the measured turbulence does not account for the internal transport, or the above simplistic model is deficient. Therefore, additional experiments are needed to thoroughly study this point.

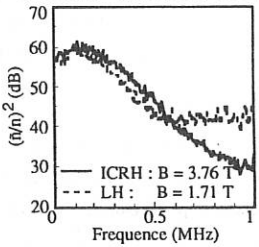

Fig.7 Power spectra of $\tilde{n}/n$.

5) Conclusions

Similarity experiments have been made in Tore Supra to investigate the ρ^* scaling of local transport and global confinement. A local analysis showed that in L regimes the electron and effective transport are gyro-Bohm, the ion transport is rather Goldston, as found in other tokamaks. On the other hand, in the ohmic SOC regime, the electron and effective transport are Bohm, and the ion transport is B-independent. All these results are consistent with those obtained from global analysis. For these experiments, when using a simplistic model, it seems that the measured density fluctuations and the internal transport do not follow the same trend.

[1] Petty C.C, Luce T.C, et al., Phys. Rev. Lett., **74**, 1763 (1995)

[2] Zou X.L. *et al.*, *22nd EPS Conf. on Contr. Fusion and Plasma Phys.*, Bournemouth, Vol.19C, I-041 (1995)

[3] Connor, J.W., Taylor, J.B., Nucl. Fusion, **17**, 1047 (1977)

[4] Harris G.R., *et al.*, Nuclear Fusion, **32**, 1967 (1992)

[5] Truc A., Quéméneur A., Hennequin P., *et al.*, Rev. Sci. Instr., **63** (7), 3716 (1992)

[6] Devynck P., Garbet X., Laviron C. *et al.*, Plasma Phys. Cont. Fusion, **35**, 65 (1993)

IMPURITY CONTENT AND SUSTAINMENT OF TORE- SUPRA SNAKES

PECQUET A.L., MATTIOLI M., CRISTOFANI P., GARBET X.
GERAUD A., GIL C.

Association Euratom-CEA sur la Fusion
Département de Recherches sur la Fusion Contrôlée
CEA-Cadarache, F-13108 St Paul-lez-Durance

Introduction

Snakes have been observed after pellet injections into Tore-Supra during ohmic as well as during ICRH discharges as it has already been reported in JET[1]. They correspond mainly to a density perturbation. For example, on Tore-Supra [2,3], high speed hydrogen pellets (1500m/s and approximately 10^{21} atoms) were injected into deuterium plasmas. In such conditions the produced snakes exhibit a m=1 n=1 helicity and rotate on a radius r_S much smaller than the radius of the q=1 surface deduced from the inversion radius of the sawteeth ($r_S/r_{q=1}$=0.5) [4]. A study of the chemical composition of the snake and the consequence upon its stability are the purposes of this paper, which is organised as follows: the first paragraph presents the chemical composition of the snake using a simplified model, simulating the oscillations of both the line integrated electron density and the soft X-ray brightnesses. It has been deduced that the carbon concentration inside the snake is larger than in the surrounding plasma. The second paragraph is devoted to the time evolution equation of the snake size, taking into account the tearing component and two additional effects, namely the resistivity increase through the carbon accumulation [5] and the bootstrap current [6].

Evaluation of the snake electron density and of the impurity content.

The snake is observed using data from the following diagnostics: 5 channels of the laser interferometer, 44 channels of the soft X-ray camera viewing the plasma vertically and 6 ECE channels interferometer giving the spatial profile of the electron temperature. The average effective charge Zeff is routinely obtained from quantitative analysis of the visible bremmstrahlung emission at wavelength around 5238Å, whereas the impurities are measured by the XUV line spectroscopy. Fig.1 shows the evolution during the snake lifetime of the central ECE signal, the soft X-ray at the snake radius and two integrated electron line densities as function of time.The early appearance of the modulations on the density indicates that the snake is already created at the end of the ablation process at t = 8.56 s. The amplitude of perturbation is almost constant during the entire snake duration . The modulations on the increasing (because of the electron temperature recovery) soft X-ray signals appear only about 80 ms later and reach a maximum of 30% of the average integrated signal around t = 8.85 s and then decreases with a time constant of 170 ms.

For more detailed investigations, the impurity content is obtained by using an impurity transport code simulating simultaneously all available experimental data (XUV line spectroscopy, soft X-ray emission and visible bremsstrahlung) [7].

Prior to pellet injection the described quantitative analysis has given a central $Z_{eff} = 1.40 \pm 0.05$, due to carbon with a central density $n_C(0)$ of about $4.5\ 10^{17}\ m^{-3}$. Pollution by oxygen, chlorine and heavy metal (mainly Fe) is negligible, as far as both visible bremsstrahlung (then Z_{eff}) and soft X-ray signals are concerned. To estimate the chemical composition of the snake, the plasma is divided in two components:

-the unperturbed background plasma obtained neglecting the snake modulations.

-the snake perturbation corresponding to the signal oscillations. The snake has been simulated as an off-axis perturbation superposed to the unperturbed, previously simulated plasma. By rotating the snake on the magnetic surface r_s the interferometer modulations are simulated supposing a parabolic density perturbation. The snake electron temperature $T_{es}(r_s)$ is taken constant in the snake (measured by ECE Fabry-Perot and Michelson interferometers). As impurity, only carbon is considered with constant concentration inside the electron density perturbation. Figure3 shows four simulations at four instants during a snake period at t=8.68 s. The simulation of the central snake electron density gives $n_{es}(0) = 5.\ 10^{19}\ m^{-3}$. From left to right the snake is at its interior, upper, exterior and lower positions At the same time for the base plasma $n_e(0) = 1.\ 10^{20}\ m^{-3}$, $T_e(r_s) \leq T_e(0) \approx 1.1$ keV. The stars show the experimental soft X-ray brightness profiles, the dashed lines show the simulations of the unperturbed base plasma. Assuming a C concentration inside the perturbation equal to that of the unperturbed plasma, it is impossible to simulate the snake oscillations on soft X-rays (dot-dashed lines). The solid lines show the final simulations. The central C density in the perturbation, superposed to the unperturbed plasma, increases from $7.5\ 10^{16}\ m^{-3}$ up to $1.7\ 10^{18}\ m^{-3}$ with a final Z_{eff} value inside the snake (parabolic density perturbation plus base plasma) of about 1.36. Figure 3 is the same as Figure 2 at 8.87 s. Now the simulation of the snake electron density has given $n_{es}(0) = 5.\ 10^{19}\ m^{-3}$. At the same time, for the base plasma, $n_e(0) = 7.\ 10^{19}\ m^{-3}$, $T_e(r_s) \leq T_e(0) = 1.5$ keV. In this case to obtain the final simulations it is necessary to increase the C density in the perturbation from $1.5\ 10^{17}\ m^{-3}$ up to $4.\ 10^{18}\ m^{-3}$ with a final Z_{eff} value inside the snake of about 2.1. Other simulations have shown that during the snake decay this latter value is not changed.

Stability criteria [3,5]

To drive the snake there are two mechanisms additional to the mode , namely:

-the variation of resistivity inside the snake due to the carbon accumulation,

-the modification of the bootstrap current induced by the presence of a large m=1, n=1 island snake perturbation.

The problem is to evaluate the contribution of each effect in terms of Δ'. To simplify the calculations we assume a monotonic current profile, consider the snake as an island of m=1 n=1

helicity and also neglect coupling terms with other modes. The qualitative time evolution of the half island size δ_s is then given by the non linear equation:

$$\frac{\partial \delta_s}{\partial t} = \frac{1}{k_1}\frac{\eta}{\mu_0}\left[\Delta' + \Delta'_\eta + \Delta'_{jbs}\right] \qquad (1)$$

where k_1=1.7, η is resistivity and Δ' is the discontinuity of the vector potential amplitude across the layer.

***Bootstrap contribution:** Δ'_{jbs}

Starting from the integrated Ampère law $\Delta'_{jb}\tilde{A}_{//} = \mu_0 \int_{-\infty}^{+\infty}\int_{-\alpha_0}^{+\alpha_0} \frac{d\alpha}{2\pi} j_{bs}(r,\alpha)\cos\alpha \; dr$ and taking for the island bootstrap current j_{bs} the expression calculated by Carrera et al.[8] leads to $\Delta'_{bs} = 1.15\sqrt{\varepsilon_s}\beta_p \frac{1}{L_n}\frac{r_s}{s_s}\frac{1}{\delta_s}$ where β_p is poloidal beta defined on r_s, L_n the density length decrease calculated faraway from the resonance and s_s the shear value at the resonant surface.

***Impurity contribution:** Δ'_η. In the same way, supposing a parabolic profile for Z_{eff} inside the snake, the relation between the parallel impurity induced current $\delta J_{s//}$ and δZ_{eff}, is given by: $\frac{\delta J_{s//}}{J_{s//}} = -\frac{\delta Z_{eff}}{2Z_{eff}}\left(1-\overline{\Psi}\right)$ and leads to $\Delta'_\eta = \frac{128}{15\pi}\frac{2-s_s}{s_s}\frac{\delta Z_{eff}}{Z_{eff}}\frac{1}{\delta_s}$

Finally the snake time evolution is governed qualitatively by the equation:

$$\frac{\partial \delta_s}{\partial t} = \frac{1}{k_1}\frac{\eta}{\mu_0}\left[\Delta' + 1.15\sqrt{\varepsilon_s}\beta_p \frac{1}{L_n}\frac{r_s}{s_s}\frac{1}{\delta_s} + \frac{128}{15\pi}\frac{2-s_s}{s_s}\frac{\delta Z_{eff}}{Z_{eff}}\frac{1}{\delta_s}\right] \qquad (2)$$

Conclusions: To simulate the experimental signals, it is necessary to increase the carbon density inside the snake. The Δ' study shows that the impurity and the bootstrap terms are destabilizing. After the snake initial phase (t>8.64s), $\frac{\delta Z_{eff}}{Z_{eff}} > 8\%$ the impurity term dominates over the current bootstrap. In the saturation phase $\partial_t \delta_s$=0, the above simplified model, implies that $\Delta' r_s = -6\frac{2-s_s}{s_s} \equiv -\frac{12}{s_s}$. For a flat q profile ,i.e. a low value of s_s, this means that Δ' is strongly negative. This suggests the presence of stabilizing effects.

References

[1]WELLER A., CHEETHAM A. D., EDWARDS A. W., et al., Phys. Rev. Lett. 59(1987) 2303.
[2]GERAUD A., CHATELIER M., DRAWIN H.W., et al. in Controlled Fusion and Plasma Physics (Proc. 20th Eur. Conf. Lisboa) ,Vol 17C, Part I, European Physical Society, Geneva (1993)163.
[3]PECQUET A-L., CRISTOFANI P., MATTIOLI M., et al. "Snake-like phenomena in Tore-Supra following pellet injection", (1996) Rep. EUR-CEA-FC 1579 CEN Cadarache.(submitted to Nucl Fusion)
[4]CRISTOFANI P., DESGRANGES C., GARBET X., et al. in Controlled Fusion and Plasma Physics (Proc. 21th Eur. Conf. Montpellier) ,Vol 18B, Part I, European Physical Society, Geneva (1994) 210.
[5]WESSON J., Plasma Phys. Control. Fusion 37 (1995) A337.
[6]THYAGARAJA A., HAAS F.A., in Controlled Fusion and Plasma Physics (Proc. 20th Eur. Conf. Lisboa,Vol 17C, Part IV, European Physical Society, Geneva (1993)1323.
[7]MATTIOLI M., DE MICHELIS C., MONIER-GARBET P. Nucl. Fusion 35, 807 (1995)
[8]CARRERA R., HAZELTINE R.D. and KOTSCHENREUTER M., Phys.Fluids 29 899 (1986)

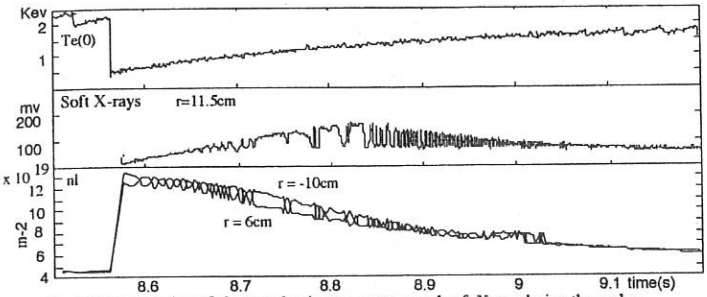

Fig 1 Time evolution of electron density temperature and soft X-ray during the snake

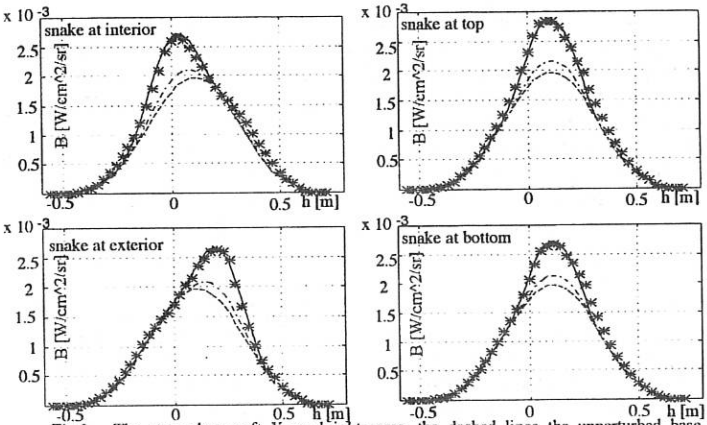

Fig 2 The stars show soft X-ray brightnesses, the dashed lines the unperturbed base plasma simulation, the dot dashed with same C concentration inside the snake as base plasma and solid lines with increased C inside the snake at t=8.68s.

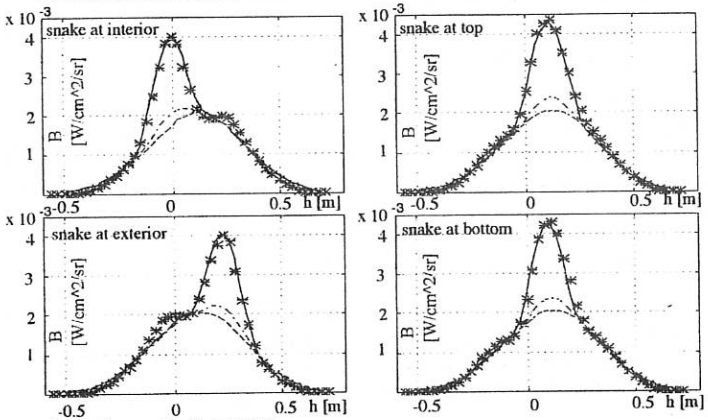

Fig 3 Same as Fig.2 at t=8.87s.

Time Dependent Transport Simulation Study for Advanced Tokamak Mode in KT-2 Tokamak

B.G. Hong and S.K. Kim

Nuclear Fusion Laboratory, Korea Atomic Energy Research Institute,
P.O. Box 105 Yusong, Taejon, Korea 305-600.

1. Introduction

In advanced tokamak operation, utilizing bootstrap current driven by pressure gradient is advantageous since it reduces power required for the non-inductive current drive. With a high bootstrap current, the current profile is naturally hollow and leads to negative magnetic shear configuration. This configuration has been thought to be promising for the advanced tokamak operation since it produces high β_N due to high-n ballooning stability and enhanced confinement due to suppression of anomalous transport mechanism such as ITG and trapped electron mode[1]. Dynamic simulation is necessary to investigate the stable route to high β_P, high bootstrap current plasma with negative shear over a central plasma region and to calculate the required auxiliary heating and current drive power. For the bootstrap current dominant plasma, the control of pressure profile by the heating and current drive methods for the alignment of the bootstrap current to the desired total current is important since the bootstrap current is strongly dependent on the pressure profile through the plasma transport. We present time-dependent simulation studies of advanced tokamak discharge in a large-aspect-ratio (LAR), medium-size, diverted tokamak KT-2 which was conceptualized[2] with a research goal of 100% non-inductive current drive exploiting high bootstrap current fraction(> 70 %). TSC[3] transport simulation code is used to determine dynamic evolution of the profiles of plasma pressure, current and bootstrap current. TSC evolves MHD equations describing transport time-scale evolution of axisymmetric tokamak plasma.

2. Dynamic Evolution of Negative Magnetic Shear Configuration

We perform TSC time-dependent transport simulations for reference KT-2 tokamak parameters; major radius R_0=1.4m, minor radius a=0.25m, elongation κ=1.8 and triangularity δ =0.6 with double null plasma.

A. Transport Model

TSC solves transport equations with respect to evolving magnetic surface containing a fixed toroidal flux. Also, plasma force balance equations are solved to maintain plasma in near equilibrium during its evolution. For details of TSC model equations, we refer the original paper in Ref. 3.

For the density profile, we take the following parametrized form ;

$$n_e(\bar{\psi}, t) = n_{0,e}(t)[\,1 - \bar{\psi}^{\alpha_N(t)}\,]^{\beta_N(t)} + n_b(t), \qquad (1)$$

where $\bar{\psi}$ is the normalized poloidal flux and $n_b(t)$ is the density at plasma boundary. The exponents $\alpha_N(t)$ and $\beta_N(t)$ can be adjusted to match the experimantal data, but in this study we used $\alpha_N(t)$=0.5 and $\beta_N(t)$=2.0.

The electron and ion thermal conductivities are modelled as[4]

$$\chi_e = \alpha_{TS}\chi_{e,s}, \qquad (2)$$

$$\chi_e = f_m(\chi_{TEM}^2 + \chi_\eta^2)^{1/2}\ F(\Phi)\ |\nabla\Phi|^{-2}, \tag{3}$$

where Φ is toroidal flux, $F(\Phi)$ is a profile factor given in Ref. 5, and

$$\chi_{TEM} = a_{122}(1.25/10^{20})\frac{n}{n(\Phi_b)}(xB_T)^{0.3}Z^{0.2}(1+\frac{a_N}{4}), \tag{4}$$

$$\chi_\eta = a_{121}(7.5/10^8)(\frac{F(\Phi_b)}{n(\Phi_b)})^{0.6}(RB_T q_{95})^{-0.8}a^{-0.2}. \tag{5}$$

Here $P(\Phi)$ is the total heating power minus the total radiated power inside the flux surface Φ.

The time averaged effect of sawtooth instability inside q=1 surface is included in Eq.(3). Thus thermal conductivity is enhanced inside the q=1 surface according to the prescription;

$$f_m = 1, \qquad \text{for } q > 1 \tag{6}$$

$$f_m = a_{124}, \qquad \text{for } q < 1 \tag{7}$$

For the calculation of bootstrap current, we use Harris's extension[6](into Plateau and Pfirsch-Schulter collisionality regime) of Hirshman's collisionless expression[7] which is valid in the neo-classical banana regime. Neoclassical corrections to resistivity are used as in Ref. 8, and the effect of sawtooth instability is taken into account by enhancing resistivity inside q=1 surface. In Eqs. (2)-(7), a_{121}, a_{122}, a_{124} and a_{126} are parameters to control transport properties.

B. Scenario I ; Off-axis Heating

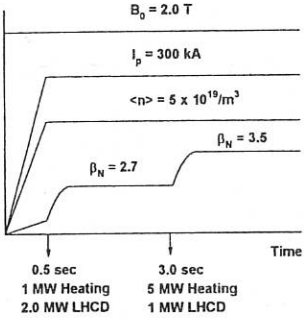

Fig. 1 Schematic of scenario I

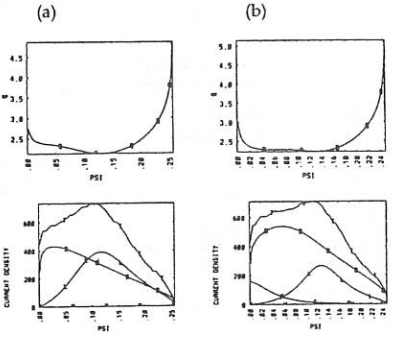

Fig. 2 q and current density profile (a) t=3.0 sec and (b) t=7.0 sec: T=total current, B=bootstrap current, L= LH current, F=FW current.

The schematic of the scenario is shown in Fig. 1. Throughout simulations, toroidal magnetic field is maintained 2.0 T for the entire simulation and plasma current is ramped from 20 kA at t=0.0 sec to at t=0.5 sec. The plasma evolves from an inboard limited circular shape at t=0.0 sec, becomes diverted at t~0.4 sec, and reaches an elongation of κ=1.8 and a triangularity of δ=0.6 at t=0.5 sec. The plasma shape and plasma currents are maintained by feedback control on PF coil currents. The electron density is programmed to increase linearly with time to the current flattop value of $\langle n\rangle \cong 5.0/10^{19}\ m^{-3}$ with peak to average value of 0.6. The effective charge Z_{eff} is set to 2.0 and the control parameters, a_{121}=0.06, a_{122}=0.4 in Eqs.(4) and (5) are used to simulate improved confinement. Deposition profiles of heating and current drive are modelled using simplified analytic formula; $S_{Heating,CD}(\Psi) = \frac{d^2(\Psi^{a_1}(1-\Psi)^{a_2}}{(\Psi-a)^2+d^2}$,

where $\hat{\psi}$ is the normalized poloidal flux, and a, d, a_1 and a_2 are profile control parameters.

At the end of plasma current ramp-up, 2 MW lower hybrid current drive with 1 MW heating is initiated and as a result, β_N increases to 2.7 with bootstrap current fraction, 57 %. The current profile redistributes from peaked OH profile to hollow profile on a long diffusive time scale. It takes more than 2.5 sec for a full relaxation of 300 kA plasma current. After the current profile has broadened sufficiently (non-monotonic q profile develops) to allow second stable regime to high-n ballooningmode, 5 MW off-axis heating with 1 MW LHCD is initiated and β_N increases to 3.5 with bootstrap current fraction = 73 %. Fig. 2 shows q and current density profiles before and after second phase heating. Due to high bootstrap current fraction(> 70 %), the current profile is hollow. Broad pressure profile due to off-axis heating cause the bootstrap current profile to peak on off-axis. A seed current(20 kA) on magnetic axis driven by fast wave controls q_0 value. Time history of q_0(Fig. 3) shows current profile is frozen after 4.0 sec.

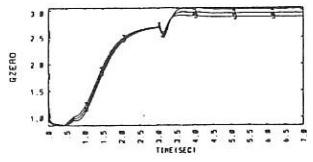

Fig. 3 q_0 as a function of time

C. Scenario II ; Central Heating

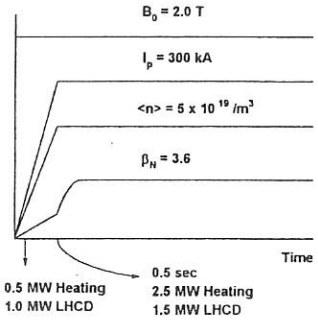

Fig. 4 Schematic of scenario II

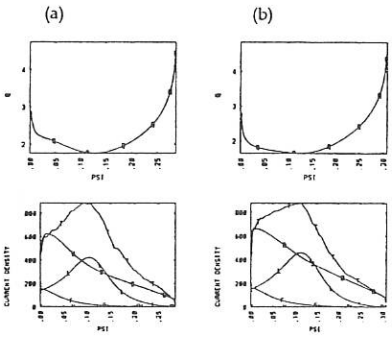

Fig. 5 q and current density profile (a) t=0.5 sec and (b) t=4.0 sec: T=total current, B=bootstrap current, L= LH current, F=FW current.

The schematic of the scenario is similar to scenario I except that we initiate heating in initial current ramp-up phase of discharge.(Fig. 4) Central electron heating by 0.5 MW heating and 1 MW LHCD increases the electrical conductivity and prevent the penetration of the inductively driven OH current by prolonging the current diffusion time. At the end of current ramp-up, 2.5 MW central heating and 1.5 MW LHCD freeze the current profile and raise plasma β_N to 3.6 and the bootstrap current fraction to 70 %. By this way, we can shorten the time which is needed for current profile redistribution and avoid MHD unstable transitions from positive to negative magnetic shear in the region of high pressure. At this state, LHCD deposition profile shifts off-axis with increasing density and controls the location and the value of q_{min} for MHD stability.

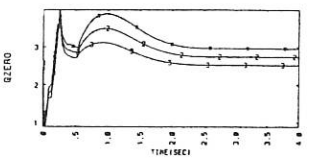

Fig. 6 q_0 as a function of time

More LHCD power is required since the bootstrap current profile peaks near the plasma center and alignment to the desired current profile is worse than scenario I. Fig. 5 shows q and current density profiles at 0.5 sec and at steady state. Due to central heating, peaked pressure profile causes the bootstrap current profile unfavorable. Control of plasma profiles is important since bootstrap current and profile are strongly dependent on plasma transport and resulting pressure profile. To increase $\beta_N > 4$, not only more heating power but strong profile control capability are required. Time history of q_0(Fig. 6) shows current profile is frozen after 2.0 sec which is shorter than 4.0 sec in senario I.

D. Sensitivity on Transport Models

We perform the simulation of scenario II with the Hirshman-Sigmar bootstrap current formulation[9] which is valid in all coollisionality regimes. The calculation shows that the magnitude of the bootstrap current is similar to the case with Harris model but the bootstrap current density near the magnetic axis is smaller, so the resulting q profile shows a larger shear in central region. When we use the Kaye-Goldston model for the thermal energy transport, the bootstrap current profile is broader and $q_{min} \sim 2$ compared to $q_{min} \sim 1.6$ with the Coppi-Tang thermal energy transport model. The details of the profiles depend on the transport models used, but the required heating and current drive power to maintain the negative magnetic shear configuration is within the KT-2 design specification.

E. MHD Stability

A trajectory of KT-2 equilibria in ℓ_i-q space indicates kink mode may be unstable but MHD stability analysis for the equilibria in steady states of the two scenarios show that n=1 external kink mode is stable in the presence of a conducting wall at 1.4 times the plasma radius. Profile optimization study based on the MHD stability analysis for the ballooning mode, the infernal mode and the kink mode has been performed and optimized profiles are found for the advanced tokamak operations in KT-2[10].

3. Summary

Through the time-dependent transport simulation, MHD stable scenarios to high β_P, high bootstrap, negative magnetic shear configuration are investigated. Two scenarios(off-axis and central heating) are considered. Simulations indicate that the advanced tokamak operation exploiting high bootstrap current in KT-2 tokamak is possible with profiles control using heating and non-inductive current drive methods.

References

[1] C. Kessel, J. Manickam, G. Rewoldt, and W. Tang, Phys. Rev. Letters **72**, 1212, (1994).
[2] I.S. Chang, et. al., "Concept Definition of KT-2", KAERI/TR-472/94, (1994).
[3] S.C. Jardin, N. Pomphrey, and J. Delucia, J. of Comp. Phys. **66**, 481, (1986).
[4] W.M. Tang, Nucl. Fusion **26**, 1605, (1986).
[5] S.C. Jardin, M.G. Bell and N. Pomphrey, Nucl. Fusion **33**, 371, (1993).
[6] G.N. Harris, EUR-CEA- FC 1436, (1991).
[7] S.P. Hirshman, Physics of Fluids **31**, 3150, (1988).
[8] S.P. Hirshman, R.J. Hawryl;uk, and B. Birge, Nucl. Fusion **17**, 611, (1977).
[9] S.P. Hirshman and D.J. Sigmar, Nucl. Fusion **21**, 1079, (1981).
[10] S. Poedts, A. De Ploey, and J.P. Goedbloed, "MHD Stability Analysis of the KT-2 Tokamak Plasma", *Rijnhuizen Report* 96-227, (1995). Also, in this conference.

Sawtooth Studies on the FTU Tokamak

F. Alladio, G. Bracco, **P. Buratti**, P. Micozzi, O. Tudisco
Associazione Euratom-ENEA sulla Fusione, Centro Ricerche Frascati,
CP 65, 00044 Frascati, Rome, Italy

1. Introduction

Sawtooth oscillations have been studied on a database including about 800 ohmic FTU discharges, in which the edge cylindrical safety factor q_a was varied between 2.2 and 8 and the volume average density $\langle n_e \rangle$ ranged from 0.3 to 2.6×10^{20} m^{-3}. Major radius and toroidal field at the plasma axis were fixed at R=0.96 m and B_T=5.6 T respectively; the radius of the last closed magnetic surface was about 0.29 m.

The main sawtooth features, namely the existence of m=1, n=1 precursor or successor oscillations, the collapse time and the period have been analysed by means of an ECE diagnostic based on a 12 channel grating polychromator.

This paper mainly deals with the influence of the Lundquist number on the sawtooth characteristics and with the diamagnetic stabilisation of the internal kink mode in the semicollisional regime.

2. Sawtooth regimes

Several distinct sawtooth regimes have been identified in FTU; each regime corresponds with a well defined region of the operation space and with a range of the Lundquist number $S=\tau_R/\tau_A$, where $\tau_R=\mu_0 r_1^2/\eta$ is the resistive diffusion time within the radius r_1 of the q=1 surface and $\tau_A=(\mu_0 m_i n_i)^{1/2}R/B_T$ is the Alfvén time. The observed regimes can be classified as follows:

A - Sawteeth with precursor m=1 oscillations are observed for $\bar{n}Rq_a / B_T > 1.2\times10^{20}$ Wb^{-1}; the the Lundquist number in this regime ranges from 2×10^5 to about 1.5×10^6. No m=1 activity is observed at the highest densities (Fig. 1a).

B - Successor oscillations substitute the precursors if $1.2 > \bar{n}Rq_a / B_T > 0.4\times10^{20}$, or $S\approx1.5\div3\times10^6$. If the density is not close to the upper bound, compound sawteeth, with full collapses interleaved by partial collapses that do not affect the plasma axis (Fig. 1b) are frequently observed interspersed with normal ones.

C - For $\bar{n}Rq_a / B_T < 0.4\times10^{20}$, i.e. close to the low density limit of the operation space, sawteeth with superimposed m=1, n=1 oscillations are observed which differ from precursors and successors as the oscillation amplitude is either constant or maximum midway between successive collapses (Fig. 1c). In this regime $S>3\times10^6$.

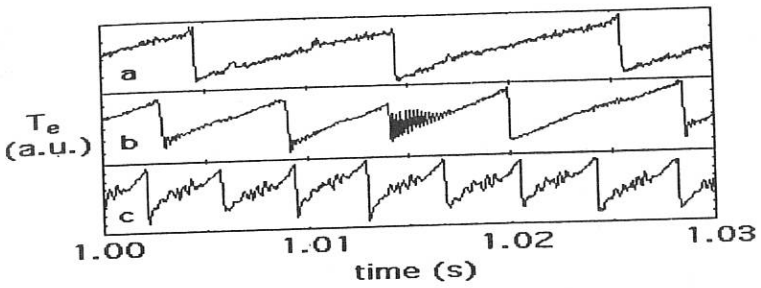

Fig. 1: *a) T_e evolution at r=2.4 cm for FTU shot #7356 (q_a=3.7, $<n_e>$=2.6×10^{20}m^{-3},S=10^6); b) T_e evolution at r=6.6 cm for FTU shot #7987 (q_a=3.7, $<n_e>$=7.5×10^{19}m^{-3}, S=2.2×10^6); c) T_e evolution at r=6.6 cm for FTU shot #7987 (q_a=3.7, $<n_e>$=2.7×10^{19}m^{-3}, S=3.3×10^6).*

3. Sawtooth period

The density dependence of the sawtooth period τ_{ST} at fixed plasma current I_p=700 kA (corresponding to q_a=3.7) is shown in Fig. 2. The increase and saturation at low and medium $<n_e>$ resembles, as usual [1], the behaviour of the ohmic energy confinement time, but at higher densities, well inside the saturated confinement regime, τ_{ST} increases again from 5 to 12 ms. Compound sawteeth are absent in this density range (and are however excluded from the τ_{ST} evaluation), so that the period increase is due to a delay in the collapse trigger. The τ_{ST} increase is not caused by a slower evolution of the q-profile between collapses, and it is associated with more peaked density profiles (see Table 1). The data presented in Fig. 2 have been obtained in nearly steady state conditions; longer sawtooth periods have been observed in conjunction with transient strong density peaking, both spontaneous and due to deep deuterium pellet injection [2]. In the latter case, sawteeth are suppressed for 70-80 ms (Fig. 3a); subsequently

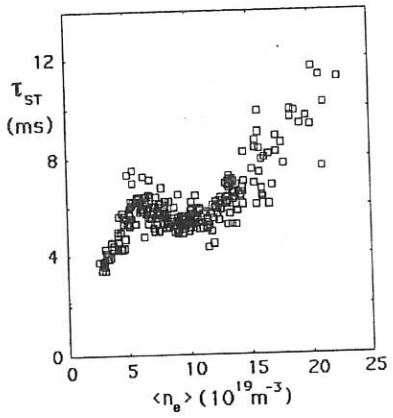

Fig. 2: *Sawtooth period versus volume average density at fixed plasma current I_p=700 kA (q_a=3.7).*

τ_{ST} decreases from 25 to 5 ms on the time scale of the peak density relaxation (Fig. 3b). The q=1 surface remains in the plasma during the sawtooth suppression period, as shown by the equilibrium reconstruction based on magnetic data and by resistive diffusion calculations.

Table 1: Sawtooth period and density peaking at the inversion radius

τ_{ST}(ms)	$n_e(10^{20}m^{-3})$	$n_e'/n_e(m^{-1})$	notes
5	1.6	0.44	gas puff
12	3	1.3	gas puff
20	4	4.8	pellet

4. Discussion

The appearance of successor oscillations, compound sawteeth and superimposed oscillations with increasing values of the Lundquist number points out a dependence of these phenomena on the weakening of resistive effects. The relative importance of the latter can be evaluated by comparing the resistive layer width $\delta_R=r_1(Ss)^{-1/3}$ (here r_1 is the radius of the q=1 surface and s is the magnetic shear at r_1) with the characteristic scale lengths for ideal, electron inertia and ion Larmor radius effects, i.e. with $\delta_H=r_1\lambda_H$, $d_e=c/\omega_{pe}$ and ρ_i respectively. The λ_H parameter is negative if the system is ideally stable; for low β, low shear plasmas we have, manipulating Eq. (9) of Ref.[3]: $\lambda_H=-0.25(r_1/R)^2s^{-1}$. We will do the comparison for the cases shown in Fig. 1c (regime C) and in Fig. 1a (regime A).

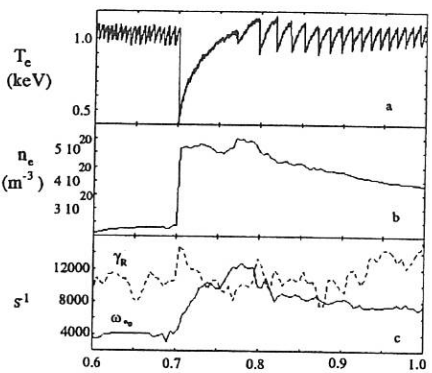

Fig. 3: *a) central T_e evolution for shot #4967 (I_p=700 kA). A pellet is injected at t=0.7 s. b) Peak density evolution. c) Resistive kink growth rate γ_R (dashed line) and electron diamagnetic frequency ω_{*e} (solid line).*

For the low density example (regime C) the relevant plasma parameters are: r_1=70 mm, $S=3.3\times10^6$, $n_e=4.7\times10^{19}$ m^{-3} and T_i=1.6 keV. Assuming s=0.1 we have: δ_R=1 mm, δ_H=−0.9 mm, d_e=0.8 mm and ρ_i=1.4 mm. Ideal effects are not negligible in this case and consequently the mode structure should be intermediate between the ones of the resistive internal kink and of the tearing mode [4], in agreement with the observation of superimposed m=1 oscillations.

For the high density example (regime A) we have: r_1=70 mm, S=1×10^6, n_e=3×10^{20} m^{-3} and T_i=0.8 keV. The ideal stability is nearly marginal in this case ($\lambda_H \approx 0$) as the pressure gradient for $r \leq r_1$ is large and the local poloidal $\beta \approx 0.4$ is close to the threshold value derived by Bussac [5]. The non-ideal characteristic lengths are: δ_R=1.5 mm, d_e=0.3 mm and ρ_i=1 mm, so that in this case resistivity is the dominant effect, although the ion Larmor radius is not negligible and the appropriate regime is the semicollisional one [6].

The correlation between sawtooth period and density peaking suggests that the existence of a quiescent phase between two collapses could be due to diamagnetic stabilisation of the internal kink. This mode is unstable for $\delta_R > (d_e, |\lambda_H|)$ [6], but non-linear calculations [7] give mode saturation at low amplitudes provided that:

$$\omega_{*e} > \gamma_R \ , \qquad (1)$$

where $\gamma_R = s\tau_A^{-1}(Ss)^{-1/3}$ is the growth rate of the resistive kink mode and $\omega_{*e} = T_e n_e'/eBr_1 n_e$ is the electron diamagnetic frequency. The calculations of Ref. [7] were done for the collisional regime ($\delta_R \gg \rho_i$); however, since the semicollisional growth rate [6] $\gamma_{sc} \approx (\rho_i/\delta_R)^{4/7}\gamma_R \approx \gamma_R$, we assume that (1) is applicable in our case. As shown in Fig. 3c, the non-linear stability condition (1) is satisfied in the sawtooth free phase after pellet injection.

The shear used to evaluate γ_R was calculated by a resistive diffusion code. Typical values of 0.1 were obtained. The effect of sawtooth collapses was ignored, so that s and then γ_R are likely to be overestimated when sawteeth are frequent. The γ_R values are however much smaller than the inverse of the central T_e crash time which was as short as 5 μs in fast collapses.

Condition (1) can be translated into a stability boundary for the shear at the q=1 radius: $s < s_{cr}$; a formally similar condition was obtained for the linear stability in the collisionless regime [3]. We conclude that the trigger mechanism in both collisionless and semicollisional regimes depends on a critical shear which increases with the density gradient.

References

[1] G. Vlad, G. Bracco and P. Buratti, Nucl. Fusion 31 (1991) 1536.

[2] F. Alladio et al., Plasma Phys Control. Fusion 35 (1993) B241.

[3] L. Zacharov, B. Rogers and S. Migliuolo, Phys. Fluids B 5 (1993) 2498.

[4] G. Ara, B. Basu, B. Coppi et al., Ann. Phys. (NY) 112 (1978) 443.

[5] M. N. Bussac, R. Pellat, D. Edery and J. L. Soule, Phys. Rev. Lett. 35 (1975) 1638.

[6] F. Pegoraro, F. Porcelli, T. J. Schep, Phis. Fluids B 1 (1989) 364.

[7] D. Biskamp, Phys. Rev. Lett. 46 (1981) 1522.

Correlation among Plasma Rotation, Magnetic Configurations and Improved Confinement Regimes in Present Large Tokamak Experiments

F. Alladio, F. Crisanti, A. Mancuso, P. Micozzi
Associazione Euratom-ENEA, C.R. Frascati, C.P. 65 - 00044 Frascati, Roma, Italy
K.H. Burrell, L.L. Lao, M.S. Chu, T.H. Osborne
General Atomics, P.O. Box 85608, San Diego, California
R. Giannella, P. Lomas, D. O'Brien
JET Joint Undertaking, Abingdon, Oxon, OX14 3DB, UK

1 - Introduction

The VH-mode is obtained on the DIII-D tokamak with tangential NBI heating [1]. In this regime the global energy confinement times τ_E exceeds up to a factor of 4 the L-mode scaling. A necessary condition in order to obtain the VH-mode in DIII-D is the strong shaping of the plasma column: high elongation (κ=b/a $\geq$ 2) and high triangularity ($\delta \approx$ 0.7÷0.8). The VH phase shows a characteristic profile of the radial electric field E_r: in particular, the region where the shear of the radial electric field is strong encompasses in the VH-mode the range of normalised minor radii $0.6< \rho <1$, whereas in the H regime it is limited within $0.85< \rho <1$. There are theories invoking the shear of E_r as the cause of the anomalous transport decrease during the VH-modes and, more generally, of the improved confinement regimes: as a matter of fact, discharges in DIII-D and in other tokamaks with reversed safety factor q profile show a transport barrier located close to the shear reversal; correspondingly very large values of the plasma rotation speed and of the radial electric field are measured in the central region.

A correlation has been found [2] on DIII-D VH-mode discharges between the increase of the poloidal beta β_p (along with the energy confinement time τ_E) and a geometrical property of the plasma configuration: the ratio of the parallel Pfirsch-Schlüter current density J_{PS} and the perpendicular diamagnetic current density J_{DIA}, which is an estimate of the geodesic curvature of the magnetic field lines. The strong shaping of the plasma cross-section reduces $\left\langle J_{PS}^2/J_{DIA}^2 \right\rangle$ (averaged upon a magnetic surface). The geodesic curvature can influence the transport through the reduction of the factor of increase of the moment of inertia $(1+2\hat{q}^2)$ [3] of the magnetic configuration. These reductions are due to the reduced compression that the flux tubes suffer going from the external to the internal side of the torus. So strongly shaped plasmas have higher rotation velocities, with the same momentum source, and therefore can generate stronger radial electric fields and achieve a better stabilisation of the turbulence.

2 - Electric Field and Plasma Rotation

The relation between the radial electric field and the plasma rotation is given by the equation:

$$E_r = \frac{1}{n_i Z_i e}\left(\vec{\nabla} P_i\right)_r - \left(\vec{v} \wedge \vec{B}\right)_r \qquad (1)$$

where n_i is the density of the ion species and Z_i its charge number, e is the electron charge, P_i is the ion pressure, $\vec{B}$ is the total magnetic field (with poloidal and toroidal components $\vec{B}_p$ and $\vec{B}_\phi$) and $\vec{v}$ is fluid velocity. The gradient of P_i is effective only very near to the plasma edge, while the $\vec{v}\wedge\vec{B}$ part of E_r is $|\vec{E}|_{\vec{v}\wedge\vec{B}} \propto G(\psi)RB_p$; the flux function G is:

$$G(\psi) = -\frac{\vec{v}_\perp \cdot \vec{B}_p}{B_p^2}\frac{B^2}{RB_\phi} \qquad (2)$$

where ψ is the flux function, $\vec{v}_\perp$ is the component of $\vec{v}$ orthogonal to the magnetic field and R is the distance from the symmetry axis of the torus. If the anomalous parallel viscosity is much larger than the neo-classical one ($\nu_{eff} \gg \nu_\parallel^{NC}$), the asymptotic value of the perpendicular velocity is [4]:

$$G(\psi, t\gg\tau_G) \cong -\frac{S_G}{\rho_m \alpha \nu_{eff}} \qquad (3)$$

Here $\tau_G = 1/\nu_{eff}$ is the characteristic time of G, ρ_m is the mass density, S_G is the momentum source (proportional to the NBI power) and the geometric factor α is proportional to the ratio between the factor of increase of the moment of inertia $(1+2\hat{q}^2)$ and the square of the safety factor q : $\alpha \propto (1+2\hat{q}^2)/q^2$. In this case the geometry influences the behaviour of G (and so of the radial electric field) by a factor $1/\alpha$.

3 - Experimental Results

From an experimental point of view, a clear correlation appears between the higher values of the volume averaged radial electric field $\overline{E}_r$ measured during the VH shots and the lower value of the α volume average ($\overline{\alpha}$) which characterises them. In Fig. 1-2 an example is given for shots 75121 (VH-mode) and 75984 (H-mode), both with the same plasma current and density. The difference in $\overline{E}_r$ between H and VH shots is already observed at the beginning of the Neutral Beam Injection pulse, well before the VH phase starts; furthermore the time evolution of the radial electric field appears quite different: $\overline{E}_r$ saturates quickly in the H-mode discharges but continues to grow in the VH-mode shots. The ratio of the values of $\overline{E}_r$ between VH and H-mode reaches a factor of more than 2. The estimate of $\overline{\alpha}$ shows a difference between H and VH shots also before the NBI pulse, which spans from 10% to more than 30%, depending upon the elongation of the H-mode discharge.

Therefore the effect of the magnetic configuration upon the radial electric field seems to be stronger than the one expected from the model ($G(\psi, t\gg\tau_G) \propto 1/\alpha$). Furthermore the characteristic time of the $\overline{E}_r$ evolution ($\tau_G = 1/\nu_{eff}$) is longer during the VH-modes, implying that also the anomalous viscosity is influenced by the α factor via the turbulence suppression, due to the increased electric field. Taking into account that $G(\psi, t\gg\tau_G) \propto 1/(\alpha\nu_{eff})$, the α dependence of $\overline{E}_r$ should be more than linear. In this way a positive feedback between the increased electric field and the global energy confinement time (via the magnetic configuration effect) may be responsible for the good plasma performances observed during the VH phase.

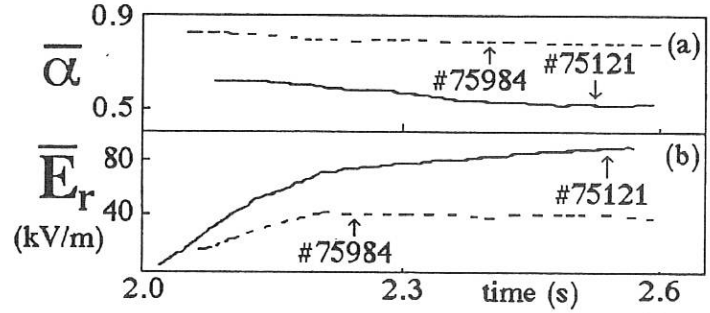

Fig. 1: Time behaviour of the quantity $\overline{\alpha}$ (a) and of the average radial electric field $\overline{E}_r$ (b) for a VH-mode DIII-D discharge 75121 (solid line) with I_p=1.6 MA and P_{NBI}=8 MW, and for an H-mode discharge 75984 (dashed line) with I_p=1.6 MA and P_{NBI}=10 MW.

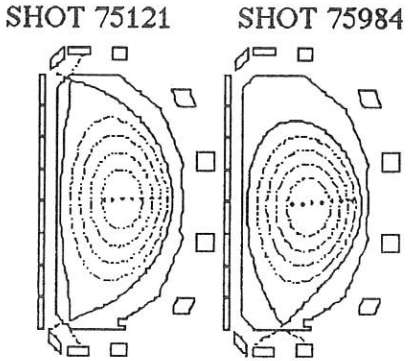

Fig. 2: Flux surface contours for the two DIII-D discharges of Fig. 1. The H-mode shot 75984 is a Single Null configuration less elongated and less triangular (κ=1.8, δ=0.4) with respect to the VH-mode shot 75121, which is a Double Null configuration with κ=2.2 and δ=0.84.

A radial validation of this model is found by analysing the shots with strongly reversed magnetic shear. Discharges in which a reversed q profile ($q_{95} \approx 6$, $q_{axis} \approx 4.5$, $q_{min} \approx 2.5$) is sustained for more than 1 sec have been obtained on DIII-D at low plasma density by operating the NBI during the ramp-up of I_p, with a shape typical of the VH-mode. When the NBI power is increased (during the flat-top of I_p), the reversed q profiles shots show a transport barrier located at $\rho \approx 0.5$ (close to the shear reversal) with very low effective heat conductivity χ_{eff} in the central region of the plasma, in which record values of ion temperature and radial electric field are measured. In Fig. 3 the behaviour of $E_r^{\vec{v}\wedge\vec{B}}$ and $2\hat{q}^2/q^2$ versus the normalised minor radius ρ is shown for a reversed shear shot and is compared with a VH-mode shot. The $2\hat{q}^2/q^2$ profile is VH-like in the external zone, but in

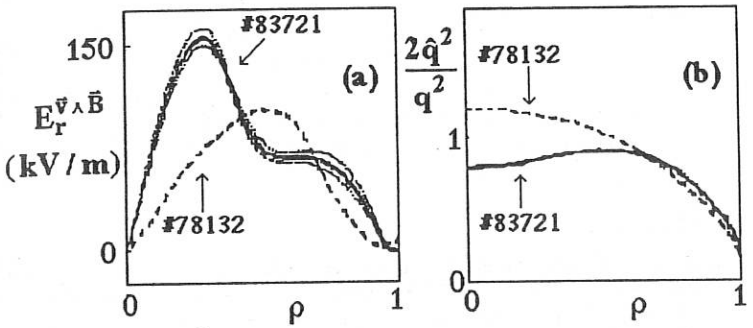

Fig. 3: Profiles of $E_r^{\vec{v}\wedge\vec{B}}$ (a) and of $2\hat{q}^2/q^2$ (b) vs. the normalised radius ρ for a VH-mode (shot 78132 at t=2.6 sec) and for a corresponding reversed shear discharge (shot 83721 at t=1.65 sec). The error bars of the diagnostics that measures the radial electric field is also shown for the non-monotonic q profile case.

the central region it is lower with respect to the VH-mode, corresponding to an electric field and a plasma rotation that are strongly peaked for $\rho < 0.5$.

In JET, although a clear correlation between the toroidal rotation and the magnetic inertia $1+2\hat{q}^2$ is observed, there is no evidence of a correlation between high confinement and triangularity. Up to now the achieved triangularity is $\delta \leq 0.56$. An experiment is proposed to achieve a larger triangularity (δ~0.7÷0.8) in the new divertor configuration (Mark-II) at a current level up to 2.5 MA. In this way it should be possible to obtain values of the $\overline{\alpha}$ parameter of the same order of DIII-D.

4 - Conclusions

The following picture of the improved transport regimes of tokamak plasmas is suggested. The additional heating tends to increase the turbulence level of the plasma: this phenomenon causes the confinement degradation with the injected power. On the other hand, if the same additional heating is able to act also as a net momentum source, the induced plasma rotation can provide an electric field which seems to be able to stabilise the plasma turbulence. The quality of the confinement regime which is obtained in a tokamak discharge is given by the balance between those opposite effects. In this framework the magnetic configuration plays a key role, since a low value of the geodesic curvature can allow a high rotation speed with a moderate level of injected power.

References

[1] Osborne, T.H., Burrell, K.H., et al., Nucl. Fusion **35** (1995) 23

[2] Alladio, F., Report Euratom-ENEA RT/ERG/FUS/94/26 (1994)

[3] Hirshman, S.P., Nucl. Fusion **18** (1978) 917

[4] Alladio, F., Micozzi, P., Report Euratom-ENEA RT/ERG/FUS/95/21 (1995)

Modelling the Dependence of Sawtooth Stability on ICRH Power in Tokamak Plasmas

KG McClements, RO Dendy, RJ Hastie and TJ Martin
UKAEA, Fusion, Culham, Abingdon, Oxfordshire, OX14 3DB,
United Kingdom (UKAEA/Euratom Fusion Association)

1. Introduction

Sawtooth stabilization has been achieved in several tokamaks for a limited period using ion cyclotron resonance heating (ICRH): experiments of this type in JET are described in Ref. [1]. In one discharge (hereinafter discharge A), the central electron temperature T_{e0} initially exhibited sawtoothing behaviour, but rose to a steady value shortly after the onset of ICRH. This steady state persisted for about 1s, during which MHD activity was absent. A sawtooth collapse in T_{e0} then followed, triggered by an instability with toroidal and poloidal mode numbers $n = 1$, $m = 1$. In a second discharge described in Ref. [1] (hereinafter discharge B), sawtooth stabilization did not occur: T_{e0} rose at the onset of ICRH, but continued to exhibit sawtooth behaviour. The ICRH power $P_{\rm RF}$ was 4.3 MW in discharge A and 6 MW in discharge B. The potential energy δW associated with $m = 1$ internal kink displacements is likely to play a crucial role in determining the occurrence of sawteeth: in the ideal limit, instability occurs if and only if $\delta W < 0$. Trapped ions heated by ICRH give rise to a kinetic term in δW, which is positive and stabilizing [2]. δW is computed here for ICRH discharges in tokamak plasmas, taking into account anisotropic pressure as well as kinetic effects, and using parameters which correspond to discharges A and B.

2. Heated Minority Ion Distribution

The model distribution used in Ref. [2] is

$$F_h(\mu,\mathcal{E},r) = 2n_h(r)\left(\frac{m_h}{2\pi T_\perp(r)}\right)^{3/2} G(r)\exp\left\{-m_h\left[\frac{\mu B_0}{T_\perp(r)}+\frac{|\mathcal{E}-\mu B_0|}{T_\parallel(r)}\right]\right\}, \qquad (1)$$

where: magnetic moment μ and energy $\mathcal{E}$ are normalized to minority ion mass m_h; B_0 is magnetic induction at $R = R_0$, where R is distance from the symmetry axis and R_0 is major radius; G is a normalization factor; n_h is minority ion density; r is a minor radial coordinate; and $T_\parallel$, $T_\perp$ are determined by a model of ICRH power deposition proposed by Stix [3]. On a given flux surface, maximum power deposition occurs at $R = R_0$, where $\mu B_0 = v_\perp^2/2$ and $|\mathcal{E}-\mu B_0| = v_\parallel^2/2$. If $B = B_0(1-\epsilon\cos\theta)$, where θ is poloidal angle and $\epsilon \equiv r/R_0$, the locus of constant F_h in the outer midplane is defined by

$$v_\parallel^2 = \left(\frac{T_\parallel}{T_\perp}\right)\frac{u^2 - v_\perp^2(1-(T_\perp/T_\parallel)\,\epsilon)}{1-\epsilon} \qquad \left[v_\perp^2 < v_\parallel^2(1/\epsilon-1)\right], \qquad (2)$$

and

$$v_\perp^2 = \frac{u^2 + v_\parallel^2\,(T_\perp/T_\parallel)\,(1-\epsilon)}{1+(T_\perp/T_\parallel)\,\epsilon} \qquad \left[v_\perp^2 > v_\parallel^2(1/\epsilon-1)\right], \qquad (3)$$

where u is a constant. These two conics meet at a pitch angle corresponding to bounce reflection at $\theta = \pm 90°$, i.e. the points of maximum power deposition. The contour shape defined by Eqs. (2) and (3) depends only on $T_\parallel/T_\perp$: by adjusting the value of this parameter, it is possible to obtain distribution function contours whose shape closely resembles those obtained in full Fokker–Planck calculations [4]. Despite its simplicity, Eq. (1) thus provides a realistic representation of ion distributions heated by ICRH.

3. Evaluation of Kink Energy

The change in potential energy of a toroidal plasma undergoing an $m = 1$ internal kink displacement ξ_0 is

$$\delta W = 6\pi^2 R_0 \xi_0^2 \frac{B_0^2}{\mu_0}\left(\frac{r_1}{R_0}\right)^4 \left\{\delta\tilde{W}_{\rm k} + \delta\tilde{W}_{\rm T} + \delta\tilde{W}_{\rm shape}\right\} \equiv 6\pi^2 R_0 \xi_0^2 \frac{B_0^2}{\mu_0}\left(\frac{r_1}{R_0}\right)^4 \delta\tilde{W}, \quad (4)$$

where the safety factor $q(r_1) \equiv 1$ and $\delta\tilde{W}_{\rm k}$, $\delta\tilde{W}_{\rm T}$, $\delta\tilde{W}_{\rm shape}$ are dimensionless forms of, respectively, the kinetic, toroidal and cross-sectional shaping contributions to δW. When the mode frequency is smaller than the precessional drift frequency of the heated ions we can write

$$\delta\tilde{W}_{\rm k} = -\frac{2\sqrt{2}\pi}{3}\frac{\mu_0 m_h}{B_0 R_0}\left(\frac{R_0}{r_1}\right)^4 \int_0^{r_1} r dr \int_{1/B_{\rm min}}^{1/B_{\rm max}} d\lambda \int_0^\infty \mathcal{E}^{3/2} d\mathcal{E} \frac{\partial F_h}{\partial r}\frac{I_q^2}{I_c + sI_s}, \quad (5)$$

where $F_h = F_h(\lambda \equiv v_\perp^2/(v^2 B), \mathcal{E}, r)$, $B_{\rm min} = B_0(1-\epsilon)$, $B_{\rm max} = B_0(1+\epsilon)$, $s \equiv d\ln q/d\ln r$, and I_c, I_s, I_q are functions of λ defined in Ref. [2]. In general, $\delta\tilde{W}_{\rm k}$ is complex: this paper is concerned solely with the real part of $\delta\tilde{W}_{\rm k}$, which is given by the principal part of the λ integral in Eq. (5). A tractable expression for $\mathrm{Re}(\delta\tilde{W}_{\rm k})$ may be obtained by expanding to leading order in $1-q$ and s and integrating by parts. The final result can be evaluated numerically for prescribed radial profiles of $T_\perp$, $T_\parallel$, n_h and q. $T_\perp(r)$ is determined by the ICRH power deposition profile, which we assume to be of the form

$$P_d(R,Z) \propto \exp\left\{-\frac{(R-R_0)^2}{d^2} - \frac{Z^2}{D^2}\right\}, \quad (6)$$

where Z is vertical distance and D is much smaller than the minor radius a. The Stix model [3] predicts that $T_\perp \simeq \rho_{\rm RF}\tau_s/2n_h$, where $\rho_{\rm RF}$ is the ICRH power density coupled to minority ions and τ_s is the slowing-down time. We identify $\rho_{\rm RF}$ with the peak value of P_d on a given flux surface, in which case $T_\perp(r) \simeq T_\perp(0)\exp(-r^2/D^2)$, where $T_\perp(0)$ can be deduced empirically from direct measurements of F_h [2,5,6]: for a 4 MW ICRH discharge in JET (such as discharge A), $T_\perp(0) \simeq 140$ keV.

We assume electron temperature and density profiles of the form

$$T_e(r) = T_{e0}\left[1-(r/a)^2\right]^{\nu_{Te}}, \quad n_e(r) = n_{e0}\left[1-(r/a)^2\right]^{\nu_{ne}}, \quad (7)$$

where, in discharge A, $T_{e0} = 6.4$ keV, $\nu_{Te} = 1.90$, $n_{e0} = 2.1\times 10^{19}$ m^{-3} and $\nu_{ne} = 0.7$. At low ICRH power, $\epsilon T_\perp/T_\parallel \ll 1$ for $r \le r_1$ [2], and we can then write [7]

$$\delta\tilde{W}_{\rm T} = \frac{1}{6}\beta_p^c + \delta\tilde{W}_1 + \beta_p\delta\tilde{W}_2 + \beta_p^2\delta\tilde{W}_3, \quad (8)$$

where: $\delta\tilde{W}_1$, $\delta\tilde{W}_2$ and $\delta\tilde{W}_3$ depend on the q–profile; β_p is the beta poloidal, defined in terms of an equivalent scalar pressure $p \equiv p_{\rm bulk} + (p_\parallel + p_\perp)/2$, where $p_{\rm bulk}$ is the bulk plasma pressure and $p_\parallel$, $p_\perp$ are the parallel and perpendicular pressures of the heated minority ions; and β_p^c is defined in the same way as β_p except that p is replaced by $(p_\parallel + p_\perp + C)/2$, where

$$C = 4\pi m_h \int\int \frac{B}{|v_\parallel|}(\mu B)^2 \frac{\partial F_h}{\partial \mathcal{E}} d\mu d\mathcal{E} \simeq -4Gn_h \frac{T_\perp}{T_\parallel}(T_\parallel T_\perp)^{1/2}. \qquad (9)$$

$\beta_p^c < 0$ when $T_\perp > T_\parallel$. β_p can be split into bulk plasma ($\beta_p^{\rm bulk}$) and hot minority ion ($\beta_p^{\rm hot}$) components. To compute $\beta_p^{\rm bulk}$, we set the central bulk ion temperature and density equal to 5.5 keV and 8×10^{18} m^{-3}; to compute $\beta_p^{\rm hot}$, we assume a minority ion concentration n_h/n_e of 0.02 [2]. Finally, we set

$$q(r) = q_0[1 + \lambda_q(r/a)^{2\nu}]^{1/\nu}. \qquad (10)$$

To model the early stage of the sawtooth–free period we set $q_0 = 0.8$, $\lambda_q = 41.2$, $\nu = 2$: to model the late stage of the sawtooth–free period, we set $q_0 = 0.7$, $\lambda_q = 149.4$, $\nu = 2.5$.

The contributions to $\mathrm{Re}(\delta\tilde{W})$ at the beginning and end of the sawtooth–free period are listed in Table 1. $\mathrm{Re}(\delta\tilde{W})$ changes sign from positive to negative: our model implies that the ideal internal kink mode becomes unstable at about the same time as the end of the sawtooth–free period. The change in the q–profile is such that $|\delta\tilde{W}_{\rm T}|$ and $|\delta\tilde{W}_{\rm shape}|$ rise sufficiently rapidly to bring about destabilization. The shape term becomes more important as r_1 increases because flux surface cross–sections become less circular towards the plasma edge. $\delta\tilde{W}_{\rm shape}$ is also sensitive to ν: the sharp increase in $|\delta\tilde{W}_{\rm shape}|$ is due partly to a flattening of the q–profile at $r < r_1$.

Table 1: Safety factor parameters and contributions to δW in early stage (second column) and late stage (third column) of sawtooth–free period in discharge A.

q_0	0.8	0.7
r_1/a	0.34	0.40
$\mathrm{Re}(\delta\tilde{W}_{\rm k})$	0.0089	0.0098
$\delta\tilde{W}_{\rm T}$	−0.0015	−0.0046
$\delta\tilde{W}_{\rm shape}$	−0.0024	−0.0074
$\mathrm{Re}(\delta\tilde{W})$	0.0050	−0.0022

Fig. 1(a) shows the contributions to $\mathrm{Re}(\delta\tilde{W})$ as functions of $T_\perp(0)$. In discharge B, $T_\perp(0) \simeq 210$ keV. The change of sign in $\mathrm{Re}(\delta\tilde{W})$ can be attributed to the fact that $\mathrm{Re}(\delta\tilde{W}_{\rm k})$ scales with $\beta_p^{\rm hot}$ whereas $\delta\tilde{W}_{\rm T}$ contains a negative term which scales with $(\beta_p^{\rm hot})^2$: a sufficiently large increase in minority ion pressure is destabilizing. This change of sign is consistent with the observation that sawteeth are suppressed in discharge A but not in discharge B. Fig. 1(b) shows the contributions to $\mathrm{Re}(\delta\tilde{W})$ as functions of D: optimum stability can be achieved by minimizing the vertical extent of the ICRH power deposition profile.

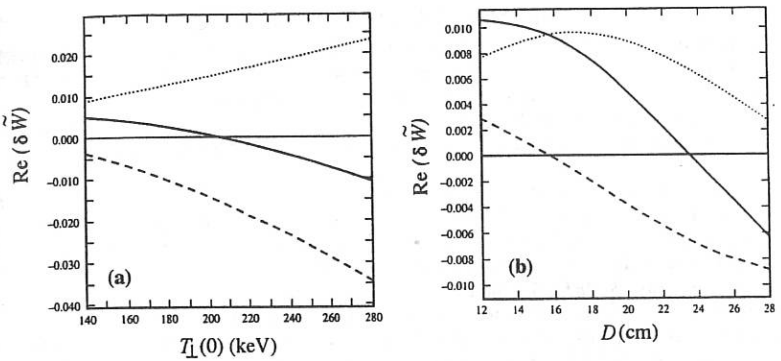

Fig.1: $\mathrm{Re}(\delta\tilde{W}_\mathrm{k})$ *(dotted line),* $\delta\tilde{W}_\mathrm{T} + \delta\tilde{W}_\mathrm{shape}$ *(dashed line) and* $\mathrm{Re}(\delta\tilde{W})$ *(solid line) as functions of (a)* $T_\perp(0)$ *and (b)* D.

4. Discussion

In a study of two ICRH JET discharges, a correlation has been found between the occurrence of sawteeth and the sign of the $m = 1$ internal kink energy δW. An increase in ICRH power can reduce δW, leading to greater instability, as observed. Sawtooth suppression is clearly associated with $\mathrm{Re}(\delta\tilde{W}) > 0$, and therefore it is logical to search for accessible parameter régimes in which $\mathrm{Re}(\delta\tilde{W}) > 0$ can be maintained. Our model indicates that stability can be enhanced by minimizing the vertical extent of the ICRH power deposition profile. We have assumed that the heated minority ions are weakly anisotropic ($\epsilon T_\perp/T_\parallel \ll 1$) and have thin banana orbit widths ($\ll r_1$): these assumptions break down when the ICRH power is very high, and in fact sawtooth stabilization has been observed in JET discharges with $P_\mathrm{RF} > 6$ MW. However, the contribution of heated ions to the Shafranov shift (represented by the β_p and β_p^2 terms in Eq. (8)) implies that instability must occur when P_RF is sufficiently high.

Acknowledgments

This work was funded by the UK Department of Trade and Industry and Euratom.

References

[1] DJ Campbell et al, *Phys. Rev. Lett.* **60** 2148 (1988)
[2] KG McClements, RO Dendy, RJ Hastie, TJ Martin, *Phys. Plasmas* in press (1996)
[3] TH Stix, *Nucl. Fusion* **15** 737 (1975)
[4] RW Harvey, MG McCoy, GD Kerbel, SC Chiu, *Nucl. Fusion* **26** 43 (1986)
[5] AA Korotkov, A Gondhalekar, Proc. 21st Eur. Conf. on Contr. Fusion and Plasma Physics, Montpellier (1994), I, p.266
[6] KG McClements, RO Dendy, A Gondhalekar, these proceedings
[7] AB Mikhailovskii, *Sov. J. Plasma Phys.* **9** 190 (1983)

Study of Internal Reconnection Events on the START Tokamak

R. J. Buttery, M. K. Bevir, A. Caloutsis, D. Gates, C. G. Gimblett, M. Gryaznevich, T. C. Hender, I. Jenkins, R. Martin†, C. Ribeiro*, D. C. Robinson, A. Sykes, M. Valovič, M. J. Walsh, H. R. Wilson.

†*UKAEA Fusion, Culham, Oxon, OX14 3DB. UK.* †*UMIST, Manchester, UK.*

**University of Sao Paulo, Brazil.* (UKAEA / EURATOM Fusion Association).

Abstract

New results and analyses of Internal Reconnection Events (IREs) are presented in order to understand better the disruption immunity of START. Using new diagnostics, better reconstructions of changes in the START plasma have been possible. The equilibrium models used for this allow analysis of a range of plasma parameters and examination of various constraints in order to model the IRE. We find a modified helicity conservation model generally reproduces global parameter changes well. Studies of the behaviour of various parameters show that there are a number of 'special' properties of tight aspect ratio plasmas, most notably in responses of flux and q values to IREs, which may explain the disruption immunity.

1. Introduction

The absence of current terminating disruptions on the START device continues to be of much interest. In conventional aspect ratio tokamaks (eg JET) they rapidly terminate the plasma current, and particularly if associated with vertical displacement events, can lead to severe structural and thermal loads in a future power plant. On START no such event has been seen at tight aspect ratio ($A = R/a < 1.8$) in over 30000 discharges. However Internal Reconnection Events (IREs) are common and appear to exhibit many of the properties of a disruption (rapid increase in plasma current, negative spike in loop voltage, increase in elongation, reduction in plasma energy) but without termination of the current.

IREs on START occur under a range of plasma conditions and with varying signatures. However in a given regime, it is often possible to achieve highly reproducible effects, and thus a more detailed study of the IRE is possible. The START tokamak is now equipped with new diagnostics, including a 30 point Thomson scattering and 3 soft X-ray (SXR) cameras enabling more detailed information about plasma changes to be obtained.

2. IREs on START

While IREs occur in all operating regimes, they occur more frequently near the density and current limits in the Hugill diagram. In a typical IRE, fast CCD pictures show that on reconnection, the plasma elongates, sometimes even touching the PF coils and there is an increase in visible light intensity suggesting energy loss through the separatrix, and there is sometimes some inward motion. Afterwards the plasma quickly (2-3ms) returns to its pre-IRE parameters.

Looking at the SXR data we see various signatures. Typically there is a steady growth in emission prior to the IRE, with little or no radial motion accompanying the event. Also, the IRE can be accompanied by mode activity in the centre of the plasma, with growth of m=1 and/or m=2 modes just prior to the IRE.

The new Thomson scattering system produces detailed electron density and temperature profiles in the plasma at a single time. Thus it is possible to compile a full picture of the

IRE with a range of identical shots. Looking at a density limit IRE (shown below, against time relative to the start of plasma current rise and major radius), we see that there is a large and rapid (~ 0.2ms) fall in both electron density and temperature coincident with the plasma current rise of the IRE. The electron temperature falls more rapidly (~ 0.1ms) than the density, and slightly ahead (~ 0.1ms) of the current rise, but also recovers faster after the IRE. The magnetic axis appears to move inwards 2-3cm. In other regimes different effects are seen, eg. for broader pressure profiles, the fall in pressure prior to the IRE is much slower (~1ms).

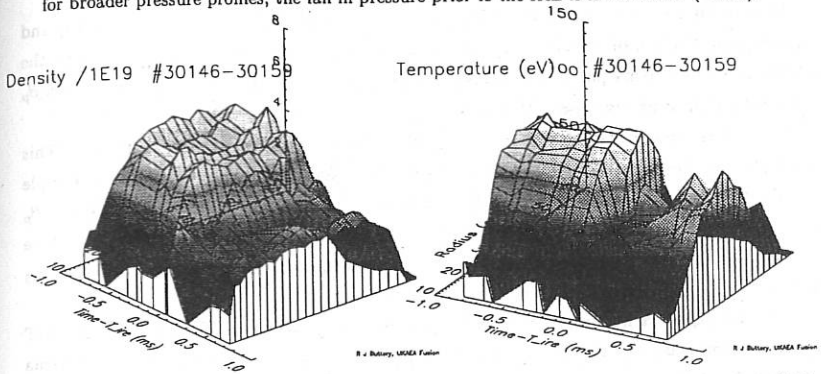

Figure 1: Electron Density and Temperature Variation during a Density Limit IRE on START

3. Modelling of IREs

Thus, as IREs occur in many differing regimes, accompanied by a wide range of effects, it is hypothesised that the disruption immunity of START results from some intrinsic property of the nature of the plasma response to changes. Earlier modelling showed the effects due to the vessel or coil casing currents to be small. In order to understand the processes better, reconstructions of the plasma have been undertaken using a free-boundary Grad-Shafranov equilibrium code.

The results of such reconstructions are given in lines 1 and 2 of the table below. This is based on the density limit shots shown above, reconstructed just before the fall in pressure and I_p rise, and at the maximum of the current rise when central pressure is at a minimum. In order to match the post-IRE state we must redistribute the current profile, thus dropping the inductance and raising central q. We then find the plasma elongates, and the observed changes in radius and vertical field are matched. The magnetic energy (ΔM.E.) also falls, consistent with the idea of a relaxation of the plasma. Here, there is also a clear rise in edge q and q_{95} and toroidal flux (ϕ) as it becomes more paramagnetic.

Case	I_p/kA	R_{axis}/m	k	$\int Pdl$	l_i	β_p	q_e	q_0	ϕ	ψ_p	ΔM.E.
Prior to IRE	*132	*0.325	1.69	*386	0.723	0.169	14	1.1	91	32	-
After IRE	*170	*0.288	2.28	*131	0.340	0.052	14.5	2.3	106	20	-379
Helicity cons'	175	.291	2.33	131	0.333	0.052	14.9	2.4	110	20	-306

*Table: Reconstruction of density limit IRE to match to plasma current, radius and vertical field on the central rod. * parameters forced to match experiment, others are therefore predictive.*

If we examine the changes in the plasma parameters more closely, we see that the post-IRE state is close to a modified helicity conservation constraint, given the same falls in β_p and l_i, as shown in line 3 of the table. The helicity constraint presumes no helicity dissipation between pre- and post-IRE states, apart from that due to the plasma motion, and is prescribed by:

$$\Delta K = -(\phi_f + \phi_i)(\psi^e{}_f - \psi^e{}_i)$$

It is found that other constraints, such conservation of toroidal flux (ϕ) or poloidal flux (ψ_p) in the plasma, or of LI_p are not such a good fit.

Thus we find we can represent the IRE well with a model allowing falls in β_p and l_i and requiring conservation of helicity, by adjusting the plasma current. This enables us to scan the behaviour of the plasma parameters across various types of IRE, by scanning in post-IRE β_p and l_i values for some given pre-IRE state.

Performing these scans confirms the trends seen in reconstructions, as described above. This technique was then used to compare with conventional tokamaks, taking as a second example a case with a JET-like aspect ratio and β_p, and scanning similar ranges of fractional falls in β_p and l_i. For A$\sim$3 we found the plasma current and elongation changes were smaller, but there was much greater inward motion of the plasma, with substantial falls in minor radius. Also q_{95} and toroidal flux fell substantially, with a modest rise in q_0.

Thus we expect a number of clear differences in the behaviour of IREs between START and conventional aspect ratio tokamaks. However this could be due to differences in A, plasma shaping, initial β_p or some other parameter. Thus before discussing these effects we attempt to analyse more rigorously, with a methodical approach in which pre-IRE conditions were maintained constant with A, with $l_i = 1$, $\beta_p = 0.6$, for a possible future spherical tokamak with I_p=1.6MA, minor radius of 1m, inboard limiter, and almost uniform vertical field. Post-IRE states were then constructed with a fall in l_i of 0.3 (to represent a partial relaxation), and various falls in β_p, to obtain the changes displayed in Fig 2. It should be noted that the complete loss of β_p case shown here is an extreme one not usually seen in experiment, but included here to highlight trends.

The same behaviour is seen for plasma current (Fig 2a) and elongation (Fig 2e) as described above. However, we now see that the radial motion of the plasma (Fig 2b) is mainly dependent on the absolute fall in the size of β_p, which may explain why strong radial motions are not seen on START, which usually has a small β_p. Note also in this figure, as the plasma is inboard limited, changes in minor radius will be double the change in radius, leading to substantial falls from the initial value of 1m for large falls in β_p. However, decreases in minor radius, would not necessarily lead to loss of plasma as, for example, increases in toroidal flux (for example if the plasma elongates, as it does at low A) may result in the plasma moving towards the magnetic axis, if the plasma follows flux surfaces.

We can use a force free assumption ($\mathbf{J} \times \mathbf{B}$=0) to calculate how the plasma motion is based a combination of the motion of poloidal and toroidal flux surfaces. The results of this are shown in Fig 2f, with losses given in terms of the percentage of poloidal flux in the initial plasma. We find these approximately match changes seen in toroidal flux (not shown here). This demonstrates

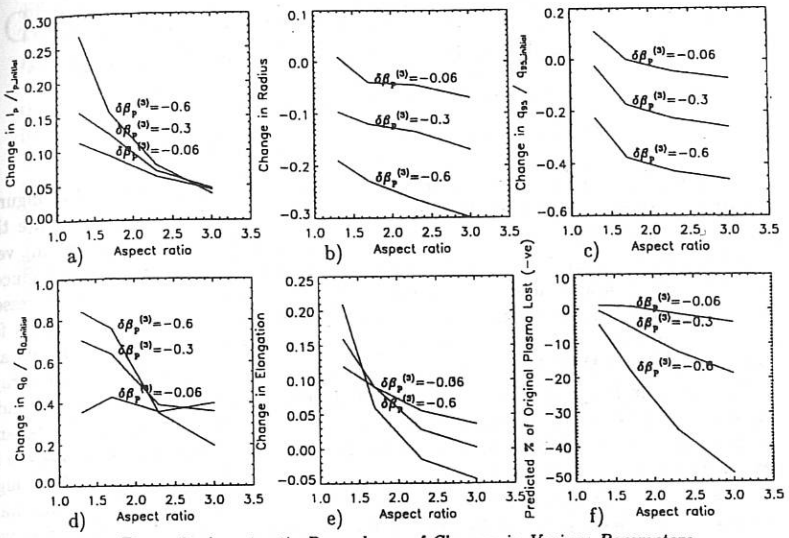

Figure 2: Aspect ratio Dependence of Changes in Various Parameters

that unlike at low A, at conventional A we expect to loose a significant portion of the plasma. This seems a promising explanation of disruption immunity. However, there may be anomalous effects that prevent the plasma following flux surfaces.

An alternatively explanation may lie in the q behaviour. At low A, the fractional falls in edge q are lower, while the initial edge q is higher due to geometric effects. Indeed edge q and q_{95} can rise at low A if there is a substantial change in elongation (eg see table). This contrasts with the conventional aspect ratio case where the already low value of edge q falls further, raising the possibility of successive low q surfaces reaching the edge of the plasma, destabilising low m/n modes, leading to a progressively more unstable situation, and current termination.

It is also interesting to note the larger rises in central q at tight aspect ratio. This may have the benefit of removing low m/n modes that may otherwise grow and disrupt the plasma, as would be the case in the table above where q_0 rises well above 2.

4. Conclusions

We have seen internal reconnections at tight aspect ratio occur in a range of regimes with varying precursors. Reconstructions show these can be modelled with modified helicity conservation. Analysis with this model shows that the behaviour of IREs on START is substantially different to conventional tokamaks. More systematic aspect ratio scans show the origins of this may lie in flux conserving motions or q changes. Further detailed analysis, and comparison with experiment, will attempt to resolve the underlying physics of this, and isolate the critical factors, particularly with access to higher β_p regimes with the new Neutral Beam Injector on START.

This work was jointly funded by the UK Dept. of Trade and Industry and Euratom.

Halo Currents and VDEs in COMPASS–D

G.G. Castle, A.W. Morris, D. Gates, M. Valovič

UKAEA Government Division, Fusion,

Culham Laboratory, Abingdon, Oxon. OX14 3DB.

A series of experiments were performed on COMPASS–D in a single null configuration (vessel parameters $R = 0.557$ m, $a = 0.232$ m, $b = 0.385$ m) to investigate the properties of poloidal and toroidal halo currents flowing in the vacuum vessel during vertical displacement events, or VDEs. Both poloidal and toroidal halo currents are induced during a disruption and these currents can produce large forces on the vacuum vessel; these forces are a serious design consideration for ITER and also have consequences for in-vessel components and the vacuum vessel on devices such as JET. Halo currents are diagnosed on COMPASS–D by three main diagnostics: three toroidally separate arrays of $\dot{B}$ magnetic pickup coils (located at toroidal angles of $\phi = 0$, $\phi = \frac{3}{4}\pi$ and $\phi = \pi$ radians) comprising 72 distinct measurements of each field component, 3 resistive shunts, and Langmuir probes located in an X–point limiter tile. The halo shunt measurements are in qualitative agreement with the poloidal currents determined from the $\dot{B}_\phi$ coils (although the magnetically determined currents are $\sim 35\,\%$ lower on average). Peak poloidal halo currents of up to $0.55\,I_{po}$ (I_{po} is the pre–disruption plasma current) have been observed with shunt measurements. These values are similar to those seen on ASDEX-U, DIII-D, JET and JT-60 [1, 2, 3]. The large number of coils provides a unique and powerful diagnostic for halo current measurements. The full set of coils allows determination of both axisymmetric ($n = 0$) and non-axisymmetric ($n = 1$) current modes with poloidal mode numbers as high as $m = 12$.

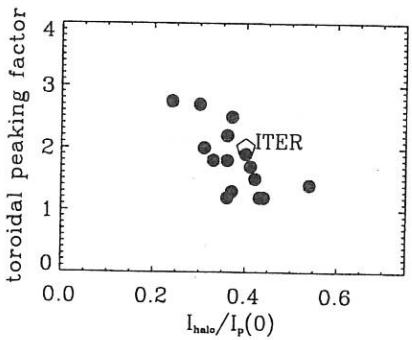

Figure 1: *Toroidal peaking factor as a function of the normalised maximum poloidal halo current, $I_\theta^{max}/I_p(0)$ on COMPASS-D, including the ITER design point for comparison. The values of I_θ^{max} are from shunt measurements.*

Vertical disruptions were induced both away from and towards the X–point and scans of B_ϕ ($B_\phi = 1.1 - 1.85\ T$, $I_{po} = 180\ kA$) and I_{po} ($I_{po} = 115 - 195\ kA$, $B_\phi = 1.2\ T$) were performed to determine the scaling of halo current magnitudes and to investigate any

differences due to conducting structures in the vessel or asymmetries in VDE direction. These scalings show that the maximum magnitude of the poloidal halo current scales like I_{po}^2 and decreases weakly with B_ϕ (i.e., there is no direct scaling with q).

The calculated peak vertical force due to the measured poloidal halo current distribution in the vessel wall interacting with the background toroidal field also scales like I_{po}^2 but decreases weakly with B_ϕ. At a given time, the toroidal peaking factor is the ratio of the maximum $\Delta B_\phi|_{max}$ as measured at two toroidally opposing locations divided by the average $\Delta B_\phi|_{max}$ between those two locations ($\Delta B_\phi|_{max}$ is the maximum ΔB_ϕ measured at a particular toroidal angle). It is a measure of the toroidal asymmetry of the poloidal halo currents. As can be seen from Figure 1, on COMPASS-D the toroidal peaking factor is close to the toroidal peaking factor for the ITER design point. The $n = 1$ asymmetric portion of the poloidal halo current can be a significant fraction ($\sim$ 50 %) of the peak poloidal halo current. Unlike observations from Alcator C-MOD [4], on COMPASS-D only a very small fraction of the halo current structure appears to rotate toroidally. As COMPASS-D has low intrinsic error fields, presumably the lack of rotation is due to some mechanism other than mode locking. Scalings of plasma elongation ($1.1 \leq \kappa \leq 1.6$) were performed which verified the increasing severity of VDEs with increasing κ. Initial indications are that the energy quench phase tends to induce poloidal halo currents that flow in such a sense as to preserve the diamagnetic portion of the toroidal flux (tending to pull plasma facing components from the vessel wall), while during the current quench phase the poloidal halo currents flow paramagnetically (tending to compress plasma facing components) and reach maximum amplitude.

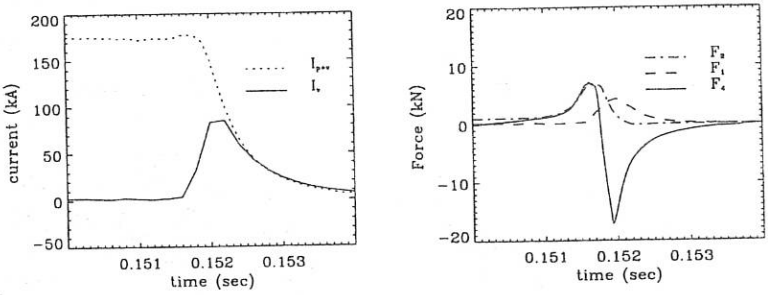

Figure 2: *The figure on the left indicates the time histories of the sum of the plasma and vessel currents, along with the vessel current for COMPASS-D shot 17110. The figure on the right displays the three main vertical magnetic forces acting on the vessel wall during the VDE.*

COMPASS-D is equipped with a set of internal and external partial Rogowski coils to measure the poloidal magnetic field distribution both inside and outside the vacuum vessel, three $\dot{B}_\phi$ Mirnov arrays at different toroidal locations, and seven flux loops for measuring toroidal voltage. These diagnostics provide the unique ability to measure all of the currents and fields producing vertical or radial $\vec{j}_\theta \times \vec{B}_{\dot{\phi}}$ or $\vec{j}_\phi \times \vec{B}_\theta$ forces on the vacuum vessel. It should be stressed that it is impossible to separate the image current and halo current contributions to these forces. The four important fields producing vertical

forces are B^0_ϕ, B^1_ϕ, B^0_θ, and B^1_θ ("0" means $m = 0$ while "1" means the $\sin\theta$ component). B^0_ϕ is determined via the current in the TF coils, B^1_ϕ is determined by integrating $\dot{B}_\phi$ from the Mirnov coils (assuming no contribution before the disruption). B^1_θ and B^0_θ are obtained by integrating over the B_θ distribution provided by the internal and external partial Rogowski coils.

If we assume that both the fields and currents may be expanded in a series of $\sin m\theta$ and $\cos m\theta$ components, then the integration over the COMPASS–D vacuum vessel shape gives the following expression for the net vertical magnetic force:

$$F_z = \pi \frac{a+b}{2} 0.872 \left(I^0_\phi B^1_\theta + I^1_\phi B^0_\theta - I^0_\theta B^1_\phi - I^1_\theta B^0_\phi \right) = F_1 + F_2 + F_3 + F_4 \qquad (1)$$

The factor of 0.872 comes from the noncircular shape of the COMPASS–D vacuum vessel. F_1, F_2, and F_4 are displayed in Figure 2 for COMPASS–D shot 17110 (F_3 was negligible and so not included). This shot was a downward-induced disruption and one can see that F_4, the force due to the poloidal halo current, has the largest effect.

The torque about the $\phi = \pi/2$ (y) axis may be calculated by assuming that the vertical force density on the vacuum vessel varies smoothly from the measurements made at $\phi = 0$ to those made at $\phi = \pi$. We assume that the vertical force density may be written as

$$\frac{1}{R}\frac{\partial \vec{F}_z}{\partial \phi} = \frac{\cos^2(\frac{\phi}{2})\, F_z(\phi = 0) + \sin^2(\frac{\phi}{2})\, F_z(\phi = \pi)}{2\pi R}\, \hat{e}_z. \qquad (2)$$

This can be reduced to the simple formula

$$N_y = \frac{1}{4}(F_z(\phi = 0) - F_z(\phi = \pi)). \qquad (3)$$

Figure 3 shows that the maximum torque increases along with the maximum vertical force.

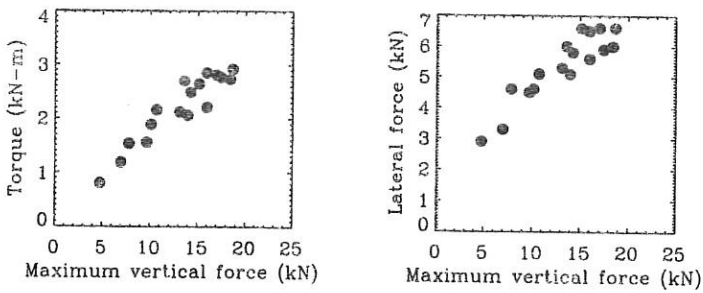

Figure 3: *Maximum torque on vacuum vessel as a function of the maximum vertical force magnitude for a set of downward VDEs, and the maximum lateral force versus maximum vertical force magnitude for the same shots. Here each quantity is the peak value during a shot, not necessarily obtained at the same time (the torque N_y may peak at a different time from when the vertical force F_z peaks).*

The lateral force in the $\phi = 0$ direction may be calculated in a manner similar to that of the torque and is given by

$$F_L = \frac{1}{4}(F_R(\phi = 0) - F_R(\phi = \pi)) \tag{4}$$

where F_R is the radial $\vec{j} \times \vec{B}$ force obtained at a given toroidal location. An important issue for ITER is estimating the worst-case stresses on the vacuum vessel during a disruption. Data from ASDEX, ALCATOR C-MOD, and COMPASS-D all show that the maximum poloidal halo current scales like $I_p(0)^2$. The greatest possible poloidal halo current would occur if all of the initial plasma energy were converted into a poloidally circulating halo current. In this case we would have

$$W_i + \frac{1}{2}L_p I_p^2(0) = \frac{1}{2}L_\theta I_\theta^2 \tag{5}$$

which clearly could exceed $I_p(0)$. This situation would of course require a mechanism that would allow such a conversion (which may or may not exist); therefore this estimate of I_θ^{max} represents an upper bound. Also, dissipation of the plasma energy through increased radiation and Ohmic losses ($\propto I_\theta^2$) will tend to lower the actual peak value.

During a VDE, the plasma is subject to several sources of vertical force. Once the plasma has moved a distance Δz from its equilibrium position, there are both stabilising and destabilising forces acting upon it. For small displacements, these forces are both proportional to Δz and I_p^2. As the plasma moves toward the wall, image currents are induced are proportional to $\Delta z I_p^2$. Once the plasma has made contact with the vessel, halo currents begin to circulate poloidally (and toroidally). These currents exert a calculable force on the vacuum vessel (once I_θ and B_ϕ are known). The linearised vertical force balance on the plasma can then be written as

$$(\alpha\,\Delta z + \beta\,\Delta \dot{z})\,I_p^2 = \hat{e}_z \cdot \oint \vec{I}_\theta \times \vec{B}_\phi\, d\theta. \tag{6}$$

Here α and β are functions of the plasma equilibrium, the control fields, and the vessel characteristics. This equation illustrates how the instantaneous vertical halo force is proportional to I_p^2, but it is not obvious why the maximum poloidal halo current should scale like $I_p(0)^2$. The time histories of Δz, α, β and I_p must play an important role. As the scaling of F_z with $I_p(0)^2$ appears to be a serious problem for ITER, more work should be undertaken to compare theory with experiment.

This work was funded by the UK Department of Trade and Industry and Euratom

References

[1] R. Yoshino, Y. Neyatani, *et al.*, *The softening of current quenches in JT60-U*, Nuclear Fusion, **33**, (1993), pp. 1559-1612

[2] R. Yoshino, Y. Neyatani, *et al.*, Proceedings of the 15th International Conference on Plasma Physics and Controlled Nuclear Fusion Research, Seville, 1994, (IAEA Vienna) pp. 685-695

[3] O. Gruber, K. Lackner, G. Pautasso, U. Seidel, B. Streibl, *Vertical Displacement Events and Halo Currents*, Plasma Physics and Controlled Fusion, 35 (1993) vol. B, pp.191-204

[4] R.S. Granetz, *Disruptions and Halo Currents in Alcator C-MOD*, Proc. 1995 APS Plasma Physics Conf.

First Results of Neutral Beam Heating in START Spherical Tokamak Plasmas

M J Walsh, R J Akers, R A Bamford, R J Buttery, P G Carolan, D M Codling, N J Conway, G F Counsell, M Cox, J Dowling, T. Edlington, M Gryaznevich, T Gunston, I Jenkins, S J Manhood, R Martin[a] M Mironov[b] K. Morel[c] A W Morris, M P S Nightingale, M O'Brien, S Ya Petrov[b] Y-K M Peng[d], M N Price, C Ribeiro[e], D C Robinson, M Singleton[f] R T C Smith, A Sykes, T N Todd, C C Tsai[d], S E V Warder, A. Whitehead
UKAEA, Fusion, Culham, Abingdon, Oxon, OX14 3DB, UK
(UKAEA/Euratom Fusion Association)

Introduction

Although originally a low-budget experiment based on spare equipment, START has been continually upgraded and can now obtain large plasmas (R = 0.34m, a = 0.27m giving 'spherical' plasmas of over 1m in overall diameter), plasma currents of over 200kA and a plasma duration of longer than 40 msec. In 1994, it was decided to augment the programme by testing the effects of additional heating by neutral beam injection using a 40keV, 0.5MW neutral beam injector lent to Culham by ORNL in the USA. To aid this, the plasma diagnostics have recently been much improved, with the addition of a 30 point Thomson scattering system, a high speed video camera capable of 40,000 fps, tomography from three new SXR cameras, 20 channel spectroscopic ion temperature diagnostics and a 16-channel Neutral Particle Analyser(NPA) capable of observing energies up to 50keV.

The ORNL beam began operation at Culham in late 1995 with tangential co-injection into START plasmas (modelling and experiment have shown that counter-injection losses are high). Since then the beam and plasma parameters have been steadily optimised. All operation is presently in hydrogen.

The Beam

An outline diagram of the beam geometry in the START experiment is shown in figure 1. It is set up to nominally inject power tangentially in the co-direction and has an impact parameter of R=0.28m. The beam has a divergence of 1.4^0 and is focussed to achieve a 1/e half-width of 13cm in the plasma. Estimates using a graphite beam-dump suggest that the beam power is ~240kW at an ion current of 43.6A at 25.5keV. The ion current reaches its flat-top in approximately 4ms. A visible spectrometer was used to show that the $H^+ : H_2^+ : H_3^+ : H_2O^+$ *ion* current ratio was 0.61 : 0.24 : 0.13 : 0.02 corresponding to *neutral* currents of E : E/2 : E/3 of 5.4 : 5.4 : 4.1A at 25.5 : 12.75 : 8.5keV or 138 : 69 : 35kWatts. The total number of particles in the beam is $\sim 10^{20}$/second.

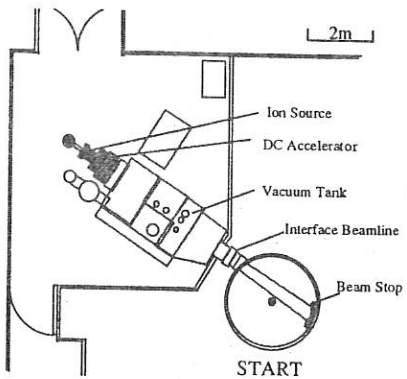

Figure 1

Results

Typical plasma parameters for a beam heated discharge are Ip~200kA,k=1.8 and R~0.32m A~1.26. Generally there is a slow increase in electron density when the beam is on. The ion temperatures (Figure 2) as measured by CXR-spectroscopy and by NPA show a

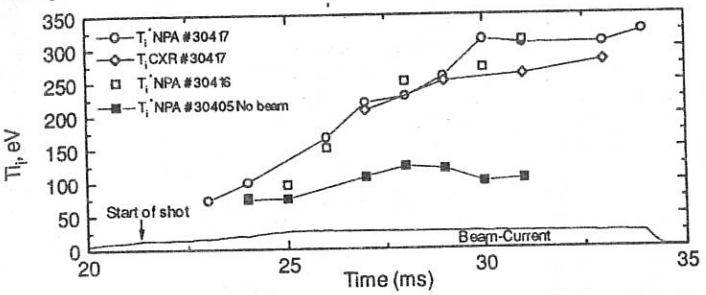

Figure 2

significant increase during the shot, from typically 100eV to greater than 250eV (error on NPA~10%, error on CXR~10%). The power radiated increases by approximately 50% during the injection to ~150kW. Figure 3 shows an electron pressure profile calculated from the 30-point Thomson scattering electron temperature and density profiles during a beam shot. A large Shafranov shift is clearly evident and SXR cameras confirm that this can be about 25% of the minor radius. This can be partially attributed to the fast-ion energy content stored in the plasma.

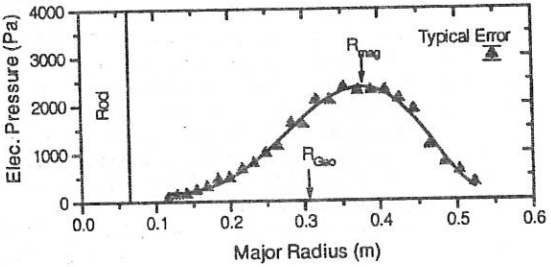

Figure 3

With counter-injection there was no clear heating as expected from the modelling.

MHD Observations

MHD characteristics of NBI heated plasmas on START have been studied using Mirnov coils, horizontal and vertical multi-chord SXR arrays and impurity ion-rotation diagnostics. The main changes have been observed in the poloidal mode structure, the rotation frequency of low *m*, *n* modes, MHD spectrum and the frequency of Internal Reconnection Events.

Low *m*, *n* mode activity shows a decrease in frequency in discharges with co-injection but an increase in counter-injection. This is in agreement with toroidal rotation measurements from spectrocopic observations. In the counter-injection shot #30026 the beam was abruptly terminated at t=32ms (figure 4).

In Figure 4 the change in the toroidal rotation measured with the CELESTE diagnostic (20 channel spectrometer) using the Boron IV-line (2823Å) is compared with the corresponding change in the low-m (predominantly m = 2) mode rotation frequency from SXR signal analysis and the Mirnov oscillation frequency evolution.

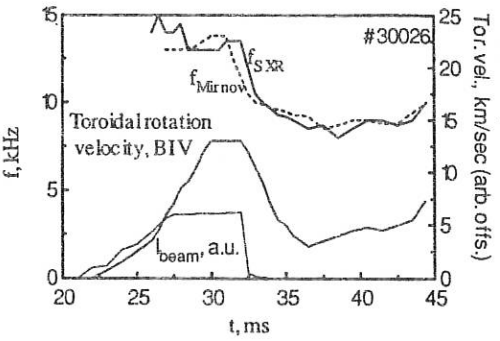

Figure 4

It has been found that shots with NBI have fewer internal reconnections than shots with similar plasma parameters without injection. Some increase in high frequency MHD activity (50-150kHz) has been observed and the possibility of NBI-driven TAE modes is under consideration.

Fast Ion Distribution

The fast-ion spectrum as measured by the NPA for 25.5keV (~240kW) injection into a 210kA, k=1.8 START discharge is shown in figure 5 below along with a modelled spectrum from the Fokker Planck Code (FPP-3D).

Results for two orientations of the NPA on the horizontal midplane are shown; the first is for the case of the NPA view being perpendicular to the plasma surface (0°) and the second is for the case of the NPA viewing angle tilted so that it is looking at 18°(toward the beam). The 18° case shows a classical fast-ion slowing down spectrum, indicating no significant anomalous fast-ion losses. Charge-exchange losses are not included in the model. Typically at these conditions, the modelling shows that we expect about 70% of the fast ion power to be confined by the plasma when orbit and shine-through losses are taken into account. Figure 5 indicates the difference in the measured fast-ion spectrum when viewing the plasma at pitch-angle $\pi/2$ (NPA angle=0°). The agreement between model and data are very good; the signal at 0° being approximately an order of magnitude lower than at 18° as predicted by the modelling. The statistical level shown in figure 5 indicates the noise level for the particular NPA setting.

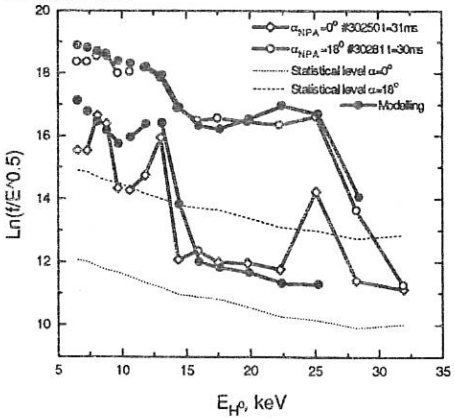

Figure 5

FPP-3D also calculates the fast ion pressure distribution. Full trajectory-averaging in the solution of the Fokker-Planck equation means that the resulting pressure distribution is significantly less peaked than would be predicted from a flux-surface averaging code (such as BANDIT-3D).

Effects on START Operating Space and Beta.

Initial attempts to test the effects of extending the operating limits of the START device with NBI have produced very encouraging results. Previous best Ohmic discharges were in deuterium and reached Murakami numbers, $n_eR/B(10^{19}m^{-2}T^{-1})$ up to ~8. With the beam (the solid points shown in figure 6) values of up to 14 (in H) have been attained. Values of $I_p/N<10^{-14}$Am have been achieved.

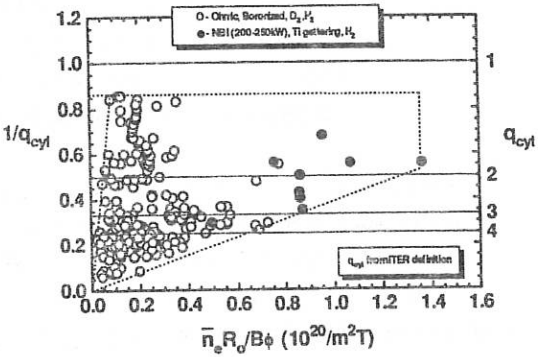

Figure 6

The installation of the NBI has allowed the initial exploration of the anticipated large beta limit space, with average betas of ~8%, and central betas greater than 40% already achieved.. The highest normalised beta so far is about 2.4. It is expected that still higher values will be attainable when the beam power is increased.

The effect on energy confinement has so far not been studied in detail as the plasma conditions change substantially with the beam, particularly in that the plasma radius tends to increase and requires additional vertical field to maintain a constant plasma size.

Conclusions

We have shown that the tight aspect ratio geometry and Ohmic plasma target of the START experiment are suitable for effective NBI. Measurements of the fast-ion spectrum indicate a classical slowing-down spectrum and no anomalous losses. Significant increases in ion temperature are observed by both NPA and CXR diagnostics. For the present START configuration, NBI discharges appear to be better conditioned than equivalent Ohmic ones. Co-injection produced high beta values while counter-injection showed little sign of heating. Thus we have demonstrated for the first time the effects of neutral beam heating at tight aspect ratio, justifying the choice of this additional heating method both for START and for the sucessor experiment MAST which is currently under construction.

Acknowledgements

This work is jointly funded by the UK Department of Trade and Industry and Euratom and by the US DoE.

(a) UMIST, Manchester UK
(b) Ioffe Institute, St. Petersburg, Russia
(c) Imperial College, London, UK.
(d) Oak Ridge National Laboratory, Tennessee, USA
(e) University of Sao Paulo, Brazil
(f) University College Cork, Ireland

Impurity Content of TdeV Plasmas from Simulations of VUV Lines, SXR and Radiation Profile Measurements

E. Haddad, R. Marchand, G. Ratel, B.C. Gregory, H.H. Mai,
D. Whyte, N. Richard, I. Condrea, C. Côté, C. Boucher.
*Centre Canadien de Fusion Magnétique**
1804 boul. Lionel Boulet Varennes, Qc, Canada, J3X 1S1
* Supported by AECL, Hydro-Québec and the INRS.

1. Introdution

The impurity levels in tokamak plasmas, generally deduced from a few specific spectroscopic lines, can have a large uncertainty due to the accuracy level of atomic and spectroscopic data (excitation, ionization, ...) and their sensitivity to the experimental electron temperature. The new approach presented here obtains the impurity levels by comparing iteratively the measured profiles of line intensities from three absolutely calibrated diagnostics with simulation results from the MIST transport code [1] and from collisional radiative line intensities [2]. The VUV spectrometer gives the low Z impurity content from analysis of spectral line radial profiles especially in the outer part of the main plasma (C IV, O V, Ne VIII, ...) [3]. The soft x-ray camera, most sensitive to higher ionisation states, permits the determination of the global metallic impurity content [4,5]. Finally a bolometer array, used to map total (spectrally integrated) radiated power, is very helpful in the identification processes: low Z impurity radiation profiles peak near the edge whereas those of medium and high Z peak in the plasma centre. The comparison is used to characterize impurity transport and levels under several conditions: a) Compact Torus injection, b) detachment during ohmic or ohmic with lower hybrid heating, c) neon injection, and d) the evolution of impurities with lower hybrid ramp up.

2. Methodology

The one-dimensional radial impurity transport code MIST solves for an impurity 'I', the set of simultaneous coupled equations for the density n_{Iq} of each ion species of charge +q, including ionization and recombination. The n_e, T_e and T_i profiles are the main code input. The adjustable parameters used to fit simulated data with experimental results are: the diffusivity, D(r); the convection velocity, v(r); and the impurity global parameter F_I (the total 'I' impurity content as

a fraction of the total number of electrons). The code is run for the three intrinsic impurities in the plasma: C and O, the major impurities in TdeV, and Fe as representative of the metallic impurities (Fe, Cr and Ni) whose total concentration in standard discharges is of the order of 10^{-4}, around the detection limit from spectroscopic lines. Despite their low density, these impurities have considerable contribution into the soft x-rays and total radiation. A fourth impurity (eg. injection of Ne, N, ...) can be added to the procedure.

The levels of Carbon and Oxygen (F_C, F_O) and transport parameters (D and v) are deduced from comparison of measured with simulated emissivity of CIV (154.8nm) and OV (63.0nm):

$I_{CIVsim}(r) = n_e(r)\ n_C3(r)\ <\sigma v(T_e(r))>_{154.8nm}$; $I_{OVsim}(r) = n_e(r)\ n_O4(r)\ <\sigma v(T_e(r))>_{63.0nm}$,

where $<\sigma v(T_e(r))>_{154.8nm}$ and $<\sigma v(T_e(r))>_{63.0nm}$ are the excitation rates [6].

The first estimate of metallic fraction F_{Fe}, in the iterative procedure is deduced by subtracting from the total Z_{eff}, the contribution of oxygen and carbon. The distribution of $n_{Fe}q(r)$ are obtained using D and v deduced from Carbon and Oxygen. The simulated soft x-ray and total radiation are obtained by summing the contributions of all ionization states of the three impurities:

$$Rad_{sim}(r) = \sum n_Cq(r)\ R_Cq(T_e(r)) + \sum n_Oq(r)\ R_Oq(T_e(r)) + \sum n_{Fe}q(r)\ R_{Fe}q(T_e(r))$$

$$SX_{sim}(r) = \sum n_Cq(r)\ X_Cq(T_e(r)) + \sum n_Oq(r)\ X_Oq(T_e(r)) + \sum n_{Fe}q(r)\ X_{Fe}q(T_e(r))$$

where n_Iq are obtained from MIST, R_Iq, is the radiation loss rate of the species I^{q+}, R_Iq is given by ADPAK [1] or by a collisional radiative model [2,7], X_Iq, is the radiation rate in the soft x-ray region (2.5-20 keV), considering the bremsstrahlung, dielectronic recombination (continuum) and line radiation. F_{Fe} is then increased or decreased in order to fit the experimental to simulated soft x-ray and total radiation profiles.

3. Applications.

Rather than an absolute determination of impurity levels, in many cases one needs rather to know how the impurities evolve during a specific experiment. Some examples are presented:

A) First, consider the estimate of the Upper limit of Tungsten concentration after the Compact Torus (CT) injection in TdeV plasma [8]. The tungsten used as coating of CT electrodes risks to contaminate the plasma. After CT injection T_e stays almost the same while many signals increase: $\bar{n}_e$ (x1.25), the central soft x-ray intensity (x1.8), the total radiation (x1.5) and Z_{eff} (x1.16). First the procedure shows that the soft x-rays and total radiation evolution can be explained by the increase of n_e and F_C,F_O, and F_{Fe} (x1.16) as given by Z_{eff}. Then we compare the central chord of total radiation increase after CT with that of injected tungsten by laser ablation

technique (F_W= $2.5x10^{-3}$) (Figs. 1 a, b). If we assume the increase is caused only by tungsten contamination, we obtain a concentration of 10^{-4} as an upper limit. Considering also that the profile shapes are peaked near the edge, that the central chord intensity increases by 45±5%, and those at the edge chord by 35±5%, the upper limit is reduced to 2.5 10^{-5}, an improvement by a factor 4, and an acceptable level for ITER applications [7] (Fig. 1c).

B) During plasma detachment the evolution of CIV radial profile (intensity and shape) is a signature of a diffusivity increase with detachment inside the separatrix near the edge (Figs 2 a,b and c).

C) After Neon injection (~1 %) at $\bar{n}_e$=6. 10^{19} m^{-3}, with LH heating, the total radiation increases in the central region of the plasma which is a signature of metallic radiation (Fig. 3), equivalent to a concentration of 10^{-4} of Fe. The source of metallic impurity can be interpreted by the relative high metal sputtering yield by Neon compared to Deuterium (factor of a few hundreds) [9] and by the exponential increase of the sputtering yield with T_e for low T_e (10-50 eV): a small increase of T_e at the edge by LH heating is sufficient to increase the sputter yield by an order of magnitude.

D) The similarity of the total radiation profiles during LH heating (ramp, 0 to 650 kW) indicates that the proportion of metallic impurity to carbon content does not increase: there is good matching between the HF antennae and the plasma (Fig. 4).

4. Discussion and conclusions

Soft x-ray and total radiation result from the supperposition of radiative processes involving many ionization states of different impurity elements. They are very useful in the identification and quantitative determination of tokamak impurity contents. The confidence level in impurity studies is greatly improved by doing analysis of the combined three diagnostics: the VUV spectrometer, the soft x-ray camera and the bolometer array.

References

[1] HULSE R.A. Nucl. Technol. Fusion 3 (1983) 259.
[2] Marchand., et al., IAEA Report INDC (NSD)-309 (1995).
[3] HADDAD E., et al., Plasma Phys. Contr. Fusion 34 (1992) 579.
[4] JANICKI C., " A Computer Code for the Modelling of Soft X-Rays", CCFM RI 370e (1992).
[5] HADDAD E., et al., to appear in Nucl. Fusion 36 No 4 (1996)
[6] ITIKAWA Y. et al., Atomic Data and Nuclear Data Tables 33, (1985) 149.
[7] POST D.E., J. of Nucl. Materials 220-222 (1995) 143.
[8] RAMAN R. et al., this conference.
[9] Eckstein W. et al, Sputtering Data, Report IPP 9/82 (1993).

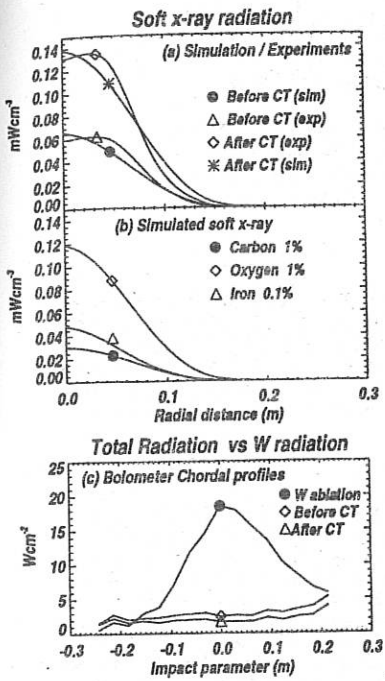

Figure 1: Simulation of Impurities with CT Injection

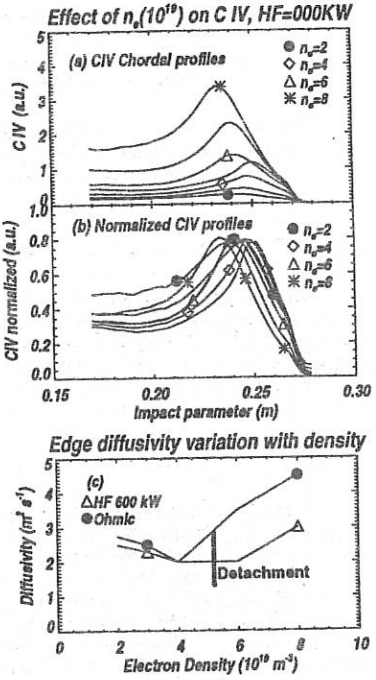

Figure 2: CIV Evolution with Density (Detachment Effects)

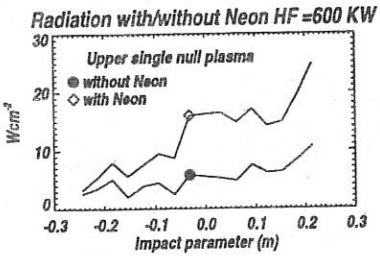

Figure 3: Central total radiation with Neon injection

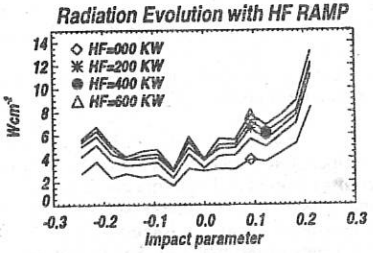

Figure 4: No increase of central radiation with a HF ramp

Enhanced Plasma Confinement after Compact Toroid Fuelling

R. Raman[1], F. Martin, M. St-Onge, G. Abel, J.-L. Lachambre, C. Côté, N. Richard, E. Haddad, N. Blanchard, R. Décoste, A. Côté, J-L. Gauvreau, P. Gierszewski[1], D. Hwang[2], A. Hirose[3], B. Quirion, H. Mai, H. McLean[2], C. Xiao[3], B. Stansfield, M. Chartré, D.Michaud

Centre Canadien de Fusion Magnétique, Varennes, Québec J3X 1S1 Canada
[1]Canadian Fusion Fuels Technology Project, Mississauga, Ontario, Canada
[2]University of California - Davis, Livermore, California, USA
[3]University of Saskatchewan, Saskatoon, Saskatchewan, Canada

Abstract:

We report the first measurements showing improvement in tokamak plasma confinement obtained after compact toroid (CT) fuelling. CT injection using the CTF device resulted in more than 20% increase in the particle inventory of TdeV without any plasma cooling or rapid loss of particles. The energy confinement time increased by >20%, the radiated power increased approximately in proportion to the electron density and the edge H_α signal dropped slightly. There was no enhancement in MHD activity.

Introduction:

Control over the density profile in a tokamak fusion reactor is desirable. Peaked density profiles can reduce the ignition margin for a reactor [1]. Peaking the density profile can increase the usable bootstrap current and increase the net output of power producing tokamaks [2]. The primary means for deep fuelling of present day tokamaks is by the injection of frozen deuterium pellets. But this scheme is not expected to extrapolate favourably for a reactor as pellets are expected to penetrate to only about 10% (r/a ~ 0.9) from the plasma edge leading to a low burn fraction of about 5%. A calculation of the burn fraction to the normalized fuel penetration depth shows that the burn fraction increases approximately linearly with the fuel penetration depth [3]. Other than representing a waste of fuel, edge fuelling may lead to excessive amounts of tritium in the fuel cycle and to large amounts of tritium being trapped in the vessel walls. Such shallow penetration can lead to high edge densities, leading to increased divertor pumping requirements and possibly limit reactor operation to below the Greenwald limit. For the International Thermonuclear Experimental Reactor (ITER), the edge density limit remains a critical issue, and the recent ASDEX Upgrade results are unfavourable in regard to H-mode confinement enhancement with density above the Greenwald limit [4]. Injection of large pellets may result in higher core neutral concentrations. On D-III-D, increasing the core neutral concentration resulted in a decrease of the H-mode confinement enhancement factor [5].

Perkins et al. [6], Parks [7] and Newcomb [8] proposed the use of spheromak compact toroid plasmoids for central fuelling of tokamak plasmas. The spheromak is a compact toroid (CT) plasma configuration with approximately equal toroidal and poloidal magnetic fields [9]. It can be formed in a magnetized Marshall gun [10] and efficiently accelerated to high velocities [11]. Central fuelling of a reactor requires injection velocities in the range of 350 to 800 km/s which can be achieved only by accelerated CTs. Recent results on CT fuelling of a tokamak [12] showed that it was possible to non-disruptively fuel a tokamak discharge and to substantially increase the particle inventory of the discharge. However, in these experiments there was a substantial drop in the plasma current, rapid cooling of the central plasma, increased MHD activity and rapid loss of the injected fuel because of plasma contamination by the CT.

Experimental results:

We present the first results in which CT fuelling led to an improvement in the tokamak behaviour. These results were obtained as a result of injection of CTs with lower impurity content which were generated after extensive electrode bakeout. Reduction of impurities was confirmed by absolutely calibrated carbon IV line emission intensity measurements, of the TdeV plasma, which have decreased by more than an order of magnitude. In addition bolometric measurements showed, for the early CT injection data, the radiated power to temporarily exceed the input ohmic power. This is no longer the case.

The CTF device [13] was used to inject a CT into the TdeV tokamak (R = 0.86m, a = 0.25 m, poloidal single null, ohmically heated discharge) operated with a toroidal field of 1.4 T and a plasma current of 160 kA and an edge q of 3.8. The line averaged electron density was in the range of 1.7 to 2.5 x 10^{19} m^{-3} with a corresponding nominal particle inventory of 3 to 5 x 10^{19} ions. The feedback controlled tokamak gas injection used to maintain a constant electron density was interrupted 2 ms before CT injection preventing gas injection for the rest of the discharge. In these experiments a deuterium CT was injected into a tokamak plasma of the same isotope.

Diagnostic traces for a typical tokamak discharge with central penetration of the CT are shown in Figure 1. The CT was injected at 802 ms. The central (r/a = 0.1) and outer (r/a = 0.9) interferometer chords show a fast rising density signal from CT fuelling indicating central penetration of the CT. The central density stays elevated while the edge density returns to about the pre-CT injection level indicating a peaking of the density profile after CT injection. In addition there is no rapid loss of particles. The main plasma bolometer signal demonstrates the lack of enhanced impurity radiation. The immediate increase in the central soft x-ray channel further indicates the lack of central cooling. Global tokamak parameters such as plasma current and loop voltage are not perturbed and there is no enhancement in MHD activity following CT injection. The increase in the C IV signal shows injection of carbon impurities, but this is small compared to earlier experiments. The transient Zeff spike (FWHM ~ 1 ms) is possibly related to the burn through of low-z impurities. As the C IV signal and the edge density return to near the pre-CT injection levels, in about 3 ms, the Zeff settles at a value about 16% higher than before CT injection.

To show the dramatic effect of CT fuelling, we compare the time history of the total particle inventory for the case of CT fuelling and CT gas valve puff alone. In order to maintain similar wall recycling conditions, two consecutive discharges were chosen. The particle inventory is calculated from the seven chord, SMM interferometer array [14]. As shown in Figure 2, for the gas injection case there is no change during the first 10 ms, after that the rate of rise is similar to that obtained during density ramp-up with gas valve feed back control (~10^{17} particles/msec). In contrast for the CT fuelling case, the initial increase is about 20 times faster. To fully realize the efficiency of CT fuelling (defined as the increase in mass of the tokamak plasma divided by mass contained in the CT), one has to compare the mass of the CT to the mass of the gas associated with the gas valve pulse. In general during CT fuelling, the coupling is more than 50% [12] and 42% for this specific case. The coupling is not 100% because in these experiments the CT length is approximately equal to the tokamak minor radius, which means that fuel that is deposited in the outer flux surfaces, or in the open field line region will not efficiently couple to the tokamak discharge. However this is not expected to be a problem for larger tokamaks as the ratio of CT length to tokamak minor radius is expected to be about 15% for an ITER class device [15]. For the case of gas valve fuelling, we find the fuel coupling efficiency to be <6%.

Since CTs are formed in the annulus between metal electrodes, the possibility of CT contamination by sputtered metal atoms must be considered. To reduce erosion and sputtering, electrodes on the CTF device are coated with tungsten. Because of the low

electron temperature of these CTs (6 to 20 eV), it has been impossible to experimentally confirm the tungsten contamination level in the CT through spectroscopic measurements of the CT plasma as the intensity of the observed lines has been very small. Measurement of multiply ionized tungsten lines requires a plasma temperature of several hundred eV. Ultimately, the amount of eroded metal atoms that contaminate the tokamak plasma should be controlled to an acceptable level. By comparing the profiles of radiated power after CT injection to that obtained after laser ablation of W targets, the upper limit to the amount of W concentration in the TdeV plasma is determined to be 2.2 x 10^{-5} after CT injection.

In Figure 3 we show the plasma diamagnetic energy and the energy confinement time calculated from diamagnetic measurements. Immediately after CT injection (at 802 ms) the plasma diamagnetic energy and the energy confinement time begin to increase and the H_α signal drops sharply. At approximately 814 ms Ep flattens and τ_E decreases. This may be the result of temporary cooling of the edge plasma since this time is correlated to the time of arrival of unused gas from the CT formation phase. After about 12 ms this trend reverses and the plasma energy and the energy confinement time both increase. At 836 ms, both these parameters reach a peak. The diamagnetic energy content has increased by 38%, and τ_E by 35%. At this time the total particle content in the discharge is 27% higher than before CT injection. Beyond t = 838 ms, although the total particle content in the discharge stays approximately the same both the diamagnetic energy and τ_E decrease. To fully realize the advantages of CT fuelling the parasitic gas load to the tokamak must be reduced possibly through the implementation of faster gas injection valves on the CT fueller. The increase in the plasma energy and the energy confinement time is consistent with the other observations that show low levels of tokamak contamination, lack of plasma cooling and absence of any enhancement in MHD activity following CT injection.

In summary, we have demonstrated the use of CT injection for tokamak fuelling without adversely affecting the tokamak plasma parameters. On the contrary, the plasma energy confinement time improves after CT fuelling. Proper injector electrode conditioning is necessary to minimize the impurity content in the CT. The dominant impurities are non-metallic; these are not expected to be a problem in a multi pulse injector in which the injector operating frequency is greater than the impurity monolayer formation time [15]. An upper limit on the metallic impurity concentration, in this first generation device, shows it to be in the range acceptable for reactor fuelling. Measured fuelling is more than an order of magnitude greater than necessary for a reactor.

Acknowledgments:

The CTF project is funded by the Canadian Fusion Fuels Technology Project. We acknowledge the assistance of Dr. W. Rowan of the TEXT tokamak and Dr. Jack Sugar of the US National Institute of Standards and Technology for providing us with the wavelength of tungsten lines. The Centre Canadien de Fusion Magnétique is funded by Atomic Energy of Canada Limited, Hydro-Québec and the Institut National de la Recherche Scientifique.

References:

[1] L.J. Perkins et al., "ITER parametric analysis and operational performance report," ITER documentation series, No. **22**, IAEA, Vienna (1991).
[2] D.R. Mikkelsen et al., Nucl. Fusion **35**, 521 (1995).
[3] W. Houlberg et al, Nucl. Fusion **34**, 106 (1994)
[4] D.Post, "Report of the fourth ITER divertor physics and divertor modelling and database expert group workshop," San Diego, CA March 11-15, (1996).

[5] R Stambaugh, "Divertor Research Summary from DIII-D," in reference 4.
[6] L.J. Perkins, S.K. Ho and J.H. Hammer, Nucl. Fusion **28**, 1365 (1988).
[7] P.B. Parks, Phys. Rev. Lett., **61**, 1364 (1988).
[8] W.A. Newcomb, Phys. Fluids B, **3**, 1818 (1991).
[9] M.N. Rosenbluth and M.N. Bussac, Nucl. Fusion **19**, 489 (1979).
[10] C.W. Barnes et al., Phys. Fluids **29**, 3415 (1986).
[11] C.W. Hartman and J.H. Hammer, Phys. Rev. lett., **48**, 929 (1982).
[12] R. Raman, F. Martin, B. Quirion et al., Phys. Rev. Lett., **73**, 3101 (1994).
[13] R. Raman, J. Thomas, D. Hwang et al., Fusion Tech., **24**, 239 (1993).
[14] J-L. Lachambre et al., Rev. Sci. Instrum. **65**, 3428 (1994).
[15] P. Gierszewski, R. Raman, D. Hwang, Fusion Tech. **28**, 619 (1995).

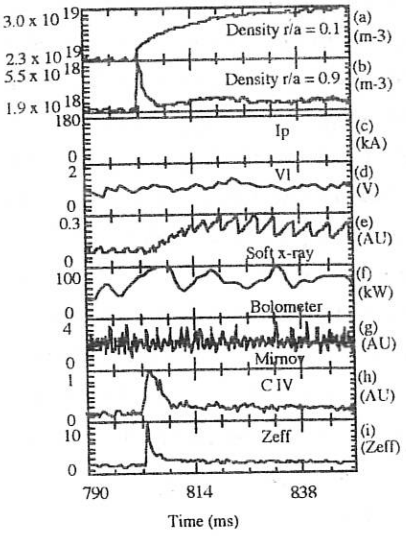

Figure 1: Time history of tokamak parameters for the central penetration case at BT = 1.4 T, (a) line averaged electron density at r/a = 0.1, (b) line averaged electron density at r/a = 0.9, (c) plasma current (Ip), (d) loop voltage (VL), (e) central chord soft x-ray signal , (f) main plasma viewing bolometer signal, (g) Mirnov coil signal, (h) carbon IV line monitor signal and (i) Zeff.

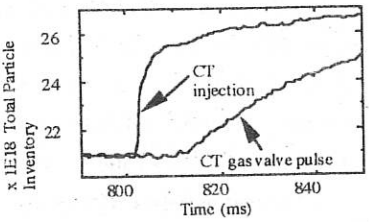

Figure 2: Comparison of the rate of particle inventory increase for the case of CT gas valve pulse and CT injection.

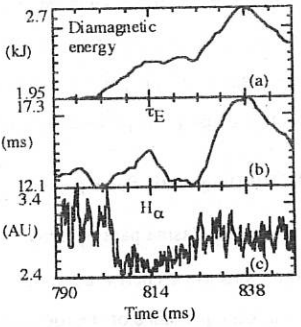

Figure 3: Time history of (a) Plasma diamagnetic energy (b) energy confinement time, (c) Hα signal.

HIBP measurements of the plasma electric potential on T-10

A.V. Melnikov, N.K. Kharchev, L.G. Zimeleva, L.G. Eliseev, V.A. Vershkov,
Institute of Nuclear Fusion, Russian Research Centre "Kurchatov Institute" Moscow, Russia
I.S. Bondarenko, S.M. Khrebtov, L.I. Krupnik, I.S. Nedzelskij, Yu.V. Trofimenko,
Institute of Plasma Physics, National Scientific Centre "KhIPT", Kharkov, Ukraine.

1. Introduction

The essential role of the electric field on the plasma confinement and equilibrium in the fusion devices is well recognized now [1]. The effect of the electric field on the behavior of toroidal plasmas is twofold. The first is the control of some confinement processes by static electric field. The essential effect of the intrinsic electric field on the plasma confinement through the **E*B** drift was discussed for the stellarators [2]. After discovering of the improved confinement regimes, the general significance of the static radial electric field in tokamaks was recognized also [3]. The second is the effect of the electric field fluctuations on the transport processes [4]. The Heavy Ion Beam Probing (HIBP) is the only diagnostic allowing to investigate both sides of the phenomenon of the plasma electric field. HIBP is able to measure as the potential time evolution (oscillations) in every selected point, as the radial potential profiles in different time interval of discharges. The measurements are possible both in the plasma edge and in the plasma core of the magnetic confinement systems [5]. In this report we describe the basic properties of HIBP on T-10 tokamak, and some results of the plasma potential investigation and the fluctuations of the plasma potential, density and poloidal magnetic field.

2. HIBP Diagnostic Set-Up

To study the plasma parameters in T-10 a diagnostic system for plasma probing by a beam of Cs^+ ions with energy up to 210 keV was developed [6] The specific feature of this system is the presence of the toroidal steering electrostatic plates before the energy analyzer entrance. These plates correct toroidal displacement of the secondary ions. The power supply provides the measurements during the 5 ms of the correcting pulse flat top every 20

ms. The calculated detector grid in the midplane of the plasma column is almost horizontal. It allows to observe the outer plasma area 18-28 cm by the Cs^+ beam with the energies 120-160 keV for toroidal magnetic field B = 1.5 T. The spatial resolution of measurements L = 5-10 mm, temporal resolution was limited by the data acquisition system (the bandwidth 20 kHz).

3. Experimental Results

The measurements on T-10 tokamak (R=150 cm, a=30 cm) were made in the regimes with the magnetic field B=1.5T, and current I=135-170 kA, pulse duration up to 600 ms. The sharp gas turn-off in 250 ms is associated with the transition to regime with high impurity confinement (S-B transition [7]). Fig 1 demonstrates the time evolution of the main plasma parameters in this regime. The 350 V difference in t1 and t2 moments with equal density indicates the dependence of the potential not only from the density, but also to the gas feed, similar to [6]. The potential increase in the internal (r = 18 cm) regions in comparison with the phase of the density rump up indicates the increase of ion confinement (see also Fig.2). It could be explained by the relaxation of the instability accompanying the gas puff and it shows the ion nature of this instability.

The pellet injection into the low density plasma leads to the decrease of the plasma potential for the time of the density increase, Figs 3,4. It corresponds to the known tendency of the growing up of the negative potential with density [6]. Two lower curves in Fig 5. confirm it also.

Fig. 5 demonstrates the negative potential well towards minor axis in MHD quiet regimes. MHD active regimes have the potential well with twice smaller depth. The difference in the potential value between of the discharges with and without MHD activity can reach 400-600 V. In MHD-active regimes electric field is very low, almost zero, where $q \sim 2$ (19 cm < r < 25 cm). The absolute potential reference was made on the basis of the absolute calibration of analyzer on the He gas target. Along with the plasma potential, HIBP is able to measure the plasma density (the total secondary ion current is proportional to plasma density $I_{tot} \propto n L$) and poloidal magnetic field, which produces the ion toroidal displacement.

Plasma electric potential, density and magnetic potential oscillations were observed in the frequency range 1 kHz (Fig. 6). The decrease of the poloidal field oscillations b_p/B_t and increase of the density ones towards the edge coincide with probe measurements [8]. The region of the high level poloidal field oscillations coincides with $q \sim 2$ zone.

Acknowledgment

This work was partly supported by Russian Fundamental Research Foundation. Grant N 96-02-18702. Authors are grateful to Dr. V. Sergeev for the collaboration in pellet injection experiment.

References

[1] K.Ida, Y.Muira, S-I Itoh et al., NIFS-313, Nagoya, Japan , 1994.

[2] L.M.Kovrizhnykh , Nucl. Fusion, vol. **24**, p 435, 1984.

[3] S-I Itoh, K. Itoh., Phys.Rev.Lett., vol. **60**, p2276, 1988.

[4] B.B.Kadomtsev, Plasma Turbulence. London-New York. Academic press,1965.

[5] Yu. N. Dnestrovskij et al., IEEE Trans. on Plasma Sci., **22**, N4, p 310, 1994.

[6] A.V.Melnikov et al., IEEE Trans. on Plasma Sci., **22**, N4, p 363, 1994.

[7] V.V. Alikaev et al.,Plasma Phys and Contr Fus., 30, p381, 1988.

[8] S.J. Zweben and R.J. Taylor, Nucl.Fusion, 21, p193, 1981.

Figure captions

Fig.1. The time evolution of the main plasma parameters and the electric potential.

Fig.2. The time variation of the potential relative to the value in the puff switch-off moment in three radial positions for several discharges.

Fig.3.The the density and potential correlation in the pellet injection. Long case.

Fig.4.The the density and potential correlation in the pellet injection. Short case.

Fig.5. The potential profiles for the various types of MHD activity.

Fig. 6. Plasma potential, density and poloidal field oscillation (last scaled to 10^3) profiles.

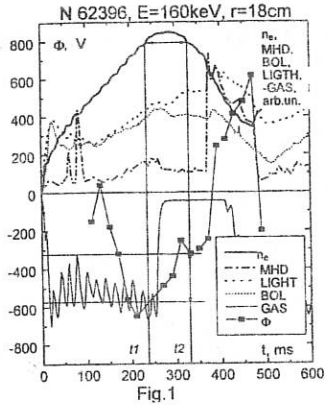

Fig.1

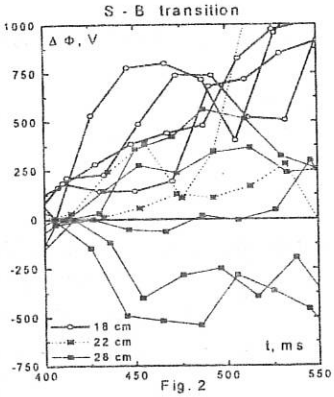

Fig. 2

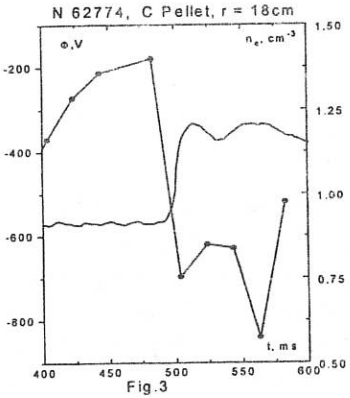

Fig.3

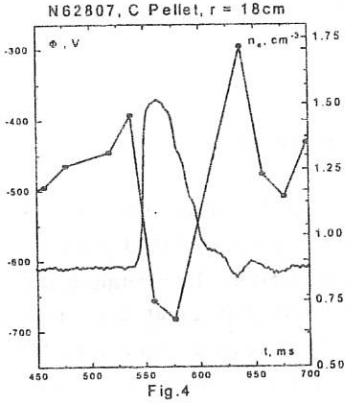

Fig.4

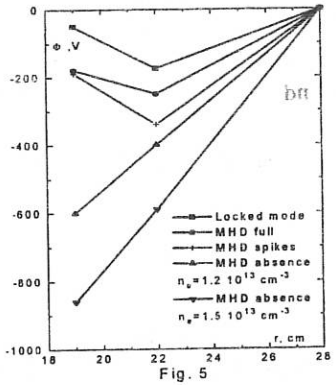

Fig. 5

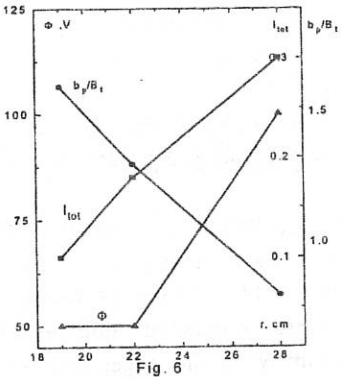

Fig. 6

TOROIDAL η_i MODE STABILITY AT LARGE TEMPERATURE GRADIENTS

A. Jarmén

Institute for Electromagnetic Field Theory and Plasma Physics
EURATOM-NFR *Association*
Chalmers University of Technology
S-412 96 Göteborg, Sweden

Introduction

It is well known that the ion temperature gradient (ITG) or η_i mode ($\eta_i=[(1/T_i)(dT_i/dr)]/[(1/n_o)(dn_o/dr)]=L_n/L_T$, L_n=density scale length, L_T=temperature scale length) has an instability threshold (η_{ilow}) around one for density scale lengths of the order of the magnetic field curvature radius L_B[1-3]. It is the purpose of the present work to show, in a basic toroidal gyrokinetic description assuming isotropic η_i and no collisions, the existence of a high η_i stabilization at $\eta_i=\eta_{iup}\approx 10$ or larger (cf Refs. 2 and 4). The lowest η_{iup} is found to occur at wavelengths corresponding to $k_\perp^2\rho_i^2\approx 1$ ($k_\perp$ = perpendicular wavenumber, ρ_i = ion Larmor radius). It is also shown that the density gradient (small L_n) is stabilizing - lowering the growthrate and the upper η_i stability threshold.

The η_i modes are assumed to be one of the driving sources for drift wave turbulence causing anomalous particle and heat transport[5,6]. One may expect that an upper η_i threshold can give rise to enhanced confinement regimes that do not require proximity to the edge. One example could be the interior transport barriers recently observed in all major tokamaks. Equilibria with

large η_i can occur e.g. in regions with negative shear[7] in combination with high heating power.

Formulation

We assume a perturbation of the form $\exp(jk_{\|}x_{\|}+jk_{\perp}x_{\perp}-j\omega t)$ where $k_{\|}$ and $k_{\perp}$ are along and perpendicular to the background magnetic field respectively and an electrostatic electric field $E=-\nabla\phi$ where ϕ is the electrostatic potential. We neglect parallel ion motion (assuming $\omega/k_{\|}>>v_{thi}$), electron and ion trapping and collisions in order to concentrate on the main toroidal η_i mode characteristics. In a gyrokinetic ion description the ion density response may be derived from the ion gyrokinetic equation. Assuming a Maxwellian ion velocity distribution one obtains

$$\frac{\delta n_i}{n_0}=Q\frac{e\phi}{T_i}\equiv(-1+I)\frac{e\phi}{T_i}$$

where

$$I=\int\frac{\omega+\omega_{*i}(v^2)}{\omega+\omega_{Di}(v)}J_0^2\left(\frac{k_{\perp}v_{\perp}}{\omega_{ci}}\right)f_{Mi}dv$$

and

$$\omega_{*i}(v^2)=\frac{cT_i}{eB_0^2}\left[1+\eta_i\left(\frac{mv^2}{2T_i}-\frac{3}{2}\right)\right][\nabla(\ln n_0)\times B_0]\cdot k_{\perp}$$

$$\omega_{Di}(v)=\frac{cm}{eB_0^3}\left(\frac{1}{2}v_{\perp}^2+v_{\|}^2\right)(\nabla B_0\times B_0)\cdot k_{\perp}$$

ω_{*i} and ω_{Di} are the ion diamagnetic and the ion magnetic frequency respectively (magnetic drift = ∇B drift + curvature drift).

In the regime under consideration $k_{\|}v_{thi}<<\omega<<k_{\|}v_{the}$ the electrons are assumed to be adiabatic. From the parallel equation of motion for the electrons neglecting electron inertia we then obtain a

Boltzmann distribution for the electron density, which, assuming $e\phi/T_e<<1$, gives $\delta n_e/n_o=e\phi/T_e$. Using now the quasineutrality condition, $\delta n_e=\delta n_i$, the dispersion relation may be written $Q=1/\tau$, where $\tau=T_e/T_i$.

Results

Fig. 1 shows the upper η_i stability threshold derived from the dispersion relation as a function of $\varepsilon_n(\varepsilon_n=2L_n/L_B$, $L_B=$ magnetic field curvature radius) with $b_o=k_\perp^2\rho_i^2$ as a parameter ($\rho_i=\sqrt{T_i}/m_i/\omega_{ci}=$ ion Larmor radius). The threshold is strongly reduced by smaller ε_n. The lowest values occur at $b_o\approx1$. Fig. 2 shows the stability thresholds in the η_i-b_o plane with ε_n as a parameter. We note that the upper threshold goes to infinity as $b_o\rightarrow0$. As $b_o>1$ it is increased again (not shown in the figure). The lower η_i threshold is around one in both of the figures.

Fig. 3 shows the normalized frequency and growthrate as a function of η_i with b_o as a parameter. We note that the mode propagation is in the ion drift direction and that the frequency increases almost linearly from low values at the lower η_i threshold to around $2\omega_{*i}$ at the upper η_i threshold.

The formalism requires the wavelength of the mode to be small compared to relevant background inhomogeneities. In a linear study as here we may assume propagation principally in the poloidal direction, $\lambda\approx\lambda_\theta$, and the relevant background scale length to compare is L_B. If the mode is mainly localized to the outer part of the torus, however, (medium or strong ballooning), where the directions of L_B and θ are perpendicular, a restriction on L_B may not be nessecary either. The condition $\lambda<<L_B$ is fullfilled by e.g. $b_o=0.25$, $\rho_i=0.25$ cm and $L_B=300$ cm. The formalism also requires the Larmor radius to be smaller than the scale lengths which is fullfilled by e.g. $\varepsilon_n=0.15$ and $\eta_i=\eta_{iup}\approx25$ (Fig. 1).

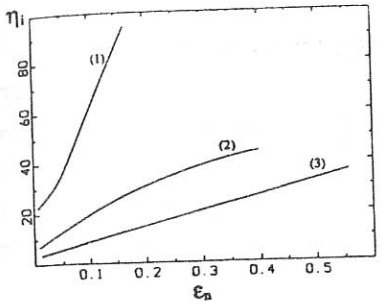

Fig. 1. η_i upper stability threshold versus ε_n for τ=1 and b_o=0.1 (1), b_o=0.25 (2), b_o=0.5 (3).

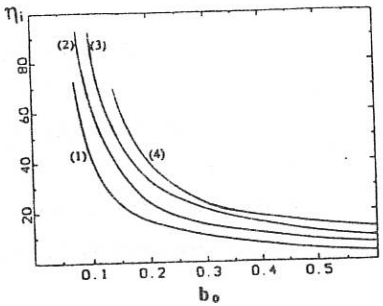

Fig. 2. η_i upper stability threshold versus b_o for τ=1 and ε_n=0.05 (1), ε_n=0.1 (2), ε_n=0.15 (3), ε_n=0.2 (4).

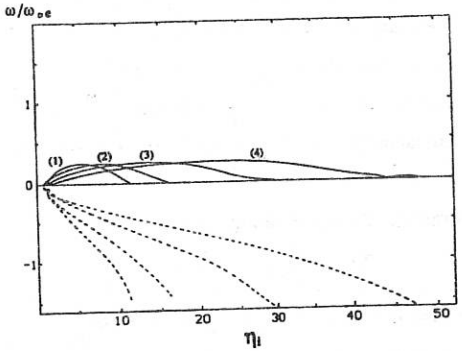

Fig. 3. Normalized growthrate γ/ω_{*e} (full line) and real frequency ω_r/ω_{*e} (dashed line) as a function of η_i for τ=1, ε_n=0.15 and b_o=1 (1), b_o=2 (2), b_o=4 (3), b_o=9 (4).

References

1. F. Pegoraro and B. Coppi, Nucl. Fusion 17, 969 (1977).
2. A. Jarmén, P. Andersson and J. Weiland, Nucl. Fusion 27, 941 (1987).
3. F. Romanelli, Phys. Fluids B1, 1018 (1989).
4. H. Song and A.K. Sen, Phys. Fluids B5, 2808 (1993).
5. W. Horton, D. Lindberg, J.Y. Kim, J.Q. Dong, G.W. Hammet, S.D. Scott, M.C. Zarnsdorf and S. Hamaguchi, Phys. Fluids B4, 953 (1992).
6. J. Weiland and H. Nordman, Nucl. Fusion 31, 390 (1991).
7. C. Kessel, J. Manickam, G. Rewoldt and W.M. Tang, Phys. Rev. Lett 72, 1212 (1994).

Formation of Transport Barriers

V Rozhansky, M Tendler*, S Voskoboynikov

St.Petersburg State Technical University, 195251, St. Petersburg, Russia

*Alfven Lab., Euroatom NER Association, Royal Institute of Technology, Stockholm, Sweden

1. Introduction

A simple model of the formation of the transport barriers at the edge region of a tokamak is presented. The particle continuity equation with the diffusion coefficient which depends on the shear of the poloidal $\vec{E} \times \vec{B}$ drift has been solved numerically. Therefore, the paradigm of the shear suppression [1-3] was applied to the dynamics of the formation of the transport barriers. The special emphasis was made on the detailed dynamics of L-H and H-L transitions including the pellet-caused H-mode (PCH mode) [4], [5]. The main experimentally observed typical features of the barrier formation [2-5] are reproduced by the numerical simulation.

2. Model

Inside the transport barrier the diffusion equation has been solved

$$\frac{\partial n}{\partial t} - \frac{\partial}{\partial x}[D(\alpha)\frac{\partial n}{\partial x}] = 0 \,, \qquad (1)$$

where x is the dimensionless distance from separatrix $x=(r-a)\Theta/\rho_{ci}$, ρ_{ci}/Θ is the poloidal gyroradius, time t is measured in units $(\rho_{ci}/\Theta)^2/D^{(mnn)}$. The parameter α is proportional to the shear of radial electric field $\alpha \sim |dE_r/dr|$. Electric field is supposed to be neoclassical with the toroidal rotation damped by the anomalous inertia and viscosity [6]

$$E_r^{(NEO)} = \frac{T_i}{e}[\frac{d\ln n}{dr} + (1-k)\frac{d\ln T_i}{dr}]. \qquad (2)$$

where k is the numerical coefficient, dependent on collisionality. This field is observed in the L-regime, while for the steep density profiles typical for H-mode additional equation for electric field is to be solved [6]. Leaving this for the future publication we shall focus here on the initial phase of the barrier formation when Eq.(2) is still an exact one. Assuming that the density gradient is steeper than the temperature gradient, the diffusion coefficient is governed by the second derivative $d^2 lnn/dr^2$. Hence we shall specify

$$\alpha = \frac{\rho_{ci}^2}{\Theta^2}|\frac{d^2\ln n}{dr^2}| = |\frac{d^2\ln n}{dx^2}|. \qquad (3)$$

The chosen dependence $D(\alpha)$ is shown in Fig. 1. The values $\alpha_{1,2}$ can be estimated from the comparison of the decorrelation frequency associated with the shear of the rotation with the diffusion decay [1]. For the modeling we chose $\alpha_1=0.5$, $\alpha_2=1$ and $D^{(max)}/D^{(min)}=10$. The Eq.(1) has been solved in the region $0\le x\le 1$ with the boundary conditions $n(x=0)=1$, $Ddn/dx(x=1)=\Gamma$. The point $x=0$ defines the separatrix and $x=1$ - the interface of the transport barrier with the hot core, Γ is a given particle flux from the core.

3. Qualitative analysis

For small Γ stationary profile is determined by $D^{(max)}$, depends linearly on x with gradual slope

$$n(x)=1+\Gamma x/D^{(max)}. \qquad (4)$$

In Fig. 2 the local flux $D(\alpha)dn/dx$ is plotted versus dn/dx for the linear profile $n(x)=1+\beta x$ at separatrix $x=0$. Since $\alpha=\beta^2/(1+\beta x)^2$ for linear profile the local particle flux start to decrease at gradient $\beta=\alpha_1^{1/2}$ and to increase again at $\beta=\alpha_2^{1/2}$. The character of the steady state solution depends on the relation between Γ and $\Gamma^{(max)}$. If $\Gamma< \Gamma^{(max)}$ than the steady state linear profile given by Eq.(4) can exist. On the contrary for $\Gamma> \Gamma^{(max)}$ the steady state solution corresponds to the steep density gradient at the separatrix which can be associated with the H-mode. The relation between Γ and $\Gamma^{(max)}$ depends, of course, on the ion temperature and density at the separatrix. For larger temperatures and smaller densities the value of $\Gamma^{(max)}$ is smaller since the shear suppression is more effective, and it is easier to reach H-regime for the same particle flux Γ. If one starts from a linear profile given by Eq.(4), and then owing to additional heating or density decrease Γ becomes larger than $\Gamma^{(max)}$, the L-H transition must take place. On the contrary, to obtain H-L transition the particle flux must fall below $\Gamma^{(min)}$.

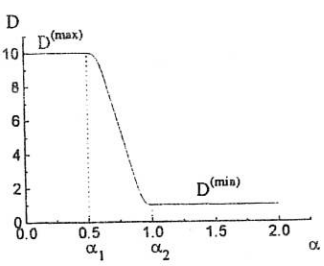

Fig. 1.

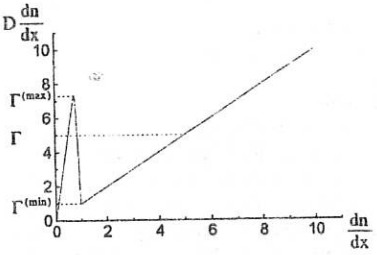

Fig. 2.

4. Results of the simulation

To solve numerically Eq.(1) the small artificial viscosity was added. In Figs. 3-6 results for the initial profile given by Eq.(4) are presented. The initial density gradient was $\beta=\Gamma/D^{(max)}$ with $\Gamma=7.5>\Gamma^{(max)}$. The density profiles in Fig. 3 and deviations Δn from initial profile in Fig. 4 are shown for the moments: 1-$t=0$ (initial profile), 2-$t=0.0005$, 3-$t=0.001$, 4-$t=0.005$, 5-$t=0.01$, 6-$t=0.05$, 7-$t=0.1$, 8-$t=0.5$, 9-$t=1$, 10-$t=4$. It is clearly seen that very quickly the density perturbation near the separatrix start to increase while the diffusion coefficient (Fig. 5) and the particle flux to SOL $\Gamma(0)$ in Fig. 6 simultaneously start to decrease. After the fast diffusion time $t_f=x^2/D^{(max)}$ (for $x=1$ $t_f=0.1$) the diffusion coefficient is suppressed in the whole transport barrier and the futher transiton occur with the slow diffusion time $t_s=x^2/D^{(min)}$. It is interesting to note that at small times the region of the suppressed diffusion coefficients propagates even faster than according to $x^2=4D^{(max)}t$. If one starts modeling from the profile 10 it is not sufficient to make the flux $\Gamma<\Gamma^{(max)}$ for H-L transition, we can obtain transition for $\Gamma\leq 0.25$ which is smaller than $\Gamma^{(min)}$, Figs. 7-8. The final steady state profile coincides with Eq.(4).

The possibility of stimulating the L-H transition by the injection of a slow pellet observed in [4], [5] was modeled, see Figs. 9-10. To the initial profile Eq.(4) which was close to the point of transition with $\Gamma<\Gamma^{(max)}$ ($\Gamma=6.75$) the small 5% density perturbation was added. When the maximum of the perturbation was centered at $x<0.3$ it was sufficient to cause the transition, Figs. 9-10. Evolution at larger times was similar to Fig. 3. The 1% perturbation caused similar evolution for $x<0.3$, while for $x>0.3$ no transition was observed-the perturbation just spread and disappeared owing to diffusion.

Some other different boundary conditions were employed and will be reported elsewhere.

Acknowledgments

The work was supported by the RFFI grant N 95-01-00524 and partially by the Swedish Institute.

References

[1] Biglari H, Diamond PH & Terry PW, *Phys. Fluids* **B2** 11 (1990)
[2] Groebner RJ, *Phys. Fluids* **B5** 2343 (1993)
[3] Moyer RA et al, Phys, Plasmas **2** 2397 (1995)
[4] Askinasi LG et al, *Phys. Fluids* **B5** 2420 (1993)
[5] Kapralov VG, Rozhansky VA, Khlopenkov KV, *In Controlled Fusion and Plasma Physics (Proc. 22nd Eur. Conf. Bournemouth. 1995)* **19C** 117 (1995)
[6] Rozhansky V, Tendler M, Phys. Fluids **B4** 1877 (1992)

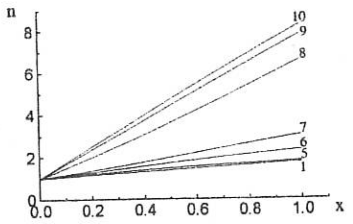

Fig. 3. Density evolution during L-H transition, $\Gamma=7.5>\Gamma^{(max)}$.

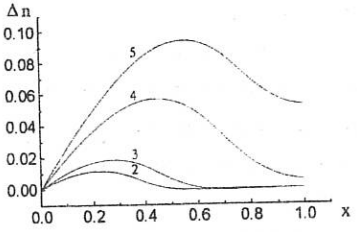

Fig. 4. Evolution of the deviation from the linear profile Eq. (4) during L-H transition, $\Gamma=7.5>\Gamma^{(max)}$.

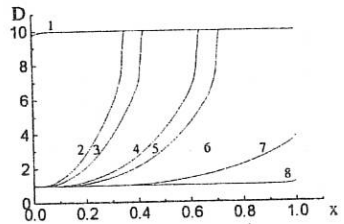

Fig. 5. Evolution of the diffusion coefficient during L-H transition, $\Gamma=7.5>\Gamma^{(max)}$.

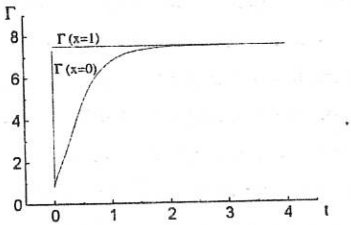

Fig. 6. Particle fluxes during L-H transition. $\Gamma=7.5>\Gamma^{(max)}$.

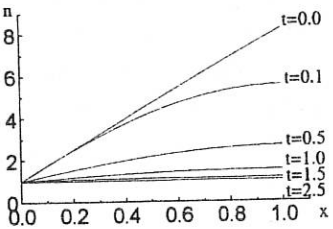

Fig. 7. H-L transition, density evolution.

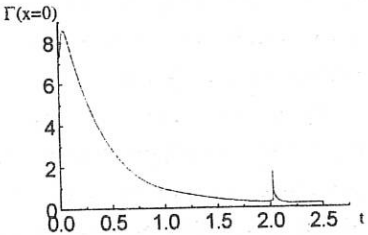

Fig. 8. Particle flux during H-L transition

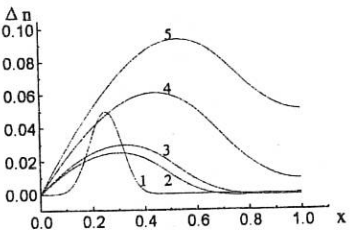

Fig. 9. Pellet-caused L-H transition $\Gamma<\Gamma^{(max)}$. ($\Gamma=6.75$).

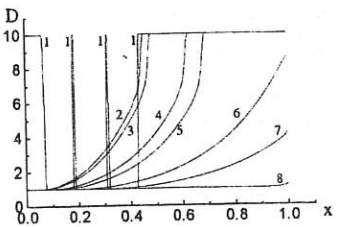

Fig. 10. Diffusion coefficient during pellet-caused L-H transition $\Gamma<\Gamma^{(max)}$. ($\Gamma=6.75$).

TRANSVERSE CURRENT IN A BRAIDED MAGNETIC FIELD.

I. Kaganovich, V. Rozhansky, M. Tendler*

Physico - Technical Department, St. Petersburg State Technical University, Russia

* Fusion Plasma Physics, Euratom - NFR Association, Alfven Lab., Royal Institute of Technology, Stockholm, Sweden

1. Introduction

The issue of cross-field conductivity is important for determining the potential profile in various magnetic field configurations addressed in the context of fusion research. The interest is further enhanced by the large body of evidence obtained on many tokamaks that the formation of transport barriers is consistent with the paradigm that increased shear in the ExB flow leads to a suppression of plasma turbulence, thereby improving confinement.

For a collisionless plasma, the issue of cross-field current in a stochastic magnetic field has been considered in [1,2]. The current was assumed to be carried by test electrons, ignoring restrictions imposed by the ambipolarity constraint.

Here, the cross-field conductivity of a plasma is addressed assuming a braided magnetic field with a given level of magnetic fluctuations. In contrast to [1,2], the ambipolarity constraint is employed locally. The current is divergence free throughout the plasma column. This constraint implies that the parallel electron current arising due to electron flow along a braided magnetic field line is short-circuited by ion flow across the field. Since parallel to magnetic field electrons are much more mobile than ions a significant ambipolar electric field has to arise, thereby suppressing the electron current. Hence the value of the transverse current obtained in [1,2] is the upper estimate. In reality, difference is shown to be large. The resulting net current averaged over the flux surface is governed by the cross-field conductivity of ions. This effective conductivity is caused by the ion viscosity and inertia and becomes large for small scales typical for magnetic field perturbations. Yet the considerable enhancement of the transverse current occurs even in regularly perturbed magnetic field. Furthermore the transverse current is amplified by stochastic characteristics of the magnetic field.

The resulting averaged cross-field conductivity is shown to be proportional to the squared magnetic field perturbations. The analysis quantified below corresponds to the calculation of cross-field conductivity in a tokamak with ergodic limiter, it has also significant reference to tokamaks and RFP's with a large degree of intrinsic stochasticity. Since the underlying physics

is the same for all toroidally symmetric configurations, we adopt, for simplicity, a slab geometry, where the unperturbed magnetic field is assumed to be given.

2. Model

A slab geometry is considered with the plasma parameters depending on the x-coordinate normal to the flux surfaces. The unperturbed magnetic field is given by

$$\vec{B} = B_z\vec{e}_z + B_y(x)\vec{e}_y = B[\vec{e}_z + \Theta(x)\vec{e}_y], \quad \Theta(x) = B_y / B_z << 1 \tag{1}$$

Here, the y-axis corresponds to the poloidal direction in a tokamak, the z-axis - to the toroidal one and the x-axis - to the radial one. The unperturbed plasma density and plasma potential are denoted as $n_0(x)$ and $\varphi_0(x)$, respectively. The magnetic field perturbation is $\vec{B}' = \sum \vec{B}'_{\vec{k}} \exp(i\vec{k}\vec{r})$ with $k_z \ll k_y$. Its impact is the most pronounced near the resonance flux surfaces, where $k_{II}(x) = (k_y B_y(x) + k_z B_z)/B \to 0$. We shall start from the case when the mean free path $\lambda_{mfp} << k_{II}^{-1}$, so that we solve the fluid equations [3]:

$$\text{div}\ \vec{\Gamma}_i = 0,\ \text{div}\ \vec{j} = 0,\ \ m_i n(\vec{u}\nabla)\vec{u} = -\nabla p + \frac{1}{c}[\vec{j}\times\vec{B}] - \nabla\cdot\vec{\pi}\,, \tag{2}$$

$$\vec{j}_{II} = \sigma_{II}\vec{b}\left(-\nabla\varphi + \frac{T_e}{e}\nabla \ln n + \frac{1.71}{e}\nabla T_e\right) \tag{3}$$

where $\vec{\Gamma}_i$ is ion flux, $\vec{j}$ is current, u is plasma velocity, σ_{II} is parallel conductivity, $\vec{b} = \vec{B}/B$, and $\vec{\pi}$ is the ion viscosity tensor.

3. Transverse current for collisional case $\lambda_{mfp} k_{II} << 1$

In the absence of the transverse transport the solution of the linearized Eqs.(2,3) corresponds to the constant density, temperature and potential along the magnetic field lines, and to the zero currents and drift velocities. Inertia and viscosity arise due to the drifts in the perturbed electric field. Similar effect is produced by the cross-field anomalous diffusion which wash out density perturbations, and cause particle fluxes [5]. Inertia and viscosity result in the transverse ion currents. Thus, the parallel electron current j_{II} arises to close the circuit. The averaged transverse electron current is $j_x = \langle j_{II} b_x \rangle$. Substituting the expression for j_{II} from Eq. (3) with self-consisted electric field one obtains:

$$j_x = \frac{1}{2}\sum_{\vec{k}_\perp} \mathrm{Re}\left\{ |b_{x,\vec{k}}|^2 \sigma_{II} I_\sigma(k_{II}) \left[\frac{T_{e0}}{e}\frac{\partial \ln n_0}{\partial x} - \frac{\partial p_0}{\partial x} + 1.71 \cdot I_T(k_{II}) \frac{\partial T_{e0}}{\partial x} \right] \right\}, \tag{4}$$

$$I_\sigma(k_{II}) = \frac{\sigma_\perp k_\perp^2}{\sigma_{II} k_{II}^2 + \sigma_\perp k_\perp^2}\ \ I_T(k_{II}) = \frac{(\chi_{i\perp} k_\perp^2 + i\omega_{ei}\vec{k}_\perp)}{\chi_{II} k_{II}^2 + (\chi_{i\perp} k_\perp^2 + i\omega_{ei}\vec{k}_\perp)}\ \ \vec{u}_{ei} = \frac{c}{B}\left(\frac{e\partial\varphi_0}{\partial x} - \frac{\partial \ln p_{e0}}{n_0 \partial x} \right) \tag{5}$$

where the factors $I_{\sigma,T}$ arise due to the local ambipolarity constraint. In the limit $u_{e\perp} \to 0$, when $\sigma_\parallel k_\parallel^2 << \sigma_\perp k_\perp^2$ (i.e. ignoring the local ambipolarity constraint), Eq.(4) is similar to the result of [4] for electron heat conductivity. The contribution to perpendicular conductivity from perpendicular viscosity can be calculated according to [3] $\sigma_{\perp\vec{k},\nu} = -2\eta_i k_\perp^2 c^2 / B^2$, where η_i is the ion transverse viscosity coefficient [3]. The contribution from inertia term is $\sigma_{\perp\vec{k},i} = i \cdot m_i c^2 \left(\vec{u}_{i\perp}\vec{k}\right) n / B^2$, $\sigma_{\perp\vec{k}} = \sigma_{\perp\vec{k},\nu} + \sigma_{\perp\vec{k},i}$. There is also contribution from the parallel viscosity caused by the parallel fluxes which arises from the wash out of the density perturbations by the anomalous diffusion. The resulting current is proportional to the density gradient. It was calculated in [5].

The main contribution to the sum over $k_\perp$ in Eq.(4) is determined by the resonances in Eq.(5). This yields values of $k_\parallel \sim k_{\parallel\sigma}$ for two first terms in Eq.(4) and $\sim k_{\parallel T}$ for the third one. The value of $k_{\parallel\sigma}$ is given by the estimate $k_{\parallel\sigma} = \sqrt{|\sigma_\perp|/|\sigma_\parallel|}\, k_\perp$. It yields:

$$j_x = \frac{\sigma_\parallel D_{st}}{L_\sigma}\left[\frac{T_{e0}}{e}\frac{\partial \ln n_0}{\partial x} - \frac{\partial \varphi_0}{\partial x} + 1.71\frac{\partial T_{e0}}{\partial x}\frac{L_\sigma}{L_T}\right] \qquad (6)$$

where $D_{st} = \pi \cdot b^2 / (2\Theta \cdot \delta k_y)$, δk_y is the difference between two neighboring k_y, $L_{\sigma,T} = k^{-1}_{\parallel\sigma,T}$. The resulting current depends on the ion cross-field local conductivity. From Eq.(6) it follows that the conductivity is significantly enhanced even in non-stochastic magnetic field, if the decorrelation occurs due to transverse collisional transport (it corresponds to 'double streaming regime' in classification of enhanced diffusion [6]). If the magnetic field is stochastic (when Kolmogorov's length of exponential divergence $L_k = \left(\delta k_y \Theta / k_y^2 \Theta'^2 b^2\right)^{1/3} < 1/(\Theta \cdot \delta k_y)$, the local transverse transport is amplified due to the exponential divergence of neighboring magnetic lines. This effect is less important if $L_k > L_\sigma$. In contrast, when $L_k < L_\sigma$ quasilinear theory is not valid and fractal structure of magnetic field lines has to be taking into account. The estimate of conductivity in this case can be obtained by method proposed in [4]. The result coincides with (6) if we replace L_σ by factor $\sim L_k \ln(L_\sigma / L_k)$. If differs from the Rochester-Rosenbluth result for diffusion of 'test' electrons [6] by logarithmic factor.

4. Transverse current for collisionless case $\lambda_{mfp} k_\parallel >> 1$.

Employing the electron kinetic equation in the drift approximation one can obtain for the Maxwellian distribution function (f):

$$\langle j_{\perp x}\rangle = \sum_{\vec{k}} \int dv_{\parallel} |b_{x\vec{k}}|^2 \frac{v_{\parallel}^2 f}{2m_e} *$$

$$* \mathrm{Re}\left[\left(\frac{\partial \ln n_0}{\partial x} - \frac{1}{T_{e0}}\frac{\partial \varphi_0}{\partial x} + I_T(k_{\parallel})\left(\frac{m_e v^2}{2T_{e0}} - \frac{3}{2}\right)\frac{\partial T_{e0}}{\partial x}\right)\cdot \frac{I_\sigma(k_{\parallel})}{i(k_{\parallel}v_{\parallel} + \vec{k}_{\perp}\vec{u}_{e\perp}) - \nu_{eff}}\right] \quad (7)$$

where ν_{eff} is a frequency of electron phase decorrelation. It is governed by stochastic processes: for the transverse diffusion $\nu_{eff} \equiv \max\left(D_{\perp}k_{\perp}^2; \left(1/6k_{\parallel}'^2 D_{\perp} v_{\parallel}^2\right)^{1/3}\right)$; for randomization in stochastic magnetic lines with the correlation lengths $l_{\perp}; l_{\parallel}$ it is given by $\nu_{eff} \equiv v_{\parallel}l_{\parallel} + u_{\perp}l_{\perp}$. The transverse conductivity in collisionless case is controlled by the ion inertia; the parallel electron conductivity $\sigma_{\parallel} = e^2 n/m_e \nu_{eff}$ is determined by ν_{eff}. Similar to the collisional case the transverse current depends on local ion conductivity. Indeed if magnetic field is stochastic, the current obtained in [1,2] should be reduced by factor $\sim \ln(L_\sigma / L_k)$ times. The ratio L_σ / L_k is very small and the value of $\ln(L_\sigma / L_k)$ is about 2-5. It yields that the influence of the local ambipolarity is important.

5. Conclusions:

Here, the cross-field current in a braided magnetic field is addressed. In contrast to [1,2], the ambipolarity constraint is employed locally. Since electrons are much more mobile than ions a significant ambipolar electric field has to arise, thereby suppressing the electron current. Hence the value of the transverse current obtained in [1,2] is the upper estimate. In reality, difference is shown to be large. The resulting current is governed by the cross-field conductivity of ions. It is strongly enhanced due to the small scale of the magnetic field perturbations. Yet the considerable enhancement of the transverse current occurs even in regularly perturbed magnetic field. Furthermore the transverse current is amplified for stochastic magnetic field.

Acknowledgment: The work was supported by RBRF grant N 9602 16919a and partially by the Swedish Institute and Humboldt Foundation

References

1) R.W. Harvey, M.G. McCoy, J.Y. Hsu, A.A. Mirin, Phys Rev. Lett., 47, (1981), 102

2) A.V. Gurevich, K.P. Zybin, Ya.N. Istomin, Nuclear Fusion, Vol. 27, N3, (1987), 453

3) S.I.Braginski. Rev.Plasma Physics ed. by M.Leontovich, v.1 (1963) , 193.

4) B.B. Kadomtsev and O.P. Pogutse, Plasma Phys. Controlled Nucl. Fusion Res.
Proc. 7th Int Conf. (Innsbruck,1978), (IAEA, Vienna), Vol.1,649

5) I. Kaganovich, V. Rozhansky, M. Tendler, in Proc. 10th ICPP, Foz do Iguacu Brazil, p33

6) J.H. Misgvich, M.Vlad, F. Spineanu, R. Balescu, Comments Plasma Phys. Contr. Fusion, Vol.17 (1995), 45

Studies of Turbulence in the JET Divertor Plasmas

I. García-Cortés[1], C. Hidalgo[1], J.R. Martín-Solís[2], S. Ali-Arshad[3], S. Clement[3], S.J. Davies[3], J. Lingertat[3], A. Loarte[3], G.F. Matthews[3] and R.D. Monk[3]

1) Asociación EURATOM-CIEMAT, 28040 Madrid, SPAIN
2) Universidad Carlos III de Madrid, 28911 Madrid, SPAIN
3) JET Joint Undertaking, Abingdon, Oxfordshire, OX14 3EA, UK

Experimental Setup

The experiments considered in this paper were carried out in single null discharges during the JET Mark I pumped divertor phase [1] under different plasma conditions. The 4 Hz sweeping of the strike point at the target plates has allowed the measurement of fluctuation profiles both in the divertor plasma strike zones and private flux region (PFR) using the target Langmuir probes. To determine the strike point position at the divertor plates we used the criteria based on the floating potential sign at the target-probes and calculations from equilibrium reconstruction codes. The position of the strike point is uncertain by at least 1cm. A poloidal cross section of the target showing the JET Mark I Langmuir probe array [2] is shown in fig.1.The turbulence was characterised by four probes, two of them (5 cm toroidally apart) located in the inner strike zone of the divertor and other two in the outer zone.

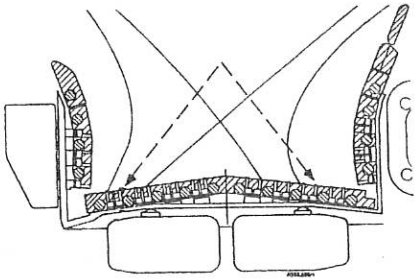

Fig.1. Poloidal cross section of the divertor target showing the Langmuir probe array. The arrows show the probes used for fluctuation measurements

Fluctuation Levels and Turbulence Spectra

Radial profiles of ion saturation current (I_{sat}), fluctuation levels of I_{sat} ($\tilde{I}_{sat}$ and $\tilde{I}_{sat}/I_{sat}$) and floating potential (ϕ_f) in the SOL and PFR are shown in figure 2 for the discharge 34112 [I_p=1.6-2.0 MA, B_T=2.6 T, $\bar{n}_e$~2 x 10^{19} m^{-3}] during the ohmic phase. Measurements were taken at the outer divertor target. The I_{sat} fluctuations rise as the probe approaches the separatrix from the SOL side and increase even further when the probe is in the PFR, defining the separatrix as the radius where the floating potential changes sign (vertical line in the figure 2). The $\tilde{I}_{sat}/I_{sat}$ is almost constant in the SOL with a value of 5%, increasing up to 15% in the PFR.

In the SOL region most of the power in the fluctuation spectra is dominated by frequencies below 50kHz. Higher frequencies (up to 300kHz) become non-negligible in the spectra close to the separatrix and in the PFR. In the PFR there exists a low density and temperature (< 10 eV) plasma, originated by diffusion from the SOL. This plasma presents strong radial gradients in density and temperature, short connection lengths, and a large variety of atomic processes which could account for the observed increase in the level of fluctuations.

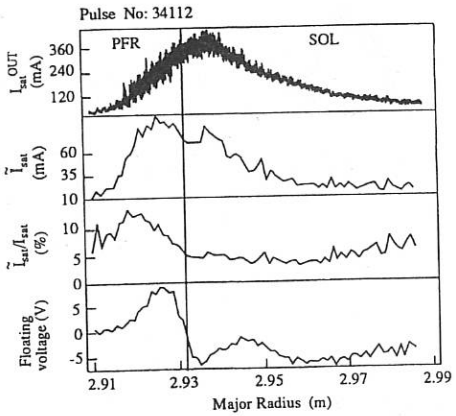

Fig.2. Radial profiles of raw data, fluctuation levels and normalised fluctuations of ion saturation current, and the mean value of the floating potential for the discharge 34112. Separatrix is defined as the radius where the floating potential changes sign (vertical line) Measurements were taken at the outer divertor plates.

In/Out Turbulence Asymmetries

Comparative studies of the turbulence structure in the inner and outer divertor regions have been carried out under different plasma conditions (Ohmic, L and H) modes. Figures 3a and 3b show the radial profile of the ion saturation current signals measured at the inner and outer target plates during sweeping of the strike points in the ELM free H-mode of the pulse 35457 (I_p=2 MA, B_T=2.6 T, $\bar{n}_e$~3 x 10^{19} m^{-3} and 7 MW of NBI heating). In this case the divertor electron density and temperatures were in the range n_e~1.5 x 10^{19} m^{-3} and T_e~10-15 eV, at the strike points. Significant differences between the level of fluctuations measured at the inner and outer target plates are generally observed at both sides of the separatrix (SOL and PFR), which are directly observed in the raw data (see figure 3). In the SOL region, fluctuation levels are systematically higher at the outer divertor plate. As shown in figure 3c at the inner side the normalised level of fluctuations ($\tilde{I}_{sat}/I_{sat}$) is 2-3 % in the SOL region and about 15 % in the PFR close to the separatrix. The fluctuation levels observed at the outer divertor are about 5-10 % in the SOL and about 25 % in the PFR. The corresponding frequency spectra, for measurements taken close to the inner-outer strike points in the SOL region, are shown in figure 3d. Note that the level of high frequency fluctuations, 30-200 kHz, is higher at the outer divertor plate. Similar results have been found in Ohmic plasmas.

Curvature driven instabilities could account for the large in-out asymmetry observed in the SOL turbulence during JET discharges [3]. However it should be noted that curvature driven instabilities may not explain the observed increase in the level of fluctuations when crossing the separatrix from the outer SOL into the private flux region.

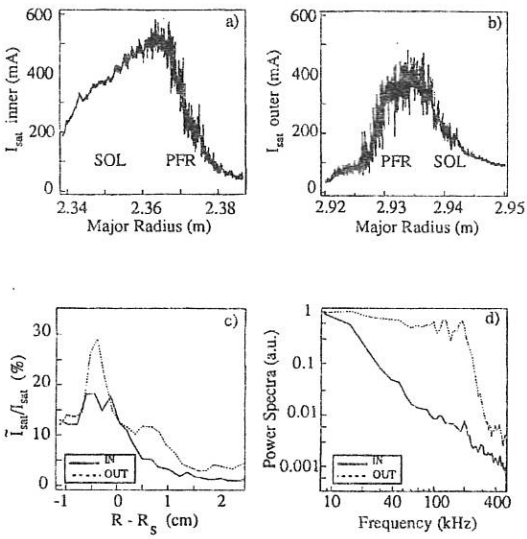

Fig.3. Time evolution of: a) I_{sat} at the inner and b) I_{sat} at the outer region. c) $\tilde{I}_{sat}/I_{sat}$ at the inner (continuos line) and outer divertor (dash line) and (d) their frequency spectra calculated at 0cm<R-R_S<1cm. Measurements were taken in the H-mode phase of the shot 35457. Note the sign convention is: the radial position is always defined positive when the probe is in the SOL and negative when the probe is in the PFR

Turbulence in Detached Plasmas

H-mode detached plasmas have been produced at JET by introducing an impurity into the divertor to enhance radiation. Fluctuation profiles during the H-mode detached phase with nitrogen seeding have been investigated. The time evolution of plasma parameters for the pulse 34361[I_p=2 MA, B_T=2.5 T, $\bar{n}_e$~5 x $10^{19}m^{-3}$ and P_{NBI}=11 MW] is shown in figure 4. Measurement of fluctuations were taken after nitrogen gas puffing, in the detached phase. The radial profile of $\tilde{I}_{sat}/I_{sat}$ is shown in fig.5 for the inner divertor plate. The level of fluctuations in the plasma strike zone is in the range 10-20% and rises up to 20-30% in the proximity of the strike point. It is interesting to compare the fluctuation levels in the detached phase with those in non detached plasmas. As shown in figure 3c the $\tilde{I}_{sat}/I_{sat}$ of a non-detached plasma at the inner target during the H mode is below 3% (shadow zone in fig. 5) at least a factor 5 smaller than in the detached phase. The high radiation level of these plasmas could be affecting turbulence through radiative instabilities and the presence of high neutral densities and low temperatures during the detachment in the divertor region could also drive instabilities.

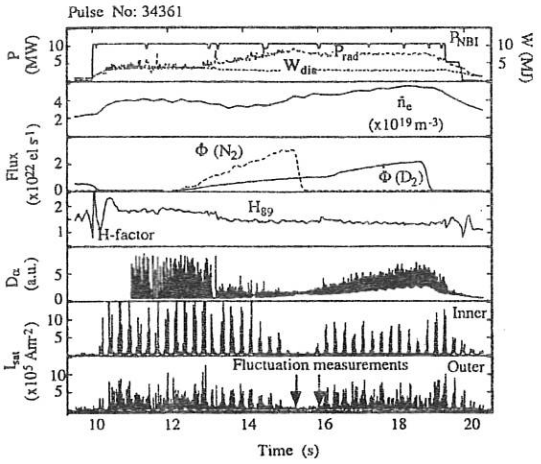

Fig.4 H-mode discharge in which a radiative detached divertor plasma is established by nitrogen seeding. Pulse number 34361.

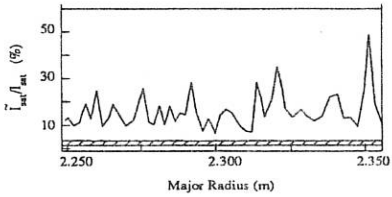

Fig.5 Radial profile of $\tilde{I}_{sat}/I_{sat}$ in the detached phase. The shadow zone corresponds to the level of $\tilde{I}_{sat}/I_{sat}$ of a non-detached plasma at the inner target during the H mode phase. The nominal position of the separatrix is at R=2.36m.

Summary

The turbulence spectra as well as their amplitudes have been found to be sensitive to the plasma conditions at the JET-divertor region . The results can be summarised as:

-In ohmic shots, the level of fluctuation ($\tilde{I}_{sat}/I_{sat}$) is in the range of 5% at the plasma strike zones with fluctuations dominated by frequencies below 50 kHz. However, this level goes up to 15 % close to the separatrix and in the PFR, with the frequency spectra up to 200 kHz.

-Significant in/out asymmetries in $\tilde{I}_{sat}/I_{sat}$ and spectral characteristics have been found in ohmic and H mode regimes. In the SOL region, these levels are higher at the outer divertor plate.

-Fluctuation levels in H mode detached plasmas are higher than in non-detached phases.

References

1.Bertolini E. and the JET Team, Fusion Engineering and Design **30** (1995) 53.
2.Matthews G.F., Davies S.J. et al, Contrib. Plasma Physics Vol. 36 (1996) 29.

NONLINEAR EVOLUTION OF MHD INSTABILITIES IN TOKAMAK PLASMAS WITH HOLLOW CURRENT PROFILES

E.K. Maschke , **X. Litaudon**, M. Berroukeche*, B.Saramito*

Association EURATOM-CEA sur la Fusion
D.R.F.C. , Centre de Cadarache
F-13108 Saint-Paul-lez-Durance CEDEX (France)

I. Introduction

Plasmas with hollow current profiles are obtained in experiments aiming at "advanced scenarios" in tokamaks with lower hybrid current drive or off-axis heating. The corresponding q-profiles are non-monotonic and often have two resonant surfaces of the same helicity q=m/n with low numbers m,n. In such situations, double as well as simple tearing modes may be unstable. In this paper we present numerical investigations of these instabilities and try to interprete experimental observations made on the tokamaks Tore Supra [1,2] and RTP[3]. We use a modular code based on an exact scalar representation of toroidal MHD [4] which allows to write all systems of "reduced MHD" equations of various complexity (up to the full MHD equations) in essentially the same form. Here we restrict ourselves to Strauss type equations in cylindrical geometry with perturbations having a single helicity.

II. Evolution of double tearing modes

As a typical example we present the linear and nonlinear features of the instability of helicity m/n = 2 for the hollow current profile shown in Fig.1 . In Fig. 2 we show the radial structure of the perturbed flux ψ , the perturbed current j , the electric potential Φ, and the vorticity density w of the unstable linear mode m=2, n=1. The time evolution of the single-helicity solution of the nonlinear equations has a first period during which the growth is dominated by the exponential growth of the fundamental mode m=2, n=1, followed by a period of explosive growth of all modes as shown in Fig. 3 . In the first period two magnetic islands are present and perturb the current profile of the m=0, n=0 mode as shown in Fig.4. During the explosive phase the current profile of the m=0, n=0 mode is flattened out over a large portion of the region between the two q=2 surfaces.

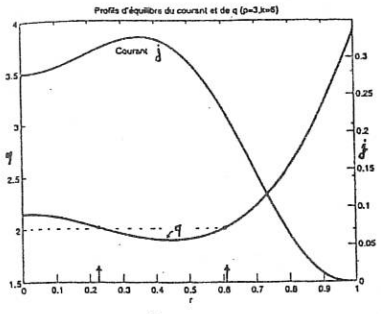

Fig. 1

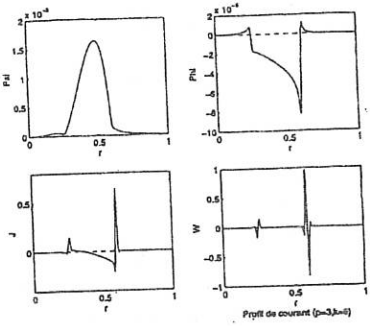

Fig.2

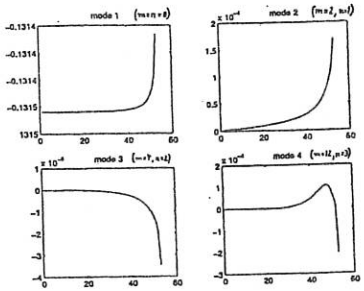

Fig.3

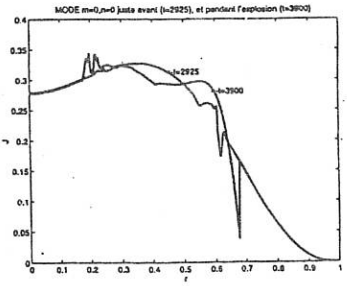

Fig.4

Similar behaviour can be demonstrated for current profiles having two magnetic surfaces where either q=3 or q=4. Of course, the linear growth rate and the details of the nonlinear evolution depend strongly on the particular form of the equilibrium profiles.

III. Evolution of simple tearing modes

In contrast to the case of the double tearing instability presented in the preceding Section, the simple tearing modes appearing in the case of current profiles having only one rational surface q=m/n with low m and n usually saturate at a level which may not be detected in an experiment. This may be the reason why certain discharges with hollow current profiles are found [1] to have no detectable MHD activity although linear theory predicts instability.

IV. Sequence of reconnection events in plasmas with hollow current profiles

In Tore Supra [2] , sawtooth oscillations of the electron temperature, located near the surface q=2, have been observed. A m=2 magnetic perturbation appears to be accompanied by a m=3 perturbation probably connected with the q=3/2 surface. The two perturbations rotate initially with different rotation frequencies, but the two frequencies gradually approach each other and finally the two perturbations lock shortly before the sawtooth crash. A numerical simulation of this behaviour requires calculations in toroidal geometry with equilibrium flow, and will not be treated here except for some general discussion in Section V below.

In RTP an interesting saw-tooth pattern has been observed [3] in experiments with off-axis heating leading to hollow current profiles. A sequence of rapid saw-tooth oscillations of the electron temperature at about half-radius, interrupted periodically by a larger saw-tooth crash in the plasma center, is interpreted by the authors[3] in terms of the evolution of the current profile and the associated q profile. We have adopted this point of view and show in Figs. 5 and 6 a possible sequence of situations which may lead to the observed saw-tooth pattern. The curves labelled (a) correspond to a situation where there is only one rational surface of low m,n .

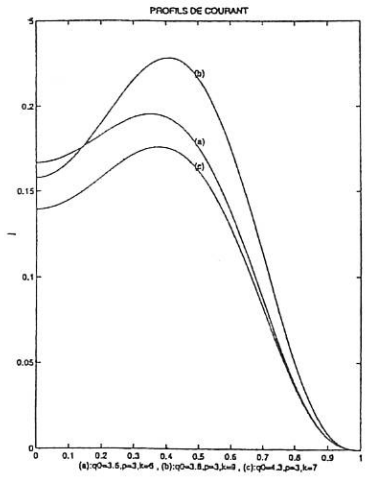

Fig.5

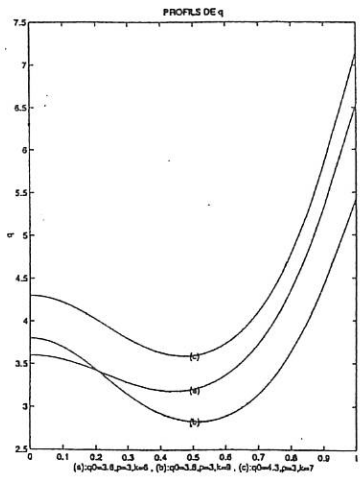

Fig.6

A simple tearing mode could be unstable but would saturate at a low amplitude, as we have said above. The off-axis heating then leads to profiles of the type of the curves labelled (b), for which a double tearing mode m/n = 3/1 is unstable and leads to a crash of the temperature in the radial interval between r = O.3 and r = O.6 . A slower evolution leads finally to the situation shown by the curves labelled (c), where the double tearing mode m/n = 4/1 is unstable, leading to the large crash which includes the center of the plasma.
Up to now we have studied only these three situations without trying to simulate the combined evolution of profiles and instabilities. More complete calculations are planned.

V. Conclusion

Our calculations indicate that double tearing modes can have explosive growth and may explain the crash of saw-tooth oscillations, contrary to simple tearing modes which often saturate at small amplitude. More work including toroidicity and the effects of plasma rotation is in progress.

Acknowledgements

Part of the numerical results presented here has been obtained using the attribution of computer time on the machines of IDRIS (Orsay, France). Discussions with N. Lopez Cardozo and M.R. de Baar are gratefully acknowledged

References

[1] Equipe Tore Supra (presented by X.Litaudon), Proceedings 11 th Topical Conf. on Radio Frequency Power in Plasmas, Palm Springs CA, 1995, R.Prater and V.S.Chan Eds., AIP Press, p.40.
[2] S.Turlur et al., 22 nd EPS Conf. on Contr. Fusion and Plasma Physics, Bournemouth, 1995), Europhysics Conference Abstracts.
[3] M. R. de Baar et al., this conference.
[4] E.K. Maschke and J. Morros Tosas, Plasma Phys. Controlled Fusion 31 (1989) 563.

---

*) Present address: Université Blaise Pascal (Clermont-Ferrand), Dépt. de Mathématiques appliquées. F-63177 Aubière CEDEX, France

ANALYSIS OF PELLET FUELLING EFFICIENCY FROM THE INTERNATIONAL PELLET ABLATION DATABASE

A.Géraud, L.R.Baylor *, IPADBASE Collaboration

Association Euratom-CEA sur la Fusion Contrôlée,CE Cadarache, 13108 Saint Paul Lez Durance, France
* Oak Ridge National Laboratory, Oak Ridge, TN, USA

INTRODUCTION

During the last two decades, much effort has been devoted to the study of pellet-plasma interactions, mainly focusing on ablation and transport modification caracterization. These studies have yielded an extensive validation of a NGS-like scaling law for pellet penetration and a comprehensive description of PEP modes. Compared with these well documented subjects, the question of the pellet fuelling efficiency (η=Increase of the Plasma Content / Pellet Content) has been by far less addressed. This point is nevertheless of crucial importance since it governs the performances of pellet injectors required in a reactor to achieve efficient fuelling and isotopic tailoring with the aim to reduce wall tritium inventory. Some results have already been published for TORE SUPRA [1], ASDEX-U[2], JET [3], and TFTR [4], but no comprehensive study has been presented yet. Recently, such a study has become possible using the International Pellet Ablation Database (IPADBASE [5]). In this paper, the values of the fuelling efficiency η over a sample of ≈150 pellets from TORE SUPRA, JET, TFTR, T-10, DIII-D is presented and its behavior with pellet penetration, additionnal power and plasma confinement regime is discussed.

THE INTERNATIONAL PELLET ABLATION DATABASE

IPADBASE was initially intended to furnish experimental data to the different theoretical ablation models developped in order to predict the penetration and the mass deposition in a next step tokamak such as ITER. This database has been assembled from pellet injection experimental data around the world covering a wide range of pellet and plasma characteristics. In the initial configuration presented in this paper, data from JET, Tore Supra, DIII-D, FTU, TFTR, T-10 and ASDEX-U have been included. It contains pellet parameters such as mass, velocity and penetration

Device	vp (m/s)	Np (10^{20} at)	Ip (MA)	Bt (T)	ne(0) ($10^{20}m^{-3}$)	Te(0) (keV)	Padd (MW)
ASDEX-U	240-1200	1.7-4.3	0.6-1	1.3-2.7	0.2-2.2	0.25-3.5	0-8 (NB)
DIII-D	515-1100	1 - 20	0.5-2	1.6-2.1	0.22-1.3	1.4-4.2	0-11.5 (NB)
FTU	1350-1800	0.4-1.8	0.3-0.9	5.6-7	0.5-2.24	1.1-1.9	0
JET	460-1350	3-80	2.2-5.2	2.8	0.22-0.76	1.5-4.2	0-13.5 (NB)
T-10	400-800	0.2-0.45	0.2-0.4	2.85	0.4-0.75	1-2.8	0
TFTR	1000-2250	14-35	1.6	4.4	0.17-0.5	5.8-7.7	7-21 (NB)
Tore Supra	600-3300	0.4-36	0.6-2	2.5-4.1	0.17-0.72	1.5-5	0-5.4 (LH, ICR)

Table 1: Pellet and plasma characteristics range considered in IPADBASE (version 1.0)

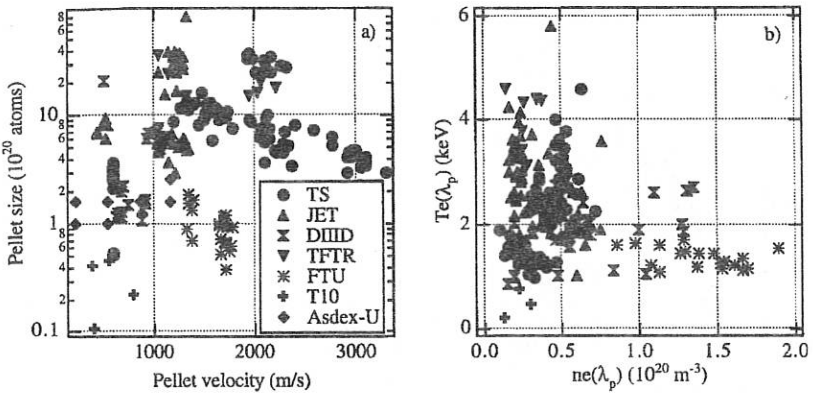

Fig.1: Pellet mass and velocity (a) and plasma electron density and temperature at the end of the ablation process (b), identified by machine

depth, a description of the magnetic geometry of the plasma, the plasma electron density and temperature profiles and some characteristics of the additional heating. Table 1 gives the range of plasma and pellet parameters from the seven machines considered. Pellet parameters are detailed in Fig.1a and the plasma range is represented in Fig.1b in a Te(λ_p) versus ne(λ_p) diagram, where Te(λ_p) and ne(λ_p) are the values of the temperature and density at the end of the pellet trajectory.

FUELLING EFFICIENCY

Among the available data, the pellet content N_p measured by a microwave cavity and the increase of the plasma content dNe can be extracted to calculate a fuelling efficiency defined as the ratio $\eta = dNe/N_p$. This has been done for the machines equipped with a calibrated microwave cavity: DIII-D, JET, T10, TFTR and Tore Supra. The accuracy of such a measurement is typically ± 25% and the error on dNe can be estimated to be less than ± 5% if the time resolution of the density measurement is high enough to avoid missing the peak density after pellet injection; this is the case for the selected pellets, with a time resolution between 2 and 24 ms. Such inaccuracy is large enough to hide any possible general trend for a particular machine with a limited range of parameters, but by putting together data from the different machines, a better global view can be expected.

As an exception, a wide range of pellet injection and plasma conditions on Tore Supra is available and has been used as support of the discussion. This large Tore Supra database is due to having both a centrifugal pellet injector for repetitive injection at low velocity and a two-stage light gas gun with different gun barrel diameters allowing pellet velocity in the 3 km/s range. In other respects pellet injection experiments in lower hybrid (LH) current drive scenarios have shown significantly modified penetration depths. Intermediate penetration has been obtained by notching the LH power and firing pellets after a delay corresponding to the slowing down time of the fast electrons driven by the LH wave [2]. A plot of the Tore Supra fuelling efficiency η versus the pellet penetration depth is given in Fig.2. It is shown that the Tore Supra data can be well fitted by an exponential law if we take into account the uncertainty on the pellet mass measurements. Also

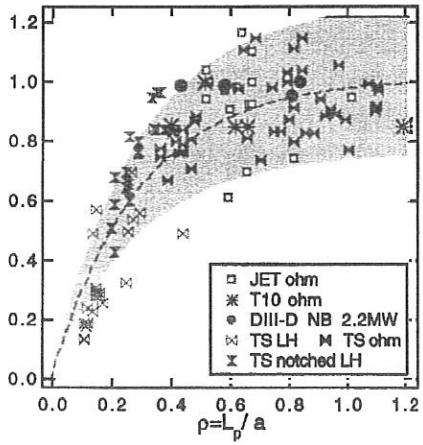

Fig.2 : Fuelling efficiency versus normalized pellet penetration depth in JET, T10 and TORE SUPRA for ohmically and LH heated plasma.
The dashed curve is the fit deduced from Tore Supra data (ohmic+notched LH + LH) :

$$\eta = 1 - \exp(-\rho/\rho_0) \quad \text{with } \rho_0 = 0.29$$

The gray zone corresponds to the pellet content uncertainty of ± 25%.
The notched LH regime, obtained by injecting pellets ≈ 50 ms after switching off the LH power (2MW), allowed a partial recovery of the pellet penetration depth on Tore Supra relatively to the LH case. Some pellets fired into DIII-D NB heated plasmas at low power (≈ 2MW) have been added on the curve.

plotted are the data extracted from IPADBASE for ohmic shots from JET and T10 and for weakly NB heated DIII-D plasmas. The Tore Supra fit remains valid for all these pellet injection experiments.
The same presentation is given in Fig.3 for pellets fired into NB, ICR and LH plasmas, taking again the Tore Supra pellets as a fitting reference. Although the ICR power on Tore Supra was limited to 3MW for the selected data, the saturation level of the exponential fit is clearly reduced to a value ≈ 0.8. This behavior is confirmed when η is plotted for JET (NB, 7-11 MW), TFTR (NB, 7-21 MW) and DIII-D (NB, 2.2-11.5 MW). On DIII-D, except for the shots at low power, pellets were injected during ELMy H mode regime. Like on Asdex-U [2] where η is similar for L-mode and ELMy H-mode conditions as soon as pellets reach mid-radius, η does not seem to be affected by the ELMs for the pellet penetration considered ($\rho \approx 0.5$).
By making the assumption that the saturation level is a function of the additonal power per particle and keeping the characteristic length ρ_0 obtained in ohmic regime, all the data have been fitted by the expression given in Fig.4. Considering the inaccuracy in the determination of the experimental value of η, the agreement can be considered as acceptable for ion heating. In the electron heating case (LH, 1-3 MW), where the higher η in Fig.3 or 4 are obtained with 3 MW and high pellet speed, η does not appear to be reduced with the applied power.

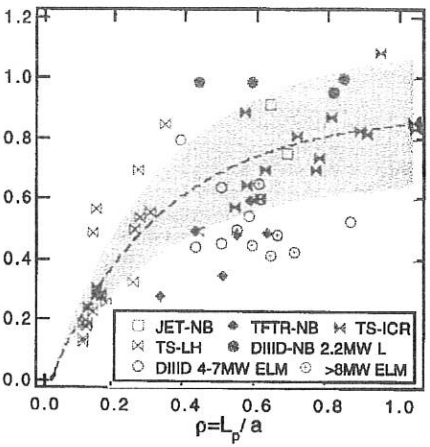

Fig.3: η versus normalized penetration depth in JET, TFTR, DIII-D NB heated plasmas and in Tore Supra LH and ICR heated plasmas. The dashed curve is the fit deduced from Tore Supra data (ICR and LH).

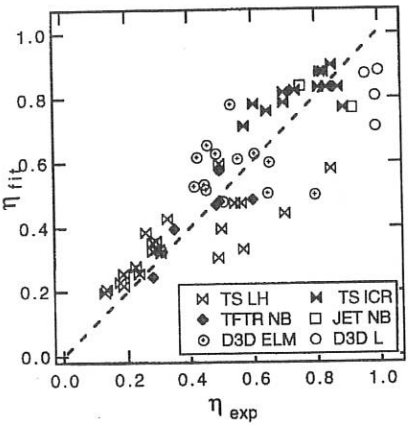

Fig.4 : Comparison of fuelling efficiency for additional heating cases with scaling using regression analysis for all the IPADBASE data. To clarify, pellets fired into ohmic plasmas are not plotted. The best fit gives :

$$\eta = 1 - e^{-\frac{p}{0.29}} - 0.24\left(\frac{Padd}{Ne}\right)^{0.65}$$

where P *[MW]* is the total additional power and Ne *[e20]* the total number of particles in the plasma.

DISCUSSION AND CONCLUSION

A statistical analysis of the fuelling efficiency η has been undertaken using the wide range of experiments included in a first version of the International Pellet Ablation Database that we hope to further extend. This analysis shows some global behaviors :

- An exponential dependence of η on the penetration depth is deduced mainly from Tore Supra owing to the availability of data for normalized penetration depth between 0.1 and 0.4. This experimental observation is not yet understood but investigations on charge exchange losses and fast outwards transport, observed in particular in JET, TFTR and Tore Supra, are in progress.

- A reduction of η, already reported for individual machines, is clearly seen when increasing the power for NB or ICRF heating, i.e. for heating driving fast ions. In the case of electron heating, although only data from LH additional power limited to 3 MW are available in the database, such a reduction does not appear so clearly. This observation must be confirmed by other electron heating experiments (LH and ECRH) at higher levels of power and high pellet velocity in order to compare with ion heating for moderate pellet penetration. This can be done on Tore Supra, where 6 MW of LH power and pellet velocity in the 4 km/s range are available.

- The ELM activity does not affect η for the pellet penetration considered in the present database. Nevertheless more data concerning this regime should be added for moderate penetration in the ELM extension zone. The ELM effect could be of crucial importance [2] in a machine like ITER in which the pellet penetration will be possibly limited to the ELM extension zone.

References

[1] Géraud A. *et al.*, 19th EPS (Innsbruck, 1992),Vol.16C-I, 159
[2] Lang P.T. *et al.*, 22nd EPS (Bournemouth, 1995), Vol.19C-II, 449
[3] Schmidt G.L. *et al.*, 19th EPS (Innsbruck, 1992), Vol.16C-I, 255
[4] Owens D.K. *et al.*, IAEA-TECDOC-534, IAEA, Vienna (1989) 191
[5] IPADBASE collaboration, to be published in Nuc.Fus.

INDEX